

## **Magnetic Resonance Elastography**

# **Magnetic Resonance Elastography**

Physical Background and Medical Applications

*Sebastian Hirsch, Jürgen Braun, and Ingolf Sack*

**WILEY-VCH**

#### **The Authors**

##### ***Dr. Sebastian Hirsch***

Charité–Universitätsmedizin Berlin  
Department of Radiology  
Charitéplatz 1  
10117 Berlin  
Germany

##### ***Dr. Jürgen Braun***

Charité–Universitätsmedizin Berlin  
Department of Medical Informatics  
Hindenburgdamm 30  
12200 Berlin  
Germany

##### ***Prof. Ingolf Sack***

Charité–Universitätsmedizin Berlin  
Department of Radiology  
Charitéplatz 1  
10117 Berlin  
Germany

#### **Cover**

The cover images were kindly provided by the authors.

■ All books published by Wiley-VCH are carefully produced. Nevertheless, authors, editors, and publisher do not warrant the information contained in these books, including this book, to be free of errors. Readers are advised to keep in mind that statements, data, illustrations, procedural details or other items may inadvertently be inaccurate.

**Library of Congress Card No.:** applied for

#### **British Library Cataloguing-in-Publication Data**

A catalogue record for this book is available from the British Library.

#### **Bibliographic information published by the Deutsche Nationalbibliothek**

The Deutsche Nationalbibliothek lists this publication in the Deutsche Nationalbibliografie; detailed bibliographic data are available on the Internet at <http://dnb.d-nb.de>.

© 2017 WILEY-VCH Verlag GmbH & Co. KGaA,  
Boschstr. 12, 69469 Weinheim, Germany

All rights reserved (including those of translation into other languages). No part of this book may be reproduced in any form – by photoprinting, microfilm, or any other means – nor transmitted or translated into a machine language without written permission from the publishers. Registered names, trademarks, etc. used in this book, even when not specifically marked as such, are not to be considered unprotected by law.

**Print ISBN:** 978-3-527-34008-8

**ePDF ISBN:** 978-3-527-69604-8

**ePub ISBN:** 978-3-527-69602-4

**Mobi ISBN:** 978-3-527-69603-1

**oBook ISBN:** 978-3-527-69601-7

**Cover Design** Schulz Grafik-Design, Fußgönheim,  
Germany

**Typesetting** SPi Global Private Limited, Chennai, India

**Printing and Binding**

Printed on acid-free paper

## Contents

<b>About the Authors</b>	<i>xiii</i>
<b>Foreword</b>	<i>xv</i>
<b>Preface</b>	<i>xvii</i>
<b>Acknowledgments</b>	<i>xix</i>
<b>Notation</b>	<i>xxi</i>
<b>List of Symbols</b>	<i>xxiii</i>
<b>Introduction</b>	<i>1</i>
<b>Part I Magnetic Resonance Imaging</b>	<b>7</b>
<b>1 Nuclear Magnetic Resonance</b>	<b>9</b>
1.1 Protons in a Magnetic Field	9
1.2 Precession of Magnetization	10
1.2.1 Quadrature Detection	11
1.3 Relaxation	13
1.4 Bloch Equations	14
1.5 Echoes	15
1.5.1 Spin Echoes	15
1.5.2 Gradient Echoes	17
1.6 Magnetic Resonance Imaging	17
1.6.1 Spatial Encoding	18
1.6.1.1 Slice Selection	19
1.6.1.2 Phase Encoding	19
1.6.1.3 Frequency Encoding	20
<b>2 Imaging Concepts</b>	<b>23</b>
2.1 <i>k</i> -Space	23
2.2 <i>k</i> -Space Sampling Strategies	26
2.2.1 Segmented Image Acquisition	27
2.2.1.1 Fast Low-Angle Shot (FLASH)	27
2.2.1.2 Balanced Steady-State Free Precession (bSSFP)	28
2.2.2 Echo-Planar Imaging (EPI)	30
2.2.3 Non-Cartesian Imaging	32



- 2.3 Fast Imaging 33
- 2.3.1 Fast Imaging Strategies 33
- 2.3.2 Partial Fourier Imaging 34
- 2.3.3 Parallel Imaging 35
- 2.3.3.1 GRAPPA 36
- 2.3.4 Impact of Fast Imaging on SNR and Scan Time 37

### **3 Motion Encoding and MRE Sequences 41**

- 3.1 Motion Encoding 43
- 3.1.1 Gradient Moment Nulling 44
- 3.1.2 Encoding of Time-Harmonic Motion 46
- 3.1.3 Fractional Encoding 50
- 3.2 Intra-Voxel Phase Dispersion 51
- 3.3 Diffusion-Weighted MRE 52
- 3.4 MRE Sequences 53
- 3.4.1 FLASH-MRE 53
- 3.4.2 bSSFP-MRE 55
- 3.4.3 EPI-MRE 57

## **Part II Elasticity 61**

### **4 Viscoelastic Theory 63**

- 4.1 Strain 63
- 4.2 Stress 67
- 4.3 Invariants 68
- 4.4 Hooke's Law 69
- 4.5 Strain-Energy Function 70
- 4.6 Symmetries 71
- 4.7 Engineering Constants 75
- 4.7.1 Young's Modulus and Poisson's Ratio 75
- 4.7.2 Shear Modulus and Lamé's First Parameter 76
- 4.7.3 Compressibility and Bulk Modulus 77
- 4.7.4 Compliance and Elasticity Tensor for a Transversely Isotropic Material 79
- 4.8 Viscoelastic Models 80
- 4.8.1 Elastic Model: Spring 81
- 4.8.2 Viscous Model: Dashpot 82
- 4.8.3 Combinations of Elastic and Viscous Elements 83
- 4.8.4 Overview of Viscoelastic Models 89
- 4.9 Dynamic Deformation 92
- 4.9.1 Balance of Momentum 92
- 4.9.2 Mechanical Waves 96
- 4.9.2.1 Complex Moduli and Wave Speed 98
- 4.9.3 Navier–Stokes Equation 99
- 4.9.4 Compression Modulus and Oscillating Volumetric Strain 100
- 4.9.5 Elastodynamic Green's Function 101
- 4.9.6 Boundary Conditions 103

4.10	Waves in Anisotropic Media	104
4.10.1	The Christoffel Equation	105
4.10.2	Waves in a Transversely Isotropic Medium	106
4.11	Energy Density and Flux	110
4.11.1	Geometric Attenuation	113
4.12	Shear Wave Scattering from Interfaces and Inclusions	114
4.12.1	Plane Interfaces	115
4.12.2	Spatial and Temporal Interfaces	118
4.12.3	Wave Diffusion	121
4.12.3.1	Green's Function of Waves and Diffusion Phenomena	125
4.12.3.2	Amplitudes and Intensities of Diffusive Waves	126
<b>5</b>	<b>Poroelasticity</b>	<b>131</b>
5.1	Navier's Equation for Biphase Media	133
5.1.1	Pressure Waves in Poroelastic Media	136
5.1.2	Shear Waves in Poroelastic Media	140
5.2	Poroelastic Signal Equation	142
<b>Part III Technical Aspects and Data Processing</b>		<b>145</b>
<b>6</b>	<b>MRE Hardware</b>	<b>147</b>
6.1	MRI Systems	147
6.2	Actuators	153
6.2.1	Technical Requirements	153
6.2.2	Practicality	153
6.2.3	Types of Mechanical Transducers	154
<b>7</b>	<b>MRE Protocols</b>	<b>161</b>
<b>8</b>	<b>Numerical Methods and Postprocessing</b>	<b>165</b>
8.1	Noise and Denoising in MRE	165
8.1.1	Denoising: An Overview	165
8.1.2	Least Squares and Polynomial Fitting	167
8.1.3	Frequency Domain ( $k$ -Space) Filtering	168
8.1.3.1	Averaging	168
8.1.3.2	LTI Filters in the Fourier Domain	170
8.1.3.3	Band-Pass Filtering	172
8.1.4	Wavelets and Multi-Resolution Analysis (MRA)	172
8.1.5	FFT versus MRA <i>in vivo</i>	174
8.1.6	Sparsen Approximations and Performance Times	175
8.2	Directional Filters	176
8.3	Numerical Derivatives	179
8.3.1	Matrix Representation of Derivative Operators	182
8.3.2	Anderssen Gradients	183
8.3.3	Frequency Response of Derivative Operators	186
8.4	Finite Differences	187

<b>9</b>	<b>Phase Unwrapping</b>	<b>191</b>
9.1	Flynn's Minimum Discontinuity Algorithm	193
9.2	Gradient Unwrapping	195
9.3	Laplacian Unwrapping	196
<b>10</b>	<b>Viscoelastic Parameter Reconstruction Methods</b>	<b>199</b>
10.1	Discretization and Noise	201
10.2	Phase Gradient	204
10.3	Algebraic Helmholtz Inversion	205
10.3.1	Multiparameter Inversion	207
10.3.2	Helmholtz Decomposition	207
10.4	Local Frequency Estimation	208
10.5	Multifrequency Inversion	210
10.5.1	Reconstruction of $\varphi$	211
10.5.2	Reconstruction of $ G^* $	213
10.6	$k$ -MDEV	214
10.7	Finite Element Method	217
10.7.1	Weak Formulation of the One-Dimensional Wave Equation	218
10.7.2	Discretization of the Problem Domain	219
10.7.3	Basis Function in the Discretized Domain	220
10.7.4	FE Formulation of the Wave Equation	221
10.8	Direct Inversion for a Transverse Isotropic Medium	224
10.9	Waveguide Elastography	225
<b>11</b>	<b>Multicomponent Acquisition</b>	<b>229</b>
<b>12</b>	<b>Ultrasound Elastography</b>	<b>233</b>
12.1	Strain Imaging (SI)	235
12.2	Strain Rate Imaging (SRI)	235
12.3	Acoustic Radiation Force Impulse (ARFI) Imaging	235
12.4	Vibro-Acoustography (VA)	237
12.5	Vibration-Amplitude Sonoelastography (VA Sono)	237
12.6	Cardiac Time-Harmonic Elastography (Cardiac THE)	237
12.7	Vibration Phase Gradient (PG) Sonoelastography	238
12.8	Time-Harmonic Elastography (1D/2D THE)	238
12.9	Crawling Waves (CW) Sonoelastography	238
12.10	Electromechanical Wave Imaging (EWI)	239
12.11	Pulse Wave Imaging (PWI)	239
12.12	Transient Elastography (TE)	240
12.13	Point Shear Wave Elastography (pSWE)	240
12.14	Shear Wave Elasticity Imaging (SWEI)	240
12.15	Comb-Push Ultrasound Shear Elastography (CUSE)	241
12.16	Supersonic Shear Imaging (SSI)	241
12.17	Spatially Modulated Ultrasound Radiation Force (SMURF)	241
12.18	Shear Wave Dispersion Ultrasound Vibrometry (SDUV)	241
12.19	Harmonic Motion Imaging (HMI)	242

<b>Part IV</b>	<b>Clinical Applications</b>	<b>243</b>
<b>13</b>	<b>MRE of the Heart</b>	<b>245</b>
13.1	Normal Heart Physiology	245
13.1.1	Cardiac Fiber Anatomy	247
13.1.2	Wall Shear Modulus versus Cavity Pressure	249
13.2	Clinical Motivation for Cardiac MRE	250
13.2.1	Systolic Dysfunction versus Diastolic Dysfunction	250
13.3	Cardiac Elastography	252
13.3.1	<i>Ex vivo</i> SWI	253
13.3.2	<i>In vivo</i> SDUV	253
13.3.3	<i>In vivo</i> Cardiac MRE in Pigs	254
13.3.4	<i>In vivo</i> Cardiac MRE in Humans	256
13.3.4.1	Steady-State MRE (WAV-MRE)	256
13.3.4.2	Wave Inversion Cardiac MRE	259
13.3.5	MRE of the Aorta	260
<b>14</b>	<b>MRE of the Brain</b>	<b>263</b>
14.1	General Aspects of Brain MRE	264
14.1.1	Objectives	264
14.1.2	Determinants of Brain Stiffness	264
14.1.3	Challenges for Cerebral MRE	264
14.2	Technical Aspects of Brain MRE	265
14.2.1	Clinical Setup for Cerebral MRE	265
14.2.2	Choice of Vibration Frequency	266
14.2.3	Driver-Free Cerebral MRE	269
14.2.4	MRE in the Mouse Brain	270
14.3	Findings	271
14.3.1	Brain Stiffness Changes with Age	272
14.3.2	Male Brains Are Softer than Female Brains	273
14.3.3	Regional Variation in Brain Stiffness	274
14.3.4	Anisotropic Properties of Brain Tissue	274
14.3.5	The <i>in vivo</i> Brain Is Compressible	276
14.3.6	Preliminary Findings of MRE with Functional Activation	277
14.3.7	Demyelination and Inflammation Reduce Brain Stiffness	277
14.3.8	Neurodegeneration Reduces Brain Stiffness	279
14.3.9	The Number of Neurons Correlates with Brain Stiffness	280
14.3.10	Preliminary Conclusions on MRE of the Brain	280
<b>15</b>	<b>MRE of Abdomen, Pelvis, and Intervertebral Disc</b>	<b>283</b>
15.1	Liver	283
15.1.1	Epidemiology of Chronic Liver Diseases	286
15.1.2	Liver Fibrosis	287
15.1.2.1	Pathogenesis of Liver Fibrosis	289
15.1.2.2	Staging of Liver Fibrosis	291
15.1.2.3	Noninvasive Screening Methods for Liver Fibrosis	292
15.1.2.4	Reversibility of Liver Fibrosis	293

15.1.2.5	Biophysical Signs of Liver Fibrosis	293
15.1.3	MRE of the Liver	294
15.1.3.1	MRE in Animal Models of Hepatic Fibrosis and Liver Tissue Samples	294
15.1.3.2	Early Clinical Studies and Further Developments	295
15.1.3.3	MRE of Nonalcoholic Fatty Liver Disease	303
15.1.3.4	Comparison with other Noninvasive Imaging and Serum Biomarkers	304
15.1.3.5	MRE of the Liver for Assessing Portal Hypertension	307
15.1.3.6	MRE in Liver Grafts	309
15.1.3.7	Confounders	310
15.2	Spleen	311
15.2.1	MRE of the Spleen	311
15.3	Pancreas	314
15.3.1	MRE of the Pancreas	315
15.4	Kidneys	315
15.4.1	MRE of the Kidneys	316
15.5	Uterus	318
15.5.1	MRE of the Uterus	318
15.6	Prostate	319
15.6.1	MRE of the Prostate	320
15.7	Intervertebral Disc	321
15.7.1	MRE of the Intervertebral Disc	322
<b>16</b>	<b>MRE of Skeletal Muscle</b>	<b>325</b>
16.1	<i>In vivo</i> MRE of Healthy Muscles	326
16.2	MRE in Muscle Diseases	330
<b>17</b>	<b>Elastography of Tumors</b>	<b>333</b>
17.1	Micromechanical Properties of Tumors	333
17.2	Ultrasound Elastography of Tumors	336
17.2.1	Ultrasound Elastography in Breast Tumors	337
17.2.2	Ultrasound Elastography in Prostate Cancer	338
17.3	MRE of Tumors	339
17.3.1	MRE of Tumors in the Mouse	340
17.3.2	MRE in Liver Tumors	342
17.3.3	MRE of Prostate Cancer	344
17.3.3.1	<i>Ex Vivo</i> Studies	344
17.3.3.2	<i>In Vivo</i> Studies	345
17.3.4	MRE of Breast Tumors	345
17.3.4.1	<i>In Vivo</i> MRE of Breast Tumors	346
17.3.5	MRE of Intracranial Tumors	347
<b>Part V</b>	<b>Outlook</b>	<b>351</b>
	Dimensionality	351
	Sparsity	352
	Heterogeneity	353
	Reproducibility	353

<b>A</b>	<b>Simulating the Bloch Equations</b>	<i>355</i>
<b>B</b>	<b>Proof that Eq. (3.8) Is Sinusoidal</b>	<i>357</i>
<b>C</b>	<b>Proof for Eq. (4.1)</b>	<i>359</i>
<b>D</b>	<b>Wave Intensity Distributions</b>	<i>361</i>
D.1	Calculation of Intensity Probabilities	<i>361</i>
D.2	Point Source in 3D	<i>362</i>
D.3	Classical Diffusion	<i>363</i>
D.4	Damped Plane Wave	<i>365</i>
	<b>References</b>	<i>367</i>
	<b>Index</b>	<i>417</i>

## About the Authors



*Sebastian Hirsch* studied physics at Johannes Gutenberg University in Mainz, Germany. Since 2009 he has been working in the Elastography group at Charité – Universitätsmedizin Berlin, Germany. His work has focused on the development of fast magnetic resonance imaging methods suitable for accelerating MR elastography and on the investigation of poroelastic properties of biological tissue. In 2015, he obtained a PhD in physics from Humboldt University of Berlin.



*Jürgen Braun* studied chemistry and received his PhD degree in physical chemistry from the Albert Ludwig University of Freiburg for his dissertation about NMR studies in liquids and solids. He is currently working as an Assistant Professor at the Charité – Universitätsmedizin Berlin and is Associate Director of the Institute for Medical Informatics. His research interests include medical imaging with a focus on elastography, medical engineering, and image processing.



*Ingolf Sack* studied physical chemistry and received his PhD in solid-state NMR at Free University of Berlin, Germany. He is a full Heisenberg professor of the German Research Foundation for Experimental Radiology and Elastography at Charité – Universitätsmedizin Berlin. His research activities span from NMR spectroscopy, MRI, biomechanics, acoustics, and rheology to medical ultrasound, signal processing, and image analysis. He leads an interdisciplinary team of scientists who has pioneered pivotal developments in elastography of the liver, muscle, heart, and brain.

You can contact the authors by sending an e-mail to [mre-book@charite.de](mailto:mre-book@charite.de).

## Foreword

Many diseases cause profound changes in the mechanical properties of tissue and the normal function of tissues like skeletal muscle, heart, lungs, and gut are deeply rooted in the complex mechanical characteristics of their constituent cells. Research now provides growing evidence of the importance of tissue matrix mechanics on cellular function. Cells react to the dynamic and static properties of their matrix environment through a process known as mechano-transduction. It is now known that mechanobiology plays an important role in the origin of many disease processes, including organ fibrosis and cancer.

Magnetic resonance elastography (MRE) has emerged as a versatile technology to reliably assess the mechanical properties of tissue. It has a proven ability to quantitatively interrogate a range of novel mechanical biomarkers in almost all regions of the body.

An important milestone in the evolution of MRE was the demonstration that it can serve as a reliable, painless, and less-expensive alternative to liver biopsy for assessing liver fibrosis. This transformed MRE from a research technique into a clinical tool that is now routinely used in patient care worldwide. In 2009, MRE became available as a Food and Drug Administration (FDA)-approved upgrade for magnetic resonance imaging (MRI) scanners. The installed base of MRE reached over 550 systems worldwide in 2015 and is expanding rapidly.

A remarkable aspect of the development of MRI over the last three decades is that most innovations and new applications of the technology were developed by researchers in the academic medical community and not by industry. MRI truly is a modality that has been continually reinvented by its users. MRE is similar in this regard and this book has been written by individuals who served as pioneering explorers of many of the frontiers of MRE.

With broad and deep coverage of the field of MRE, this book addresses a full range from fundamental principles to clinical applications. It provides a concise overview of the medical and biological perspectives that drive the applications. It nicely integrates important concepts in MR physics, viscoelastic theory, and signal processing and provides access in one volume to important background content that can be difficult to find elsewhere.



This book should be read cover-to-cover. It provides a one-stop, in-depth review of MRE technology and applications and is a wonderful source of information for students, engineers, scientists, and physicians.

*Richard L. Ehman*  
*Professor of Radiology*  
*Blanche R. & Richard J. Erlanger*  
*Professor of Medical Research*  
*Mayo Clinic*

## Preface

The principal aim of this book is to provide a comprehensive introduction to magnetic resonance elastography (MRE). Technically, MRE is based on two main research fields: magnetic resonance imaging (MRI) and viscoelastic theory – two vast topics with virtually no overlap in academic curricula. This motivated us to write a textbook that allows physicists and engineers who want to commence research in this field to quickly gather all information that is necessary to comprehend the rather intricate and complex concepts underlying MRE. The scope of the book spans the theoretical background as well as various practical and technical aspects.

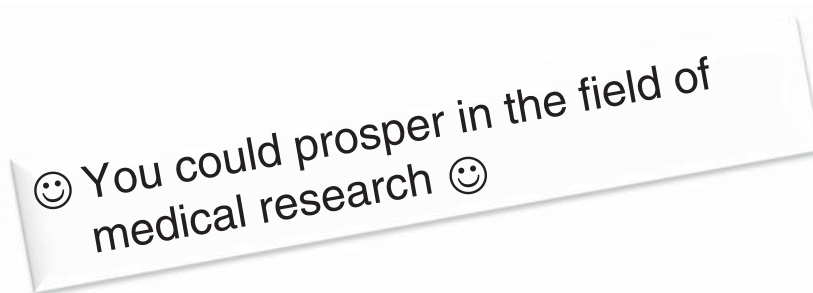
A second goal of this book is to provide the background for using MRE as a clinical routine method. We have therefore compiled data from the literature that provide the preclinical and clinical foundations for measuring viscoelastic properties for diagnostic purposes. While the number of relevant publications by far exceeds the amount of information that could possibly be published in a single book, we aimed to discuss the application of MRE to various organs in the human body from its inception up to the current state of the art. This part of the book is less theoretical and technical than the preceding parts and can serve as a valuable reference also for scientists without a strong background in physics, engineering, or related fields.

This work is a joint effort by the members of the elastography group at Charité – Universitätsmedizin Berlin, Germany, as well as our clinical collaborators from the Department of Radiology, the Clinic for Pediatric Endocrinology and Diabetology and the Ultrasound Research Laboratory of Charité. We strove to combine our expertise and experience to facilitate entry into the fascinating research field that is MRE. In doing so, we tried to maintain a balanced view on the globally distributed research activities in this field.

We acknowledge that the part of the book discussing various methods of reconstructing viscoelastic parameters from MRE measurements is biased toward a school of thought that favors a concept that can be characterized as “inversion of the wave equation,” as opposed to different approaches based on finite elements methods (FEM). This is not meant to be a statement on the superiority of the former method over the latter, it rather reflects the educational background of the members in our research group. FEM is a highly sophisticated field with applications in various engineering disciplines, and its use for viscoelastic parameter calculation in MRE must not be understated. However, for lack of personal experience and familiarity with the method, we restrict the discussion to a general overview and refer the inclined reader to specialized literature on FEM in general or its use in MRE in particular.

This is the first edition of the book. While we put a lot of work into ensuring that all information is correct, we are fully aware that errors are inevitable in a book of this volume. We therefore kindly ask our readers to point out any mistakes you encounter or points that are not explained clearly, so that one day we will be able to release a revised and improved edition. All feedback is highly appreciated. You can contact the authors by sending e-mails to the address given below, or post your comments to the errata page available in the website mentioned below.

We hope that you will enjoy reading this book and that it will be a reliable guide on your journey through the exciting field of MRE, and we wish you all the best for your studies and research! Or, to say it with the infallible words of a fortune cookie:



Berlin, February 2016  
mre-book@charite.de  
<http://www.wiley-vch.de/ISBN/978-3-527-34008-8>

*Sebastian Hirsch  
Jürgen Braun  
Ingolf Sack*

## Acknowledgments

Writing a textbook about a field as vast as magnetic resonance elastography (MRE) is a huge effort and requires the collaboration of many people, everyone being a specialist in their own field. We cordially thank everyone who has contributed to this book, be it through writing a section of text, revising it for factual soundness or intelligibility, or providing feedback, inspiration, and insight. We sincerely thank all our coauthors for expanding the scope of this book beyond what we would have been able to write ourselves, and for their invaluable contributions to the following chapters:

- Heiko Tzschätzsch: “4.11 Energy Density and Flux,” “4.12 Shear Wave Scattering from Interfaces and Inclusions” and “12 Ultrasound Elastography”
- Eric Barnhill: “8.1 Noise and Denoising in MRE” and “8.3 Numerical Derivatives”
- Abbas Samani: “10.7 Finite Element Method”
- Thomas Elgeti: “13 MRE of the Heart”
- Christian Hudert “15.1 Liver”
- Jing Guo: “16 MRE of skeletal muscle”
- Thomas Fischer and Anke Thomas: “17.2 Ultrasound Elastography of Tumors”

Research is essentially a matter of teamwork, and none of us would have been able to write this book if we had not benefited in many ways from the hard work of the Elastography team at Charité – Universitätsmedizin Berlin. We are particularly indebted to our current team: Eric Barnhill, Florian Dittmann, Jing Guo, Selçan Ipek-Ugay, Andreas Fehlner, Clara Körting, Christian Rudolph, Mehrgan Shahryari, and Heiko Tzschätzsch. We are grateful for the continuing support from our long-standing former colleagues Dieter Klatt, Uwe Hamhaber, Dagmar Krefting, and Sebastian Papazoglou. We also cordially thank Annette Kögel and Sabine Sassmann for their help with numerous administrative matters.

All our motivation for research in MRE comes from the clinic. We have been blessed with clinicians from Charité who were always open to think in a new direction toward unprecedented imaging parameters, measurement systems, and diagnostic applications and who never gave us the feeling that surprising results and crazy ideas cannot be turned into diagnostic value eventually. Our special gratitude therefore goes to Christian Althoff, Patrick Asbach, Daniel Baumgart, Thomas Elgeti, Thomas Fischer, Agnes Flöel, Florian Freimann, Bernd Hamm, Robert Hättasch, Karl-Titus Hoffmann, Christian Hudert, Korinna Jöhrens, Fabian Knebel, Thomas Kröncke, Axel Lipp, Stephan Marticorena-Garcia, Friedemann Paul, Martin Reiß-Zimmermann,

Rolf Reiter, Michael Scheel, Rajan Somasundaram, Barbara Steiner, Kaspar-Josche Streitberger, Matthias Taupitz, Anke Thomas, Edzard Wiener, and Jens Würfel.

We are also very thankful to radiographers Yvonne Kamm, Andrea Hassenpflug, Cynthia Kraut, and Susan Pikol for their support in performing clinical magnetic resonance elastography (MRE) studies.

Research is likely to get stuck unless it receives continuous inspiration from the outside world. We are therefore very grateful to our scientific colleagues worldwide for ongoing discussion, exchange of ideas, and their valuable opinions on many of our oftentimes fuzzy scientific ideas: Angela Ariza, Johannes Bernarding, Richard Ehman, Philippe Garteiser, Stefan Hetzer, Carmen Infante-Duarte, Paul Janmey, Josef Käs, Charlotte Klein, Oliver Klein, Arunark Kolipaka, Armando Manduca, Matthew McGarry, Joyce McLaughlin, Jason Millward, Keith Paulsen, Donald Plewes, Neil Roberts, Anthony Romano, Tim Salcudean, Eyk Schellenberger, Jörg Schnorr, Ralph Sinkus, Ligin Solamen, Thomas Tolxdorff, Bernard Van Beers, Jonathan Vappou, Susanne Wagner, and John Weaver.

Expanding the scope of MRE to a continually increasing number of organs requires constant adaptations of existing hardware and the development of completely novel designs. This would not have been possible without the help from our technical partners: Ivo Cermak, Toni Drießle, Tassilo Heinze, Robert Klaua, Dietmar Otto, Michael Schultz, and Manh Nguyen Trong.

We are particularly thankful to Bettina Herwig for correcting and improving the language in the book and therewith becoming involuntary familiar with the details of MRE.

Finally, our utmost gratitude goes to our families whom we barely saw during long phases of writing this book.

*Sebastian Hirsch  
Jürgen Braun  
Ingolf Sack*

## Notation

Much attention was paid to keep the mathematical notation throughout the book as consistent and self-explanatory as possible. The following conventions were used:

- Matrices, tensors, and vectors are denoted by bold, upright Latin or Greek letters:  $\mathbf{a} = \mathbf{C} \cdot \mathbf{b}$ .
- Unit vectors are denoted by a hat symbol:  $\hat{\mathbf{x}} = \frac{\mathbf{x}}{|\mathbf{x}|}$ .
- Integral transforms are denoted, depending on the context, by either a caligraphic letter or a diacritic symbol:  $\mathcal{F}[u] \equiv \tilde{u}$  for the Fourier transform of  $u$ ,  $\mathcal{L}[u] \equiv \bar{u}$  for the Laplace transform.
- The bullet  $\bullet$  is used exclusively to denote the scalar product of two vectors or vector-valued expressions:  $\mathbf{a} \bullet \mathbf{b}$ ,  $\nabla \bullet \mathbf{u} \equiv \text{div } \mathbf{u}$ .
- Multiplication between a vector and matrix, or multiplication with a scalar quantity, is denoted by a smaller dot:  $\mathbf{A} \cdot \mathbf{b}$ .
- Where appropriate, temporal derivatives are marked by a dot, and spatial derivatives by an apostrophe:  $\frac{\partial g}{\partial t} = \dot{g}$ ,  $\frac{\partial f}{\partial x} = f'$ .
- Summation over an index is always specified explicitly by the sum symbol. Summation over repeated indices (Einstein's sum convention) is *never* implied.
- Only indices or exponents that take numerical values are printed in italic; super- or subscripts that serve as a specification are always printed upright:  $x_i$ ,  $a^b$ ,  $u_{\text{shear}}$ .
- The complex unit is always represented by an upright letter to make it distinguishable from an index:  $\sqrt{-1} = i \leftrightarrow u_i, i \in \mathbb{N}$ .
- Matrices and vectors are surrounded by parentheses when all elements are listed explicitly:

$$\begin{pmatrix} a \\ b \\ c \end{pmatrix} = \begin{pmatrix} \cos \alpha & -\sin \alpha & 0 \\ \sin \alpha & \cos \alpha & 0 \\ 0 & 0 & 1 \end{pmatrix} \cdot \begin{pmatrix} x \\ y \\ z \end{pmatrix}.$$

- Brackets are used to denote that vectors or matrices are constructed by concatenating other vectors or matrices:  $\mathbf{A} = [\mathbf{a}, \mathbf{b}, \mathbf{c}]$  denotes that the matrix  $\mathbf{A}$  is assembled by concatenating three column vectors along the horizontal dimension.
- In equations, parentheses  $()$ , brackets  $[\ ]$ , and curly braces  $\{ \}$  are used interchangeably for grouping terms and to denote precedence:  $a \cdot (b + c) \equiv a \cdot [b + c] \equiv a \cdot \{b + c\}$ .

## List of Symbols

The following table lists commonly used mathematical symbols. Note that some symbols are reused in a local context to denote something else, but this will always be explained in the text.

### Roman symbols

<b>B</b>	magnetic field
<b>C</b>	elasticity tensor
<b>c</b>	curl of the displacement field (shear strain)
<b>d</b>	divergence of the displacement field (volumetric strain)
<b>E</b>	Young's modulus
<b>G</b>	linear magnetic gradient field
<b>G*</b>	complex shear modulus
<b>I</b>	MR image
<b>i</b>	imaginary unit ( $i = \sqrt{-1}$ )
<b>K</b>	bulk (compression) modulus
<b>k</b>	wave vector
<b>M</b>	P-wave modulus
<b>M</b>	magnetization
<b>P</b>	vector of energy flux density
<b>S</b>	(complex) MR signal; entropy
<b>S</b>	compliance tensor
<b>T</b>	vibration period
<b>T<sub>1</sub>, T<sub>2</sub>, T<sub>2</sub>*</b>	longitudinal / transverse relaxation times
<b>TE</b>	echo time
<b>TR</b>	repetition time
<b>u</b>	displacement field

### Greek symbols

<b><math>\alpha</math></b>	springpot interpolation parameter; flip angle
<b><math>\delta</math></b>	Kronecker delta, Dirac delta distribution
<b><math>\epsilon</math></b>	strain tensor
<b><math>\eta</math></b>	viscosity
<b><math>\kappa</math></b>	compressibility
<b><math>\lambda</math></b>	wave length, first Lamé's parameter

$\mu$	(real-valued) shear modulus
$\boldsymbol{\mu}$	magnetic moment of a spin
$\nu$	Poisson's ratio
$\xi$	encoding efficiency
$\rho$	mass density
$\boldsymbol{\sigma}$	stress tensor
$\phi$	MR signal phase, oscillation phase
$\varphi$	phase of the complex shear modulus ( $G^*$ )
$\omega$	angular vibration frequency, angular precession frequency

**Mathematical operators**

$\nabla$	gradient operator
$\Delta$	Laplacian operator
$\mathcal{F}$	(continuous) Fourier transform
$\mathcal{L}$	Laplace transform
FFT	fast Fourier transform (discrete)
tr	trace (of a matrix)
$\mathbb{N}$	natural numbers
$\mathbb{Z}$	integer numbers
$\mathbb{R}$	rational numbers
$\mathbb{C}$	complex numbers
$\mathbb{1}$	identity operator/identity matrix
$\star$	convolution operator



## Introduction

Approximately 50 000 years ago, during an age called *upper paleolithic revolution* [1], mankind began to develop finer tactile senses and greater perceptual capabilities than ever before. This great mystery of human evolution endowed our ancestors with the tools and the intellectual prowess to investigate the origins of pain and disease. The tools they probably used – auscultation, palpation, and sight – are still valuable tools for diagnostic routine in modern clinical practice. The knowledge that ancient physicians had accumulated by observing their patients and the precision with which they drew their conclusions is exemplified in the Ebers Papyrus, one of the oldest and most beautiful medical books of humanity, which was written during the reign of pharaoh Ahmose I (1560–1525 BCE). As shown in Figure 1, Ahmose’s doctors paid significant attention to palpation: manually deforming and shifting soft tissue layers and carefully sensing the resistance of tissue against that deformation provided them with an incredibly rich source of diagnostic information. The wealth of information attainable through palpation is still being explored today. On the one hand, physicists have developed mechanical models of soft biological tissues that describe how structures on several length scales, from the cellular level to larger fibers or vascular trees, translate to the macroscopic level, affecting the haptic sensation that we perceive with our fingers. On the other hand, modern biological and biophysical research has revealed that altered mechanical properties play a key role in the progression of numerous diseases, from fibrosis to tumors. It has even been suggested that these mechanical cues can precede other signs or symptoms of diseases (see Figure 2).

Viscoelastic properties are one of the three main determinants of haptic sensation, the other two being temperature and surface texture. Viscoelasticity provides a framework to classify the response of a material when a force is applied to it. On the coarsest scale, viscoelasticity is comprised of the complementary concepts of *elasticity* and *viscosity*. Elastic materials can be deformed when a force is applied, but they will immediately return to their original shape when the force is removed. Objects such as a steel spring and gelatin dessert (“jelly,” “jello”) are typical examples exhibiting elastic behavior. Viscous materials, on the other hand, also deform when a force is applied; however, they will remain in their deformed shape after removal of the force. Honey and other thick liquids are examples of such material properties. However, most materials possess both elasticity and viscosity at the same time. For example, according to the above classification, a rubber ball and metal ball would both be classified as elastic, since they both tend to return to their original shape after deformation. Yet, when a rubber ball and a metal ball bounce up from a hard surface after being dropped from the same

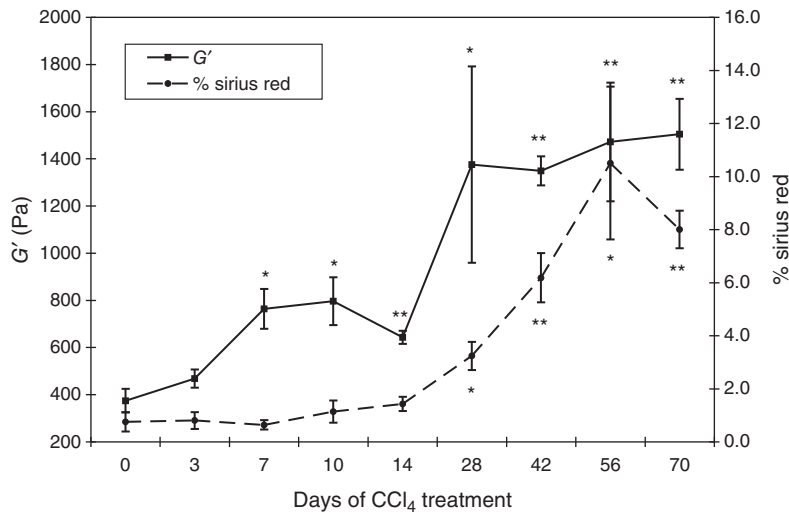


**Figure 1** Papyrus Ebers, Columns 107 (right) and 108 (left). Demarcated sections highlight descriptions of palpation examinations. *Ebers 872*: If a swelling presents spherical and stiff and recedes pressure of the fingers, then it originates from the vessel and should be treated with a heated knife. *Ebers 873*: If a swelling at internal layers of the skin appears nodular and feels compliant, like air-filled cavities, then it is a tumor of the vessels and you should not treat it (with a knife), but rather use remedies or incantations to improve the condition of the vessel in all affected areas of the human body. *Ebers 867*: If a swelling in any part of the body feels elastic under the fingers and comes apart under constant pressure, it is of fat and should be treated with the knife. *Ebers 868*: If a swelling has the property of a son (or daughter, metastasis?) and it can be found isolated or spread and feels moderately solid, then it should be treated with the knife. (Nonliteral translation by the authors, based on the German text of Wolfhart Westendorf, *Handbuch der ägyptischen Medizin*, 1999, volume 2, pg. 547, kindly provided by Marko Stuhr, Mayen, Germany. Reproduced with permission of Universität Leipzig.)

height, the metal ball will reach a greater height than the rubber ball.<sup>1</sup> The reason is that the rubber ball converts a portion of the energy that was used to deform it into heat, whereas the metal ball restores almost all of the deformation energy back into kinetic energy, and therefore bounces back with higher velocity. Viscosity is also a measure of how much of the deformation energy is converted into heat. Therefore, in addition to being elastic, the rubber ball is characterized by a much higher viscosity than the metal ball. We can therefore define what we call a “square of viscoelasticity,” shown in Figure 3, that allows us to compare viscoelastic properties of different materials. The four corners are characterized by the extreme cases found in solid bodies (excluding liquids): “highly viscous/highly elastic<sup>2</sup>” (rubber), “purely elastic” (spring), “low elasticity/high viscosity” (marshmallow), and “low elasticity/low viscosity” (jelly).

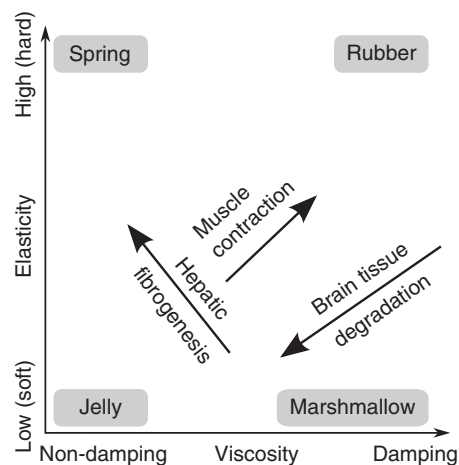
1 <http://sciencenotes.org/why-a-glass-ball-bounces-higher-than-a-rubber-ball/>

2 It is important to note here that, in contrast to colloquial use, “highly elastic” does not mean “easily deformable.” On the contrary, it means “very resistant to deformation.”



**Figure 2** Example of the importance of mechanical tissue properties in disease: Stiffness (storage modulus  $G'$ ) measured by shear oscillatory rheometry in fibrosis-induced rat livers. Fibrosis is characterized by the accumulation of excess and abnormal extracellular matrix material. Samples were stained for the presence of collagen by sirius red, which detects primarily type I collagen. The time axis indicates time since initiation of fibrosis. Significant changes relative to day 0 are demarcated by asterisks (\* $P < 0.05$ , \*\* $P < 0.005$ ). The data suggest that an increase in liver stiffness precedes fibrosis and that increased liver stiffness may play an important role in initiating early fibrosis. (Georges 2007 [2]. Reproduced with permission of American Journal of Physiology.)

**Figure 3** The “square of viscoelasticity:” viscoelastic properties can be characterized in a two-dimensional plot in terms of viscosity and elasticity. The arrows indicate how viscoelasticity of human organs is affected when the liver becomes fibrotic, when a muscle contracts or when the brain undergoes degradation. (Sack 2013 [3]. Reproduced with the permission of Royal Society of Chemistry.)



Different materials – including different types of organic tissue – can be characterized in terms of their elasticity and viscosity and thus be represented by a point within the square of viscoelasticity. If a disease alters the viscoelastic properties of a specific type of tissue, for example, the liver, healthy and diseased tissue would therefore appear as two different points in the diagram.

Diagnosis of disease can therefore be performed by comparing the viscoelastic properties of a potentially diseased organ to those of a healthy one. This is the

foundation of manual palpation. Through years of experience, physicians develop a sense of the “correct” properties of different organs, and they can detect deviations based on the haptic feedback that they receive when manually deforming the tissue. While this method is very powerful, it has two major drawbacks:

- Assessment of tissue elasticity through a physician is qualitative rather than quantitative, and hence subjective. For a widely applicable clinical instrument, a quantitative method that also allows less experienced examiners to detect disease based on numbers rather than sensation is desirable.
- Noninvasive assessment of tissue viscoelasticity is only feasible for a few organs that can be palpated through the skin. This excludes most deeper organs as well as those shielded by bones, such as the brain.

Both limitations can be overcome when medical imaging is employed to replace palpation, leading to “elastography.” Elastography can be separated into two independent steps: application of a force that causes tissue deformation and detection of the response of the tissue to that force. Ultrasound (US) imaging or magnetic resonance imaging (MRI) are capable of performing the latter, since they are both sensitive to tissue motion on the order of micrometers. For achieving tissue deformation, various approaches exist. Most of them rely on the application of an external force that is transmitted through skin and bones into the organ of interest. In magnetic resonance elastography (MRE), the most common type of applied force is harmonic vibration, which stimulates mechanical waves that propagate through the body. By detecting the displacement induced by these waves, viscosity and elasticity of tissue can be retrieved quantitatively through wave inversion algorithms.

Mechanical testing and MRE experiments performed on *phantoms*<sup>3</sup> has revealed that minute structural changes can lead to huge differences in viscoelastic properties. For example, the addition of less than one mass percent of agarose, a gelling agent extracted from seaweed, turns liquid water into a solid block, thus increasing its elasticity by many orders of magnitude. Furthermore, Guo and Posnansky demonstrated that adding a small amount of structured elements, such as paper strips, to a homogeneous gel induces viscous properties [4, 5]. In the context of clinical diagnosis, this means that small structural modifications on the cellular level can translate into well-measurable changes in the viscoelastic parameters of the whole organ. The same applies to findings published by Lambert et al. [6], who analyzed the influence of microscatterers on macroscopically observed wave characteristics. These results suggest that elastography is capable of providing insight into structural alterations that occur far below the spatial resolution of the underlying imaging technique. Furthermore, typical resolution-limiting relations, such as the Abbe limit stating that optical systems cannot resolve objects that are smaller than half a wavelength, do not apply to MRE, since information on the microscopic scale is merely deduced from phenomena observed on much larger scales, and not imaged directly.

In order to extract structural information from MRE measurements, *viscoelastic* models are used that establish a relationship between the viscoelastic parameters of a material and its response to deformation. The complexity of these models ranges from

---

<sup>3</sup> Phantoms are simple model systems, such as a block of gelatin, used to isolate one particular aspect of viscoelasticity from the plethora of concomitant physiological processes that coexist in living tissue and render measurements more challenging.

simple linear models, such as Hooke's law, to much more refined exponential models that are closely related to highly advanced mathematical disciplines, including fractional calculus. Models of the latter type, for example, the *springpot model*, can be used to characterize the frequency dependency – the *dispersion* – of viscoelastic parameters. Their application requires more input information, such as data acquired at different vibration frequencies. In return, their internal parameters can be directly linked to very specific aspects of the cellular structure of tissue. In addition to being a clinically relevant instrument for early and noninvasive diagnosis of disease and monitoring progression of disease and therapy, its explicit dependence on microscopic structure has rendered MRE a highly valuable tool for fundamental clinical and preclinical research.

In the first two parts of this book, we will present a comprehensive discussion of the physical principles underlying MRI and viscoelastic theory. In the third part, we will proceed to demonstrate how these inherently unrelated concepts merge into MRE. We will also discuss various numerical and computational methods for data processing in MRE that can serve as a guide to the reader to develop the ideal experimental setup tailored to his/her specific requirements. Finally, in the fourth part, we will review examination strategies and results that were published by the global MRE community on MRE applied to various organs.

Berlin, February 2016.

## Part I

### Magnetic Resonance Imaging

This chapter explains the physical principles behind magnetic resonance imaging (MRI). It is subdivided into two parts. In the first part, we will explore the nuclear magnetic resonance (NMR) effect. The physical phenomenon of NMR is the basis for magnetic resonance imaging, and has also applications outside the field of medical imaging. In (bio)chemistry, NMR spectroscopy is used as a tool to unravel the structure of molecules and to quantify bond lengths. We will show how NMR can be manipulated in different ways to generate *echo* signals and investigate their properties.

The second part will illustrate how the NMR effect can be exploited to generate images. The mechanisms underlying spatial encoding will be discussed, and the most important signal sampling and imaging strategies will be presented. Finally, more specialized techniques and concepts that are relevant for magnetic resonance elastography (MRE) will be introduced.

## 1

## Nuclear Magnetic Resonance

### 1.1 Protons in a Magnetic Field

<sup>1</sup>H-Nuclear magnetic resonance (NMR) is based on the manipulation of the magnetic moments of hydrogen nuclei (protons) in a strong magnetic field. A static magnetic field,  $\mathbf{B}_0$ , typically with a field strength of 1.5 or 3 T in clinical magnetic resonance imaging (MRI) scanners, induces macroscopic magnetization in the proton population inside a given object. Microscopically,  $\mathbf{B}_0$  defines a quantization axis for the proton spin  $\mathbf{S}$ . Henceforth, we assume that  $\mathbf{B}_0$  is aligned with the  $z$ -axis of the coordinate system:  $\mathbf{B}_0 = (0, 0, B_0)^T$ . The proton has a spin quantum number  $S = \frac{1}{2}$ , meaning that  $|\mathbf{S}| = \sqrt{S(S+1)}\hbar = \sqrt{\frac{3}{4}}\hbar$ . Projection of  $\mathbf{S}$  onto  $\mathbf{B}_0$  can assume one of two possible values,  $S_z = \pm \frac{1}{2}\hbar$ , whereas the  $x$ - and  $y$ -components of the spin,  $S_x$  and  $S_y$ , according to the quantum mechanical uncertainty principle, remain undetermined. The proton spin is associated with a magnetic moment

$$\boldsymbol{\mu} = \gamma \mathbf{S}, \quad (1.1)$$

with the *gyromagnetic ratio*  $\gamma = 2\pi \cdot 42.58 \text{ MHz/T}$  for protons [7]. Thus, the  $z$ -component of the magnetic moment can assume either of two values

$$\mu_z = \pm \frac{1}{2} \gamma \hbar, \quad (1.2)$$

while  $\mu_x$  and  $\mu_y$  form an arbitrary and undetermined transverse magnetization component in the  $xy$ -plane. For each of the two possible values of  $\mu_z$ , the potential energy of the respective state is

$$E = -\mathbf{B}_0 \bullet \boldsymbol{\mu} = -B_0 \cdot \mu_z, \quad (1.3)$$

indicating that the parallel alignment ( $\uparrow\uparrow$ ) of  $\mu_z$  with  $\mathbf{B}_0$  has lower energy than the antiparallel ( $\uparrow\downarrow$ ) orientation<sup>1</sup> [8]. The energy gap between the two states is therefore

$$\delta E = E_{\uparrow\downarrow} - E_{\uparrow\uparrow} = 2 \cdot B_0 \cdot \mu_z = \gamma \cdot B_0 \cdot \hbar. \quad (1.4)$$

<sup>1</sup> Note that the sign conventions are somewhat misleading. For a magnetic field, the  $\mathbf{B}$ -vector points from the north pole to the south pole. However, a magnetic dipole vector  $\boldsymbol{\mu}$  points from the south pole to the north pole. The antiparallel orientation therefore means that the north poles of the field and the dipole are aligned, creating a repulsive torque that tries to flip the dipole by  $180^\circ$ , which explains why the antiparallel state possesses a higher potential energy than the parallel state.

Since protons are fermions, the distribution of the entire population of  $N$  protons over these two states is governed by a Fermi statistics [9]:

$$N_{\uparrow\uparrow} = N \cdot \frac{e^{-E_{\uparrow\uparrow}/k_B T}}{e^{-E_{\uparrow\uparrow}/k_B T} + e^{-E_{\uparrow\downarrow}/k_B T}} \quad (1.5)$$

$$N_{\uparrow\downarrow} = N \cdot \frac{e^{-E_{\uparrow\downarrow}/k_B T}}{e^{-E_{\uparrow\uparrow}/k_B T} + e^{-E_{\uparrow\downarrow}/k_B T}}. \quad (1.6)$$

The magnetic moments of protons in the parallel and antiparallel states cancel each other out. However, at human body temperature of  $37^\circ\text{C}$ , the parallel, lower energy state has a slightly larger population than the excited antiparallel state. The excess population, with respect to the total population,

$$\delta N = \frac{N_{\uparrow\uparrow} - N_{\uparrow\downarrow}}{N} = \frac{e^{-E_{\uparrow\uparrow}/k_B T} - e^{-E_{\uparrow\downarrow}/k_B T}}{e^{-E_{\uparrow\uparrow}/k_B T} + e^{-E_{\uparrow\downarrow}/k_B T}}$$

is in the order of  $10^{-6}$  at typical field strengths of clinical MRI scanners of 1.5 T or 3 T. This imbalance causes a small net magnetization

$$\mathbf{M}_0 = \delta N \rho |\mu_z| \hat{\mathbf{z}}, \quad (1.7)$$

with average proton density  $\rho$  and the unit vector  $\hat{\mathbf{z}}$  along the  $z$ -axis.  $\mathbf{M}_0$  is aligned with the static  $\mathbf{B}_0$  field. Manipulation of this magnetization by means of additional time-dependent magnetic fields is the basis for all types of MR experiments. Despite the quantum mechanical nature of individual protons, the macroscopic magnetization can be treated in a classical way, since individual protons are never probed in MR imaging [9]. For a single proton, the transverse component of the magnetic moment (i.e., the projection of  $\boldsymbol{\mu}$  onto the  $xy$ -plane) would have to be taken into account. However, by averaging over a large number of protons (in the order of Avogadro's constant,  $N_A \approx 6 \cdot 10^{23}$ ), these contributions cancel each other out, so that no net transverse magnetization is observed in the equilibrium state.

## 1.2 Precession of Magnetization

For an arbitrary orientation of magnetization  $\mathbf{M}$  with respect to the direction of  $\mathbf{B}_0$ , the time evolution of  $\mathbf{M}$  is characterized by [10]:

$$\frac{\partial \mathbf{M}}{\partial t} = \gamma \mathbf{M} \times \mathbf{B}_0. \quad (1.8)$$

Total magnetization  $\mathbf{M}(t)$  can be decomposed into a longitudinal component  $\mathbf{M}_{\parallel}(t) = M_{\parallel}(t) \cdot \hat{\mathbf{z}}$  and a transverse component  $\mathbf{M}_{\perp}(t)$  so that

$$\mathbf{M}(t) = \mathbf{M}_{\parallel}(t) + \mathbf{M}_{\perp}(t). \quad (1.9)$$

This allows us to separate Eq. (1.8) into

$$\frac{\partial \mathbf{M}_{\parallel}}{\partial t} = \gamma \mathbf{M}_{\parallel} \times \mathbf{B}_0 = \mathbf{0} \quad (1.10)$$

$$\frac{\partial \mathbf{M}_{\perp}}{\partial t} = \gamma \mathbf{M}_{\perp} \times \mathbf{B}_0. \quad (1.11)$$



Equation (1.11) describes the precession of the transverse magnetization about the axis defined by  $\mathbf{B}_0$ . The angular frequency of precession in a magnetic field of strength  $B$  is  $\omega = \gamma B$ , corresponding to the energetic separation  $\delta E = \gamma B \hbar$  of the two states of  $\mu_z$  of a single spin. If the magnetic field is solely determined by the static field  $\mathbf{B}_0$ , all magnetization precesses at the same frequency  $\omega_0$ , which is also called *Larmor frequency*. In the presence of additional magnetic fields,  $\mathbf{B} = \mathbf{B}_0 + \delta\mathbf{B}$ , Eq. (1.8) becomes

$$\frac{\partial \mathbf{M}}{\partial t} = \gamma \mathbf{M} \times (\mathbf{B}_0 + \delta\mathbf{B}) \quad (1.12)$$

$$= \gamma \mathbf{M}_\perp \times \mathbf{B}_0 + \gamma \mathbf{M} \times \delta\mathbf{B}. \quad (1.13)$$

The right-hand side of Eq. (1.13) is a superposition of the previously mentioned precession of transverse magnetization and a rotation of full magnetization  $\mathbf{M}$  about the axis defined by the arbitrary field vector  $\delta\mathbf{B}$ . In order to simplify the description, a coordinate transform can be performed from the static laboratory system to a reference frame (designated by primed symbols, e.g.,  $\mathbf{M}'$ ) that rotates about the  $z$ -axis with the Larmor frequency  $\omega_0$ . Since this system rotates in synchrony with  $\mathbf{M}_\perp$ , transverse magnetization appears static and the first precession term in Eq. (1.13) vanishes. If  $\delta\mathbf{B}$  is designed to rotate at the Larmor frequency in the transverse plane and to be aligned with the  $x'$ -axis,  $\delta\mathbf{B}' = B'_1 \cdot \hat{\mathbf{x}}'$ , the rotating-frame version of Eq. (1.13) can be formulated as

$$\frac{\partial \mathbf{M}'}{\partial t} = \gamma B'_1 (\mathbf{M}' \times \hat{\mathbf{x}}'), \quad (1.14)$$

or alternatively for a flip around the  $y'$ -axis:

$$\frac{\partial \mathbf{M}'}{\partial t} = \gamma B'_1 (\mathbf{M}' \times \hat{\mathbf{y}}'). \quad (1.15)$$

In general, for an arbitrary vector  $\boldsymbol{\omega}' = (\omega'_1, \omega'_2, \omega'_3)^T = \gamma \mathbf{B}'$ , the motion of the magnetization is given by

$$\frac{\partial \mathbf{M}'}{\partial t} = (\mathbf{M}' \times \boldsymbol{\omega}'). \quad (1.16)$$

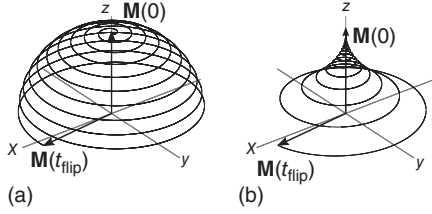
Figure 1.1 illustrates how such a  $\mathbf{B}_1$ -field can tilt the longitudinal magnetization from its initial equilibrium state into the transverse plane. Since the rotation frequency of the magnetization about the direction of  $\mathbf{B}'_1$  is given by  $\omega_F = \gamma B'_1$ , the flip angle<sup>2</sup> can be calculated as  $\alpha(t) = \omega_F \cdot t = \gamma B'_1 \cdot t$ . Arbitrary flip angles can thus be achieved by suitable combinations of  $B_1$  field strength and the duration for which the field is switched on. Figure 1.1 illustrates the special case with  $\alpha = 90^\circ$ .

A numerical method to simulate spin behavior under different kinds of applied magnetic fields is described in Appendix A.

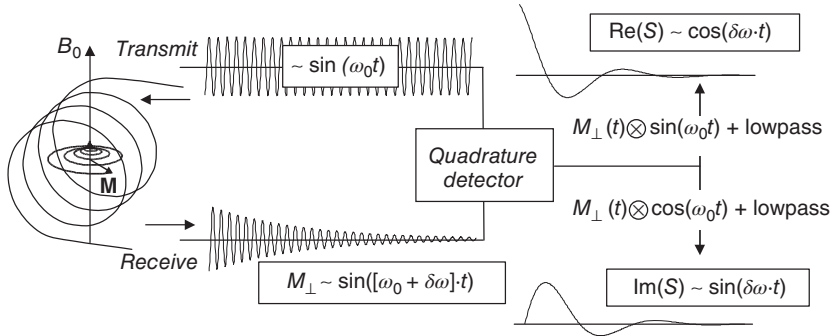
### 1.2.1 Quadrature Detection

A precessing transverse magnetization induces a sinusoidal voltage signal  $S(t) = S_0 \cdot \sin((\omega_0 + \delta\omega)t) \cdot \exp\left(-\frac{t}{T_{\text{decay}}}\right)$  in a conductor loop (usually referred to as a *receive coil*), as shown in Figure 1.2.  $\delta\omega$  denotes a small offset from  $\omega_0$  due to additional magnetic

<sup>2</sup> “Flip angle” always refers to the angle by which a  $\mathbf{B}_1$ -pulse tilts the magnetization away from the direction of  $\mathbf{B}_0$ . The subscript “F” in  $\omega_F$  refers to “flip.”



**Figure 1.1** Time evolution of magnetization as seen from the laboratory frame. The black line traces the tip of  $\mathbf{M}(t)$  over time. (a) During a  $90^\circ$ -pulse, the longitudinal equilibrium magnetization is tipped toward the transverse plane. The combination of precession at Larmor frequency and the tipping induced by the  $B_1$  pulse causes the magnetization to spiral on a spherical shell from the  $z$ -axis toward the  $xy$ -plane. (b) After the  $B_1$  pulse, the magnetization precesses at Larmor frequency. The transverse component of  $\mathbf{M}$  decays with time constant  $T_2^*$ , whereas the longitudinal component relaxes back toward the equilibrium value  $\mathbf{M}(0)$  with time constant  $T_1$  (see Section 1.3).



**Figure 1.2** Illustration of the quadrature detection step of the MR signal acquisition. Details are explained in the text.

fields. The signal decay time constant<sup>3</sup> is either  $T_2$  or  $T_2^*$ , depending on the type of echo (spin echo vs gradient echo, see Sections 1.5.1 and 1.5.2). The Larmor frequency  $\omega_0$  is irrelevant, and the desired information is only contained in the offset frequency  $\delta\omega$  (see Section 1.6.1). In order to isolate  $\delta\omega$ , *quadrature detection* [11, pg. 371] is deployed.

Through quadrature detection, the received signal is divided into two branches and each is multiplied by either  $\cos(\omega_0 t)$  or  $\sin(\omega_0 t)$ . Because of the trigonometric relations

$$\sin \alpha \cdot \sin \beta = \frac{1}{2} (\cos(\alpha - \beta) - \cos(\alpha + \beta)) \quad (1.17)$$

and

$$\sin \alpha \cdot \cos \beta = \frac{1}{2} (\sin(\alpha - \beta) + \sin(\alpha + \beta)) \quad (1.18)$$

the product signal is a sum of two signals, one oscillating with  $\delta\omega$  and the other with  $2\omega_0 + \delta\omega$ . Since  $\delta\omega \ll \omega_0$ , a suitable low-pass filter will block the high frequency signal, so that the slow component  $\delta\omega$  is obtained. The two filtered signals (from the sine and cosine branch) represent the real and imaginary parts of  $S$ . The conversion to magnitude

<sup>3</sup> The different types of signal relaxation and their sources will be discussed in Section 1.3.

and phase can then be performed according to

$$|S| = \sqrt{|\operatorname{Re}(S)|^2 + |\operatorname{Im}(S)|^2} \quad (1.19)$$

$$\phi = \arctan\left(\frac{\operatorname{Im}(S)}{\operatorname{Re}(S)}\right). \quad (1.20)$$

The signal magnitude is proportional to the magnitude of transverse magnetization  $|\mathbf{M}_\perp|$ , and the phase  $\phi$  is the angle between  $\mathbf{M}_\perp$  and the  $x'$ -axis of the rotating frame.

### 1.3 Relaxation

The above discussion of precessing magnetization did not take dissipative interaction between spins and their environment into account. Since the parallel and antiparallel orientation of a magnetic moment with respect to  $\mathbf{B}_0$  differ by energy  $\delta E = \gamma \hbar B_0$ , the interaction of a spin with its surroundings can change the orientation of its magnetic moment. This effect gives rise to *relaxation effects*, which are crucial for MRI signal and contrast generation.

In the thermal equilibrium state, the resultant magnetization  $\mathbf{M}_0$  is aligned with  $\mathbf{B}_0$ , which defines the  $z$ -axis of the coordinate system. At any time point  $t$ , the total magnetization  $\mathbf{M}(t)$  can be decomposed into longitudinal and transverse component, as introduced in Eq. (1.9). The presence of transverse magnetization indicates a perturbation of the equilibrium state. Through interaction with the microscopic lattice of the medium, excess energy is dissipated over time, so that the magnetization relaxes to the initial longitudinal state. The rate of change of the longitudinal magnetization component is proportional to its deviation from the equilibrium state:

$$\frac{\partial \mathbf{M}_\parallel}{\partial t} = \frac{1}{T_1} (\mathbf{M}_0 - \mathbf{M}_\parallel). \quad (1.21)$$

$T_1$  is the time constant of this relaxation process. It is dependent on the magnetic field strength and material properties. The range of  $T_1$  in the human body at  $37^\circ\text{C}$  and  $B_0 = 1.5\text{ T}$  ranges from 50 (muscle) to 4500 ms (cerebrospinal fluid) [10].

Thus far, spins have been treated as noninteracting particles. This is a rough approximation, since every spin is exposed to not only the external magnetic field but also the magnetic moments of its immediate surroundings. These interactions overlay with  $\mathbf{B}_0$ , so that every spin experiences a magnetic field as a sum of those two contributions. Hence, if the field strength is variable in space,  $B = B(\mathbf{r})$ ,  $\omega$  will also become position-dependent. This implies that magnetization vectors precessing at different locations will dephase over time, thus diminishing the resultant transverse magnetization. This effect is characterized by a first-order differential equation

$$\frac{\partial \mathbf{M}_\perp}{\partial t} = -\frac{1}{T_2} \mathbf{M}_\perp, \quad (1.22)$$

which is solved by a real-valued exponential function

$$\mathbf{M}_\perp(t) = \mathbf{M}_\perp(0) \cdot e^{-\frac{t}{T_2}} \quad (1.23)$$

with time constant  $T_2$  characterizing the signal decay due to loss of coherence of the precession phase. Locally,  $T_2$  is an indicator of proton mobility. Mobile protons, such as

those in free water, traverse regions of increased and reduced field strength in relatively short time periods, so that opposing effects on the spin phase can partially cancel out, thus slowing signal decay and prolonging  $T_2$ . Stationary protons, on the other hand, are subject to the same magnetic environment for extended periods of time and are therefore less likely to experience cancellation of the effect. Regions of low proton mobility are therefore characterized by small  $T_2$  values.  $T_2$  depends on the magnetic field strength of the MR scanner, with higher field strengths leading to shorter  $T_2$ . At a given field strength, different types of biological tissue have characteristic  $T_2$  values (e.g., at 3 T: liver – 42 ms, skeletal muscle – 50 ms, white matter – 69 ms, gray matter – 99 ms, and blood – 275 ms [12]).

Inhomogeneity of the static field  $\mathbf{B}_0$  is another cause of signal dephasing. These deviations are caused by the magnetic material response of the tissue. The external field can be amplified or attenuated regionally, depending on the local susceptibility distribution inside the object. Interfaces (between organs or between an organ and air or fluid) and iron-rich regions induce abrupt spatial variation of susceptibility and therefore strongly affect the magnetic field. Spatial variation of  $\mathbf{B}_0$  leads to position-dependent precession frequencies, which have a similar effect as the aforementioned spin–spin interactions. The decay time constant due to  $\mathbf{B}_0$  inhomogeneity is denoted  $T_i$ . The compound effect of both dephasing mechanisms is quantified by  $T_2^* = \left(\frac{1}{T_2} + \frac{1}{T_i}\right)^{-1}$ , and the corresponding differential equation and its solution are given by

$$\frac{\partial \mathbf{M}_\perp}{\partial t} = -\frac{1}{T_2^*} \mathbf{M}_\perp \quad (1.24)$$

$$\text{and } \mathbf{M}_\perp(t) = \mathbf{M}_\perp(0) \cdot e^{-\frac{t}{T_2^*}}. \quad (1.25)$$

The decay of transverse magnetization due to dephasing is always faster than the restoration of longitudinal magnetization,  $T_2^* < T_2 < T_1$ . The effect of the inhomogeneity contribution  $T_i$  can be reversed through *spin echoes* (SE), which will be discussed in Section 1.5.1. In that case, the signal decays with the time constant  $T_2$  rather than the shorter  $T_2^*$ , yielding a stronger signal and hence better image quality. In NMR spectroscopy, the  $T_2$  or  $T_2^*$  decay curve is sampled, and its Fourier transform (a Lorentz curve) is analyzed as the signal of interest.

## 1.4 Bloch Equations

The precession of the transverse component of magnetization and the relaxation effects are combined in the Bloch equation:

$$\frac{d\mathbf{M}}{dt} = \gamma \mathbf{M} \times \mathbf{B} + \frac{1}{T_1} (M_0 - M_\parallel) \hat{\mathbf{z}} - \frac{1}{T_2} \mathbf{M}_\perp, \quad (1.26)$$

where  $\mathbf{B}$  is the total magnetic field, which can have contributions in addition to  $\mathbf{B}_0$ , but it is assumed that its deviation from the  $z$ -direction (the direction of  $\mathbf{B}_0$ ) is small.<sup>4</sup> In the

<sup>4</sup> Notable other contributions are magnetic field gradients, with a magnitude of typically tens of millitesla, the  $B_1$  field with a strength of tens of microtesla, and the chemical shift, which modulates the precession frequency by approximately 3.5 ppm (parts per million) between fat and water. All these contributions are therefore very small compared to the strength of the static  $B_0$  field of typically 1.5 or 3 T and do not change the direction of  $\mathbf{B}$  significantly.

absence of additional fields, that is, when  $\mathbf{B} = \mathbf{B}_0$ , the solution to the Bloch equation is given by [10]:

$$M_x(t) = \exp\left(-\frac{t}{T_2}\right) \cdot (M_x(0) \cdot \cos(\omega_0 t) + M_y(0) \cdot \sin(\omega_0 t)) \quad (1.27)$$

$$M_y(t) = \exp\left(-\frac{t}{T_2}\right) \cdot (M_y(0) \cdot \cos(\omega_0 t) - M_x(0) \cdot \sin(\omega_0 t)) \quad (1.28)$$

$$M_{\parallel}(t) = M_{\parallel}(0) \cdot \exp\left(-\frac{t}{T_1}\right) + M_0 \cdot \left(1 - \exp\left(-\frac{t}{T_1}\right)\right). \quad (1.29)$$

For the transverse components  $M_x$  and  $M_y$ , this represents a rotation about the  $z$ -axis with angular frequency  $\omega_0$  and exponentially decaying amplitude. The longitudinal component relaxes from its excited state  $M_{\parallel}(0)$  to the equilibrium value  $M_0$ . The three equations, (1.27)–(1.29), can be written equivalently in matrix form as follows:

$$\begin{pmatrix} M_x(t) \\ M_y(t) \\ M_{\parallel}(t) \end{pmatrix} = \begin{pmatrix} e^{-t/T_2} \cos(\omega_0 t) & e^{-t/T_2} \sin(\omega_0 t) & 0 \\ -e^{-t/T_2} \sin(\omega_0 t) & e^{-t/T_2} \cos(\omega_0 t) & 0 \\ 0 & 0 & e^{-t/T_1} \end{pmatrix} \begin{pmatrix} M_x(0) \\ M_y(0) \\ M_{\parallel}(0) \end{pmatrix} + \begin{pmatrix} 0 \\ 0 \\ M_0(1 - e^{-t/T_1}) \end{pmatrix}. \quad (1.30)$$

Additional  $B_1$  fields are used to induce magnetization flips, as explained in Section 1.2, usually as pulsed fields with a duration of a few milliseconds. For most imaging applications, it is sufficient to assume the flips to be instantaneous, so that Eqs. (1.27)–(1.29) (or Eq. (1.30)) can be used to describe the situation before and after the pulse, with an abrupt change of  $M_x$ ,  $M_y$ ,  $M_{\parallel}$  (and potentially the precession phase) in between.

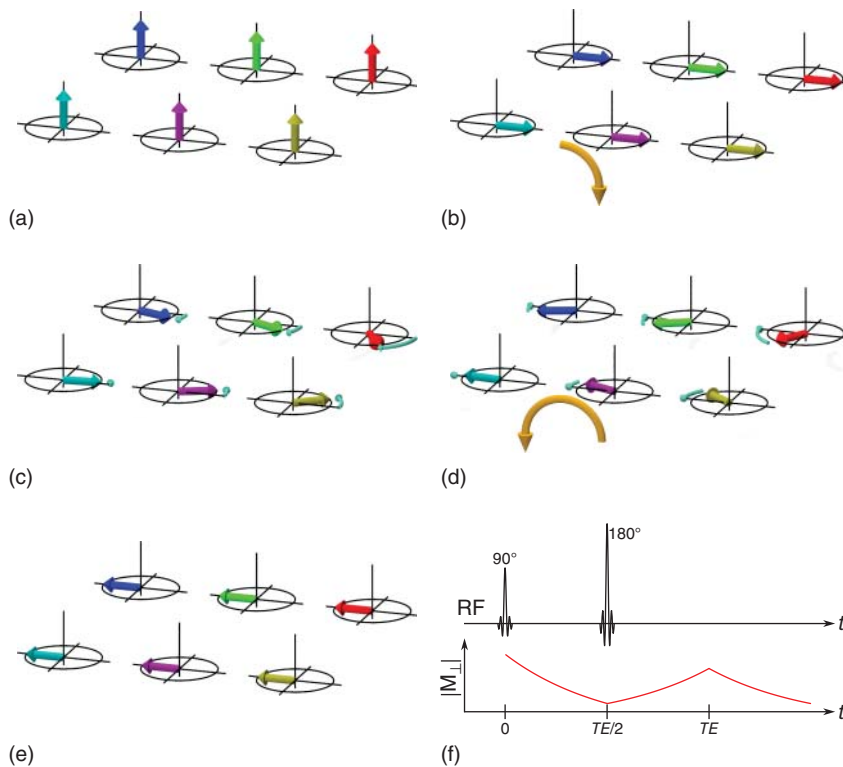
Maxwell's equations state that time-varying magnetic fields are always accompanied by an electric field, thus forming an electromagnetic field. Due to its frequencies of 63 and 126 MHz on 1.5- and 3-T MR scanners, respectively, a pulsed electromagnetic field is referred to as a *radiofrequency* (RF) pulse.

## 1.5 Echoes

Thus far, we have seen how RF pulses can be used to flip the magnetization coherently from the  $z$ -axis into the  $xy$ -plane to generate a measurable MR signal. However, due to relaxation effects, the signal amplitude will decrease exponentially as the transverse magnetization dephases. The signal following immediately after an excitation pulse is called *free induction decay* (FID), and its decay constant is  $T_2^*$ , the shortest of the three relaxation constants  $T_1$ ,  $T_2$ , and  $T_2^*$ . *Spin echoes* and *gradient echoes* are two mechanisms that allow one to modulate and partially recover these signal losses. In the following sections, we will explain the underlying principles.

### 1.5.1 Spin Echoes

Spin echoes deploy a  $180^\circ$  RF-pulse to reverse the dephasing of the in-plane magnetization after an excitation. The process is illustrated in Figure 1.3.



**Figure 1.3** Illustration of the spin-echo principle, from the rotating-frame perspective. The arrows correspond to six isochromats at different positions within the imaging plane with different precession frequencies. The direction of the static magnetic field is upward. (a) Equilibrium. (b) Excitation ( $90^\circ$  pulse). (c) Free precession. (d)  $180^\circ$  pulse. (e) Echo formation. (f) Timing diagram.

Each arrow in Figure 1.3 represents the magnetization of an isochromat (ensemble of spins with the same precession frequency) at different positions in the imaging plane. The precession frequencies of the isochromats are distinct from one another due to deviations of the magnetic field strength caused by susceptibility effects or  $B_0$  inhomogeneity. Initially, all isochromats are in thermal equilibrium and their magnetic moments are aligned with the magnetic field along the  $z$ -axis (Figure 1.3a). An RF pulse is irradiated (shown as a  $90^\circ$  pulse, but arbitrary flip angles are possible) and generates transverse magnetization. Directly after the pulse, the magnetization vectors of all isochromats are in phase (b). The isochromats start to precess about the direction of the magnetic field at their individual precession frequencies  $\omega_p(x, y)$ , indicated by the length of the circular arrows. After a certain time  $t = TE/2$  of free precession, the magnetization vectors have dephased, so that their vector sum  $|\mathbf{M}_\perp|$  is smaller than after the initial RF pulse (c). Next, a  $180^\circ$  pulse is deployed, which flips the in-plane magnetization (d). During the next  $TE/2$  interval, the isochromats continue to precess freely at their individual precession frequencies  $\omega_p(x, y)$ . Finally, at time  $t = TE$  after the excitation pulse, all isochromats are realigned, so that their magnetization vectors add up to maximum amplitude, causing a peak in the recorded MR signal.  $TE$  is referred to as *echo time*.

The refocusing pulse can only reverse the effect of spatially dependent precession frequencies due to magnetic field inhomogeneities. As explained in Section 1.3, interactions between spins lead to longitudinal ( $T_1$ ) and transverse ( $T_2$ ) relaxation and cause additional decoherence and hence reduce the magnitude of the transverse magnetization over time. If  $TE$  is short compared to  $T_1$ , such that  $T_1$  relaxation during signal evolution is negligible (which is a realistic assumption for most pulse sequences), the echo amplitude can be approximated by  $|S_0| \propto |\mathbf{M}_\perp(TE)| \approx |\mathbf{M}_\perp(0)| \cdot \exp(-TE/T_2)$ .

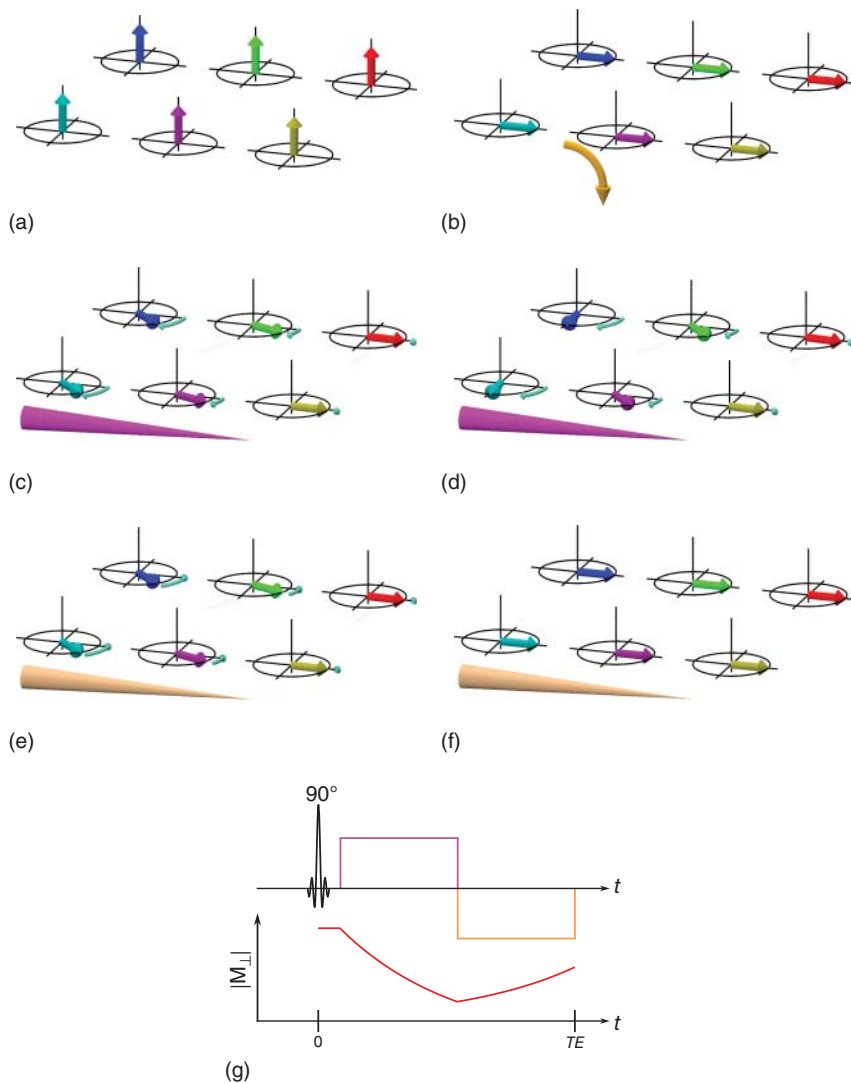
### 1.5.2 Gradient Echoes

Gradient echoes use a pair of dephaser–rephaser gradients rather than a refocusing pulse to generate an MRI echo signal. The working principle is illustrated in Figure 1.4. As in the case of a spin echo, the equilibrium longitudinal magnetization (a) is fully or partially flipped into the transverse plane by an RF pulse of arbitrary flip angle (b). Next, a dephasing gradient (see Section 1.6.1) is applied along the readout axis (indicated by the purple cone), imposing precession frequency dispersion along that axis (c)–(d). The vector sum  $|\mathbf{M}_\perp|$  of the precessing magnetization thus decreases. Eventually, the dephasing gradient polarity is reversed (e), indicated by the changed color of the cone. For every isochromat, the amplitude of the gradient-induced field strength modulation is constant, but the sign changes. Spins that initially experience a strong positive field offset due to the dephaser gradient subsequently experience a strong negative field offset. This affects the local precession frequency (in the rotating frame) in the same way; rapidly precessing spins continue to precess rapidly, but the precession direction is inverted. Finally, the rephasing gradient eliminates the effect of the dephasing gradient (at the instance for which the area under the rephaser gradient waveform is equal to the area under the dephaser) and  $|\mathbf{M}_\perp|$  is maximized.

Spatial modulation of the precession frequency due to  $B_0$  field inhomogeneity was neglected in Figure 1.4. However, this introduces an additional contribution to spin dephasing and cannot be compensated for by the rephasing gradient. Therefore, in contrast to a spin echo sequence, where decay of the echo amplitude is primarily governed by  $T_2$ , the gradient echo amplitude reduces as  $|\mathbf{M}_\perp(TE)| = |\mathbf{M}_\perp(0)| \cdot \exp(-TE/T_2^*)$ , with  $T_2^* < T_2$  (see Section 1.3). For a fixed  $TE$ , the gradient echo will thus have lower signal amplitude (and hence lower signal-to-noise ratio) than a spin echo.

## 1.6 Magnetic Resonance Imaging

The previous sections have described how the NMR effect can be used to generate and manipulate a signal from an ensemble of spins in a magnetic field. This mechanism is sufficient to obtain time-resolved spectra that provide information on relaxation times and chemical compounds contained in a sample. However, the methods introduced so far can only access global properties of an object – we have not yet described how to associate a signal with its position of origin, which is the prerequisite for any imaging modality. In this section, we will therefore explain a process for encoding spatial information in the MR signal and demonstrate how this information can be used to convert a signal into an image. We will then look into different data sampling strategies and finally present some methods for accelerating the imaging process.



**Figure 1.4** Illustration of the gradient echo principle, from the rotating-frame perspective. The arrows correspond to six isochromats with different precession frequencies at different positions within the imaging plane. The direction of the static magnetic field is upward. The cone indicates direction and polarity of the gradient. Further explanations are given in the text. (a) Equilibrium. (b) Excitation ( $90^\circ$  pulse). (c) Dephasing gradient. (d) Dephasing gradient. (e) Rephasing gradient. (f) Echo formation. (g) Timing diagram.

### 1.6.1 Spatial Encoding

Mathematically, an image can be described as a discrete two-dimensional signal, where each pixel can be assigned a unique position in space. In order to generate images from the voltage induced by the precessing transverse magnetization in receive coils, it is necessary to establish a mechanism for spatial encoding of information. The received



signal  $S(t)$  can then be interpreted as a superposition of the signals from isochromats (ensembles of spins with the same precession frequency) at different locations, and image reconstruction comprises the decomposition of this compound signal into spatially resolved information.

Three distinct steps are carried out to achieve spatial encoding in three-dimensional space. Each of them requires the application of a *gradient* field. Gradients generate a magnetic field parallel to the  $z$ -axis, with the magnitude being linearly dependent on one coordinate:

$$\mathbf{B}(x, y, z) = G_x x \cdot \hat{\mathbf{z}} \quad (1.31)$$

for an  $x$ -gradient with amplitude  $G_x$ , and analogously for  $y$  and  $z$ . These magnetic fields add to  $\mathbf{B}_0$ , so that the resultant magnetic field becomes

$$\mathbf{B}(x, y, z) = (B_0 + G_x x + G_y y + G_z z)\hat{\mathbf{z}}. \quad (1.32)$$

Sequential application of three orthogonal gradients leads to three-dimensional spatial encoding of the MRI signal.

#### 1.6.1.1 Slice Selection

As described in Section 1.2, a transverse rotating magnetic field  $\mathbf{B}_1$  can be used to tilt magnetization away from its longitudinal equilibrium state and into precessing transverse magnetization. This only works if the rotation frequency  $\omega$  of  $\mathbf{B}_1$  matches the spin precession frequency  $\omega_p$ . Assuming that a  $z$ -gradient field is active while the  $\mathbf{B}_1$ -pulse is applied,  $\omega_p$  becomes position-dependent<sup>5</sup>:

$$\omega_p(x, y, z) = \gamma B(x, y, z) = \gamma(B_0 + G_z \cdot z). \quad (1.33)$$

This implies that  $\mathbf{B}_1$  can only flip spins at the  $z$ -location  $z_0$  for which the resonance condition is fulfilled, that is, where  $\omega_p(x, y, z_0) = \omega$ . If, instead of being monofrequent,  $\mathbf{B}_1$  is designed to be a superposition of precession frequencies with equal amplitudes over a frequency range  $(\omega - \delta, \omega + \delta)$ , it will flip all spins in the range  $(z_0 - \Delta z, z_0 + \Delta z)$  with  $\Delta z = \frac{\delta}{\gamma G_z}$ . A waveform with uniform amplitude over the interval  $(\omega - \delta, \omega + \delta)$ , constituting a rectangular pulse in frequency space, corresponds to a sinc<sup>6</sup> in the time domain. Hence, a combination of a *slice-select* gradient and a sinc-shaped  $\mathbf{B}_1$ -pulse can be used to excite only the spins within a slice of arbitrary orientation and thickness. This process is called *slice selection* (SS).

#### 1.6.1.2 Phase Encoding

*Phase encoding* (PE)<sup>7</sup> is the first of two in-plane spatial encoding steps following slice-selective excitation. A phase-encoding gradient,  $\mathbf{G}_{PE}$ , is turned on for a limited time  $T_{PE}$ . Its direction lies in the imaging plane, perpendicular to the slice-select gradient. This introduces in-plane dispersion of the precession frequency along the direction of the gradient. Let us assume that the magnetization is excited in such a

<sup>5</sup>  $B_1$  is about three orders of magnitude smaller than typical gradients, and five to six orders of magnitude smaller than  $B_0$ ; therefore, its effect on the resonance frequency is negligible.

<sup>6</sup>  $\text{sinc}(t) = \frac{\sin(t)}{t}$ .

<sup>7</sup> PE in the context of MRI is not related to a technique of the same name used for digital data transmission, also known as Manchester coding.

way that it has zero phase offset in the rotating reference frame after excitation. For simplicity, we will assume further that the imaging plane corresponds to the  $xy$ -plane (i.e., SS along the  $z$ -axis) and that the phase-encoding direction coincides with the  $y$ -axis,  $\mathbf{G}_{\text{PE}} = G_{\text{PE}} \cdot \hat{\mathbf{y}}$ . After application of the phase-encode gradient pulse, the offset phase is given by

$$\begin{aligned}\phi(\mathbf{r}) &= \mathbf{r} \bullet \left( \gamma \int_0^{T_{\text{PE}}} (\mathbf{B}(x, y, z, t) - \mathbf{B}_0) dt \right) \\ &= \gamma \int_0^{T_{\text{PE}}} \mathbf{r} \bullet (G_{\text{PE}} \cdot \hat{\mathbf{y}}) dt \\ &= \gamma \cdot G_{\text{PE}} \cdot y \cdot T_{\text{PE}}.\end{aligned}\quad (1.34)$$

This implies that the  $y$ -position of a previously excited spin is now encoded in its precession phase.

### 1.6.1.3 Frequency Encoding

The second in-plane encoding axis is referred to as *frequency encoding* or *readout (RO)* direction. After PE, a readout gradient  $\mathbf{G}_{\text{RO}}$ , perpendicular to the slice selection and phase-encoding directions, is applied while the MR signal is sampled by means of an analog-to-digital converter (ADC) connected to the receive coil(s).<sup>8</sup> If the frequency-encoding axis coincides with the  $x$ -axis and  $t = 0$  denotes the time at which  $\mathbf{G}_{\text{RO}}$  is switched on, phase evolution can be expressed as

$$\phi(x, y, z, t) = \gamma(G_{\text{PE}} \cdot y \cdot T_{\text{PE}} + G_{\text{RO}} \cdot x \cdot t). \quad (1.35)$$

The receive coil will “see” this signal (after quadrature detection) as a superposition of all individual signals averaged over space:

$$\tilde{S}(t) = \iiint_{z_0 - \Delta z}^{z_0 + \Delta z} S_0(x, y, z) \cdot \exp(i\phi(x, y, z, t)) dz dy dx, \quad (1.36)$$

where  $S_0(x, y, z)$  is the magnitude of the signal emitted at location  $\mathbf{r} = (x, y, z)$ . If we use  $\phi$  from Eq. (1.35) and substitute  $k_y = \gamma \cdot G_{\text{PE}} \cdot T_{\text{PE}}$  and  $k_x(t) = \gamma \cdot G_{\text{RO}} \cdot t$ , this can be rewritten as

$$\tilde{S}(k_x, k_y) = \iiint_{z_0 - \Delta z}^{z_0 + \Delta z} S_0(x, y, z) \cdot \exp(i(k_x \cdot x + k_y \cdot y)) dz dy dx, \quad (1.37)$$

which is the 2D Fourier transform of the in-plane magnetization (averaged over slice thickness  $2 \cdot \Delta z$  along the  $z$ -direction). This means that  $S_0(x, y, z)$  can be recovered from the signal  $\tilde{S}(k_x, k_y)$  if sufficient data points in  $k$ -space, spanned by unit vectors  $\hat{\mathbf{k}}_x$  and  $\hat{\mathbf{k}}_y$ , are sampled and then subjected to a discrete inverse 2D Fourier transform. Since  $k_x$  is explicitly time-dependent by definition, a line in  $k$ -space with fixed  $k_y$  can be sampled by recording the MR signal over time, while the readout gradient is switched on.  $k_y$  is defined by the area under the phase-encoding gradient waveform prior to signal readout, determined by its amplitude  $G_{\text{PE}}$  and duration  $T_{\text{PE}}$ . Different lines in

<sup>8</sup> Most modern MRI scanners use arrays of receive coils, rather than a single coil. Smaller coils, embedded in a flexible mat or a rigid assembly, can be positioned closer to the object of interest than a single larger coil, enabling increased signal quality. Furthermore, parallel imaging (see Section 2.3.3) requires multiple coils with different spatial sensitivity profiles.

$k$ -space can therefore be acquired sequentially by changing the product  $G_{\text{PE}} \cdot T_{\text{PE}}$ . A more elaborate method for sampling an entire  $k$ -space with a single excitation will be discussed in Section 2.2.2.

If readout of a  $k$ -space line were started immediately after the excitation of a transverse magnetization component,  $T_2^*$  relaxation would cause the signal amplitude to drop continuously along that line so that the amplitude at one end of the line would be larger than that at the opposite end. This asymmetry would inevitably cause image artifacts after Fourier transform. One technique to overcome such issues is to refocus the signal so that its amplitude reaches a local maximum at a certain time  $TE$  after excitation. The local signal maximum is called an *echo*, and the interval  $TE$  between the excitation and the echo is referred to as *echo time*. If readout is performed symmetrically around the echo, so that the first half of the  $k$ -space line is sampled on the rising slope of the signal envelope and the second half on the falling slope, the signal amplitude is distributed symmetrically over the line (see Figure 2.4 for an example).

## 2

## Imaging Concepts

2.1  $k$ -Space

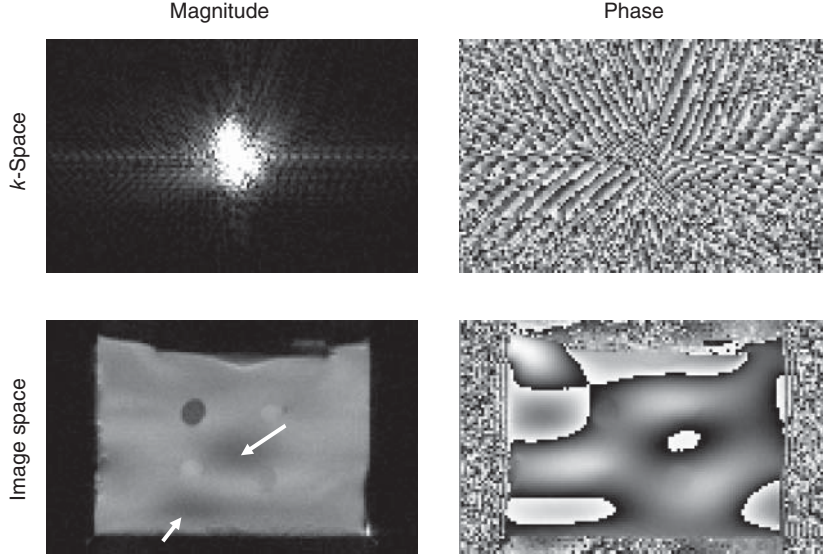
It was mentioned earlier that the acquired signal in MRI is the  $k$ -space representation of the spatial distribution of transverse magnetization (see Eq. (1.37)). The MRI data acquisition process consists of filling  $k$ -space line by line, and then an image is calculated from the complete  $k$ -space. We will now look at the image reconstruction process and discuss some relationships between acquisition parameters in  $k$ -space and the corresponding parameters of the reconstructed images.

$k$ -Space is a two- (representing a single image slice) or three-dimensional (representing a volume to be reconstructed into multiple slices) discrete space equipped with an orthogonal coordinate system. The coordinates are typically referred to as  $k_x$ ,  $k_y$ , and  $k_z$  (hence the name).<sup>1</sup> Alternatively, to draw the connection to MR image acquisition, the axes can also be labeled in terms of readout (RO) and phase-encode (PE) directions, as we will do below. For Cartesian imaging techniques,  $k$ -space points are sampled on a rectilinear grid, whereas non-Cartesian MR acquisition schemes sample data points on a curvilinear or irregular grid. Each data point in  $k$ -space is a complex number. Points that are close to the center of  $k$ -space represent low spatial frequencies, corresponding to the coarse structure of the image. Higher spatial frequencies are encoded in the periphery of  $k$ -space and capture small details, which ultimately define the image resolution.

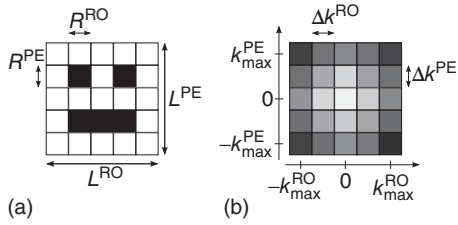
In the simplest case, image reconstruction is carried out by applying an inverse discrete Fourier transform (DFT) to the  $k$ -space data. Since  $k$ -space can be either two-dimensional or three-dimensional, the appropriately dimensioned version of the DFT has to be used. In general, one-dimensional DFTs can be performed along all spatial dimensions successively. A fast Fourier transform (FFT) algorithm is most commonly chosen because of its speed and ubiquity. An example is presented in Figure 2.1, where magnitude and phase of both  $k$ -space and image space are shown for a 2D data set.

The *Nyquist–Shannon sampling theorem* establishes a correlation between the size and resolution of an MR image and the geometric parameters of the corresponding  $k$ -space [10]. Let  $L^{\text{PE}}$  and  $L^{\text{RO}}$  denote the size of the image along the PE and RO axes, respectively, and  $R^{\text{PE}}$  and  $R^{\text{RO}}$  the spatial resolution in the image, that is, the distance between the centers of adjacent pixels or voxels. The Nyquist–Shannon theorem states

<sup>1</sup>  $k$  is the classical symbol for wave number.



**Figure 2.1** Example of MRI image of an agarose gel phantom with two soft and two hard inclusions, in  $k$ -space and image space representation. The conversion between the two representations can be achieved by a two-dimensional Fourier transform. The white arrows in the lower left image indicate signal cancellation due to intra-voxel phase dispersion (see Section 3.2), caused by excessive vibration amplitudes. The inclusions are visible in the magnitude image as bright and dark disks. The phase image is affected by phase wraps, which would have to be removed by unwrapping before further processing.



**Figure 2.2** An image (a) and its associated  $k$ -space (b) with the relevant parameters. The RO and PE axes are horizontal and vertical, respectively, as commonly found in MRI literature.  $R$  represents the pixel spacing (resolution),  $L$  the spatial extent of the image,  $\Delta k$  the distance between adjacent points in  $k$ -space, and  $k_{\max}$  identifies the corners of  $k$ -space.

that

$$k_{\max}^{\text{PE}} = \frac{1}{2 \cdot R^{\text{PE}}} \quad (2.1)$$

$$k_{\max}^{\text{RO}} = \frac{1}{2 \cdot R^{\text{RO}}} \quad (2.2)$$

$$\Delta k^{\text{PE}} = \frac{1}{L^{\text{PE}}} \quad (2.3)$$

$$\Delta k^{\text{RO}} = \frac{1}{L^{\text{RO}}}, \quad (2.4)$$

where  $k_{\max}^{\text{PE}}$  and  $k_{\max}^{\text{RO}}$  designate the coordinates of the corner points of the acquired  $k$ -space and  $\Delta k^{\text{PE}}$  and  $\Delta k^{\text{RO}}$  represent the distance between adjacent sample points in  $k$ -space. A graphical illustration of these parameters is presented in Figure 2.2.

The total number of pixels in the image can be calculated as

$$N_{\text{pixels}} = \frac{L^{\text{RO}}}{R^{\text{RO}}} \cdot \frac{L^{\text{PE}}}{R^{\text{PE}}}. \quad (2.5)$$

In *k*-space, PE lines are sampled between  $-k_{\text{max}}^{\text{PE}}$  and  $+k_{\text{max}}^{\text{PE}}$  in steps of  $\Delta k^{\text{PE}}$ . The total number of PE lines is therefore

$$N_{\text{lines}} = \frac{2 \cdot k_{\text{max}}^{\text{PE}}}{\Delta k^{\text{PE}}} = \frac{2 \cdot \frac{1}{2 \cdot R^{\text{PE}}}}{\frac{1}{L^{\text{PE}}}} = \frac{L^{\text{PE}}}{R^{\text{PE}}}. \quad (2.6)$$

The number of sample points in each PE line is given by

$$N_{\text{RO}} = \frac{2 \cdot k_{\text{max}}^{\text{RO}}}{\Delta k^{\text{RO}}} = \frac{2 \cdot \frac{1}{2 \cdot R^{\text{RO}}}}{\frac{1}{L^{\text{RO}}}} = \frac{L^{\text{RO}}}{R^{\text{RO}}}. \quad (2.7)$$

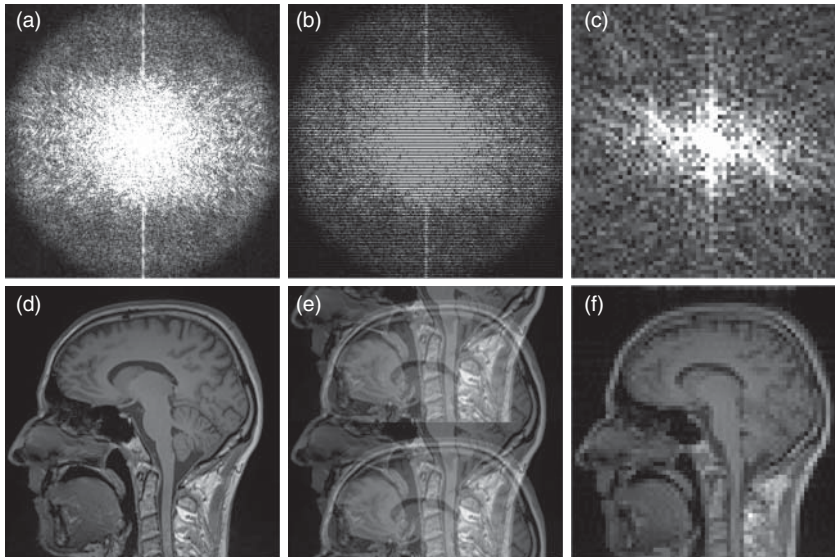
The total number of sample points in the full *k*-space is therefore

$$N_{\text{sample points}} = \frac{L^{\text{RO}}}{R^{\text{RO}}} \cdot \frac{L^{\text{PE}}}{R^{\text{PE}}} = N_{\text{pixels}}. \quad (2.8)$$

Thus, Eqs. (2.1)–(2.4) imply that the number of data points is the same in the image and its associated *k*-space. This fact can also be understood from a different perspective: DFT is a unitary operation; therefore, information is neither gained nor lost during transformation, maintaining the number of data points.

Violating Eqs. (2.1) and (2.2) will reduce image resolution, whereas breaching Eqs. (2.3) and (2.4) effectively decreases the field of view (FOV) and leads to fold-in (aliasing) of all objects that are located outside the FOV (Figure 2.3). Along the RO axis, band-pass filtering of the raw MR signal can suppress these fold-ins. Along the PE axis, care has to be taken to ensure that the object does not exceed the FOV, since there is no easy fix for this type of fold-ins.

Image size and resolution along the RO and PE axes are in principle mutually independent; however, for the sake of simplicity, let us assume that they are equal – which is not an uncommon situation at all – and hence drop the indices PE and RO. For an image with a size of  $N \times N$  pixels,  $N \times N$  data points have to be sampled in *k*-space. While readout of a single line in *k*-space is usually a fast process that only takes few milliseconds, each *k*-space line requires its own phase-encoding step. In highly segmented sequences, such as FLASH, each readout requires its own excitation pulse, such that the total acquisition time is proportional to the number of *k*-space lines. In other sequences, such as EPI, where several or all lines are acquired in one readout train following a single excitation pulse, the total acquisition time is only weakly affected by the number of *k*-space lines, whereas the echo time is approximately proportional to that number. Long echo times render the sequence more sensitive to signal relaxation (governed by either  $T_2$  or  $T_2^*$ , depending on the type of pulse sequence), resulting in a poorer signal-to-noise ratio (SNR). In summary, an excessive number of PE lines either increases total acquisition time or decreases image quality. Therefore, various strategies to decrease the number of necessary *k*-space lines without severe penalties have been conceived and will be presented in this chapter. These strategies are collectively referred to as *fast imaging*.



**Figure 2.3** Illustration of  $k$ -space artefacts occurring when the Nyquist–Shannon theorem is violated. (a,d)  $k$ -Space (magnitude) and image space representation of a fully sampled ( $256 \times 256$ )  $T_1$ -weighted MRI scan. In (b), every second line in  $k$ -space was set to zero (simulating exclusion of these lines from data acquisition). According to Eq. (2.3), this halves the field of view (FOV) in the direction of the skipped lines. Since the object is larger than the reduced FOV, ghosting occurs, as shown in (e). In (c), only the central  $64 \times 64$   $k$ -space points were used for image reconstruction. The resulting image (f) has reduced resolution, as predicted by Eqs. (2.1) and (2.2).

## 2.2 $k$ -Space Sampling Strategies

Despite a plethora of different MR pulse sequences – EPI, RARE, HASTE, TSE, MP-RAGE to name a few – imaging in general can be understood as a modular procedure including at least the following steps:

- 1) *Excitation*: Creation of transverse magnetization through application of one or more radiofrequency (RF) pulses. This step usually includes the slice selection process discussed above. For more sophisticated imaging techniques, it can also include saturation pulses to selectively suppress certain types of tissue (e.g., fat, blood, or free water). However, these applications are beyond the scope of this book, and we refer to the literature [10, 11] for further information.
- 2) *Signal manipulation*: This part of image generation can include additional RF pulses, gradients, and delays for manipulation of longitudinal or transverse magnetization. The  $180^\circ$  pulse of a spin-echo sequence and the dephasing gradient of a gradient-echo sequence are typical examples. In more specialized scenarios, motion sensitization (for magnetic resonance elastography (MRE) or diffusion-sensitive imaging) can be performed here through the addition of appropriate gradient waveforms. The phase-encoding step can be part of either this step or the following one.
- 3) *Readout*: The final step is sampling of the MR signal. Different strategies exist, from the collection of a single  $k$ -space point per excitation pulse to the acquisition of an entire  $k$ -space in a single-shot sequence. This component can include the PE gradient (if it is not part of the second step), and it has to include the RO gradient.

The first two steps can be understood with the concepts already discussed. In the following section, we will concentrate on the third step. The basis for virtually all MRI experiments is Eq. (1.37), that is, the fact that a fully sampled *k*-space can be converted into an image by means of an inverse Fourier transform. However, there are many different strategies of filling *k*-space.

The simplest case comprises the acquisition of a single *k*-space line for each excitation pulse. The line to be acquired is determined by the area under the phase-encoding gradient before signal readout. Signal sampling in the presence of the RO gradient introduces frequency dispersion along the RO axis, as explained in Section 1.6.1.3. Let us assume that the size of the final image along the RO axis is  $L_x$ . Two pixels from opposite ends of the image are then separated by frequency  $\delta\nu = \frac{1}{2\pi} \gamma G_{\text{RO}} \cdot L_x$ , where  $G_{\text{RO}}$  is the amplitude of the RO gradient. The quantity  $\delta\nu$  is called the *bandwidth*.  $\delta\nu$  is the largest frequency that has to be resolved to reconstruct the image. According to the Nyquist–Shannon theorem, the signal has to be sampled in steps of  $\delta t = \frac{1}{2\delta\nu}$ .  $\delta t$  is usually referred to as *dwell time* or the sampling time per data point.

Increasing the bandwidth – by increasing RO gradient amplitude  $G_{\text{RO}}$  – leads to a larger spectral separation of signals from adjacent voxels. At the same time, the dwell time decreases so that individual *k*-space line can be sampled faster. However, reducing data acquisition time has a negative impact on the SNR, as will be shown in Section 2.3.4.

### 2.2.1 Segmented Image Acquisition

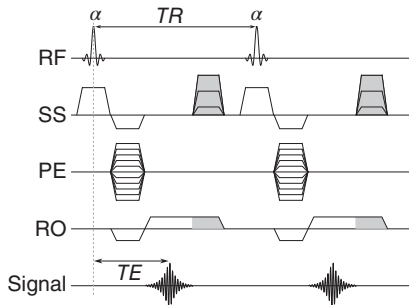
In general, segmented acquisition refers to a sampling strategy that requires several excitation→readout cycles for acquiring a full *k*-space. There are numerous concepts for partitioning *k*-space; however, we will concentrate in the following chapter on the most common one, which involves the acquisition of a single line (one phase-encoding step) after each excitation.

#### 2.2.1.1 Fast Low-Angle Shot (FLASH)

FLASH [13] (fast low-angle shot<sup>2</sup>) is a spoiled and segmented gradient-echo sequence. In general, each repetition of the acquisition loop shown in Figure 2.4 acquires one line in *k*-space, each time with a different PE gradient, illustrated by the superimposed PE gradient shapes. Very short echo times and repetition times (on the order of 10 ms) can be achieved. With a 90° excitation pulse, this would cause problems, since  $T_1$  is much shorter than  $TR$ , so that there is hardly any longitudinal magnetization when the second RF pulse is applied. As a remedy, much smaller flip angles – on the order of 15° – are used. Those low-angle RF pulses do not flip the entire longitudinal magnetization  $M_{\parallel}$  into the transverse plane, but only the fraction  $M_{\parallel} \cdot \sin(\alpha)$ , while the complementary portion,  $M_{\parallel} \cdot \cos(\alpha)$ , remains on the longitudinal axis. Hence, for  $\alpha = 15^\circ$ , each RF pulse flips about 26% of the available longitudinal magnetization into the transverse plane. During each  $TR$  interval, a certain amount of transverse magnetization relaxes back to the longitudinal orientation. After a number of repetitions (typically 20–40), an equilibrium is reached, in which the amount of magnetization that is flipped by each pulse is equal to the amount of longitudinal magnetization that relaxes between RF pulses. This *steady state* guarantees that the signal intensity is the same for all acquired

<sup>2</sup> FLASH is the name used in the original publication. SPGR and T1-FFE are alternate names for this sequence.





**Figure 2.4** Timing diagram of a FLASH pulse sequence, according to [14]. Two iterations of the acquisition loop are shown; in practice, one repetition is required for each PE line. Spoiler gradients are shaded in gray. The superimposed PE gradients indicate that a different gradient is used in each iteration; the same holds true for the slice-select spoiler gradient. Abbreviations: SS – slice-selection gradient, PE – phase-encoding gradient, RO – readout gradient, RF – radiofrequency pulses,  $TE$  – echo time.

$k$ -space lines. This technique removes the need to wait for full recovery of longitudinal magnetization after each excitation, and hence accelerates the imaging process significantly.<sup>3</sup> The flip angle that maximizes transverse magnetization in the steady state is called *Ernst angle*, which can be calculated as [11]

$$\alpha_E = \arccos(e^{-TR/T_1}). \quad (2.9)$$

RF pulses do not only convert longitudinal into transverse magnetization, they also have an effect on the existing transverse magnetization. Here, the analysis is more complicated, since the effect of an RF pulse on transverse magnetization depends not only on the flip angle but also on the phase of the pulse relative to the phase of the precessing magnetization. Three or more pulses in quick succession can generate a number of additional echoes (*stimulated echoes* or *Hahn echoes* [10], which are beyond the scope of this book) that can interfere with signal acquisition. In order to circumvent this issue, FLASH employs a process called *gradient spoiling*. Spoiler gradients are shaded in gray in Figure 2.4. They are used to deliberately dephase transverse magnetization with the goal of minimizing (or, ideally, nulling) the resultant transverse magnetization vector. Any subsequent RF pulse will then “see” only the longitudinal magnetization. In each repetition of the acquisition loop, a slice-select spoiler gradient with a different amplitude is deployed to prevent coherent buildup of remaining transverse magnetization due to imperfect spoiling.

The scheme shown in Figure 2.4 represents the basic implementation of a FLASH pulse sequence. If the sequence is used for MRE, additional motion-encoding gradients (MEGs) are required to detect induced tissue vibration. This can easily be done by inserting an appropriate MEG (see Section 3.1) waveform between the slice-select and PE gradients; however, doing so will increase both the echo time and repetition time.

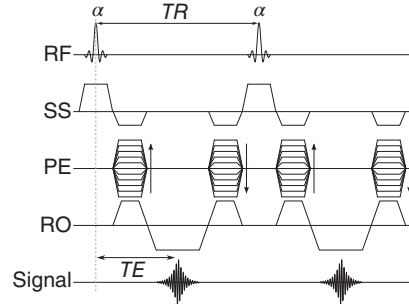
#### 2.2.1.2 Balanced Steady-State Free Precession (bSSFP)

*Balanced steady-state free precession* (bSSFP<sup>4</sup>) [15] is an alternative steady-state imaging strategy. It is very similar to FLASH; a sequence diagram is presented in Figure 2.5. In contrast to FLASH, the gradients on each axis are fully balanced for each loop iteration, preventing spoiling of transverse magnetization. Instead, the RF pulses are deployed in such a way that part of the remaining longitudinal magnetization can contribute to

<sup>3</sup> As a rule of thumb, the longitudinal equilibrium magnetization is reached after  $5 \cdot T_1$  in the case of a  $90^\circ$  pulse.

<sup>4</sup> Also known as BFFE, FIESTA, and True FISP.

**Figure 2.5** Two repetitions of the acquisition loop of a balanced steady-state free precession (bSSFP) sequence, according to [14]. Gradients along all three axes are balanced for each  $TR$  interval. The vertical arrows along the PE axis indicate that the PE gradient and its rewinder are of equal magnitude but opposite polarity. For a list of abbreviations, see Figure 2.4.



the steady state, thus leading to potentially higher signal amplitudes than with use of a FLASH sequence. If all RF pulses have the same phase in the rotating reference frame and are orthogonal to the in-plane magnetization, then each pulse has two effects:

- 1) Flipping longitudinal magnetization into the transverse plane.
- 2) Flipping part of the transverse magnetization onto the negative longitudinal axis.

If the increase in transverse magnetization per RF pulse due to the first effect is larger than the decrease in transverse magnetization due to the second effect, the overall signal amplitude is larger than for a FLASH sequence, which annihilates the remaining transverse magnetization component prior to each RF pulse.

However, the situation becomes much more complicated if the pulses (and hence the axis about which the magnetization is flipped) are not orthogonal to the transverse magnetization. In this case, the flipping effect of a pulse has to be decomposed into two components. While part of the transverse magnetization is again flipped onto the negative axis, the remaining in-plane component is then rotated by a certain angle in the transverse plane so that the phase of the transverse magnetization changes. Over a series of several RF pulses, this leads to the generation of complex magnetization patterns, including all sorts of Hahn echoes and stimulated echoes that will interfere with data acquisition.

Let us imagine that there is a linear gradient  $\mathbf{g}$  of the static magnetic field, due to  $B_0$  inhomogeneities or improper shimming, such that

$$\mathbf{B}(\mathbf{r}) = (B_0 + \delta B(\mathbf{r})) \cdot \hat{\mathbf{e}}_z \quad (2.10)$$

$$\delta B(\mathbf{r}) = \mathbf{r} \cdot \mathbf{g}. \quad (2.11)$$

The modulation of  $\mathbf{B}$  induces a position-dependent shift  $\delta\omega(\mathbf{r}) = \gamma \mathbf{r} \cdot \mathbf{g}$  of the spin resonance frequency. Therefore, if the initial RF pulse excites all spins with a common phase  $\Psi_0$ , then the phase distribution at the beginning of the next pulse,  $TR$  later, will be

$$\Psi(TR) = \Psi_0 + \delta\omega \cdot TR = \Psi_0 + \gamma \mathbf{r} \cdot \mathbf{g}. \quad (2.12)$$

Note that the right-hand side of Eq. (2.12) depends explicitly on the position  $\mathbf{r}$  of the spin so that the phase of the magnetization is not homogeneous throughout the object. This means that it is not possible to apply an RF pulse that has the same phase, relative to the magnetization, at all positions within the imaging plane.<sup>5</sup> Therefore, the steady-state

<sup>5</sup> This is the case when a single-channel RF transmit system is used. Multichannel excitation, using several independent transmit coils, can be employed to generate spatially varying  $B_1$  fields, but this is beyond the scope of this book.

magnetization will vary across the object, giving rise to inhomogeneous image intensity. Reference [16] contains a comprehensive mathematical treatment of this phenomenon. In summary, a gradient  $\mathbf{g}$  imposes a periodic intensity modulation with period

$$\lambda = \frac{1}{\gamma \cdot g \cdot TR}, \quad (2.13)$$

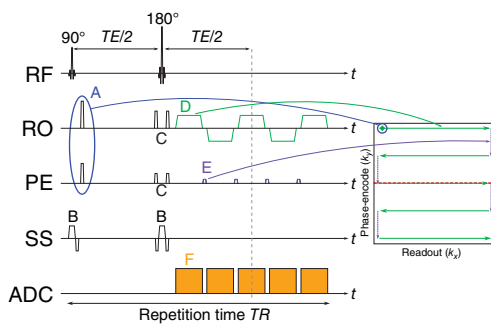
which manifests itself as a pattern of bright and dark stripes perpendicular to  $\mathbf{g}$  (*banding*). An example of banding is shown in the top right image of Figure 3.9. Since bSSFP was used as the basis for MRE in the past [17–19], its specific properties when used for harmonic motion detection will be discussed in Section 3.4.2.

### 2.2.2 Echo-Planar Imaging (EPI)

Echo-planar imaging (EPI, [20]) is an extremely fast MR imaging strategy that allows acquisition of an entire 2D image with a single RF excitation. In contrast to other techniques that are constrained to the acquisition of a single or several  $k$ -space lines, EPI is capable of acquiring a full 2D  $k$ -space following a single excitation pulse. An oscillating RO gradient is combined with short intermittent PE gradient pulses (“*blips*”) to sample  $k$ -space in a zigzag pattern. EPI can be implemented as either a gradient-echo or spin-echo pulse sequence. The following discussion focuses on the spin-echo case, the gradient-echo case is analogous.

As explained in Section 1.5.1, an excitation pulse followed by a  $180^\circ$  pulse with delay  $TE/2$  will result in the formation of a spin echo signal at time  $TE$ . Figure 2.6 depicts the basic principles of the EPI sequence. For the sake of clarity, minor details have been omitted from the figure. A full description can be found in [11] or [21], a concise explanation is given below (the letters A to E refer to Figure 2.6).

The  $90^\circ$  pulse flips the longitudinal magnetization into the transverse ( $xy$ ) plane. Due to the *slice-select gradient* B, only a slice of a certain thickness rather than the full volume is excited. The negative lobe of the slice-select gradient rewinds the phase dispersion caused by the gradient so that after the end of the waveform, all spins in the  $xy$ -plane precess in phase (neglecting dephasing effects such as  $B_0$  inhomogeneities and dipole interaction). The *prephasing gradients* A create an in-plane phase dispersion, allowing  $k$ -space sampling to begin in one corner of the 2D  $k$ -space. The  $180^\circ$  refocusing pulse flips the transverse magnetization, leading to the formation of a spin echo at time  $TE$  with respect to the  $90^\circ$  pulse. The crusher gradients C surrounding the refocusing pulse serve to compensate for imperfect inversion (i.e., spatial deviations from



**Figure 2.6** Diagram of the EPI sequence and its  $k$ -space trajectory. An explanation is given in the text. RF denotes radiofrequency pulses. RO, PE, and SS refer to readout, phase-encode, and slice-select axes, the three orthogonal gradient directions used for spatial encoding. ADC (analog-to-digital converter) indicates recording of an RF signal. Repetition time ( $TR$ ) is the duration of the acquisition of one slice.

the expected nominal flip angle of  $180^\circ$  due to  $B_0$  or  $B_1$  inhomogeneities) and suppress undesirable *free induction decay* (FID, [11]) signal, which would otherwise interfere with the spin echo signal. In order to understand this concept, it is important to note that the effect of two gradients with the same polarity before and after a  $180^\circ$  pulse will have opposite effects on the spins, that is, if the first gradient causes dephasing, the second one will rephase the signal.

Signal sampling starts immediately after the refocusing pulse. A trapezoidal RO gradient  $\textcircled{R}$  is applied while the analog-to-digital converter (ADC) samples the resultant gradient echo signal, acquiring a single line in *k*-space<sup>6</sup> (indicated by the uppermost green arrow on the right-hand side of Figure 2.6). Once the line has been recorded, the RO gradient is turned off and a short PE gradient pulse  $\textcircled{E}$  (a *blip*) is deployed, shifting the following RO to the next line in *k*-space (purple dashed arrow on the right-hand side of Figure 2.6). Then the next RO gradient is deployed with inverse polarity, sampling the second line of *k*-space in the opposite direction. This pattern of PE blips and alternating RO gradients is repeated until all of *k*-space has been sampled. A two-dimensional FFT can be used to convert the measured signal into an image of that slice. For clarity, Figure 2.6 illustrates the acquisition of only five lines. Typically, however, a train of 64–256 lines is sampled after a single excitation within approximately 20–100 ms. This highly efficient sampling scheme makes EPI one of the fastest MRI techniques available.

After acquisition of a 2D *k*-space, a different slice can be acquired by repeating the process with a shifted center frequency of the RF pulses to excite a different region. Alternatively, the same slice could be acquired again, either with some parameters changed or with identical parameters for signal averaging. The time required for the acquisition of a single slice is called *repetition time* and denoted by *TR*. Since the main part of the magnetization is in the transverse plane after the first image acquisition, one has to wait for it to return to the longitudinal state before it can be flipped again by the next  $90^\circ$  pulse. This limits the minimum time between acquisitions of the same slice to the order of 1–1.5 s at 1.5 T. However, while the magnetization in one slice relaxes back toward thermal equilibrium, a different slice can be scanned to reduce total scanning time.

The oscillating RO gradient produces a series of gradient echoes. Meanwhile, the RF refocusing pulse generates a spin echo signal, which acts as the envelope for the amplitude of the individual gradient echoes. Because of the symmetry property of the spin echo discussed in Section 1.5.1, the spin echo amplitude is maximum at time  $TE/2$  after the refocusing pulse. The sequence timing exploits this by adapting the readout train, such that the center line of *k*-space (the dashed red line in Figure 2.6) is sampled at that time. This guarantees maximum SNR for the low spatial frequencies that constitute the center of *k*-space and ultimately determine the overall image contrast. Conversely, the *k*-space periphery is sampled at lower signal amplitudes, thus imposing a limitation on the maximum attainable image resolution.

In the standard implementation of EPI, the time slot between the two RF pulses (the first  $TE/2$  interval) is basically unused, with the exception of the acquisition of some autocalibration data, which have been omitted from Figure 2.6. The overall timing is determined by the duration of the readout train. The second  $TE/2$  interval is the duration between the refocusing pulse and the readout of the center of *k*-space and

<sup>6</sup> Sampling of a *k*-space line is shown here as a continuous process, whereas in reality the signal is temporally binned into typically 64–256 discrete data points.

is thus determined by the number of  $k$ -space lines to be sampled and the gradient performance. The temporal separation of the  $90^\circ$  and  $180^\circ$  pulses is set to be equal to this required  $TE/2$  interval. The empty time slot between the two RF pulses can be used for MRE-relevant motion encoding, as described in Chapter 3.

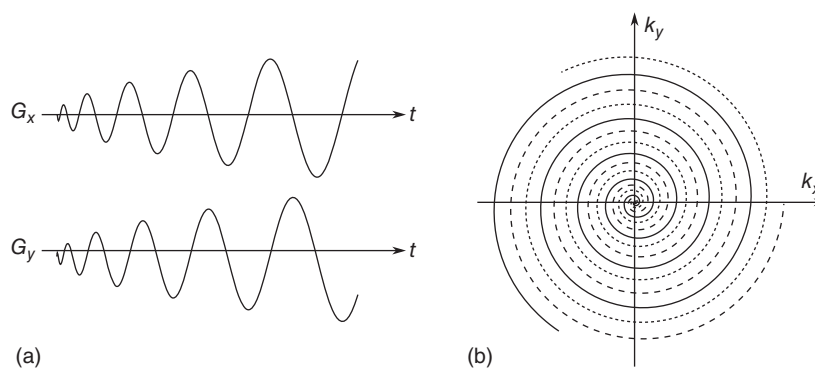
### 2.2.3 Non-Cartesian Imaging

Non-Cartesian imaging strategies constitute an exception to the assumption that data are acquired on a Cartesian grid in  $k$ -space. While Cartesian  $k$ -space sampling has the advantage that image reconstruction can be performed directly by applying an FFT (which requires data on a Cartesian grid), numerous imaging techniques exist that overcome the constraint of a Cartesian  $k$ -space, for example, by reading data along spiral or radial trajectories. For the reconstruction of such  $k$ -spaces, two fundamental approaches exist: either the data are re-gridded onto the Cartesian grid by interpolation or other mathematical procedures, or the canonical Fourier transform is replaced with a variant that can deal with nonuniform sampling.

Non-Cartesian sampling and image reconstruction are very wide fields of research, and in this book we can only scratch the surface. Reasons for opting for such a strategy are faster data acquisition, lower demands on gradient performance, lower gradient slew rates (causing less peripheral nerve stimulation), and reduced scanner noise. Depending on the implementation of the sequence, not all of these advantages can be exploited at the same time.

As an example of non-Cartesian imaging, we will discuss an EPI-based approach with a spiral readout trajectory, which was proposed by Johnson in [22].

Typically, each readout in a spiral or radial sequence starts at the center of  $k$ -space. This means that no pre-phasing gradients (such as  $\textcircled{A}$  in Figure 2.6) or in-plane phase-encoding gradients are required. Instead, the RO gradient consists of a superposition of the in-plane gradients (for 2D sampling) or all three gradients (for 3D sampling) during signal RO, as shown in Figure 2.7. In the case of a spiral sequence, a hybrid approach is employed: One three-dimensional  $k$ -space is sampled in multiple



**Figure 2.7** Spiral  $k$ -space sampling, as described in [23] and used in [22]. The RO gradient waveforms for one spiral arm are shown on (a). Note that for spiral imaging there is no in-plane PE gradient; both gradients act as RO gradients. (b) Three spirals are superimposed by modifying the phase of the gradient waveforms. Note that the sampling density is higher in the center of  $k$ -space than in the periphery, which can be exploited for correcting subject motion [22].

shots following the excitation of a thick slab. Each readout follows a spiral trajectory (in the  $k_x k_y$ -plane), whereas the  $k_z$ -position is determined by a short PE gradient along the  $z$ -axis prior to readout. Since a spiral covering an entire 2D  $k$ -space would take too long to acquire, an interleaved scheme is used, in which several spiral arms are superimposed to obtain a fully sampled  $k$ -space.

## 2.3 Fast Imaging

### 2.3.1 Fast Imaging Strategies

Many applications require fast image acquisition, to either increase patient comfort by shortening the total scan time or to optimize image quality by reducing repetition time in single-shot sequences. However, in Section 2.1, we explained that the number of  $k$ -space points to be sampled is determined by the desired image size and resolution, and that violating these relationships will lead to severe image artifacts. Nevertheless, several techniques exist to accelerate the acquisition process, by either exploiting redundancy in the MR signal or complementing image reconstruction with additional information. In this section, we will discuss the most common methods and their relevance to MRE.

The most obvious strategy to reduce the number of PE lines is to restrict the FOV along the PE direction. Equation (2.8) states that a reduction of pixels translates to the same reduction of required  $k$ -space points. Instead of a square image, one can acquire a rectangular image with dimensions  $N_x \times N_y$ . From here on, we will identify  $x$  with the RO axis and  $y$  with the PE direction, as is common in MRI literature. If we require isotropic resolution ( $R^x = R^y$ ), then Eqs. (2.1) and (2.2) dictate that  $k_{\max}^x = k_{\max}^y = k_{\max}$ . However, if we introduce a scaling factor  $0 < p < 1$  such that  $L^y = p \cdot L^x$ , the distance between adjacent  $k$ -space points becomes direction-dependent:

$$\Delta k^x = \frac{1}{L^x} \quad (2.14)$$

$$\Delta k^y = \frac{1}{L^y} = \frac{1}{p \cdot L^x} = \frac{\Delta k^x}{p} > \Delta k^x. \quad (2.15)$$

According to Eq. (2.6), this reduces the number of  $k$ -space lines by a factor  $\frac{1}{p} > 1$ , whereas the number of points in each line remains unaffected. This method is applicable if the object to be imaged does not exceed the FOV along the PE axis, otherwise fold-in artifacts will occur. In many practical applications, the object to be imaged is longish or ellipsoidal in shape. In these cases, the image can be oriented in such a way that the long axis is aligned with the RO axis and the short axis with the PE axis. Reducing the PE FOV is then possible without risk of fold-in artifacts. In other cases, there are factors that constrain the choice of image orientation (e.g., sequences relying on high gradient performance sometimes require the image to be aligned with the gradient coordinate system of the scanner), and FOV reduction is not an option. In any case, this strategy can be combined with the more complex methods described in the following paragraphs.

### 2.3.2 Partial Fourier Imaging

The (continuous or discrete) Fourier transform has one very useful property when applied to real-valued data. Let  $I(x, y)$  designate an image in which every pixel is characterized by one real number (the gray value, or intensity, at that point). Its Fourier-transformed counterpart

$$\tilde{I}(k_x, k_y) = \mathcal{F} [I(x, y)](k_x, k_y) \quad (2.16)$$

features a symmetry relation:

$$\tilde{I}(k_x, k_y) = \tilde{I}(-k_x, -k_y)^*, \quad (2.17)$$

where the asterisk denotes complex conjugation. In other words, there is a level of redundancy in  $k$ -space, since every data point  $(k_x, k_y)$  contains the same information as its point-symmetric counterpart  $(-k_x, -k_y)$ . Consequently, full image information is contained in one-half of  $k$ -space, and sampling the entire  $k$ -space can be considered a waste of time. This can be exploited by restricting data acquisition to the upper half of  $k$ -space, only acquiring PE lines with  $k_y \geq 0$ , and then calculating the points in the lower half through complex conjugation. In practice, a few lines of the lower half are sampled to increase noise robustness. The partial Fourier factor  $PF$  denotes the portion of the full  $k$ -space that is actually sampled. Typical values for clinical applications are  $PF \in \left\{ \frac{5}{8}, \frac{6}{8}, \frac{7}{8} \right\}$ . Image acquisition time is reduced by the same factor  $PF$ , and the *acceleration factor* is therefore given by

$$R = \frac{1}{PF}. \quad (2.18)$$

However, there is a price to pay for the accelerated image acquisition. In real-world applications, each acquisition is tainted by a certain amount of noise. Therefore, each sample point  $\tilde{I}(k_x, k_y)$  consists of the “actual” value  $\tilde{I}_0(k_x, k_y)$  (the value that would be acquired under hypothetical noise-free conditions) and noise  $\tilde{n}(k_x, k_y)$ :

$$\tilde{I}(k_x, k_y) = \tilde{I}_0(k_x, k_y) + \tilde{n}(k_x, k_y). \quad (2.19)$$

Noise is a random quantity, and the values of  $\tilde{n}$  are not correlated between different sample points. Therefore, in general,  $\tilde{n}(k_x, k_y) \neq \tilde{n}(-k_x, -k_y)^*$ . If one acquires a full  $k$ -space, the Fourier transform involves a kind of averaging between point-symmetric data points, so that the impact of noise is reduced. On the other hand, if the partial Fourier technique is used, no such averaging occurs since only one value is known for every pair of points. In general, the SNR is related to acquisition parameters via [10]

$$\text{SNR} \propto \sqrt{T_s} \cdot V, \quad (2.20)$$

where  $T_s$  is the sampling time (the time during which data are actively sampled, independent of other time parameters such as echo time, repetition time, or total imaging time) and  $V$  is the volume of a single voxel. As a consequence, partial Fourier imaging reduces the SNR by a factor of  $\sqrt{PF}$ . Section 2.3.4 will explain how this drawback can – in some cases – be partially compensated for through echo time reduction.

Unfortunately, the symmetry in Eq. (2.17) only exists in the case of real-valued image data. If one is only interested in a magnitude image that depicts the signal amplitude in each pixel, partial Fourier imaging is a viable acceleration method. If the signal phase

is also of interest, the image data become complex, and  $k$ -space points become decoupled, such that the value of one point cannot be calculated from its point-symmetric counterpart any more. In that case, partial Fourier techniques cannot be applied.

### 2.3.3 Parallel Imaging

The use of multiple small, localized coils instead of one large-volume resonator for receiving the MR signal was introduced originally to increase image quality. As a rule of thumb, a circular receive coil has a “sensitivity depth” that is approximately equal to its diameter, meaning that small coils can only pick up signals that originate in their vicinity and are blind to signals farther away from their surface. While this may look like a drawback at first, there are some major advantages. First, the major part of the noise in an MR image is caused by random signal from parts of the body outside the FOV. Electronic noise in the coils and signal amplifiers only plays a minor role. The volume resonator (or *body coil*) that is built into clinical MR scanners covers a relatively large volume. This can be an advantage in some cases, for example, when one wants to acquire a large FOV to get an overview of the subject’s anatomy at the beginning of an examination. However, it also implies that every body part within the resonator contributes to the noise level of the acquired image, thus oftentimes dramatically affecting image SNR. Furthermore, there is an air gap between the subject and the volume resonator, since it has to accommodate subjects of very different physique. Removing a receiving antenna from the signal source leads to a decrease in signal amplitude, constituting another limitation for the SNR attainable with the body coil.

Surface coils, on the other hand, are available either as flexible mats that can be wrapped around the body part of interest or embedded in rigid plastic housings that are adapted to the shape of a certain body part (such as head coils). They are usually small in diameter ( $\sim 10$  cm) and are therefore only sensitive to signals from their proximity. An image acquired with a single surface coil has a strong intrinsic geometric weighting, with high signal amplitudes on the surface and a pronounced signal decrease toward the interior parts of the body that are farther away from the coil.

However, several of those small coil elements can be combined into arrays with fixed or flexible geometry (head coils with 64 or more individual coil elements are not uncommon). One image can be reconstructed from each of the coils, with a specific geometric weighting due to the position of that coil relative to the FOV. In the most basic implementation, the magnitudes of those individual images are combined in a sum-of-squares manner, achieving more or less homogeneous intensity across the image. In order to avoid image artifacts, it is crucial to perform a measurement of noise correlation between individual coils and apply a phase correction to the signals from the individual coils to account for geometric effects (if two coils “see” a spin from different angles, the signals they pick up will differ by a phase that corresponds to the difference angle) and differences in signal travel time. The data required for these corrections are usually collected at the beginning of a multicoil acquisition.

The use of multiple localized coils for accelerating data acquisition is termed *parallel imaging*. It is based on the fact that, under ideal circumstances, the image information acquired by different coils from the same object only differs in terms of the geometric weighting effect induced by the spatial sensitivity profiles of the coils. In other words, no two images from two different coils are equal, meaning that there is a specific intrinsic set



of information contained in each single-coil signal. Parallel imaging exploits this fact by intentionally acquiring undersampled  $k$ -spaces and then mathematically approximating the missing data based on the intrinsic geometric information. Typically, one or more PE lines are skipped so that only every  $g$ -th line is acquired. As a consequence, the distance between measured PE lines,  $\Delta k^{\text{PE}}$ , is increased by the same factor  $g$ . According to Eq. (2.3), the FOV in the PE direction is reduced by  $g$ , causing fold-in artifacts for anything outside the FOV. Parallel imaging reconstruction removes these artifacts by exploiting the additional spatial information in each single-coil signal.

Most of the currently available parallel imaging techniques can be broadly subdivided into two categories:

- Image space-based methods calculate individual images for every single-coil  $k$ -space. Due to violation of Eq. (2.3), the resulting images are tainted by fold-in artifacts. The additional spatial information from the single-coil images are used to mathematically resolve the bias causing fold-ins, so that artifact-free images can be calculated for each coil. Finally, those individual images, which still differ in their spatial weighting, are combined to generate one compound image with homogeneous sensitivity profile. The most common representative of this category is SENSE (Sensitivity Encoding, [24]).
- $k$ -space-based methods reconstruct complete  $k$ -spaces for each individual coil before combining the single-coil images. Missing  $k$ -space lines are approximated from adjacent acquired lines and information on spatial coil sensitivity distribution. The most prominent example from this category is GRAPPA (Generalized Autocalibrating Partially Parallel Acquisition, [25]).

Other techniques exist to resolve bias in incomplete  $k$ -spaces, for example, by employing temporal regularization [26] or requiring nonstandard scanner hardware, such as nonlinear gradient coils [27]. However, these methods are beyond the scope of this book.

In early implementations of parallel imaging, information on the geometric arrangement of the coil elements had to be incorporated manually. In SENSE and GRAPPA, a number of *autocalibration scans* (ACS) are performed prior to each scan, usually by sampling a few PE lines close to the center of  $k$ -space, and allow for automated determination of image reconstruction parameters.

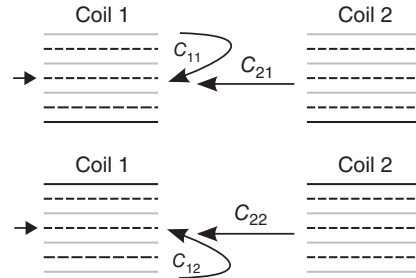
The following section will concentrate on GRAPPA. Further information on other techniques can be found in the literature [11, 28, 29].

### 2.3.3.1 GRAPPA

As a  $k$ -space-based technique, GRAPPA aims at assembling complete  $k$ -spaces for each individual coil prior to Fourier transform. The basic idea is to approximate the missing PE lines in each single-coil  $k$ -space as a superposition of the adjacent acquired lines from the  $k$ -spaces of all coils. Superposition weights are determined from a set of autocalibration scans performed prior to image acquisition.

Figure 2.8 illustrates the reconstruction procedure for the case of two coils and an acceleration factor of  $g = 2$ . Solid lines are acquired PE lines, whereas dashed lines are skipped and have to be reconstructed. The top row shows one option for estimating the unknown line indicated by the arrow on the left in the  $k$ -space of coil 1 from the block of three acquired gray lines in each of the single-coil  $k$ -spaces.  $C_{11}$  and  $C_{21}$  represent sets of complex weighting factors with which each line is multiplied prior to being summed

**Figure 2.8** Principle of GRAPPA reconstruction for a setup with two coils. Solid lines are acquired while dashed lines are skipped, but are required for artifact-free image reconstruction. The top and bottom rows demonstrate two options for reconstructing the line marked by the arrow on the left-hand side from different blocks of three acquired lines, indicated in gray.



up to obtain an approximation for the missing line. The lower row in the figure portrays a second option to reconstruct the same line from a different block of three acquired lines using different weights  $C_{12}$  and  $C_{22}$ , respectively. Note that each  $C_{ij}$  contains one complex factor for each line in the block.  $C_{ij}$  depends only on the position of the line to be reconstructed *relative* to the block of lines used, and not on the absolute position of the line in  $k$ -space. The missing lines in the  $k$ -space of coil 2 can be reconstructed in a similar way, using different weighting factors. In GRAPPA, each missing line is reconstructed using different blocks, and the results are then combined to achieve optimal image quality. The process is performed for every missing line in each of the single-coil  $k$ -spaces. Eventually, every complete  $k$ -space can be converted to an artifact-free image. However, since each of the images is an approximation of the signal that one of the coils “sees,” each image is modulated with the spatial sensitivity profile of its associated coil. In order to generate one image with homogeneous sensitivity, the individual images are combined, by either sum-of-squares or more complex algorithms.

The determination of the weighting factors is accomplished by acquiring a few contiguous lines in the center of  $k$ -space prior to the actual scan. The weights can then be determined by fitting blocks of acquired lines to another acquired line and treating the weighting factors as unknowns, thus obtaining sets of weights that yield the closest approximation.

### 2.3.4 Impact of Fast Imaging on SNR and Scan Time

For the discussion of the impact of fast imaging on signal quality, it is necessary to divide MR sequences into two distinct categories. On the one hand, there are segmented sequences, such as FLASH or bSSFP, in which each PE line requires a full excitation  $\rightarrow$  phase-encoding  $\rightarrow$  readout cycle. On the other hand, single-shot sequences, such as EPI, acquire a full  $k$ -space after a single excitation. The following discussion will be restricted to those two extreme cases. Many sequences are hybrids of the two, acquiring two or more  $k$ -space lines with one excitation pulse. In these cases, the analysis of the effect of fast imaging on SNR and scan time is more complex, but can still be derived from the principles outlined in the following paragraphs.

In the case of FLASH, repetition time  $TR$  corresponds to the length of one excitation  $\rightarrow$  phase-encoding  $\rightarrow$  readout cycle with acquisition of a single PE line. The total acquisition time for  $N_{\text{phase}}$  PE lines is therefore  $TR \cdot N_{\text{phase}}$ . Reducing the number of PE lines will therefore decrease the number of repetitions and hence the total acquisition time, but has no effect on the timing of each of the acquisition cycles. In particular, echo time

$TE$  is unaffected by the use of fast imaging. This means that the intrinsic SNR reduction by the square root of the acceleration factor,  $\sqrt{R}$ , cannot be compensated for. The only benefit of parallel imaging is hence the reduction of the total acquisition time, which can improve patient comfort and patient throughput. Since a FLASH sequence typically has rather high intrinsic SNR, it affords moderate acceleration.

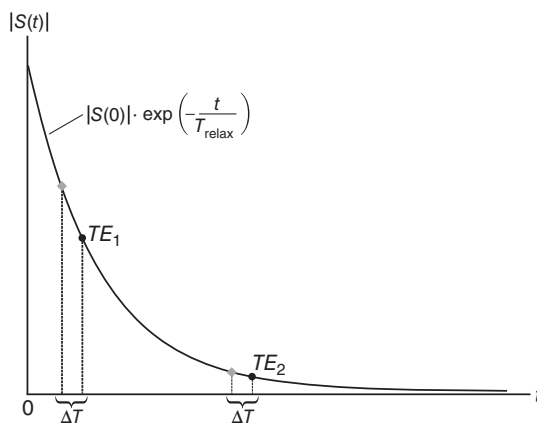
For EPI sequences, repetition time  $TR$  designates the duration from the excitation pulse to the end of the readout of an entire  $k$ -space. Echo time  $TE$ , on the other hand, is measured from the excitation pulse to the readout of the  $k$ -space centerline, which typically occurs in the middle of the full readout train. Parallel imaging shortens the length of the RO train, moving the centerline readout closer to the excitation pulse, leading to a reduction of both echo time and repetition time. After the excitation pulse, the magnitude of the precessing longitudinal magnetization decays exponentially, with either  $T_2$  (for spin-echo EPI) or  $T_2^*$  (for gradient-echo EPI). The signal amplitude at the time of centerline RO is therefore given by

$$|S(TE)| = |S(0)| \cdot \exp\left(-\frac{TE}{T_{\text{relax}}}\right), \quad (2.21)$$

where  $|S(0)|$  is the signal magnitude immediately after excitation and  $T_{\text{relax}}$  represents either  $T_2$  or  $T_2^*$ . From Eq. (2.21) it is obvious that shortening  $TE$  will increase the signal amplitude. If the signal amplitude is taken into account as another parameter affecting SNR, Eq. (2.20) can be extended to

$$\text{SNR} \propto \sqrt{T_s} \cdot V \cdot \exp\left(-\frac{TE}{T_{\text{relax}}}\right). \quad (2.22)$$

Sampling time  $T_s$  is proportional to the number of PE lines and is therefore reduced by acceleration factor  $R$  if fast imaging is applied. This translates to a reduction of the SNR by a factor of  $\sqrt{R}$ . At the same time, the echo time is also reduced by a factor of approximately  $R$ , thus increasing SNR due to higher signal amplitude. The result of these two counteracting effects basically depends on the echo time and relaxation time, as illustrated in Figure 2.9. If  $TE$  is short compared to  $T_{\text{relax}}$ , acquisition occurs in a region in which the exponential relaxation curve is steep, so that a small reduction of  $TE$  can achieve a significant increase in signal strength. For longer  $TE$ , the acquisition is located



**Figure 2.9** Effect of shortening echo time on signal magnitude. The black dots indicate signal strength for two arbitrarily chosen echo times  $TE_1$  and  $TE_2$ . The gray diamonds represent the signal amplitudes resulting when two echo times are reduced by the same amount  $\Delta T$ . Obviously, the gain in signal amplitude is much larger for shorter echo times.

on the flat section of the signal relaxation envelope, and a variation of  $TE$  has virtually no effect on signal strength.

In summary, for single-shot sequences,  $TE$ ,  $TR$ , and total scan time are reduced if fast imaging is employed. The degree to which the acceleration-induced SNR loss can be compensated depends on the actual values of  $TE$  and  $T_{\text{relax}}$ , and no general estimate is possible.

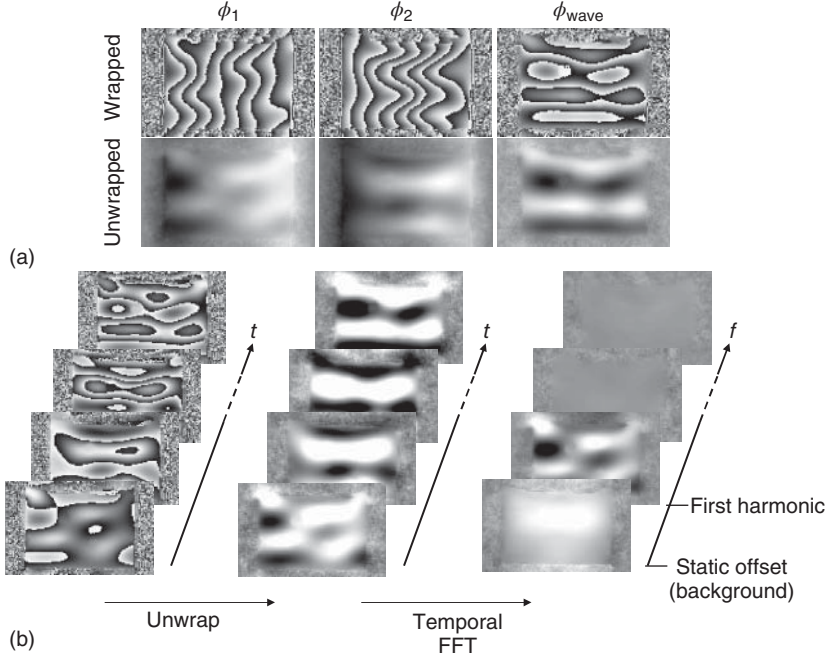
## 3

## Motion Encoding and MRE Sequences

The principle underlying MRE is to encode information on coherent tissue motion into the phase of the complex MRI signal. During postprocessing, the signal phase is converted into a displacement field, which is then subjected to an inversion algorithm to derive viscoelastic material parameters. Since the relevant information is stored in the signal phase, as opposed to the signal magnitude as in most other MRI applications, MRE is a *phase-contrast* MRI technique. Due to the constrained reconstruction of the signal phase, which is always mapped to the interval  $-\pi \leq \phi < \pi$ , irrespective of the true values of  $\phi$ , *phase unwrapping* has to be employed to obtain physically correct values. Phase unwrapping will be discussed in Chapter 9. An example of a wrapped and an unwrapped phase image can be seen in Figure 3.1a.

In this book we will only cover *time-harmonic* MRE, in which time-harmonic waves are used to induce tissue displacement. Other methods, based on image acquisition during (or before and after) nonharmonic motion, exist, but are rarely used [30, 31]. In dynamic MRE, where wave-induced displacement amplitudes are typically one to two orders of magnitude smaller than the spatial resolution of the image (tens to hundreds of micrometers versus  $\sim 2$  mm), a highly efficient mechanism for motion detection is required. MR sequences can be equipped with a *motion-encoding gradient (MEG)* to sense wave fields. By storing displacement information in the phase of the complex MR signal, motion sensitivity becomes decoupled from image resolution. This distinguishes phase-contrast MRI from strain imaging techniques [32], in which deformation information is retrieved from the image magnitude and is bound to image resolution. However, the signal phase is also sensitive to inhomogeneities of  $\mathbf{B}_0$  and modulations of the magnetic field due to a spatially varying susceptibility distribution. The resulting phase image is therefore a superposition of information from different sources. A separation of the wave information from the other contributions is not possible with only a single image.

Magnetic field inhomogeneities and susceptibility effects are usually static (time-independent). Wave propagation, on the other hand, is an intrinsically dynamic process with well-defined behavior in the time domain. The key to isolating wave information is to acquire several images at different phases of the wave oscillation cycle. At least two images are necessary to calculate *phase difference images*, from which the motion information can be extracted: assume that the phase of each image



**Figure 3.1** Illustration of wave image processing. In (a), two raw, wrapped phase images  $\phi_1$  and  $\phi_2$  with opposite vibration phase are shown. After unwrapping, each image is a superposition of the propagating wave and the static background. Taking the phase difference image, as prescribed by Eq. (3.3), removes most of the background while preserving the wave information. In (b), a stack of images, capturing the wave at different phases of the vibration cycle, is first subjected to unwrapping and then temporally Fourier-transformed. In the resulting frequency-resolved representation, the static offset caused by the susceptibility and  $\mathbf{B}_0$  inhomogeneity background is contained in the zero-frequency component, whereas the wave information falls into the first harmonic frequency image. The higher harmonic frequencies contain no information, since only the first harmonic frequency was mechanically stimulated.

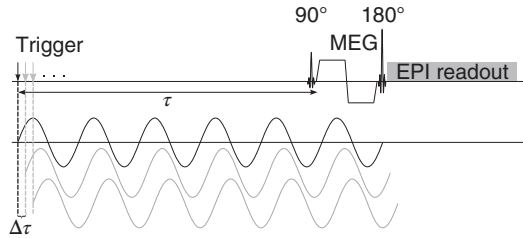
is a superposition of a static background,  $\phi_0$ , and the wave-induced contribution,  $\phi_{\text{wave}}$ , which is the quantity of interest. Since the background is static, it is identical for both images. The two images are acquired such that they depict the wave at two different oscillation phases, which are separated by  $180^\circ$ . The second image hence depicts the wave with an inverted sign. We can therefore write the phases of the two images as

$$\phi_1 = \phi_0 + \phi_{\text{wave}} \quad (3.1)$$

$$\phi_2 = \phi_0 - \phi_{\text{wave}}. \quad (3.2)$$

Because of phase wraps in  $\phi_1$  and  $\phi_2$ , it is not possible to take the difference of the two images to discard the background signal, as this would lead to artifacts. However, the problem can be solved in the complex domain:

$$\phi_{\text{wave}} = \frac{1}{2} \arg \left( \frac{e^{i\phi_1}}{e^{i\phi_2}} \right) = \frac{1}{2} \arg \left( e^{i(\phi_1 - \phi_2)} \right) = \frac{1}{2} \arg \left( e^{2i\phi_{\text{wave}}} \right). \quad (3.3)$$



**Figure 3.2** Diagram of a spin echo EPI-MRE sequence. At the start of the sequence, the MRI scanner sends a trigger (indicated by the black arrow) to the vibration generator to initiate mechanical vibration. The following delay is calculated in such a way that the offset  $\tau$  between the trigger and the MEG is exactly 100 ms. In the next repetition,  $\tau$  is decreased by  $\Delta\tau$  (first gray arrow), so that the MEG encodes a slightly shifted wave propagation phase. One iteration of this diagram captures a single slice. EPI-MRE and other MRE sequences will be discussed more thoroughly in Section 3.4.

A wave image that was calculated in such a way from two wave images with opposite oscillation phase is referred to as a *phase difference image*. The process is shown in Figure 3.1b.

Typically, more than two oscillation phases are acquired, and a one-dimensional Fourier transform then separates static from dynamic effects. A comprehensive explanation of the mechanism will be given in Section 3.1. This requires synchrony between vibration and image acquisition. The general principle is outlined in Figure 3.2. A trigger signal is sent by the MR scanner to the vibration generator to initiate vibration. After a certain delay  $\tau$  to allow for wave propagation into the region of interest, the imaging sequence is started and a single image is acquired. Different wave phases can be captured by repeating the process with different delays  $\tau$ . If the mechanical frequency is  $f$ , and  $N$  wave phases are acquired,  $\tau$  is reduced  $N$  times in steps of  $\Delta\tau = \frac{1}{f \cdot N}$ , so that one vibration cycle is sampled with  $N$  equidistant data points. In the following sections, we will first explain how motion information is stored in the phase of MR images and how it can be recovered in postprocessing. We will then proceed to discuss several common MRE imaging sequences.

### 3.1 Motion Encoding

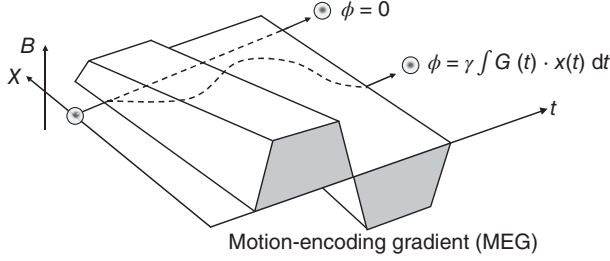
MRE is not the only MR modality that requires quantification of motion. Diffusion MRI and flow-sensitive MRI also rely on deriving motion information from MRI scans.<sup>1</sup> This section will explain the general working principle behind phase-contrast motion encoding and how it is used to quantify time-harmonic motion.

In the presence of a gradient field  $\mathbf{G}(t)$ , a spin with trajectory  $\mathbf{x}(t)$  accumulates a phase

$$\phi(t) = \phi(t_0) + \gamma \int_{t_0}^t \mathbf{G}(t') \bullet \mathbf{x}(t') dt'. \quad (3.4)$$

A graphical depiction of this mechanism is presented in Figure 3.3.

<sup>1</sup> In flow-sensitive MRI, information on constant coherent motion is encoded into the phase of the MRI signal in a way very similar to MRE. In diffusion MRI, on the other hand, incoherent diffusive motion is encoded as a loss of signal magnitude.



**Figure 3.3** Illustration of phase accumulation for a moving spin in the presence of a motion-encoding gradient in the  $x$ -direction. For the static spin, the effects of the positive and negative lobes of the MEG compensate each other, so that the net phase after the MEG is zero. The moving spin experiences the two lobes at different locations, and hence with different strength, so that a net phase remains. The spin phase after the MEG depends on the actual spin trajectory, and can be calculated using (3.4) (with  $\phi(t_0) = 0$ ).

For the following discussion, we will set  $\phi(t_0) = 0$ , which is not strictly necessary because any additional existing phase offsets will be removed by the temporal Fourier transform over the acquired wave propagation steps. However, before we explain how time-harmonic motion can be encoded, we have to first look at the effect of different families of gradients on the phase accumulated by stationary and moving spins.

### 3.1.1 Gradient Moment Nulling

Any smooth trajectory  $\mathbf{x}(t)$  of a signal-generating particle can be expanded into a Taylor series at  $t_0$ :

$$\mathbf{x}(t) = \mathbf{x}(t_0) + \dot{\mathbf{x}}(t_0) \cdot (t - t_0) + \frac{1}{2} \ddot{\mathbf{x}}(t_0) \cdot (t - t_0)^2 + \mathcal{O}(t^3). \quad (3.5)$$

Substituting Eq. (3.5) into Eq. (3.4) yields [11, pg. 336]

$$\begin{aligned} \phi(t) &= \phi(t_0) + \gamma \int_{t_0}^t \left( \mathbf{G}(t') \cdot \mathbf{x}(t_0) + \mathbf{G}(t') \cdot \dot{\mathbf{x}}(t_0) \cdot (t' - t_0) \right. \\ &\quad \left. + \frac{1}{2} \mathbf{G}(t') \cdot \ddot{\mathbf{x}}(t_0) \cdot (t' - t_0)^2 + \dots \right) dt' \\ &= \phi(t_0) + \mathbf{M}_0(t) \cdot \mathbf{x}(t_0) + \mathbf{M}_1(t) \cdot \dot{\mathbf{x}}(t_0) + \frac{1}{2} \mathbf{M}_2 \cdot \ddot{\mathbf{x}}(t_0) + \dots \end{aligned} \quad (3.6)$$

with the  $k$ th *gradient moment*

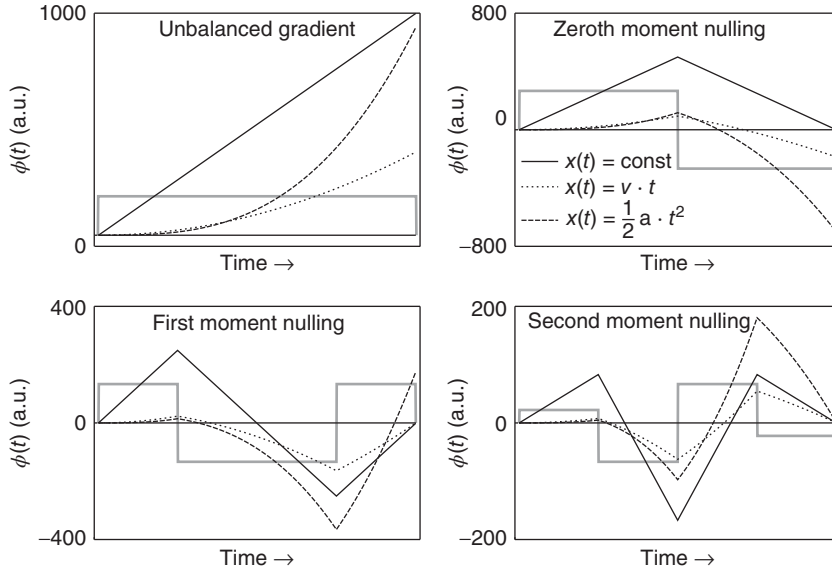
$$\mathbf{M}_k(t) = \int_{-\infty}^t \mathbf{G}(t') \cdot t'^k dt'. \quad (3.7)$$

Shifting the lower integration limit from  $t_0$  to  $-\infty$  is permissible, since in the previous section we required that  $\mathbf{G}(t)$  be zero for  $t < t_0$ . The translation invariance

$$\int_{-\infty}^t \mathbf{G}(t') \cdot (t' - t_0)^k dt' = \int_{-\infty}^t \mathbf{G}(t') \cdot t'^k dt'$$

that is implicitly used in the last step of Eq. (3.6) is only true if all gradient moments  $0, \dots, (k - 1)$  vanish. This is the case for all MEG waveforms considered in this book. We will use the term “ $k$ th moment nulling” (abbreviated as 0mn, 1mn, and 2mn) to indicate





**Figure 3.4** Effect of an unbalanced gradient and zeroth, first, and second gradient moment nulling on a stationary spin outside the scanner isocenter (solid line) and on spins with constant velocity (dotted line) or constant acceleration (dashed line). The plots were obtained by calculating the integral in Eq. (3.4) for different gradient shapes and spin trajectories. The gradient waveform is represented by the thick gray line. The three curves in each diagram represent the phase encoded by the respective gradient for the three types of motion. The scaling of the y-axis is arbitrary, but consistent across all plots. It is clearly visible that for the unbalanced gradient, all motion types (including stationary) lead to a nonzero phase for all spins. As the order of gradient moment nulling increases, higher orders of the Taylor expansion of the spin trajectory (Eq. (3.5)) are suppressed at the end of the gradient, thus rendering the spin phase insensitive to these types of motion.

that all gradient moments up to (and including)  $\mathbf{M}_k$  are zero. Because of the resulting time-translation invariance, we will henceforth use a time axis that is defined by the start ( $t_0 = 0$ ) and end ( $t = T$ ) of the gradient waveform. Since we are only interested in the total effect of the MEG on the signal phase of a particle,  $\phi(T)$  is the relevant quantity. In Figure 3.4, we illustrate the effect of different orders of gradient moment nulling on three types of nonharmonic motion.

$\mathbf{M}_0 = \mathbf{0}$  is the prerequisite for stationary spins not accumulating a position-dependent phase by nulling the term  $\mathbf{x}(0)$  in the series expansion of  $\mathbf{x}(t)$ . This implies that the total area under the gradient waveform has to be zero. A commonly used waveform with this property is a sine or its trapezoidal approximation. Higher-order gradient moment nulling can be employed to suppress artifacts induced by laminar, turbulent, or pulsatile flow of blood or cerebrospinal fluid.

If the first gradient moment is also nulled ( $\mathbf{M}_0 = \mathbf{0}$  and  $\mathbf{M}_1 = \mathbf{0}$ ), the constant-velocity term  $t \cdot \dot{\mathbf{x}}(0)$  is eliminated from Eq. (3.5) in addition to the static position-dependent contribution. Particles moving at constant speed, as in constant-velocity flow, will not acquire an additional phase from the MEG. A cosine or its rectangular approximation constitutes a suitable waveform.

Second-order gradient moment nulling ( $\mathbf{M}_0 = \mathbf{0}$ ,  $\mathbf{M}_1 = \mathbf{0}$ , and  $\mathbf{M}_2 = \mathbf{0}$ ) can be implemented as a train of four trapezoids of equal duration with relative amplitudes (+1/3,

$-1, +1, -1/3$ ), constituting two cycles. In addition to the effects of first-order moment nulling,  $\mathbf{M}_2 = \mathbf{0}$  suppresses the constant-acceleration term  $t^2 \cdot \ddot{\mathbf{x}}(0)$  in Eq. (3.5), so that particles accelerating at a constant rate will not accumulate signal phase. This effect becomes relevant in the presence of pulsating or turbulent flow.

### 3.1.2 Encoding of Time-Harmonic Motion

We assume that the spin undergoes harmonic oscillation about its equilibrium position  $\mathbf{x}_0$  with initial phase  $\psi$ ,

$$\mathbf{x}(t) = \mathbf{x}_0 + \mathbf{u}_0 \cdot \sin(\Omega t + \psi).$$

We will further center the gradient on the time axis and require that  $\mathbf{G}(t)$  is zero everywhere outside the interval  $-\frac{T}{2} \leq t \leq \frac{T}{2}$  and that its direction does not change over time. Therefore, it can be factorized into  $\mathbf{G}(t) = \hat{\mathbf{G}}_0 \cdot g(t)$ , where the hat denotes a unit vector. If we are only interested in the total accumulated phase after the gradient,  $\phi(t \geq \frac{T}{2})$ , Eq. (3.4) can be rewritten as

$$\phi(\psi) = \gamma \left( \mathbf{x}_0 \cdot \hat{\mathbf{G}}_0 \int_{-T/2}^{T/2} g(t) dt + \mathbf{u}_0 \cdot \hat{\mathbf{G}}_0 \int_{-T/2}^{T/2} g(t) \sin(\Omega t + \psi) dt \right). \quad (3.8)$$

Note that on the left-hand side, we introduce a dependence on the oscillation phase  $\psi$ . The gradient waveform  $g(t)$  is usually chosen in such a way that the area under the waveform is zero and the first integral in Eq. (3.8) vanishes.  $\phi(\psi)$  is a sinusoidal function with period  $2\pi$  with respect to  $\psi$  (see Appendix B for a proof). The phase and amplitude of  $\phi(\psi)$  are determined by the gradient waveform  $g(t)$ , oscillation frequency  $\Omega$ , oscillation amplitude  $|\mathbf{u}_0|$ , and the angle between the gradient and oscillation polarization, represented by the scalar product  $\hat{\mathbf{G}}_0 \cdot \hat{\mathbf{u}}_0$ .

We now demonstrate the calculation of *encoding efficiency*,  $\xi$ , of a given gradient waveform  $g(t)$  for a vibration with frequency  $\Omega$ . This will allow us to derive physical oscillation amplitudes  $\tilde{u}(\mathbf{r})$  from the measured Fourier-transformed MR signal phase  $\tilde{\phi}_i(\mathbf{r})$  via

$$\tilde{u}_i(\mathbf{r}) = \xi \tilde{\phi}_i(\mathbf{r}). \quad (3.9)$$

The tilde denotes the Fourier-transformed quantity, evaluated at the vibration frequency  $\Omega$ . Encoding efficiency is defined as the maximum phase offset caused by the gradient waveform for a vibration with unit amplitude and polarization parallel to the gradient direction, such that  $\hat{\mathbf{u}}_0 \cdot \hat{\mathbf{G}}_0 = 1$ :

$$\xi = \max_{\psi} \left( \gamma \int_{-T/2}^{T/2} g(t) \sin(\Omega t + \psi) dt \right). \quad (3.10)$$

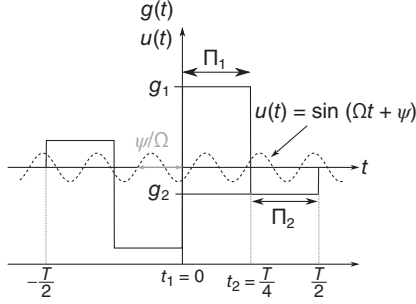
We will analyze two cases, corresponding to symmetric and antisymmetric gradient shapes.<sup>2</sup> Symmetric gradients obey

$$g(t) = g(-t), \quad (3.11)$$

whereas antisymmetric gradients satisfy

$$g(t) = -g(-t). \quad (3.12)$$

<sup>2</sup> There is no requirement that MEGs actually fulfill either of these conditions, but all typically used MEGs belong to either class for a number of reasons.



**Figure 3.5** Illustration of an MEG waveform with second-order gradient moment nulling and a sinusoidal vibration with angular frequency  $\Omega$  and phase offset  $\psi$  (dashed). The gradient can be composed from a train of plateaus with height  $g_i$  and duration  $\Pi_i$ , as discussed in the text. Since the gradient is antisymmetric with respect to the origin, accumulated phase (integral over  $g(t) \cdot u(t)$ ) is greatest when  $\psi = 0$ , according to Eq. (3.18). Because of the symmetry between the MEG and the oscillation, the part for  $t < 0$  contributes the same as the part for  $t > 0$ , so that we only calculate the latter and double the result.

For simplicity, we assume that the gradient waveform is a sequence of  $n$  plateaus with height  $g_i$ , starting point  $t_i$ , and duration  $\Pi_i$ , as outlined in Figure 3.5. This requirement will be lifted later on, so that the results can be applied to arbitrary symmetric and antisymmetric gradient waveforms. The encoding efficiencies of commonly used MEG waveforms are presented in Table 3.1.

With the above simplifications, we can rewrite the integral as

$$\phi(\psi) = \gamma \cdot \sum_{i=1}^n g_i \cdot \int_{t_i}^{t_i + \Pi_i} \sin(\Omega t + \psi) \pm \sin(-\Omega t + \psi) dt, \quad (3.13)$$

where the plus and minus signs belong to symmetric and antisymmetric MEGs, respectively. Executing the integral yields

$$\begin{aligned} \phi(\psi) = \gamma \cdot \sum_{i=1}^n g_i \cdot \left[ -\frac{1}{\Omega} (\cos(\Omega(t_i + \Pi_i) + \psi) - \cos(-\Omega t_i + \psi)) \right. \\ \left. \pm \frac{1}{\Omega} (\cos(-\Omega(t_i + \Pi_i) + \psi) + \cos(-\Omega t_i + \psi)) \right]. \end{aligned} \quad (3.14)$$

In order to identify the vibration phase  $\psi$  that yields the largest phase contribution, we take the derivative with respect to  $\psi$  and equate it to zero:

$$\begin{aligned} 0 \stackrel{!}{=} \frac{d\phi}{d\psi} = \frac{1}{\Omega} \sum_{i=1}^n g_i \cdot \left[ \sin(\Omega(t_i + \Pi_i) + \psi) - \sin(\Omega t_i + \psi) \right. \\ \left. \pm (-\sin(-\Omega(t_i + \Pi_i) + \psi) + \sin(-\Omega t_i + \psi)) \right]. \end{aligned} \quad (3.15)$$

We note that every term of the sum comprises two pairs of the form

$$\sin(X + \psi) \pm (-\sin(-X + \psi)). \quad (3.16)$$

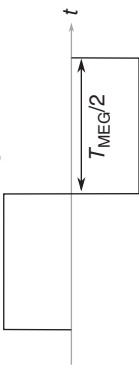
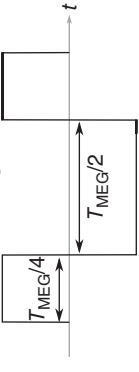
The whole sum certainly vanishes if each of those pairs vanishes, that is, if

$$\sin(X + \psi) - \sin(-X + \psi) = 0 \Rightarrow \psi = \frac{\pi}{2} \text{ for symmetric MEGs} \quad (3.17)$$

$$\text{or } \sin(X + \psi) + \sin(-X + \psi) = 0 \Rightarrow \psi = 0 \text{ for antisymmetric MEGs.} \quad (3.18)$$

In other words, the motion-induced phase is maximized if the vibration and the MEG have the same type of symmetry with respect to  $t = 0$ . This guarantees that the contributions of  $t < 0$  and  $t > 0$  to the integral are equal, so that the terms  $\sin(-\Omega t + \psi)$  and  $\sin(\Omega t + \psi)$  can be combined to yield  $2 \cdot \sin(\Omega t + \psi)$ . The final formula for calculating

**Table 3.1** Encoding efficiencies for motion-encoding gradient shapes with zeroth- and first-order gradient moment nulling.

Waveform	Zeroth moment nulling	First moment nulling
		
$ \xi $ for rectangular gradients with one cycle ( $N = 1$ )	$\left  \frac{\gamma g (1 - \cos(\pi T_{\text{MEG}} f_{\text{mech}}))}{\pi f_{\text{mech}}} \right $	$\left  \frac{\gamma g (\sin(\pi T_{\text{MEG}} f_{\text{mech}}) - 2 \sin(\frac{1}{2} \pi T_{\text{MEG}} f_{\text{mech}}))}{\pi f_{\text{mech}}} \right $
$ \xi $ for rectangular gradients with $N$ cycles	$\left  \frac{\gamma g}{\pi f_{\text{mech}}} \sum_{k=1}^N (-1)^k (\cos((k-1)\pi T_{\text{MEG}} f_{\text{mech}}) \dots - \cos(k\pi T_{\text{MEG}} f_{\text{mech}})) \right $	$\left  \frac{\gamma g}{\pi f_{\text{mech}}} \sum_{k=1}^N (-1)^{k+N-1} (2 \sin((k-1/2)\pi T_{\text{MEG}} f_{\text{mech}}) \dots - \sin(k\pi T_{\text{MEG}} f_{\text{mech}}) \dots - \sin((k-1)\pi T_{\text{MEG}} f_{\text{mech}})) \right $
$ \xi $ for sinusoidal approximation with $N$ cycles	$\left\{ \begin{array}{l} \left  \frac{\gamma g T_{\text{MEG}} \cdot \sin(\pi N T_{\text{MEG}} f_{\text{mech}})}{\pi (T_{\text{MEG}}^2 f_{\text{mech}}^2 - 1)} \right  \quad \text{if } f_{\text{mech}} \neq \frac{1}{T_{\text{MEG}}} \\ \left  \frac{\gamma g N T_{\text{MEG}}}{2} \right  \quad \text{if } f_{\text{mech}} = \frac{1}{T_{\text{MEG}}} \end{array} \right.$	$\left\{ \begin{array}{l} \left  \frac{\gamma g T_{\text{MEG}} f_{\text{mech}} \cdot \sin(\pi N T_{\text{MEG}} f_{\text{mech}})}{\pi (T_{\text{MEG}}^2 f_{\text{mech}}^2 - 1)} \right  \quad \text{if } f_{\text{mech}} \neq \frac{1}{T_{\text{MEG}}} \\ \left  \frac{\gamma g N T_{\text{MEG}}}{2} \right  \quad \text{if } f_{\text{mech}} = \frac{1}{T_{\text{MEG}}} \end{array} \right.$

$T_{\text{MEG}} = 1/f_{\text{MEG}}$  is the duration of one gradient cycle,  $f_{\text{mech}}$  the frequency of the vibration,  $N$  the number of MEG cycles,  $\gamma$  the gyromagnetic ratio and  $g$  the amplitude of the gradient (mT/m). The second and third row represent the solution of Eq. (3.19) for rectangular (=trapezoidal with infinite slew rate) gradient waveforms with 1 and  $N$  cycles, respectively. The last row gives encoding efficiencies for harmonic gradients, in which the rectangular gradients are replaced with a sine (0mm) or cosine (1mm) waveform. The encoding efficiency of trapezoidal and rectangular MEGs is generally slightly higher than that of sinusoidal ones.

encoding efficiency thus reads

$$\xi(\Omega, T) = 2 \gamma \cdot \sum_{i=1}^n g_i \cdot \int_{t_i}^{t_i+\Pi_i} \sin(\Omega t + \psi) dt \quad (3.19)$$

with  $\psi$  chosen according to Eqs. (3.17) and (3.18).

By decreasing plateau durations  $\Pi_i$  and simultaneously increasing their number  $N$ , we can approximate arbitrary gradient waveforms (such as trapezoidal or sinusoidal) by a sequence of infinitely short plateaus. The relations derived above are therefore also valid for arbitrary MEGs, as long as they are compatible with one of the symmetry constraints, that is, Eq. (3.11) or Eq. (3.12). However, for gradient waveforms that are not closely approximated by a small number of plateaus, such as sinusoids, it might be more appropriate to calculate the integral

$$\xi(\Omega, T) = 2 \gamma \cdot \int_0^{T/2} g(t) \cdot \sin(\Omega t + \psi) dt \quad (3.20)$$

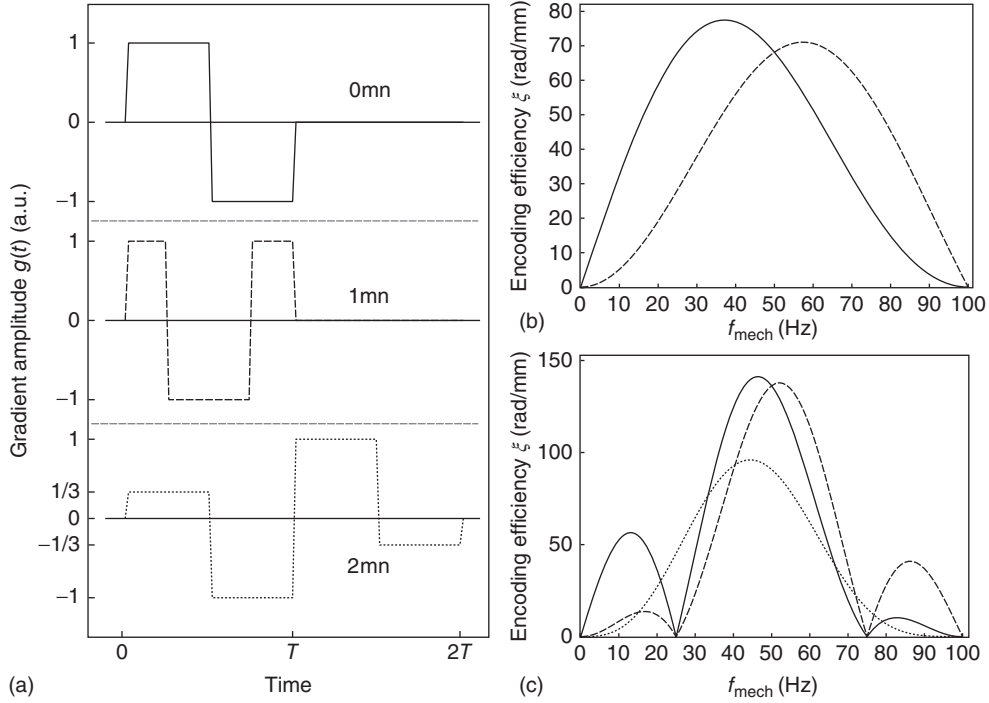
with the same optimum phase  $\psi$  as above.

Returning to the three archetypical waveforms representing zeroth, first, and second gradient moment nulling that we introduced in Section 3.1.1 and illustrated in Figure 3.4, we can now analyze their sensitivity to harmonic motion. In Figure 3.6, the encoding sensitivity of the three gradients is plotted as a function of the vibration frequency for a fixed gradient timing.

Figure 3.6b corresponds to the encoding efficiency of a 20 ms waveform with zeroth (0mn) and first (1mn) moment nulling, that is, one cycle at an MEG frequency of 50 Hz. The sensitivity maximum for 1mn is shifted toward higher frequencies. While the peak values for the two curves are similar, the 1mn waveform exhibits significantly lower sensitivity to low mechanical vibration frequencies, indicating that it is less susceptible to distortions induced by cardiac motion ( $\sim 1$  Hz).

In Figure 3.6c, the sensitivity profiles for 40 ms waveforms are shown. For 0mn and 1mn, this corresponds to two cycles of the configuration shown in Figure 3.6a, whereas, for 2mn, only one cycle of the compound waveform is employed. 2mn provides even more robustness against low-frequency artifacts than 1mn at the cost of a lower peak sensitivity and broader frequency spectrum. For 0mn and 1mn, peak encoding efficiency and spectral selectivity (width of the central peak) are better if two cycles are employed. However, the sensitivity nulls at odd multiples of the first subharmonic frequency have to be taken into account, especially in acquisitions with multiple simultaneous mechanical vibration frequencies [18, 33] (see Chapter 11).

In practice, gradient waveform  $g(t)$  and vibration frequency  $\Omega$  are chosen to meet the demands of wave mechanics, image resolution, signal quality, and hardware performance. A balanced waveform is used for  $g(t)$ , so that the  $\mathbf{x}_0$ -dependent term in Eq. (3.8) is nulled. Wave images are then recorded as illustrated in Figure 3.2.  $\mathbf{G}$  is applied to three orthogonal axes in repeated acquisitions. For each direction of  $\mathbf{G}$ ,  $N$  wave phases (typically  $N = 4$  or  $N = 8$ ) are recorded by gradually decreasing the delay  $\tau$ . The phase values  $\phi(\tau_i)$ ,  $i = 1, \dots, N$ , represent  $N$  equidistant points across one cycle of the vibration. However, these values can be tainted by the static background of the phase image, higher harmonics of the vibration frequency, and mechanical resonances of the patient table or MR scanner. In order to separate these effects from the actual vibration signal, a

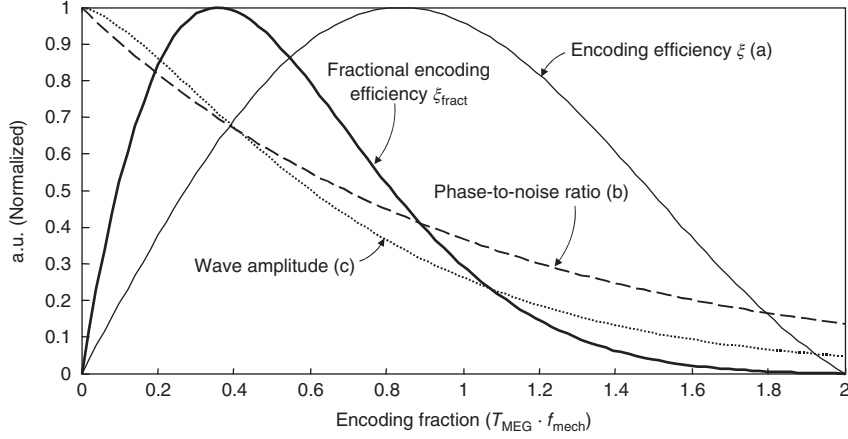


**Figure 3.6** Different orders of gradient moment nulling. (a) Waveforms with zeroth (solid), first (dashed), and second (dotted) order moment nulling (mn), composed of individual trapezoidal shapes. For zeroth and first mn, one cycle with period  $T$  is shown. Second mn can only be implemented with an even number of cycles, each with period  $T$ . (b) Encoding sensitivity for one cycle with zeroth and first mn with  $T = 20$  ms and gradient amplitude 20 mT/m in the mechanical vibration frequency range 0–100 Hz. (c) Encoding sensitivity for two cycles with  $T = 20$  ms. All constellations where  $f_{\text{mech}} < \frac{1}{T}$  are referred to as *fractional encoding*.

discrete Fourier transform is performed with respect to  $\tau_{ij}$ , and the frequency component  $\tilde{\phi}$  is extracted. The oscillation amplitude  $\tilde{u}$  is then calculated according to Eq. (3.9).

### 3.1.3 Fractional Encoding

The sensitivity profiles in Figure 3.6 indicate that vibration frequency and MEG frequency do not necessarily have to be equal. Encoding schemes with  $f_{\text{mech}} < f_{\text{MEG}}$  were conceived by Rump et al. [18] and termed *fractional encoding*. In general, longer motion-encoding periods with multiple MEG cycles offer superior sensitivity characteristics, but they also require longer echo times, thus resulting in lower signal quality due to  $T_2$  decay and longer total acquisition duration. Selecting a suitable MEG waveform is therefore often a compromise between sensitivity and signal quality, as illustrated in Figure 3.7. As an example, the optimal motion-encoding period  $T_{\text{MEG}}$  for a BSSFP-MRE sequence ( $T_2^*$  weighting) is given in [18] as



**Figure 3.7** Illustration of the contributions that determine the motion sensitivity in a sequence with fractional encoding as a function of  $T_{\text{MEG}} \cdot f_{\text{mech}}$ . The final fractional encoding efficiency (bold solid line) is a product of three contributions:  $a$ ,  $b$ , and  $c$ , where  $a$  represents the encoding efficiency, as explained in Figure 3.6. Contribution  $b$  quantifies the phase-to-noise ratio (PNR), which decreases exponentially with either  $T_2$  or  $T_2^*$ , depending on the type of sequence. The third contribution,  $c$ , relates to the damping of the wave according to the Voigt model (Section 4.8.3), which is larger for higher vibration frequencies. The curves were plotted for the following parameters:  $T_{\text{MEG}} = 20$  ms ( $a$ ,  $c$ ),  $f_{\text{mech}} = 50$  Hz ( $b$ ),  $T_2^* = 20$  ms, Voigt model for  $c$ :  $E = 1$  kPa,  $\eta = 1$  Pa s,  $\rho = 1000$  kg/m<sup>3</sup>, evaluated at a depth of 1 cm.

$$T_{\text{MEG}}^{(\text{opt})} = \frac{1}{2} T_2^* + \frac{1}{2} \sqrt{(T_2^*)^2 + 8\pi^2 T_2^* \frac{T_{\text{MEG}}}{T_{\text{vib}}} \cdot \frac{\eta}{\mu}}, \quad (3.21)$$

where  $\eta$  is the viscosity and  $\mu$  the shear modulus of the tissue.

## 3.2 Intra-Voxel Phase Dispersion

MR imaging involves discretizing a continuous body into a set of cubic or cuboidal voxels with finite volumes. The value assigned to each voxel is the contrast-generating physical quantity  $Q$  (e.g., proton density or relaxation time), averaged over the voxel. It is hence implicitly assumed that the spatial variation of  $Q$  occurs on a length scale much larger than the voxel dimensions, so that approximating the continuous quantity  $Q(\mathbf{r})$  with a discrete quantity  $Q(\mathbf{r}_i)$  is feasible.

As motion encoding affects the phase of the MR signal, care has to be taken when selecting the motion-encoding parameters. The MR scanner only “sees” the aggregate signal from each voxel, which is equivalent to the complex sum of all single-spin signals. If the phase dispersion introduced by the MEG is so strong that the phase varies by as much as  $2\pi$  across one voxel, the individual signal contributions will cancel out, and there is little to no resulting signal.<sup>3</sup> This effect is called “intra-voxel phase dispersion;” an example can be seen in the magnitude image of Figure 2.1, indicated by arrows.

<sup>3</sup> It is important to keep the periodic nature of the signal phase  $\phi$  in mind: If  $\phi$  is uniformly distributed over  $0 \leq \phi < 2\pi$ , the average phase is  $\langle \phi \rangle = \pi$ . However, for the signal-relevant quantity  $e^{i\phi}$ , averaging yields  $\langle e^{i\phi} \rangle = 0$ , or, more generally,  $\langle e^{i\phi} \rangle \neq e^{i\langle \phi \rangle}$ .

On the other hand, if motion encoding is too weak, there will be no signal cancellation in one voxel; however, the average motion signal phases of adjacent voxels will also be very similar, and their spatial derivatives will hence be small. Noise can therefore easily become the dominating factor in acquisitions with low motion sensitivity. The same can happen if the wavelength of the mechanical waves is in the range of spatial resolution. It is therefore crucial to select the MEG waveform and amplitude, vibration frequency, and imaging resolution in a way that achieves sufficient signal amplitude and acceptable signal-to-noise ratio (SNR) in the spatial derivatives of the displacement field.

Glaser et al. proposed an algorithm to derive shear stiffness from the modulation of the MRI magnitude image induced by intra-voxel phase dispersion, instead of relying on phase image [34].

### 3.3 Diffusion-Weighted MRE

It was mentioned earlier in this section that diffusion-weighted MRI (DWI, diffusion-weighted imaging) is an alternative way to encode motion information in the MR signal. However, there are notable differences between DTI and MRE regarding both the type of motion and the encoding mechanism. DTI uses gradients similar to the MEGs in MRE to manipulate the phase of moving spins. Typically, a gradient shape with zeroth moment nulling is utilized (even though there is usually a gap between the two gradient lobes to maximize encoding efficiency). As a result, stationary spins receive no accrued phase, whereas moving spins accumulate a phase offset depending on their respective trajectory (see Figure 3.4). In contrast to MRE, which aims at detecting *coherent* wave motion, DTI is sensitized to *incoherent* diffusive motion. In a highly diffusive medium, spins that originate from the same voxel at the beginning of the diffusion-encoding process are likely to end up in different locations after the encoding step due to the random nature of diffusion. Since each of these diffused spins reaches the final voxel on a different trajectory, they all possess different offset phases. Therefore, when the MR signal is sampled, the vector sum of the spins within one voxel is smaller than that in the nondiffusive case, where every spin stays in its original voxel. The diffusion-encoding gradients thus cause a signal decrease (relative to the same acquisition without diffusion weighting), and the magnitude of that decrease can be used to quantify diffusion-related material parameters [11].

The fact that both the type of motion (coherent vs incoherent) and storage mechanism (signal phase vs signal magnitude) in MRE and DTI are orthogonal was exploited by Yin et al. [35], who combined these two methods into one technique, called diffusion MRE (dMRE). The strength of the diffusion-weighting effect is quantified by the  $b$ -value. For rectangular gradients, the  $b$ -value can be calculated as  $b = \gamma^2 G^2 T^2 (\delta t - T/3)$ , where  $T$  is the duration of each gradient lobe and  $\delta t$  their temporal separation [11]. High  $b$ -values correspond to strong signal dephasing for moving spins; values up to  $b = 1500 \text{ s/mm}^2$  are common. For a typical MRE waveform with an MEG frequency of 50 Hz, corresponding to two rectangular lobes with a duration of 10 ms each and an amplitude of 30 mT/m, the  $b$ -value is approximately  $43 \text{ s/mm}^2$ . The diffusion sensitivity of MRE is therefore low. Yin et al. overcame this issue by using optimized gradient waveforms that simultaneously accommodate the demands of MRE and DTI.



### 3.4 MRE Sequences

Many pulse sequences can be and have been used for MRE. This section is not meant as an exhaustive treatment of all MRE sequences ever employed. Instead, we will have a look at how the previously discussed sequences – FLASH, bSSFP, and EPI – can be used for MRE. We will also analyze how the properties of the derived sequences differ from the original sequences.

In general, two steps are necessary to convert an arbitrary pulse sequence into an MRE sequence. First, MEGs have to be inserted between excitation and signal read-out to encode tissue oscillation into the signal phase. Second, synchronization has to be established between the sequence and the vibration generator to acquire images at well-defined points of the oscillation cycle. The most common way of achieving this is by having the sequence send trigger pulses – either as a TTL<sup>4</sup> signal via a coaxial cable or as light pulses through an optical fiber – from the scanner to the vibration generator to initiate vibration. The other direction, triggering image acquisition from the vibration generator, is also possible; however, one has to ensure that the latency of the scanner and its fluctuation are small compared to the vibration period.<sup>5</sup>

#### 3.4.1 FLASH-MRE

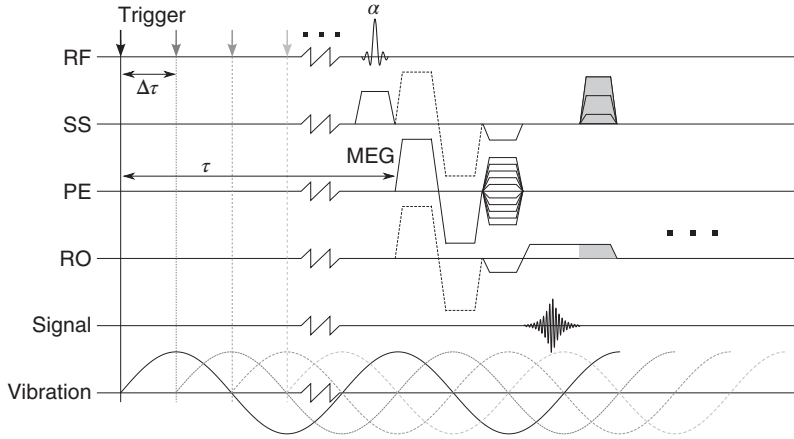
Converting a FLASH sequence, as shown in Figure 2.4, into an MRE sequence [36] is a rather straightforward task. A sequence diagram is shown in Figure 3.8. Each acquisition loop begins with the scanner sending a trigger signal to the vibration generator, which in turn activates the oscillation (black solid arrow and sinusoid). After a delay  $\tau$  (indicated by the interrupted time axis) to allow for wave propagation into the organ of interest, image acquisition is started. The acquisition loop shown acquires one  $k$ -space line and is repeated for all  $N_{\text{PE}}$  phase-encode lines, and for all slices in a multislice acquisition. After that, the delay between the trigger and the sequence is reduced by  $\Delta\tau = \frac{T_{\text{vib}}}{N_t}$  (first gray arrow and sinusoid), where  $T_{\text{vib}}$  is the vibration period and  $N_t$  the desired number of wave propagation phases. The scan is then repeated with this adjusted delay, thus sampling a different wave propagation phase. The whole process is repeated until all phase propagation steps (here, four) have been acquired. Finally, the whole acquisition can be repeated with the MEG applied to a different axis in order to acquire different projections of the tissue displacement field. The overall number of iterations of the acquisition loop is

$$N_{\text{iterations}} = N_{\text{slices}} \cdot N_{\text{PE}} \cdot N_t \cdot N_{\text{projections}}. \quad (3.22)$$

The addition of the MEG prolongs both the echo time and the repetition time compared to the standard FLASH sequence. Being a gradient-echo (GE) technique, FLASH is sensitive to signal decay governed by  $T_2^*$ , which can be significantly shorter than  $T_2$ . Short MEG periods are therefore desirable to keep the increase of  $TE$  small. The MEG period,  $T_{\text{MEG}}$ , does not have to match the vibration period, as explained in

<sup>4</sup> TTL = transistor–transistor logic, an electronic standard for signal transmission and processing based on voltage levels.

<sup>5</sup> The same is true if the scanner triggers the vibration generator; however, the latter usually has a lower latency due to its significantly lower complexity.



**Figure 3.8** Schematic timing diagram of a FLASH-MRE sequence. In order to acquire the full displacement field, the MEG is applied on all three gradient axes in successive acquisitions, as indicated by the dashed lines. The gray gradients represent spoilers, as explained in Section 2.2.1.1. The scaling of gradient amplitudes and the time axis is not accurate.

Section 3.1, and it is common to keep the former significantly shorter than the latter by fractional encoding (see Section 3.1.3). As illustrated in Figure 3.6, an increasing mismatch between  $T_{\text{vib}}$  and  $T_{\text{MEG}}$  leads to a decrease in motion-encoding sensitivity. As a consequence, care must be taken in selecting an MEG period that does not affect image quality too strongly while maintaining a reasonable motion sensitivity for the desired vibration frequency.

An increase in repetition time has both positive and negative effects. On the positive side, a longer  $TR$  leaves more time for  $T_1$ -driven signal relaxation between RF pulses, thus augmenting steady-state magnetization and signal quality. The flip angle has to be adapted, using the equation for the Ernst angle (see Eq. (2.9)). If several slices are to be acquired, they can be scanned in an interleaved manner to increase the repetition time for each slice. For example, after acquisition of one  $k$ -space line of slice #1, the same line can be acquired in all other slices. Since remaining transverse magnetization is spoiled at the end of each  $TR$  interval and the RF pulses are slice-selective, there is no interference between slices. In the Ernst angle equation, the repetition time has then to be replaced with  $N_{\text{slices}} \cdot TR$ .

On the negative side, the increase in repetition time translates into an increase in acquisition time by a factor of approximately  $N_{\text{repetitions}} \cdot (T_{\text{MEG}} + \tau)$  in comparison to the standard FLASH sequence.<sup>6</sup>

An alternative approach to FLASH-MRE prescribes an integer ratio of the vibration period to repetition time:

$$\frac{TR}{T_{\text{vib}}} = n \quad (3.23)$$

$$\text{or } \frac{T_{\text{vib}}}{TR} = n \quad \text{with } n \in \mathbb{N}. \quad (3.24)$$

<sup>6</sup> This is not exactly true, since the delay  $\tau$  includes the time for the excitation pulse, which is also present in the normal FLASH sequence. However, the duration of the RF pulse ( $\sim 2$  ms) short compared to  $\tau$  ( $\sim 50$ – $100$  ms in human applications).

In the former case, by virtue of its periodicity, the vibration waveform  $v(t)$  fulfills the relation

$$v(t + TR) = v(t + n \cdot T_{\text{vib}}) = v(t). \quad (3.25)$$

This means that the same vibration phase is sampled in each iteration of the acquisition loop, without the need for triggering. Therefore, one trigger pulse can be sent at the beginning of the acquisition, and then all  $k$ -space lines of all slices can be acquired during continuous vibration, without the inclusion of the delay  $\tau$  in each  $TR$ . In order to sample different wave propagation phases, it is still necessary to resynchronize the vibration; however, this only needs to be done after all phase-encode lines of all slices and for all projections have been acquired. The number of trigger pulses and  $\tau$  delays hence reduces from  $N_{\text{slices}} \cdot N_{\text{PE}} \cdot N_t \cdot N_{\text{projections}}$  to  $N_t$ , which can significantly accelerate the acquisition. Echo time is not affected, as  $\tau$  is not contained in  $TE$ . This acceleration mechanism requires Eq. (3.23) to be satisfied, which can limit the choice of other sequence parameters or require the incorporation of fill times into  $TR$ .

In the second case (Eq. (3.24)), the vibration period is larger than the repetition time, so that in the second repetition of the acquisition loop a different wave propagation phase is sampled. The integer ratio between  $TR$  and  $T_{\text{vib}}$  guarantees that after  $n$  repetitions,  $n$  different wave phases have been recorded during continuous vibration, so that no resynchronization between the scanner and the vibration generator is required, given that the internal clocks of the two devices are sufficiently precise. The acquired  $k$ -space lines have then to be reordered to ensure that every  $k$ -space contains only lines recorded at the same wave propagation phase.

### 3.4.2 bSSFP-MRE

Because of the similarity between bSSFP and FLASH, most of the timing-related considerations regarding FLASH-MRE are also valid for bSSFP-MRE. However, due to the absence of spoiling in bSSFP, transverse magnetization is carried over from one  $TR$  interval to the next, rendering the signal generation far more complex. The first application of bSSFP-MRE was published by Bieri et al. [17]. The following discussion is based on analyses presented in [17, 19].

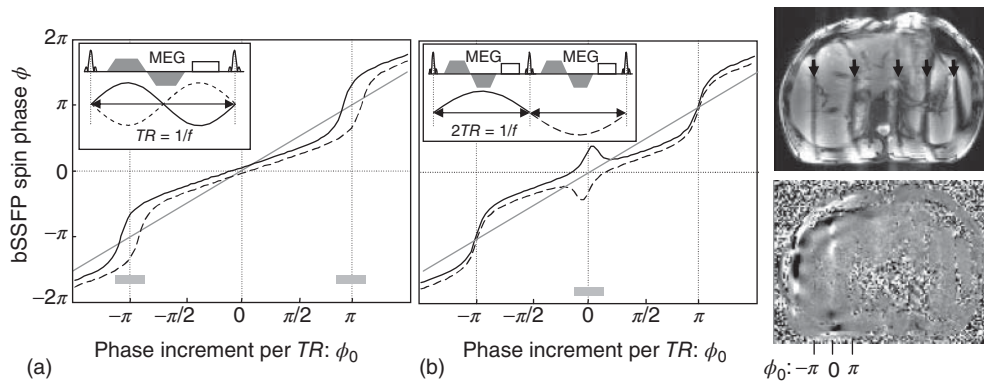
As in the case of FLASH-MRE, bSSFP-MRE matches the sequence repetition time  $TR$  and the vibration period in order to acquire images of multiple vibration phases. Two images with opposite vibration phase can then be combined into one phase difference image that is devoid of the static susceptibility background (see Eq. (3.3)).

Since transverse magnetization is not spoiled after each acquisition, as in the case of FLASH, the steady state depends on the offset phase being accumulated during each shot. Let us assume that  $\phi_0$  is the *static* phase increment per shot, unrelated to motion effects. It is composed of contributions from an inhomogeneous susceptibility distribution across the object and  $\mathbf{B}_0$  inhomogeneities resulting from imperfect shimming. In a spoiled sequence, the relationship between that phase increment  $\phi_0$  and the phase  $\phi$  of the acquired MRI signal would be simply

$$\phi = \phi_0, \quad (3.26)$$

since the spoiling at the end of each single acquisition destroys the transverse magnetization component, so that each excitation pulse generates a fresh precessing

magnetization with a well-defined phase. However, in bSSFP, the remaining transverse magnetization at the end of each shot is flipped by the next RF pulse, and the phase of the in-plane magnetization after the pulse is determined by the phase of the magnetization before the pulse relative to the flip axis (the direction of the  $B_1$  field in the oscillating reference frame). In order to separate the irrelevant static background from the motion-induced phase contribution, phase difference images are calculated from pairs of images with identical timing relative to the vibration, but opposite signs of the flip angle. The nonlinear phase response of bSSFP causes the phase of the resulting phase difference image,  $\phi_{\text{wave}}$ , to depend on the phase increment per shot,  $\phi_0$ . This is illustrated in Figure 3.9 for two cases, one with  $TR = \frac{1}{f_{\text{vib}}}$ , and one with  $TR = \frac{1}{2f_{\text{vib}}}$ . Obviously, the phase response is very different for these two scenarios. In the first case, motion sensitivity is maximized when the phase increment per  $TR$  is  $\phi_0 = \pm\pi$ . In the second case, on the other hand, optimal sensitivity results from  $\phi_0 = 0$ . We will first discuss the latter scenario, which is conceptually simpler. The situation  $\phi_0 = 0$  corresponds to an ideal medium with a homogeneous susceptibility distribution and perfect shimming, such that the Larmor frequency is constant across the entire volume of interest and (in the absence of oscillation) all spins precess in-phase. This requirement cannot be fulfilled under real-world conditions. Small field gradients lead to two effects. First, it generates banding artifacts, as explained in Section 2.2.1.2. Second, since  $\phi_0$  becomes position-dependent, the encoding sensitivity and hence the conversion factor  $\xi$  between the MR signal phase and the physical



**Figure 3.9** Illustration of the nonlinear phase response of bSSFP. The solid and dashed lines correspond to the MR signal phase ( $\phi$ ) as a function of the phase increment per  $TR$  ( $\phi_0$ ) for two acquisitions with opposite oscillation phase. For a fixed value of  $\phi_0$ , the motion-related phase  $\phi_{\text{wave}}$  is half the vertical distance of the two curves. The gray rectangles indicate ranges of  $\phi_0$  with optimal motion sensitivity. In (a), one  $TR$  matches one vibration cycle, so that the wave has to be inverted (dashed sinusoidal) in order to acquire the second phase image. In (b), one  $TR$  matches half an oscillation cycle, so that two images with opposite oscillation phase are sampled automatically without the need to invert the oscillation. The two images on the right-hand side illustrate the position dependence of motion sensitivity of a sequence of type (b). The magnitude image (top) suffers from banding, as explained in Section 2.2.1.2. The phase image (bottom) exhibits vertical stripes of high ( $\phi_0 = 0$ ) and low ( $\phi_0 = \pm\pi$ ) motion sensitivity, as explained in the text. This modulates the physically correct displacement field and causes problems for the reconstruction of elastic moduli.

displacement (see Section 3.1.2) can also differ depending on the position within the object. Since the field gradients cannot be easily measured, it is unfeasible to quantify these parameters for every voxel in the image. Therefore, the reconstructed displacement field is subject to spatial modulation, even if the wave amplitude is constant. The calculation of elastic moduli is hampered by that modulation, which is indistinguishable from viscous damping. This is shown in the two MR images in Figure 3.9, where a horizontal field gradient causes vertical bands of high and low motion sensitivity.

For the first case, where optimal motion sensitivity is achieved if  $\phi_0 = \pm\pi$  (or, more accurately, if  $\phi_0$  is an odd integer multiple of  $\pi$ ), perfect shimming ( $\phi_0 = 0$ ) leads to very poor motion sensitivity. However, the motion sensitivity can be increased *locally* by applying a linear magnetic field gradient, and thus imposing a spatial modulation onto  $\phi_0$ . Assume that we turn on a gradient along the  $x$ -axis,  $G_x$ , for a short time  $\tau$  during each  $TR$  interval. As a consequence, the offset phase becomes

$$\phi_0(x) = \gamma \cdot G_x \cdot x \cdot \tau. \quad (3.27)$$

This implies that in regions where  $\phi_0(x)$  is close to an odd multiple of  $\pi$ , motion sensitivity is maximized. Between those optimum bands, however, motion sensitivity is strongly decreased. Using this technique, the displacement field can only be evaluated in regions of high motion sensitivity, rendering it unsuitable for most extended organs. Since the additional gradient cannot be balanced during the  $TR$  interval (otherwise, its effect on  $\phi_0$  would be reversed), referring to such a sequence as a *balanced* SSFP is not technically correct, but that distinction is usually not made. If the gradient is so strong (or long) that the bands of high and low motion sensitivity become smaller than one voxel, the sequence becomes a FLASH sequence and the gradient acts as a spoiler gradient that effectively destroys all transverse magnetization. From this last point, we can see that bSSFP possesses locally a higher motion sensitivity than a FLASH sequence. However, the spatial variation of motion sensitivity is a major drawback for most applications, so that bSSFP-MRE is not used any more.

### 3.4.3 EPI-MRE

Being one of the fastest sampling schemes available, EPI is a natural candidate for data acquisition in MRE. Its capability to acquire either entire images (single-shot EPI) or several  $k$ -space lines (segmented EPI) after a single excitation pulse drastically reduces overall scan time. This gain can be reinvested in the acquisition of more data (e.g., three orthogonal projections of the displacement field, more slices, or several vibration frequencies), which would lead to unfeasibly long examination times with slower pulse sequences.

EPI can be implemented as either a gradient echo (GE) or spin echo (SE) technique. Both have been successfully applied for MRE (see Table 7.1). SE-EPI is usually slower than GE-EPI because of the requirement to first let the magnetization dephase and then to wait for it to rephase after the refocusing pulse. GE-EPI, on the other hand, induces dephasing artificially by means of a gradient, and signal sampling can start immediately after the dephasing gradient. SE-EPI is sensitive to  $T_2$  signal decay, whereas the GE-EPI signal is modulated by the faster  $T_2^*$  decay.

MEGs can be inserted into an SE-EPI sequence in two ways. One option is shown in Figure 3.1. The whole MEG is placed between the  $90^\circ$  and  $180^\circ$  pulses. This time slot is usually empty in standard EPI sequences and its only purpose is to allow for dephasing of transverse magnetization, which is then refocused by the  $180^\circ$  pulse. Using this time slot for the MEG therefore does not increase  $TE$  and  $TR$ . However, that time slot is usually rather short (a few milliseconds), requiring a short (and hence high-frequency) MEG, which has low sensitivity to low vibration frequencies. In order to increase sensitivity for low frequencies, it can become necessary to prolong the MEG, thus stretching the separation between the two RF pulses. Due to the inherent symmetry of SE-EPI,<sup>7</sup> increasing the interpulse interval by an amount  $\Delta t$  will increase echo time by  $2 \cdot \Delta t$ .

In some scenarios, it can be advantageous to split the MEG waveform into two parts and arrange these on both sides of the refocusing pulse, as illustrated in Figure 3.10. Such cases arise if the MEG waveform is composed of several cycles with a relatively high frequency, yielding an MEG train that is longer than half the readout train (e.g., in segmented EPI acquisitions). In these cases, the duration of the MEG dictates the length of  $TE/2$ . In order to restore the symmetry required for SE-EPI, a fill time has to be inserted between the refocusing pulse and the EPI readout.<sup>8</sup> This effectively increases the echo time and leads to inferior signal quality due to  $T_2$  signal decay (see Figure 3.10a). If the required fill time is longer than half the MEG train, substituting that fill time with the second half of the MEG will reduce echo time.<sup>9</sup> The second MEG following the inversion pulse also has to be inverted, since gradients before and after an  $180^\circ$  pulse have opposite effects on transverse magnetization. In addition, the “gap” between the two parts of the MEG has to be an integer multiple of the MEG period to ensure that the two parts act coherently. This is straightforward, since the first MEG section can be shifted freely between the two RF pulses, and results in a shorter  $TE$  and hence in better SNR (see Figure 2.9). Another benefit of placing the MEGs symmetrically around the refocusing pulse is that it avoids the effects of concomitant gradient fields,<sup>10</sup> as discussed in [37], which can cause artifacts.

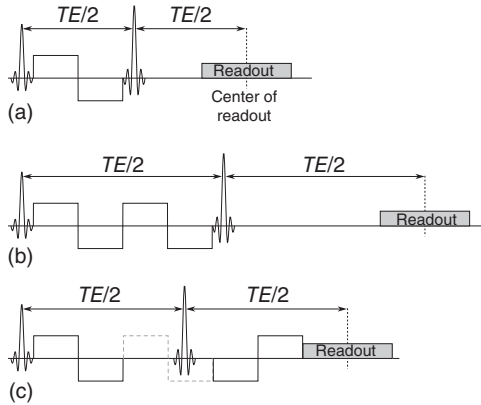
Due to the long readout train, EPI is particularly susceptible to  $B_0$  inhomogeneity. Even small uncompensated field fluctuations can accrue to significant deviations of the  $k$ -space trajectory, if multiple lines are sampled in quick succession. This will inevitably lead to image artifacts, especially to geometric distortions in regions adjacent to air-filled cavities, such as the parts of the brain surrounding the paranasal sinuses. The effect can be attenuated by shortening the readout train, for example, by increasing readout bandwidth, but this again decreases the SNR. Field inhomogeneities are not too much of an issue at 1.5 T, but they gain importance at 3 T and beyond. However, single-shot SE-EPI has already been performed successfully at 7 T [38].

<sup>7</sup> The first half of  $TE$ , defined as the distance between the  $90^\circ$  and  $180^\circ$  pulses, has to be equal to the time between the  $180^\circ$  pulse and the center of signal readout (see Figure 2.6).

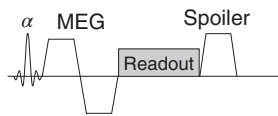
<sup>8</sup> Alternatively, the EPI readout could be stretched by, for example, reducing the readout bandwidth, but this does not solve the underlying problem.

<sup>9</sup> Strictly speaking, the MEG does not have to be divided into two identical parts. Any subdivision is valid.

<sup>10</sup> Concomitant gradient fields refer to deviations of a magnetic field gradient from the ideal profile. Even though each gradient coil produces a field that changes *mainly* along one axis, there is always a dependence on the other two axes if the field is expanded up to the second order of a Taylor series. These concomitant fields can cause nonlinearities in the encoded motion information. In most cases, these effects are simply ignored.



**Figure 3.10** Different ways of placing MEGs within a spin-echo sequence. (a) A spin-echo sequence with one MEG cycle is shown. If the resulting motion sensitivity is insufficient, a second MEG cycle can be added. (b) The second MEG is appended to the first one. Because of the inherent symmetry of spin-echo sequences, a fill time has to be inserted before the readout so that the refocusing pulse is in the center of the  $TE$  interval. (c) the MEG is instead inserted between the refocusing pulse and the readout. The timing between the MEGs has to be such that the gap is an integer multiple of the MEG period (shown in dashed gray). Since the refocusing pulse inverts the spin phase, the second MEG has to be of opposite polarity relative to the first one. A fill time has to be inserted in the first half of  $TE$  to maintain spin-echo symmetry. This constellation leads to a significantly shorter  $TE$  than in (b). The fill time in (b) could be used for a third MEG cycle; however, in media with short  $T_2$ , the increase in  $TE$  would cause significant signal loss, so that (c) would be the better compromise for that scenario.



**Figure 3.11** Simplified timing diagram of a GE-EPI sequence, as used in [39]. Only the image acquisition part is shown, vibration and synchronization are analogous to Figure 3.8. In the original publication, a segmented image acquisition strategy was used, so the process illustrated here has to be repeated several times to obtain a complete  $k$ -space. The MEG can be applied to all three gradient axes in successive scans.

The structure of GE-EPI sequences is simpler than that of their SE counterpart. Due to the absence of a refocusing gradient, there is only one possible location for the MEG. A simplified diagram of the sequence used in [39] is shown in Figure 3.11. Because of the  $T_2^*$  sensitivity of GE sequences, it is usually not advisable to use a single-shot sampling strategy; segmented image acquisition is used instead. The spoiler gradient at the end of the sequence nulls the remaining in-plane magnetization, so that subsequent RF pulses do not generate undesirable echoes. Segmented data acquisition generally renders GE-EPI sequences slower than single-shot SE-EPI sequences.

**Part II**

**Elasticity**



## 4

## Viscoelastic Theory

Elasticity and viscosity are two physical concepts that describe the response of a solid body to an external force. Both cases include a deformation of the body as a consequence of that force. Initially, the body will exert an opposing force and resist deformation. In a purely elastic body, this opposing force will restore the initial shape after the external force has been removed. The resistance of a viscous medium decreases over time as it “flows” into a new shape that is in equilibrium with the external forces. After the removal of the force, the body will stay in its new shape and will not return to the original pre-deformation state. Real materials usually have intermediate characteristics, exhibiting viscous and elastic properties at the same time.

Viscoelasticity theory is an extremely rich and wide field, and a comprehensive discussion is far beyond the scope of this book. We therefore introduce a couple of restraints to narrow the topic down to a more manageable size:

- *Linear elasticity*: Viscoelastic parameters are constant and do not depend on the degree of deformation.
- *Small strains*: Deformations are small compared to the size of the object.
- *Isotropy*: Viscoelastic properties do not depend on the direction along which a force acts.
- *Smooth variation of viscoelastic parameters*: We assume that viscoelastic properties do not change abruptly and that their spatial derivatives are negligibly small compared to the variation of displacement amplitudes.

These assumptions are usually sufficient to explain most phenomena encountered in magnetic resonance elastography (MRE). However, sometimes general models are needed, such as anisotropy for the highly fibrous and ordered structure of muscles or neural fibers, and in Section 4.10 we will look beyond these constraints.

### 4.1 Strain

The response of a medium to deformation can be described in terms of *strain* and *stress*. Strain represents the deflection of a mass point from its original position in the undeformed body. Stress quantifies the forces counteracting deformation throughout the medium. Both stress and strain are physical quantities which can – at least in principle – be measured directly, whereas the relationship between them is subject to physical modeling.

*Magnetic Resonance Elastography: Physical Background and Medical Applications*, First Edition.  
Sebastian Hirsch, Jürgen Braun, and Ingolf Sack.

© 2017 Wiley-VCH Verlag GmbH & Co. KGaA. Published 2017 by Wiley-VCH Verlag GmbH & Co. KGaA.

In the following section, a continuous medium will be represented as a number of discrete masses arranged on a rectangular lattice. This formalism is useful to illustrate the key concepts of elasticity; however, it is not limited to highly ordered systems such as perfect crystals. All findings are also applicable to more unstructured systems, such as biological tissue. The following sections are based on the presentation in [40] and [41].

The deformation of a three-dimensional object can be described in terms of its associated *displacement field*  $\mathbf{u}$  in the sense that every point  $\mathbf{r}$  is shifted to a different position  $\mathbf{r} + \mathbf{u}(\mathbf{r})$ . A deformation can change the distance between two points. In the undisturbed state, the distance between points  $\mathbf{r}$  and  $\mathbf{r} + \delta\mathbf{r}$  is  $D = |\delta\mathbf{r}|$ . The deformation shifts these points to  $\mathbf{r} + \mathbf{u}(\mathbf{r})$  and  $\mathbf{r} + \delta\mathbf{r} + \mathbf{u}(\mathbf{r} + \delta\mathbf{r})$ , respectively, as shown in Figure 4.1. The variation  $\delta\mathbf{u} = \mathbf{u}(\mathbf{r} + \delta\mathbf{r}) - \mathbf{u}(\mathbf{r})$  for infinitesimal distances  $\delta\mathbf{r}$  is then

$$\delta u_i = \sum_{j=1}^3 \frac{\partial u_i}{\partial r_j} \delta r_j. \quad (4.1)$$

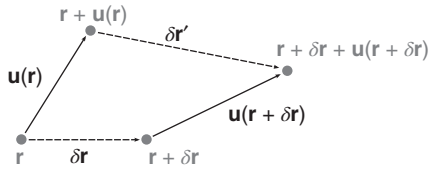
In Appendix C, it will be shown that this can equally be expressed as [41]

$$\delta u_i = \frac{1}{2} \left( \frac{\partial u_i}{\partial r_j} + \frac{\partial u_j}{\partial r_i} \right) + \frac{1}{2} ((\nabla \times \mathbf{u}) \times \delta\mathbf{r})_i. \quad (4.2)$$

The first term on the right-hand side of Eq. (4.2) is referred to as an *infinitesimal strain tensor* :

$$\begin{aligned} \epsilon_{ij} &= \frac{1}{2} \left( \frac{\partial u_i}{\partial r_j} + \frac{\partial u_j}{\partial r_i} \right) = \frac{1}{2} (\nabla \mathbf{u} + (\nabla \mathbf{u})^T) \\ &= \begin{pmatrix} \frac{\partial u_1}{\partial r_1} & \frac{1}{2} \left( \frac{\partial u_1}{\partial r_2} + \frac{\partial u_2}{\partial r_1} \right) & \frac{1}{2} \left( \frac{\partial u_1}{\partial r_3} + \frac{\partial u_3}{\partial r_1} \right) \\ \frac{1}{2} \left( \frac{\partial u_1}{\partial r_2} + \frac{\partial u_2}{\partial r_1} \right) & \frac{\partial u_2}{\partial r_2} & \frac{1}{2} \left( \frac{\partial u_2}{\partial r_3} + \frac{\partial u_3}{\partial r_2} \right) \\ \frac{1}{2} \left( \frac{\partial u_1}{\partial r_3} + \frac{\partial u_3}{\partial r_1} \right) & \frac{1}{2} \left( \frac{\partial u_2}{\partial r_3} + \frac{\partial u_3}{\partial r_2} \right) & \frac{\partial u_3}{\partial r_3} \end{pmatrix}. \end{aligned} \quad (4.3)$$

where  $\epsilon$  is a symmetric ( $\epsilon_{ij} = \epsilon_{ji}$ ) tensor of rank 2 which can be expressed as a  $3 \times 3$  matrix. Due to its symmetry, only six of nine entries are independent. The second term in Eq. (4.2) corresponds to an infinitesimal rotation in the vicinity of point  $\mathbf{r}$ .



**Figure 4.1** Nomenclature used for positions and displacements in a solid body. The two points  $\mathbf{r}$  and  $\mathbf{r} + \delta\mathbf{r}$  are subject to a displacement  $\mathbf{u}$ . Dashed lines represent connections between points before and after a deformation. Solid lines correspond to displacements. Points and their position vectors before and after deformation are shown in gray.

### Linear strain theory

The linear approximation made in Eq. (4.1) by using only the first-order rather than the full (infinite) Taylor series has huge implications for the applicability of that equation. It basically constitutes the foundation of linear elasticity, which deals with small, or rather infinitesimal, strains. However, real-world strains are always finite quantities, so that Eq. (4.1) and all subsequent derivations are always approximations rather than exact descriptions. In MRE, it is generally reasonable to apply this approximation, since the strains are usually very small ( $10^{-4}$ – $10^{-2}$ ). However, other scenarios involving large deformations require a more precise theory, called *finite strain theory*. In this book, we will always use infinitesimal strain theory and discard second and higher orders of strain quantities, which are dominated by the linear order in the regime of small strains.

The trace of the strain tensor,  $\text{tr}(\epsilon) = \nabla \cdot \mathbf{u}$ , quantifies a change in volume according to  $V' = V \cdot (1 + \text{tr}(\epsilon))$  for a small-volume element  $V$ . The off-diagonal elements of  $\epsilon$  parametrize shear strain.

Figure 4.2 depicts the shear strain caused by a force acting in the horizontal direction. The associated displacement field obviously has only a horizontal component. The vertical sides of the rectangle are tilted by an angle  $\theta$ . We can calculate the four spatial derivatives of the two-dimensional displacement field. Since we already know that the vertical component  $u_2 = 0$ , we deduce  $\frac{\partial u_2}{\partial r_1} = 0$  and  $\frac{\partial u_2}{\partial r_2} = 0$ . For the horizontal component, we find

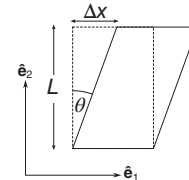
$$\begin{aligned} \frac{\partial u_1}{\partial r_1} &= 0 \quad (\text{the displacement is constant along horizontal lines}) \\ \frac{\partial u_1}{\partial r_2} &= \frac{\Delta x}{L} = \tan \phi. \end{aligned}$$

The strain tensor, as defined in Eq. (4.3), is

$$\epsilon = \begin{pmatrix} 0 & \frac{1}{2} \tan \phi \\ \frac{1}{2} \tan \phi & 0 \end{pmatrix}.$$

We can readily see that the main diagonal of the strain tensor contains only zeros, since the area of the rectangle does not change under shear deformation. This result can be generalized to 3D shear deformations: Let  $\theta_{ij}$ , ( $i \neq j$ ) be the change in the angle between the  $i$ -axis and  $j$ -axis caused by deformation.<sup>1</sup> With the definition  $\gamma_{ij} = \tan \theta_{ij}$ , the strain

**Figure 4.2** Geometrical representation of shear strain. The dashed rectangle represents the undeformed state and the solid trapezoid the deformed body.



<sup>1</sup> Hence,  $\theta$  in Figure 4.2 is  $\theta_{12}$  and  $\theta_{21}$ , since the angle between the two sides of the rectangle changes from  $90^\circ$  to  $90^\circ - \theta$ .

tensor for pure shear strain has the form

$$\epsilon = \begin{pmatrix} 0 & \gamma_{12}/2 & \gamma_{13}/2 \\ \gamma_{21}/2 & 0 & \gamma_{23}/2 \\ \gamma_{31}/2 & \gamma_{32}/2 & 0 \end{pmatrix}.$$

For small deformations, we can linearize the tangent function:

$$\gamma_{ij} = \tan \phi_{ij} \approx \phi_{ij}.$$

The definition of  $\theta_{ij}$  as the difference angle between two sides of a cube implies that  $\theta_{ij} = \theta_{ji}$  and hence  $\gamma_{ij} = \gamma_{ji}$ .

A deformation can be described equivalently by using the *deformation gradient* [42] instead of the strain tensor. Every point of a material under deformation can be labeled with a pre-deformation coordinate  $\mathbf{r}$  and a post-deformation coordinate  $\mathbf{r}'$ . The relation between these two coordinates then is

$$\mathbf{r}' = \mathbf{r} + \mathbf{u}(\mathbf{r}), \quad (4.4)$$

as shown in Figure 4.1. The *deformation gradient*  $\mathbf{F}$  is defined as the derivative of the deformed coordinate with respect to the undeformed coordinate:

$$\begin{aligned} \mathbf{F} &= \nabla_{\mathbf{r}} \mathbf{r}' \\ \implies F_{ij} &= \frac{\partial r'_i}{\partial r_j}, \end{aligned}$$

where  $\nabla_{\mathbf{r}}$  denotes differentiation with respect to  $\mathbf{r}$ . Inserting Eq. (4.4) yields

$$\mathbf{F} = \nabla_{\mathbf{r}}(\mathbf{r} + \mathbf{u}(\mathbf{r})) = \mathbb{1} + \nabla_{\mathbf{r}} \mathbf{u} \quad (4.5)$$

with the  $3 \times 3$  identity matrix  $\mathbb{1}$ . In first-order approximation, we can write  $\mathbf{u}(\mathbf{r}) = \nabla \mathbf{u}(\mathbf{r}) \cdot \mathbf{r}$ , dropping the subscript  $\mathbf{r}$  on the gradient operator, and therefore we can express Eq. (4.4) as

$$\mathbf{r}' = \mathbf{r} + \mathbf{u}(\mathbf{r}) = (\mathbb{1} + \nabla \mathbf{u}) \cdot \mathbf{r} = \mathbf{F} \cdot \mathbf{r}. \quad (4.6)$$

The deformation gradient can thus be interpreted as the linear transform that maps the undeformed to the deformed state.

We can now calculate the magnitude of deformation

$$\begin{aligned} \mathbf{F}^T \mathbf{F} &= (\mathbb{1} + (\nabla \mathbf{u}))^T \cdot (\mathbb{1} + \nabla \mathbf{u}) \\ &= \mathbb{1} + \nabla \mathbf{u} + (\nabla \mathbf{u})^T + (\nabla \mathbf{u})^T \cdot \nabla \mathbf{u} \\ &= \mathbb{1} + 2 \cdot \epsilon + \mathcal{O}((\nabla \mathbf{u})^2). \end{aligned}$$

If we omit the quadratic terms of  $\nabla \mathbf{u}$ , which is permissible in the small-strain regime, we obtain the relationship

$$\epsilon = \frac{1}{2} (\mathbf{F}^T \mathbf{F} - \mathbb{1}). \quad (4.7)$$

Alternatively, the link between  $\mathbf{F}$  and  $\epsilon$  can be expressed as

$$\epsilon = \frac{1}{2} (\mathbf{F} + \mathbf{F}^T) - \mathbb{1}. \quad (4.8)$$

The deformation gradient is used in finite strain theory to describe and study arbitrary deformations. However, for this book and MRE in general, the strain formulation is preferred over the deformation form.

## 4.2 Stress

The strain tensor is a purely phenomenological description of the deformation of a body; it contains no information on the cause of deformation. The forces acting at a point in a solid body can be fully represented by a decomposition into force components parallel and perpendicular to the faces of a small cubic volume element around that point. This yields three forces for each of the three pairs of mutually parallel faces of the cube, resulting in a total of nine components. The forces, normalized to the area  $A$  of one face of the cube, are termed *stresses*. The nine stress components are summarized in the *stress tensor*  $\sigma$ , where the element  $\sigma_{ij}$ ,  $i, j \in \{1, 2, 3\}$  represents the stress along the  $i$ th Cartesian axis on the surface orthogonal to the  $j$ th axis. We assume that the cube is aligned with the coordinate system. Let  $A_j$  denote the area of the face orthogonal to the  $\hat{e}_j$  basis vector and  $F_i$  the force acting on that face in the direction of  $\hat{e}_i$ , then the elements of the stress tensor can be represented as

$$\sigma_{ij} = \frac{F_i}{A_j}, \quad (4.9)$$

as illustrated in Figure 4.3.

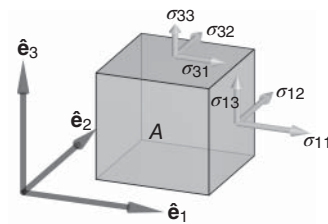
The diagonal components  $\sigma_{ii}$  act orthogonally on the three surfaces. In other words, these forces are directed either toward or away from the center of the cube, and they either compress or expand the volume. The off-diagonal entries  $\sigma_{ij}$ ,  $i \neq j$  characterize stresses tangential to their respective surfaces. They exert a torque on the volume element, causing shear deformation while preserving volume. If the resultant torque of all stresses does not vanish, the cube will rotate. Therefore, the necessary and sufficient condition for a static (equilibrium) configuration is that  $\sigma_{ij} = \sigma_{ji}$  for all pairs ( $i \neq j$ ), so that all torque components cancel. In Figure 4.3, this is shown for stresses  $\sigma_{31}$  and  $\sigma_{13}$ , which act on the same edge and with the same strength, therefore balancing each other. The same must be true for all other pairs of tangential stress components. This condition implies that only six of the nine entries of the stress tensor are independent as long as bulk rotation of the object is prevented.

On the other hand, the diagonal elements,  $\sigma_{ii}$ , compress or expand the volume. Since they act orthogonally on the surfaces of the cube rather than tangentially, they do not cause rotation.

If the stress tensor is evaluated at the location of a surface with outward normal vector  $\hat{n}$ , the projection on  $\hat{n}$  is called (*surface*) *tension* or *traction*:

$$\tau_i = \sum_{j=1}^3 \sigma_{ij} n_j = \sum_{j=1}^3 \sigma_{ji} n_j. \quad (4.10)$$

**Figure 4.3** Definition of the nomenclature to denote stress tensor elements  $\sigma_{ij}$ . The same convention is also used for the strain tensor elements  $\epsilon_{ij}$ .



Hence,  $\tau_i$  represents the force acting on the surface along the  $i$ th Cartesian direction. Using the outward normal vector in the definition implies that forces pulling on the surface (trying to extend the enclosed volume) are positive, whereas compressive forces are negative.

### 4.3 Invariants

We can see easily from Figure 4.3 that the individual elements of the stress tensor,  $\sigma_{ij}$  (and analogously for the strain tensor elements,  $\epsilon_{ij}$ ) change if the coordinate system is rotated. Being second-order tensors, stress and strain tensors depend on the orientation of the coordinate system. However, linear algebra states that three independent invariants exist for each tensor:

$$I_1 = \text{tr}(\epsilon) = \epsilon_{11} + \epsilon_{22} + \epsilon_{33} \quad (4.11)$$

$$I_2 = \frac{1}{2} (\text{tr}(\epsilon^2) - \text{tr}(\epsilon)^2) = \epsilon_{12}^2 + \epsilon_{13}^2 - \epsilon_{11}\epsilon_{22} + \epsilon_{23}^2 - \epsilon_{11}\epsilon_{33} - \epsilon_{22}\epsilon_{33} \quad (4.12)$$

$$I_3 = \det(\epsilon) = (\epsilon_{22}\epsilon_{33} - \epsilon_{23}^2)\epsilon_{11} - (\epsilon_{12}\epsilon_{33} - \epsilon_{13}\epsilon_{23})\epsilon_{12} + (\epsilon_{12}\epsilon_{23} - \epsilon_{13}\epsilon_{23})\epsilon_{13}. \quad (4.13)$$

These invariants and their implications apply analogously to the stress tensor. We can see that  $I_1$  represents volumetric strain, which is therefore independent of the choice of the coordinate system. However, none of the constants reflects the shear strain elements, meaning that shear strain actually depends on the coordinate system. The symmetry of the strain tensor guarantees the existence of three eigenvalues  $\lambda_i$ , which are determined by the equation

$$\det(\epsilon - \lambda_i \cdot \mathbf{1}) = 0 \quad \text{for } i = 1, 2, 3. \quad (4.14)$$

The eigenvalues can alternatively be expressed in terms of the three invariants:

$$\lambda_i^3 - I_1 \cdot \lambda_i^2 + I_2 \cdot \lambda_i - I_3 = 0 \quad \text{for } i = 1, 2, 3. \quad (4.15)$$

Each eigenvalue is associated with an eigenvector, and the three eigenvectors constitute an orthonormal basis. It is therefore possible to express the strain tensor in the coordinate system defined by the eigenvectors:

$$\epsilon' = \begin{pmatrix} \lambda_1 & 0 & 0 \\ 0 & \lambda_2 & 0 \\ 0 & 0 & \lambda_3 \end{pmatrix}. \quad (4.16)$$

This means that in the eigenvector system the full deformation can be expressed by three axial strains, with no shear. These strains are termed *principal strains*. On the basis of these principal strains, the *maximum shear*,  $\gamma_{\max}$ , strain can be calculated as the difference between the maximum and the minimum principal strain:

$$\gamma_{\max} = \text{maximum principal strain} - \text{minimum principal strain}. \quad (4.17)$$

An alternative method of calculating maximum shear strain of a 3D displacement field is *octahedral shear strain* (OSS), which was introduced into MRE by McGarry et al. [43]. OSS is defined as

$$\text{OSS} = \frac{2}{3} \sqrt{(\epsilon_{11} - \epsilon_{22})^2 + (\epsilon_{11} - \epsilon_{33})^2 + (\epsilon_{22} - \epsilon_{33})^2 + 6 \cdot (\epsilon_{12}^2 + \epsilon_{22}^2 + \epsilon_{33}^2)}. \quad (4.18)$$

OSS can be quantified for each voxel separately, giving rise to its use as a spatially resolved measure of shear wave amplitudes to estimate signal quality or to compare wave amplitudes in different subjects.

As a consequence of the quadratic terms in Eq. (4.18), it would not yield sound results if the complex wave  $u_0 \cdot e^{i\omega t}$  was inserted for the strain. Only strain derived from the real or imaginary part of the complex oscillation is suitable for the calculation of OSS. Therefore, OSS is not a constant quantity, but it oscillates about its mean at twice the drive frequency  $\omega$ . Because of that oscillation, OSS measured at a single time point is not a reliable measure of image quality; instead, the average over the full oscillation cycle has to be calculated. This in turn requires some preprocessing of the acquired wave fields, for example, to ensure that there are no temporal phase wraps between time points. While some MRE data processing methods contain these steps as part of their standard pipeline, others, such as those based on gradient unwrapping (see Section 9.2), follow a different path and do not provide the quantities required for OSS calculation, so that OSS estimation cannot be easily integrated into these pipelines.

#### 4.4 Hooke's Law

Stress and strain are not independent of one another. The relationship between the two depends on the type of material and its characteristics. Hooke's law models the relationship between the two tensors in a linear manner:

$$\sigma_{ij} = \sum_{k,l=1}^3 C_{ijkl} \epsilon_{kl}. \quad (4.19)$$

According to this relationship, every single stress  $\sigma_{ij}$  is a function of the full strain field  $\epsilon$ . A medium whose stress-strain relationship is accurately described by Eq. (4.19) is classified as *linear elastic*.  $\mathbf{C}$  is a fourth-order tensor with  $3^4 = 81$  elements. The strain tensor  $\epsilon$  is symmetric by definition (Eq. (4.3)). Equation (4.26) implies that the stress tensor  $\sigma$  possesses the same symmetry, which imposes some constraints on the elements of  $\mathbf{C}$ , namely  $C_{ijkl} = C_{jikl} = C_{ijlk} = C_{klij}$ , so that only 21 of its elements are independent. As a formal simplification, *Voigt notation* can be introduced to replace four-digit indices with two-digit indices according to the following scheme:

$$\begin{array}{lll} 11 \rightarrow 1, & 22 \rightarrow 2, & 33 \rightarrow 3, \\ 23 \rightarrow 4, & 13 \rightarrow 5, & 12 \rightarrow 6. \end{array}$$

Hooke's law (Eq. (4.19)) can then be formulated as a matrix equation:

$$\begin{pmatrix} \sigma_{11} \\ \sigma_{22} \\ \sigma_{33} \\ \sigma_{23} \\ \sigma_{13} \\ \sigma_{12} \end{pmatrix} = \begin{pmatrix} C_{11} & C_{12} & C_{13} & C_{14} & C_{15} & C_{16} \\ C_{12} & C_{22} & C_{23} & C_{24} & C_{25} & C_{26} \\ C_{13} & C_{23} & C_{33} & C_{34} & C_{35} & C_{36} \\ C_{14} & C_{24} & C_{34} & C_{44} & C_{45} & C_{46} \\ C_{15} & C_{25} & C_{35} & C_{45} & C_{55} & C_{56} \\ C_{16} & C_{26} & C_{36} & C_{46} & C_{56} & C_{66} \end{pmatrix} \begin{pmatrix} \epsilon_{11} \\ \epsilon_{22} \\ \epsilon_{33} \\ 2\epsilon_{23} \\ 2\epsilon_{13} \\ 2\epsilon_{12} \end{pmatrix}. \quad (4.20)$$

The factor 2 for the off-diagonal elements of the strain tensor results from summation over identical elements, for example,  $\epsilon_{23} + \epsilon_{32} = 2\epsilon_{23}$ . Note that introducing Voigt

notation does not actually reduce  $\mathbf{C}$  from a fourth-order to a second-order tensor. Transformations, such as reflections or rotations, have to operate on  $C_{ijkl}$  rather than on  $C_{mn}$ , as will be demonstrated in Section 4.6.

Hooke's law can equivalently be formulated using the *compliance* tensor  $\mathbf{S}$ , which is the inverse of the elasticity tensor:  $\mathbf{S} = \mathbf{C}^{-1}$ . Equation (4.19) then reads

$$\epsilon_{ij} = \sum_{k,l=1}^3 S_{ijkl} \sigma_{kl}. \quad (4.21)$$

#### Compliance versus elasticity

The two formulations, Eqs. (4.19) and (4.21), represent the same physical situation, but from different points of view.  $\sigma = \mathbf{C} \cdot \epsilon$  describes the distribution of stresses if the deformation (strain) of a body is known, whereas  $\epsilon = \mathbf{S} \cdot \sigma$  gives the deformation if the acting forces (stresses) are prescribed. Stating this might seem trivial; however, there are some important implications to be considered. Since  $\sigma$  and  $\epsilon$  are second-order tensors and  $\mathbf{C}$  and  $\mathbf{S}$  fourth-order tensors, each element of  $\sigma$  is a weighted sum of *all* elements of  $\epsilon$ , and vice versa. Analogously, there is no one-to-one correspondence between the elements of  $\mathbf{S}$  and  $\mathbf{C}$ .

The most suitable representation of Hooke's law therefore depends on the scenario under consideration. If strain is the independent quantity, and stress as a function of strain is to be derived, using  $\mathbf{C}$  is the more natural choice. Conversely, if the stress is known and the strain has to be determined,  $\mathbf{S}$  is the preferable choice for the parametrization.

## 4.5 Strain-Energy Function

A body can be deformed in two ways. First, an external force can be applied to the surface. Second, the body can be heated or cooled. In both scenarios, energy is either transferred into the body or drained from it. This implies that a deformation is associated with a change in internal energy. It is shown in [41] that the rate of change of the internal energy density  $U$  can be represented as

$$\dot{U} = \dot{Q} + \sum_{i,j=1}^3 \sigma_{ij} \dot{\epsilon}_{ij}, \quad (4.22)$$

where  $Q$  is the heat per unit volume. The differential of  $U$  is thus given by

$$dU = dQ + \sum_{i,j=1}^3 \sigma_{ij} d\epsilon_{ij}. \quad (4.23)$$

According to the laws of thermodynamics, the differential of heat is related to the absolute temperature  $\Theta$  and the entropy per unit volume  $S$  via  $dQ = \Theta dS$ , yielding

$$dU = \Theta dS + \sum_{i,j=1}^3 \sigma_{ij} d\epsilon_{ij}. \quad (4.24)$$



If a deformation occurs in an adiabatic, reversible way, the entropy does not increase ( $dS = 0$ ), such that

$$dU = \sum_{i,j=1}^3 \sigma_{ij} d\epsilon_{ij}. \quad (4.25)$$

Taking the derivative with respect to the strain component  $\epsilon_{ij}$  leads us to

$$\sigma_{ij} = \frac{\partial U}{\partial \epsilon_{ij}}. \quad (4.26)$$

Hence, the stresses within a body under deformation can be derived from the internal energy density. A function with the property exhibited by  $U$  in Eq. (4.26) is called *strain-energy function*.<sup>2</sup> For an irreversible process, an increase in entropy ( $dS > 0$ ) renders the step from Eq. (4.24) to Eq. (4.25) invalid. In that case, a more general strain-energy function  $W$  has to be used instead of the internal energy  $U$  in Eq. (4.26). We will therefore use  $W$  from here on.

From Eq. (4.26), it follows that  $W$  must be of the form

$$W = \frac{1}{2} \cdot \sum_{i,j=1}^3 \sigma_{ij} \epsilon_{ij} = \frac{1}{2} \cdot \sum_{i,j,k,l=1}^3 C_{ijkl} \epsilon_{ij} \epsilon_{kl}. \quad (4.27)$$

Since  $\sigma$  and  $\epsilon$  are related via a first-order differential in Eq. (4.26), an arbitrary offset can be added to  $W$  without affecting the stress–strain relation. It is hence possible to define the undeformed equilibrium state as  $W = 0$ . Furthermore, in equilibrium, all stresses  $\sigma_{ij}$  have to vanish, since otherwise they would constitute a driving force causing deformation, contradicting the assumption of an undeformed state. Therefore, according to Eq. (4.26), the equilibrium state is a stationary point of  $W$  with respect to strains  $\epsilon_{ij}$ .

## 4.6 Symmetries

In Section 4.4, it was explained that the 81 elements of the most general linear elasticity tensor  $C_{ijkl}$  can be reduced to 21 independent elements through a series of symmetry arguments, so that  $\mathbf{C}$  can be represented by a symmetric  $6 \times 6$  matrix. In this chapter, we will demonstrate how this fact can be derived from material symmetries.

The elasticity tensor  $C_{ijkl}$  and the compliance tensor  $S_{ijkl}$  are both fourth-order tensors. Hence, in order to transform them from one coordinate system to another, four “copies” of the transformation matrix  $\mathbf{Q}$  are required:

$$C'_{ijkl} = \sum_{a,b,c,d=1}^3 Q_{ia} Q_{jb} Q_{kc} Q_{ld} C_{abcd} \quad (4.28)$$

and analogously for  $S'_{ijkl}$  (we will use  $\mathbf{C}$  throughout this chapter, but the same arguments hold for  $\mathbf{S}$ ).

If a material possesses a symmetry, this means that there is an associated transformation matrix  $\mathbf{Q}$  that leaves the system invariant, such that  $C_{ijkl} = C'_{ijkl}$  for all entries. The

<sup>2</sup> Despite its name, the strain-energy function represents an energy density. In order to obtain the actual energy stored in a body due to deformation, one has to integrate over the whole volume.

most commonly found symmetries in real-world materials are mirror symmetry (the associated transform is a reflection about the mirror plane) and rotations.

A reflection about a plane orthogonal to one of the three coordinate axes can be represented in matrix form as

$$\mathbf{P}^{(1)} = \begin{pmatrix} -1 & 0 & 0 \\ 0 & 1 & 0 \\ 0 & 0 & 1 \end{pmatrix}, \quad \mathbf{P}^{(2)} = \begin{pmatrix} 1 & 0 & 0 \\ 0 & -1 & 0 \\ 0 & 0 & 1 \end{pmatrix}, \quad \mathbf{P}^{(3)} = \begin{pmatrix} 1 & 0 & 0 \\ 0 & 1 & 0 \\ 0 & 0 & -1 \end{pmatrix}. \quad (4.29)$$

Rotations, on the other hand, have the form

$$\mathbf{R}^{(1)} = \begin{pmatrix} 1 & 0 & 0 \\ 0 & \cos \phi & -\sin \phi \\ 0 & \sin \phi & \cos \phi \end{pmatrix}, \quad \mathbf{R}^{(2)} = \begin{pmatrix} \cos \phi & 0 & -\sin \phi \\ 0 & 1 & 0 \\ \sin \phi & 0 & \cos \phi \end{pmatrix},$$

$$\mathbf{R}^{(3)} = \begin{pmatrix} \cos \phi & -\sin \phi & 0 \\ \sin \phi & \cos \phi & 0 \\ 0 & 0 & 1 \end{pmatrix}, \quad (4.30)$$

with rotation angle  $\phi$  for rotations about the  $\hat{\mathbf{e}}_1$ -,  $\hat{\mathbf{e}}_2$ -, and  $\hat{\mathbf{e}}_3$ -axes, respectively.

In order to demonstrate how the presence of symmetries reduces the number of independent elements of  $\mathbf{C}$  and  $\mathbf{S}$ , we will follow the arguments presented in [42]. For the simplest case, assume that the medium is symmetric with respect to the  $\hat{\mathbf{e}}_2\hat{\mathbf{e}}_3$ -plane at  $r_1 = 0$ . Such a medium is called *monoclinic*. A reflection of the  $r_1$  component must leave the components of  $\mathbf{C}$  invariant, since both the stress and strain components change their signs:

$$\sigma_{ij} = \sum_{k,l=1}^3 C_{ijkl} \epsilon_{kl} \quad \text{in the basis } \{\hat{\mathbf{e}}_1, \hat{\mathbf{e}}_2, \hat{\mathbf{e}}_3\}$$

$$\sigma'_{ij} = \sum_{k,l=1}^3 C'_{ijkl} \epsilon'_{kl} \quad \text{in the basis } \{-\hat{\mathbf{e}}_1, \hat{\mathbf{e}}_2, \hat{\mathbf{e}}_3\}$$

$$C'_{ijkl} = C_{ijkl} \quad \forall i, j, k, l = 1, 2, 3. \quad (4.31)$$

The transform that achieves a flip of the  $\hat{\mathbf{e}}_1$ -axis has the form

$$\mathbf{r}' = \mathbf{P}^{(1)} \mathbf{r} \quad (4.32)$$

with  $\mathbf{P}^{(1)}$  from Eq. (4.29). Inserting  $\mathbf{P}^{(1)}$  into the transformation equation (4.28), we obtain

$$C'_{ijkl} = \sum_{a,b,c,d=1}^3 P_{ia}^{(1)} P_{jb}^{(1)} P_{kc}^{(1)} P_{ld}^{(1)} C_{abcd}. \quad (4.33)$$

$\mathbf{P}^{(1)}$  has the form of an identity matrix, apart from the entry  $-1$  in  $P_{11}^{(1)}$ . This implies that every element  $C'_{ijkl}$  with  $n$  occurrences of the value  $1$  among its four indices is proportional to  $(-1)^n C_{ijkl}$ . Therefore, for each element with an odd number of  $1$ 's, such as  $C_{1112}$  or  $C_{1234}$ , we obtain  $C'_{ijkl} = -C_{ijkl}$ . Together with the requirement of Eq. (4.31), this implies that each of these elements has to be zero. The existence of a plane of symmetry therefore reduces the number of independent viscoelastic parameters from 21 in the general case to 13.

An analogous argument can be used to analyze *orthotropic* materials with three perpendicular planes of symmetry.<sup>3</sup> In this case, elements with an odd number of 2's or 3's among their four indices vanish as well, and only nine independent parameters remain. The orthotropic elasticity tensor reads in Voigt notation

$$\mathbf{C} = \begin{pmatrix} C_{11} & C_{12} & C_{13} & 0 & 0 & 0 \\ C_{12} & C_{22} & C_{23} & 0 & 0 & 0 \\ C_{13} & C_{23} & C_{33} & 0 & 0 & 0 \\ 0 & 0 & 0 & C_{44} & 0 & 0 \\ 0 & 0 & 0 & 0 & C_{55} & 0 \\ 0 & 0 & 0 & 0 & 0 & C_{66} \end{pmatrix}. \quad (4.34)$$

Finally, the highest degree of symmetry that can be found in an anisotropic medium is referred to as *transverse isotropy*. This term designates a material that has isotropic properties in a given plane and different properties along the normal vector of that plane. For example, there is no distinguished direction in a bundle of aligned fibers in the plane orthogonal to the fibers, whereas the direction along the fibers stands out (see Figure 4.5). Mathematically, transverse isotropy is characterized by rotational symmetry about one axis for arbitrary rotation angles. This is equivalent to the existence of infinitely many (nonperpendicular) symmetry planes that all contain the fiber direction as a tangent vector.

If we assume that the fibers are aligned with the  $\hat{\mathbf{e}}_3$ -axis, the symmetry-preserving rotation is  $\mathbf{R}^{(3)}$ , as given for arbitrary rotation angles  $\phi$  in Eq. (4.30) above. The elements of the elasticity tensor transform according to

$$C'_{ijkl} = \sum_{a,b,c,d=1}^3 R_{ia}^{(3)} R_{jb}^{(3)} R_{kc}^{(3)} R_{ld}^{(3)} C_{abcd}. \quad (4.35)$$

Since every plane that has a normal vector in the  $\hat{\mathbf{e}}_1\hat{\mathbf{e}}_2$ -plane is a symmetry plane of the material, this includes specifically the plane orthogonal to  $\hat{\mathbf{e}}_1$ , which was taken as the symmetry plane in the discussion of a monoclinic medium. By the same argument as above, all eight coefficients  $C'_{ijkl}$  with an odd number of 1's across their subscripts have to be zero. However, rotation symmetry prescribes additional relations that do not hold in the monoclinic case. As an example, take the transformation of the component<sup>4</sup>

$$\begin{aligned} C'_{1323} &= R_{11} R_{33} R_{21} R_{33} \cdot C_{1313} + R_{12} R_{33} R_{21} R_{33} \cdot C_{2313} \\ &\quad + R_{11} R_{33} R_{22} R_{33} \cdot C_{1323} + R_{12} R_{33} R_{22} R_{33} \cdot C_{2323}. \end{aligned} \quad (4.36)$$

Of course, the full transformation according to Eq. (4.35) contains more terms than shown here; however, since  $R_{31} = R_{13} = R_{23} = R_{32} = 0$ , only the four terms listed above remain. Of these, we know from the above argument that  $C_{2313}$  and  $C_{1323}$  are zero, since they have an odd number of 1's among their indices. The same is true for  $C_{1323}$  on the

<sup>3</sup> There cannot be a medium with only two perpendicular planes of symmetry, because the reflection about two such planes automatically establishes symmetry about a third perpendicular plane.

<sup>4</sup> We drop the superscript that denotes the rotation axis for the matrix  $\mathbf{R}$  to improve readability.

left-hand side of the equation, so that we obtain (with  $R_{33} = 1$ )

$$\begin{aligned}
0 &= R_{11} R_{21} \cdot C_{1313} + R_{12} R_{22} \cdot C_{2323} \\
\Rightarrow 0 &= \cos \phi \cdot \sin \phi \cdot C_{1313} + (-\sin \phi) \cdot \cos \phi \cdot C_{2323} \\
\Rightarrow 0 &= \cos \phi \cdot \sin \phi \cdot (C_{2323} - C_{1313}) \\
\Rightarrow C_{2323} &= C_{1313}.
\end{aligned}$$

Similar considerations finally lead us to a stress–strain relation of the form

$$\begin{pmatrix} \sigma_{11} \\ \sigma_{22} \\ \sigma_{33} \\ \sigma_{23} \\ \sigma_{31} \\ \sigma_{12} \end{pmatrix} = \begin{pmatrix} C_{1111} & C_{1122} & C_{1133} & 0 & 0 & 0 \\ C_{1122} & C_{1111} & C_{1133} & 0 & 0 & 0 \\ C_{1133} & C_{1133} & C_{3333} & 0 & 0 & 0 \\ 0 & 0 & 0 & C_{1313} & 0 & 0 \\ 0 & 0 & 0 & 0 & C_{1313} & 0 \\ 0 & 0 & 0 & 0 & 0 & \frac{C_{1111} - C_{1122}}{2} \end{pmatrix} \cdot \begin{pmatrix} \epsilon_{11} \\ \epsilon_{22} \\ \epsilon_{33} \\ 2\epsilon_{23} \\ 2\epsilon_{31} \\ 2\epsilon_{12} \end{pmatrix}. \quad (4.37)$$

There are only five independent parameters left for a transverse isotropic medium. Notably, the last element,  $C_{1212}$ , has been substituted with a linear combination of  $C_{1111}$  and  $C_{1122}$ . This justifies the term “plane of isotropy” for the  $\hat{\mathbf{e}}_1\hat{\mathbf{e}}_2$ -plane, since shear deformations within that plane are governed by the same elastic constants as axial deformations, analogous to isotropic materials. By contrast, shear strains with an out-of-plane component ( $\epsilon_{23}$  and  $\epsilon_{31}$ ) are governed by constant  $C_{1313}$ , which is unrelated to all other tensor elements. Using Voigt notation, the elasticity tensor can be equivalently written as [42]

$$\mathbf{C} = \begin{pmatrix} C_{11} & C_{12} & C_{13} & 0 & 0 & 0 \\ C_{12} & C_{11} & C_{13} & 0 & 0 & 0 \\ C_{13} & C_{13} & C_{33} & 0 & 0 & 0 \\ 0 & 0 & 0 & C_{44} & 0 & 0 \\ 0 & 0 & 0 & 0 & C_{44} & 0 \\ 0 & 0 & 0 & 0 & 0 & \frac{C_{11} - C_{12}}{2} \end{pmatrix}. \quad (4.38)$$

Since  $\boldsymbol{\sigma}$  and  $\boldsymbol{\epsilon}$  share the same symmetry properties, the same line of arguments applies to  $\mathbf{S}$ , which has the same form and the same number of independent parameters as  $\mathbf{C}$ . We will give explicit expressions for  $\mathbf{S}$  and  $\mathbf{C}$  for the transverse isotropic case in Section 4.7.4.

The highest possible degree of symmetry is *isotropy*, which means that the elastic properties do not depend on the direction of strains and stresses. This case can be derived from the transverse isotropic case by introducing either  $\hat{\mathbf{e}}_1$  or  $\hat{\mathbf{e}}_2$  as another rotational symmetry axis for arbitrary rotation angles. By the same argument as above, we find that

$$C_{2222} = C_{3333} \quad \Rightarrow C_{22} = C_{33} \quad (4.39)$$

$$C_{1122} = C_{1133} \quad \Rightarrow C_{12} = C_{13} \quad (4.40)$$

$$C_{1313} = C_{1212} \quad \Rightarrow C_{44} = \frac{C_{11} - C_{12}}{2}. \quad (4.41)$$

The elasticity tensor for an isotropic medium hence has the form

$$\mathbf{C} = \begin{pmatrix} C_{11} & C_{12} & C_{12} & 0 & 0 & 0 \\ C_{12} & C_{11} & C_{12} & 0 & 0 & 0 \\ C_{12} & C_{12} & C_{12} & 0 & 0 & 0 \\ 0 & 0 & 0 & \frac{C_{11}-C_{12}}{2} & 0 & 0 \\ 0 & 0 & 0 & 0 & \frac{C_{11}-C_{12}}{2} & 0 \\ 0 & 0 & 0 & 0 & 0 & \frac{C_{11}-C_{12}}{2} \end{pmatrix}. \quad (4.42)$$

Obviously, a linear isotropic medium is characterized by only two elastic constants,  $C_{11}$  and  $C_{12}$ . The physical meaning of these constants will be discussed in Section 4.7.

## 4.7 Engineering Constants

The symmetry transforms we used in Section 4.6 to calculate the elasticity tensors  $\mathbf{C}$  for different degrees of symmetry apply identically to the compliance tensor  $\mathbf{S}$ . For the linear isotropic case, we can therefore represent the stress–strain relation as

$$\begin{pmatrix} \epsilon_{11} \\ \epsilon_{22} \\ \epsilon_{33} \\ 2\epsilon_{23} \\ 2\epsilon_{31} \\ 2\epsilon_{12} \end{pmatrix} = \begin{pmatrix} S_{11} & S_{12} & S_{12} & 0 & 0 & 0 \\ S_{12} & S_{11} & S_{12} & 0 & 0 & 0 \\ S_{12} & S_{12} & S_{11} & 0 & 0 & 0 \\ 0 & 0 & 0 & 2 \cdot (S_{11} - S_{12}) & 0 & 0 \\ 0 & 0 & 0 & 0 & 2 \cdot (S_{11} - S_{12}) & 0 \\ 0 & 0 & 0 & 0 & 0 & 2 \cdot (S_{11} - S_{12}) \end{pmatrix} \cdot \begin{pmatrix} \sigma_{11} \\ \sigma_{22} \\ \sigma_{33} \\ \sigma_{23} \\ \sigma_{31} \\ \sigma_{12} \end{pmatrix}. \quad (4.43)$$

As in the case of the isotropic elasticity tensor, the compliance tensor only depends on two constants,  $S_{11}$  and  $S_{12}$ . In the following sections, we analyze the physical meaning of these parameters and their relationship to the three principal types of strain: uniaxial loading, shear, and volumetric strain.

### 4.7.1 Young's Modulus and Poisson's Ratio

Imagine a block of isotropic material that is subjected to a pushing force from above ( $\hat{\mathbf{e}}_3$ ), but is not constrained on its sides, as shown in Figure 4.4. This scenario is known as uniaxial loading. The only acting stress is  $\sigma_{33}$ . From Eq. (4.43), we gather that

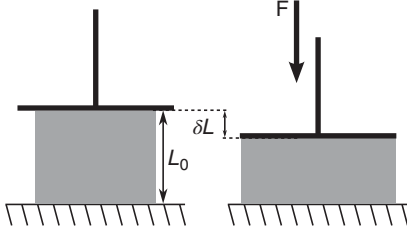
$$\epsilon_{11} = \epsilon_{22} = S_{12} \cdot \sigma_{33} \quad (4.44)$$

$$\epsilon_{33} = S_{11} \cdot \sigma_{33} \quad (4.45)$$

$$\epsilon_{23} = \epsilon_{13} = \epsilon_{12} = 0. \quad (4.46)$$

Not surprisingly, the strains orthogonal to the acting stress are equal since the medium is isotropic. Furthermore, all shear strains are zero, indicating that purely axial stress can only cause axial strains and no shear deformation. For the strain along the acting stress, we introduce *Young's modulus*,  $E$ , such that

$$\epsilon_{33} = \frac{1}{E} \sigma_{33}. \quad (4.47)$$



**Figure 4.4** Diagram of applying uniaxial loading to a body to quantify its Young's modulus. The force acting on the plate on top of the body generates a stress according to  $\sigma_{33} = \frac{F}{A}$ , where  $A$  is the contact area between the body and the pressure plate. The resulting strain is  $\epsilon_{33} = \frac{\delta L}{L_0}$ . Since the body is not constrained laterally, it can expand perpendicular to the direction of the acting stress. The in-plane strains are then determined by Poisson's ratio, as explained in the text.

For the transverse strains, we introduce a second parameter, *Poisson's ratio*  $\nu$ , such that

$$\epsilon_{11} = \epsilon_{22} = -\frac{\nu}{E}\sigma_{33}. \quad (4.48)$$

For positive values of  $\nu$ , Eq. (4.48) indicates that compressive strain ( $<0$ ) along one axis is compensated by expansive strain ( $>0$ ) in the transverse plane, and vice versa. For  $\nu = \frac{1}{2}$ , the medium is perfectly incompressible, whereas  $\nu = 0$  represents a perfectly compressible medium, in which strains and stresses along different axes are uncoupled. Most real-world materials possess intermediate properties, with  $0 < \nu < \frac{1}{2}$ , where higher values represent reduced compressibility. *Auxetic* materials are characterized by negative Poisson's ratios, which means that compressive stress along one axis also causes compression in the transverse plane. Such a behavior is caused by special geometries of the microscopic structure. An example of an auxetic material is paper.

With these definitions of Young's modulus and Poisson's ratio, we find that

$$S_{11} = \frac{1}{E} \quad (4.49)$$

$$S_{12} = -\frac{\nu}{E}. \quad (4.50)$$

In an anisotropic medium, the response of the object depends on the direction along which a stress acts. This implies that Poisson's ratio depends on the direction of deformation. The more general definition is therefore

$$\nu_{ij} = -\frac{\partial \epsilon_{jj}}{\partial \epsilon_{ii}}. \quad (4.51)$$

Young's modulus becomes dependent on the direction of the strain as well. A representation for a compliance tensor of an anisotropic medium will be given in Section 4.7.4.

#### 4.7.2 Shear Modulus and Lamé's First Parameter

A second type of deformation occurs when a body is subjected to shear strain (see Figure 4.2 for a graphical representation). Shear stresses and strains are represented by the off-diagonal elements  $\sigma_{ij}$  and  $\epsilon_{ij}$  ( $i \neq j$ ). From Eq. (4.43) we can see that, for pure shear strain, the individual components are uncoupled. The proportionality constant between stress and strain is the shear modulus  $\mu$ :  $\epsilon_{ij} = \frac{1}{\mu}\sigma_{ij}$ . Therefore, we have  $S_{44} = \frac{1}{\mu}$ .

In the representation of the compliance tensor used in Eq. (4.43), the last three diagonal entries were given by

$$S_{44} = 2 \cdot (S_{11} - S_{12}). \quad (4.52)$$

By substituting  $S_{11} = \frac{1}{E}$  and  $S_{12} = -\frac{\nu}{E}$ , we obtain

$$S_{44} = \frac{1}{\mu} = 2 \cdot \left( \frac{1}{E} + \frac{\nu}{E} \right) = 2 \cdot \frac{1 + \nu}{E}. \quad (4.53)$$

The shear modulus is thus not an independent quantity, but it is related to Young's modulus and Poisson's ratio via

$$\mu = \frac{E}{2(1 + \nu)}. \quad (4.54)$$

We now know all parameters that are necessary to represent the compliance tensor of a linear isotropic medium with physically meaningful quantities:

$$\begin{pmatrix} \epsilon_{11} \\ \epsilon_{22} \\ \epsilon_{33} \\ 2\epsilon_{23} \\ 2\epsilon_{31} \\ 2\epsilon_{12} \end{pmatrix} = \begin{pmatrix} \frac{1}{E} & -\frac{\nu}{E} & -\frac{\nu}{E} & 0 & 0 & 0 \\ -\frac{\nu}{E} & \frac{1}{E} & -\frac{\nu}{E} & 0 & 0 & 0 \\ -\frac{\nu}{E} & -\frac{\nu}{E} & \frac{1}{E} & 0 & 0 & 0 \\ 0 & 0 & 0 & \frac{1}{\mu} & 0 & 0 \\ 0 & 0 & 0 & 0 & \frac{1}{\mu} & 0 \\ 0 & 0 & 0 & 0 & 0 & \frac{1}{\mu} \end{pmatrix} \cdot \begin{pmatrix} \sigma_{11} \\ \sigma_{22} \\ \sigma_{33} \\ \sigma_{23} \\ \sigma_{31} \\ \sigma_{12} \end{pmatrix}. \quad (4.55)$$

It is important to note that Young's modulus and Poisson's ratio are not by any means distinguished quantities for the representation of elastic properties. Many other parameters can be used instead. However, due to the fact that the compliance (and elasticity) tensors in isotropic materials depend only on two parameters, any pair of elastic constants can be converted to any other pair.<sup>5</sup> One useful parametrization is the pair  $(\mu, \lambda)$ , where  $\lambda$  is *Lamé's first parameter*. It can be calculated from  $E$  and  $\nu$  as

$$\lambda = \frac{E\nu}{(1 + \nu) \cdot (1 - 2\nu)}. \quad (4.56)$$

Unlike the previously discussed parameters,  $\lambda$  does not have a direct physical interpretation. We can see that, in the case of a perfectly incompressible material ( $\nu = \frac{1}{2}$ ), the denominator becomes 0 and hence  $\lambda = \infty$ . For perfect compressibility ( $\nu = 0$ ), on the other hand,  $\lambda = 0$ . We can hence conclude that  $\lambda$  reflects how easily a material can be compressed, however; it is *not* identical to compressibility or the compression modulus, which we will denote by  $\kappa$  and  $K$ , respectively. Rather,  $\lambda$  combines  $K$  and  $\mu$  and can become negative. The significance of Lamé's first parameter will become more obvious in Section 4.9, when we decompose arbitrary deformation fields into pure shear and pure compression components.

### 4.7.3 Compressibility and Bulk Modulus

From the above discussion it is clear that the Poisson's ratio is closely linked to the *compressibility*  $\kappa$  of a medium. The terms *compression* and, its opposite, *expansion*, refer to

<sup>5</sup> A very useful conversion table can be found at [https://en.wikipedia.org/wiki/Bulk\\_modulus](https://en.wikipedia.org/wiki/Bulk_modulus)

volumetric strain

$$\text{tr}(\epsilon) = \epsilon_{11} + \epsilon_{22} + \epsilon_{33}, \quad (4.57)$$

which is a scalar quantity. Volumetric strain is effected by axial stresses  $\sigma_{ii}$ . We will assume that axial stresses act along all three coordinate axes, and that there are no shear stresses. Under these circumstances, Eq. (4.55) reduces to

$$\begin{pmatrix} \epsilon_{11} \\ \epsilon_{22} \\ \epsilon_{33} \end{pmatrix} = \begin{pmatrix} \frac{1}{E} & -\frac{\nu}{E} & -\frac{\nu}{E} \\ -\frac{\nu}{E} & \frac{1}{E} & -\frac{\nu}{E} \\ -\frac{\nu}{E} & -\frac{\nu}{E} & \frac{1}{E} \end{pmatrix} \cdot \begin{pmatrix} \sigma_{11} \\ \sigma_{22} \\ \sigma_{33} \end{pmatrix}. \quad (4.58)$$

Calculating volumetric strain according to Eq. (4.57) yields

$$\begin{aligned} \text{tr}(\epsilon) &= -2\frac{\nu}{E} \cdot (\sigma_{11} + \sigma_{22} + \sigma_{33}) + \frac{1}{E} (\sigma_{11} + \sigma_{22} + \sigma_{33}) \\ &= \frac{1-2\nu}{E} \cdot (\sigma_{11} + \sigma_{22} + \sigma_{33}). \end{aligned} \quad (4.59)$$

As mentioned in Section 4.1, volumetric strain can be understood as the relative volume change of a body under deformation:

$$\text{tr}(\epsilon) = \frac{\Delta V}{V}. \quad (4.60)$$

On the other hand, the axial stresses  $\sigma_{ii}$  quantify the forces per area that push (or pull) orthogonal to the surface of a cube aligned with the coordinate system (see Figure 4.3). This is the equivalent of a differential pressure  $\Delta p$  that transforms the body from the original to the deformed state.<sup>6</sup> We can therefore define

$$\Delta p = -\frac{1}{3} (\sigma_{11} + \sigma_{22} + \sigma_{33}). \quad (4.61)$$

By convention, when describing pressures, the minus sign indicates that an increase in pressure yields compression, whereas a pressure decrease causes expansion. We can now reformulate Eq. (4.59) as

$$\begin{aligned} \frac{\Delta V}{V} &= -3\Delta p \cdot \frac{1-2\nu}{E} \\ \Rightarrow \kappa &\equiv -\frac{1}{V} \frac{\partial V}{\partial p} = \frac{3(1-2\nu)}{E}, \end{aligned} \quad (4.62)$$

where we switched from finite differences to true derivatives to be more mathematically correct. The quantity  $\kappa$  is called *compressibility*. Its inverse is referred to as *bulk modulus* or *compression modulus*:

$$K \equiv \frac{1}{\kappa} = \frac{E}{3(1-2\nu)}. \quad (4.63)$$

The derivative  $\frac{\partial V}{\partial p}$  is always negative, since a pressure increase reduces the volume and vice versa, such that  $K, \kappa \geq 0$ . Low compressibility (and a high bulk modulus) indicates a stiff material that permits only a small volume change for a given pressure, whereas high

<sup>6</sup> We do not know, nor care about, the initial pressure that the undeformed state is balanced with, since it does not contribute to the volumetric deformation.



compressibility (low bulk modulus) characterizes easily compressible materials.  $\kappa = 0$  and  $K = \infty$  represent incompressible materials.

From Eq. (4.62), it is readily seen that perfect incompressibility ( $\kappa = 0$ ) implies  $\nu = 1/2$  or an infinitely large Young's modulus  $E$ . The first case corresponds to material that can be elongated or jolted with no change in its volume (requiring contraction perpendicular to the direction of elongation or expansion perpendicular to the direction of compression), while in the second case the material is resistant to any such deformation.

#### 4.7.4 Compliance and Elasticity Tensor for a Transversely Isotropic Material

It was shown in Section 4.6 that a transversely isotropic medium is characterized by five independent parameters. The stress–strain relation, using stress as the independent quantity, for such a medium with the symmetry plane perpendicular to the 3-axis, has the form

$$\epsilon = \mathbf{S} \cdot \sigma = \begin{pmatrix} 1/E_1 & -\nu_{21}/E_1 & -\nu_{31}/E_3 & 0 & 0 & 0 \\ -\nu_{21}/E_1 & 1/E_1 & -\nu_{31}/E_3 & 0 & 0 & 0 \\ -\nu_{13}/E_1 & -\nu_{13}/E_1 & 1/E_3 & 0 & 0 & 0 \\ 0 & 0 & 0 & 1/\mu_{13} & 0 & 0 \\ 0 & 0 & 0 & 0 & 1/\mu_{13} & 0 \\ 0 & 0 & 0 & 0 & 0 & 1/\mu_{12} \end{pmatrix} \cdot \begin{pmatrix} \sigma_{11} \\ \sigma_{22} \\ \sigma_{33} \\ 2\sigma_{23} \\ 2\sigma_{13} \\ 2\sigma_{12} \end{pmatrix}, \quad (4.64)$$

which is the inverse of Eq. (4.20). Apart from the factor 2 for the last three entries of  $\epsilon$ ,  $\sigma$  and  $\epsilon$  have the same form. The block structure of the compliance matrix in Eq. (4.64) ensures that the axial stresses ( $\sigma_{ii}$ ) translate to purely axial strains ( $\epsilon_{jj}$ ). Compression or elongation along each axis causes a strain along the same axis, with the respective Young's modulus  $E_i$  ( $E_1 = E_2 \neq E_3$ ) as the proportionality constant. In addition, deformation also occurs along the other two axes, which is governed by the ratio of Poisson's ratio to Young's moduli. Coupling between in-plane stresses and strains is quantified by the in-plane Young's modulus  $E_1$ , the Poisson's ratio  $\nu_{21}$ , and the in-plane shear modulus  $\mu_{12}$ . Coupling between in-plane and through-plane components depends on  $E_1$ ,  $E_3$ ,  $\nu_{31}$ , and  $\nu_{13}$ . Symmetry of the compliance tensor requires that  $\nu_{13} = \nu_{31} \cdot \frac{E_1}{E_3}$ .

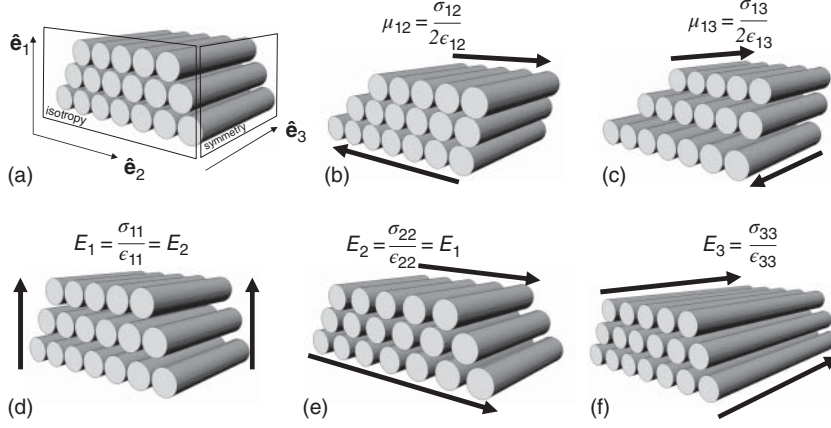
The last three entries of the stress and strain vectors correspond to shear deformation. They are independent of axial deformation, and coupling between stress and strain is parametrized by the shear moduli  $\mu_{12}$  and  $\mu_{13}$ . The in-plane shear modulus is not independent, but determined by the other parameters:

$$\mu_{12} = \frac{E_1}{2(1 + \nu_{21})}. \quad (4.65)$$

Hence, there are a total of five independent elastic parameters in the compliance tensor of a transversely isotropic medium:  $E_1$ ,  $E_3$ ,  $\nu_{12}$ ,  $\nu_{31}$ , and  $\mu_{13}$  (Figure 4.5).

Since  $\mathbf{S}$  is a positive definite matrix,<sup>7</sup> it can be inverted to yield the elasticity tensor  $\mathbf{C}$ . For a transversely isotropic medium, the elasticity tensor has the form displayed in

<sup>7</sup> This is a consequence of the strain-energy function being zero for the undeformed state and yielding positive values for all deformed states. If this were not the case, it would imply the existence of a deformed state with a lower potential energy than the undeformed state.



**Figure 4.5** (a) Shear moduli in a fiber-reinforced transversely isotropic material with planes of symmetry ( $\hat{e}_1\hat{e}_3, \hat{e}_2\hat{e}_3$ ) and a plane of isotropy ( $\hat{e}_1\hat{e}_2$ ). Different types of deformation probe different mechanical moduli: shear deformation perpendicular (b) and parallel (c) to the fibers probes the two shear moduli,  $\mu_{12}$  and  $\mu_{13}$ , respectively. Axial deformation along a single axis probes Young's moduli  $E_1 = E_2$  and  $E_3$  (d-f).

Eq. (4.38), with

$$\begin{aligned}
 C_{11} = C_{22} &= \frac{E_1}{1 + \nu_{21}} \frac{1 - \nu_{31}^2 E_1 / E_3}{D} \\
 C_{33} &= \frac{(1 - \nu_{21}) E_3}{D} \\
 C_{12} &= \frac{E_1}{1 + \nu_{21}} \frac{\nu_{21} + \nu_{31}^2 E_1 / E_3}{D} \\
 C_{13} = C_{23} &= \frac{E_1 \nu_{31}}{D} \\
 C_{44} = C_{55} &= \mu_{13} \\
 C_{66} &= \mu_{12} \quad \text{with} \\
 D &= 1 - \nu_{21} - 2\nu_{31}^2 \frac{E_1}{E_3}.
 \end{aligned} \tag{4.66}$$

## 4.8 Viscoelastic Models

The term *viscoelastic* is composed of *viscous* and *elastic*. As outlined above, these two properties characterize different types of responses of a medium to an external force. This section will first analyze viscous and elastic behavior separately and then proceed to combine them into a number of viscoelastic models.

In the following discussion, we will neglect inertia, which in reality gives rise to oscillatory effects and is a prerequisite for mechanical wave propagation. Hence, the models

to be introduced here are abstract and do not apply to real materials. One way to imagine such media is to separate structure from mass: remove all mass from a material, so that only its structure – the component responsible for transmitting forces across the body – remains. That way, mechanical coupling between different regions of the medium is preserved, while its mass density is decreased to zero, allowing for instantaneous acceleration and deceleration without requiring infinitely large forces.

#### 4.8.1 Elastic Model: Spring

A purely elastic medium deforms when a force is applied, but will immediately return to its original state once the force is removed. In other words, deformation of an elastic medium is a fully reversible process. This has a number of implications:

- 1) The fact that the body returns to its original shape means that no energy is dissipated during deformation. The free energy of the medium can increase during deformation (since deforming usually requires work to be performed on a body), but this energy is later released when the original state is restored. Therefore, an elastic medium can store energy but will not convert it to heat.
- 2) The response of an elastic body to deformation can be analyzed without considering its history. Purely elastic media therefore do not exhibit hysteresis.

A model system for purely elastic media is a (massless) spring. In the one-dimensional case, stress and strain are scalar quantities and the stress–strain relation can be parametrized through Young’s modulus  $E$  of the spring:

$$\sigma_e = E\epsilon. \quad (4.67)$$

The strain is the change in length relative to the original length  $L_0$  of the spring:

$$\epsilon = \frac{\Delta L}{L_0}. \quad (4.68)$$

If a certain amount of stress,  $\sigma_0$ , is applied, the spring is shortened or elongated to  $L = L_0 + \Delta L$ , such that

$$\Delta L = \frac{L_0}{E}\sigma_0. \quad (4.69)$$

In agreement with the convention introduced in Section 4.2, positive stresses indicate pulling forces, associated with an elongation of the spring and hence  $\Delta L > 0$ , whereas compressive stresses, causing a shortening of the spring, are characterized by  $\sigma < 0$  and  $\Delta L < 0$ . Since the spring is considered massless, the strain can follow the stress without delay, as no mass has to be accelerated or decelerated.<sup>8</sup> As a consequence, Eq. (4.67) is also valid for time-dependent deformation:

$$\sigma_e(t) = E\epsilon(t). \quad (4.70)$$

Caution is in order when the terminology related to elasticity is used in a quantitative sense. Elasticity is *not* a synonym for “deformability” or “compliance” but rather the opposite. High elasticity means that large stresses are necessary to achieve even a small deformation. It might be more intuitive to refer to the (elastic) modulus rather than to elasticity when a quantitative statement or a comparison is intended.

<sup>8</sup> This is, of course, an idealized assumption and real-world springs always possess a certain mass, which causes them to oscillate about stationary points. Oscillations and waves will be discussed in Section 4.9.

#### 4.8.2 Viscous Model: Dashpot

In contrast to an elastic medium, a viscous body “flows” out of shape under stress and does not return to its original shape once the load is removed. A highly viscous medium resembles liquids such as honey or crude oil; however, in this treatment, we again neglect inertia, so that the model does not have a real-world counterpart.

The fact that a viscous medium retains its deformed state even after the stress is removed means that the work performed during deformation has been converted to a different form of energy and is not available for performing mechanical work. In most cases, internal friction during deformation converts the mechanical work into heat, which is an irreversible process.

The model system for a purely viscous medium is a *dashpot*, a piston immersed in a pot filled with a viscous fluid, such as oil. The piston can move through the oil, but due to the viscosity of the fluid, friction causes resistive forces. Since friction is proportional to the velocity of the moving piston, the stress–strain relation of a dashpot accounts for the rate of change of the strain:

$$\sigma_v = \eta \dot{\epsilon}, \quad (4.71)$$

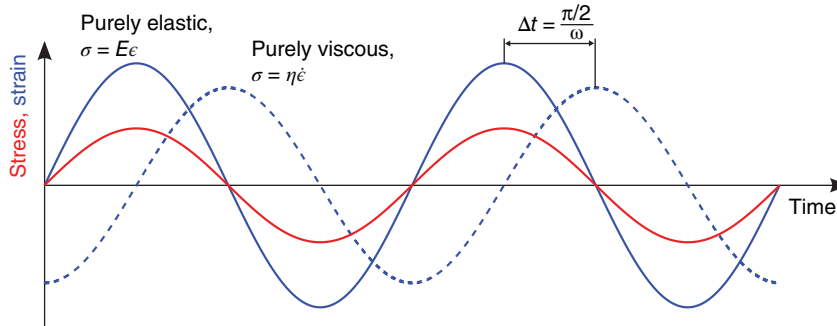
where  $\eta$  quantifies the viscosity of the fluid. For a constant stress  $\sigma_0$ , Eq. (4.71) implies a constant deformation velocity  $\dot{\epsilon}$ , meaning that the strain increases linearly with time. Hence, there is no equilibrium under a constant stress condition, and the medium will continue to “flow apart” until the stress is removed, at which point the body will retain its shape. Furthermore, the medium does not resist the deformation itself – even large deformation can be effected by small stresses over long periods of time.

#### Real-valued and complex moduli

Thus far, we have not discussed the range of values of elastic moduli. Young’s modulus  $E$  of an ideal spring and the viscosity  $\eta$  of an ideal dashpot are both real-valued positive quantities. However, if we analyze the stress–strain relations, Eqs. (4.70) and (4.71), for an oscillating stress  $\sigma(t) = \sigma_0 \cdot \exp(i\omega t)$  with amplitude  $\sigma_0$  and angular frequency  $\omega$ , something remarkable happens:

$$\begin{aligned} \epsilon &= \frac{\sigma(t)}{E} = \frac{\sigma_0}{E} \cdot \exp(i\omega t) && \text{(spring)} \\ \dot{\epsilon} &= \frac{\sigma(t)}{\eta} \implies \epsilon(t) = \frac{\sigma_0}{\eta} \cdot \left(-\frac{i}{\omega}\right) \cdot \exp(i\omega t) && \text{(dashpot)} \end{aligned}$$

A graphical representation of this scenario is given in Figure 4.6. Keeping in mind that  $E$ ,  $\eta$ ,  $\sigma_0$ , and  $\omega$  are all real-valued positive quantities, we find that, for the spring, strain is just a scaled version of stress. For the dashpot, on the other hand, the factor  $i$  introduces a phase shift of  $90^\circ$  between the two, such that strain lags behind stress by one quarter of an oscillation period. If we condense Eqs. (4.70) and (4.71) into the general form of the one-dimensional version of Hooke’s law,  $\sigma = Z\epsilon$ , with a viscoelastic modulus  $Z$ , we note that  $Z$  can be a complex quantity. If  $Z$  is strictly real, it characterizes a purely elastic medium, such as a spring. Conversely, if  $Z$  is purely imaginary, it represents a perfectly viscous medium. In most real-world cases,  $Z$  is located in the first quadrant of the complex plane, with  $\text{Re}(Z), \text{Im}(Z) > 0$ , which is characteristic of a medium that exhibits both elastic and viscous properties.



**Figure 4.6** The real part of an oscillating stress (red) with frequency  $\omega$ , and the resulting strain in a purely elastic (solid) and a purely viscous (dashed) medium. The elastic strain is in phase with the acting stress, whereas the viscous strain lags behind the stress by one quarter of the oscillation period.

### 4.8.3 Combinations of Elastic and Viscous Elements

Springs and dashpots can be combined in a manner very similar to the combination of resistors and inductors in electrical circuits, and the resultant systems will exhibit hybrid characteristics. The two most basic ways of combining two elements is to assemble them either in series or in parallel and to apply a stress to the compound system. The parallel arrangement of a spring and a dashpot is called *Voigt model* (or *Kelvin–Voigt model*), whereas the serial alignment is referred to as *Maxwell model*.

An electrical analogy can be used to understand how stresses and strains behave in arbitrarily complex arrangements of viscoelastic elements. In electrical circuits, if resistors are arranged in series, the same current will flow through all of them, but the voltage across each element will be different. On the other hand, in a parallel arrangement, the voltage across each element will be equal to the voltage applied to the circuit, but the currents through each branch depend on the resistance of that branch, and the total current through the system equals the sum of all currents.

If we equate strain with voltage and stress with current, the same rules hold for elastic networks. In a serial arrangement, all elements experience the same stress, while the strain in each element depends on its viscoelastic parameters. Conversely, in a parallel arrangement, strain is identical in each element, while the stresses differ and the total stress is the sum of the stresses in each branch. This can be easily understood if one imagines a parallel arrangement of a spring and an infinitely sturdy steel bar. The bar will prevent the spring from being compressed, so it sustains the full stress applied to the system, whereas the spring remains unloaded. If the bar is gradually weakened, the spring will start to receive a part of the applied stress and will hence shorten. Ultimately, if the bar is removed (or becomes infinitely weak), the spring has to support the full stress, and its Young's modulus will dictate the strain of the system.

In theory, the set of equations resulting from these considerations is sufficient to understand arbitrary arrangements of springs and dashpots:

- Serial arrangement of  $N$  elements:

$$\sigma = \sigma_1 = \sigma_2 = \dots = \sigma_N \quad (4.72)$$

$$\epsilon = \sum_{i=1}^N \epsilon_i. \quad (4.73)$$

- Parallel arrangement of  $N$  elements:

$$\sigma = \sum_{i=1}^N \sigma_i \quad (4.74)$$

$$\epsilon = \epsilon_1 = \epsilon_2 = \dots = \epsilon_N. \quad (4.75)$$

However, there is a major drawback in the formulation of the stress–strain relations for a spring (Eq. (4.67)) and a dashpot (Eq. (4.71)): the stress in a spring depends on the strain, whereas the dashpot stress depends on the strain rate. Hence, simply inserting these stress–strain relations into the above composition rules would lead to differential equations, which would have to be solved for  $\epsilon$  and  $\dot{\epsilon}$  simultaneously. In complex networks with many elements, this can become a challenging task. However, in the frequency domain representation, these differential equations morph into much simpler algebraic expressions. The standard procedure is therefore to perform the calculations in the Laplace domain. The frequency-resolved modulus  $G^*(\omega)$  can then be obtained by substituting the Laplace domain variable  $s$  with  $i\omega$ .

### The Laplace transform

The Laplace transform is an integral transform defined as

$$\mathcal{L}[f(t)](s) = \int_{0^-}^{\infty} e^{-st} f(t) dt. \quad (4.76)$$

It converts a function  $f(t)$ , defined in the time domain ( $t \in \mathbb{R}$ ), into a function that depends on a complex frequency variable  $s \in \mathbb{C}$ . As a shorthand notation for the rather clumsy left-hand side of Eq. (4.76), we will use the overbar to indicate pairs of functions and their Laplace transforms:  $\bar{f}(s) \equiv \mathcal{L}[f(t)](s)$ . The  $0^-$  in the lower integration bound is meant to indicate that an impulse function at the origin,  $\delta(0)$ , fully contributes to the integral.

The integral in Eq. (4.76) does not necessarily converge for all values of  $s$ . For example, if  $f(t) = 1$ , the integral converges only for  $\text{Re}(s) > 0$ . The imaginary part of  $s$  has no effect on the convergence of the integral, and the region of convergence (ROC) is always<sup>a</sup> determined by a condition  $\text{Re}(s) > a$  or  $\text{Re}(s) \geq a$ , with  $-\infty \leq a \leq +\infty$ . However, the function resulting from the evaluation of Eq. (4.76) is usually defined for a larger range of  $s$ , usually the entire complex plane without isolated points at which  $\bar{f}(s)$  has poles.

The Laplace transform has a number of useful properties, which will be listed here without proof:

- Linearity:

$$\mathcal{L}[a \cdot f(t) + b \cdot g(t)](s) = a \cdot \bar{f}(s) + b \cdot \bar{g}(s) \quad (4.77)$$

for  $a, b \in \mathbb{C}$ .

- Differentiation:

$$\mathcal{L} \left[ \frac{df}{dt} \right] (s) = s \cdot \bar{f}(s) - f(0). \quad (4.78)$$

For higher-order derivatives, the relation reads

$$\mathcal{L} [f^{(n)}(t)] (s) = s^n \cdot \bar{f}(s) - \sum_{k=1}^n s^{k-1} f^{(n-k)}(0). \quad (4.79)$$

- Laplace transform of the Heaviside step function:

$$\mathcal{L} [\Theta(t)] (s) = \frac{1}{s} \quad (4.80)$$

with

$$\Theta(t) = \begin{cases} 0 & : t \leq 0 \\ 1 & : t > 0 \end{cases} \quad (4.81)$$

This property is used when instantaneous loading or unloading is to be modeled.

- Time shifting:

$$\mathcal{L} [f(t - \tau) \cdot \Theta(t - \tau)] = e^{-\tau s} \bar{f}(s) \quad (4.82)$$

for  $\tau \in \mathbb{R}$ .

- Inverse transform:

$$f(t) = \mathcal{L}^{-1}[\bar{f}(s)] = \lim_{q \rightarrow \infty} \frac{1}{2\pi i} \int_{c-iq}^{c+iq} e^{st} \bar{f}(s) ds, \quad (4.83)$$

where  $c \in \mathbb{R}$  is larger than the real part of all poles of  $\bar{f}(s)$  in the complex plane. Equation (4.83) prescribes the evaluation of a line integral parallel to the imaginary axis in the complex plane. However, evaluating this integral can be nontrivial, and instead, inverse transforms are often calculated through algebraic manipulation and with the help of transformation tables, which are available in textbooks or on the internet.<sup>b</sup>

The relevance of the Laplace transform in the context of viscoelasticity arises from the fact that Eq. (4.79) can be used to rewrite differential equations together with their initial value conditions in the time domain to algebraic equations in the Laplace domain, where they are easier to solve. Each term in the sum represents the initial value condition for one of the derivatives.

<sup>a</sup>Convergence analysis in general is more complicated than outlined here. Refer to mathematical literature for a more rigorous treatment of this topic.

<sup>b</sup>For example, [https://en.wikipedia.org/wiki/Laplace\\_transform#Table\\_of\\_selected\\_Laplace\\_transforms](https://en.wikipedia.org/wiki/Laplace_transform#Table_of_selected_Laplace_transforms)

Because of the linearity of the Laplace transform, sums of stresses or strains translate to sums of their transformed counterparts, such that the structure of the composition laws is the same in the time domain and the Laplace domain. Due to the differentiation rule of the Laplace transform (Eq. (4.78)), strain rate  $\dot{\epsilon}$  becomes  $s \cdot \bar{\epsilon}(s) - \epsilon(0)$ . We

will now illustrate how to apply the composition rule in conjunction with the Laplace transform to obtain the stress–strain relation for the Voigt model (see Figure 4.7).

The constitutive equation for the Voigt model corresponds to the composition rule for parallel alignment:

$$\begin{aligned} \sigma &= \sigma_{\text{spring}} + \sigma_{\text{dashpot}} = E\epsilon + \eta\dot{\epsilon} \\ \text{and } \epsilon &= \epsilon_{\text{spring}} = \epsilon_{\text{dashpot}}. \end{aligned} \quad (4.84)$$

After Laplace transform, this becomes

$$\bar{\sigma} = E\bar{\epsilon} + \eta s\bar{\epsilon} - \underbrace{\eta \epsilon(0)}_{=0} \quad (4.85)$$

$$\bar{\epsilon} = \left( s + \frac{E}{\eta} \right)^{-1} \cdot \frac{1}{\eta} \bar{\sigma}, \quad (4.86)$$

where we assumed that the initial strain at  $t = 0$  vanishes.

We will now analyze the strain response of the Voigt model to a boxcar stress, which corresponds to instantaneously applying a constant stress  $\sigma_0$  to the system at  $t = 0$  and releasing the stress at  $t = T$ . Such a stress can be written as

$$\sigma(t) = \sigma_0 \cdot (\Theta(t) - \Theta(t - T)), \quad (4.87)$$

where  $\Theta(t)$  is the Heaviside step function. We can then obtain the Laplace transform of  $\sigma$  using Eqs. (4.80) and (4.82):

$$\bar{\sigma} = \sigma_0 \cdot \left( \frac{1}{s} - \frac{e^{-sT}}{s} \right). \quad (4.88)$$

We used the fact that  $\sigma(0) = 0$ , according to the definition of the Heaviside function.<sup>9</sup>

Inserting Eq. (4.88) into Eq. (4.86) yields

$$\bar{\epsilon} = \left( s + \frac{E}{\eta} \right)^{-1} \frac{\sigma_0}{\eta} \left( \frac{1}{s} - \frac{e^{-sT}}{s} \right), \quad (4.89)$$

which can be rewritten as

$$\bar{\epsilon} = \frac{\sigma_0}{\eta} \left( \frac{1}{s \left( s + \frac{E}{\eta} \right)} - \frac{e^{-sT}}{s \left( s + \frac{E}{\eta} \right)} \right). \quad (4.90)$$

From a Laplace transformation table<sup>10</sup> we gather that  $\frac{\alpha}{s(s+\alpha)}$  is the Laplace transform of  $(1 - e^{-\alpha t}) \cdot \Theta(t)$ . With  $\alpha = \frac{E}{\eta}$ , the first term inside the bracket of Eq. (4.90) hence corresponds to  $\frac{1}{\alpha}(1 - e^{-\alpha t}) \cdot \Theta(t)$ , whereas the second term is a time-shifted version:  $\frac{1}{\alpha}(1 - e^{-\alpha(t-T)}) \cdot \Theta(t - T)$ . Combining these results, the solution in the time domain can

<sup>9</sup> There are different conventions for the value of the Heaviside function at  $t = 0$ . Other definitions prescribe  $\Theta(0) = 1$  or  $\Theta(0) = \frac{1}{2}$ . In these cases, some formulas used here might look different (and represent different physical scenarios).

<sup>10</sup> For example, [https://en.wikipedia.org/wiki/Laplace\\_transform#Table\\_of\\_selected\\_Laplace\\_transforms](https://en.wikipedia.org/wiki/Laplace_transform#Table_of_selected_Laplace_transforms)



be expressed as

$$\epsilon(t) = \frac{\sigma_0}{E} \left( \underbrace{\left(1 - e^{-\frac{E}{\eta}t}\right) \cdot \Theta(t)}_{\textcircled{1}} - \underbrace{\left(1 - e^{-\frac{E}{\eta}(t-T)}\right) \cdot \Theta(t-T)}_{\textcircled{2}} \right). \quad (4.91)$$

A graphical representation is shown in Figure 4.7. For a physical interpretation, we perform a temporal decomposition. The first term  $\textcircled{1}$  characterizes the response to the application of the stress after  $t = 0$ , when the second term  $\textcircled{2}$  is still zero due to the delayed step function.  $\textcircled{1}$  is an exponential approach from zero toward  $\frac{\sigma_0}{E}$ , with a time constant  $\frac{E}{\eta}$ . To analyze the behavior after the removal of the stress at  $t = T$ , we evaluate Eq. (4.91) for  $t > T$ , when both step functions yield 1. We perform a variable substitution,  $t' = t - T$ , so that  $t' = 0$  marks the beginning of the relaxation process:

$$\epsilon(t' > 0) = \frac{\sigma_0}{E} \cdot \left(1 - e^{-\frac{E}{\eta}T}\right) \cdot e^{-\frac{E}{\eta}t'}. \quad (4.92)$$

The last factor is a time-dependent decay, again with a time constant  $\frac{E}{\eta}$ . The factor in the brackets is a constant scaling factor that quantifies which fraction of the maximum attainable strain,  $\frac{\sigma_0}{E}$ , was reached during application of the stress over duration  $T$ . From Eqs. (4.91) and (4.92) we can gain insights into the roles that the spring and the dashpot play in the Voigt model. The maximum strain for a given stress,  $\frac{\sigma_0}{E}$ , depends only on the spring. The dashpot cannot limit the strain, since, as discussed above, it is sensitive to the strain rate but not to the strain itself. However, the dashpot contributes to the decay constant  $\frac{E}{\eta}$ . In this constellation, the dashpot counteracts the spring and delays the otherwise immediate response. Increasing viscosity  $\eta$  of the Voigt model hence slows down the dynamic response of the system, whereas increasing the elastic modulus  $E$  has an accelerating effect.

We will now look at how we can calculate the viscoelastic parameters of a compound system from the parameters of the individual constituents. First, we choose the origin of the time axis so that  $t = 0$  always represents the undeformed, strain-free state and, so that we can always neglect the term  $\epsilon(0)$  which arises when the Laplace transform is applied to temporal derivatives (see Eq. (4.78)). Next, we introduce the *complex modulus*  $G^*$ , which can simultaneously represent viscous and elastic properties in a single complex number.<sup>11</sup> Two parameterizations are commonly used to represent  $G^*$ :

$$G^* = G' + iG'' \quad (4.93)$$

$$\text{and } G^* = |G^*| \cdot e^{i\varphi}. \quad (4.94)$$

$G'$  and  $G''$  denote real and imaginary parts; the prime does *not* indicate derivatives.  $|G|$  is sometimes used as a shorthand notation for  $|G^*|$ , and occasionally the same quantity is referred to as *absG*.  $\varphi$  is the *phase angle*, and its range extends from 0 (pure elasticity) to  $\frac{\pi}{2}$  (pure viscosity). Its tangent is referred to as *loss tangent* and it quantifies the ratio

<sup>11</sup> Note that the asterisk only marks  $G^*$  as a complex quantity, it does *not* denote complex conjugation. This notation has become standard in the elastography community.

of viscous to elastic behavior:

$$\tan(\varphi) = \frac{G''}{G'}. \quad (4.95)$$

In the Laplace domain,  $G^*$  represents the ratio of stress to strain:

$$\overline{G}^*(s) = \frac{\overline{\sigma}(s)}{\overline{\epsilon}(s)}. \quad (4.96)$$

We can see that  $\overline{G}^*$  depends on the Laplace domain variable  $s$ . We will see shortly that this translates into a frequency dependency of the viscoelastic properties of a material.

The advantage of the introduction of  $G^*$  is that we can now represent springs and dashpots analogously in the Laplace domain:

$$\overline{\sigma}(s) = \overline{G}^*(s) \cdot \overline{\epsilon}(s) \quad \text{for a spring with } \overline{G}^*(s) = E \quad (4.97)$$

$$\overline{\sigma}(s) = \overline{G}^*(s) \cdot \overline{\epsilon}(s) \quad \text{for a dashpot with } \overline{G}^*(s) = \eta s. \quad (4.98)$$

Obviously,  $\overline{G}^*$  is constant for a spring, whereas it depends on  $s$  for a dashpot.

We now revisit the strain and stress rules, Eqs. (4.72)–(4.75), for parallel and serial arrangements of elements. For a parallel arrangement of two components with complex moduli  $G_1^*$  and  $G_2^*$ , we obtain

$$\begin{aligned} \overline{\epsilon}(s) &= \overline{\epsilon}_1(s) = \overline{\epsilon}_2(s) \quad \text{and} \quad \overline{\sigma}(s) = \overline{\sigma}_1(s) + \overline{\sigma}_2(s) \\ \Rightarrow \overline{\sigma}(s) &= \overline{G}_1^*(s) \cdot \overline{\epsilon}_1(s) + \overline{G}_2^*(s) \cdot \overline{\epsilon}_2(s) \\ &= (\overline{G}_1^*(s) + \overline{G}_2^*(s)) \cdot \overline{\epsilon}(s) = \overline{G}^*(s) \cdot \overline{\epsilon}(s) \\ \text{with } \overline{G}^*(s) &= \overline{G}_1^*(s) + \overline{G}_2^*(s). \end{aligned} \quad (4.99)$$

For a serial arrangement, a Maxwell model, we similarly derive

$$\begin{aligned} \overline{\epsilon}(s) &= \overline{\epsilon}_1(s) + \overline{\epsilon}_2(s) \quad \text{and} \quad \overline{\sigma}(s) = \overline{\sigma}_1(s) = \overline{\sigma}_2(s) \\ \Rightarrow \overline{\epsilon}(s) &= \frac{\overline{\sigma}_1(s)}{\overline{G}_1^*(s)} + \frac{\overline{\sigma}_2(s)}{\overline{G}_2^*(s)} \\ &= \overline{\sigma}(s) \cdot \left( \frac{1}{\overline{G}_1^*(s)} + \frac{1}{\overline{G}_2^*(s)} \right) = \frac{\overline{\sigma}(s)}{\overline{G}^*(s)} \\ \text{with } \frac{1}{\overline{G}^*(s)} &= \frac{1}{\overline{G}_1^*(s)} + \frac{1}{\overline{G}_2^*(s)}. \end{aligned} \quad (4.100)$$

We can see that these rules are very similar in form to the composition laws for resistances in electrical circuits, but the rules for parallel and serial arrangements are reversed. In fact, had we used inverse moduli (compliances) instead of  $G^*$ , the rules would be formally identical to their electrical counterparts. However, we refrained from this step to avoid introducing new physical quantities that do not really help to advance the understanding of this matter.

From Eqs. (4.97) and (4.98) we can see that only the complex modulus of the dashpot explicitly depends on the Laplace domain variable  $s$ , whereas the one of the spring is truly a constant. We obtain a frequency-resolved representation of  $G^*(s)$  by substituting

$s = i\omega$ , where  $\omega$  is an angular frequency.<sup>12</sup> The resultant quantity  $\overline{G}^*(\omega)$  can be interpreted as a representation of the viscoelastic properties of the medium if an oscillating strain is applied at frequency  $\omega$ . For  $\omega = 0$ , one obtains the properties under static conditions. A spring is not frequency dependent, since, according to Eq. (4.70), it responds instantaneously to arbitrary stresses. For a dashpot, on the other hand, the stress is proportional to strain rate  $\dot{\epsilon}$ . If we assume an oscillating deformation,  $\epsilon(t) = \epsilon_0 \cdot e^{-i\omega t}$ , we can see that  $\dot{\epsilon} \propto \omega$ . The physical explanation is that at a constant amplitude, deformation has to occur faster at higher frequencies, which causes higher damping in a viscous material than at low frequencies and speeds.

#### 4.8.4 Overview of Viscoelastic Models

In addition to the models just discussed, numerous other types of varying complexity exist. A spring and a dashpot are clearly only capable of representing pure elasticity or pure viscosity. A combination of one spring and one dashpot leads to the Voigt model (parallel arrangement) or the Maxwell model (serial arrangement). These are capable of representing viscoelastic properties, while their suitability for modeling actual viscoelastic materials is still limited. For example, the Voigt model does not predict the frequency dependence of  $G'$  as observed in biological tissue. The Maxwell model, on the other hand, has a higher viscosity ( $G''$ ) in the low-frequency range, thus being more akin to a viscous fluid than solid tissue. The addition of more elements to a model increases the number of parameters and hence the number of degrees of freedom. The *Zener model*, also known as *standard linear solid (SLS) model*, is an example for a system composed of three elements: a spring in parallel to a Maxwell model, which better approximates the properties of biological tissue. Some important viscoelastic models and their properties are summarized in Figure 4.7.

##### Springpot and fractional viscoelasticity

All viscoelastic models discussed so far incorporate a finite number of dashpots and springs. In *fractional viscoelasticity* theory, the properties of viscoelastic materials are modeled either as an infinite sequence of springs and dashpots (see the *fractal ladder* in Figure 4.7), or by means of *fractional calculus*, a mathematical discipline that aims at extending the concept of the  $n$ th derivative,  $\frac{d^n}{dt^n}$ , to noninteger parameters (see, e.g., [44] for a mathematical overview and the application to viscoelasticity). The relevant property of fractional derivatives is most easily expressed in the Fourier domain:

$$\mathcal{F} \left[ \frac{d^\alpha}{dt^\alpha} f(t) \right] (\omega) = (i\omega)^\alpha \mathcal{F} [f(t)](\omega). \quad (4.101)$$

<sup>12</sup> By substituting  $s$  with  $i\omega$  in the definition of the Laplace transform, Eq. (4.76), the Laplace transform becomes a one-sided Fourier transform,  $\mathcal{F} [f](\omega) = \int_0^\infty e^{-i\omega t} f(t) dt$ . Since we implicitly assume that the object is in an undeformed state for  $t \leq 0$ , stress and strain are zero for  $t < 0$  and we can hence shift the lower integration bound from 0 to  $-\infty$  without changing the result of the integral when applied to  $\sigma(t)$  or  $\epsilon(t)$ . The substitution  $s \rightarrow i\omega$  hence yields the full frequency spectrum.

For integer values  $\alpha = n \in \mathbb{N}$ , this reproduces the well-known relation for the Fourier transform of the  $n$ th derivative. Applying Eq. (4.101) to the dashpot law, Eq. (4.71), and denoting the Fourier transform with a tilde, we obtain

$$\tilde{\sigma}(\omega) = \eta(i\omega)^\alpha \cdot \tilde{\epsilon}(\omega), \quad (4.102)$$

which tells us that, for any given oscillation frequency  $\omega$ , the phase shift between stress and strain in such an element is given by  $(i\omega)^\alpha$ , which is a powerlaw. For  $\alpha = 0$ , the system thus represents a spring with modulus  $E = \eta$ . For  $\alpha = 1$ , the system reduces to a dashpot with viscosity  $\eta$ . For  $0 < \alpha < 1$ , the system exhibits intermediate behavior that cannot be reproduced by a combination of a finite number of springs and dashpots. In order to maintain the purity of the constants,<sup>3</sup> we re-parametrize the model as

$$\eta \rightarrow E^{1-\alpha} \cdot \eta^\alpha, \quad (4.103)$$

so that now  $\eta$  always represents the viscous properties for  $\alpha = 1$  and  $E$  Young's modulus for the case  $\alpha = 0$ . The resultant model

$$\tilde{\sigma}(\omega) = E^{1-\alpha}(i\omega\eta)^\alpha \cdot \tilde{\epsilon}(\omega) \quad (0 \leq \alpha \leq 1) \quad (4.104)$$

or, equivalently in the Laplace domain,

$$\bar{\sigma}(s) = E^{1-\alpha}(s \cdot \eta)^\alpha \cdot \bar{\epsilon}(s) \quad (0 \leq \alpha \leq 1) \quad (4.105)$$

is referred to as a *springpot* [45]. The fractional ladder shown in Figure 4.7 is a special case of the springpot with  $\alpha = 0.5$  and has a straightforward geometric representation in terms of an infinite sequence of springs and dashpots. The complex modulus of the springpot in the Laplace domain is

$$\bar{G}^* = E^{1-\alpha}(\eta s)^\alpha \quad (0 \leq \alpha \leq 1). \quad (4.106)$$

The springpot powerlaw parameter  $\alpha$  can be expressed in terms of the real and imaginary parts of the complex modulus:

$$\alpha = \frac{\pi}{2} \cdot \arctan\left(\frac{\text{Im}(\bar{G}^*)}{\text{Re}(\bar{G}^*)}\right). \quad (4.107)$$



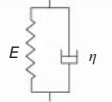
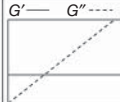
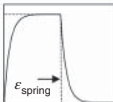
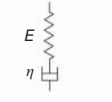

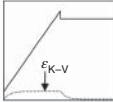
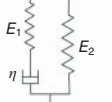
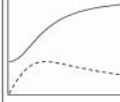
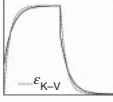
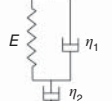
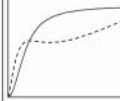
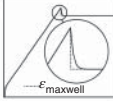
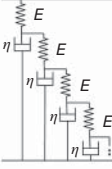

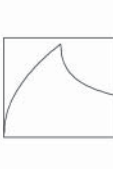
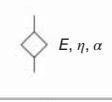
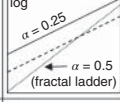
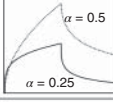

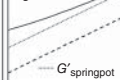
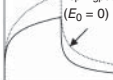
Sometimes, the *phase angle*  $\varphi$  from the definition of the complex shear modulus (cf. Eq. (4.94)) is used instead of  $\alpha$ :

$$\varphi = \arctan\left(\frac{\text{Im}(\bar{G}^*)}{\text{Re}(\bar{G}^*)}\right) = \frac{2}{\pi} \cdot \alpha \quad (4.108)$$

and its tangent is referred to as the *loss tangent*, representing the ratio of viscous to elastic properties

$$\tan(\varphi) = \frac{\text{Im}(\bar{G}^*)}{\text{Re}(\bar{G}^*)} = \frac{\sin\left(\frac{\pi\alpha}{2}\right)}{\cos\left(\frac{\pi\alpha}{2}\right)}. \quad (4.109)$$

<sup>3</sup>Having  $\eta$  denote elasticity rather than viscosity for  $\alpha = 0$  is somewhat awkward, and the physical dimension of  $\eta$  would be  $\text{Pa s}^\alpha$ .

Spring (Hookean)		Dashpot (Newtonian)			
		$S' = \frac{1}{E}$	$G^* = E$		
		$S' = \frac{1}{\eta s}$	$G^* = \eta s$		
Model	Schematic	Compliance $S^*$	Modulus $G^*$	$G^* (s = i\omega)$	$\epsilon(t)$
Kelvin–Voigt (K–V)		$\frac{1}{\frac{1}{S'} + \frac{1}{S''}}$	$E + \eta s$		
Maxwell		$S' + S''$	$\frac{E\eta s}{E + \eta s}$		
Zener (SLS)		$\frac{1}{\frac{1}{S'_1 + S''} + \frac{1}{S'_2}}$	$\frac{(E_1 + E_2)\eta s + E_1 E_2}{E_2 + \eta s}$		
Jeffreys		$\frac{1}{\left(\frac{1}{S'} + \frac{1}{S''}\right) + S''_2}$	$\frac{(E + \eta_1 s)\eta_2 s}{E + \eta_1 s + \eta_2 s}$		
Fractal ladder		$\frac{1}{S'' + S' + \frac{1}{\frac{1}{S''} + \frac{1}{S' + \frac{1}{S''} + \frac{1}{S' + \frac{1}{S''} + \dots}}}}$ $S^* = \frac{1}{\frac{1}{S''} + \frac{1}{S' + S^*}}$	$\eta s + \frac{1}{\frac{1}{E} + \frac{1}{\eta s + \frac{1}{\frac{1}{E} + \frac{1}{\eta s + \dots}}}}$ $G^* = \eta s + \frac{1}{\frac{1}{E} + \frac{1}{G^*}}$ $\approx \sqrt{E\eta s} \quad (\eta \ll E)$		
Springpot (generalized fractal ladder)		$S' \left(\frac{S''}{S'}\right)^\alpha \quad (0 \leq \alpha \leq 1)$	$E^{1-\alpha} \eta^\alpha s^\alpha$		
Kelvin–Voigt fractal derivative		$\frac{1}{\frac{1}{S'} \left(\frac{S''}{S'}\right)^\alpha + \frac{1}{S'_0}}$	$E^{1-\alpha} \eta^\alpha s^\alpha + E_0$		

**Figure 4.7** Summary of important viscoelastic models in elastography assembled from basic spring and dashpot elements. Compliance  $S^*$  and modulus  $G^*$  are analytically given in the Laplace domain  $s$  (bars over the symbols, denoting the Laplace domain, have been omitted to improve readability).  $G^*$  is plotted over the angular frequency  $\omega = 0, \dots, 100 \cdot 2\pi s^{-1}$ . “log” refers to double logarithmic plots to better illustrate powerlaw behavior. The rightmost column, on a time axis spanning 0.2 s, shows strain  $\epsilon(t)$  in response to a boxcar stress spanning the first half of the time axis, that is,  $\sigma(0 \leq t \leq 0.1 s) = 1$  Pa. Further simulation parameters correspond to typical values encountered in elastography of biological tissues (e.g.,  $E = E_1 = 1$  kPa),  $\eta = 10$  Pa s,  $\eta_1 = 1$  Pa s,  $\eta_2 = 10$  Pa s,  $\alpha = 0.25$ ,  $E_0 = 0.2$  kPa).

## 4.9 Dynamic Deformation

The considerations thus far have concentrated on static scenarios or the relaxation of a system following a single deformation. In this section, we will extend these concepts to incorporate dynamic aspects, which ultimately serve as the basis for the modeling of elastic wave propagation through viscoelastic materials.

### 4.9.1 Balance of Momentum

The discussion of viscoelastic models in Section 4.8 neglected the mass of springs and dashpots, which allowed for instantaneous responses to applied stresses. For any real-world scenario, mass has to be taken into account. This has two implications:

- Strains cannot follow stresses instantaneously, since finite forces can only cause finite accelerations. In this sense, mass has a delaying effect because of the momentum associated with its motion. For example, the oscillation frequency of an unattenuated harmonic oscillator with spring constant  $D$  and mass  $m$  is given by  $\omega = \sqrt{\frac{D}{m}}$ .
- In the same way that inertia delays the response to a stress, it also leads to overshooting (unless the inertia is compensated for by strong viscous effects). Imagine an elastic system that was deformed and returns to its zero-strain state once the stress is relieved. Upon reaching the undeformed state, however, the individual mass points that constitute the medium still have a momentum that is proportional to strain relaxation rate  $\dot{\epsilon}$ . Since there is no resultant stress (and hence no associated force) in the undeformed state, the system will not stop at the zero-strain state but will overshoot and generate an opposing stress, causing a deceleration and a reversal of the direction of motion, again toward the undeformed state. The process repeats itself, either infinitely in the case of a purely elastic medium or with an exponential attenuation in the presence of viscosity. If the medium is linear (stress and strain are related via a proportionality constant), the system performs a harmonic oscillation about its equilibrium state. This is the local equivalent of mechanical waves.

The interaction between stresses and inertial effects is described by the *balance of momentum*. Basically, this is a reformulation of Newton's law

$$\mathbf{F} = m\mathbf{a}, \quad (4.110)$$

where  $\mathbf{F}$  is the force acting on a body and  $\mathbf{a}$  is the resulting acceleration. Since we are only interested in motion associated with deformation of elastic bodies, we equate the acceleration with the second time derivative of the displacement field:  $\mathbf{a} = \ddot{\mathbf{u}}$ . In continuum mechanics, the total mass of the body is usually not considered, since strains and stresses are local rather than global quantities (i.e., they can vary in space), and hence their effects are also local. Instead, mass density  $\rho$  is used. In incompressible homogeneous media,  $\rho$  is constant throughout the body, which is a good approximation for MRE.

Forces in continuous media can broadly be subdivided into two categories: stresses and body forces. While stresses arise from deformation, body forces have origins that are not related to viscoelastic properties. They act upon each infinitesimal volume element separately, and the total force can be calculated from a volume integral over the body. One example is gravitation, which is of the form

$$\mathbf{b}(\mathbf{r}) = g\rho(\mathbf{r}) \cdot \hat{\mathbf{e}}_z, \quad (4.111)$$

if we assume that the body is near the earth's surface and that it is small enough to neglect spatial variation of the gravitation field  $g$ . Despite the name, body forces are rather force densities, and the actual force is obtained by multiplication with the volume element. The total gravitational force is then

$$\mathbf{B} = \hat{\mathbf{e}}_z \iiint_{\text{body}} g \rho(\mathbf{r}) \, dV. \quad (4.112)$$

As explained in Section 4.2, the elements of the stress tensor,  $\sigma_{ij}$ , represent the force (per unit area) acting along the  $i$ th Cartesian axis on the surface with normal vector  $\hat{\mathbf{e}}_j$  of an infinitesimal cubic volume element. The total force acting on this volume element can thus be calculated by

$$\mathbf{F} = \int_{\partial S} \boldsymbol{\sigma} \cdot d\mathbf{A} + \mathbf{B}, \quad (4.113)$$

where  $\partial S$  is the surface of the volume element and  $\mathbf{A}$  is the oriented<sup>13</sup> surface element. According to Gauss's theorem, the surface integral can be rewritten as a volume integral of the divergence<sup>14</sup> of the integrand:

$$\mathbf{F} = \int_V \nabla \cdot \boldsymbol{\sigma} \, dV + \mathbf{B}, \quad (4.114)$$

where  $(\nabla \cdot \boldsymbol{\sigma})_j = \sum_{i=1}^3 \frac{\partial \sigma_{ij}}{\partial r_i}$ . Forces acting on the surface of a body are therefore reflected in the displacement field throughout the body, and the volume integral reconstructs the total force by collecting the local deformations.

Newton's law, Eq. (4.110), holds true not only for the bulk material but also for each infinitesimal volume element individually. Therefore, it can also be formulated in a local version in terms of force densities:

$$\mathbf{f} = \frac{\partial \mathbf{F}}{\partial V} = \frac{\partial m}{\partial V} \mathbf{a} + \frac{\partial \mathbf{B}}{\partial V} = \rho \ddot{\mathbf{u}} + \mathbf{b}, \quad (4.115)$$

where bulk density  $\rho$  replaces bulk mass  $m$ .

In the absence of body forces ( $\mathbf{b} = \mathbf{0}$ ), substituting Eq. (4.114) into Eq. (4.115), the derivative cancels the volume integration, and one obtains

$$f_j = \rho \ddot{u}_j = (\nabla \cdot \boldsymbol{\sigma})_j = \sum_{i=1}^3 \frac{\partial}{\partial r_i} \sigma_{ij}. \quad (4.116)$$

We can now insert the general version of Hooke's law (Eq. (4.19)) and the definition of the infinitesimal strain tensor (Eq. (4.3)):

$$\begin{aligned} \rho \ddot{u}_j &= \sum_{i,k,l=1}^3 \frac{\partial}{\partial r_i} C_{ijkl} \epsilon_{kl} \\ &= \sum_{i,k,l=1}^3 \frac{1}{2} C_{ijkl} \cdot \left( \frac{\partial^2 u_k}{\partial r_i \partial r_l} + \frac{\partial^2 u_l}{\partial r_i \partial r_k} \right). \end{aligned} \quad (4.117)$$

<sup>13</sup> Pointing along the outward surface normal.

<sup>14</sup> Note that we use the notation  $\nabla \cdot \boldsymbol{\sigma}$  for the divergence of the second-order tensor  $\boldsymbol{\sigma}$ , rather than  $\nabla \bullet \boldsymbol{\xi}$  for the divergence of a vector  $\boldsymbol{\xi}$ . The divergence of  $\boldsymbol{\sigma}$  is a vector, hence the expression  $\nabla \cdot \boldsymbol{\sigma}$  is equivalent to the multiplication of a row vector with a square matrix, whereas  $\bullet$  denotes scalar multiplication between two vectors.

We neglected the spatial variation of the elasticity tensor  $\mathbf{C}$ , since we generally restrict the discussion to relatively homogeneous materials with slowly varying mechanical properties. Equation (4.117) is a second-order partial differential equation with a second-order temporal derivative on the left-hand side and a second-order spatial derivative on the right-hand side. This is a characteristic property of a *wave equation*.

We will now derive an explicit form of the wave equation for a linear isotropic medium. We begin by calculating the elasticity tensor from the compliance tensor given in Eq. (4.55) through matrix inversion. However, instead of using Poisson's ratio  $\nu$ , Young's modulus  $E$ , and the shear modulus  $\mu$  (only two of which are independent, with the third one being a function of the other two, as explained in Section 4.7.2), we prefer to parametrize the result in terms of  $\mu$  and bulk modulus  $K$ , since these are the two most easily graspable parameters in the context of wave mechanics, as we will illustrate below. Therefore, we refer to a conversion table<sup>15</sup> and find the relations

$$E = \frac{9K\mu}{3K + \mu} \quad (4.118)$$

$$\nu = \frac{3K - 2\mu}{2(3K - \mu)}. \quad (4.119)$$

Inverting the compliance tensor and performing these substitutions finally yields<sup>16</sup>

$$\begin{pmatrix} \sigma_{11} \\ \sigma_{22} \\ \sigma_{33} \\ \sigma_{23} \\ \sigma_{31} \\ \sigma_{12} \end{pmatrix} = \begin{pmatrix} K + \frac{4}{3}\mu & K - \frac{2}{3}\mu & K - \frac{2}{3}\mu & 0 & 0 & 0 \\ K - \frac{2}{3}\mu & K + \frac{4}{3}\mu & K - \frac{2}{3}\mu & 0 & 0 & 0 \\ K - \frac{2}{3}\mu & K - \frac{2}{3}\mu & K + \frac{4}{3}\mu & 0 & 0 & 0 \\ 0 & 0 & 0 & \mu & 0 & 0 \\ 0 & 0 & 0 & 0 & \mu & 0 \\ 0 & 0 & 0 & 0 & 0 & \mu \end{pmatrix} \cdot \begin{pmatrix} \epsilon_{11} \\ \epsilon_{22} \\ \epsilon_{33} \\ 2\epsilon_{23} \\ 2\epsilon_{31} \\ 2\epsilon_{12} \end{pmatrix}. \quad (4.120)$$

Here, the upper-left  $3 \times 3$  submatrix couples the axial strains, whereas the lower-right matrix establishes a one-to-one relationship between shear strains and stresses, relating only to the off-diagonal entries of the stress and strain tensor. We can hence represent the axial stresses as

$$\sigma_{ii} = \sum_{k=1}^3 \left( K - \frac{2}{3}\mu \right) \epsilon_{kk} + 2\mu\epsilon_{ii} \quad (4.121)$$

$$= \left( K - \frac{2}{3}\mu \right) \nabla \cdot \mathbf{u} + 2\mu\epsilon_{ii} \quad (4.122)$$

and the shear stresses as

$$\sigma_{ij} = 2\mu\epsilon_{ij} \quad (i \neq j). \quad (4.123)$$

<sup>15</sup> Such as [https://en.wikipedia.org/wiki/Bulk\\_modulus](https://en.wikipedia.org/wiki/Bulk_modulus).

<sup>16</sup> Performing these calculations manually is tedious and not particularly insightful. We therefore refrain from showing intermediate steps and recommend to use symbolic calculation software for such tasks.



We combine these expressions by multiplying them with Kronecker- $\delta$  symbols:

$$\begin{aligned}
\sigma_{ij} &= \sigma_{ij} \cdot \delta_{ii} + \sigma_{ij} \cdot (1 - \delta_{ij}) \\
&= \sigma_{ii} \cdot \delta_{ij} + \sigma_{ij} \cdot (1 - \delta_{ij}) \\
&= \left( \left( K - \frac{2}{3}\mu \right) \nabla \bullet \mathbf{u} + 2\mu\epsilon_{ij} \right) \cdot \delta_{ij} + 2\mu\epsilon_{ij} \cdot (1 - \delta_{ij}) \\
&= \delta_{ij} \cdot \left( K - \frac{2}{3}\mu \right) \nabla \bullet \mathbf{u} + 2\mu\epsilon_{ij}.
\end{aligned} \tag{4.124}$$

Substituting this expression into the balance of momentum (Eq. (4.116)) yields

$$\rho \ddot{\mathbf{u}}_j = \sum_{i=1}^3 \frac{\partial}{\partial r_i} \left( \delta_{ij} \left( K - \frac{2}{3}\mu \right) \cdot \nabla \bullet \mathbf{u} + 2\mu\epsilon_{ij} \right) \tag{4.125}$$

$$= \sum_{i=1}^3 \frac{\partial}{\partial r_i} \left( \delta_{ij} \left( K - \frac{2}{3}\mu \right) \cdot \sum_{k=1}^3 \frac{\partial u_k}{\partial r_k} + 2\mu \frac{1}{2} \left( \frac{\partial u_i}{\partial r_j} + \frac{\partial u_j}{\partial r_i} \right) \right) \tag{4.126}$$

$$= \sum_{i,k=1}^3 \delta_{ij} \left( K - \frac{2}{3}\mu \right) \frac{\partial^2 u_k}{\partial r_i \partial r_k} + \sum_{i=1}^3 \mu \left( \frac{\partial^2 u_i}{\partial r_i \partial r_j} + \frac{\partial^2 u_j}{\partial r_i^2} \right). \tag{4.127}$$

In the first step, the definition of the infinitesimal strain tensor (Eq. (4.3)) is used. In the second step, the spatial derivatives of the parameters  $\mu$  and  $K$  are neglected, as explained above. The last line can be expressed in vector notation as

$$\rho \ddot{\mathbf{u}} = \left( K - \frac{2}{3}\mu \right) \nabla(\nabla \bullet \mathbf{u}) + \mu \nabla(\nabla \bullet \mathbf{u}) + \mu \Delta \mathbf{u} \tag{4.128}$$

$$= \left( K + \frac{1}{3}\mu \right) \nabla(\nabla \bullet \mathbf{u}) + \mu \Delta \mathbf{u}. \tag{4.129}$$

Equation (4.129) is called *Navier equation*<sup>17</sup> [46]. It can equivalently be formulated as

$$\rho \ddot{\mathbf{u}} = \left( K + \frac{4}{3}\mu \right) \nabla(\nabla \bullet \mathbf{u}) - \mu \nabla \times (\nabla \times \mathbf{u}), \tag{4.130}$$

because of the vector calculus identity

$$\nabla \times (\nabla \times \mathbf{v}) = \nabla(\nabla \bullet \mathbf{v}) - \Delta \mathbf{v} \quad \text{for } \mathbf{v} : \mathbb{R}^3 \rightarrow \mathbb{R}^3. \tag{4.131}$$

In most textbooks, the Navier equation is represented in terms of  $\mu$  and  $\lambda$  as

$$\rho \ddot{\mathbf{u}} = (\lambda + \mu) \nabla(\nabla \bullet \mathbf{u}) + \mu \Delta \mathbf{u} \tag{4.132}$$

$$\text{or } \rho \ddot{\mathbf{u}} = (\lambda + 2\mu) \nabla(\nabla \bullet \mathbf{u}) - \mu \nabla \times (\nabla \times \mathbf{u}), \tag{4.133}$$

respectively. However, since  $\lambda$  has no physical interpretation of its own, we will stick with Eqs. (4.129) and (4.130).

<sup>17</sup> Also called Navier–Cauchy or Lamé–Navier equation.

**Helmholtz decomposition**

*Helmholtz's theorem* states that any well-behaved<sup>a</sup> three-dimensional vector field  $\Psi$  can be decomposed into two complementary fields,  $\Psi_L$  and  $\Psi_T$ , with the following properties:

$$\nabla \bullet \Psi_T \equiv \text{div } \Psi_T = 0 \quad (4.134)$$

$$\nabla \times \Psi_L \equiv \text{curl } \Psi_L = \mathbf{0} \quad (4.135)$$

$$\Psi = \Psi_L + \Psi_T. \quad (4.136)$$

The indices L and T refer to “longitudinal” and “transverse,” respectively, for reasons that will become obvious later on. The divergence of a vector field is the sum of its three axial derivatives,  $\nabla \bullet \Psi = \sum_{i=1}^3 \frac{\partial \Psi_i}{\partial r_i}$ , whereas the curl consists of the tangential derivatives:  $\nabla \times \Psi = \sum_{i,j,k=1}^3 \epsilon_{ijk} \frac{\partial \Psi_j}{\partial r_i} \hat{\mathbf{e}}_k$ , with the Levi-Civita symbol  $\epsilon_{ijk}$  and the unit vector along the  $k$ th dimension,  $\hat{\mathbf{e}}_k$ . The Helmholtz decomposition theorem hence guarantees that any displacement vector field  $\mathbf{u}$  can be expressed as the sum of one field  $\mathbf{u}_L$  with vanishing curl and one divergence-free field  $\mathbf{u}_T$ .

It was explained in Section 4.1 that the diagonal elements  $\epsilon_{ii}$  of the strain tensor represent compression, whereas the off-diagonal entries correspond to shear deformation. From the definition of the infinitesimal strain tensor given in Eq. (4.3),  $\epsilon_{ij} = \frac{1}{2} \left( \frac{\partial u_i}{\partial r_j} + \frac{\partial u_j}{\partial r_i} \right)$ , it is obvious that there is a one-to-one correspondence between the diagonal elements of  $\epsilon$  and  $\mathbf{u}_L$  on the one hand and the off-diagonal elements of  $\epsilon$  and  $\mathbf{u}_T$  on the other hand. In other words, any displacement field  $\mathbf{u}$  is a superposition of two fields, one causing pure volumetric strain (compression or dilatation), and the other pure shear deformation. Hence, we can express the total displacement field as

$$\begin{aligned} \mathbf{u} &= \mathbf{u}_L + \mathbf{u}_T \quad \text{with} \\ \nabla \bullet \mathbf{u}_T &= 0 \\ \text{and } \nabla \times \mathbf{u}_L &= \mathbf{0}. \end{aligned}$$

<sup>a</sup>Sufficiently smooth and fast decaying.

**4.9.2 Mechanical Waves**

The Navier equation is a second-order partial differential equation. From the representation Eq. (4.130) it becomes obvious that the right-hand side can be separated into two parts. The first term,  $\nabla (\nabla \bullet \mathbf{u})$ , is essentially the gradient of a scalar function. Because of the general vector calculus identity

$$\nabla \times (\nabla f) = \mathbf{0} \quad \text{for } f : \mathbb{R}^3 \rightarrow \mathbb{R} \quad (4.137)$$

this term is curl-free and hence represents pure volumetric strain (compression or dilation). Conversely, the second term,  $\nabla \times \nabla \times \mathbf{u}$ , is divergence-free due to the identity

$$\nabla \bullet (\nabla \times \mathbf{v}) = 0 \quad \text{for } \mathbf{v} : \mathbb{R}^3 \rightarrow \mathbb{R}^3. \quad (4.138)$$

It therefore represents pure shear strain. Equation (4.130) hence exposes the separability of the displacement field into its longitudinal (compressional) and transverse (shear) components, as required by the Helmholtz theorem (Eqs. (4.134)–(4.136)). However, performing the same separation on the left-hand side of the Navier equation is less straightforward, as in most experimental situations the measured displacement field  $\mathbf{u}$  is the sum of compressional and shear components. In these cases, it becomes advantageous to apply either the curl or the divergence operator to the whole equation to filter out the undesirable field component. With the definitions

$$\mathbf{c} \equiv \nabla \times \mathbf{u} \quad (4.139)$$

$$d \equiv \nabla \cdot \mathbf{u} \quad (4.140)$$

we obtain

$$\begin{aligned} \rho \ddot{\mathbf{c}} &= -\mu \nabla \times \nabla \times \mathbf{c} \\ &= \mu (\Delta \mathbf{c} - \underbrace{\nabla(\nabla \cdot \mathbf{c})}_{=0}) \\ &= \mu \cdot \Delta \mathbf{c} \end{aligned} \quad (4.141)$$

$$\text{and } \rho \ddot{d} = \left(K + \frac{4}{3}\mu\right) \nabla \cdot (\nabla d) = M \cdot \nabla \cdot (\nabla d) \quad (4.142)$$

$$= M \cdot \Delta d \quad \text{with } M = \left(K + \frac{4}{3}\mu\right). \quad (4.143)$$

These two equations have the form of wave equations that govern the propagation of transverse ( $\mathbf{c}$ , subscript T) and longitudinal ( $d$ , subscript L) waves. Through comparison with the standard form of the wave equation,

$$\ddot{\chi} = c^2 \Delta \chi \quad (4.144)$$

for arbitrary scalar or vector functions  $\chi$ , we obtain the propagation velocities

$$c_T = \sqrt{\frac{\mu}{\rho}} \quad (4.145)$$

$$c_L = \sqrt{\frac{M}{\rho}} = \sqrt{\frac{K + \frac{4}{3}\mu}{\rho}}. \quad (4.146)$$

The parameter  $M = K + \frac{4}{3}\mu$  designates the *P-wave modulus*.<sup>18</sup> Since  $M > \mu$ , the longitudinal wave travels faster than the transverse wave.

A solution to Eq. (4.144) has the form

$$\chi(\mathbf{r}, t) = \chi_0 \cdot \exp(\pm i \cdot (\mathbf{k} \cdot \mathbf{r} - \omega t))$$

$$\chi(\mathbf{r}, t) = \chi_0 \cdot \exp(\pm i \cdot (\mathbf{k} \cdot \mathbf{r} - \omega t))$$

for vector and scalar fields, respectively, with polarization  $\chi_0$ , amplitude  $\chi_0$ , wave vector  $\mathbf{k}$  and angular frequency  $\omega$ . These functions are harmonic both in time and space. As

<sup>18</sup> The “P” stands for “primary.” Pressure waves are the fastest kind of waves released during an earthquake, and they are therefore the first waves to be detected by remote seismographs. The slower shear waves arrive later and are hence denoted “secondary” or S-waves in seismology. Coincidentally, S and P can also be understood as mnemonics for shear and pressure, respectively.

a consequence, if  $\chi$  and  $\chi$  are associated with  $\nabla \bullet \mathbf{u}_L$  and  $\nabla \times \mathbf{u}_T$ , the corresponding displacement fields must fulfill a wave equation as well:

$$\ddot{\mathbf{u}}_{L/T} = c_{L/T}^2 \Delta \mathbf{u}_{L/T}. \quad (4.147)$$

There is no coupling between the individual field components, so that Eq. (4.147) can be solved for each component separately:

$$\ddot{u}_i = c^2 \Delta u_i. \quad (4.148)$$

In isotropic materials, propagation velocity is the same for all three components.

For the transverse field, the divergence has to vanish:

$$\nabla \bullet \mathbf{u}_T = \pm \mathbf{k} \bullet \mathbf{u}_0 \cdot i \cdot \exp(\pm i \cdot (\mathbf{k} \bullet \mathbf{r} - \omega t)) \stackrel{!}{=} 0.$$

This is only possible if the wave vector  $\mathbf{k}$  is orthogonal to the polarization  $\mathbf{u}_0$ , so that  $\mathbf{k} \bullet \mathbf{u}_0 = 0$ , hence the designation “transverse.” In other words, for a transverse/shear wave, the deflection is always perpendicular to the propagation direction.

The longitudinal wave, on the other hand, is characterized by the condition

$$\nabla \times \mathbf{u}_L = \pm \mathbf{u}_0 \times \mathbf{k} \cdot i \cdot \exp(\pm i \cdot (\mathbf{k} \bullet \mathbf{r} - \omega t)) \stackrel{!}{=} \mathbf{0},$$

necessitating that  $\mathbf{u}_0 \times \mathbf{k} = \mathbf{0}$ , so that the polarization must be parallel to the propagation direction.

In three-dimensional space, for any given direction of the wave vector, there are hence two linearly independent polarizations for the transverse wave and only one for the longitudinal wave. In an isotropic medium, the two transverse polarizations behave identically, whereas, in an anisotropic medium, they can have different propagation velocities.

#### 4.9.2.1 Complex Moduli and Wave Speed

We previously introduced the complex shear modulus  $G^*$  (Eqs. (4.93) and (4.94)). In a viscoelastic medium, the shear wave equation (4.141) can be written with  $G^*$  instead of the real-valued shear modulus  $\mu$ , which represents only elasticity. The wave equation then reads

$$\rho \ddot{\mathbf{c}} = G^* \Delta \mathbf{c}, \quad (4.149)$$

or

$$\rho \ddot{\mathbf{u}} = G^* \Delta \mathbf{u}, \quad (4.150)$$

if  $\mathbf{u}$  is free of compressional waves. In the purely elastic case, the shear wave velocity is given by  $c_T = \sqrt{\frac{\mu}{\rho}}$ . For a viscoelastic medium, the corresponding expression,  $\sqrt{\frac{G^*}{\rho}}$ , becomes complex, with the real part representing wave speed and the imaginary part quantifying the frequency-dependent exponential attenuation coefficient,  $\Gamma(\omega)$ , in a plane-wave model:

$$\mathbf{u}(\mathbf{r}, t) = \mathbf{u}_0 \cdot e^{i(\mathbf{k} \bullet \mathbf{r} - \omega t) - \Gamma(\omega) \cdot \hat{\mathbf{k}} \bullet \mathbf{r}}. \quad (4.151)$$

The damping constant for the two parameterizations  $((G', G'')$  and  $(|G^*|, \varphi)$ ) reads

$$\Gamma(\omega) = \omega \operatorname{Im} \left( \sqrt{\frac{\rho}{G^*(\omega)}} \right) = \frac{\omega \cdot \sqrt{\rho \cdot (\sqrt{G'^2 + G''^2} - G')}}{\sqrt{2} (G'^2 + G''^2)} \quad (4.152)$$

$$\text{or } \Gamma(\omega) = \frac{\omega \cdot \sqrt{\rho \cdot (1 - \cos(\varphi))}}{\sqrt{2}|G^*|}, \quad (4.153)$$

where the frequency dependence of  $G''$  and  $G^*$  has been dropped for improved legibility. For the wave speed, we obtain

$$c(\omega) = \frac{1}{\operatorname{Re} \left( \sqrt{\frac{\rho}{G^*(\omega)}} \right)} = \sqrt{\frac{2 (G'^2 + G''^2)}{\rho (G' + \sqrt{G'^2 + G''^2})}} \quad (4.154)$$

$$\text{or } c(\omega) = \sqrt{\frac{2|G^*|}{\rho \cdot (1 + \cos(\varphi))}}. \quad (4.155)$$

Note that these equations only hold true if  $G' > 0$ , that is, they are not applicable to purely viscous media, in which the plane wave approach is invalid.

### 4.9.3 Navier–Stokes Equation

In the discussion so far, we have assumed that all positions are measured in a static reference frame. This is an admissible assumption if the individual mass points oscillate about their equilibrium positions, and if the oscillation amplitudes are small. This approach is called *Eulerian* description. However, in the presence of flow, or large amplitudes, particle motion can be more appropriately described by tracking the individual mass points as they traverse across the object. In that case, the position becomes time-dependent, so that instead of  $\mathbf{u}(\mathbf{r}, t)$  with a time-independent equilibrium position vector  $\mathbf{r}$ , we have to consider the trajectory of the particle  $\mathbf{r}(t)$ . Hence, the displacement field has to be parametrized as

$$\mathbf{u}(\mathbf{r}(t), t). \quad (4.156)$$

This approach is called *Lagrangian* description. Taking temporal derivatives of  $\mathbf{u}$  in the static reference frame then requires total derivatives rather than partial ones:

$$\frac{d\mathbf{u}}{dt} = \frac{\partial \mathbf{u}}{\partial t} + \frac{\partial \mathbf{r}}{\partial t} \bullet \nabla \mathbf{u} = \frac{\partial \mathbf{u}}{\partial t} + \mathbf{v} \bullet \nabla \mathbf{u} = \left( \frac{\partial}{\partial t} + \mathbf{v} \bullet \nabla \right) \mathbf{u}, \quad (4.157)$$

where  $\mathbf{v} = \frac{\partial \mathbf{r}}{\partial t}$  is the (local) flow velocity and  $\nabla \mathbf{u}$  is a tensorial derivative, that is,  $(\nabla \mathbf{u})_{ij} = \frac{\partial u_i}{\partial r_j}$ . A derivative of the form of Eq. (4.157) is called *material derivative*.

The analogue of the Navier equation (4.132) in the presence of flow is known as *Navier–Stokes equation*. It can be formulated as

$$\rho \left( \frac{\partial \mathbf{v}}{\partial t} + (\mathbf{v} \bullet \nabla) \mathbf{v} \right) = -\nabla p + \mu \cdot \Delta \mathbf{v} + (\lambda + \mu) \cdot \nabla (\nabla \bullet \mathbf{v}) + \mathbf{f}, \quad (4.158)$$

with fluid pressure  $p$  and body force density  $\mathbf{f}$ . In the case of an incompressible fluid, the volumetric strain, as quantified by  $\nabla \bullet \mathbf{v}$ , vanishes, and the Navier–Stokes equation reduces to

$$\rho \left( \frac{\partial \mathbf{v}}{\partial t} + (\mathbf{v} \cdot \nabla) \mathbf{v} \right) = -\nabla p + \mu \cdot \Delta \mathbf{v} + \mathbf{f}. \quad (4.159)$$

As a note of mathematical curiosity, it has not yet been proven at the time of writing that solutions to the Navier–Stokes equation always exist in three-dimensional space, and that existing solutions are always smooth. The Clay Mathematics Institute has included these two proofs in its list of Millennium Problems, and their solution will be rewarded with one million US-\$.<sup>19</sup> MRE usually focuses on solid bodies and small strains, therefore the Navier equation will be used instead of the Navier–Stokes equation throughout this book.

#### 4.9.4 Compression Modulus and Oscillating Volumetric Strain

In elastography experiments, the compression modulus  $K$ , like the shear modulus  $\mu$ , is not a directly measurable quantity; it can only be calculated from stress and strain. This section discusses a simple relationship that can be used to detect changes in  $K$  between different physiological states of body tissue by quantifying induced oscillating strain.

As discussed in Section 4.7.3, a pressure change  $\Delta P$  can alter the volume of a compressible material. For a linear medium, the relationship between the pressure change and the volume change  $\Delta V$  is linear:

$$\Delta P = -K \frac{\Delta V}{V}. \quad (4.160)$$

Equation (4.160) is not restricted to a static context but is also valid in a dynamic setting. If an oscillating pressure  $\tilde{P} = P_0 \cdot \exp(-i\omega t)$  acts on the medium, the relation can be stated as

$$\tilde{P} = -K \frac{\Delta \tilde{V}}{V}, \quad (4.161)$$

where  $\Delta \tilde{V}$  denotes the oscillation of the volume about its equilibrium value  $V$  at angular frequency  $\omega$ . Mathematically, this corresponds to the temporally Fourier-transformed displacement field  $\mathbf{U}(\omega)$ , evaluated at the oscillation frequency. In the general case of a viscoelastic medium,  $K$  is a complex number, with the real and imaginary parts representing elastic and viscous behaviors, respectively. Taking the magnitude of both sides of the equation leads to

$$|\tilde{P}| = |K| \cdot \frac{|\Delta \tilde{V}|}{V}.$$

The normalized volume change  $|\Delta \tilde{V}|/V$  is equivalent to the divergence of the pressure-induced displacement field, that is, the volumetric strain:

$$|\tilde{P}| = |K| \cdot |\nabla \bullet \mathbf{U}|. \quad (4.162)$$

This implies that a measurement of the magnitude of the oscillating volumetric strain is representative of the oscillating pressure magnitude, with the magnitude of the complex compression modulus as the proportionality constant.

<sup>19</sup> <http://www.claymath.org/millennium-problems/navier%E2%80%93stokes-equation>

#### 4.9.5 Elastodynamic Green's Function

In the previous derivation of the wave equation, no explicit assumptions about the source of the waves were made. In this section, we present a general tool to solve the wave equation for arbitrary external forces. These source terms can be incorporated into the Navier equation by adding localized and time-dependent force terms:

$$\rho \ddot{\mathbf{u}} - (\lambda + \mu) \nabla(\nabla \cdot \mathbf{u}) - \mu \Delta \mathbf{u} = \mathbf{f}(\mathbf{r}, t). \quad (4.163)$$

This is an inhomogeneous version of the Navier equation, with the inhomogeneity term  $\mathbf{f}(\mathbf{r}, t)$ .

Inhomogeneous differential equations of the form

$$\hat{D}y(r) = f(r) \quad (4.164)$$

with an arbitrary differential operator  $\hat{D}$  can be solved if *Green's function*  $G(r)$  of  $\hat{D}$  is known. Green's function is the solution to a modified version of the differential equation with the inhomogeneity term replaced by a Dirac delta pulse  $\delta(r)$ :

$$\hat{D}G(r) = \delta(r). \quad (4.165)$$

The inhomogeneity term  $f(r)$  can then be expressed as

$$f(r) = \int_{-\infty}^{\infty} \delta(r - r') f(r') dr' = \int_{-\infty}^{\infty} \hat{D}G(r - r') f(r') dr'. \quad (4.166)$$

If the differential operator  $\hat{D}$  commutes with the integration, so that the two can be swapped, the solution to Eq. (4.164) can be calculated as

$$f(r) = \hat{D}y(r) = \hat{D} \int_{-\infty}^{\infty} G(r - r') f(r') dr' \quad (4.167)$$

$$\Rightarrow y(r) = \int_{-\infty}^{\infty} G(r - r') f(r') dr'. \quad (4.168)$$

This means that the solution to an inhomogeneous differential equation can be expressed as the integral over the source distribution  $f(r)$ , where each source is weighted with Green's function  $G(r, r')$  at that position.<sup>20</sup> If the source terms have an additional time dependence, such that  $f(r) \rightarrow f(r, t)$ , Green's function inherits the time dependence:  $G(r, r') \rightarrow G(r, r'; t, t')$ . In that case, Green's function describes how a distortion at the space-time coordinate  $(t', r')$  affects the solution at the coordinate  $(t, r)$ . The meaning of this statement will become clearer in the next paragraph.

The elastodynamic Green's function for homogeneous and isotropic medium is the solution to Eq. (4.129) or Eq. (4.130) with a source or body force term of unit strength

$$f(\mathbf{r}, t; \mathbf{r}', t') = \delta(\mathbf{r} - \mathbf{r}') \cdot \delta(t - t'). \quad (4.169)$$

Green's function describes the displacement field at  $(t, \mathbf{r})$  caused by a  $\delta$ -pulse at  $(t', \mathbf{r}')$ . Due to the vector nature of the displacement field, two additional indices are necessary to account for the direction of the deflection (polarization, index  $j$ ) and the direction of

<sup>20</sup> Mathematically, this is equivalent to a convolution of the source term with Green's function of the system.

the force (index  $k$ ). Unidirectional pulses cause both shear and pressure waves, so that Green's function is often divided into three parts:

$$G_{jk}^s(\mathbf{r} - \mathbf{r}', t - t') = -\frac{1}{4\pi\rho c_s^2} \cdot (\gamma_j\gamma_k - \delta_{jk}) \cdot \frac{1}{|\mathbf{r} - \mathbf{r}'|} \cdot \delta\left(t - t' - \frac{|\mathbf{r} - \mathbf{r}'|}{c_s}\right), \quad (4.170)$$

$$G_{jk}^p(\mathbf{r} - \mathbf{r}', t - t') = \frac{1}{4\pi\rho c_p^2} \cdot \gamma_j\gamma_k \cdot \frac{1}{|\mathbf{r} - \mathbf{r}'|} \cdot \delta\left(t - t' - \frac{|\mathbf{r} - \mathbf{r}'|}{c_p}\right), \quad (4.171)$$

$$G_{jk}^c(\mathbf{r} - \mathbf{r}', t - t') = \frac{1}{4\pi\rho} \cdot (3\gamma_j\gamma_k - \delta_{jk}) \cdot \frac{1}{|\mathbf{r} - \mathbf{r}'|^3} \int_{|\mathbf{r} - \mathbf{r}'|/c_p}^{|\mathbf{r} - \mathbf{r}'|/c_s} \tau'' \delta(t - t' - \tau) d\tau, \quad (4.172)$$

where  $\gamma_j = (r_j - r'_j)/|\mathbf{r} - \mathbf{r}'|$  are the direction cosines of the vector connecting  $\mathbf{r}$  and  $\mathbf{r}'$ . The constants  $c_s$  and  $c_p$  represent the propagation velocities of the shear and compression waves.  $G_{jk}^s$  and  $G_{jk}^p$  describe the shear and pressure far-field, respectively, whereas  $G_{jk}^c$  represents the *coupling field* or *near-field*. It comprises the shear and pressure near field. The complete Green's function is

$$G_{jk} = G_{jk}^s + G_{jk}^p + G_{jk}^c. \quad (4.173)$$

A graphical representation of these three terms is shown in Figure 4.8. One way to think about Green's function is that it evaluates the displacement field at  $(t, \mathbf{r})$  and keeps track of the contribution from events happening at  $(t', \mathbf{r}')$ . The full field can then be reconstructed by summing up all these contributions through integration over  $t'$  and  $\mathbf{r}'$ . The expression  $t - t' - |\mathbf{r} - \mathbf{r}'|/c$  in the argument of the delta function in Eqs. (4.170) and (4.171) states that a source at  $(t', \mathbf{r}')$  can only contribute to the displacement at  $(t, \mathbf{r})$  if the time between emission ( $t'$ ) and detection ( $t$ ) is equal to the travel time of the signal between those two points ( $|\mathbf{r} - \mathbf{r}'|/c$ ). Furthermore, since  $|\mathbf{r} - \mathbf{r}'|/c \geq 0$ , an event can only have an effect after it has happened ( $t \geq t'$ ), reflecting a manifestation of *causality*.

The response of an elastic medium to a point source with arbitrary time dependence is obtained by convolution of Green's function with the time dependence of the source. Moreover, the Green's function can be used to express the displacement field resulting from surface traction<sup>21</sup>  $\boldsymbol{\tau}(\mathbf{r}, t)$  that acts on some region  $R \subseteq S$ , where  $S$  is the surface bounding the given volume. The remainder  $S \setminus R$  is assumed to be traction free. The field can then be expressed implicitly as

$$u_j(\mathbf{r}, t) = \int_{-\infty}^{\infty} \iiint_V \sum_{k=1}^3 G_{jk}(\mathbf{r} - \mathbf{r}', t - t') f_k(\mathbf{r}', t') dV(\mathbf{r}') dt' + \text{boundary terms}. \quad (4.174)$$

The first term in Eq. (4.174) can be interpreted in the sense of Huygens' principle. Every surface point with nonzero traction radiates a point source field. The second term requires knowledge of the displacement field itself at the surface and corresponds to possible surface effects such as Rayleigh waves or head waves. These effects have to be calculated on a case-by-case basis, and no general solution can be given here.

If we assume that the source of the vibration is a rigid plate that is attached to the object without slip on an area  $R \subseteq S$  and that the plate vibrates along the 3-direction, we

<sup>21</sup> Traction is the force per area acting on a boundary or surface. See Eq. (4.10) for the definition.



can represent the force term as

$$f_1 = f_2 = 0 \quad (4.175)$$

$$f_3(\mathbf{r}', t') = \begin{cases} \zeta \cdot \exp(i\omega t') & \text{if } \mathbf{r}' \in R \\ 0 & \text{otherwise.} \end{cases} \quad (4.176)$$

The amplitude of the oscillating force,  $\zeta$ , must have the dimension force/area, in contrast to the case force/volume when the force is located within the body. We can therefore reduce the volume integral in Eq. (4.174) to a surface integral over the contact surface  $R$ . Furthermore, Green's function does not take into account reflection at the boundaries, assuming instead that waves will only travel through the object once and then disappear (this is the equivalent of assuming perfectly absorbing boundary conditions). We therefore introduce  $\Lambda$  to denote the length of the longest straight line that originates in  $R$  and ends somewhere on the surface of the object. As a result, the maximum travel time of the wave through the object is given by  $\tau = \frac{\Lambda}{c}$ , where  $c$  is the propagation velocity. We finally want the model to be *causal*, meaning that the behavior of the system at any given time is only determined by the "vibration history" and not by the vibration happening in the future. This allows us to also restrict the integration bounds for the temporal integral to 0 and  $\tau$ , meaning that we look back in time no further than  $\tau$  and not at all into the future. With these simplifications, we can express the displacement field as

$$u_j(\mathbf{r}, t) = \zeta \int_0^{\Lambda/c} \int_R G_{j\beta}(\mathbf{r} - \mathbf{r}', t - t') \cdot \exp(i\omega t') \, dA(\mathbf{r}') \, dt', \quad (4.177)$$

with the scalar surface element  $dA$ .

#### 4.9.6 Boundary Conditions

The general solution of a differential equation defines a whole class of functions, since each integration step introduces an arbitrary constant of integration. To narrow down this solution space to a single solution, further information about the system has to be incorporated. This is achieved by introducing *boundary conditions*, which specify the behavior of the system on the boundary of the problem domain. The number of independent boundary conditions is equal to the order of the differential equation, as every condition fixes one constant of integration.

Generally, boundary conditions can be categorized into four types. Let  $S$  be the boundary of the object under investigation:

- 1) *Dirichlet* boundary condition: This boundary condition prescribes displacement on the boundary, which, in the case of a rigid (nondeformable) boundary, is

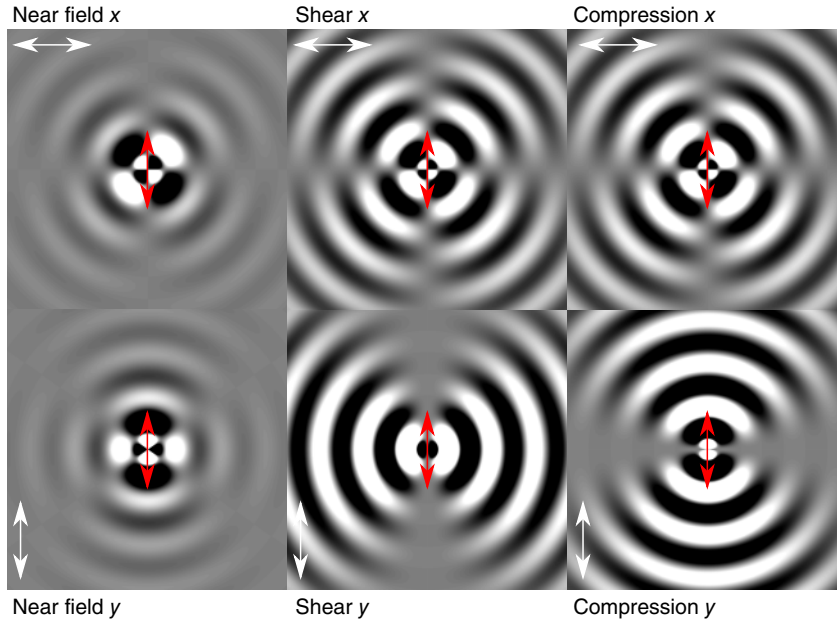
$$\mathbf{u}(\mathbf{r}) = \mathbf{0} \quad \text{for } \mathbf{r} \in S.$$

- 2) *von Neumann* boundary condition: Traction  $\boldsymbol{\tau}$  on the surface is prescribed. A traction-free surface can be characterized by

$$\boldsymbol{\tau}(\mathbf{r}) = \mathbf{0} \quad \text{for } \mathbf{r} \in S. \quad (4.178)$$

- 3) *Sommerfeld* (nonreflecting) boundary condition:

$$\partial_{\mathbf{n}} u = iku \quad \text{for } \mathbf{r} \in S, \quad (4.179)$$



**Figure 4.8** 2D simulation of the field generated by a point source according to Eqs. (4.170)–(4.172). The source is located in the center of the image and oscillates in the  $y$ -direction, as indicated by the red arrows. The  $x$  (horizontal) and  $y$  (vertical) components of the resulting displacement fields are shown, as indicated by the white arrows. The simulation was performed assuming shear wave and pressure wave velocity to be identical, which is unphysical but helps to appreciate the patterns created by each mode. As a consequence, the  $x$  components of the shear and compression fields are identical, which would not be the case if the velocities were different. Note that the near field decreases much faster with the distance from the source than the far fields.

where  $\partial_{\mathbf{n}}$  is the derivative along the surface normal and  $k$  is the wave number. Sommerfeld boundary conditions suppress the reflection of an incident wave.

- 4) Mixed boundary conditions: Different parts of the boundary can be governed by different boundary conditions. For example,  $S$  might be subdivided into two nonoverlapping regions  $S_1$  and  $S_2$ , such that  $S = S_1 \cup S_2$  and  $S_1 \cap S_2 = \emptyset$ .  $S_1$  could be characterized by prescribed displacement  $\mathbf{u}$  and  $S_2$  by traction  $\boldsymbol{\tau}$ .

Boundary conditions will be considered in Section 8.4 in the context of numerical field simulations. Examples of such simulated wave fields for different boundary conditions in 1D and 2D are shown in Figure 8.15.

## 4.10 Waves in Anisotropic Media

The wave phenomena discussed in the previous sections were derived under the assumption of an isotropic medium. However, many real-world materials exhibit anisotropy, implying that viscoelastic moduli depend on the direction in which a force is applied. In such materials, different wave modes exist, which are characterized by the orientation of polarization and propagation directions relative to the principal axes of

the material structure. In this section, we will first discuss the mathematical treatment of waves in a generally anisotropic medium, and then we will focus on a transversely anisotropic medium to highlight some of the effects that differentiate such a medium from an isotropic one.

The Navier equation (4.129) is only valid for isotropic media. In the anisotropic case, more than two parameters are required to represent the viscoelastic properties of the material. The general balance of momentum equation for an oscillating displacement field  $u_i \propto \exp(i\omega t)$  in an anisotropic medium reads (cf. Eqs. (4.116) and (4.117))

$$-\rho\omega^2 u_i + \sum_{j,k,l=1}^3 \frac{\partial}{\partial r_j} \left( C_{ijkl}(\mathbf{r}) \frac{\partial}{\partial r_k} u_l \right) = 0, \quad (4.180)$$

or, if we assume spatially constant viscoelastic parameters,

$$-\rho\omega^2 u_i + \sum_{j,k,l=1}^3 C_{ijkl} \frac{\partial^2}{\partial r_j \partial r_k} u_l = 0. \quad (4.181)$$

In contrast to the isotropic case, Eq. (4.181) is a system of three coupled differential equations for the three spatial components of the displacement field. No analytical solution exists for the general case. Furthermore, the solution also depends on the aforementioned terms in Green's function, including boundary conditions, polarization, and propagation direction of the waves. Nevertheless, in the next section, we will present a useful tool for the treatment of such cases.

#### 4.10.1 The Christoffel Equation

There is no closed-form solution to Eq. (4.181), neither for anisotropy nor for a general geometry including boundary conditions. Therefore, we limit our discussion to plane waves with harmonic frequency  $\omega$ . This approach ignores boundaries, but accounts for specific polarization and propagation directions, which ultimately determine the wave fields in anisotropic media, such as muscles or neuronal fiber tracts. Consider a plane wave

$$u_i = u_{0i} e^{i(\mathbf{k} \cdot \mathbf{x} - \omega t)}, \quad (4.182)$$

where the  $u_{0i}$  are constants determining the initial polarization and amplitude of the wave and  $\mathbf{k}$  is the wave vector with length  $k = \omega/c$ , with the phase velocity of the wave,  $c$ . Inserting Eq. (4.182) into Eq. (4.181), we obtain

$$\sum_{j,k,l=1}^3 (C_{ijkl} k_j k_k - \rho\omega^2 \delta_{il}) u_{0i} = 0 \quad \text{for } i = 1, 2, 3. \quad (4.183)$$

Here,  $\delta_{il}$  is the Kronecker delta and  $c_{ijkl} = C_{ijkl}/\rho$ . Nontrivial solutions (for which at least one  $u_{0i} \neq 0$ ) for the components  $u_i$  exist only for angular frequencies  $\omega$  that satisfy the characteristic equation

$$\det \left( \sum_{j,k=1}^3 C_{ijkl} k_j k_k - \rho\omega^2 \delta_{il} \right) = 0, \quad (4.184)$$

which is referred to as *Christoffel equation*. Equation (4.184) is of order  $d$  in  $\omega^2$ , where  $d$  is the spatial dimension. Consequently, in three-dimensional space, there exist three solutions called *modes*.<sup>22</sup> These modes are characterized by the relative orientation of their polarization ( $\mathbf{u}_0$ ) with respect to their propagation direction ( $\mathbf{k}$ ) as *quasi-transverse* (two modes) and *quasi-longitudinal* (one mode). The Christoffel equation establishes a relationship between the frequency  $\omega$  of a wave and its wave vector  $\mathbf{k}$ . Compatible pairings  $(\omega, \mathbf{k})$  are representations of plane waves in four-dimensional (3D + time) Fourier-transformed space. Hence, for a fixed value of  $\omega$ , solutions  $\mathbf{k}$  represent waves with frequency  $\omega$  that propagate in different directions. This means that a single plane wave spreads into different directions like a wave package rather than a conventional single wave, giving rise to the notion of group velocity. In other words, the set of wave vectors for a given value of  $\omega$  defines a surface of constant angular frequency in the Fourier domain. The exact relationship between  $\mathbf{k}$  and  $\omega$  is determined by the elastic properties of the material in the form of the elasticity tensor  $\mathbf{C}$ . By dividing Eq. (4.184) through  $|\mathbf{k}|$ , one obtains a corresponding equation, whose solutions are surfaces of constant *phase velocity*  $c$ , since  $c = \frac{\omega}{|\mathbf{k}|}$ . Although these surfaces are given in  $k$ -space or wave normal space, their symmetry properties translate identically into position space. This makes them particularly useful for analyzing waveforms.

In an anisotropic medium, phase speed depends on the direction of  $\mathbf{k}$ . The direction of energy transport is given by the aforementioned *group velocity*<sup>23</sup>

$$\mathbf{v} = \nabla_{\mathbf{k}}\omega(\mathbf{k}), \quad (4.185)$$

where  $\nabla_{\mathbf{k}}$  denotes the gradient with respect to the wave vector  $\mathbf{k}$ . The direction of  $\mathbf{v}$  in anisotropic media differs from the direction of  $\mathbf{k}$ .

#### 4.10.2 Waves in a Transversely Isotropic Medium

In Section 4.7.4, we presented the explicit form of the elasticity and compliance tensors for a transversely isotropic medium. In analogy to the procedure in Section 4.9.1, we substitute the stress gradient  $\nabla \cdot \boldsymbol{\sigma}$  into the balance of momentum (Eq. (4.116)). As a result, we obtain the equation of motion for elastic waves in a material featuring transverse isotropy with the parametrization defined by Eqs. (4.20) and (4.66):

$$\rho \ddot{\mathbf{u}} - \underbrace{(\mathbf{A}_1 \partial_1^2 + \mathbf{A}_2 \partial_2^2 + \mathbf{A}_3 \partial_3^2 + \mathbf{A}_4 \partial_1 \partial_2 + \mathbf{A}_5 \partial_1 \partial_3 + \mathbf{A}_6 \partial_2 \partial_3)}_{\equiv \hat{\mathbf{L}}} \mathbf{u} = \mathbf{0}, \quad (4.186)$$

<sup>22</sup> Every possible solution for  $\omega^2$  corresponds to two distinct physical solutions,  $+\omega$  and  $-\omega$ . These represent waves with opposite propagation directions but otherwise identical properties, so that they are counted as one mode rather than two.

<sup>23</sup> The difference between phase velocity,  $\mathbf{c}$ , and group velocity,  $\mathbf{v}$ , is that phase velocity represents the speed at which a wave of a single frequency propagates through a medium, whereas group velocity quantifies the speed of the envelope of a wave packet (a superposition of waves with different frequencies). In isotropic media,  $\mathbf{c}$  and  $\mathbf{v}$  are always parallel, whereas in anisotropic media their directions can differ.

with  $\mathbf{u} = \mathbf{u}(\mathbf{r}, t)$ ,  $\partial_i \equiv \frac{\partial}{\partial r_i}$  and

$$\begin{aligned} \mathbf{A}_1 &= \begin{pmatrix} C_{11} & 0 & 0 \\ 0 & \mu_{12} & 0 \\ 0 & 0 & \mu_{13} \end{pmatrix}, & \mathbf{A}_2 &= \begin{pmatrix} \mu_{12} & 0 & 0 \\ 0 & C_{11} & 0 \\ 0 & 0 & \mu_{23} \end{pmatrix}, \\ \mathbf{A}_3 &= \begin{pmatrix} \mu_{13} & 0 & 0 \\ 0 & \mu_{23} & 0 \\ 0 & 0 & C_{33} \end{pmatrix}, & \mathbf{A}_4 &= \begin{pmatrix} 0 & C_{12} + \mu_{12} & 0 \\ C_{12} + \mu_{12} & 0 & 0 \\ 0 & 0 & 0 \end{pmatrix}, \\ \mathbf{A}_5 &= \begin{pmatrix} 0 & 0 & C_{13} + \mu_{13} \\ 0 & 0 & 0 \\ C_{13} + \mu_{13} & 0 & 0 \end{pmatrix}, & \mathbf{A}_6 &= \begin{pmatrix} 0 & 0 & 0 \\ 0 & 0 & C_{23} + \mu_{23} \\ 0 & C_{23} + \mu_{23} & 0 \end{pmatrix}. \end{aligned}$$

Matrices  $\mathbf{A}_1$ ,  $\mathbf{A}_2$ , and  $\mathbf{A}_3$  are multiplied with second-order uniaxial derivatives  $\partial_i^2 \mathbf{u}$  in Eq. (4.186). These three matrices are diagonal, indicating that pure axial strain results in pure axial stress and vice versa, as already discussed in Section 4.7.4. These three terms hence represent volumetric deformation. The second set of matrices,  $\mathbf{A}_4$ ,  $\mathbf{A}_5$ , and  $\mathbf{A}_6$ , has symmetric pairs of off-diagonal entries as the only nonvanishing elements. They are multiplied with second-order mixed derivatives ( $\partial_i \partial_j \mathbf{u}$ ,  $i \neq j$ ), which represent shear deformation along different axes.

As an example of how to use such a model for elastography, we follow the path described in [47]. First, we impose the assumption of incompressibility by requiring that the volumetric strain vanishes,

$$\epsilon_{11} + \epsilon_{22} + \epsilon_{33} \equiv \frac{\partial u_1}{\partial r_1} + \frac{\partial u_2}{\partial r_2} + \frac{\partial u_3}{\partial r_3} = 0. \quad (4.187)$$

This induces relations between the viscoelastic parameters, namely

$$v_{31} = \frac{1}{2} \quad (4.188)$$

$$v_{12} = 1 - \frac{1}{2} \frac{E_1}{E_3} \quad (4.189)$$

for the anisotropic Young's moduli and Poisson's ratios. Therefore, we have reduced the number of parameters in the original transversely isotropic model from five (in Eq. (4.66)) to three, which obey the inequality

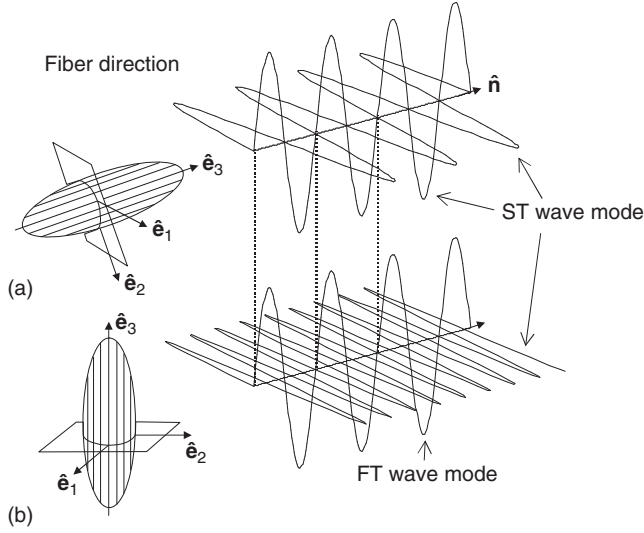
$$\mu_{12} \neq \mu_{13} \neq \frac{E_3}{3}. \quad (4.190)$$

For an isotropic medium, all three terms would be equal.

We now solve the Christoffel equation (4.184) for the transversely isotropic case. With the introduction of the normalized wave vector,  $n_i = \frac{k_i}{|\mathbf{k}|}$ , the Christoffel equation reads [48]

$$\det (C_{ijkl} n_j n_k - \rho c^2 \delta_{il}) = 0. \quad (4.191)$$

As explained in Section 4.10.1, there are three solutions for  $c$ , corresponding to three different wave modes. One mode corresponds to a longitudinal mode, which we are not interested in, since we assume incompressibility of the tissue. The other two modes are referred to as the *fast transverse* (FT) and the *slow transverse* (ST) modes, depending on the orientation of the polarization relative to the fibers (see Figure 4.9).



**Figure 4.9** Illustration of the nomenclature for shear waves in a transversely isotropic medium. Wave modes polarized parallel to the fiber direction are referred to as “fast transverse” (FT), whereas those polarized perpendicular to the fibers are called “slow transverse” (ST). (Klatt 2010 [49]. Reproduced with permission of Institute of Physics Publishing.)

- The FT mode applies to waves that are polarized parallel to the fibers. The velocity of this mode is

$$\rho c_{\text{FT}}^2 = (4\mu_{13} - \mu_{12} - E_3) \cdot (n_3^4 - n_3^2) + \mu_{13}. \quad (4.192)$$

If such a wave propagates within the plane of isotropy ( $n_3 = 0$ ), the wave speed is governed exclusively by  $\mu_{13}$ , whereas all three elastic constants affect the speed if the propagation direction has an out-of-plane component. Since shear waves cannot propagate along their polarization direction, the FT mode does not apply to waves that travel along the fibers. The direction dependence of the FT mode is shown in the last column of Figures 4.10 and 4.11.

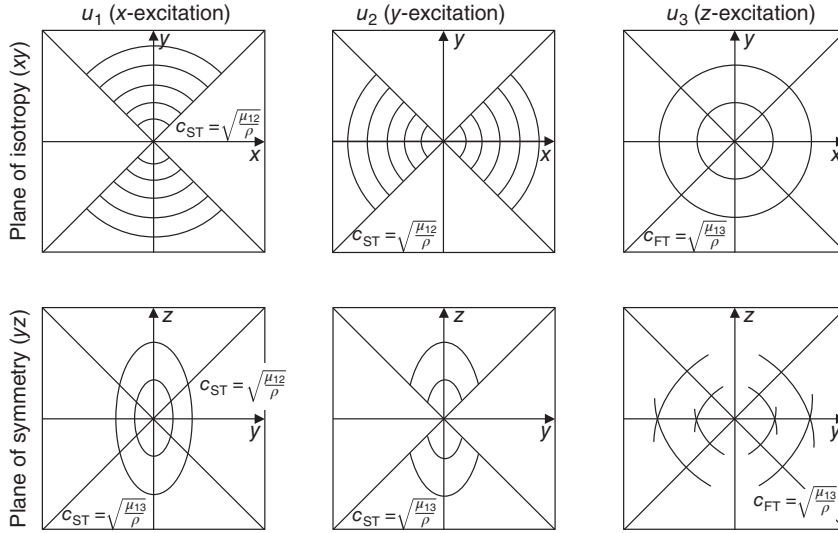
- The ST mode corresponds to shear wave propagation with polarization parallel to the plane of isotropy, as illustrated in Figure 4.9. Wave speed in that case is

$$\rho c_{\text{ST}}^2 = \mu_{12}(n_1^2 + n_2^2) + \mu_{13}n_3^2. \quad (4.193)$$

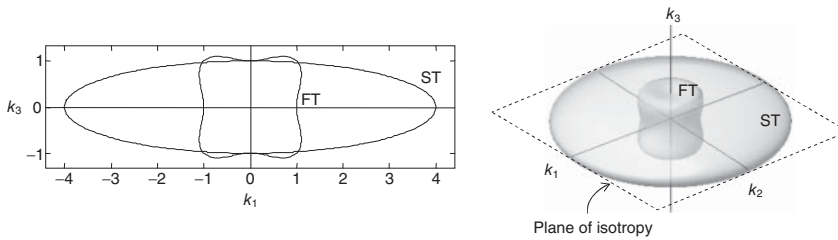
Waves propagating strictly within the plane of isotropy ( $n_3 = 0$ ) are governed by  $\mu_{12}$ . Propagation parallel to the fibers ( $n_3 = 1$ ) is characterized by  $\mu_{13}$ . Waves traveling in an oblique direction are described by a combination of  $\mu_{12}$  and  $\mu_{13}$  (but not  $E_3$ , as in the case of the FT mode). This is shown in the first two columns of Figures 4.10 and 4.11.

Note that the terminology “fast” and “slow” only makes sense if  $\mu_{13} > \mu_{12}$ , which does not necessarily have to be the case. Furthermore, the fast and slow modes can propagate at the same velocity for specific directions.<sup>24</sup> The categorization into slow and fast can

<sup>24</sup> For example,  $c_{\text{ST}} = \sqrt{\frac{\mu_{13}}{\rho}}$  for  $n_3 = 1$  and  $c_{\text{FT}} = \sqrt{\frac{\mu_{13}}{\rho}}$  for  $n_3 = 0$ .



**Figure 4.10** Shear wave modes in a transversely isotropic medium with fibers along the z-axis. The first row represents wave propagation in the plane of isotropy (xy-plane) and the second row depicts one plane of symmetry (yz-plane). The three columns represent three orthogonal modes of excitation along the three principal axes. The curved lines indicate wave fronts emanating from the center of the image. Since only shear waves are considered here, propagation cannot be parallel to the polarization direction. (Klatt 2010 [49]. Reproduced with permission of Institute of Physics Publishing.)



**Figure 4.11**  $k$ -Space representation of iso surfaces representing constant wave velocity for fast transverse and slow transverse shear modes, that is, the solutions of the Christoffel equation (4.184) for fixed values of  $c$  and  $\rho$ , plotted in 2D and 3D. The oblate ellipsoid represents the slow transverse mode (Eq. (4.193), basically describing an ellipsoid with half axes  $\sqrt{\frac{1}{\mu_{12}}}$  and  $\sqrt{\frac{1}{\mu_{13}}}$ ). The more irregular surface corresponds to the fast transverse wave mode, reflecting the more complex structure of Eq. (4.192). Note that this representation is given in un-normalized  $k$ -space; therefore, the coordinates are actual  $k$ -values rather than their normalized equivalents ( $n_1, n_2, n_3$ ). (Papazoglou 2006 [48]. Reproduced with permission of Wiley.)

therefore sometimes be misleading, and it is better to classify these waves as “polarized parallel to the fibers” and “polarized perpendicular to the fibers.”

In Sections 10.8 and 10.9, we will discuss two methods that can be used to obtain viscoelastic parameters from wave fields measured in anisotropic or transversely isotropic media.

### 4.11 Energy Density and Flux

*This section was coauthored by Heiko Tzschätzsch from the Department of Radiology, Charité – Universitätsmedizin Berlin, Germany.*

In some applications of MRE, such as cardiac MRE (which will be discussed in Chapter 13), information on tissue elasticity is derived directly from wave amplitudes without inversion of the wave equation. Therefore, it is important to understand the relationship between wave amplitudes and elastic tissue properties. Valuable insights can be gained from analyzing energy transport by plane waves in an isotropic medium.

A traveling wave gives rise to changes in the potential and kinetic energy of the medium. Potential energy is the result of local deformation, whereas kinetic energy manifests itself in the deflective motion of mass points. The strain-energy function introduced in Section 4.2,

$$W = \frac{1}{2} \cdot \sum_{i,j=1}^3 \sigma_{ij} \epsilon_{ij} = \frac{1}{2} \cdot \sum_{i,j,k,l=1}^3 C_{ijkl} \epsilon_{ij} \epsilon_{kl}, \quad (4.194)$$

only accounts for potential energy density. Kinetic energy, on the other hand, is given by

$$T = \frac{1}{2} \rho \dot{\mathbf{u}}^2 = \frac{1}{2} \rho \sum_{i=1}^3 \dot{u}_i^2, \quad (4.195)$$

where  $u_i$  denotes the components of the displacement field. The total energy density is the sum of the two:

$$\Phi = W + T. \quad (4.196)$$

The energy enclosed in a volume  $V$  can be calculated as the volume integral

$$E = \iiint_V \Phi(\mathbf{r}) dV. \quad (4.197)$$

We will now investigate how the propagation of waves affects the distribution of energy within a medium, following the path outlined in [50].

Gauss's divergence theorem, which we already used on page 93, states that the volume integral of a scalar function  $\Theta(\mathbf{x})$  can be equivalently calculated as the surface integral over a vector field  $\Psi$  if  $\Psi$  is the divergence of  $\Theta(\mathbf{x})$ :

$$\iiint_V \Theta(\mathbf{x}) d\mathbf{x} = \oiint_{\partial V} \Psi(\mathbf{x}) \cdot d\mathbf{A} \quad (4.198)$$

with  $\Theta(\mathbf{x}) = \nabla \cdot \Psi(\mathbf{x})$ ,

where  $\partial V$  is the closed surface of  $V$  and  $d\mathbf{A}$  is the oriented surface element with an outward-pointing normal vector. We now apply this theorem to the total energy and assume that the temporal derivative of the total energy density,  $\dot{\Phi}$ , can be expressed as the negative divergence of a three-dimensional vector field  $\mathbf{P}$ ,

$$\dot{\Phi}(\mathbf{x}) = -\nabla \cdot \mathbf{P}(\mathbf{x}) \quad (4.199)$$



(the purpose of the minus symbol will become obvious later), and that we can hence rewrite Eq. (4.197) as

$$\dot{E} = - \oint_{\partial V} \mathbf{P}(\mathbf{x}) \cdot \hat{\mathbf{n}}(\mathbf{x}) \, dA. \quad (4.200)$$

Equation (4.199) has the characteristic form of a *continuity equation*. The vector entity  $\mathbf{P}$  is the *energy flux density*.<sup>25</sup> Equation (4.200) then states that the change of the total energy enclosed in a volume  $V$  is equal to the energy flux through the surface of the volume and that energy cannot be created nor destroyed in the volume itself. By virtue of the minus sign that we introduced in the definition of flux in Eq. (4.199),  $\mathbf{P}$  points in the direction of energy transport.

In the next step, we will link energy flux density to the displacement field  $\mathbf{u}$  induced by a propagating wave. The change of energy density can be expressed as

$$\dot{\Phi} = \dot{W} + \dot{T}. \quad (4.201)$$

Using Eq. (4.194), we obtain for the potential energy component

$$\begin{aligned} \dot{W} &= \frac{1}{2} \cdot \sum_{i,j,k,l=1}^3 C_{ijkl} \cdot (\epsilon_{ij} \dot{\epsilon}_{kl} + \dot{\epsilon}_{ij} \epsilon_{kl}) = \sum_{i,j,k,l=1}^3 C_{ijkl} \cdot \epsilon_{ij} \dot{\epsilon}_{kl} \\ &= \sum_{i,j=1}^3 \sigma_{ij} \dot{\epsilon}_{ij} = \frac{1}{2} \sum_{i,j=1}^3 \sigma_{ij} \left( \frac{\partial \dot{u}_i}{\partial r_j} + \frac{\partial \dot{u}_j}{\partial r_i} \right) = \sum_{i,j=1}^3 \sigma_{ij} \frac{\partial \dot{u}_i}{\partial r_j}. \end{aligned} \quad (4.202)$$

For the kinetic energy density, on the other hand, we obtain using Eq. (4.195):

$$\dot{T} = \frac{1}{2} \rho \cdot \sum_{i=1}^3 \frac{\partial \dot{u}_i^2}{\partial t} = \rho \cdot \sum_{i=1}^3 \dot{u}_i \ddot{u}_i \quad (4.203)$$

We can now calculate the rate of change of the total energy by volumetric integration:

$$\begin{aligned} \dot{E} &= \iiint_V (\dot{T} + \dot{W}) \, dV = \iiint_V \sum_{i,j=1}^3 \sigma_{ij} \frac{\partial \dot{u}_i}{\partial r_j} \, dV + \iiint_V \rho \cdot \sum_{i=1}^3 \dot{u}_i \ddot{u}_i \, dV \\ &\stackrel{(1)}{=} \iiint_V \sum_{i,j=1}^3 \left( \frac{\partial}{\partial r_j} (\sigma_{ij} \cdot \dot{u}_i) - \dot{u}_i \frac{\partial \sigma_{ij}}{\partial r_j} \right) \, dV + \iiint_V \rho \cdot \sum_{i=1}^3 \dot{u}_i \ddot{u}_i \, dV \\ &\stackrel{(2)}{=} \oint_{\partial V} (\boldsymbol{\sigma} \cdot \dot{\mathbf{u}}) \cdot \hat{\mathbf{n}} \, dA + \underbrace{\sum_{i=1}^3 \iiint_V \dot{u}_i \left( \rho \ddot{u}_i - \sum_{j=1}^3 \frac{\partial \sigma_{ij}}{\partial r_j} \right) \, dV}_{=0} \\ &= \oint_{\partial V} (\boldsymbol{\sigma} \cdot \dot{\mathbf{u}}) \cdot \hat{\mathbf{n}} \, dA. \end{aligned} \quad (4.204)$$

In step (1), we performed integration by parts in the first integral. In step (2), we invoked Gauss's divergence theorem to convert the volume integral of the first term into a surface integral. We then merged the two remaining volume integrals. The term in the

<sup>25</sup>  $\mathbf{P}$  is the mechanical counterpart to the *Poynting vector* in electrodynamics.

parentheses is a component-wise formulation of the balance of momentum (Eq. (4.116)) and hence yields zero in the absence of external forces.

By comparing the last line of Eq. (4.204) with Eq. (4.200), we can identify

$$\mathbf{P} = -\boldsymbol{\sigma} \cdot \dot{\mathbf{u}}. \quad (4.205)$$

In isotropic media, the energy flux  $\mathbf{P}$  is parallel to the wave vector  $\mathbf{k}$ , which means that a propagating wave transports energy. In anisotropic media, however, the directions can differ, as discussed in Section 4.10.1.

In order to establish the relationship between elastic parameters and average energy flow, we will now analyze a pure shear wave  $\mathbf{u}(\mathbf{r}, t) = \mathbf{u}_0 \cdot \sin(\mathbf{k} \cdot \mathbf{r} - \omega t)$  propagating along the  $x$ -axis. Its wave vector is  $\mathbf{k} = (k, 0, 0)^T$ , and the polarization is  $\mathbf{u}_0 = (0, u_{02}, u_{03})^T$ . Obviously, the wave only depends on the  $x$ -coordinate, and the only non-vanishing components of the strain tensor are  $\epsilon_{12} = \epsilon_{21} = -\frac{1}{2}ku_{02} \cdot \cos(\mathbf{k} \cdot \mathbf{r} - \omega t)$  and  $\epsilon_{13} = \epsilon_{31} = -\frac{1}{2}ku_{03} \cdot \cos(\mathbf{k} \cdot \mathbf{r} - \omega t)$ . Since these are shear strains, the corresponding stresses are obtained through multiplication with  $2\mu$ . The energy flux vector thus reads

$$P_1 = \sum_{j=2}^3 ku_{0j}\mu \cdot \cos(\mathbf{k} \cdot \mathbf{r} - \omega t) \cdot u_{0j}\omega \cdot \cos(\mathbf{k} \cdot \mathbf{r} - \omega t) \quad (4.206)$$

$$= k\mu\omega \cdot \cos^2(\mathbf{k} \cdot \mathbf{r} - \omega t) \cdot (u_{02}^2 + u_{03}^2) \quad (4.207)$$

$$= \sqrt{\rho\mu}\omega^2 \cdot \cos^2(\mathbf{k} \cdot \mathbf{r} - \omega t) \cdot \mathbf{u}_0^2 \quad (4.208)$$

$$P_{2,3} = 0 \quad (4.209)$$

with the substitutions  $k = \frac{\omega}{c}$  and  $c = \sqrt{\frac{\mu}{\rho}}$ . Energy flows along the  $x$ -axis parallel to the propagation of the wave. The time average over the  $\cos^2$  term yields an additional factor  $\frac{1}{2}$ , such that the time-averaged components of the energy flux become

$$\bar{P}_1 = \frac{1}{2}\sqrt{\rho\mu} \cdot \mathbf{u}_0^2 \quad (4.210)$$

$$\bar{P}_{2,3} = 0 \quad (4.211)$$

$$\Rightarrow |\bar{\mathbf{P}}| = |\bar{P}_1| = \frac{1}{2}\omega^2 u_0^2 \cdot \sqrt{\rho\mu}. \quad (4.212)$$

For a constant flux, we therefore derive the proportionality

$$|\mathbf{u}| \propto \sqrt[4]{\mu}. \quad (4.213)$$

The magnitude of the energy flux is also referred to as *wave intensity*:

$$I = |\mathbf{P}| = \sqrt{\rho\mu}\omega^2 \mathbf{u}^2. \quad (4.214)$$

We conclude this discussion by examining the distribution of the total energy into potential and kinetic contributions. Again, we insert a monochromatic plane wave

$$\mathbf{u}(\mathbf{r}, t) = \mathbf{u}_0 \cdot \sin(\mathbf{k} \cdot \mathbf{r} - \omega t) \quad (4.215)$$

into Eq. (4.195) and obtain

$$T = \mathbf{u}_0^2 \rho \omega^2 k^2 \cos^2(\mathbf{k} \cdot \mathbf{r} - \omega t). \quad (4.216)$$

The time average is then

$$\langle T \rangle_t = \frac{1}{2} \mathbf{u}_0^2 \rho \omega^2 k^2, \quad (4.217)$$

since  $\frac{1}{2\pi} \int_0^{2\pi} \cos^2(t) dt = \frac{1}{2}$ .

For the potential energy density, we insert the plane wave into Eq. (4.194):

$$\begin{aligned} W &= \frac{1}{2} \sum_{i,j,l,m=1}^3 C_{ijlm} \frac{1}{2} (u_{0i}k_j + u_{0j}k_i) \cos(\mathbf{k} \cdot \mathbf{r} - \omega t) \\ &\quad \cdot (u_{0l}k_m + u_{0m}k_l) \cos(\mathbf{k} \cdot \mathbf{r} - \omega t) \\ &= \cos^2(\mathbf{k} \cdot \mathbf{r} - \omega t) \sum_{i,j,l,m}^3 C_{ijlm} u_{0j} u_{0m} k_i k_l. \end{aligned} \quad (4.218)$$

Again, the time average over the  $\cos^2$  term yields  $\frac{1}{2}$ , so that

$$\langle W \rangle_t = \frac{1}{2} \sum_{i,j,l,m}^3 C_{ijlm} u_{0j} u_{0m} k_i k_l. \quad (4.219)$$

$T$  and  $W$  being energy *densities* implies that these relations hold true for arbitrarily small volumes, hence it is correct even for individual particles.

Locally, for a fixed position  $\mathbf{r}$ , a plane wave reduces to a harmonic oscillator. From the virial theorem, we know that in the case of a potential  $W(r) \propto \cdot |r|^n$ , the time averages of potential and kinetic energy (densities) behave as

$$2 \cdot \langle T \rangle_t = n \cdot \langle W \rangle_t. \quad (4.220)$$

Since a harmonic oscillator is characterized by  $n = 2$ , we gather that  $\langle T \rangle_t = \langle W \rangle_t$ . Over the course of one oscillation period, kinetic and potential energies contribute therefore equally to the total energy, and the total energy density can hence be calculated as  $\Phi = 2 \cdot \langle W \rangle_t = 2 \cdot \langle T \rangle_t$ , depending on which information on the system is available. There is no need to look at the time average of  $\Phi$ , since the total energy is not subject to change as long as dissipation is neglected.

#### 4.11.1 Geometric Attenuation

Conservation of energy gives rise to a phenomenon known as “geometric attenuation.” We assume that a point source emits waves at a constant power  $\Pi$ . The waves propagate away from the source at velocity  $c$ . The medium is purely elastic, so that no energy is lost. Over the time interval  $0 \leq t \leq \delta t$ , the energy emitted by the source is

$$E = \Pi \cdot \delta t. \quad (4.221)$$

At a time  $t > \delta t$ , that energy is contained in a spherical shell with outer radius  $R(t) = c \cdot t$  and shell thickness  $\delta R = c \cdot \delta t$ . The volume of the shell is given by

$$\begin{aligned} V &= \frac{4\pi}{3} \cdot (R^3 - (R - \delta R)^3) = \frac{4\pi}{3} (3R^2 \cdot \delta R - 3R \cdot \delta R^2 - \delta R^3) \\ &\approx 4\pi R^2 \cdot \delta R \end{aligned} \quad (4.222)$$

if  $R \gg \delta R$ . The energy density is therefore

$$\Phi = \frac{E}{V} = \frac{E}{4\pi R^2 \cdot \delta R}. \quad (4.223)$$

Obviously, the energy density decreases as  $\frac{1}{R^2}$ , since a fixed amount of the energy is spread over an increasingly larger shell. We gather from Eqs. (4.194) and (4.195) that both potential energy density  $W$  and kinetic energy density  $T$  are proportional to the square of the displacement field.<sup>26</sup> We can thus conclude that

$$\begin{aligned} \Phi &= W + T \propto \mathbf{u}^2 \\ \Phi &\propto \frac{1}{R^2} \implies |\mathbf{u}| \propto \frac{1}{R}. \end{aligned} \quad (4.224)$$

Therefore, the amplitude of a spherical wave from a point source propagating in three dimensions decreases as  $\frac{1}{R}$ . This effect is called *geometric attenuation*. Note that this is the case in a purely elastic, nondissipative medium. The loss of wave amplitude does not correspond to a loss of energy, but it is only caused by the reduction of energy density caused by an increase in the illuminated volume. Total energy is preserved:

$$E^{\text{total}} = \int \Phi(\mathbf{r}, t) dV = \Pi \cdot t \quad \text{for } t \geq 0 \quad (4.225)$$

if the point source was switched on at  $t = 0$ .

Note that geometric attenuation only occurs for waves propagating outward from a spatially restricted source. For plane waves, which are modeled to originate from an infinite plane, no such effect is observed since the volume that is illuminated by a certain amount of energy does not increase over time. In a dissipative medium, geometric attenuation and dissipative damping coexist.

## 4.12 Shear Wave Scattering from Interfaces and Inclusions

*This section was coauthored by Heiko Tzschätzsch from the Department of Radiology, Charité – Universitätsmedizin Berlin, Germany.*

Wave scattering occurs when an elastic wave hits a surface at which the elastic properties change discontinuously. It is a phenomenon that looks very different on different length scales. A natural length scale is defined by the *mean free path length*. This is the average distance that a wave can travel before it is scattered by a material inhomogeneity. If the mean free path length is much larger than the size of the object through which the wave travels, waves are highly unlikely to be scattered and traverse the object mostly unhindered. Conversely, if the mean free path length is significantly shorter than the object size, incident waves undergo multiple scattering events before leaving the object. In this case, each scattered wave travels in a different direction, and phase coherence between waves scattered at different positions is lost. The superposition principle leads to spatially dependent *speckle patterns* of the wave intensity. In the macroscopic image, only the resultant intensity distribution is observed.<sup>27</sup> As it becomes impossible

<sup>26</sup> Kinetic energy is proportional to  $\dot{\mathbf{u}}^2$  rather than  $\mathbf{u}^2$ ; however, a wave has the form  $\mathbf{u}_0 \cdot f(\mathbf{r}, t)$ , so that  $\mathbf{u}^2 \propto \dot{\mathbf{u}}^2$ .

<sup>27</sup> This phenomenon is the contrast-generating mechanism in conventional medical ultrasound imaging.

to observe individual waves in a strongly scattering environment, the wave equation cannot be applied to describe the observations. Instead, the dynamics of wave intensity is characterized by a diffusion-type differential equation (see Section 4.12.3).

On the microscopic scale, the interaction between a single wave and a single scatterer, such as an inclusion, is analyzed. Since, in general, an elastic medium supports both shear (S) and pressure (P) waves, a shear wave can also yield a scattered pressure wave and vice versa. This phenomenon is called *mode conversion*. If the surface of the elastic discontinuity, henceforth called *interface*, is a plane, one usually decomposes the shear wave into a wave whose vector of polarization lies within the interface and a shear wave whose vector of polarization meets with the interface at an angle. The first type is called shear horizontal (SH) wave, while the other is called shear vertical (SV) wave. An SH wave produces only scattered SH waves, while an SV wave produces scattered SV and P waves. The wave equation is still valid for these individual wave components, and certain kinds of continuity conditions have to be considered at the interface.

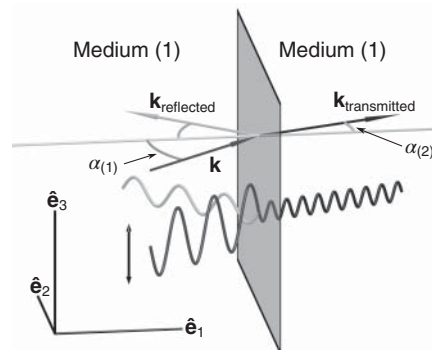
If all scatter processes are considered elastic, that is, without loss of energy, scattering does not affect the frequency of the waves. However, due to geometric effects and variations in elastic material properties, the wavelengths of incident, scattered and transmitted waves can differ.

It is customary to distinguish between *welded* and *nonwelded* interfaces. Welded interfaces are characterized by the condition that displacement and traction across the interfaces are continuous. For a nonwelded interface, on the other hand, only traction across the interface is continuous, whereas displacement is allowed to be discontinuous. The discontinuity in displacement can be interpreted as slip. If the degree of discontinuity is proportional to the traction across the interface, then this scenario is called *linear slip*.

#### 4.12.1 Plane Interfaces

In this section, we will take a closer look at the behavior of a plane wave incident on a plane interface between two different media, designated (1) and (2). The situation is illustrated in Figure 4.12. We choose Cartesian coordinates such that the interface coincides with the  $\hat{e}_2\hat{e}_3$ -plane at  $r_1 = 0$ . The wave travels in the positive  $\hat{e}_1$ -direction (but not necessarily parallel to the  $\hat{e}_1$ -axis), hitting the interface at an angle  $\alpha_{(1)}$  between its wave

**Figure 4.12** Illustration of reflection and transmission of an incident wave with wave vector  $\mathbf{k}$  at an interface between two different media. Medium (2) is softer than medium (1), therefore the wavelength of the transmitted wave is shorter than the wavelength of the incident and reflected waves. The amplitudes of the incident, transmitted, and reflected waves are such that the conservation of energy is fulfilled and that continuity of the displacement at the interface according to Eq. (4.229) is maintained.



vector  $\mathbf{k}$  and the  $\hat{\mathbf{e}}_1$ -axis. The wave vector is assumed to lie in the  $\hat{\mathbf{e}}_1\hat{\mathbf{e}}_2$ -plane,<sup>28</sup> while the polarization vector (black double-ended arrow) points in the  $\hat{\mathbf{e}}_3$ -direction, that is, parallel to the interface. Thereby the elastic wave is characterized as an SH wave. Scattering will change the wave vector  $\mathbf{k}$  for the reflected and transmitted waves. However, the horizontal component  $k_2$  of the wave vector is preserved. This parameter is the same for the incident, transmitted, and reflected waves, whereas all other components of  $\mathbf{k}$  are subject to change.<sup>29</sup>

We designate the incident, reflected, and transmitted waves by  $\mathbf{u}_i$ ,  $\mathbf{u}_r$ , and  $\mathbf{u}_t$ , respectively. They can be expressed as

$$\begin{aligned}\mathbf{u}_i &= \exp \left[ i\omega \left( \frac{k_2}{\omega} r_2 + \frac{\cos \alpha_{(1)}}{c_{(1)}} r_1 - t \right) \right] \hat{\mathbf{e}}_3, \\ \mathbf{u}_r &= R_A \cdot \exp \left[ i\omega \left( \frac{k_2}{\omega} r_2 - \frac{\cos \alpha_{(1)}}{c_{(1)}} r_1 - t \right) \right] \hat{\mathbf{e}}_3, \\ \mathbf{u}_t &= T_A \cdot \exp \left[ i\omega \left( \frac{k_2}{\omega} r_2 + \frac{\cos \alpha_{(2)}}{c_{(2)}} r_1 - t \right) \right] \hat{\mathbf{e}}_3,\end{aligned}\quad (4.226)$$

where  $c_{(1)}$  and  $c_{(2)}$  are the shear wave speeds in the left and right compartments,  $\alpha_{(2)}$  is the angle between the transmitted wave vector and the  $\hat{\mathbf{e}}_1$ -axis and  $\hat{\mathbf{e}}_3$  denotes the Cartesian unit vector in the corresponding direction. The reflection and transmission coefficients  $R_A$  and  $T_A$  are calculated by imposing boundary conditions at the elastic interface. The subscript “A” refers to “amplitude,” to distinguish the coefficients from similar coefficients, which will be calculated for energy flow later on. Since all three waves are polarized along the  $\hat{\mathbf{e}}_3$ -axis, we only need to consider that component of the displacement field and will henceforth drop the index 3. We will use the indices (1) and (2) to refer to quantities measured in the left and right half spaces of Figure 4.12, respectively. The displacements on either side of the boundary thus read

$$u^{(1)}\hat{\mathbf{e}}_3 = \mathbf{u}_i + \mathbf{u}_r \quad (4.227)$$

$$\text{and } u^{(2)}\hat{\mathbf{e}}_3 = \mathbf{u}_t, \quad (4.228)$$

and the boundary conditions at  $x_1 = 0$ , defining a linear slip interface, require

$$u^{(2)} - u^{(1)} = \xi \tau_{13}^{(1)} = \xi \tau_{13}^{(2)} \quad \text{and} \quad \tau_{13}^{(2)} - \tau_{13}^{(1)} = 0, \quad (4.229)$$

where  $\xi$  is the specific compliance of the interface and

$$\tau_{13}^{(i)} = \rho_{(i)} c_{(i)}^2 \frac{\partial u^{(i)}}{\partial x_1} \quad \text{for } i = 1, 2. \quad (4.230)$$

The notation used in Eq. (4.230) indicates that the traction in either compartment can be chosen to evaluate the right-hand side of the first equation in Eq. (4.229). Inserting

<sup>28</sup> The coordinate system can always be rotated to fulfill these assumptions.

<sup>29</sup> Imagine a billiard ball that bounces off the cushion on one side of the table. The velocity component parallel to the cushion will be preserved, while the normal component is reflected and possibly decreased due to inelastic effects.

Eq. (4.226) into Eq. (4.229) yields for  $R_A$  and  $T_A$ :

$$\begin{aligned} R_A &= \frac{\rho_{(1)}c_{(1)} \cos \alpha_{(1)} - \rho_{(2)}c_{(2)} \cos \alpha_{(2)} - \Delta}{\rho_{(1)}c_{(1)} \cos \alpha_{(1)} + \rho_{(2)}c_{(2)} \cos \alpha_{(2)} - \Delta}, \\ T_A &= \frac{2\rho_{(1)}c_{(1)} \cos \alpha_{(1)}}{\rho_{(1)}c_{(1)} \cos \alpha_{(1)} + \rho_{(2)}c_{(2)} \cos \alpha_{(2)} - \Delta}, \end{aligned} \quad (4.231)$$

where

$$\Delta = i\xi\omega\rho_{(1)}\rho_{(2)}c_{(1)}c_{(2)} \cos \alpha_{(1)} \cos \alpha_{(2)}.$$

If we assume equal densities,  $\rho_{(1)} = \rho_{(2)} = \rho$ , the scenario can be described by Snell's law

$$\frac{\sin \alpha_{(1)}}{\sin \alpha_{(2)}} = \frac{c_{(1)}}{c_{(2)}}. \quad (4.232)$$

The formulas for  $R_A$  and  $T_A$  thus read

$$R_A = \frac{c_{(1)} \cos \alpha_{(1)} - c_{(2)} \cos \alpha_{(2)} - \Delta/\rho}{c_{(1)} \cos \alpha_{(1)} + c_{(2)} \cos \alpha_{(2)} - \Delta/\rho} \quad (4.233)$$

$$T_A = \frac{2c_{(1)} \cos \alpha_{(1)}}{c_{(1)} \cos \alpha_{(1)} + c_{(2)} \cos \alpha_{(2)} - \Delta/\rho} \quad (4.234)$$

$$\text{with } \Delta = i\xi\omega\rho^2c_{(1)}c_{(2)} \cos \alpha_{(1)} \cos \alpha_{(2)}. \quad (4.235)$$

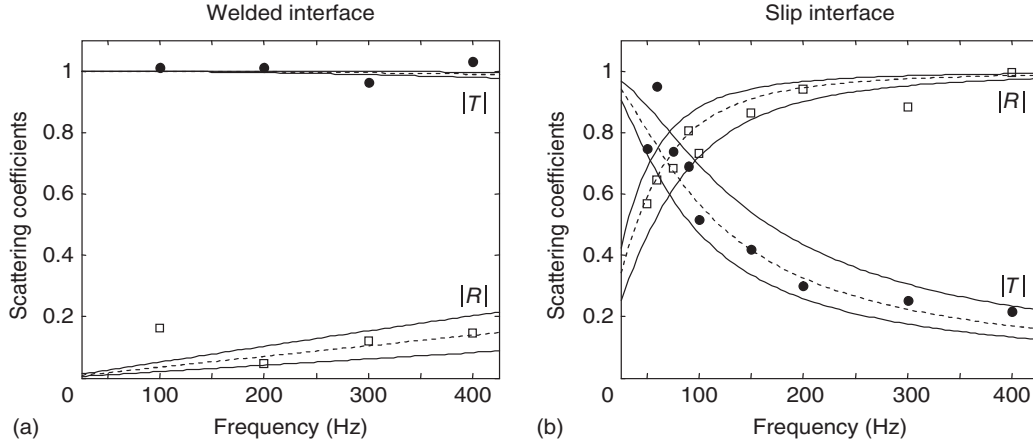
Even for the purely elastic case, the frequency dependence of  $\Delta$  introduces frequency dependence of the transmission and reflection coefficients. In the simplest case, two pieces of the same material,  $\rho_{(1)} = \rho_{(2)} = \rho$  and  $c_{(1)} = c_{(2)} = c$ , are in contact along a surface with specific compliance  $\xi$ . For an incident wave propagating perpendicular to the surface ( $\alpha_{(1)} = 0$  and  $\alpha_{(2)} = 0$ ), we obtain

$$R_A = -\frac{i\xi\omega\rho c}{2 - i\xi\omega\rho c} \quad (4.236)$$

$$T_A = \frac{2}{2 - i\xi\omega\rho c}. \quad (4.237)$$

The plot of  $R_A$  and  $T_A$  versus frequency, as shown in Figure 4.13, illustrates that transmission decreases at higher frequencies. As a consequence, cranial ultrasound suffers from the fact that low wave amplitudes are achievable in the brain, since the high-slip interface between the brain and the skull reflects most of the ultrasound energy in the megahertz frequency range.

Specific compliance  $\xi$  was introduced as a phenomenological parameter quantifying the degree of "weldedness" between two elastic compartments. A three-layer model can provide more physical insight. In such a model, a layer with thickness  $d$  and wave speed  $\bar{c}$  is sandwiched between the two compartments. Assume that the two outer compartments have the same mechanical properties ( $c_{(1)} = c_{(2)} = c$ ). The reflection and transmission coefficients for an incident wave with a wave vector orthogonal to the middle



**Figure 4.13** Plot of transmission and reflection coefficients for a welded (a) and slip interface (b). The points correspond to measurements performed using MRE on two blocks made of the same agarose gel, either with a direct contact interface, or with a layer of a more liquid gel as a lubricant to allow slip. The dashed lines represent least-squares fits of Eqs. (4.236) and (4.237), respectively, while the solid lines indicate the margins of error. (Papazoglou 2007 [51]. Reproduced with permission of Institute of Physics Publishing.)

layer ( $\alpha_{(1)} = 0$ ) then read

$$R_A = \frac{(\bar{c}^2 - c^2) \sin(\omega d / \bar{c})}{2i\bar{c}c \cos(\omega d / \bar{c}) + (\bar{c}^2 + c^2) \sin(\omega d / \bar{c})} \quad \text{and}$$

$$T_A = \frac{2i\bar{c}c}{2i\bar{c}c \cos(\omega d / \bar{c}) + (\bar{c}^2 + c^2) \sin(\omega d / \bar{c})}. \quad (4.238)$$

In the limit of vanishing layer thickness,  $d \rightarrow 0$  and  $\bar{c} \ll c$ , Eq. (4.238) reduces to Eq. (4.231) with  $\alpha_{(1)} = \alpha_{(2)} = 0$  and

$$\xi = \frac{d}{\rho \bar{c}}. \quad (4.239)$$

Viscosity  $\eta$  can be incorporated into this model by replacing real-valued phase speed  $\bar{c}$  with its viscoelastic equivalent according to Eq. (4.155). For a Voigt model (see Section 4.8.3) with shear modulus  $\mu$  and viscosity  $\eta$ , we obtain

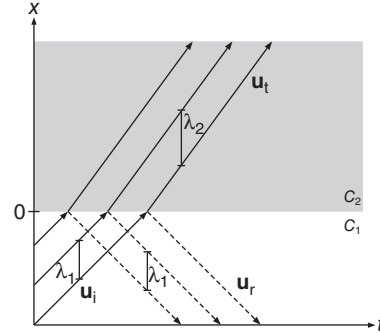
$$\bar{c}(\omega) = \sqrt{\frac{2(\mu^2 + \omega^2 \eta^2)}{\rho (\mu + \sqrt{\mu^2 + \omega^2 \eta^2})}}. \quad (4.240)$$

#### 4.12.2 Spatial and Temporal Interfaces

The discussion thus far has focused on spatial interfaces between media with different mechanical properties, as illustrated in Figure 4.14. However, the same formalism can be used to analyze wave effects at temporal interfaces, when the properties of a single homogeneous medium change instantaneously, for example, in myocardial muscle, which periodically alternates between relaxation and contraction (see Chapter 13).



**Figure 4.14** Example of a spatial interface between two media with wave speeds  $c_1$  (white) and  $c_2$  (gray). The wave propagates along the  $x$ -direction and is refracted at  $x = 0$ . The slope  $\frac{\Delta x}{\Delta t}$  corresponds to the wave speed.



Rather than looking at wave amplitudes before and after the refraction process, we will conduct the following analysis based on energy flux [50]. We introduced energy flux in Eq. (4.205) as

$$P_j = - \sum_{i=1}^3 \sigma_{ij} \dot{u}_i. \quad (4.241)$$

In addition to the previously introduced amplitude-related transmission and reflection coefficients,  $T_A$  and  $R_A$ , we can now introduce similar quantities that relate to the transmitted and reflected portions of the energy flux:

$$T_E \equiv \frac{|\overline{\mathbf{P}_t}|}{|\overline{\mathbf{P}_i}|} \quad (4.242)$$

$$R_E \equiv \frac{|\overline{\mathbf{P}_r}|}{|\overline{\mathbf{P}_i}|}. \quad (4.243)$$

The subscripts  $i$ ,  $t$ , and  $r$  again refer to the incident, transmitted, and reflected components of the wave. Because of the conservation of energy, the relation  $|\mathbf{P}_i| = |\mathbf{P}_t| + |\mathbf{P}_r|$  requires that  $T_E + R_E = 1$ .

In the case of perpendicular incidence and a slip-less interface (see Figure 4.14), as prescribed by the boundary conditions (Eqs. (4.227)–(4.230)), we obtain

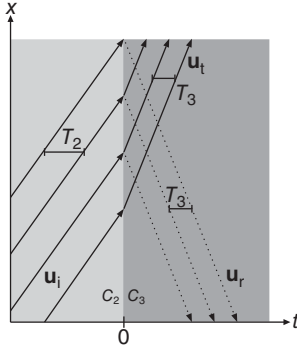
$$T_E = \frac{4\rho_1 c_1 \rho_2 c_2}{(\rho_1 c_1 + \rho_2 c_2)^2} \quad (4.244)$$

$$\text{and } R_E = \left( \frac{\rho_1 c_1 - \rho_2 c_2}{\rho_1 c_1 + \rho_2 c_2} \right)^2. \quad (4.245)$$

Now we analyze the effect of an instantaneous change in elastic material properties on a wave propagating through a homogeneous medium. For example, the medium could be the cardiac muscle undergoing contraction (systole) and relaxation (diastole) cycles. The change occurs at  $t = 0$ , as illustrated in Figure 4.15. The governing boundary conditions are comparable to those at a welded spatial interface:

$$\mathbf{u}_i(\mathbf{r}, 0) = \mathbf{u}_t(\mathbf{r}, 0) + \mathbf{u}_r(\mathbf{r}, 0) \quad (4.246)$$

$$\dot{\mathbf{u}}_i(\mathbf{r}, 0) = \dot{\mathbf{u}}_t(\mathbf{r}, 0) + \dot{\mathbf{u}}_r(\mathbf{r}, 0). \quad (4.247)$$



**Figure 4.15** Example of a temporal interface. The wave propagates in the  $x$ -direction. At  $t = 0$ , the properties of the medium change instantaneously, and the wave speed increases from  $c_2$  to  $c_3$ , causing a shortening of the cycle period,  $T$  (thus increasing the frequency), of both the reflected and the transmitted waves. The slope  $\frac{\Delta x}{\Delta t}$  represents wave speed.

The second condition is a formulation of the conservation of linear momentum. The sudden change in elastic modulus does not affect the instantaneous displacement pattern. Hence, the wavelength remains constant, whereas wave speed  $c = \sqrt{\frac{\mu}{\rho}}$  changes. Therefore, according to  $c = \lambda \cdot f$ , the frequency has to change. This is equivalent to tuning a guitar by adjusting the tension of the string while the string is oscillating, thus modulating the pitch instantaneously.

The above boundary conditions translate into the following amplitude ratios:

$$T_A = \frac{A_t}{A_i} = \frac{1}{2} \left( 1 + \frac{c_2}{c_3} \right) \quad (4.248)$$

$$R_A = \frac{A_r}{A_i} = \frac{1}{2} \left( 1 - \frac{c_2}{c_3} \right). \quad (4.249)$$

These equations indicate that, in any case, there will always be both a transmitted wave (which continues to propagate in the direction of the incident wave) and a reflected wave that propagates in the opposite direction.

For the energy-related transmission and reflection coefficients, we obtain

$$T_E = \frac{1}{4} \frac{c_3}{c_2} \left( \frac{c_3}{c_2} + 1 \right)^2 \quad (4.250)$$

$$R_E = \frac{1}{4} \frac{c_3}{c_2} \left( \frac{c_3}{c_2} - 1 \right)^2, \quad (4.251)$$

and thus for their sum

$$T_E + R_E = \frac{1}{2} \frac{c_3}{c_2} \left( \left( \frac{c_3}{c_2} \right)^2 + 1 \right). \quad (4.252)$$

Obviously, this expression cannot be equal to unity if  $c_2 \neq c_3$ . If the material stiffens ( $c_3 > c_2$ ), the energy of the wave after the transition is larger than before ( $T_E + R_E > 1$ ). Since the instantaneous displacement is not affected by the sudden change in elastic modulus, the potential energy associated with the deformation rises in that case. Increasing the elastic modulus thus requires energy in order to satisfy the conservation of energy. Conversely, after the transition, a decrease in elasticity causes the waves to have less energy than before ( $T_E + R_E < 1$ ), so that this process releases energy. Consequently, in contrast to spatial interfaces, energy flux is not constant in the case of temporal interfaces. This is a clear limitation of wave amplitude-based cardiac elastography.

In the presence of both temporal and spatial interfaces (as in the beating heart muscle), both temporal and spatial reflections occur and the resulting wave field will be a superposition of spatially and temporally scattered waves. Therefore, cardiac elastography has focused on time intervals around systole and diastole, during which the shear modulus is approximately constant, thus taking temporal variations out of the equation.

**4.12.3 Wave Diffusion**

In this section, we will analyze waves and diffusion on a one-dimensional grid with node spacing  $\Delta x$  and discrete time steps  $\Delta t$ , based on the discussion presented in [52]. This will illustrate similarities and differences between the apparently unrelated phenomena of waves and diffusion. The latter becomes relevant in strongly scattering media, where the mode of energy transport changes from linear propagation to a diffusive regime.

We denote by  $P(x_j, t_i)$  the probability of finding a wave<sup>30</sup> or a particle at grid node  $x_j$  at time point  $t_i$ . For an unattenuated propagating wave, we assume that the wave propagates in the direction of increasing  $x$ , and that the time steps are chosen such that a time step corresponds to the time the wave needs to travel from one grid point to the next. Hence, we will observe a wave at  $(x_j, t_i)$  only if it was seen at the left neighboring node at time  $t_{i-1}$ :

$$P(x_j, t_i) = P(x_{j-1}, t_{i-1}). \tag{4.253}$$

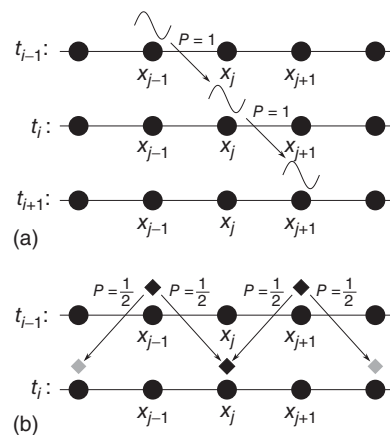
This is shown graphically in Figure 4.16a. Conversely, if we know that the wave is at  $(x_j, t_i)$ , we will find it at  $(x_{j+1}, t_{i+1})$  with probability

$$P(x_j, t_i) = P(x_{j+1}, t_{i+1}). \tag{4.254}$$

Adding Eqs. (4.253) and (4.254) and dividing the result by 2 yields

$$P(x_j, t_i) = \frac{1}{2}P(x_{j-1}, t_{i-1}) + \frac{1}{2}P(x_{j+1}, t_{i+1}). \tag{4.255}$$

**Figure 4.16** Illustration of discrete waves (a) and random walk (b). If the wave is at  $(x_{j-1}, t_{i-1})$ , then the probabilities  $P(x_j, t_i)$  and  $P(x_{j+1}, t_{i+1})$  are all equal to 1. For the random walk, we show all possibilities that lead to the particle (indicated by the diamond) being found at  $(x_j, t_i)$ .



<sup>30</sup> Since waves are extended rather than localized phenomena, “finding a wave” really means finding a specific wave phase, e.g., the peak (or maximum), at a given time and position.

This simple equation reveals an important quality of unattenuated plane waves : we can mirror space and time simultaneously, that is,

$$t_{i-1} \leftrightarrow t_{i+1} \quad \text{and} \quad x_{j-1} \leftrightarrow x_{j+1} \quad (4.256)$$

without changing Eq. (4.255). In other words, under time reversal, a propagating wave looks exactly same as the original wave propagating in the opposite direction [53]. From thermodynamics, we know that processes which can run forward and backward are isentropic; a wave traveling through a nondissipative medium therefore does not affect the entropy of the medium.

We will now apply the same formalism to a diffusive process. The mechanism underlying diffusion is the *random walk*. In the one-dimensional grid with discrete time, a random walk of a single particle can be described like this: at each point  $(x_j, t_i)$ , the particle transits with probability  $p_l = \frac{1}{2}$  to the left neighbor  $x_{j-1}$ , and with the same probability  $p_r = \frac{1}{2}$  to the right neighbor  $x_{j+1}$ . It arrives at one of the two neighbors  $x_{j\pm 1}$  at the next time step  $t_{i+1}$ , and the process begins anew.

Since the rules of the random walk do not allow a particle to stay at a given position, the probability of finding it at  $P(x_j, t_i)$  is determined by the probabilities of finding it at  $t_{i-1}$  at one of the neighboring positions  $x_{j\pm 1}$ , multiplied by  $\frac{1}{2}$ , since the particle could also move away toward  $x_{j\pm 2}$  as shown in Figure 4.16b. Hence,

$$P(x_j, t_i) = \frac{1}{2}P(x_{j-1}, t_{i-1}) + \frac{1}{2}P(x_{j+1}, t_{i-1}). \quad (4.257)$$

By comparing Eqs. (4.255) and (4.257), we can see that the only difference between waves and diffusion is the direction of the time step in the last term. However, this tiny difference has a huge physical implication: if we perform the time-and-space reversal defined by Eq. (4.254) on Eq. (4.257), we obtain

$$P(x_j, t_i) = \frac{1}{2}P(x_{j+1}, t_{i+1}) + \frac{1}{2}P(x_{j-1}, t_{i+1}), \quad (4.258)$$

which is clearly not the same as the original equation. Thus, a diffusion process played backward would not resemble to the original diffusion process. Diffusion is usually defined with respect to an initial distribution of the concentration  $C(x)$  of a substance. Each particle contributing to that concentration performs an independent random walk, and, over time, the concentration always evolves toward a uniform distribution,  $C(x, t \rightarrow \infty) = \text{const}$ , with equal concentration everywhere. From thermodynamics, we know that, of all possible concentration distributions, the uniform distribution has the highest entropy. A diffusion process running backward in time would therefore entail moving from the maximum-entropy state to a lower-entropy state. According to the second law of thermodynamics, this is impossible.

We can derive the wave equation and diffusion equation from these simple principles. For the wave equation, we can perform two index substitutions on Eq. (4.253):

$$(t_i \rightarrow t_{i-1}) \implies P(x_j, t_{i-1}) = P(x_{j+1}, t_i) \quad (4.259)$$

$$(x_j \rightarrow x_{j-1}) \implies P(x_j, t_{i+1}) = P(x_{j-1}, t_i). \quad (4.260)$$

Adding the two equations and subtracting  $2 P(x_j, t_i)$  on both sides yields

$$\begin{aligned} P(x_j, t_{i+1}) - 2 P(x_j, t_i) + P(x_j, t_{i-1}) &= P(x_{j+1}, t_i) \\ &\quad - 2 P(x_j, t_i) + P(x_{j-1}, t_i). \end{aligned} \quad (4.261)$$

By comparing this equation with the discrete first- and second-order derivative operators, Eqs. (8.23b) and (8.27), which we will discuss later, we can see that we have a second-order temporal derivative on the left-hand side and a second-order spatial derivative on the right-hand side:

$$\Delta t^2 \frac{\partial^2 P(x, t)}{\partial t^2} = \Delta x^2 \frac{\partial^2 P(x, t)}{\partial x^2}. \quad (4.262)$$

As stated earlier in this section, time step  $\Delta t$  and node spacing  $\Delta x$  are correlated such that  $\Delta t$  is the time that the wave needs to propagate from one node to the next. Hence, the wave velocity is given by  $c = \frac{\Delta x}{\Delta t}$ . We therefore arrive at the general form of the wave equation

$$\frac{\partial^2 P}{\partial x^2} = \frac{1}{c^2} \frac{\partial^2 P}{\partial t^2}. \quad (4.263)$$

In order to derive the diffusion equation, we subtract  $P(x_j, t_{i-1})$  from both sides of Eq. (4.257):

$$P(x_j, t_i) - P(x_j, t_{i-1}) = \frac{1}{2}P(x_{j-1}, t_{i-1}) - P(x_j, t_{i-1}) + \frac{1}{2}P(x_{j+1}, t_{i-1}). \quad (4.264)$$

In analogy to Eqs. (8.23b) and (8.27), we can see that the right-hand side is a discrete forward difference (with  $\Delta t = 1$ ) as an approximation to the first temporal derivative, whereas the left-hand side is again a second-order spatial derivative (with  $\Delta x = 1$ ). Therefore, in the limit  $\Delta x \rightarrow 0$ ,  $\Delta t \rightarrow 0$ , we can write

$$\Delta t \frac{\partial P(x, t)}{\partial t} = \frac{\Delta x^2}{2} \frac{\partial^2 P(x, t)}{\partial x^2} \quad (4.265)$$

$$\frac{\partial P(x, t)}{\partial t} = D \frac{\partial^2 P(x, t)}{\partial x^2}. \quad (4.266)$$

The term  $\frac{\Delta x^2}{2 \Delta t}$  is called *diffusion coefficient* and quantifies how easily a particle can move through the surrounding medium. One notable difference between waves and diffusion is the scaling behavior: if we scale time and space homogeneously with a positive parameter  $\lambda$ , such that  $\Delta t \rightarrow \lambda \cdot \Delta t$  and  $\Delta x \rightarrow \lambda \cdot \Delta x$ , we can see that the wave equation is invariant, since  $\lambda$  cancels out. However, in the case of the diffusion equation, the diffusion coefficient  $D$  will depend explicitly on the scaling parameter:  $D \rightarrow \lambda D$ . In other words, the propagation velocity of a wave is independent of the length scale on which the wave is observed, and the value of  $c$  is also valid in the infinitesimal limit  $c = \frac{\Delta x}{\Delta t}$ . For diffusion, on the other hand, the concept of an instantaneous particle velocity is not applicable. We only observe the particle at discrete time points at discrete positions, and we can conclude that the *average* velocity of the particle during that time must have been  $\frac{\Delta x}{\Delta t}$ . The dependence of  $D$  on the scaling parameter  $\lambda$  tells us that the average particle velocity for a given diffusion coefficient  $D$  depends on the observation scale. Conversely, maintaining the same particle velocity at different length scales would require adapting the diffusion coefficient. This can be understood as a manifestation of the stochastic nature of diffusion: if a particle moves to the right with a probability of  $\frac{1}{2}$ , the probability of two consecutive steps to the right is  $\frac{1}{2} \cdot \frac{1}{2} = \frac{1}{4}$ . Hence, if we average

the velocity over two time steps rather than one, we have the following situation:

$$\begin{aligned}
 (\text{LL}) \quad & \rightarrow \quad P(x_{j-2}, t_{i+2}) &= 1 \cdot \frac{1}{2} \cdot \frac{1}{2} = \frac{1}{4} & \quad d = 2\Delta x \\
 (\text{LR,RL}) \quad & \rightarrow \quad P(x_j, t_{i+2}) &= 2 \cdot \frac{1}{2} \cdot \frac{1}{2} = \frac{1}{2} & \quad d = 0 \\
 (\text{RR}) \quad & \rightarrow \quad P(x_{j+2}, t_{i+2}) &= 1 \cdot \frac{1}{2} \cdot \frac{1}{2} = \frac{1}{4} & \quad d = 2\Delta x.
 \end{aligned}$$

“L” and “R” indicate a step to the left or to the right, and  $d$  is the distance by which the particle is removed from the starting point after two steps. The average distance traveled by a particle during an interval  $2\Delta t$  is therefore

$$\langle d \rangle_{2\Delta t} = \frac{1}{4} \cdot 2\Delta x + \frac{1}{2} \cdot 0 + \frac{1}{4} \cdot 2\Delta x = \Delta x, \quad (4.267)$$

and the average velocity is  $\langle v \rangle_{2\Delta t} = \frac{\Delta x}{2\Delta t}$ , which is only half of the value  $\langle v \rangle_{\Delta t} = \frac{\Delta x}{\Delta t}$  obtained for a single time step  $\Delta t$ . This explains why the diffusion coefficient, as a marker of particle mobility, has explicit scale dependence. In any real-world situation, grid spacing is determined by the microscopic structure of the medium (e.g., by the mean free path length between particle collisions), and this spacing determines the diffusion coefficient.

#### Scaling property of the wave equation

In contrast to diffusion, the wave velocity is independent of the spatial and temporal scale of the network:  $\langle c \rangle_{\Delta t} = \langle c \rangle_{2\Delta t}$  and  $\langle c \rangle_{\Delta x} = \langle c \rangle_{2\Delta x}$ . This property translates to the viscoelastic parameters that determine the wave speed. Therefore, shear waves can serve as a probe even for scale-invariant structures, such as the hierarchical geometry of biological tissue. In other words, structures occurring on a given length scale do not only affect the wave speed (and hence elasticity) on that length scale, but also on all other scales. The shear modulus is therefore sensitive to structures that are much smaller than the wavelengths of the waves from which it was calculated.

From a different perspective, we can interpret the diffusion equation (4.266) and the wave equation (4.263) as two special cases of the more general partial differential equation

$$\frac{\partial^2 \chi}{\partial r^2} - b \cdot \frac{\partial^\alpha \chi}{\partial t^\alpha} = 0 \quad (4.268)$$

with  $\left(\alpha = 1, b = \frac{1}{D}\right)$  for diffusion and  $\left(\alpha = 2, b = \frac{1}{c^2}\right)$  for waves. This raises the question whether there exists a physically meaningful connection between these apparently unrelated phenomena. In fact, with the methods of *fractional calculus*, the above equation can be generalized to noninteger values of  $\alpha$ . For  $1 < \alpha < 2$ , we introduce the domain of *diffusive waves*, which describe phenomena in between classical waves and diffusive behavior.

A good overview of fractional calculus and its application to viscoelasticity can be found in [44]. The mathematical framework of fractional calculus is beyond the scope of this book, and we will therefore only discuss the results in a qualitative manner without rigorous mathematical treatment. Fractional derivative and integration operators

generalize the respective operations in a similar way as exponentiation with noninteger arguments does for algebraic expressions. For example, in analogy to

$$x^{\frac{1}{2}} \cdot x^{\frac{1}{2}} = x^{\frac{1}{2} + \frac{1}{2}} = x^1 = x, \quad (4.269)$$

we find

$$\frac{d^{\frac{1}{2}}}{dt^{\frac{1}{2}}} \frac{d^{\frac{1}{2}}}{dt^{\frac{1}{2}}} \chi = \frac{d^{\frac{1}{2} + \frac{1}{2}}}{dt^{\frac{1}{2} + \frac{1}{2}}} \chi = \frac{d^1}{dt^1} \chi = \frac{d}{dt} \chi, \quad (4.270)$$

so that  $\frac{d^{\frac{1}{2}}}{dt^{\frac{1}{2}}}$  can be characterized as the operator that has to be applied twice to obtain the first temporal derivative of its operand. Analytical expressions for differential and integral operators of arbitrary noninteger order  $\alpha$  are given in [44]. However, we will restrict the following discussion to a more intuitive approach based on Green's functions.

#### 4.12.3.1 Green's Function of Waves and Diffusion Phenomena

As discussed earlier (see Section 4.9.5), inhomogeneous differential equations can be solved for arbitrary inhomogeneity terms if Green's function of the related homogeneous differential equation is known. In Section 4.9.5, we explained that Green's function  $G(x, x', t, t')$  describes how an event at one space-time point  $(t', x')$  affects the situation at another point  $(t, x)$ . Since we are dealing with *causal* phenomena, we require that the cause precedes the consequence, so that in the following discussion we will always imply  $t' \leq t$  (and  $t = t'$  implies  $x = x'$  because of finite propagation velocities). In a one-dimensional domain, the wave equation has a Green's function

$$G_{\text{wave}}(x, x', t, t') = \delta((t - t') - |x - x'|/c) \quad (4.271)$$

with wave propagation velocity  $c$ . This implies that for any space-time point  $(t, x)$ , the wave field is fully determined by the sum of all distributions that occurred at other space-time points  $(t', x')$  such that  $t - t' = |x - x'|/c$ . Hence, any excitation is assumed to propagate along a straight line, since otherwise it would not be able to travel the distance  $|x - x'|$  in time  $t - t'$ .

Green's function for the one-dimensional diffusion equation (4.266) is [44]

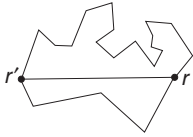
$$G_{\text{diff}}(x, x', t, t') = \frac{1}{\sqrt{4\pi D \cdot (t - t')}} \cdot \exp\left(-\frac{(x - x')^2}{4D \cdot (t - t')}\right). \quad (4.272)$$

By comparing this form with the Gaussian normal distribution with mean  $\mu$  and standard deviation  $\sigma$

$$f(x|\mu, \sigma) = \frac{1}{\sigma\sqrt{2\pi}} \cdot \exp\left(-\frac{(x - \mu)^2}{2\sigma^2}\right) \quad (4.273)$$

we see that the diffusion Green's function has the shape of a bell curve with center  $\mu = x'$  and standard deviation  $\sigma = \sqrt{2D \cdot (t - t')}$ . Because of the causality relation  $t \geq t'$ , the argument under the square root cannot become negative.

The difference between wave propagation and diffusion is therefore that the diffusion Green's function does not impose as strict limits on the spatiotemporal relationship between causes and consequences as the wave Green's function. In other words, wave propagation requires motion along a straight line at wave speed  $c$  between the cause of an event and its consequence elsewhere. For diffusion, the time for the propagation is



**Figure 4.17** Three out of infinitely many possible paths from  $r$  to  $r'$ . Since the path lengths differ, waves emitted at  $r'$  at the same time will arrive at  $r$  with different delays. Therefore, phase coherence between waves is lost, and the resulting intensity at  $r$  cannot be predicted.

not as strictly coupled to the spatial distance between the two points, so that information does not necessarily have to propagate along the shortest path or at a fixed velocity to have an effect.

What happens if the wave no longer travels along a straight line? In the previous sections, we have explained how scattering can change the propagation direction of a wave. In the case of multiple scattering, there are several (actually, infinitely many) paths a wave could take between two points  $r' = (t', x')$  and  $r = (t, x)$ , each with a different length. As scattering has no effect on the wave velocity, the partial waves that travel from  $r'$  to  $r$  have different transit times. Therefore, the strict relationship between the geometric distance of  $r'$  and  $r$  and the travel time has to be loosened to account for all partial waves arriving at  $r$  simultaneously, irrespective of the path they followed starting from  $r'$ . Thus, the  $\delta$ -peak of the original wave Green's function, Eq. (4.271), becomes "smeared," and with an increasing number of scatterers approaches the shape of the diffusion Green's function (4.272). This intermediate regime between the two pure phenomena is called "diffusive waves."

In media with a randomly distributed scatterers, there is no restriction on the lengths of possible paths from  $r'$  to  $r$ . If the scatterer density is sufficiently high, the distribution of path lengths approaches a continuum. As a consequence, the phase of each partial wave arriving at  $r$  becomes arbitrary (depending on the length of its trajectory), and phase coherence between these partial waves is lost (see Figure 4.17). The superposition of all partial waves therefore yields random amplitudes, as we will discuss in the next paragraphs.

#### 4.12.3.2 Amplitudes and Intensities of Diffusive Waves

##### Energy transport of diffusion versus propagating waves

Despite the apparent similarity of the differential equations of propagating waves (Eq. (4.144)) and diffusion (Eq. (4.266)), there are some fundamental differences that need to be pointed out. First, the wave equation prescribes a finite propagation velocity  $c$ ; the wave can travel neither faster nor slower than  $c$ . It is therefore possible to calculate how far an unscattered wave propagates in a given time interval. The diffusion equation, on the other hand, does not make any statement about the velocity of the diffusing particles. The underlying theory of Brownian motion states that the kinetic energy of the particles is distributed according to a Boltzmann statistic, which covers the whole range from zero to infinite velocity. This implies that immediately after the beginning of the diffusion process, the probability of finding diffusing particles at arbitrarily large distances is larger than zero. As the diffusion process continues, the particle cloud spreads out, and the probability of finding particles at large distances increases. In the long-time limit  $t \rightarrow \infty$ , the diffusion Green's function (Eq. (4.272)) converges toward a spatial constant, meaning that the probability of finding a particle at a specific location is the same as finding it everywhere else.



Since classical waves are not discretized phenomena, we cannot speak of the “probability of finding a wave” at a specific location; but we can look at the amplitudes of the waves as a function of the distance from the source. In the case of a point source, a portion of energy that was emitted by the source over an interval  $t_0 \leq t \leq t_1$  is distributed evenly over a spherical shell with inner radius  $R = c \cdot (t - t_0)$  and thickness  $\Delta R = c \cdot (t_1 - t_0)$ . The volume of the shell is  $4\pi R^2 \cdot \Delta R \propto t^2$ . This means that the energy content of the shell spreads across an increasing volume and that the energy density inside the shell decreases as  $\frac{1}{R^2} = \frac{1}{c^2 t^2}$ . Therefore, the wave intensity (see Eq. (4.214)) of an unattenuated point source decreases as the squared distance from the source. This has two implications. First, the energy emitted by a point source is always located in a spherical shell with finite thickness. This is not the case for diffusion, since the concentration tends toward a spatially constant distribution. Second, the wave model is suitable for treating a continuously emitting source. The diffusion model, on the other hand, is based on a fixed amount of a substance that is initially constrained to an infinitely small volume and diffuses from there; it does not allow for a continuously emitting source (in other words, the volume integral over the concentration is a time-independent constant).

An unscattered plane wave of the general form

$$\mathbf{u}(\mathbf{r}, t) = \mathbf{u}_0 \cdot e^{i(\mathbf{k} \cdot \mathbf{r} - \omega t)} \quad (4.274)$$

has the same amplitude  $|\mathbf{u}_0|$  everywhere. We can then calculate the normalized wave intensity  $I$  as

$$I(\mathbf{r}) = \frac{|\mathbf{u}(\mathbf{r})|^2}{\langle |\mathbf{u}(\mathbf{r})|^2 \rangle_S}, \quad (4.275)$$

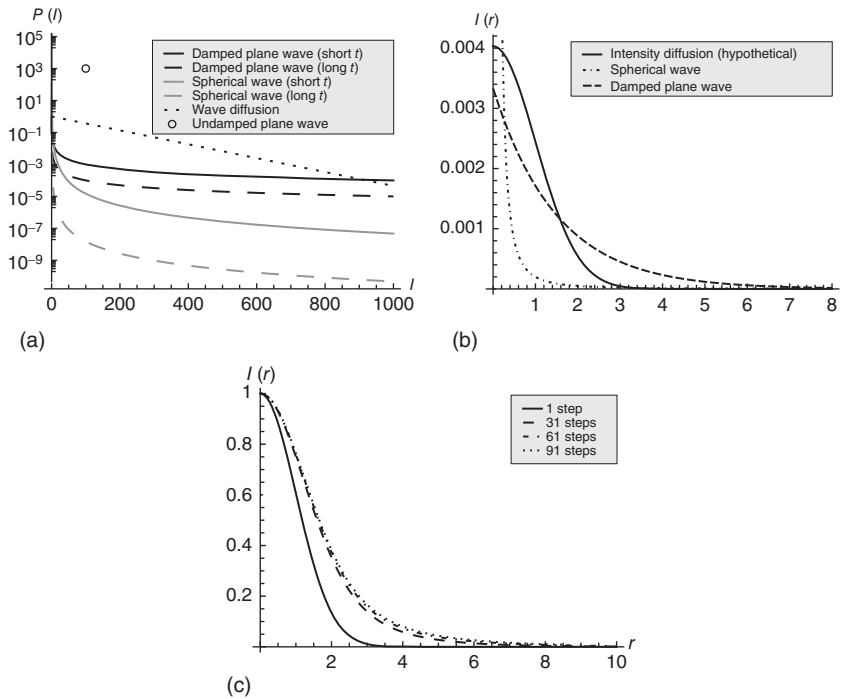
which is the local wave intensity divided by the mean intensity over a region  $S$ . Since the amplitude and hence the intensity is constant, the nominator and denominator yield the same value and therefore  $I(\mathbf{r}) = 1$ .

Alternatively, we can look at the probability of finding a certain value  $I$  of the normalized intensity in a given spot. For the probability distribution in a plane wave, we find

$$P(I) = \begin{cases} 1 & \text{if } I = 1 \\ 0 & \text{else.} \end{cases} \quad (4.276)$$

In a strongly scattering medium, there is a continuum of paths between two points  $r'$  and  $r$ , each with its own phase offset determined by the path length. In practice, it is virtually impossible to calculate the partial waves along all paths and to superimpose them to obtain the resultant field intensity at a given point. Therefore, we will switch from the microscopic view of individual scatter processes to the macroscopic view that only takes into account wave intensities, without paying tribute to the underlying exact scatterer geometry.

The superposition of many (multiply) scattered and unscattered waves becomes incoherent, since the phase of each individual wave depends on the distance it has traveled, which in turn depends on its trajectory. Therefore, local intensity is subject to interference effects, and wave intensity becomes dependent on space. In this scenario, the intensity probability distribution yields a continuum rather than the sharp peak of Eq. (4.276)



**Figure 4.18** Intensity profiles and radial profiles for different real and hypothetical types of wave phenomena. (a) Intensity probabilities for different types of waves. See Table 4.1 for the corresponding formulas. (b) Radial intensity profiles. The diffusive wave scenario does not account for speckle patterns and is therefore unphysical. (c) Hypothetical case of wave diffusion with a single excitation and multiple repeated excitations. The curves are normalized to unity amplitude at the origin to illustrate how repeated excitation makes the curve broader and flatter. This plot results from the application of the diffusion equation to intensity (see Appendix D.3), which is unphysical.

and approaches a decaying exponential function [54] (see Figure 4.18)

$$P(I) \propto e^{-I}. \quad (4.277)$$

Note that this relation is derived assuming interference between scattered waves, which is not included in the classical formulation of diffusion processes. For comparison, the same calculation for classical diffusion is performed in Appendix D.3, and the result is very different from the one above. The main reason for the difference is that interference can lead to local extrema of the amplitude, called “speckles,” which are higher than the amplitude at the source. Because of these speckle patterns, it becomes infeasible to explicitly derive a radial intensity distribution  $I(r)$ . The radial intensities labeled “wave diffusion” in Figure 4.18b correspond to a hypothetical case of intensity diffusion which is further discussed in Appendix D.3, but does not occur as a physical phenomenon, since it would violate conservation of energy. It is only presented here to outline the difference between “classical” diffusion of particles and the diffusion of waves in a strongly scattering environment. In the context of classical diffusion, the diffusing quantity is real-valued (e.g., concentration of a solution), so that interference effects are precluded. The analysis of speckle patterns in strongly scattering media can convey information on the scatterer density [55].

**Table 4.1** Intensity probability functions for different types of waves.

Type	Intensity probability function
Unattenuated spherical wave (3D)	$P(I) = \frac{3}{2} \frac{I^{-5/2}}{c^3(t-t_0)^3}$
Damped plane wave	$P(I) = \frac{L}{2 c(t-t_0)I}$
Diffusive waves	$P(I) \propto e^{-I}$

Derivations and explanations are presented in Appendix D. See Figure 4.18a for plots of the functions.

We now look at the propagation of a wavefront emanating from a plane source. We define the wavefront as the component of the wave that has traveled the largest distance from the source since the time of emission. This implies that at all times the wavefront consists only of nonscattered wave components, since any scattering is a deflection from a straight line of propagation and hence reduces the speed at which the wave moves from the source. In other words, the wave contains only the components of the wave that were transmitted at each single scattering event. We assume that the scatterer density is constant throughout the medium, so that the average time between two scattering events is  $\tau_s$ , and that  $T_A$  and  $R_A$  are identical for each scatterer. Each scatterer only permits a fraction  $T_A$  of the incident wave amplitude to pass and remain part of the wave front; the reflected part does not contribute to the wavefront any more. Therefore, the reduction of wave amplitude per time interval  $\Delta t$  is given by

$$A(t + \tau_s) = A(t) \cdot T_A. \quad (4.278)$$

We also know that, for sufficiently small intervals  $\tau_s$ , we can represent  $A(t + \tau_s)$  by the first order of the Taylor series around  $t$ :

$$A(t + \tau_s) = A(t) + \dot{A}(t) \cdot \tau_s. \quad (4.279)$$

Combining the right-hand sides of these two equations yields

$$A(t) \cdot T_A = A(t) + \dot{A}(t) \cdot \tau_s \quad (4.280)$$

$$\Rightarrow \dot{A}(t) = \frac{T_A - 1}{\tau_s} A(t) \quad (4.281)$$

$$\Rightarrow A(t) = A(0) \cdot \exp(-(1 - T_A)/\tau_s \cdot t). \quad (4.282)$$

The amplitude of the unscattered wavefront therefore decays exponentially with time with a decay constant  $\Lambda = \frac{1-T_A}{\tau_s} \geq 0$ , and, since the propagation velocity is constant, exponentially with the distance from the source. Note that the wave amplitude decreases even in nonabsorbing materials. However, the intensity of the scattered waves is not lost, but concentrated in the area “behind” the wavefront. In this region, superposition of multiply scattered wave occurs, and the phase relation depends on the lengths of the different geometric paths that the interfering partial waves have taken and the times at which they were emitted from the source.

In summary, elastic scattering does not constitute a dissipative process and hence does not cause energy loss. Only the radial distribution of wave energy emanating from a source is modulated compared to the nonscattering case, and energy propagation is slower, as the major portion of the energy lags behind the unscattered wavefront.

## 5

### Poroelasticity

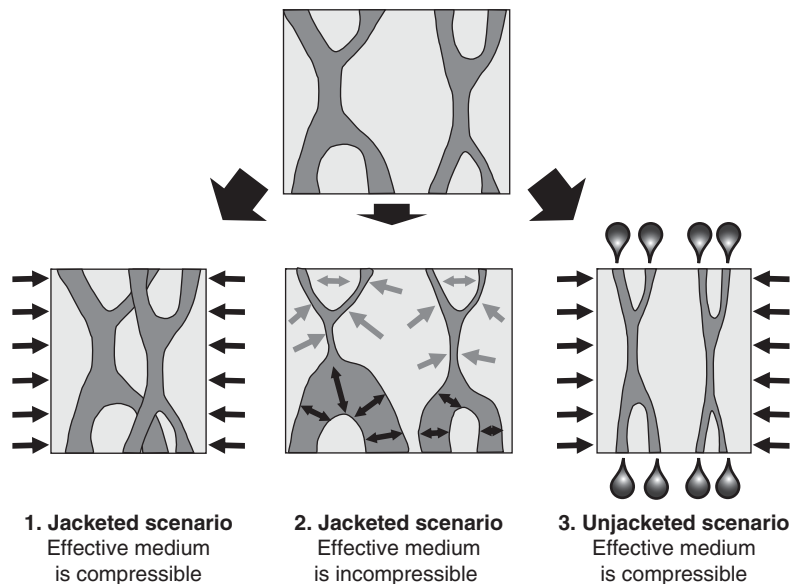
In this chapter, we will discuss the poroelastic tissue model, which contrasts more common monophasic models that were the basis for all previous discussions. We will describe the mathematical framework to characterize and assess poroelasticity with MRE, and demonstrate the implications of the model for wave propagation.

Part of the following theory is original work, which we developed for addressing some fundamental aspects of MR poroelastography. MRE cannot detect waves in different tissue compartments – such as parenchyma, blood, and interstitial water – separately. Instead, MRE integrates the phase signal within a voxel into an “effective medium” motion. The presence of multiple tissue compartments gives rise to multiple wave modes that do not exist in monophasic, isotropic materials. The origin of these wave modes can be explained by extension of Navier’s equation to multiphasic media without consideration of viscosity and fluid flow, as it is addressed by Darcy’s law. Specific attention will be paid to the fact that the coupled equations converge toward the well-known monophasic equation of motion in the limit of a single compartment.

Human tissue typically has a water content of approximately 70–85% [56, 57]. With a compression modulus of 2.2 GPa, water is considered incompressible in most elastography experiments. Consequently, MRE usually makes the assumption that tissue can undergo shear deformation but does not permit compression.

In the 1940s and 1950s, Maurice Biot introduced the theory of poroelasticity, extending previous work by Karl von Terzaghi. Biot’s research was aimed at describing the behavior of fluid-drained soils and rocks under pressure. Initially, he was only interested in the long-term characteristics of soil consolidation under a given stress [58, 59]. Later, Biot extended his theory to the dynamic regime to analyze wave propagation through poroelastic media [60, 61].

Poroelastic behavior arises from the interaction of the two compartments of a biphasic medium, in which a solid but porous matrix is fully permeated by a fluid. The pores form a contiguous and interconnected space, so that fluid motion through the matrix is possible. This model, originally derived for soil, is also applicable to biological tissue, in which vascular trees permeate the solid tissue matrix, constituting a biphasic medium. Another type of poroelastic tissue is found in the lung, where – in a simplistic view – solid tissue is interspersed with air-filled compartments. In any case, the biphasic structure is visible only on the microscale, whereas in the macroscopic view (determined by the voxel size in MRE), only a homogeneous *effective* medium is observed.



**Figure 5.1** Illustration of three scenarios for mechanical testing of a poroelastic material. On top, a tissue volume consisting of fluid space (dark gray) and solid (light gray) is shown. The fluid is assumed incompressible. Applying a pressure can yield different results, depending on the properties of the solid and the interaction between the compartments. In scenario 1, the solid is compressed whereas the fluid volume is preserved, resulting in a compressible effective medium. In scenario 2, one phase can locally expand if the other phase can be pushed out of the way. The total volume is preserved (the effective medium is thus incompressible), and the local distribution of the two phases is temporarily altered. In scenario 3, fluid is allowed to leave the system, thus resulting in a compressible effective material even when both phases are incompressible. The term “jacketed” refers to testing conditions that surround the material with an impermeable jacket that prevents fluid from being squeezed out.

As long as none of the two phases is truly incompressible, one can envision three modes of volumetric deformation (Figure 5.1). In the first mode, the two phases undergo compression and dilatation in synchrony. This means that the bulk density is subject to temporal and spatial variation, just as in the case of a compressible monophasic medium. In the second scenario, both constituents undergo out-of-phase deformation, with one being compressed while the other expands. In that case, the density of one phase increases while that of the other decreases, so that the change in bulk density can be much smaller than that of the individual phases. A third volumetric deformation mode exists even if both constituents are truly incompressible. In that case, a deformation of the matrix (which compresses the pore space, but not the matrix phase itself) can be balanced by an outflow of fluid into an external reservoir. Conversely, if fluid is forced into the medium by an external pressure, the pore space might dilate to accommodate the influx of fluid. This scenario is referred to as “unjacketed condition” in the literature. On a microscopic scale, this means that one phase is locally substituted partially or fully by the other phase. This mechanism requires the existence of an external fluid reservoir. Furthermore, the duration of a compression–dilatation cycle has to be long enough for fluid exchange to take place. This requirement is more likely to be fulfilled in a quasi-static or low-frequency scenario

than in the dynamic range typically probed by MRE. Poroelastic MRE aims to quantify dynamic poroelastic properties that occur on the same timescales as the vibration (tens of milliseconds). In the ultrasonic elastography community, mainly long-term poroelastic effects (on the order of many seconds) are addressed.

While the theory of poroelasticity became popular in the 1950s, it has been used mainly in geophysics as a tool for the analysis of rocks and soil under transient and long-term stresses. The application of a poroelastic model in the context of biological imaging of tissue was suggested by Leiderman et al. [62]. Berry et al. demonstrated poroelastic behavior of a tofu phantom under uniaxial compressive stress by ultrasound elastography [63]. Perrinez et al. demonstrated the feasibility of MR poroelastography in tofu phantoms [64, 65].

In Biot's dynamic framework, there are two constants that establish a coupling between the solid and the fluid. The first parameter, henceforth referred to as the *coupling modulus*  $H$ , characterizes how a stress in one compartment results in a strain of the other compartment, and vice versa. The second parameter, denoted  $\rho_{12}$ , has the dimension of a mass density, but is always negative. It quantifies the energy transfer from one compartment to the other due to friction caused by relative motion. However, it is important to note that this is not a dissipative process, meaning that kinetic energy is exchanged between the phases, but not converted into heat.

The composition of a biphasic material is characterized by the *porosity*  $f$ , which is defined as the fraction of fluid contained in a volume element of the bulk material:

$$f = \frac{V^f}{V}, \quad (5.1)$$

where  $V^f$  is the volume occupied by the fluid in the volume element  $V$ . If we assume that every pore of the matrix is filled with fluid (i.e., there are no air bubbles or "empty space"), the volume fractions of the two phases have to add up to unity, so that the volume fraction of the solid becomes  $1 - f$ . Bulk density is therefore

$$\rho = f \cdot \rho^f + (1 - f) \cdot \rho^s. \quad (5.2)$$

Indices "s" and "f" refer to the quantities associated with the solid and the fluid, respectively.

## 5.1 Navier's Equation for Biphasic Media

In this section, we will derive an analog of Navier's equation for a biphasic medium that will allow us to analyze wave propagation in such a material.

The total stress acting on the medium can be separated into stresses for the individual compartments:

$$\boldsymbol{\sigma} = f \cdot \boldsymbol{\sigma}^f \cdot \mathbb{1} + (1 - f) \cdot \boldsymbol{\sigma}^s. \quad (5.3)$$

The deformation of the solid is described by a  $3 \times 3$  stress tensor, whereas the fluid can be characterized by a single scalar stress value  $\sigma^f$ .

In contrast to the previous (visco)elastic models, a stress in one compartment arises not only from its own deformation but also from the deformation of the other compartment. This results in a set of coupled equations that can be combined into the elasticity

tensor of a biphasic medium:

$$\begin{pmatrix} (1-f)\sigma_{xx}^s \\ (1-f)\sigma_{yy}^s \\ (1-f)\sigma_{zz}^s \\ (1-f)\sigma_{yz}^s \\ (1-f)\sigma_{xz}^s \\ (1-f)\sigma_{xy}^s \\ f\sigma^f \end{pmatrix} = \begin{pmatrix} (1-f)(K^s + \frac{4}{3}\mu^s) & (1-f)(K^s - \frac{2}{3}\mu^s) & (1-f)(K^s - \frac{2}{3}\mu^s) & & & & f(1-f) \cdot H \\ (1-f)(K^s - \frac{2}{3}\mu^s) & (1-f)(K^s + \frac{4}{3}\mu^s) & (1-f)(K^s - \frac{2}{3}\mu^s) & & & & f(1-f) \cdot H \\ (1-f)(K^s - \frac{2}{3}\mu^s) & (1-f)(K^s - \frac{2}{3}\mu^s) & (1-f)(K^s + \frac{4}{3}\mu^s) & & & & f(1-f) \cdot H \\ & & & (1-f)\mu^s & & & \\ & & & & (1-f)\mu^s & & \\ & & & & & (1-f)\mu^s & \\ f(1-f) \cdot H & f(1-f) \cdot H & f(1-f) \cdot H & & & & fK^f \end{pmatrix} \cdot \begin{pmatrix} \epsilon_{xx}^s \\ \epsilon_{yy}^s \\ \epsilon_{zz}^s \\ 2\epsilon_{yz}^s \\ 2\epsilon_{xz}^s \\ 2\epsilon_{xy}^s \\ \theta \end{pmatrix} \quad (5.4)$$

with the volumetric strain of the fluid  $\theta = \epsilon_{xx}^f + \epsilon_{yy}^f + \epsilon_{zz}^f$ . Zero entries are not shown for improved readability. The upper left  $6 \times 6$  matrix is the usual elasticity tensor of an elastic solid, representing both shear and volumetric strains. The only difference is the weighting by the solid volume fraction  $1-f$ . The entry  $fK^f$  in the lower right corner corresponds to fluid stress induced by fluid strain. We assume here that the fluid does not support shear strains so that off-diagonal entries in the fluid strain tensor  $\epsilon^f$  vanish. Finally, the first three entries in the last row and last column represent the coupling between axial strains on the solid and fluid strain, and vice versa, via the coupling modulus  $H$ . The weighting of all entries of the elasticity tensor with either  $f$ ,  $1-f$ , or  $f(1-f)$  ensures that the model reproduces a monophasic medium in the limits  $f = 1$  (pure fluid) and  $f = 0$  (pure solid).

In analogy to the derivation of Navier's equation (cf. Section 4.9), we will now derive balance of momentum equations from this representation of the stress tensor by calculating  $\nabla \cdot \sigma^s$ :

$$\begin{aligned} (1-f)(\nabla \cdot \sigma^s)_j &= (1-f) \sum_{i=1}^3 \frac{\partial}{\partial r_i} \left[ \left( \sum_{k=1}^3 \left( K^s - \frac{2}{3}\mu^s \right) \epsilon_{kk}^s + 2\mu^s \epsilon_{ii}^s + fH\theta \right) \cdot \delta_{ij} \right. \\ &\quad \left. + 2\mu^s \cdot \epsilon_{ij}^s \cdot (1 - \delta_{ij}) \right] \\ &= (1-f) \sum_{i=1}^3 \frac{\partial}{\partial r_i} \left[ \left( \left( K^s - \frac{2}{3}\mu^s \right) \nabla \bullet \mathbf{u}^s + fH\theta \right) \cdot \delta_{ij} + 2\mu^s \epsilon_{ij}^s \right]. \end{aligned} \quad (5.5)$$

This derivation is very similar to the steps performed in the derivation of Navier's equation (Eqs. (4.124)–(4.127)). In vector notation,<sup>1</sup> the same result can be represented as

$$(1-f)\nabla \cdot \boldsymbol{\sigma}^s = (1-f) \cdot \left[ \left( K^s + \frac{1}{3}\mu^s \right) \nabla(\nabla \cdot \mathbf{u}^s) + fH\nabla\theta + \mu^s \Delta \mathbf{u}^s \right]. \quad (5.6)$$

Performing the same calculations for the fluid stress tensor, as given in the last component of Eq. (5.4), we obtain

$$f \cdot \boldsymbol{\sigma}^f = f(1-f)H \cdot \sum_{i=1}^3 \epsilon_{ii}^s + fK^f\theta, \quad (5.7)$$

with  $\theta = \sum_{i=1}^3 \frac{\partial u_i^f}{\partial r_i} = \nabla \cdot \mathbf{u}^f$ . Applying the gradient operator to derive the resultant force yields

$$f\nabla\boldsymbol{\sigma}^f = f(1-f)H\nabla(\nabla \cdot \mathbf{u}^s) + fK^f\nabla(\nabla \cdot \mathbf{u}^f). \quad (5.8)$$

We can thus equate these deformation-induced forces to the mass acceleration, according to Newton's law in analogy to Navier's equation for homogeneous media (see Section 4.9.1)

$$\rho_{11}\ddot{\mathbf{u}}^s + \rho_{12}\ddot{\mathbf{u}}^f = (1-f) \cdot \nabla \cdot \boldsymbol{\sigma}^s \quad (5.9)$$

$$\rho_{12}\ddot{\mathbf{u}}^s + \rho_{22}\ddot{\mathbf{u}}^f = f \cdot \nabla\boldsymbol{\sigma}^f. \quad (5.10)$$

In these equations, we have the acceleration terms on the left-hand side and the acting forces on the right-hand side. The acceleration terms need some explanation: Through the coupling between the two phases, a force acting on either phase will not only accelerate that phase, but due to the interaction it will also have an accelerating effect on the other phase [60]. This effect is quantified by the coupling density  $\rho_{12}$ . It can be parameterized in terms of pore geometry [66]

$$\rho_{12} = -(T-1)f\rho^f, \quad (5.11)$$

where  $T$  is the *tortuosity* of the pore space. There are different definitions for the tortuosity of a curve. The most intuitive one is the ratio of the length of the curve,  $L$ , to the distance  $D$  of its end points<sup>2</sup>:  $T = \frac{L}{D}$ , as shown in Figure 5.2. The tortuosity of a straight line is 1, whereas any other geometry results in  $T > 1$ . From this definition, we can see that  $\rho_{12}$  is always negative. The densities  $\rho_{11}$  and  $\rho_{22}$  are related to the densities of the solid and the fluid,  $\rho^s$  and  $\rho^f$ , respectively, via<sup>3</sup>

$$\rho_{11} = (1-f)\rho^s - \rho_{12} \quad (5.12)$$

$$\rho_{22} = f\rho^f - \rho_{12}. \quad (5.13)$$

Hence, we find for the bulk density of the compound material

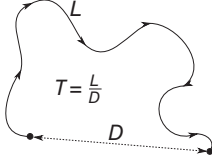
$$\rho = f\rho^f + (1-f)\rho^s = \rho_{11} + \rho_{22} + 2\rho_{12}. \quad (5.14)$$

1 As explained on page 93, the term  $\nabla \cdot \boldsymbol{\sigma} \equiv \sum_{i,j=1}^3 \frac{\partial \sigma_{ij}}{\partial r_i} \hat{\mathbf{e}}_j$  yields a vector.

2 Sometimes the square of that ratio is used instead.

3 We chose this notation to be consistent with the notation introduced by Biot [60].





**Figure 5.2** Illustration of the definition of tortuosity of a line that is used in the text.  $L$  is the length of the curve and  $D$  is the Euclidean distance of its endpoints.

By substituting the definitions (Eqs. (5.12) and (5.13)) into Eqs. (5.9) and (5.10), we can understand how  $\rho_{12}$  is correlated with energy transfer:

$$(1-f)\rho^s \ddot{\mathbf{u}}^s + \rho_{12}(\ddot{\mathbf{u}}^f - \ddot{\mathbf{u}}^s) = (1-f) \cdot \nabla \cdot \boldsymbol{\sigma}^s \quad (5.15)$$

$$f\rho^f \ddot{\mathbf{u}}^f + \rho_{12}(\ddot{\mathbf{u}}^s - \ddot{\mathbf{u}}^f) = f \cdot \nabla \boldsymbol{\sigma}^f. \quad (5.16)$$

The interaction term vanishes when both compartments are accelerated in the same direction, whereas it is maximized when the compartments undergo opposite accelerations. In a one-dimensional system, assume that the solid experiences a positive acceleration ( $\ddot{\mathbf{u}}^s > 0$ ). If the acceleration of the fluid is either negative or positive, but smaller than the solid acceleration, the interaction term in Eq. (5.15) will be positive because  $\rho_{12} < 0$ . This means that the left-hand side comprises two contributions with equal sign: one accelerates the solid, whereas the other accelerates the fluid in the same direction as the solid.

The displacement field  $\mathbf{u}^s$  usually contains both shear deformation and volumetric strain.<sup>4</sup> We will therefore use the same strategy as in Section 4.9.2: invoke the Helmholtz theorem (Eqs. (4.134)–(4.136)) to separate the equations of motion into a rotational ( $\nabla \times \mathbf{u}$ ) and a compressional ( $\nabla \cdot \mathbf{u}$ ) component.

### 5.1.1 Pressure Waves in Poroelastic Media

Applying the divergence operator to Eqs. (5.9) and (5.10), we obtain

$$\rho_{11} \cdot \nabla \bullet \ddot{\mathbf{u}}^s + \rho_{12} \cdot \nabla \bullet \ddot{\mathbf{u}}^f = (1-f) \cdot \nabla \bullet (\nabla \cdot \boldsymbol{\sigma}^s) \quad (5.17)$$

$$\rho_{12} \cdot \nabla \bullet \ddot{\mathbf{u}}^s + \rho_{22} \cdot \nabla \bullet \ddot{\mathbf{u}}^f = f \cdot \nabla \bullet (\nabla \boldsymbol{\sigma}^f). \quad (5.18)$$

We can now substitute the expressions (Eqs. (5.8) and (5.6)) into Eqs. (5.18) and (5.17) and use the shorthand notation  $\theta \equiv \nabla \bullet \mathbf{u}^f$  and  $\zeta \equiv \nabla \bullet \mathbf{u}^s$ :

$$\rho_{11} \ddot{\zeta} + \rho_{12} \ddot{\theta} = (1-f) \cdot \left( K^s + \frac{4}{3} \mu^s \right) \nabla \bullet \nabla \zeta + Hf(1-f) \nabla \bullet \nabla \theta \quad (5.19)$$

$$\rho_{22} \ddot{\theta} + \rho_{12} \ddot{\zeta} = f(1-f)H \nabla \bullet \nabla \zeta + fK^f \nabla \bullet \nabla \theta, \quad (5.20)$$

where we exploited the vector identity  $\Delta \mathbf{u}^s = \nabla^2 \mathbf{u}^s = \nabla(\nabla \bullet \mathbf{u}^s) - \nabla \times \nabla \times \mathbf{u}^s$  and discarded the rotational part.<sup>5</sup> Furthermore, we rewrite the above formulas using the scalar Laplacian  $\Delta X \equiv \nabla \bullet \nabla X$  and the P-wave modulus of the solid  $M^s \equiv K^s + \frac{4}{3} \mu^s$ :

$$\rho_{11} \ddot{\zeta} + \rho_{12} \ddot{\theta} = (1-f) \cdot M^s \cdot \Delta \zeta + f(1-f)H \cdot \Delta \theta \quad (5.21)$$

$$\rho_{22} \ddot{\theta} + \rho_{12} \ddot{\zeta} = f(1-f)H \cdot \Delta \zeta + fK^f \cdot \Delta \theta. \quad (5.22)$$

<sup>4</sup> The fluid phase, which can be either a liquid or a gas, may not support shear deformation if its viscosity is low. However, in the case of a viscous liquid, there can also be a shear component in  $\mathbf{u}^f$ .

<sup>5</sup> Doing so is legitimate, because  $\nabla \bullet (\nabla \times \boldsymbol{\chi}) = 0$  for any 3D vector field  $\boldsymbol{\chi}$ .

Next, we assume that both  $\theta$  and  $\zeta$  are plane compression waves with oscillation frequency  $\omega$  and wave number  $k$ . We can therefore write<sup>6</sup>

$$\theta(\mathbf{r}, t) = \theta_0 \cdot e^{-i\omega t} \cdot e^{i\mathbf{k} \cdot \mathbf{r}} \quad (5.23)$$

$$\zeta(\mathbf{r}, t) = \zeta_0 \cdot e^{-i\omega t} \cdot e^{i\mathbf{k} \cdot \mathbf{r}}. \quad (5.24)$$

Substituting these expressions into Eqs. (5.21) and (5.22) and reordering the terms leads us to

$$((1-f)M^s k^2 - \rho_{11}\omega^2) \cdot \zeta = (\rho_{12}\omega^2 - f(1-f)k^2 H) \cdot \theta \quad (5.25)$$

$$(fK^f k^2 - \rho_{22}\omega^2) \cdot \theta = (\rho_{12}\omega^2 - f(1-f)k^2 H) \cdot \zeta \quad (5.26)$$

with  $k = |\mathbf{k}|$ . Multiplying these two equations and dividing the result by the product  $\theta \cdot \zeta$  yields<sup>7</sup>:

$$((1-f)M^s k^2 - \rho_{11}\omega^2) \cdot (fK^f k^2 - \rho_{22}\omega^2) = (\rho_{12}\omega^2 - f(1-f)k^2 H)^2. \quad (5.27)$$

For a fixed oscillation frequency  $\omega$  and a given set of material parameters, Eq. (5.27) is a biquadratic equation in the wave number  $k$  (meaning that the only powers of  $k$  are  $k^0$ ,  $k^2$ , and  $k^4$ ), with a maximum of four distinct solutions. We can substitute  $Q = k^2$  and solve the equation algebraically. The solution has the form

$$Q_{\pm} = A \cdot (B \pm \sqrt{C}) \cdot \omega^2 \quad (5.28)$$

with

$$A = \frac{1}{2f(1-f)(M^s K^f - H^2 f(1-f))} \quad (5.29)$$

$$B = \rho_{11} f K^f + \rho_{22} (1-f) M^s - 2\rho_{12} f (1-f) H \quad (5.30)$$

$$C = \rho_{11}^2 f^2 K^{f^2} + \rho_{22}^2 (1-f)^2 M^{s^2} + 2f(1-f)M^s K^f \cdot (2\rho_{12}^2 - \rho_{11}\rho_{22}) \\ - 4\rho_{11}\rho_{12} f^2 (1-f) K^f H + 4\rho_{11}\rho_{22} f^2 (1-f)^2 H^2 - 4\rho_{22}\rho_{12} f(1-f)^2 M^s H. \quad (5.31)$$

We denote the two solutions of Eq. (5.28) by  $Q_+$  and  $Q_-$ , depending on which option for the  $\pm$  sign under the square root was chosen. These two solutions correspond to two waves with different values of  $k^2$  and hence different wavelengths. The full set of solutions is given by  $(k_+, -k_+, k_-, -k_-)$  with  $k_{\pm} = \sqrt{Q_{\pm}}$ , representing waves of two different wavelengths propagating in two opposite directions. The propagation velocity of the two waves can then be calculated as  $c = \frac{\omega}{k}$ .

We will now demonstrate that this poroelastic theory is compatible with the standard monophasic theory in the sense that in the limits  $f = 0, f = 1$  and vanishing interaction, the equations reduce to those of a monophasic medium.

For the case  $f = 0$  (pure solid), the relevant densities become

$$\rho_{12} = 0, \quad \rho_{11} = \rho^s \quad \text{and} \quad \rho_{22} = 0 \quad (5.32)$$

<sup>6</sup> The same results are obtained if one assumes that  $\theta$  and  $\zeta$  are superpositions of plane waves, which can be recovered from their spatial spectra via  $\theta(\mathbf{r}, t) = \frac{1}{\sqrt{2\pi}} \int \hat{\theta}(\mathbf{k}, t) \cdot \exp(i\mathbf{k} \cdot \mathbf{r}) d\mathbf{k}$  (and analogously for  $\zeta(\mathbf{r}, t)$ ).

Inserting this expression into Eqs. (5.21) and (5.22) and using the fact that  $\exp(i\mathbf{k} \cdot \mathbf{r})$  for different  $\mathbf{k}$  are independent leads to the same equations, but some additional calculation steps are required.

<sup>7</sup> Dividing by  $\theta \cdot \zeta$  is permissible, since both functions are complex harmonic functions that never disappear, unless their amplitude is zero, in which case there would be no waves to look at anyway.

according to Eq. (5.11), Eq. (5.12) and Eq. (5.13), respectively. Inserting these substitutions into Eq. (5.25) yields

$$(M^s k^2 - \rho^s \omega^2) \cdot \theta = 0, \quad (5.33)$$

whereas Eq. (5.26) vanishes completely. The result is a pressure wave equation for the monophasic solid medium. Conversely, for  $f = 1$  (pure fluid) and  $\rho_{12} = 0$ , it follows from Eqs. (5.12) and (5.13) that  $\rho_{11} = 0$  and  $\rho_{12} = \rho^f$ . Hence, Eq. (5.25) vanishes and Eq. (5.26) is reduced to

$$(K^f k^2 - \rho^f \omega^2) \cdot \zeta = 0, \quad (5.34)$$

which is the pressure wave equation for the monophasic fluid.

Finally, in the case of vanishing interaction ( $\rho_{12} = 0$  and  $H = 0$ ) with arbitrary volume fraction, the equations of motion (5.25) and (5.26) decouple to

$$((1-f)M^s k^2 - \rho_{11} \omega^2) \zeta = 0 \quad (5.35)$$

$$(fK^f k^2 - \rho_{22} \omega^2) \theta = 0, \quad (5.36)$$

which are wave equations for two independently oscillating media. According to Eqs. (5.12) and (5.13), we can substitute  $\rho_{11} = (1-f)\rho^s - \rho_{12} = (1-f)\rho^s$  and  $\rho_{22} = f\rho^f - \rho_{12} = f\rho^f$ , we can see that the waves are independent of the volume fraction:

$$(M^s k^2 - \rho^s \omega^2) \zeta = 0 \quad (5.37)$$

$$(K^f k^2 - \rho^f \omega^2) \theta = 0. \quad (5.38)$$

Equations (5.28)–(5.31) represent the most general solution for compressional waves in a nondissipative biphasic medium with poroelastic interactions. We will now introduce some simplifications to reduce the number of independent parameters in Eq. (5.28), since we are primarily interested in the effect of the coupling parameters  $H$  and  $\rho_{12}$ .

First, we assume equal densities of the fluid and the solid,  $\rho^s = \rho^f$ . This is justified, since in biological tissue (with the exception of the lungs, which are air-filled) both phases consist mainly of water. Usually,  $1050 \text{ kg/m}^3$  is used as tissue density, which is sufficiently close to the density of pure water ( $1000 \text{ kg/m}^3$ ). For the same reason, we make the assumption that the compression moduli of the two phases are identical to that of water,  $K^s = K^f = 2.2 \text{ GPa}$ . The shear modulus of tissue is typically several orders of magnitude smaller than that ( $\sim 2 \text{ kPa}$  for human liver and brain), so that we can neglect this contribution and approximate  $M^s = K^s + \frac{4}{3}\mu^s \approx K^s \equiv K$ . We also set the volume fraction arbitrarily to  $f = 0.5$ , assuming equal amounts of solid and fluid. Together with the assumption of equal densities of the fluid and the solid, this implies  $\rho_{11} = \rho_{22} \equiv \rho'$ . Inserting these identities into Eq. (5.27), multiplying the parentheses, and ordering by powers of  $Q$  yield

$$\frac{1}{4} \left( K^2 - \frac{1}{4} H^2 \right) Q^2 + \left( \frac{1}{2} \rho_{12} \omega^2 H - \rho' \omega^2 K \right) Q + (\rho'^2 - \rho_{12}^2) \omega^4 = 0. \quad (5.39)$$

We now have to distinguish two cases:  $K^2 \neq \frac{1}{4} H^2$  and  $K^2 = \frac{1}{4} H^2$ . In the first case, the coefficient of  $Q^2$  is distinct from zero. The solution of Eq. (5.39) is

$$Q_{\pm} = \frac{4\omega^2(\rho' \pm \rho_{12})}{2K \pm H}, \quad (5.40)$$

where the same sign has to be used in the nominator and denominator. Resubstituting  $\rho' = \frac{1}{2}\rho - \rho_{12}$  thus yields the solutions

$$Q_+ = \frac{2\omega^2 \rho}{2K + H} \quad (5.41)$$

$$Q_- = \frac{4\omega^2(\frac{1}{2}\rho - 2\rho_{12})}{2K - H}. \quad (5.42)$$

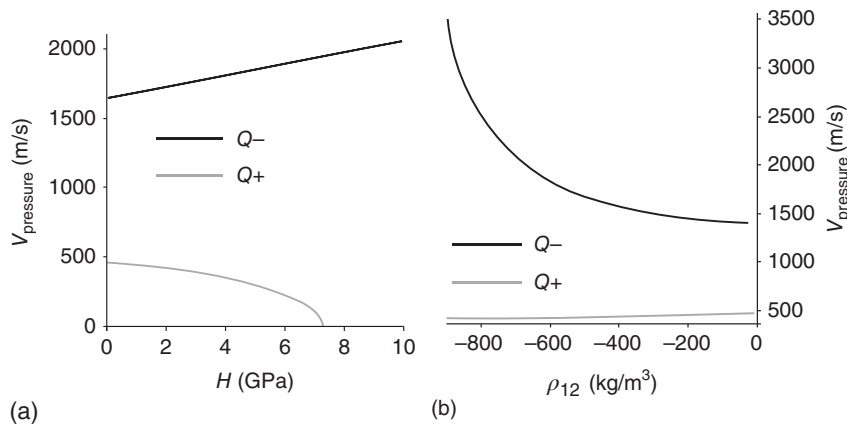
There are hence two different wavelengths  $\lambda_{\pm} = 2\pi/\sqrt{Q_{\pm}}$ , and two opposite propagation directions (because of  $Q = k^2 \Rightarrow k = \pm\sqrt{Q}$ ). The solution  $Q_+$  only depends on the coupling modulus  $H$ , but not on the coupling density  $\rho_{12}$ . Since  $\rho_{12}$  was introduced as the coefficient of friction-like energy transfer related to the relative motion of the two compartments, its absence in the expression for  $Q_+$  can only mean that this represents the case with no relative motion between the compartments, that is, the scenario in which fluid and solid oscillate in phase ( $\mathbf{u}^s = \mathbf{u}^f$ ). Conversely, the second solution,  $Q_-$ , represents the opposite case in which the effect of relative motion is maximized, corresponding to an opposed-phase motion of the compartments ( $\mathbf{u}^s = -\mathbf{u}^f$ ).

For the special case  $K = \pm\frac{1}{2}H$ , however, the coefficient of  $Q^2$  in Eq. (5.39) vanishes and we have a linear equation in  $Q$  instead. Since both  $K$  and  $H$  are positive quantities, we only need to consider the case  $K = \frac{1}{2}H$ . The solution of Eq. (5.39) then reads

$$Q = \frac{\omega^2(\rho' + \rho_{12})}{K} = \frac{1}{2} \frac{\omega^2 \rho}{K}, \quad (5.43)$$

where  $\rho$  is the bulk density of the fluid and the solid (which we assumed to be equal) and we used  $\rho' = \frac{1}{2}\rho - \rho_{12}$ . Therefore, in this special case, the poroelastic medium behaves like a monophasic medium with density  $\rho$ , but with only half the wave velocity.

We illustrate the dependence of the wave speeds for the two wave modes on the poroelastic parameters,  $H$  and  $\rho_{12}$ , in Figure 5.3, for viscoelastic parameters that are closer to biological tissue than the simplified model discussed above. We can clearly



**Figure 5.3** Plot of the pressure wave speed for the two modes in a poroelastic medium for the following parameters:  $K = M = 2.2$  GPa (assuming the compressibility of water),  $\rho^s = \rho^f = 1000$  kg/m<sup>3</sup>,  $f = 0.9$ . (a)  $H$  variable,  $\rho_{12} = -500$  kg/m<sup>3</sup>. (b)  $\rho_{12}$  variable,  $H = 1$  GPa.

see that in the absence of poroelastic interaction, two wave modes with speeds of approximately 500 and 1500 m/s exist. The speed of the slower mode further decreases as the poroelastic parameters increase, whereas the faster mode becomes even faster with stronger interaction. The literature on poroelasticity in the context of MRE is relatively sparse, and different researchers have used different poroelastic models. The suitability of the model presented above for poroelastic MRE yet remains to be evaluated. A study performed by Dai et al. [67] in the human lung has revealed the existence of two distinct compression modes propagating at different velocities. In the low-frequency regime, the wave speeds were found to be <10 and <30 m/s, respectively. Wave propagation in a poroelastic medium composed of air and lung tissue is thus much slower than that in pure air. The effect can be explained by the fact that the presence of lung tissue has a much larger effect on the bulk density than on the effective compression modulus, thus slowing the wave down.

### 5.1.2 Shear Waves in Poroelastic Media

In order to analyze rotational (shear) waves, we apply the curl operator to Eqs. (5.15) and (5.16):

$$(1-f)\rho^s\ddot{\mathbf{c}}^s + \rho_{12}(\ddot{\mathbf{c}}^f - \ddot{\mathbf{c}}^s) = (1-f)\nabla \times \nabla \cdot \boldsymbol{\sigma}^s \quad (5.44)$$

$$f\rho^f\ddot{\mathbf{c}}^f + \rho_{12}(\ddot{\mathbf{c}}^s - \ddot{\mathbf{c}}^f) = f \cdot \nabla \times \nabla \boldsymbol{\sigma}^f = \mathbf{0}, \quad (5.45)$$

with  $\mathbf{c}^{f/s} = \nabla \times \mathbf{u}^{f/s}$ . The right-hand side of the second equation vanishes, since the gradient of a scalar function is always curl-free.<sup>8</sup> We can therefore solve Eq. (5.45) for  $\ddot{\mathbf{c}}^f$ :

$$\ddot{\mathbf{c}}^f = -\frac{\ddot{\mathbf{c}}^s}{\frac{f\rho^f}{\rho_{12}} - 1} \quad (5.46)$$

and substitute this result into Eq. (5.44):

$$\ddot{\mathbf{c}}^s \left( (1-f)\rho^s - \rho_{12} \left( 1 + \frac{\rho_{12}}{f\rho^f - \rho_{12}} \right) \right) = (1-f)\nabla \times \nabla \cdot \boldsymbol{\sigma}^s. \quad (5.47)$$

In order to simplify the right-hand side, we apply the curl operator to Eq. (5.6):

$$\begin{aligned} (1-f)\nabla \times \nabla \cdot \boldsymbol{\sigma}^s &= (1-f) \cdot \left[ \left( K^s + \frac{1}{3}\mu^s \right) \nabla \times \nabla (\nabla \cdot \mathbf{u}^s) + fH\nabla \times \nabla \theta + \mu^s \nabla \times \Delta \mathbf{u}^s \right] \\ &= (1-f)\mu^s \nabla \times \Delta \mathbf{u}^s \\ &= (1-f)\mu^s \Delta \mathbf{c}^s. \end{aligned} \quad (5.48)$$

In the first step, we exploited the fact that the curl of a gradient vanishes. The validity of the second step follows from the vector calculus identity

$$\Delta \boldsymbol{\xi} = \nabla (\nabla \cdot \boldsymbol{\xi}) - \nabla \times \nabla \times \boldsymbol{\xi} \quad (5.49)$$

for an arbitrary vector field  $\boldsymbol{\xi}$ .

<sup>8</sup> The vanishing fluid stress is a manifestation of the model assumption that the fluid does not support shear stresses. This does *not* mean that the fluid cannot be subjected to shear deformation, but that the fluid will not resist shear deformation.

We therefore obtain the equation of motion for a shear wave in a poroelastic medium:

$$\left( (1-f)\rho^s - \rho_{12} \left( 1 + \frac{\rho_{12}}{f\rho^f - \rho_{12}} \right) \right) \ddot{\mathbf{c}}^s = (1-f)\mu^s \Delta \mathbf{c}^s. \quad (5.50)$$

Note that instead of a coupled system of equations, as in the case of compressional waves, we only obtain one (vector) equation for shear waves. This can be explained by the fact that the fluid does not support shear deformation; it therefore merely follows the displacement of the matrix, which allowed us to write down the explicit relationship between  $\ddot{\mathbf{c}}^s$  and  $\ddot{\mathbf{c}}^f$  in Eq. (5.46).

Equation (5.50) is a wave equation for the porous matrix. By comparing with the standard shear wave equation of a monophasic medium (cf. Eq. (4.141)),

$$\rho \ddot{\mathbf{c}} = \mu \cdot \Delta \mathbf{c}, \quad (5.51)$$

we can see that the poroelastic medium behaves like an effective medium with shear modulus

$$\mu_{\text{effective}} = (1-f)\mu^s \quad (5.52)$$

and effective density

$$\rho_{\text{effective}} = \left( (1-f)\rho^s - \rho_{12} \left( 1 + \frac{\rho_{12}}{f\rho^f - \rho_{12}} \right) \right). \quad (5.53)$$

Obviously, the shear modulus of the effective medium is equal to the matrix shear modulus weighted by the solid volume fraction. This modulus would be obtained by a (quasi-) static indentation experiment. In the dynamic case, the mass to be accelerated by the acting stresses is given by  $\rho_{\text{effective}}$  and includes the fluid and solid masses along with their kinetic coupling density  $\rho_{12}$ . The fluid behaves as a “parasitic” mass, which has to be accelerated by the matrix in order for the poroelastic medium to undergo deformation. The propagation velocity of the shear wave is

$$v_{\text{shear}} = \sqrt{\frac{\mu_{\text{effective}}}{\rho_{\text{effective}}}} = \sqrt{\frac{(1-f)\mu^s}{\left( (1-f)\rho^s - \rho_{12} \left( 1 + \frac{\rho_{12}}{f\rho^f - \rho_{12}} \right) \right)}}. \quad (5.54)$$

If we substitute  $\rho_{12}$  with the tortuosity,  $T$ , according to Eq. (5.11), and assume equal densities of the two phases,  $\rho^s \approx \rho^f = \rho$ , we obtain

$$v_{\text{shear}} = \sqrt{\frac{\mu^s}{\rho}} \cdot \sqrt{\frac{1-f}{1-\frac{f}{T}}} = v_{\text{matrix}} \cdot \sqrt{\frac{1-f}{1-\frac{f}{T}}} \leq v_{\text{matrix}}. \quad (5.55)$$

The effective-medium shear wave propagation velocity is therefore equal to the matrix shear wave velocity weighted by the square-root term. This weighting factor is always between 0 and 1, since, by definition,  $T \geq 1$ . For  $f = 0$  (a solid slab of the matrix material), Eq. (5.55) reproduces the matrix shear wave velocity. For  $f = 1$  (pure fluid without matrix), the shear wave velocity becomes zero, in accordance with the model assumption that the fluid does not support shear waves. The poroelastic shear wave is therefore slower than the monophasic shear wave because of the parasitic mass of the fluid.

## 5.2 Poroelastic Signal Equation

The magnetic resonance imaging (MRI) signal is a superposition of signals from all hydrogen atoms within an excited volume, and a decomposition into partial signals from the fluid and solid phase of a poroelastic model is intractable. The poroelastic equations of motion, (5.19) and (5.20), hence cannot be solved directly for the poroelastic parameters, since the displacement fields  $\mathbf{u}^f$  and  $\mathbf{u}^s$  cannot be separated. However, an analysis of the signal equation will reveal that it is possible to garner information about local expansion or compression for certain poroelastic scenarios.

If equal densities  $\rho^s = \rho^f = \rho$  and incompressibility are assumed for both the matrix (s) and the fluid (f) phase of a poroelastic model, fluid displacement or influx does not lead to a change of the bulk density, since one material is merely replaced with the other material of the same density. The continuity equation

$$\frac{\partial \rho}{\partial t} + \nabla \cdot \mathbf{j} = 0 \quad (5.56)$$

with mass flux  $\mathbf{j}$  therefore reduces to

$$\frac{\partial \rho}{\partial t} = 0 \quad \Rightarrow \quad \nabla \cdot \mathbf{j} = 0 \quad (5.57)$$

because of the incompressibility constraint.

MRI does not detect bulk material densities, as it is only sensitive to the proton signal from hydrogen atoms. In the biphasic poroelastic tissue model, each hydrogen atom belongs either to the matrix or to the fluid compartment. Because water content differs between interstitial water and the surrounding tissue matrix, the MRI-relevant partial hydrogen densities  $\rho_{\text{MRI}}^f$  and  $\rho_{\text{MRI}}^s$  are distinct. The continuity equation

$$\frac{\partial}{\partial t} (\rho_{\text{MRI}}^f + \rho_{\text{MRI}}^s) + \nabla \cdot (\mathbf{j}_{\text{MRI}}^f + \mathbf{j}_{\text{MRI}}^s) = 0 \quad (5.58)$$

therefore cannot be simplified to the form of Eq. (5.57).

In this model, the total hydrogen density,  $\rho_{\text{MRI}} = \rho_{\text{MRI}}^f + \rho_{\text{MRI}}^s$ , is not constant with respect to time. Rather, it will change as fluid is squeezed out or drawn into the matrix, changing the relative volumes of matrix and fluid in the overall material. The motion-encoding mechanism deployed in MRE is only sensitive to motion, not to hydrogen density, hence only the hydrogen fluxes  $\mathbf{j}_{\text{MRI}}^s$  and  $\mathbf{j}_{\text{MRI}}^f$  are detectable. The hydrogen signal from a voxel is measured as a superposition of all spins contained in that voxel and no separation into contributions from the matrix and the fluid is possible. Given this constraint, MRE quantifies the overall hydrogen flux  $\mathbf{j}_{\text{MRI}} = \mathbf{j}_{\text{MRI}}^f + \mathbf{j}_{\text{MRI}}^s$  and the continuity equation reads

$$\frac{\partial}{\partial t} \rho_{\text{MRI}} + \nabla \cdot \mathbf{j}_{\text{MRI}} = 0. \quad (5.59)$$

This implies that finite hydrogen fluxes are observable if the two compartments possess different hydrogen densities, such that  $\frac{\partial \rho_{\text{MRI}}}{\partial t} \neq 0$ . In that case, signals from inward and outward mass fluxes – even though perfectly balanced in terms of mass density – will not fully cancel out, resulting in a phase signal indicative of the motion of the compartment with the higher hydrogen density. The divergence of the hydrogen flux is therefore an indicator of local compression or dilatation, and the magnitude  $|\nabla \cdot \mathbf{j}_{\text{MRI}}|$  serves as a

measure of local compressibility. In the case of time-harmonic particle oscillations with trajectory  $\mathbf{u}(\mathbf{r}, t)$ , the oscillating flux of signal-generating particles can be represented as

$$\mathbf{j}_{\text{MRI}}(\mathbf{r}, t) = \rho_{\text{MRI}}(\mathbf{r}, t) \cdot \mathbf{u}(\mathbf{r}, t). \quad (5.60)$$

If one or both phases are compressible, Eq. (5.58) is still valid, but a change in the signal densities will arise not only from a change in the volumetric composition but also from actual compression or dilatation of the two phases.

The complex MRI signal from each compartment  $c$  at the time of the signal readout can be parameterized as follows:

$$S_c(\mathbf{r}) \propto \rho_c(\mathbf{r}) \cdot f_c(\mathbf{r}) \cdot n_c^{\text{H}}(\mathbf{r}) \cdot \exp(i\omega t) \cdot \exp\left(-\frac{TE}{T_2}\right) \cdot \exp(i\phi_{0,c}), \quad (5.61)$$

where  $\rho_c$  is the bulk density of that compartment,  $f_c$  its volume fraction and  $n_c^{\text{H}}$  the fraction of signal-generating hydrogen atoms in that phase,  $TE$  is the echo time of the MR sequence and  $T_2$  is the transverse signal decay constant of the compartment.<sup>9</sup>  $\phi_{0,c}$  is the phase offset induced by motion encoding and field inhomogeneities.<sup>10</sup> The constant hidden behind the proportionality sign is determined by the magnetic field strength of the scanner, flip angle of the radiofrequency pulses, geometry of the transmit and receive coils, and characteristics of the receiver electronics. We will henceforth consider the echo time fixed and condense the signal equation into a more compact form:

$$S_c(\mathbf{r}, t) = |S_c(\mathbf{r})| \cdot \exp(i\omega t + \phi_{0,c}). \quad (5.62)$$

We replace the time dependence of  $S_c$  with the complex phase at the time of the readout,  $\phi_c = \phi_{0,c} + \omega t_{\text{readout}}$ , and drop the explicit dependence on the position for the sake of brevity.

The signal from the voxel can be described as the superposition of the signals  $S_c = |S_c| \cdot \exp(i\phi_c)$ , where  $c \in \{1, 2\}$  iterates over the two compartments of the poroelastic model. The compound signal at the time of the readout is therefore

$$S = |S| \cdot \exp(i\phi) = S_1 + S_2 = |S_1| \cdot \exp(i\phi_1) + |S_2| \cdot \exp(i\phi_2). \quad (5.63)$$

A trigonometric analysis of these vectors (Figure 5.4) yields

$$|S| = \sqrt{|S_1|^2 + |S_2|^2 - 2|S_1||S_2| \cdot \cos(\phi_2 - \phi_1)} \quad (5.64)$$

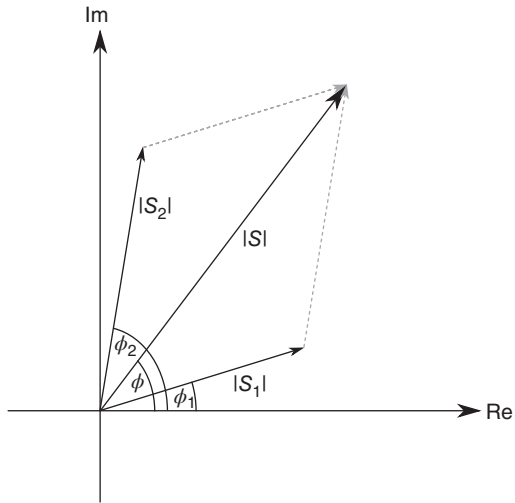
$$\phi = \phi_1 + \arcsin\left(\frac{|S_2|}{\sqrt{|S_1|^2 + |S_2|^2 - 2|S_1||S_2| \cdot \cos(\phi_2 - \phi_1)}}\right). \quad (5.65)$$

If the composition of the medium inside a given volume element changes, through either compression/dilatation or one compartment being partially replaced by the other, this will affect the phase  $\phi$  of the compound signal, which is the quantity of interest in MRE. In the case of in-phase oscillation of the two compartments (requiring compressible constituents), the change of the signal phase can be translated into a change of the bulk density via Eqs. (5.59) and (5.60). For opposed-phase motion, both in the

<sup>9</sup> If a gradient-echo sequence is used instead of a spin-echo sequence, the relevant time constant is  $T_2^*$ .

<sup>10</sup> The motion information can be separated from susceptibility artifacts by temporal Fourier transform or some other form of temporal normalization.





**Figure 5.4** The detected MRE signal in a biphasic poroelastic model. The contributions  $S_1 = |S_1| \cdot \exp(i\phi_1)$  and  $S_2 = |S_2| \cdot \exp(i\phi_2)$  from the two compartments add to form the combined signal  $S = |S| \cdot \exp(i\phi)$ .

compressible and incompressible cases, the influx of one compartment into a volume element is balanced by the outflow of the other phase. The signal of the compound MR signal is then representative of the difference of these two effects, and its sign is indicative of the motion with the larger signal amplitude.

## **Part III**

### **Technical Aspects and Data Processing**

## 6

### MRE Hardware

#### 6.1 MRI Systems

MRE is neither limited to a specific MRI system nor does it require high magnetic field strengths. Since motion information in MRE is encoded in the phase of the complex MR signal, signal-to-noise ratio (SNR) and contrast of the signal magnitude are of importance for the provision of sufficient phase-to-noise ratio only. As in all other phase contrast-based MRI techniques, a homogeneous magnetic field is favorable to avoid phase wraps. Furthermore, the gradient system of the MR scanner should be capable of delivering balanced gradients with great fidelity to avoid spoiling the signal and guarantee a linear relationship between displacement field and accumulated spin phase. Much effort of vendors of clinical MRI systems has been devoted to reduce those artifacts making the implementation of fast and robust MRE sequences easier today than in the early days of MRE. A review of the literature demonstrates that MRE can be implemented on any type of MRI scanners at almost all field strengths across a wide range of vibration frequencies, as long as the imaging sequence is synchronized to the tissue vibration. In fact, the timing of an MRE sequence with respect to the induced mechanical motion is a strong requirement for capturing waves at different phases of their propagation through the tissue. In the simplest case, TTL (transistor–transistor logic) or optical trigger pulses are sent from the scanner to the vibration generator to initiate vibration. In more complex implementations, the duration of the trigger pulses can be modulated to convey further information to the vibration generator, for example, to switch the vibration frequency during a multifrequency measurement [68]. Finally, possible interactions between actuators and MRI, leading to imaging artifacts, have to be excluded. For this reason, nonmetallic drivers are mostly used for clinical examinations (see Section 6.2). The power supply of those actuators is based on either pneumatic vibrations requiring waveguide ducts or electrical signals requiring filters to suppress electromagnetic interference (EMI). Observing these principal requirements enables researches and physicians to run MRE as a robust method for basic research as well as in clinical applications. A comprehensive list of experiments that have been conducted in the fields of preclinical and clinical MRE is beyond the scope of this book. However, Tables 6.1 and 6.2 give an overview on experiments performed on representative systems including relevant parameters.

Table 6.1 Overview of various MRE parameters used for clinical studies.

Organ/ disease	References	Subjects	B <sub>0</sub> (T)	Sequence	Encoding	MEG amplitude (mT/m)	Vibration frequency (Hz)	Actuator	TE/TR (ms)	Averages	Resolution RO × PE × SS (mm)
Brain	[69]	v	1.5	SE-EPI	3D, fe	35	10–50 (cont)	PZ	55/1350	1	2.0×2.0×2.0
	[70]	v	na	SE-EPI	3D	na	60	EM	62/3600	1	3.3×3.3×3.0
	[71]	v	1.5	SE-EPI	1D, fe, pd	35	25–62.5	EM	148/3000	1	1.5×1.5×6.0
	[38]	v	7.0	SE-EPI	3D	50	40–60	EM	76/5640	1	1.0×1.0×1.0
	[72]	p+c	1.5	SE-EPI	3D	35	50/60	PZ	99/7210	1	2.0×2.0×2.0
	[73, 74]	p+c	1.5	SE-EPI	1D, fe, pd	35	25–62.5	EM	149/3000	1	1.5×1.5×6.0
	[75]	p+c	1.5	SE-EPI	3D, fe, pd	35	25–62.5	EM	149/3000	1	2.5×2.5×6.0
	[76]	p+c	3.0	SE-EPI	3D, pd	40	60	EM	61/1500	1	4.0×4.0×4.0
	[76]	p+c	3.0	SE-EPI	3D, pd	40	60	EM	62/3600	1	3.0×3.0×3.0
	[77, 78]	p	1.5	SE-EPI	1D, pd	35	25–62.5	EM	149/3000	1	1.5×1.5×6.0
Heart	[79, 80]	p+c	1.5	ss GRE	3D, fe	25	500	EM	3.3/5.2	1	2.5×2.6×7.0
	[47]	v	1.5	SE-EPI	3D, fe	na	30–60	EM	98/4500	2	2.5×2.5×2.5
Muscle	[81]	v	3.0	SE	3D	na	60	EM	66/1000	1	2.0×2.0×2.0
	[82]	v	3.0	SE-EPI	1D	na	50	EM	56/1600	1	1.8×1.8×10
	[83]	p	1.5	GRE	1D	na	90	PN	10–60/ 100–350	na	na
Lung	[84]	p	1.5	GRE	1D	na	90	PN	19/275	1	0.9×3.8×na
	[85]	v	1.5	SE-EPI	3D, fe	20	50	EM	23/980	7	3.1×3.1×10.0
	[86]	v	1.5	SE-EPI	1D, fe	40	50	EM	12/320	na	3.8×7.6×15.0

Liver	[69]	v	1.5	SE-EPI	3D, fe	32	10–50 (cont)	PZ	55/1350	1	2.7 × 2.7 × 5.0
	[87]	v	1.5	GRE	1D	na	60	PN	26/100	1	1.3–1.6 × 3.4–4.4 × 6.0–10
	[88]	p+c	1.5	GRE	1D	na	60	PN	23/50	1	1.3–1.6 × 5.0–6.6 × 10.0
	[89]	p+c	1.5	SE-EPI	1D, pd	20	25–62.5	EM	64/500	1	2.3 × 4.7 × 10.0
	[90]	p	3.0	SE-EPI	3D	na	50	na	40/560	1	4.0 × 4.0 × 4.0
	[91]	p	1.5	GRE	1D	na	60	PN	27/100	1	1.4 × 4.2 × 10.0
			3.0						20/50	1	1.4 × 4.4 × 10.0
	[92]	p	1.5	GRE	1D	na	60	PN	23/50	1	1.3–1.6 × 5.0–6.6 × 10.0
	[93]	p	1.5	GRE	1D	na	60	PN	25/50	1	1.3–1.7 × 5.0–6.8 × 10.0
	[94]	p	3.0	GRE	1D	na	60	PN	20/50	1	1.9 × 7.5 × 10.0
	[95]	p	1.5	SE-EPI	3D	35	25–60	PZ	54/1820	1	2.7 × 2.7 × 5.0
	[96]	p	1.5	GRE	3D, fe	na	28, 56, 84	EM	9/111	1	5.0 × 3.0 × 4.0
	[97]	p+c	1.5	GRE	1D	na	60	PN	25/50	1	1.3–1.6 × 5.0–6.6 × 10.0
	[98]	v	1.5	SE-EPI	3D, fe	30	30–60	PZ	54/1820	1	2.7 × 2.7 × 5.0
Spleen	[98]	v	1.5	SE-EPI	3D, fe	30	30–60	PZ	55/3790	1	2.5 × 2.5 × 2.5
	[99]	p+c	1.5	GRE	1D	na	60	PN	25/50	na	na × na × 7.0
Liver and spleen			3.0						20/50		na × na × 10.0
	[100]	v	1.5	SE-EPI	3D, fe	40	40, 60	PN	40/1875	1	4.0 × 4.0 × 3.0
Pancreas									40/2084		
	[101]	v	1.5	SE-EPI	3D, fe	30	50–70	EM	68/1960	2	2.0 × 2.0 × 2.0
Intervertebral disk	[102]	v	1.5	SE-EPI	3D, fe	30	30–60	PZ	55/1770	2	2.5 × 2.5 × 2.5
	[103]	v	1.5	GRE	3D	14	45, 76	EM	31/53	na	1.9 × 5.6 × 5.0
Kidney									35/92		
	[104]	p	3.0	SE-EPI	3D	na	90–150	PN	48–60/	1	3.3–4.2 × 3.3–4.2 × 3.0–4.0
									1700–1850		

(continued overleaf)

Table 6.1 (Continued)

Organ/ disease	References	Subjects	$B_0$ (T)	Sequence	Encoding	MEG amplitude (mT/m)	Vibration frequency (Hz)	Actuator	TE/TR (ms)	Averages	Resolution RO × PE × SS (mm)
Uterus and cervix	[105]	v	1.5	SE-EPI	3D, fe	30	30–60	PZ	55/1590	1	2.5 × 2.5 × 2.5
Prostate	[106]	v	3.0	seg EPI	3D, fe	60	45	HY	44/2700	2	1.5 × 1.5 × 1.5 3.0 × 3.0 × 3.0
Brain tumors	[107]	v	1.5 & 3.0	GRE	1D/3D pd	40	100–400	PZ	13/18	1–4	1.1 × 1.1 × 6.0
	[108]	p	1.5 & 3.0	SE-EPI	3D, fe	30/35	30–60	PZ	99/2400	1	2.0 × 2.0 × 2.0
Breast cancer	[109]	p	3.0	SE-EPI	3D	35	30–60	EM	71/3000	1	2.0 × 2.0 × 2.0
	[110]	p	3.0	SE-EPI	3D	40	60	PN	61/1500	1	4.3 × 4.3 × 4.0
	[111]	p	3.0	SE-EPI	3D	na	60	PN	62/3600	1	3.0 × 3.0 × 3.0
	[112]	p+c	1.5	GRE	1D, fe	na	75–300	EM	28/100–300	1	na × 1.9–2.5 × 3.0–5.0
	[113]	p+c	1.5	na	3D	na	85	EM	47/495	na	2.0 × 2.0 × 2.0
Liver tumors	[114]	p	1.5	GRE	1D	na	60	EM	26/100	1	1.3–1.6 × 3.4–4.4 × 6.0–10.0
	[115]	p	1.5	SE-EPI	3D	na	50	EM	40/560	1	4.0 × 4.0 × 4.0
Prostate cancer	[116]	p+c	3.0	ss GRE	3D, fe	48	70	EM	9/344	1	2.0 × 2.0 × 2.0

**Abbreviations:** v – healthy volunteer, p – patient, p+c – patients+controls, fe – fractional encoding, pd – phase difference, ss – steady state, seg – segmented, PZ – piezoelectric, EM – electromagnetic, PN – pneumatic, HY – hydraulic, cont – continuous, na – not available, RO – readout, PE – phase-encode, SS – slice-select, SE – spin echo, GRE – gradient echo, 1D – single displacement field component, 3D – full displacement field.

Table 6.2 Overview of various MRE parameters used for preclinical studies.

Target	Animal/ sample material	<i>In vivo</i> / <i>ex vivo</i>	References	B <sub>0</sub> (T)	Sequence	Encoding	MEG amplitude (mT/m)	Vibration frequency (Hz)	Actuator	TE/TR (ms)	Averages	Resolution RO × PE × SS (mm)
Brain	Mouse	iv	[117]	11.7	SE	3D	100	400–1200	EM	34/1000	2	0.25 × 0.25 × 0.40
	Mouse	iv	[118]	9.4	GRE	1D, pd	1000	878	PZ	6/1000	2	0.16 × 0.16 × 1.00
	Mouse	iv	[119]	9.4	SE	1D, pd	300–500	370–435	PZ	25/1000	1–2	0.20 × 0.20 × 1.00
	Mouse	ev	[120]	9.4	SE	1D, pd	300–500	400	PZ	24–34/1200	1–4	0.27 × 0.27 × 1.00
	Mouse	iv	[121–124]	7.0	GRE	1D, pd	285	900	EM	14/116	1–2	0.20 × 0.20 × 2.00
	Mouse	ev	[125]	7.0	GRE	1D, pd	285	100–800	EM	16/134	1	0.31 × 0.31 × 2.00
	Mouse	iv	[126]	7.0	SE	3D	na	1000	EM	27/1001	2	0.30 × 0.30 × 0.30
	Mouse	iv	[127]	7.0	SE	3D, pd	150	600–1800	PZ	28/1000	2	0.25 × 0.25 × 0.25
	Mouse	iv	[128]	3.0	SE	1D, pd	27		EM	80/1000	1	0.47 × 0.47 × 3.00
	Cat	iv	[129]	3.0	SE	3D	na	85	PN	50/900	na	2.00 × 2.00 × 1.80
	Rat	iv+ev	[130]	0.1	na	1D	na	180	EM	60/900	4	0.55 × 0.73 × 7.00
	Pig	iv	[131]	0.1	SE	1D	15	80–140	na	60/80	8	0.70 × 0.90 × 10.0
	Liver	Rat	ev	[132]	7.0	SE	3D	na	500–700	EM	23–30/ 503–604	na
Lung	Rat	iv	[133]	7.0	SE	3D	na	300	PZ	18/350	4	0.82 × 0.82 × 0.83
	Mouse	iv	[134]	1.5	GRE	1D, pd	18	120	EM	18/33	1	0.39 × 1.56 × 5.00
	Rat	ev	[135]	1.5	SE	1D, pd	18	200–220	EM	21/200–300	1	0.47 × 0.94 × 4.00
	Rat	ev	[136]	1.5	SE	1D	na	220	PN	12/318	na	0.47 × 0.94 × 5.00
	Pig	ev	[137]	1.5	GRE	1D	15	120	EM	8/100	1	1.56 × 3.12 × 20.0

(continued overleaf)

Table 6.2 (Continued)

Target	Animal/ sample material	<i>In vivo/ ex vivo</i>	References	$B_0$ (T)	Sequence	Encoding	MEG amplitude (mT/m)	Vibration frequency (Hz)	Actuator	TE/TR (ms)	Averages	Resolution RO × PE × SS (mm)
Kidney	Pig	iv	[138]	3.0	SE	3D	na	120	PN	64/2200	1	3.54 × 3.54 × 3.00
	Rat	iv	[139]	1.5	GRE	1D	na	300	EM	15/200	na	0.47 × 0.94 × 5.00
Prostate		ev	[140]	7.0	SE	3D	200	600–1000	EM	35–50/ 800–1200	1	1.00 × 1.00 × 1.00
Colon	Mouse	iv	[141]	7.0	SE	3D	300	1000	EM	27/1001	2	0.25 × 0.25 × 0.30
Skeletal muscle	Mouse	iv	[127]	7.0	SE	3D	300	1000	EM	15/691	na	na
Arterial wall	Pig	ev	[142]	1.5	GRE	1D	na	200	EM	na/100	na	1.37 × 5.47 × 5.00
Vascular wall	Pig/human	ev	[143]	1.5	GRE	1D	na	100–500	EM	na/100	na	0.78 × 3.12 × 5.00
Eye	Bovine	ev	[144]	1.5	GRE	1D	32	300	PZ	20/40	1	0.63 × 0.63 × 5.00
Phantom tissue	Gel	na	[145]	0.5	SE	1D, pd	250	500–1000	EM	40/500–1000	1	0.23 × 0.23 × 3.00
	Gelatine	na	[146]	3.0	GRE	3D	na	100	PZ	16/21	na	0.63 × 0.63 × 2.00
	Gelatine	na	[147]	4.7	GRE	3D, pd	80	100–400	PZ	14/200	2	0.25 × 0.25 × 0.50
	Gel, frog oocyte/ engineered tissue		[148]	11.4	GRE	1D, pd	2000	585	PZ	5/200 70/800	1	0.03 × 0.03 × 0.5 0.14 × 0.14 × 0.50
	Polysiloxane	na	[149]	9.4/ 11.7	SE GRE	1D	396 1200	200–7750	PZ	8/500 4/250	na	0.51 × 0.51 × 1.00 0.08 × 0.08 × 1.00
	Polysiloxane	na	[150]	9.4/ 11.7	GRE	3D	200 750–900	500–16000	PZ	3/100 3–4/100–600	na	0.28 × 0.28 × na 0.05 × 0.05 × na

**Abbreviations:** pd – phase difference (cf. Eq. (3.3)), PZ – piezoelectric, EM – electromagnetic, PN – pneumatic, na – not available, RO – readout, PE – phase-encode, SS – slice-select, SE – spin echo, GRE – gradient echo, 1D – single displacement field component, 3D – full displacement field.



## 6.2 Actuators

In this chapter, we will review actuator systems that have been used in clinical MRE. In general, MRE actuators can be categorized by the vibration source for generating oscillation and the transducer system for transmitting the shear waves into the target tissue. We will first recapitulate generalized criteria for the design of actuators in MRE and then review several systems proposed in the literature for clinical applications. This chapter is not concerned with actuators designed for preclinical applications. Two preclinical setups for MRE studies in the mouse brain are shown in Figure 14.3. For further reading, we refer to [151].

### 6.2.1 Technical Requirements

Vibration sources and transducers in MRE should avoid any unwanted interaction with the MRI fields. This specifically applies when imaging sequences with high demands on the homogeneity of the  $\mathbf{B}_0$  and  $\mathbf{B}_1$  fields are used. Time-varying magnetic fields emitted by the radiofrequency (RF) and gradient coils of the scanner can induce eddy currents in electrically conductive parts of the transducers. Eddy currents can cause image artifacts and heat the transducers. For these reasons, conductive materials should be avoided in the transducer design. Furthermore, MRI systems are susceptible to EMI between RF signals for imaging and any other unwanted RF signal of similar frequency. EMI can arise from electrical equipment outside the scanner room and be transferred into the MRI room through cables for the power supply or control of the actuator. Thus, all cables needed for MRE inside the scanner room must be electrically filtered to remove high-frequency components. The synchronization of actuator and MRI scanner is described in Section 6.1. Related to synchronization is the need of connecting the wave generator with the MRI control computer, which is preferably performed outside the MRI room. Taken together, most MRE actuators in clinical use have entirely nonmagnetic/nonmetallic transducers inside the MRI scanner and electrical power supply and control units placed outside the MRI room. Connections through the walls of the MRI room have to be either nonconductive (e.g., plastic tubes for air or hydraulic fluid) or fitted with electronic filters to avoid EMI-related image artifacts.

### 6.2.2 Practicality

In clinical MRE, typical excitation frequencies range from 20 to 100 Hz with excitation amplitudes up to 1 mm at the body surface. Under these conditions, safety problems due to large amplitudes and high excitation frequencies are unlikely [152]. A linear dynamic response of actuators is favorable for multifrequency MRE in a wide range of vibration frequencies. Sufficiently high wave amplitudes are required, which are normally only achievable by an efficient transfer of wave energy onto the body surface near the tissue of interest. Therefore, different applications require different transducer geometries and adaptation of the transducer position. Setup of actuator and transducer should be operator-friendly and easy to handle by physicians and radiographers in a clinical examination. The attachment of transducers to the body surface should

**Table 6.3** Mechanical actuators proposed in the literature for clinical MRE.

	Direct (d)	Rigid (r)	Pneumatic (p)	Hydraulic (h)	Invasive (i)
Lorentz coils (LC)	①				
Loudspeakers (LS)		②	③	④	
Piezoelectrical (PZ)	⑤	⑥			⑧
Pressurized air (PA)			⑦		

Power sources for motion generation vary along columns, and transmission systems vary along rows. The numbers refer to the rows of Table 6.4.

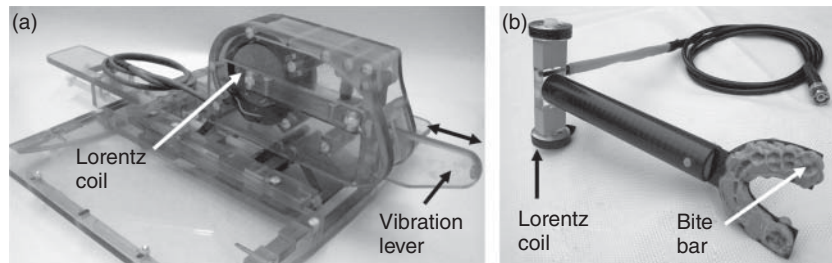
be well defined and reproducible in order to maintain high test–retest consistency. Platform-independent geometries are favorable for cross-platform and multicenter studies. Finally, yet importantly, all transducers in contact with the patient should not impose onerous vibrations. Patient comfort in MRE is highly demanded for both ethical reasons and to ensure cooperation between patient and operator.

### 6.2.3 Types of Mechanical Transducers

Four major principles of motion generation have been identified and described in the literature of clinical MRE: Lorentz coils (LC) inside the magnetic field of the MR scanner, modified loudspeakers (LS), piezoelectric elements (PZ), and pressurized air (PA). According to the literature, transmission of vibrational energy into the tissue under investigation can be classified into five principles: direct (d, i.e., no transmission, the actuator is placed within or near the field of view), rigid rods (r), pneumatic (p), hydraulic (h), and invasive (i). Table 6.3 lists mechanical transducers in MRE based on combinations of four power sources and five transmission systems. Table 6.4 shows example setups classified by the labels which correspond to the rows and columns of Table 6.3. For example, the label LS-p encodes a setup based on pneumatic (p) tubes connected to a loudspeaker (LS).

**Table 6.4** Example setups of actuators proposed in the literature for clinical MRE.

## ① LC-d



Lorentz coil-based actuators with direct transmission of vibrations. (a) Setup for prostate MRE providing transperineal excitation. (Image courtesy of Ramin Sahebjavaher and Tim Salcudean, University of British Columbia, Vancouver, Canada.) The black double arrow indicates the motion direction of the transducer. (b) Setup for brain MRE using a bite bar.

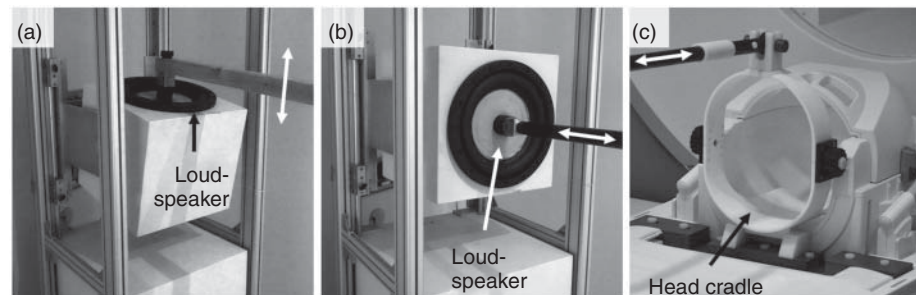
**Principle:** Lorentz force generated by alternating current in a coil which is placed inside the  $B_0$  field near the target tissue.

**App:** Prostate [153], brain [154], muscle [155], breast [156], liver [157].

**Pro:** Low hardware requirements, cost efficient, strong at higher field strengths, arbitrary waveforms possible, platform independent.

**Con:** Lorentz-coil perpendicular to  $B_0$  field, generation of heat, field distortions, electrical filtering of the power supply necessary.

## ② LS-r



Loudspeaker-based actuator with rigid transmission. (a) Vertical deflection, (b) horizontal deflection, (c) head cradle for brain MRE. White double-headed arrows indicate the motion direction of the transducer.

**Principle:** Vibration transferred from a modified loudspeaker to the body surface by a rigid rod.

**App:** Brain [74, 109], lung [85], heart [79], liver [89], muscle [47, 82], intervertebral disk [101], prostate [158].

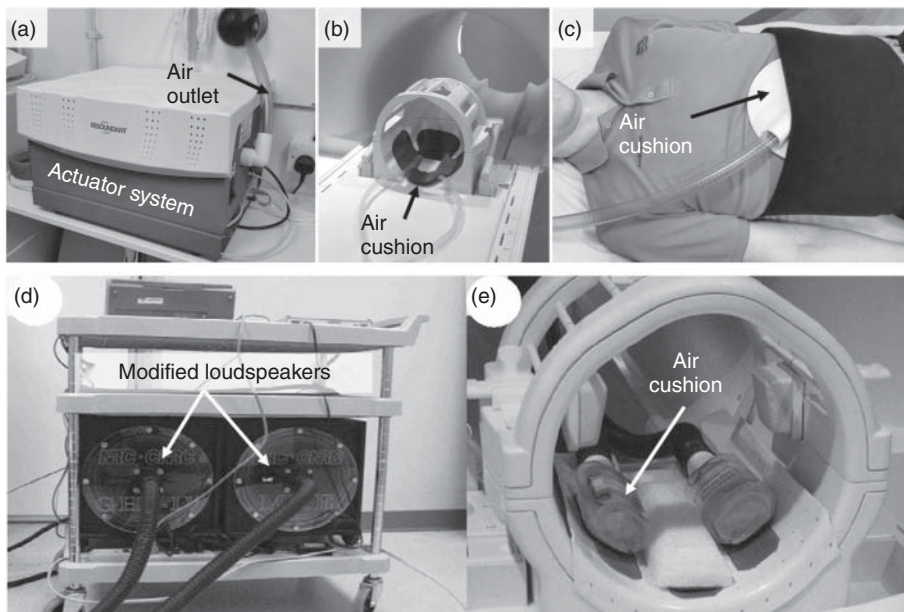
**Pro:** Transmission of arbitrary waveforms, flexible with different types of passive transducers, cost efficient, platform independent.

**Con:** Loudspeaker consists of metallic and magnetic parts, high demand on operator skills, electrical filtering of the power supply necessary.

(continued overleaf)

Table 6.4 (Continued)

## ③ LS-p



Loudspeaker-based actuators with pneumatic transmission. (a,d) Actuator systems for the generation of blast waves based on loudspeakers. (b,e) Setup for brain MRE. (c) Setup for liver MRE. (a–c) Resoundant®, Mayo Clinic, Rochester, MN, USA (courtesy of Neil Roberts, University of Edinburgh, Scotland, UK). (d,e) From [159] with permission.

**Principle:** Vibration transferred from a loudspeaker membrane to the body surface by pneumatic tubes.

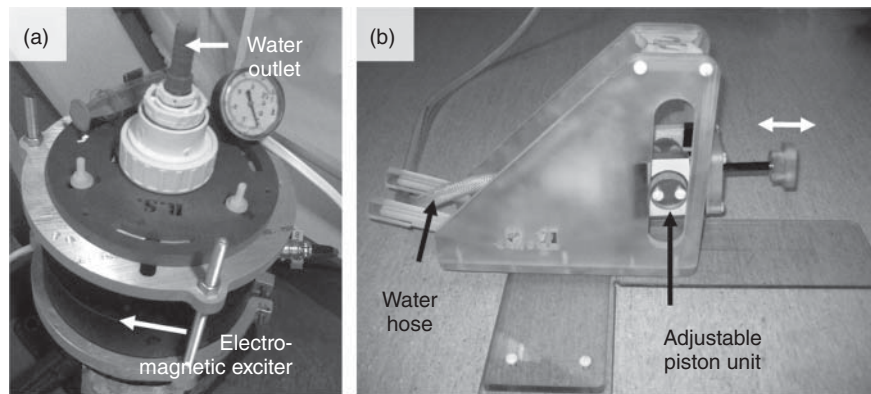
**App:** Brain [159, 160], lung [86], heart [161], aorta [162], liver [163], spleen [164], pancreas [165], kidney [108], uterus [166], muscle [167].

**Pro:** Flexible with different types of passive transducers; no electrical signals inside the MRI room, platform independent, FDA-approved device commercially available (Resoundant®), validated by a large number of clinical studies.

**Con:** Pneumatic tube requires wall ducts, possible interference of multifrequency wave signals.

Table 6.4 (Continued)

## ④ LS-h



Electromagnetic exciter (loudspeaker principle) with hydraulic transmission. (a) Hydraulic mechanism. (b) Transducer head for transperineal excitation of the prostate. The white double-headed arrow indicates the motion direction of the transducer. (Images courtesy of Ramin Sahebjavaher and Tim Salcudean, University of British Columbia, Vancouver, Canada.)

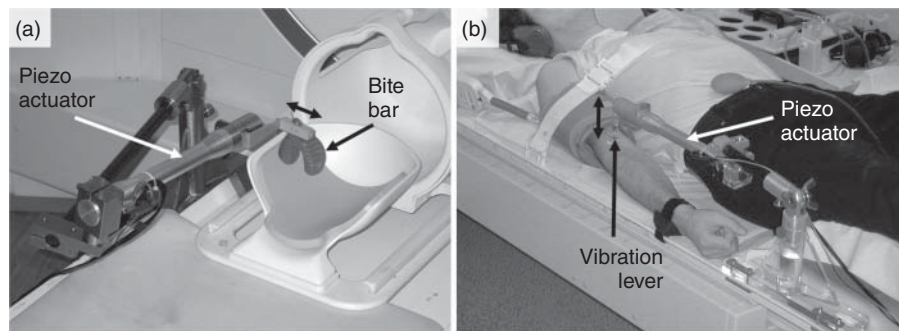
**Principle:** Vibration transferred from a loudspeaker membrane to the body surface by hydraulic tubes.

**App:** Prostate [106].

**Pro:** No electrical signals inside the MRI room, platform independent.

**Con:** Limited to lower vibration frequencies.

## ⑤ PZ-d



Piezoelectric actuator with direct transmission. (a) Setup for brain MRE using a bite bar. (b) Setup for MRE of the muscle. Black double-headed arrows indicate the motion direction of the transducer. (Images courtesy of Mark Ladd, Deutsches Krebsforschungszentrum Heidelberg, Germany.)

**Principle:** Vibration generated by a piezoelectrical actuator in vicinity to the target tissue.

**App:** Brain [169], muscle [170].

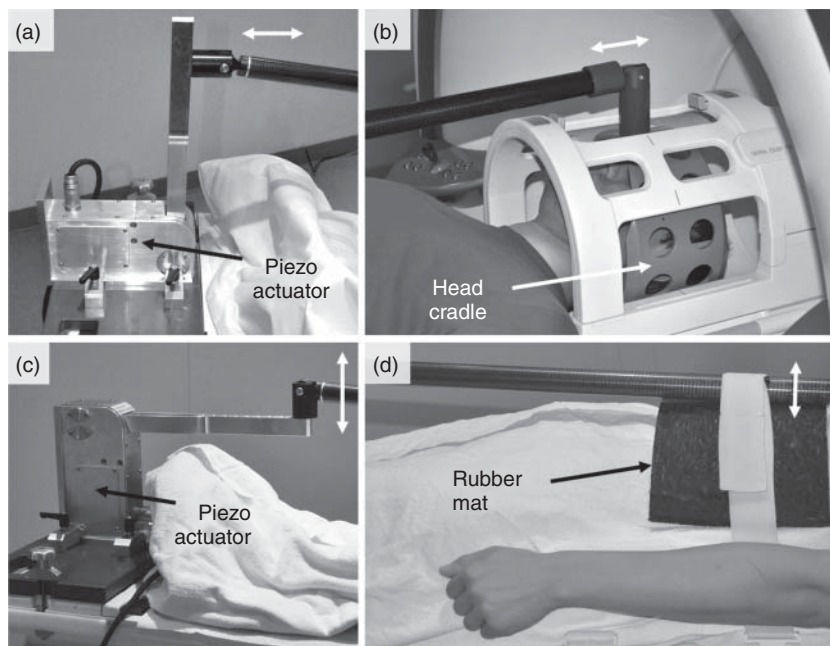
**Pro:** Arbitrary positioning relative to the  $B_0$  field, arbitrary waveforms possible, wide range of vibration frequencies applicable, platform independent.

**Con:** Metallic parts near the field of view, electrical filtering of the power supply necessary.

(continued overleaf)

Table 6.4 (Continued)

## ⑥ PZ-r



Piezoelectric actuator with rigid transmission. (a) Horizontal deflection of the vibration lever. (b) Setup for brain MRE using a head cradle. (c) Vertical deflection of the vibration lever. (d) Setup for liver MRE using a rubber mat. White double-headed arrows indicate the motion direction of the transducer.

**Principle:** Vibration transferred from a piezoelectrical actuator to the body surface by a rigid rod.

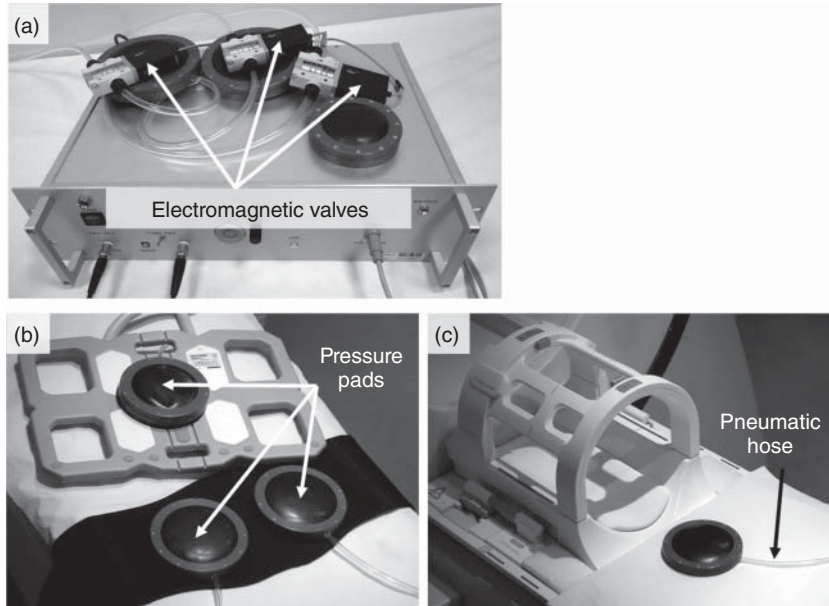
**App:** Brain [108], liver [95], spleen [98], kidney [102], uterus [105], prostate [171].

**Pro:** Transmission of arbitrary waveforms, wide range of vibration frequencies applicable, flexible with different types of passive transducers, operator friendly.

**Con:** Adaptation to different platforms necessary, filtering of the power supply necessary.

Table 6.4 (Continued)

## ⑦ PA-p



Pressurized air-based actuator with pneumatic transmission and electromagnetic valves. (a) Control unit, electromagnetic valves, and pneumatic hoses. (b) Setup for abdominal MRE using three pressure pads. (c) Setup for MRE of the brain with remote thorax-based actuation.

**Principle:** Pillow- or drum-type passive actuators are driven by pulsed pressurized air which is controlled by electromagnetic valves.

**App:** Brain [172], liver [172], prostate [173].

**Pro:** Flexible with different types of passive transducers, operator friendly, cost efficient, platform independent, high-power mechanical forces, operation from outside or inside of the MRI room feasible.

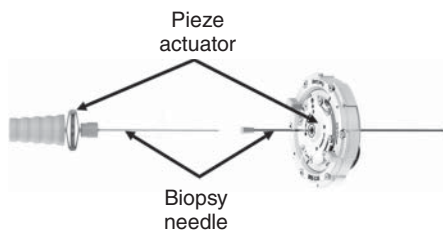
**Con:** Single-frequency rectangular pulses, forerun of 1–2 s to reach a steady state.

(continued overleaf)



Table 6.4 (Continued)

## ⑧ PZ-i



Piezoelectrical actuators with invasive transmission for interventional MRE. Both devices show a comparable technical setup consisting of a biopsy needle directly connected to the actuator unit. (Images courtesy of Nadège Corbin and Jonathan Vappou, University of Strasbourg, France.)

**Principle:** Invasive needle vibrated by a piezoelectrical actuator.

**App:** MRE-controlled MRI-guided thermal ablation [174].

**Pro:** Point source, directly at region of interest, transmission of arbitrary waveforms, wide range of vibration frequencies applicable, platform independent.

**Con:** Invasive, high demand on the skills of the operators, metal parts near the field of view, filtering of the power supply required.

---

App: application examples, Pro: advantages, Con: disadvantages. The number and label in the left column refers to Table 6.3.



## 7

## MRE Protocols

The basic types of magnetic resonance (MR) sequences used for MRE have been introduced in Section 3.4. Most MRE exams nowadays use a variant of FLASH (Section 3.4.1) or echo-planar imaging (EPI) (Section 3.4.3, segmented or single-shot), whereas other sequences, such as bSSFP (Section 3.4.2), were mainly used in the past. We present an overview over typical MRE sequences in Table 7.1. This table is by no means comprehensive, since in most occasions a basic sequence is tailored toward the specific requirements of an investigation, leading to a plethora of organ-specific MRE sequences. Discussing all of them is far beyond the scope of this book.

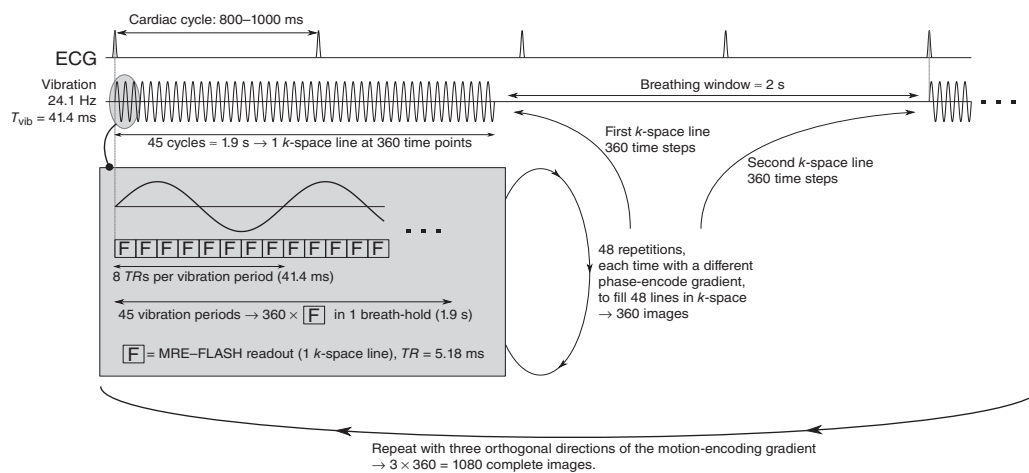
A *protocol* is a set of acquisition parameters that are used in conjunction with a specific MRI sequence to perform an MR scan. Protocol parameters are optimized toward a specific objective, such as maximizing contrast or minimizing acquisition time. By using different protocols for different organs, the same basic MR sequence can be used for multiple exams with widely differing demands on sequence timing. In MRE, protocols have to account for the amount of data required for subsequent parameter reconstruction (i.e., number of wave phases, field components, and drive frequencies), the spatial resolution, echo time (which mainly determines the SNR), and total acquisition time. Virtually every MRE study uses a different protocol that has been optimized with respect to some study-specific criteria, so that it is impossible to provide an exhaustive list of MRE protocols. Therefore, we will present three exemplary protocols that show how protocols can be used to adapt a sequence to the requirements of examining a specific organ, and refer to specialized literature for information on specific protocols.

As one example of how a protocol is used to modify a sequence to accommodate a particular set of demands, we present a detailed diagram of a FLASH-based MRE sequence for MRE of the myocardium (heart muscle) in Figure 7.1. Because of the rapid pumping motion of the heart, fast data acquisition and high temporal resolution are necessary to track the change of myocardial stiffness over the cardiac cycle. In order to fulfill this requirement without excessive electrocardiogram (ECG) triggering, the sequence acquires 360 instances of the same  $k$ -space line in quick succession. The process is repeated for every single  $k$ -space line. This contrasts most other MRE sequences, which tend to acquire a full  $k$ -space representing one point in time, before scanning the  $k$ -space corresponding another time point. Furthermore, the timing in the case of the cardiac FLASH sequence is fully determined by the duration of the FLASH kernel, leading to a  $TR$  of 5.18 ms. This duration determines virtually all other timing parameters: The temporal resolution is equal to  $TR$ , the vibration period is set

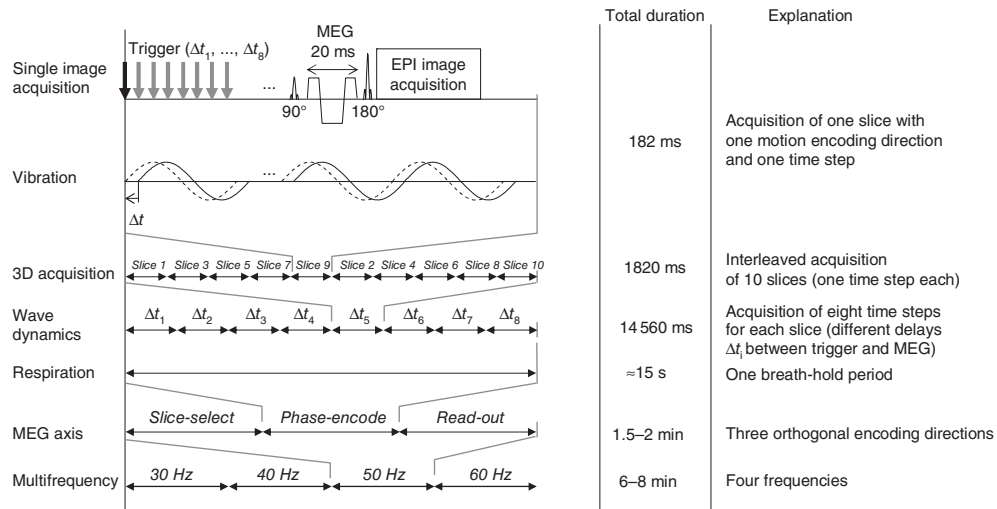
**Table 7.1** The most common sequences used for MRE, and some of their applications in human subjects. Note that the last column only presents a tiny fraction of all the investigations that have been performed and published thus far. Further details on MRE studies in various organs are presented in Part IV.

Sequence type	Published	Studied organs (selection)
Gradient echo (GRE)/FLASH	[178] [179]	Brain [180] Biceps brachii [181] Leber [182]
Balanced SSFP	[183] [184] [17]	Biceps brachii [17] Liver [185]
Segmented EPI	[39]	Biceps brachii [39]
Singleshot EPI	[186]	Brain [186] Liver [187]
Spiral EPI	[22]	Brain [22]
DENSE <sup>a)</sup>	[189]	Heart [189]

- a) *Displacement encoding with stimulated echoes* [188] uses two monopolar MEG lobes to encode motion. Between the two MEGs, transverse magnetization is flipped back to the longitudinal axis to prevent  $T_2$  signal decay.



**Figure 7.1** Sequence diagram of the FLASH-based sequence used for cardiac MRE [177]. The symbol  $F$  indicates the readout of a single  $k$ -space line with a motion-sensitized FLASH kernel, as shown in Figure 3.8, but without the trigger and the delays preceding the RF pulse. Each line in  $k$ -space is sampled at 360 time points, over approximately two cardiac cycles. The process is repeated for each of the 48  $k$ -space lines. Using GRAPPA with an acceleration factor of 2 allows for the reconstruction of 96  $k$ -space lines. The measurement is performed thrice, for three different directions of the motion-encoding gradient to sample all three Cartesian components of the displacement field.

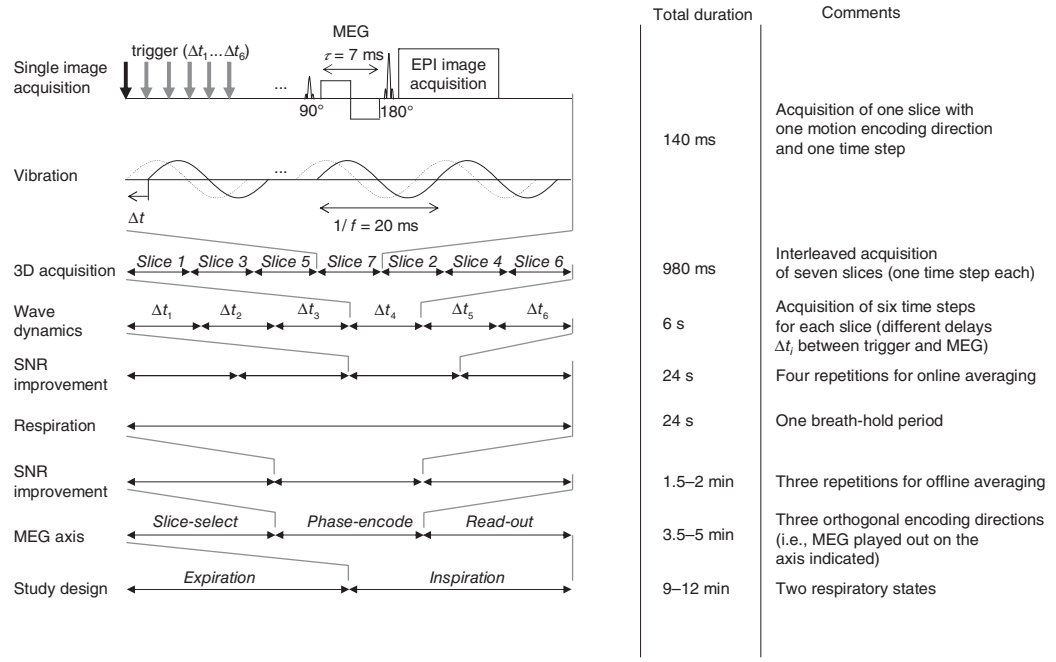


**Figure 7.2** MRE protocol of an EPI-based multifrequency exam of human liver. Each row represents a concatenation of several instances of the process illustrated in the row above. Within one breath-hold period of 15 s (“respiration”), the whole volume, consisting of 10 slices, is sampled eight times to obtain eight different points of the oscillation cycle (“wave dynamics”). A total of 12 breath-hold intervals is required to acquire three Cartesian components of the displacement field (“MEG axis”) and four frequencies. Total acquisition time is 6–8 min, depending on the duration of the recovery phases between breath-holds. (Hirsch 2014 [98]. Reproduced with permission of Wiley.)

to  $T_{\text{vib}} = 8 \cdot TR = 41.4$  ms (so that one vibration cycle is sampled with eight points), and the duration of the breath-hold is also a multiple of  $TR$ . In most other sequences,  $TR$  is decoupled from the vibration period, and synchrony is achieved via triggering and delays embedded in the sequence.

In Figures 7.2 and 7.3, we present two sample protocols for MRE exams of the liver [98] and lung [85], respectively. In both cases, MRE data acquisition has to be split into several breath-hold intervals, since respiratory motion would cause artifacts. MRE of the lung has to deal with the additional challenge that several signal averages are required because of the inherently weak MR signal attainable from lung due to its low density.

Other examples of highly customized sequences or acquisition schemes are published in [175] for MRE of the lung, and in [176] for the investigation of brain pulsation.



**Figure 7.3** MRE protocol of an EPI-based exam of human lung at a single-vibration frequency of 50 Hz. Within one breath-hold period of 24 s (“respiration”), the imaging volume, consisting of six slices, is scanned 24 times to acquire six points of the oscillation cycle (“wave dynamics”) and four repetitions for online signal averaging. This process is repeated thrice for offline averaging (thus yielding 12 signal averages). The measurement is then repeated to acquire three Cartesian components of the displacement field (“MEG axis”), and finally two different respiratory states are probed. The total measurement time is 9–12 min (depending on the duration of the recovery phases between breath-holds), split across 18 breath-hold intervals. The high number of signal averages is necessary since the lung, due to its low density, yields a very weak MR signal with intrinsically low SNR. (Hirsch 2014 [85]. Reproduced with permission of Wiley.)

## 8

### Numerical Methods and Postprocessing

#### 8.1 Noise and Denoising in MRE

*This chapter was coauthored by Eric Barnhill from the Department of Radiology, Charité – Universitätsmedizin Berlin, Berlin, Germany.*

The treatment of noise is a central issue in MRE. Denoising increases SNR of elastograms, expands the feature space resolution, and provides numerical stability for wave inversion. However, denoising techniques poorly suited to the data will achieve this stability by removing valuable information. Appropriately chosen denoising techniques will retain the structures in the data that provide meaningful information, so that this information informs the inverse problem result. Denoising in MRE must therefore not only provide stable and reproducible results, but also deliver results that relate convincingly to other available information and aid the goals of clinical diagnosis or experimental physiology.

The signal processing definition of noise is unwanted signal [190]. This is a broader definition than the colloquial use of the term, which refers to *sensor noise*. Sensor noise is stochastic and is generally high frequency with a smooth distribution, such as Gaussian, Poisson, or Rician noise. The impact of sensor noise on solutions of the inverse problem in MRE will be discussed in Chapter 10.1.

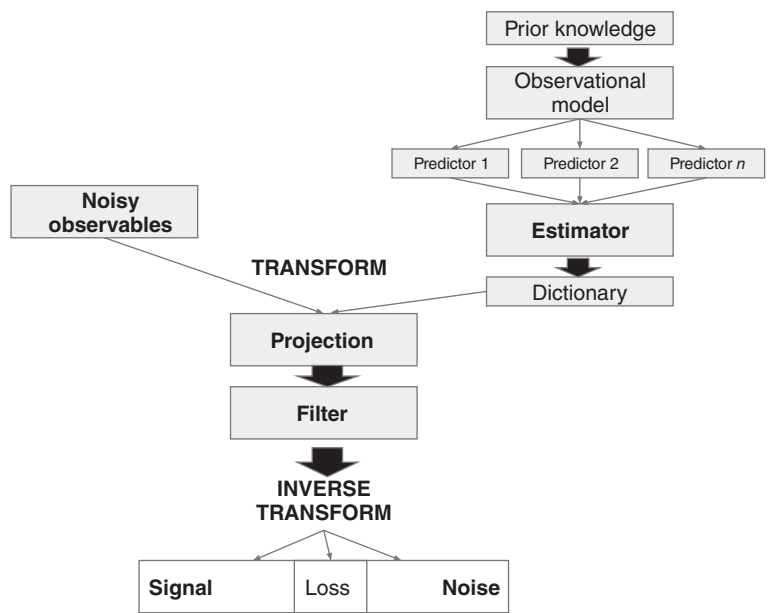
##### 8.1.1 Denoising: An Overview

In recent years, the field of denoising has progressed rapidly as it has fused signal processing with statistics. Denoising is formulated as a statistical process, in which the denoising method is a statistical *estimator* used to reconstruct an unknown signal, corrupted by noise, with minimal *risk* (i.e., minimal expected loss) [191]. This can be formulated as

$$\mathbf{y} = f\{\boldsymbol{\phi}; M\}, \tag{8.1}$$

where  $\mathbf{y} \equiv y_{1\dots m}$  is a set of noisy observations,  $\boldsymbol{\phi} \equiv \phi_{1\dots n}$  are the unknown parameters of the system, and  $M$  is an observational model linking  $\mathbf{y}$  to  $\boldsymbol{\phi}$ . We wish to find estimated parameters  $\hat{\boldsymbol{\phi}}_{1\dots n}$  to minimize the risk parameter  $R(\boldsymbol{\phi})$ , where

$$R(\boldsymbol{\phi}) = \sum_1^n v\{\hat{\boldsymbol{\phi}}; \boldsymbol{\phi}\} \tag{8.2}$$



**Figure 8.1** Process of denoising. Prior knowledge is used to construct a dictionary of predictors, known as an estimator. The noisy observables are then projected onto the estimator space to sparsify the data. A filtering or thresholding operation suppresses noise while retaining signal, and the noise-reduced signal is recovered through an inverse transform.

and  $v$  is a loss function measuring the error (most commonly, sum of squares of the residuals).

This estimation process has four steps, which we will present in both abstract mathematical form and Fourier transform terminology, which is the most ubiquitous filtering method. Figure 8.1 illustrates the general concept and Figure 8.5 visualizes the Fourier transform-based process, which will be discussed in more detail later in this section.

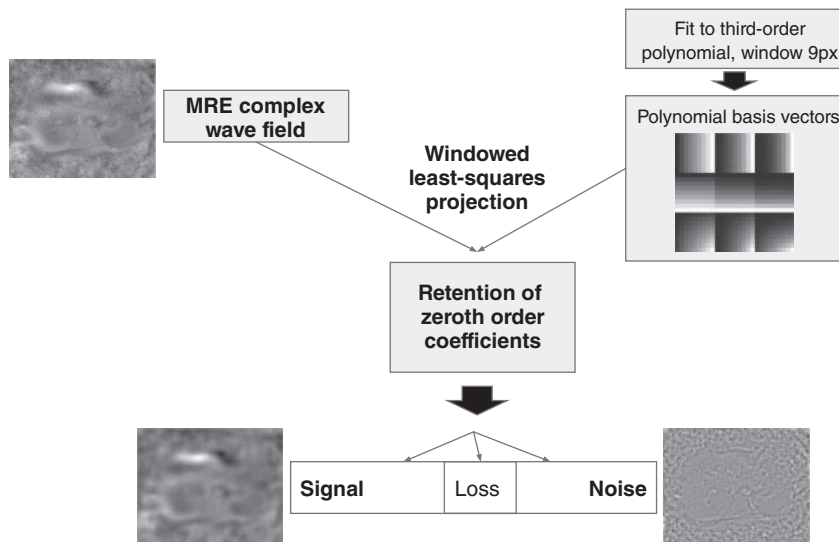
- 1) *Prior knowledge* about the signal from the observational model is used to choose, as an estimator, a *dictionary* of functions,  $\Phi_{1\dots p}$  that are well suited to the unknown signal. For the Fourier transform approach, the dictionary consists of harmonic functions.
- 2)  $\Phi$  is used to *transform* the observations by the projection  $\langle \mathbf{y}, \Phi \rangle \rightarrow F_{\mathbf{y},\Phi}$ . The goal of this transform is to make the information in the image *sparse*: the sparser the information, the lower the loss of the filtering operation and the lower the risk of the estimator. In the Fourier case, this is achieved by applying a discrete Fourier transform (DFT), most commonly as a fast Fourier transform (FFT).
- 3) Noise is separated from signal using a *filtering* operation  $F \rightarrow \hat{F}$ . A *filter* is defined as a process that suppresses some components of a signal but retains others. If the Fourier transform is used, this step corresponds to multiplying the  $k$ -space representation of the data with a function that amplifies or attenuates specific frequency bands.
- 4) Frequently, the noise-reduced parameters  $\hat{\phi}$  are then recovered through inverse transform of the thresholded data  $\langle \hat{F}, \Phi^{-1} \rangle \rightarrow \hat{\phi}$ . This corresponds to applying an inverse DFT to the modified  $k$ -space.

This framework will be illustrated through the use of three denoising approaches found in the MRE literature: least-squares polynomial smoothing using a Savitsky–Golay filter,  $k$ -space filtering using a band-pass filter, and multiresolution analysis (MRA), a method of data decomposition applying the fast wavelet transform (FWT), using complex dual-tree wavelets (CDTWs) with soft thresholding.

### 8.1.2 Least Squares and Polynomial Fitting

The ubiquitous technique of ordinary least squares (OLS) may be the most widely used form of statistical estimation, and has been used for smoothing in MRE data as well [192–194]. In a simple case common to statistics, a series of two-dimensional data points are regressed to a single line to identify significant trends. In OLS more broadly, the unknown signal is assumed using prior knowledge to be a linear, low-rank polynomial, and  $\Phi$  is a dictionary of low-rank polynomials. The data are transformed by linear projection onto the polynomial space, with  $\hat{\phi}$  determined to be the linear combination of chosen polynomial functions yielding the smallest loss  $\nu$ , with  $\nu$  the  $L^2$  norm.

To denoise data, polynomial fitting is done locally within a sliding window, modeling each window of  $m$  points in the data as a polynomial of degree  $q$ . This case is shown in Figure 8.2. Such least-squares smoothing gained widespread use after Savitsky and Golay [195] identified that the procedure could be performed using a convolution or weighted sum, about which more in the next section, and this approach is known as a Savitsky–Golay filter. A particular strength of this filter is that images are smoothed while maintaining peak values, in contrast to, for example, a moving average, which reduces the values at peaks. (However, a moving average is, technically, a Savitsky–Golay



**Figure 8.2** Schematic of denoising applied to Savitsky–Golay filtering. Prior knowledge models the data as a low-rank polynomial across a window. In this case, the data are modeled as third-order over a  $9 \times 9$  window. This yields a dictionary of ten  $9 \times 9$  basis vectors (DC not shown). Each sliding window is projected onto the polynomial basis. The data are then smoothed by retaining the zeroth-order coefficient at the center.

filter of order 1, and therefore also well described within the framework of least-squares estimators.) One way to explain this is to note that the filter is zero phase and flat in the passband, preserving lower-frequency features exactly [196]. This can be seen in the filter's frequency response, about which more information is given below.

### 8.1.3 Frequency Domain ( $k$ -Space) Filtering

The most common form of denoising, and indeed signal manipulation in general, comes from filtering in the frequency domain, with the 2D form known in MRI as  $k$ -space (see Section 2.1). While the reasons for this are many, here it is most useful to focus on the relationship of the Fourier transform to linear time-invariant (LTI) systems. Indeed, the term “filter” is often used in an offhand way to refer to LTI systems. The “time” portion of the LTI comes from audio-processing and, in the context of images and  $k$ -space, the system might be more appropriately called linear shift invariant. An LTI system produces as output a one-to-one, linear map (in other words, the transformation consists entirely of additions and multiplications by scalar) and is implemented identically at all positions in the input (hence the term shift invariant). An LTI mapping can always be expressed as a constant-coefficient difference equation (CCDE) [197]:

$$\sum_{i=0}^{N-1} a_i y[n-i] = \sum_{j=0}^{M-1} b_j x[n-j], \quad (8.3)$$

for input signal  $x$ , output signal  $y$ , and  $M$  and  $N$  input ( $a$ ) and output ( $b$ ) coefficients that are combined to produce  $y$ . If the left-hand side only consists of  $a_0$ , the system is known as a finite impulse response (FIR) filter and the response at any point can be completely characterized by a finite set of coefficients. If there are more  $a$  terms, then the filter is recursive to some degree, dependent on all previous coefficients, and is known as infinite impulse response (IIR).

An FIR filter, then, replaces each single data point with a position-independent weighted average over a neighborhood of multiple data points. As a result of this, FIR filters can be completely characterized by their response to a single unit spike (or delta function) in the data. This response is known as the *impulse response*. An FIR filter can be implemented by passing the impulse response function, known as a *kernel*, over every position in the image, replacing each pixel with a weighted average of its neighbors as specified by the impulse response. This is known mathematically as a *convolution*, although full treatment of convolution is beyond the scope of this book.

Among the many strengths of FIR filters are that such filters can be implemented algorithmically, the computation is linear to the input, the response is stable for any finite input, and the phase of the response is linear, which means that features can be expected to be preserved.

Some common FIR filtering operations in MRI and MRE are discussed below.

#### 8.1.3.1 Averaging

In the simplest case, a smoothing filter applied to a one-dimensional noisy signal replaces each data point with the average over the point and its nearest left- and right-hand-side neighbors. One rationale behind this concept is that the signal at adjacent data points is usually correlated, whereas the noise is not, so that taking the average will emphasize the signal while reducing noise.



Averaging models the measured signal,  $S_i$ , as the sum of a coherent signal  $s_i$  and a noise contribution  $n_i$ :

$$S_i = s_i + n_i, \quad (8.4)$$

where the index  $i$  enumerates the acquired data points. It is further assumed that noise is symmetrically distributed around zero, so that its mean over a large number of data points vanishes:

$$\langle n_i \rangle_i = 0. \quad (8.5)$$

If sampling is dense enough, the true signal does not change much between adjacent data points:

$$s_{i-1} \approx s_i \approx s_{i+1}. \quad (8.6)$$

We can therefore approximate  $S_i$  with the average over the three points  $i - 1$ ,  $i$ , and  $i + 1$ :

$$\begin{aligned} \check{S}_i &\equiv \frac{1}{3}(S_{i-1} + S_i + S_{i+1}) = \frac{1}{3}(s_{i-1} + s_i + s_{i+1}) + \frac{1}{3}(n_{i-1} + n_i + n_{i+1}) \\ &\approx \frac{1}{3} \cdot 3s_i + \frac{1}{3}(n_{i-1} + n_i + n_{i+1}) \\ &= s_i + \frac{1}{3}(n_{i-1} + n_i + n_{i+1}). \end{aligned} \quad (8.7)$$

Because of Eq. (8.5), the sum of three independent noise samples is probably smaller than each sample separately.<sup>1</sup> If the variation of the true signal between adjacent sample points is smaller than the average variation of noise,  $\check{S}_i$  is a better approximation to  $s_i$  than  $S_i$  alone.

More generally, we can express the smoothing of a discrete signal  $\mathbf{S} = [S_i]$  (represented as a row vector) as a convolution with a filter kernel. In the above example, the filter kernel is

$$\mathbf{K} = \left[ \frac{1}{3}, \frac{1}{3}, \frac{1}{3} \right]. \quad (8.8)$$

In order to express a higher-dimensional convolution conveniently, *stencil notation* is used for the kernel. For example, the stencil notation for a  $3 \times 3$  moving average window would be:

$$\frac{1}{9} \begin{bmatrix} 1 & 1 & 1 \\ 1 & 1 & 1 \\ 1 & 1 & 1 \end{bmatrix}. \quad (8.9)$$

In this case, the data point being convolved lies in the center of the stencil, and is being averaged with all the values around it, which are given equal weight. In order not to create signal gain, the sum of all elements of the kernel has to be equal to one:

$$\sum_{j=-p}^p K_j \stackrel{!}{=} 1. \quad (8.10)$$

<sup>1</sup> The correctness of this statement actually depends on the cumulative distribution function of noise. In some cases, averaging over more than three data points is necessary to effectively decrease the noise amplitude.

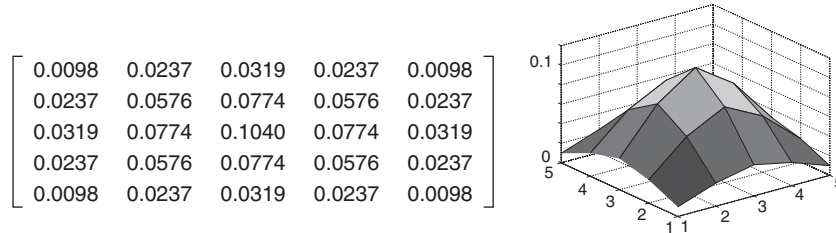


Figure 8.3 Stencil and surface plot for  $5 \times 5$  Gaussian kernel with  $\sigma = 1.3$ .

Filters where all elements are equal, such as Eq. (8.9), are referred to as *boxcar filters*, due to the similarity of their graphical representation with a railroad boxcar. However, for many applications, other filter shapes exhibit more desirable properties than a boxcar filter. For example, Gaussian-type filter kernels are ubiquitous in signal processing, with a shape corresponding to a discrete sampling of the Gaussian function

$$g(x) = \frac{1}{\sqrt{2\pi}\sigma} \cdot e^{\left(-\frac{x^2}{2\sigma^2}\right)}. \quad (8.11)$$

A 2D Gaussian kernel, assuming a  $5 \times 5$  neighborhood and a standard deviation of 1.3, is specified by the stencil and surface plot shown in Figure 8.3.

It can be seen in this case that the center is weighted more than the periphery and that values are exponentially decreasing with distance as specified in Eq. (8.11). However, time domain or image domain stencils are a poor representation to analyze the strengths and weaknesses of FIR filters. This is why they are generally analyzed in the Fourier domain.

### 8.1.3.2 LTI Filters in the Fourier Domain

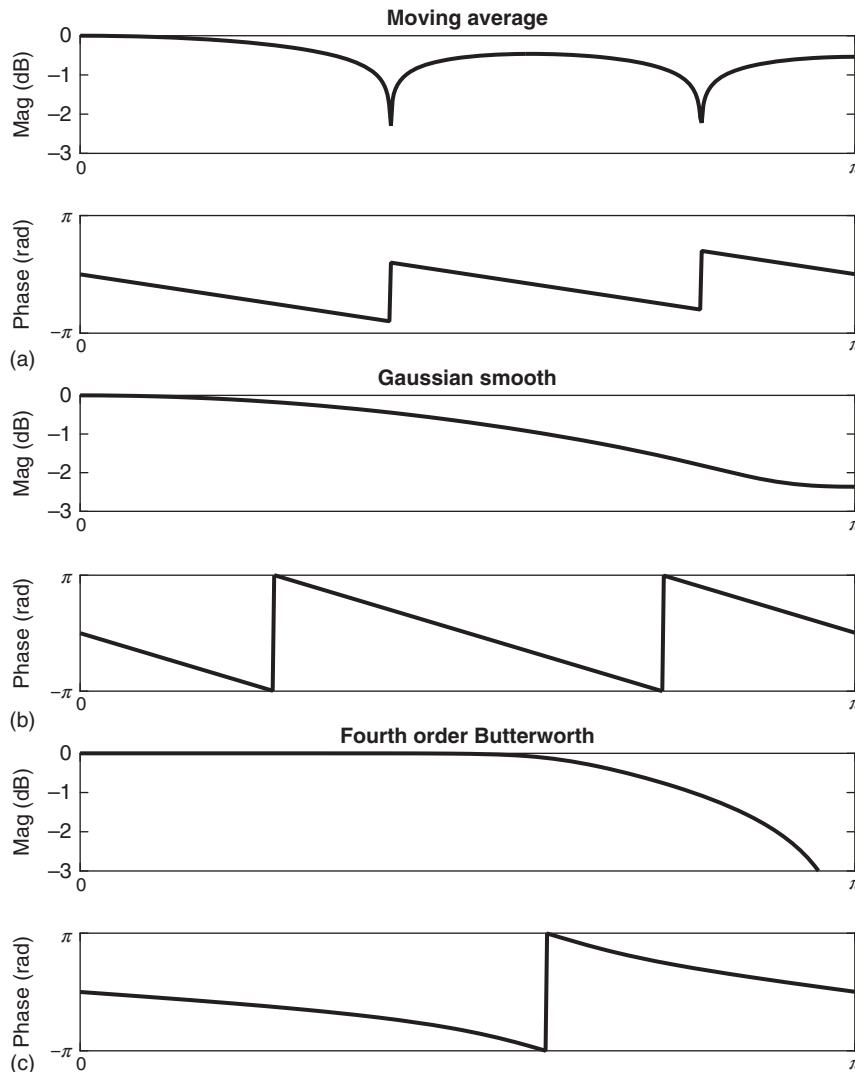
The Fourier transform diagonalizes LTI systems; that is to say, it transforms them into their sparsest basis, because the Fourier basis vectors are eigenvectors of circulant matrices, and LTI operators are always circulant. Resulting from this, convolution in the time domain, due to the properties of Fourier integrals, becomes multiplication in the Fourier domain, that is [191]

$$f_1(t) \star f_2(t) = \mathcal{F}^{-1} \left[ \tilde{f}_1(\omega) \cdot \tilde{f}_2(\omega) \right], \quad (8.12)$$

where  $\star$  is the convolution operator and  $\tilde{f}$  is the Fourier transform of  $f$ . With an LTI system, Fourier transformation turns an integral into a multiplication, or calculus into algebra.

LTI systems are analyzed in the Fourier domain by evaluation of their *frequency response* (as opposed to their impulse response in the time domain). The frequency response is generated via a discrete time Fourier transform (DTFT) analysis, which is beyond the scope of this section; the reader is referred to [197] for a detailed introduction. However, even without detailed understanding of the theory, frequency response plots are intuitive and useful for filter analysis.

A frequency response plot ranges from 0 to  $\pi$ , with 0 representing a steady constant or DC value, and  $\pi$  being the highest-frequency signal possible within the constraints of the Nyquist sampling theorem, for example, a vector alternating zeros and ones. Both magnitude and phase are plotted, with the former in decibels (dB) and the latter in



**Figure 8.4** Frequency response plots of three common filters: (a) Five-tap moving average filter; (b) Gaussian smoothing kernel, width 5,  $\sigma = 1.3$ ; (c) Fourth-order Butterworth filter, with normalized frequency cutoff of 0.6.

radians (rad). Such a plot shows the impact of any LTI on the frequency content of the image. Three relevant frequency response plots are shown in Figure 8.4 and discussed below:

- Plot (a) is the frequency response of a five-sample moving average. While averaging is straightforward in the time domain, the frequency response plot shows complications that can cause artifact. First, the “in-spectrum loss,” or attenuation of frequencies in the passband, is considerable, suggesting that a moving-average filter will remove information even within the frequencies of interest. Second, the “side lobes” found in the higher frequencies of the plot show that certain higher frequencies will be poorly

- suppressed, resulting in, for example, ringing effects. However, the phase is linear in the passband (from 0 to the first minimum in the magnitude plot), meaning there will be no distortion from this filter.
- Plot (b) is the Gaussian filter of the same width, with  $\sigma$  of 1.3. The frequency response of the Gaussian filter is considerably better behaved. There are no side lobes, such that the higher the frequency, the more it is suppressed, and this will eliminate ringing. The phase is linear, ensuring no distortion. However, the in-spectrum loss is substantial, making the Gaussian a poor choice to isolate frequency content of interest; the Gaussian affects all frequencies of the image and is thus not well “targeted.”
  - Plot (c) is a fourth-order Butterworth low-pass filter. The Butterworth filter, which will be discussed more below, is IIR, with both  $a$  and  $b$  terms in its CCDE formulation. The Butterworth shows superior performance in the frequency response magnitude: the passband is flat, which means that there is near-complete preservation of all information at the frequencies of interest, the transition region is steeper, and the higher frequencies are better suppressed. However, the phase is not linear, which means that there will be distortion of features in the image. An example of such distortion is shown in the later wavelet–Fourier comparison in Figure 8.7.

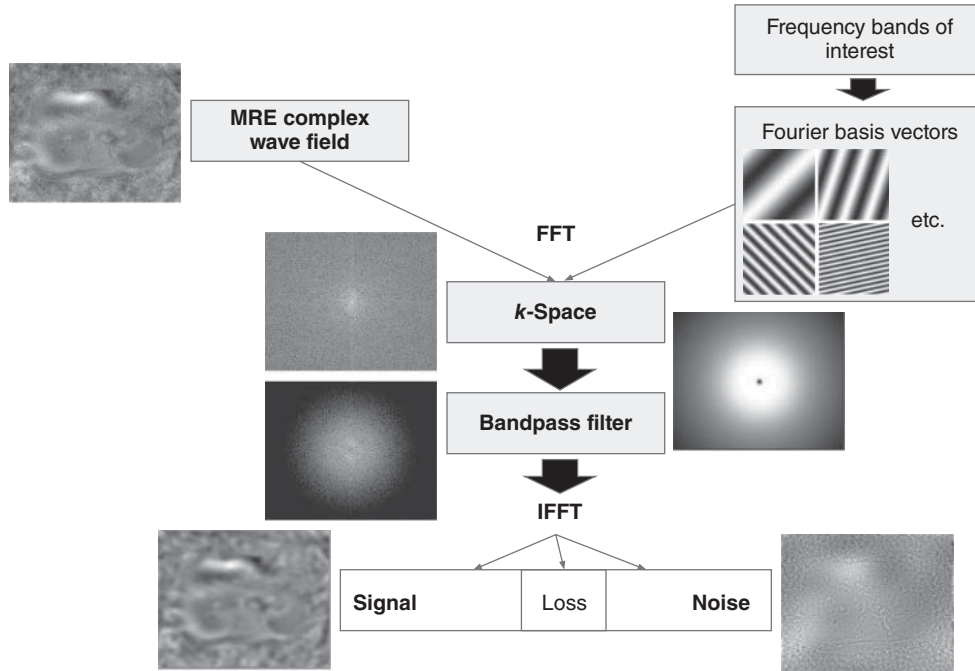
### 8.1.3.3 Band-Pass Filtering

Band-pass filtering is a frequency response-oriented approach to filtering, in which optimal filters are chosen to “pass” or “stop” various frequency content. Desired filters generally preserve the frequencies of interest as much as possible (i.e., have the flattest passband), minimize the transition band (where frequencies are semi-suppressed), minimize the “error” (passed frequencies in the stopband and vice versa), and/or have linear phase response. Filter schemas containing all of these properties are called “ideal” filters, but practical implementations require weighting some of these concerns over others. In some cases, particularly IIR filter design, the filter does not have a convenient algorithmic representation in the time domain (or image domain) and image filtering is designed in  $k$ -space. The Butterworth filter, which has a maximally flat passband for a given order, is one such filter.

$k$ -Space filtering is fit into the initial denoising schematic in Figure 8.5, using the Butterworth band-pass filter as the example filtering operation. In this case, the *prior knowledge* is that only certain spatial frequencies are of interest, which we wish to isolate. The Fourier basis is then used as the *dictionary*, and the data are projected onto it by Fourier transform. Here a 2D fourth-order Butterworth band-pass filter is then applied to the data using an element-wise multiplication. (All  $k$ -space images in the schematic are log-magnitude). The resultant image is then inverse Fourier-transformed, resulting in the smoothed “signal” image at the left-hand side and the “noise” image, which can be seen to contain both very high- and very low-frequency components, at the right-hand side.

### 8.1.4 Wavelets and Multi-Resolution Analysis (MRA)

For smooth functions, a dictionary of Fourier basis vectors will be an optimal minimax estimator for a given dictionary size [191, 198]. However, not only are images rarely smooth, but the features of greatest interest in images are often edges, textures, and



**Figure 8.5** Denoising in  $k$ -space. The dictionary used is the Fourier basis vectors in 2D; real components of a small sample are shown. The filtering operation is a Butterworth filter. This results in smoothed data with very small and very large frequencies removed.

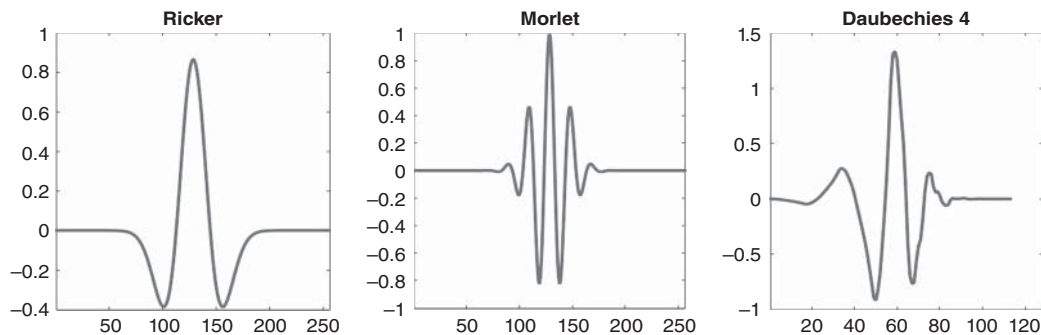
other sharp transitions that are a poor fit for a Fourier basis. Lowering the estimator risk requires sparser dictionaries. This is of importance for MRE, as MRE images contain piecewise-smooth waves with discontinuities at boundaries and interfaces. As illustrated in Figure 8.7 below, images with edges or discontinuities are not sparse in the Fourier domain and hence frequency-based denoising is a poor fit for these images. As many images contain discontinuities as features of interest, wavelets provide an appealing alternative.

A simple explanation of wavelets contains two parts. (1) A wavelet is a wavefunction with finite local support. That is, it generally appears as a single isolated wave. Some examples are shown in Figure 8.6. (2) In wavelet transforms, the idea of *frequency* is replaced with the more general idea of *scale*. A wavelet is dilated to varying scales in octave relation ( $2^j$  with  $j$  an integer), then translated like any other sliding window operator such as a moving average. A wavelet dictionary can thus be defined as [191, 199]:

$$D = \left\{ \psi_{j,n}(t) = \frac{1}{\sqrt{2^j}} \psi \left( \frac{t - 2^j n}{2^j} \right) \right\}, \quad (8.13)$$

where  $n$  represents the translation of the window relative to position  $t$  and  $j$  is the scaling coefficient that dilates or expands the wavelet to a given scale.

To complete the MRA, a wavelet is complemented by a scaling function  $\phi$  at the lowest level chosen for the analysis. The relationship between  $\phi$  and  $\psi$  is beyond the scope of this chapter, but can be found in any foundational textbook on signal processing,



**Figure 8.6** Examples of three commonly used wavelet functions. As the name suggests, they have the appearance of isolated waves. Wavelets are a sparser basis than the frequency domain for piecewise smooth images with discontinuities.

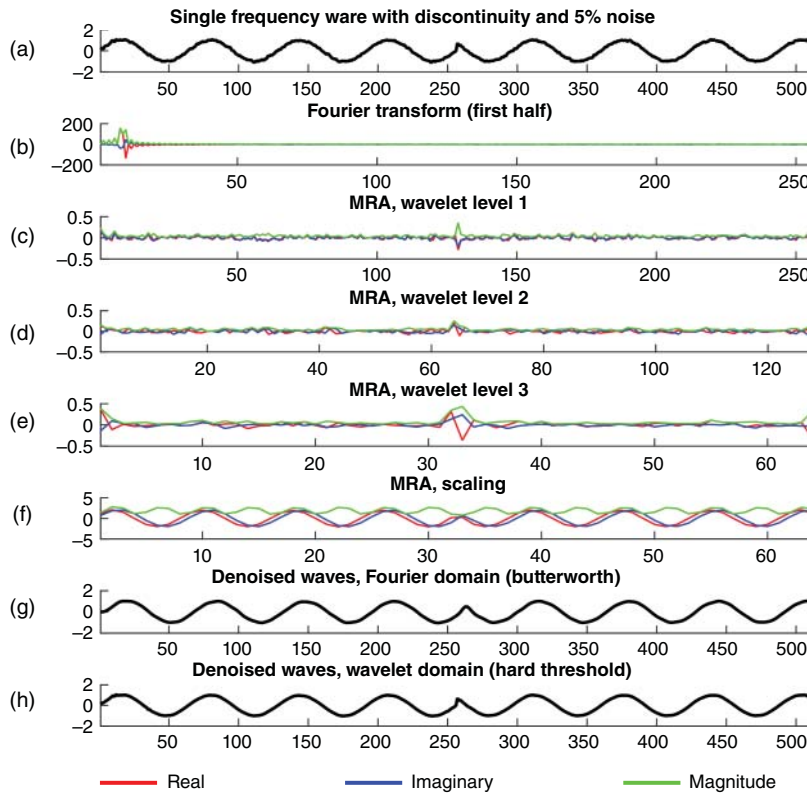
for example, [199] or [191]. For the purposes of the present discussion, the MRA takes the form of high-pass coefficients at multiple scales, and a single low-pass image at the coarsest scale, which together critically sample the image in the wavelet basis and enable its perfect reconstruction.

The advantages of wavelet bases for piecewise continuous images are shown in Figure 8.7. In Figure 8.7a, a single-frequency wave is plotted with a single discontinuity and 5% noise; Figure 8.7b shows the Fourier transform of this wave. Without the discontinuity, the wave would be a smooth function and would plot sparsely in the Fourier domain. However, the discontinuity causes ringing throughout the image, and particularly at neighboring low frequencies. As the ringing approaches the noise level, or as the artifact reaches the stopband, the information is lost. The net can be seen in Figure 8.7g. The sharp detail of the interface is lost, and its placement is distorted.

Three levels of the MRA are shown in Figure 8.7c–e and the MRA scaling function result is shown in Figure 8.7f. The MRA handles the discontinuity in a sparse and spatially resolved manner, as shown by the spike in magnitude at the spatial location of the interface at each scale. Further, the magnitude of the discontinuity is easy to separate from the surrounding noise in a filtering operation. While discussion of thresholding methods is also beyond the scope of this chapter, it can be seen in this illustration that a simple “hard threshold,” setting to zero all wavelet coefficients below some threshold, separates discontinuity from noise without error. This result is shown in Figure 8.7h. The Butterworth approach, on the other hand, smooths and shifts the discontinuity as seen in Figure 8.7g. Figure 8.8 outlines the denoising schematic in wavelet space.

### 8.1.5 FFT versus MRA *in vivo*

The impact of the sparser denoising approach is also visible *in vivo*, as illustrated in Figures 8.8 and 8.9. Figure 8.9 compares the noised image with results under several denoising techniques. A plot across a heterogeneous portion of the image allows for inspection of details. The blue line shows the noised original. The yellow line shows denoising with a divergence-free wavelet [outside the scope of this chapter/see chapter on artifact]. This method removes a small amount of low-frequency spectrum, which is most visible in the brain image, where the yellow line both rises above and falls below



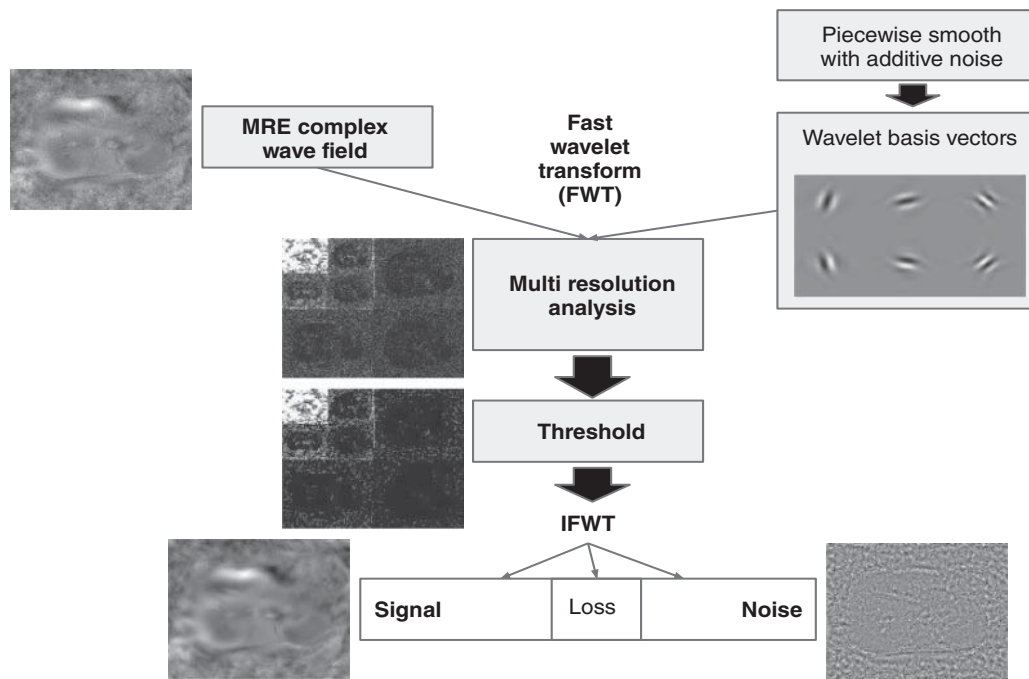
**Figure 8.7** Comparison of Fourier and complex dual-tree wavelet transforms of a (a) single-frequency wave with a discontinuity and 5% noise. The discontinuity does not have a sparse (b) Fourier representation, causing ringing throughout the image. However, the MRA handles both smooth and discontinuous elements sparsely. The Fourier domain denoise, with a fourth-order Butterworth filter, rounds and shifts the feature (g), while the wavelet domain hard thresholding maintains feature sharpness and location while removing noise (h). The lines (c) through (f) represent the wavelet decomposition from finest (c) to coarsest (f). It is obvious that the wavelet scaling function captures the global shape of the signal, whereas the finer resolutions are necessary to deal with the localized discontinuity.

the blue line. However, the image is not yet sufficiently denoised for MRE inversion. Finally, the image is denoised with CDTWs. The result is smooth enough for wave inversion, with much more detail in the curvature of the wave.

In both ideal and *in vivo* data, wavelet thresholding can preserve informational structures lost in  $k$ -space filtering that may be of clinical interest.

### 8.1.6 Sparser Approximations and Performance Times

The top-performing denoising methods often go beyond choice of a priori dictionaries. They may use machine-learning techniques, patch-based or multiscale sampling, or collaborative filtering between multiple nonlinear methods. However, many of these methods are computationally intensive, making their integration into radiological workflow a challenge. When performance is taken into account, wavelets are still



**Figure 8.8** Denoising in wavelet space. The dictionary used is one of 2D wavelets. They are applied recursively using the fast wavelet transform (FWT) to generate a multi-resolution analysis (MRA). The wavelet coefficients are then thresholded, and the image is recovered using an inverse FWT (IFWT).

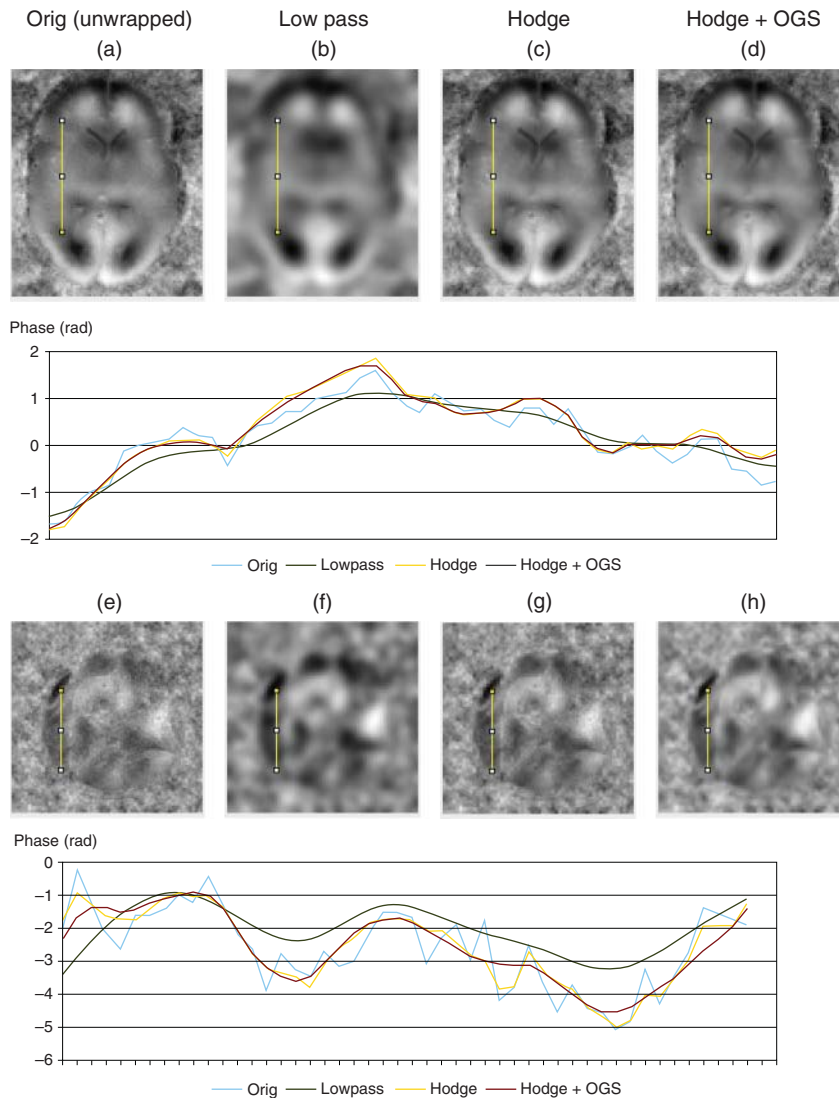
competitive for many applications. For example, CDTWs have been shown to be “optimal” [200] for waves with discontinuities, suggesting they are both fast and well suited to MRE phase data. Similarly, the well-understood relationships between image and  $k$ -space, as well the linearity of the operations, among other qualities, cause  $k$ -space filtering to still be the most widespread and useful method of image manipulation.

## 8.2 Directional Filters

In Chapter 10, we will discuss different methods for the calculation of viscoelastic moduli from MRE wave images. Waves propagating in different directions can confound reconstruction of viscoelastic parameters, unless superposition is included in the underlying model. While methods based on the full wave equation are immune to these effects (as long as all waves have the same wavelength), those based on the evaluation of the wave vector  $\mathbf{k}$  are easily biased. As a remedy, *directional filters* can be applied before inversion to separate waves with different propagation directions. Instead of suppressing noise, the  $k$ -space filters in this section will be used to pick waves that propagate in a specific direction from a complicated superposition of waves.

In order to understand directional filters, it is important to keep in mind that every point  $\mathbf{k}$  in  $k$ -space can be understood as representing a plane wave that propagates in





**Figure 8.9** Comparative denoising results on central slice of muscle and brain acquisitions. Images (a) and (e) are phase-unwrapped, but not denoised (blue lines in plot); (b) and (f) show denoising results for a low-pass filter cutoff of 10 mm (green lines in plot); (c) and (g) show the impact of the divergence-free wavelet denoising, which removes some of the low-frequency spectrum (yellow lines); (d) and (h) show the additional impact of the CDT wavelet denoising (red line). In order to study the denoising results, a vertical plot line was drawn across heterogeneous tissue features in each image. Comparison of the dark red and dark green lines shows the increase in detail from wavelet-basis multiscale filtering (red) as opposed to low-pass filtering (green), even as both produce data sufficiently smoothed for wave inversion.

the direction of  $\mathbf{k}$  with wave number  $|\mathbf{k}|$ . Therefore, if one is only interested in the waves propagating approximately in one given direction, one can cut out a wedge in  $k$ -space that is centered about the desired propagation direction. By nulling all  $k$ -space points outside the wedge, inverse Fourier transform back into image space yields the wave field resulting only from those waves whose wave vectors lie within the wedge. However, prescribing a hard cutoff in  $k$ -space will introduce artifacts in the filtered wave image, such as Gibbs ringing. It is therefore common to use instead filters with a smooth transition between the interior and the exterior of the wedge. The filter is then multiplied with the  $k$ -space representation of the wave image:

$$u_{\text{filtered}} = \mathcal{F}^{-1}[\xi(\vartheta) \cdot \mathcal{F}[u]], \quad (8.14)$$

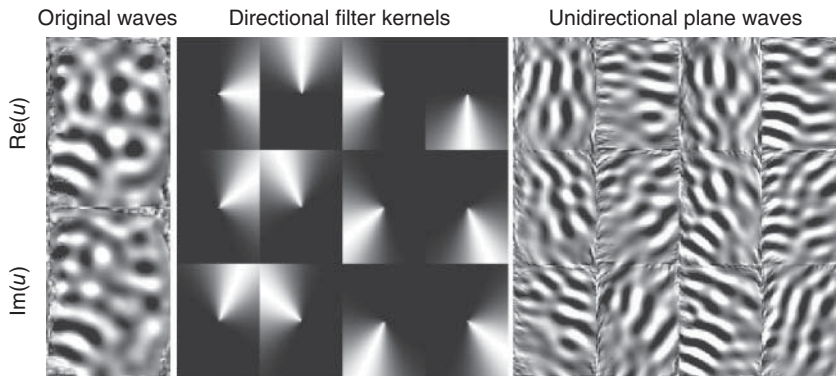
where  $\vartheta$  is the polar angle in two-dimensional  $k$ -space. Equation (8.14) can be extended to 3D by introducing a second angular variable. As an example for 2D directional filters, we define a *bank* of  $N = 12$  directional in-plane filters according to

$$\xi_n(\vartheta) = \frac{1}{\sqrt{2\pi}\sigma_\vartheta} \cdot \exp\left(-\frac{1}{2}\left(\frac{\vartheta - \vartheta_n}{\sigma_\vartheta}\right)^2\right), \quad n = 1, \dots, N \quad (8.15)$$

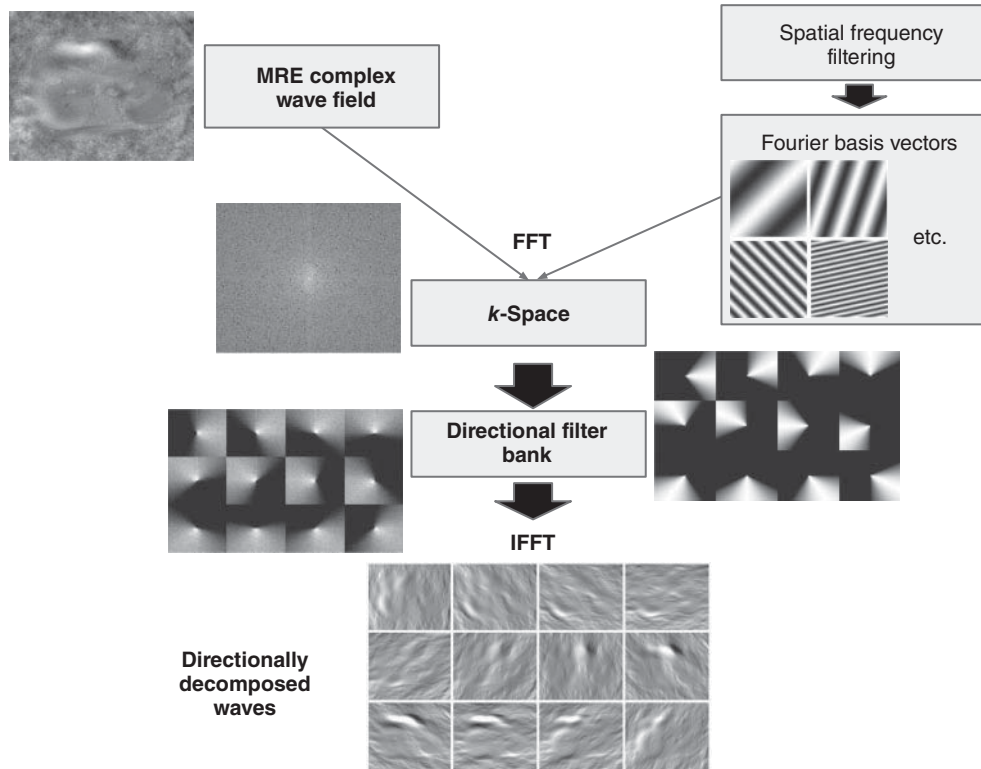
$$\text{with } \vartheta_n = 2\pi \cdot \frac{n-1}{N}. \quad (8.16)$$

The application of this filter bank to a wave field consisting of superposed plane waves is depicted in Figure 8.10. Further, this decomposition fits into our denoising schematic as another form of  $k$ -space filtering, and this is presented in Figure 8.11. In the case of directional filtering, the decomposition is lossless overall, so the result is not divided into “signal” and “noise” as in the other schematics. The noise removed is rather artifact due to inversion methodology assumptions, to be discussed further in Section 10.6.

Directional filters can be combined with wave number-based filters, such as low-pass or band-pass filters, by multiplying the directional filter kernel with a function that depends only on the radial  $k$ -space variable.



**Figure 8.10** Illustration of the effect of directional filters. Real and imaginary parts of a superposition of waves propagating in different directions are shown in the first column. The block in the center depicts 12 directional filters corresponding to Eq. (8.15) with  $N = 12$ . The block on the right-hand side represents the real part of the corresponding directionally filtered waves (shown in the same order as the filter kernels).



**Figure 8.11** Directional filtering. As spatial frequencies are targeted, prior knowledge is used to project the complex wave field onto the Fourier basis. Here, the filtering process is redundant, using a bank of filters to generate a bank of directionally decomposed waves. The waves can then be inverted using inversion assumptions that do not account for superposition.

### 8.3 Numerical Derivatives

*This chapter was coauthored by Eric Barnhill from the Department of Radiology, Charité –Universitätsmedizin Berlin, Berlin, Germany.*

The wave equations used throughout this book have been based on the infinitesimal formulation of the differential operator:

$$f'(x) \equiv \frac{df}{dx} = \lim_{h \rightarrow 0} \frac{f(x+h) - f(x-h)}{2h}. \quad (8.17)$$

However, real-world measurement processes are inherently limited to discrete sampling with a finite number of samples,  $N$ , and finite spacing (both temporally and spatially),  $\delta t$  and  $\delta x$ , respectively. In that case, we have to reformulate the quantity of interest in terms of a discrete variable<sup>2</sup>:

$$f(x), x \in \mathbb{R} \quad \longrightarrow \quad f(x_i), i \in \{1, 2, \dots, N\} \text{ and } x_{i+1} - x_i = \delta x. \quad (8.18)$$

<sup>2</sup> We will focus here on spatial discretization, since this aspect is more relevant for the chapters to follow, but the same arguments and techniques apply to temporal sampling.

We cannot apply Eq. (8.17) for the calculation of discrete derivatives, since, for  $h < \delta x$ , we do not know the value of  $f(x \pm h)$ . However, we can use the best possible approximation by choosing  $h = \delta x$ . In that case, we obtain

$$f'^{(s)}(x_i) = \frac{f(x_i + \delta x) - f(x_i - \delta x)}{2\delta x} = \frac{f(x_{i+1}) - f(x_{i-1}))}{2\delta x}. \quad (8.19)$$

The superscript (s) references the fact that  $f'^{(s)}$  is symmetric, since both the left- and right-hand-side neighbors of  $x_i$  contribute equally to the derivative. This formula is also known as the *midpoint rule*. There are also asymmetric formulations of the discrete derivative:

$$f'^{(b)}(x_i) = \frac{f(x_i) - f(x_{i-1}))}{\delta x} \quad (8.20)$$

$$f'^{(f)}(x_i) = \frac{f(x_{i+1}) - f(x_i)}{\delta x}, \quad (8.21)$$

where superscripts (b) and (f) signify “backward” and “forward,” respectively. In both cases, only one of the neighbors contributes to the derivative. The symmetric difference can also be interpreted as the arithmetic mean of forward and backward differences:  $f'^{(s)} = \frac{1}{2}(f'^{(b)}(x_i) + f'^{(f)}(x_i))$ .

It is apparent that in all three formulations the discrete derivative is just a weighted sum of the function values in the vicinity of  $x_i$ . We can therefore represent the calculation formula as

$$f'(x_i) = \sum_{q=-1,0,1} w_q \cdot f(x_{i+q}). \quad (8.22)$$

Using the discrete convolution introduced in Section 8.1.3.2 for a compact representation of Eq. (8.22), we can assemble the three weights in a vector  $\mathbf{w} = [w_{-1}, w_0, w_1]$ . The kernels for the three types of discrete differences then read

$$\mathbf{w} = \begin{cases} \frac{1}{\delta x}[-1, 1, 0] & \text{for } f'^{(b)} & (8.23a) \\ \frac{1}{\delta x}[0, -1, 1] & \text{for } f'^{(f)} & (8.23b) \\ \frac{1}{2\delta x}[-1, 0, 1] & \text{for } f'^{(s)} & (8.23c) \end{cases}$$

If we write the function values into a row vector,  $\mathbf{f} = [f_1, f_2, \dots, f_N] = [f(x_1), f(x_2), \dots, f(x_N)]$ , we can represent the derivative as

$$\mathbf{f}' = \check{\mathbf{w}} \star \mathbf{f}, \quad (8.24)$$

where  $\check{\mathbf{w}}$  denotes  $\mathbf{w}$  in reverse order. When applying the operator  $\check{\mathbf{w}}$ , care has to be taken when the values at the boundaries are to be calculated. For calculating the derivative at  $x_1$  and  $x_N$ , at least one of the values  $x_0$  and  $x_{N+1}$  is required, which do not exist. In order to obtain the derivative on the boundary nonetheless, boundary conditions are assumed. For example, the data  $\mathbf{f}$  can be zero-padded on both sides, implying that the function vanishes everywhere outside the domain  $[x_1, x_N]$ , which is an example for a Dirichlet boundary condition (see Section 4.9.6). Other boundary conditions can be used to enforce a vanishing derivative on the boundary (a von Neumann-type boundary condition), or by making  $x_1$  and  $x_N$  neighbors (periodic boundary condition). The

appropriate boundary condition is determined by the underlying physical description of the system under investigation.

The second spatial derivative,  $\Delta f$ , can be calculated by repeated application of the first discrete derivative operator. However, doing this results in suboptimal noise robustness and a kernel with width 5 rather than 3. Alternatively, we can inspect the Taylor series expansion of  $f$  at  $x_i$ :

$$f(x_i + \delta x) = f(x_{i+1}) \approx f(x_i) + f'(x_i) \cdot \delta x + \frac{1}{2} f''(x_i) \delta x^2. \quad (8.25)$$

Next, we solve the above equation for  $f''(x_i)$ :

$$f''(x_i) = \frac{2}{\delta x^2} (f(x_{i+1}) - f(x_i) - f'(x_i) \cdot \delta x) \quad (8.26)$$

$$= \frac{1}{\delta x^2} (f(x_{i-1}) - 2f(x_i) + f(x_{i+1})). \quad (8.27)$$

In the second step we used Eq. (8.19). We can now substitute the function values with the corresponding kernels, which would have the same effect when applied to  $\mathbf{f}$ :

$$\mathbf{f}'' = \frac{1}{\delta x^2} [1, -2, 1] \star \mathbf{f}. \quad (8.28)$$

In this way, we have found the representation  $\Delta = \frac{1}{\delta x^2} [1, -2, 1]$  for the kernel of the discrete one-dimensional Laplacian.

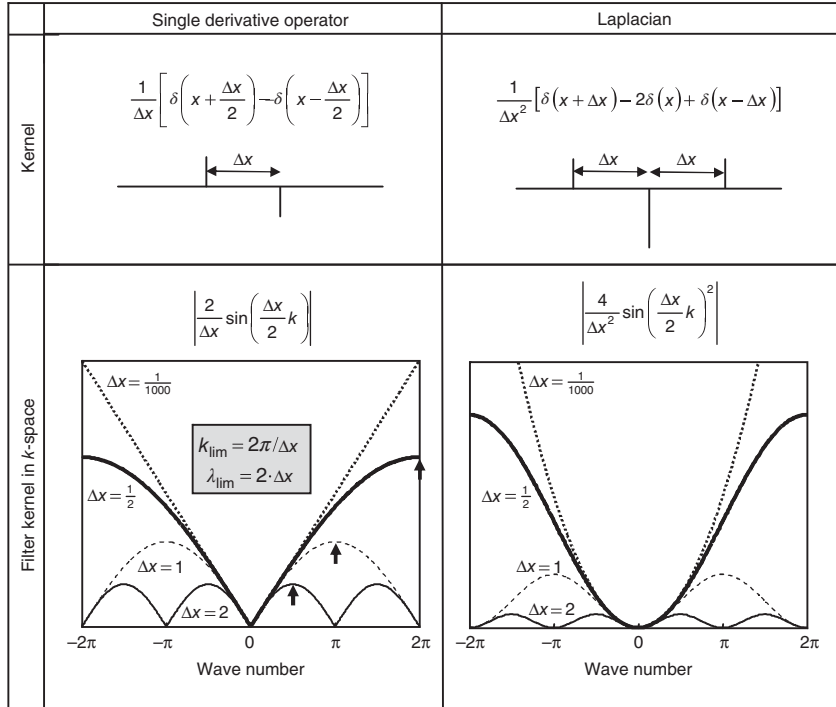
It must be borne in mind that there is no unique representation of any of these discrete derivative operators. Various convolution kernels can be designed as approximations to Eq. (8.17) with specific characteristics. One way to compare the performance of different kernels is to look at their  $k$ -space representation, that is, their Fourier-transformed counterpart. As mentioned above, one very useful property of the Fourier transform is that it translates derivatives to algebraic expressions:

$$\mathcal{F} [f'(x)](k) = -ik \mathcal{F} [f(x)](k) \quad (8.29)$$

$$\mathcal{F} [f''(x)](k) = -k^2 \mathcal{F} [f(x)](k). \quad (8.30)$$

Combining this with the Fourier convolution theorem (Eq. (8.12)), which states that the convolution of two images in image space is equivalent to multiplying their Fourier transforms in  $k$ -space, we can conclude that the ideal filter  $\tilde{\mathbf{w}}$  would have the shape  $-ik$  for the first derivative and  $-k^2$  for the second derivative in  $k$ -space. In Figure 8.13, we present several commonly used derivative kernels and their  $k$ -space representations. Obviously, all of them deviate significantly from the ideal shape, especially for higher spatial frequencies. Since noise is typically located primarily in the high-frequency regions of  $k$ -space, this can actually be an advantage over the ideal derivative operator, which tends to overweight noise-containing regions. On the other hand, real information in the high-frequency range is also suppressed by these kernels.

An alternative strategy to calculating derivatives would be to multiply  $\tilde{\mathbf{f}}$  by  $-ik$  or  $-k^2$  and inverse Fourier transform the result, which would – in theory – yield the best possible approximation to the true derivative. However, in image space, the representations of  $-ik$  and  $-k^2$  have infinite support, resulting in infinitely wide convolution kernels, rather than the compact three-element kernels of Eqs. (8.23b) and (8.23c) and Eq. (8.28). Since any real-world data vector  $\mathbf{f}$  has finite length, application of an infinitely wide kernel would result in truncation of the kernel, which in turn could introduce severe



**Figure 8.12** Illustration of the relationship between the step width  $\Delta x$  and the frequency-space characteristics of difference schemes approximating first- and second-order derivatives. In the  $k$ -space representation, the ideal characteristic is shown as the dashed straight line  $k$  (first derivative) and the dashed parabola  $k^2$  (second derivative) for a very small step size  $\Delta x = 0.001$ . Apparently, the approximation becomes better as  $\Delta x$  decreases. Both schemes ultimately fail when  $|k \cdot \Delta x| \geq \pi$  (indicated by the black arrows), which represents the Nyquist criterion. However, even when the Nyquist criterion is satisfied, the difference between the actual and ideal characteristics can be substantial, especially for larger values of  $k$ . Therefore, the stricter criterion  $k \cdot \Delta x \ll 1$  should be applied to obtain reliable numerical differences.

image artifacts, such as Gibbs ringing. A compact convolution kernel is therefore often a better choice than the mathematically exact form. If a three-element kernel is used, only the first and last data point in  $\mathbf{f}$  require special treatment as they have only one neighbor, whereas all other values are untainted by boundary effects. The standard treatment of the edge values is to revert from symmetric kernels to single-sided ones, such as the forward and backward differences (Eqs. (8.23a) and (8.23b)). This is implemented in Matlab's `gradient` function, which uses one-sided derivatives for the outermost values, and symmetric differences for all other data points.

The relationship between the spatial resolution and the  $k$ -space characteristic of numerical differences is presented in Figure 8.12.

### 8.3.1 Matrix Representation of Derivative Operators

An alternative way of representing Eq. (8.24) is to use matrix multiplication instead of the convolution. In this section, we will assume that  $\mathbf{f}$  is a column vector. We can then

express the first derivative, using single-sided differences for the edge values and symmetric differences for all other points, as

$$\mathbf{f}' = \frac{1}{2 \delta x} \underbrace{\begin{pmatrix} -2 & 2 & & & & \\ -1 & 0 & 1 & & & \\ & -1 & 0 & 1 & & \\ & & & \ddots & & \\ & & & & \ddots & \\ & & & & -1 & 0 & 1 \\ & & & & & -2 & 2 \end{pmatrix}}_{\mathbf{D}} \cdot \underbrace{\begin{pmatrix} f(x_1) \\ f(x_2) \\ f(x_3) \\ \vdots \\ \vdots \\ f(x_{N-1}) \\ f(x_N) \end{pmatrix}}_{\mathbf{f}}. \quad (8.31)$$

All values off the three main diagonals in  $\mathbf{D}$  are zero. Analogously, we can also give a matrix representation of the discrete Laplacian<sup>3</sup>:

$$\mathbf{L} = \frac{1}{\delta x^2} \begin{pmatrix} -2 & 1 & & & \\ 1 & -2 & 1 & & \\ & 1 & -2 & 1 & \\ & & & \ddots & \\ & & & 1 & -2 & 1 \\ & & & & 1 & -2 \end{pmatrix}. \quad (8.32)$$

Note that  $\mathbf{L} \neq \mathbf{D}^2$ . While  $\mathbf{D}^2$  would also be a valid representation of the Laplacian operator, it would correspond to a kernel of size 5 rather than 3, which exacerbates boundary artifacts and attenuates noise at the same time.

The advantage of the matrix representation over the convolution representation is that the matrix operators can be inverted, which constitutes a method for numerical integration and is used in finite-difference wave field simulations (see Section 8.4 or Laplace unwrapping (Section 9.3)). However, for a vector  $\mathbf{f}$  containing  $N$  values, the matrix operators are of dimension  $N^2$ , which can quickly become a challenge in terms of computer memory and computation time. Because of the tridiagonal structure of the derivative matrices, the number of nonzero values is of the order of  $N$ , whereas the number of zeros is of the order of  $N^2$ , so that a representation as a *sparse matrix* is beneficial or even mandatory.

### 8.3.2 Anderssen Gradients

Noise is one of the principal challenges when reconstructing viscoelastic parameters, as we will discuss in Section 10.1. Spatial derivatives are particularly prone to producing artifacts due to their noise-amplifying high-pass characteristics. In order to ameliorate these issues, we will describe a numerical scheme to calculate derivatives that is more resilient to noise than the ones discussed above. It is based on calculating derivatives by averaging over differentiation kernels of different sizes. The initial idea was published by Anderssen and de Hoog [201], and the first application to MRE was proposed by McLaughlin et al. [202].

<sup>3</sup> The operator shown here is valid for the case of Dirichlet boundary conditions, for which the value of  $f$  on the boundary is prescribed (see Section 4.9.6). If von Neumann boundary conditions with a fixed value of the first derivative are desired instead, the first and last elements of the main diagonal have to be  $-1$ .

In Eq. (8.23c), we introduced the symmetric difference kernel  $\frac{1}{2\delta x}[-1, 0, 1]$ . Similarly, we could introduce a kernel with a larger step as  $\frac{1}{4\delta x}[-1, 0, 0, 1]$ . More generally, we can define a derivative kernel for the 1-direction as

$$\mathbf{D}^{(1)}[s] = \frac{1}{2s \cdot \delta x} [-1, \underbrace{0, 0, \dots, 0}_{(s-1) \text{ times}}, 1] \quad \text{for } s \in \mathbb{N}. \quad (8.33)$$

The integer parameter  $s$  denotes the distance of the two points from which the derivative is calculated to the point in the center of the kernel, for which the derivative is calculated. Narrower spacing of these points (corresponding to small values of  $s$ ) constitutes better approximations to the true derivative; however, at the same time, it is also more noise-sensitive than wider spacing. Therefore, one can calculate approximations with different spacings and average over the results:

$$\mathbf{D}_n^{(1)} = \frac{1}{n} \cdot \sum_{s=1}^n \mathbf{D}^{(1)}[s] \quad \text{for } n \in \mathbb{N}. \quad (8.34)$$

In terms of computational complexity, it is more advantageous to combine the different kernels  $\mathbf{D}_n^{(1)}$  into a single kernel than to apply the convolution to each kernel separately. Because of the linearity of the convolution operation, this step is straightforward:

$$\mathbf{D}_n^{(1)} = \frac{1}{2n \cdot \delta x} \left[ -\frac{1}{n}, -\frac{1}{(n-1)}, \dots, -\frac{1}{1}, 0, \frac{1}{1}, \dots, \frac{1}{n} \right]. \quad (8.35)$$

The  $x_1$ -derivative of an  $m$ -dimensional function  $\chi(r_1, r_2, \dots, r_m)$  is

$$\frac{\partial \chi}{\partial x_1} = \check{\mathbf{D}}^{(1)} * \chi, \quad (8.36)$$

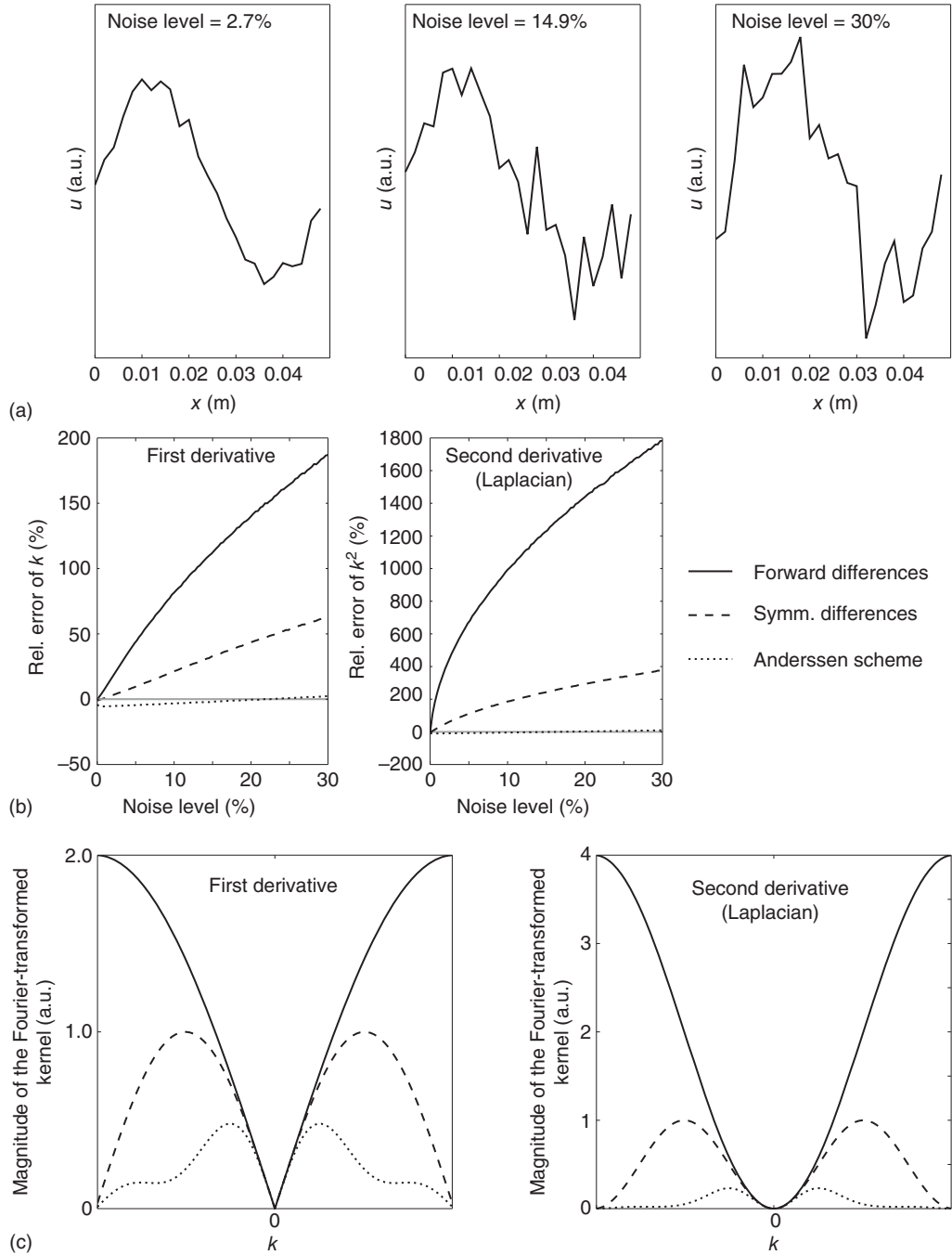
where the symbol  $\check{\phantom{x}}$  indicates reversal of the elements, as introduced on Page 180. For all other directions,  $\mathbf{D}_n^{(i)}$  can be obtained by aligning the elements of  $\mathbf{D}_n^{(1)}$  along the respective dimension  $i$ .

In [203], several other ways of improving the stability of numerical discrete derivatives are discussed. One option is to average the obtained derivatives over adjacent voxels along all dimensions (including the direction along which the derivative is taken). This publication discusses the noise characteristics of such schemes and their dependence on the sizes of the derivative kernel and the averaging window. The authors conclude that differentiation benefits from high dimensionality of the problem (since high dimensionality increases the number of points suitable for averaging within a given distance to a reference point), and that best results are achieved if the aforementioned parameters are adapted to the problem at hand.

For many applications, the authors of this book opted to employ a hybrid scheme for numerical differentiation based on a kernel of the type described by Eq. (8.35), with averaging over all dimensions *except* the one along which the derivative is calculated. In a two-dimensional scenario, for a derivative in the horizontal direction, the resulting kernel would be a  $(2n+1) \times (2n+1)$  matrix, where each row is a copy of  $\mathbf{D}_n^{(1)}$ .

In order to illustrate the effect, Figure 8.13 presents a simulation of a one-dimensional wave with different amounts of noise added. First- and second-order derivatives were calculated utilizing forward differences (Eq. (8.23b)), symmetric differences (Eq. (8.23c)), and the Anderssen scheme (Eq. (8.35)) for  $n=3$ .





**Figure 8.13** Simulation results demonstrating the noise sensitivity of different numerical derivative schemes. For the comparison, a wave with a wave speed of 1.5 m/s at a frequency of 30 Hz was simulated. Different amounts of Gaussian noise were added to the real and imaginary parts. The noise level was defined as noise level =  $\frac{E_{\text{noise}}}{E_{\text{wave}}} \cdot 100\%$ , with  $E_{\text{wave}}$  and  $E_{\text{noise}}$  denoting the energy contained in the wave and the noise spectrum, respectively. One cycle of such a wave at three different noise levels is shown in (a). First- and second-order spatial derivatives were calculated for these waves using three different schemes: forward differences (Eq. (8.23b)), symmetric differences (Eq. (8.23c)), and the Anderssen gradient scheme (Eq. (8.35)) with  $n = 3$ . (b) Shows the relative error for the calculation of the first and second (by repeated application of the operators) derivatives relative to the noiseless case. (c) The  $k$ -space representations of the three schemes are shown for the first and second derivatives.

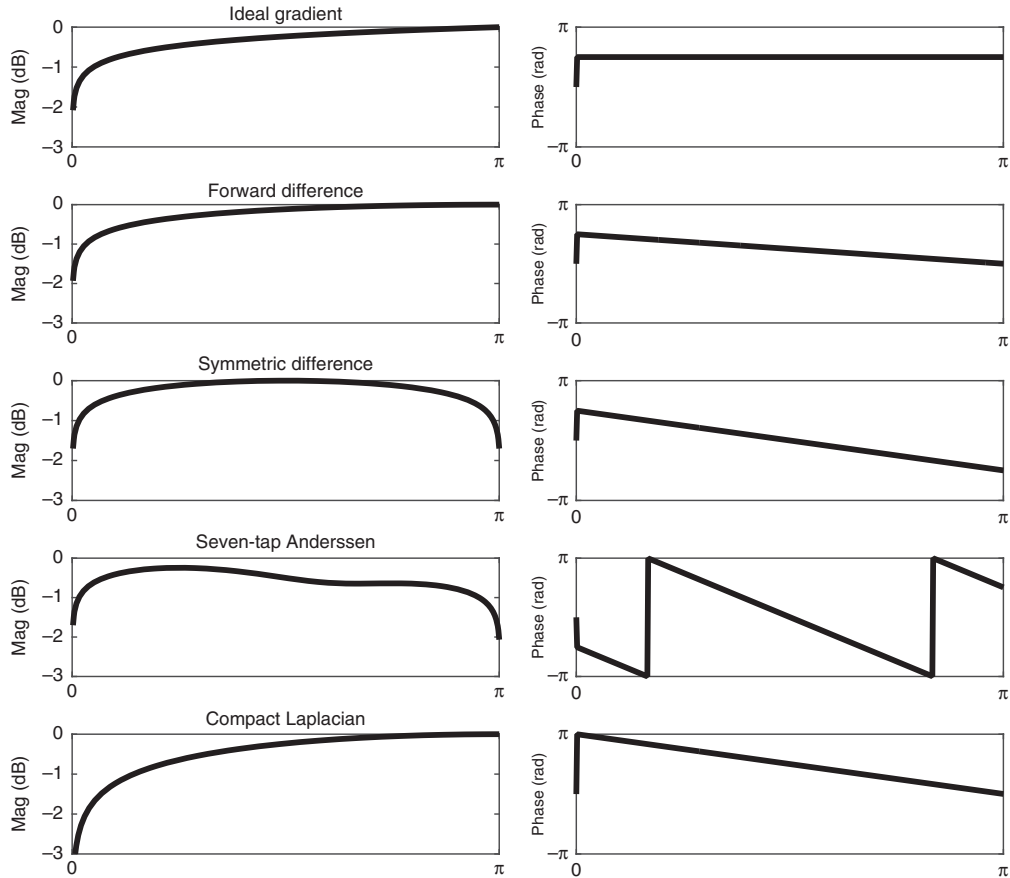


Obviously, the Anderssen gradient scheme performs much better than forward or symmetric differences. In general, all operators tend to overestimate  $k$  and  $k^2$  in the presence of noise. The reason is the overemphasis of the noisy parts of the spectrum, as will be explained in Section 10.1. However, at low noise levels, the Anderssen scheme tends to underestimate the parameters, which is a discretization artifact caused by the different kernel sizes contributing to the Anderssen kernel. Effects of discretization are also explained in Section 10.1. The last two diagrams of the figure present the frequency spectra of the first- and second-order derivatives. For the low-frequency range, close to the origin, all gradients possess similar characteristics. These low spatial frequencies typically contain the major part of the MRE-relevant signal, whereas the higher frequencies are dominated by noise. We can clearly see that, for the Anderssen gradient scheme, the weighting of the higher frequencies is much smaller than for the other two schemes, thus leading to a lower sensitivity to noise.

### 8.3.3 Frequency Response of Derivative Operators

Similar to the low-pass operators analyzed in Section 8.1.3, it is useful to analyze the frequency response of the above derivative operators to gain a deeper understanding of their properties. The frequency response for ideal, forward, symmetric, and Anderssen gradients, as well as the compact Laplace operator (in 1D), are shown in Figure 8.14.

At the top of Figure 8.14 is the “ideal gradient,” the Fourier domain gradient operator. Its phase response is constant, while it can be seen to give increasing weight to high frequencies. All the following operators have linear phase. The forward difference has a near-identical magnitude response, which is one reason for its popularity. Like the ideal gradient filter, it weighs high more than low frequencies. The symmetric differences operator attenuates this effect, and the Anderssen gradient attenuates it more, having a flatter frequency response through a large range of image frequencies. The benefits of this filter are thus seen clearly in its frequency response. Finally, the compact Laplacian operator is also presented, which has characteristics similar to the forward difference, only with a more severe weighting of high frequencies over low frequencies.



**Figure 8.14** Frequency response plots for: ideal gradient, forward difference, centered difference, Anderssen gradient, and compact Laplacian operator.

## 8.4 Finite Differences

The discrete derivative operators introduced in the previous section can be used for the calculation of numerical solutions to differential equations. This set of techniques is referred to as *finite difference methods*. As an example, we discretize the one-dimensional inhomogeneous Helmholtz equation

$$\frac{\partial^2 u}{\partial x^2} u + k^2 u = F \quad (8.37)$$

$$\rightarrow \Delta \mathbf{u} + k^2 \mathbf{1} \mathbf{u} = \mathbf{F}, \quad (8.38)$$

where  $\mathbf{u}$  and  $\mathbf{F}$  are the vectorized versions of the displacement field and the external driving force, obtained by concatenating the  $N$  spatially discretized values, as explained

---

**Algorithm 8.1** Matlab code to simulate 2D wave fields for different boundary conditions using the finite difference method. Results are shown in Figure 8.15.

---

```

k=2; % wave number
dx=0.1; % pixel spacing

% define a point source in the center of the image
F=zeros(101,101); F(51,51)=1;

si=size(F);
N = prod(size(F)); % number of pixels

% Choose boundary conditions:
BC= -1; % Dirichlet
% or
BC=0; % v. Neumann
% or
BC=1i*k*dx; % Sommerfeld

% Assemble the forward Laplacian as a sparse matrix
% from second-order derivatives in 4 directions:
E=ones(si);E(1,:)=0;
Lap_left=spdiags([-E(:) E(:) ~E(:)*BC],[0 1 0],N,N);

E=ones(si);E(end,:)=0;
Lap_right=spdiags([-E(:) E(:) ~E(:)*BC],[0 -1 0],N,N);

E=ones(si);E(:,1)=0;
Lap_up=spdiags([-E(:) E(:) ~E(:)*BC],[0 si(1) 0],N,N);

E=ones(si);E(:,end)=0;
Lap_down=spdiags([-E(:) E(:) ~E(:)*BC],[0 -si(1) 0],N,N);

Laplacian=(Lap_left+Lap_right+Lap_up+Lap_down)/dx^2;

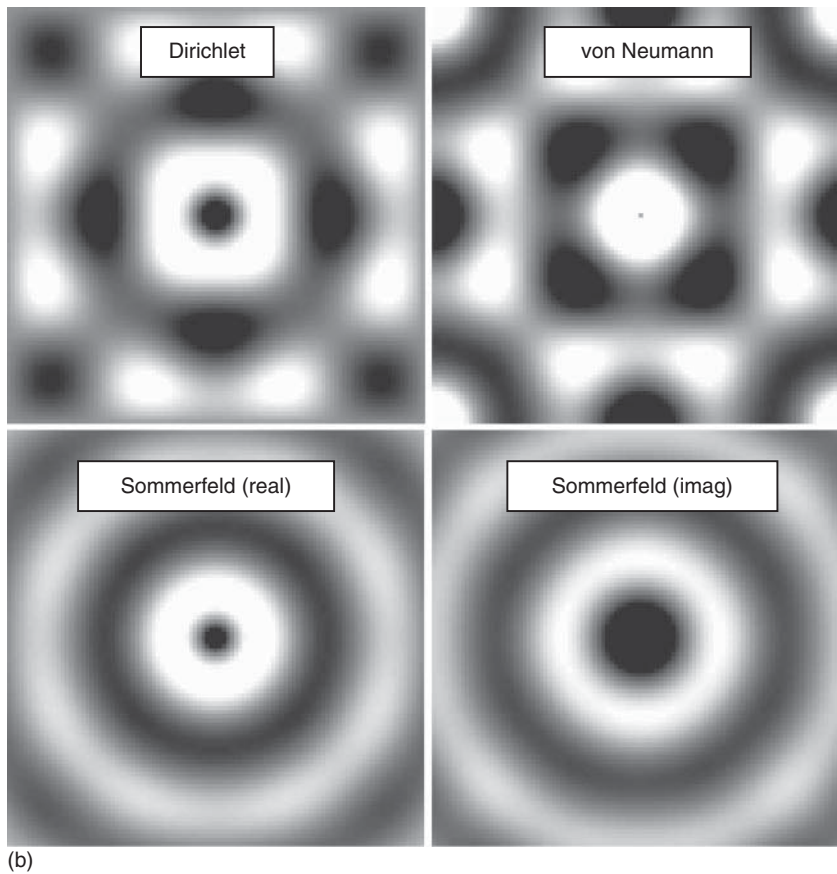
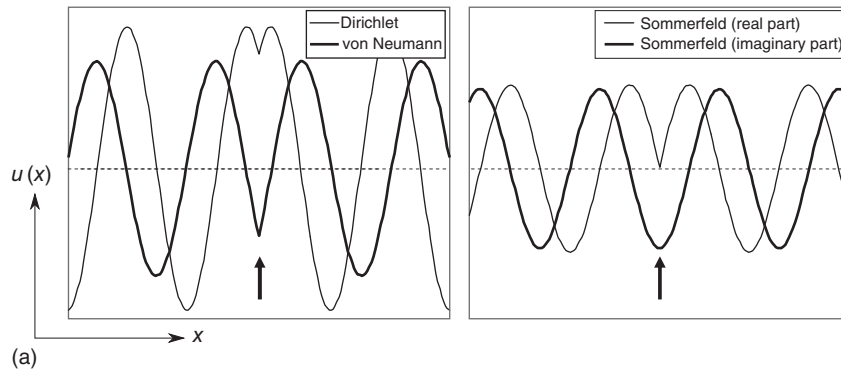
% The Helmholtz equation Lu+k^2*u = 0
Helmholtz_equ=Laplacian+spdiags(ones(N,1)*k.^2,0,N,N);

% Solve the Helmholtz equation for u and reshape the
% solution vector into an image:
Wave_image=reshape(Helmholtz_equ\F(:),si(1),si(2));

```

---

in Section 8.3,  $\Delta$  is the discrete Laplacian defined in Eq. (8.32),  $\mathbb{1}$  is the  $N \times N$  identity matrix, and  $k$  is the wave number. Since the Helmholtz equation is derived from the general wave equation for a single mode at a fixed frequency  $\omega$  (and hence a fixed wave number  $k = \frac{\omega}{c}$ ), we treat  $\mathbf{u}$  and  $\mathbf{F}$  as temporally Fourier-transformed quantities, evaluated at frequency  $\omega$ .



**Figure 8.15** 1D (a) and 2D (b) simulations of 2D wave fields from a point source in the center of the object (indicated by arrows in the 1D case) with different types of boundary conditions. The 2D simulations were performed with the code shown in Algorithm 8.1.

We can then solve the equation algebraically for  $\mathbf{u}$ :

$$\begin{aligned} \mathbf{u} &= (\Delta + k^2 \mathbb{1})^{-1} \cdot \mathbf{F} & (8.39) \\ &\Rightarrow \begin{pmatrix} u_1 \\ u_2 \\ \vdots \\ u_{N-1} \\ u_N \end{pmatrix} \\ &= \frac{1}{\delta x^2} \begin{pmatrix} (a + k^2 \delta x^2) & & & & & & & & \\ & 1 & & & & & & & \\ & & (-2 + k^2 \delta x^2) & & & & & & \\ & & & \ddots & & & & & \\ & & & & 1 & & & & \\ & & & & & (-2 + k^2 \delta x^2) & & & \\ & & & & & & 1 & & \\ & & & & & & & (a + k^2 \delta x^2) & \\ & & & & & & & & \end{pmatrix}^{-1} \cdot \begin{pmatrix} F_1 \\ F_2 \\ \vdots \\ F_{N-1} \\ F_N \end{pmatrix}. & (8.40) \end{aligned}$$

The parameter  $a$  determines the type of boundary condition:

- $a = -2$ : Dirichlet boundary conditions (values on the boundary are prescribed).
- $a = -1$ : von Neumann boundary conditions (values of the first derivative on the boundary are prescribed).
- $a = ik\Delta x - 1$ : Sommerfeld boundary conditions.

The resulting wave field  $\mathbf{u}$  can thus be directly calculated from the force field  $\mathbf{F}$ . However, care has to be taken that  $k \cdot \delta x < 1$ , since otherwise the approximation of the numerical derivative that was used to construct the discrete Laplacian becomes invalid, as illustrated in Figure 8.12. In Algorithm 8.1, we list a simple example of Matlab code for simulating 2D wave fields; and the results are shown in Figure 8.15.

As explained in the previous section, because of memory constraints and computation time, it can become mandatory to use sparse matrices for the representation of the matrix operators. In Matlab, the inversion can be performed by using the backslash operator `a\b`. A comprehensive introduction into different schemes to solve the sound wave equation using finite differences can be found in [204].

## 9

### Phase Unwrapping

In MRE, oscillation information is encoded in the phase,  $\phi$ , of the complex MRI signal. There is a linear relationship between  $\phi$  and oscillation amplitude  $u$ :  $\phi = \xi \cdot u$ . The proportionality factor  $\xi$  is the encoding efficiency (see Section 3.1). However, the MRI phase is always wrapped into the half-open interval  $[-\pi, \pi)$ , which means that *phase wraps* occur if the oscillation amplitude exceeds  $\pm \frac{\pi}{\xi}$ . These phase wraps present themselves as phase discontinuities, where the phase jumps from  $-\pi$  to  $\pi$  (or vice versa). An example is shown in Figure 9.1. Since they would cause singularities in the spatial derivatives or distort the temporal Fourier transform, phase wraps have to be removed by a process termed *phase unwrapping* prior to further processing.

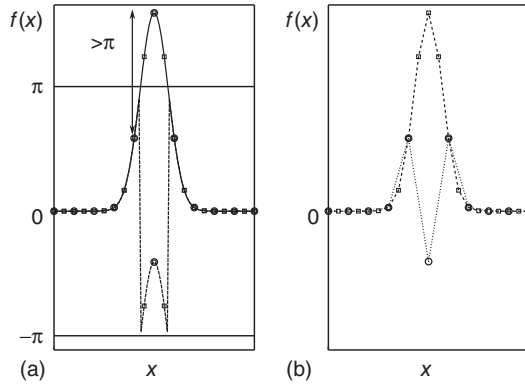
Phase unwrapping is not a problem unique to MRI; it arises in many other fields, such as interferometry or synthetic aperture radar (SAR) image reconstruction. Hence, a multitude of phase unwrapping algorithms exist, each with different strengths and weaknesses. For illustration purposes, we will discuss the unwrapping of a one-dimensional function first, before introducing more complex and useful algorithms.

Before we start the discussion, a word on notation: in this chapter,  $\phi$ , without any subscript, will always represent the physically correct phase, that is, the quantity that is to be reconstructed. We will use  $\phi_w$  to designate the wrapped phase, which is the quantity that we obtain as a result of the image acquisition process. The output of an unwrapping algorithm will be denoted  $\phi_u$ , which we also refer to as the “unwrapped phase.” For reasons that will become obvious further down, it is not always the case that  $\phi = \phi_u$ .

Let  $\phi(x)$  be a scalar function of a one-dimensional variable  $x$ , which could be either a spatial variable or time. We designate the wrapped phase as  $\phi_w(x) = \mathbf{W}\phi(x)$ , with the wrapping operator  $\mathbf{W}$ . One way to represent  $\mathbf{W}$  is by

$$\mathbf{W}\phi = \phi - 2\pi \cdot \left\lfloor \frac{\phi + \pi}{2\pi} \right\rfloor, \tag{9.1}$$

where the brackets  $\lfloor \ ]$  denote rounding toward negative infinity. In other words, if  $\phi$  is outside the interval  $[-\pi, \pi)$ , it is shifted by adding or subtracting integer multiples of  $2\pi$  until it falls into that interval.



**Figure 9.1** Wrapping and unwrapping of a smooth one-dimensional function. The solid and dashed lines on (a) represent the function before and after wrapping according to Eq. (9.1). The circles and boxes indicate samplings of the wrapped data at two sampling rates (differing by a factor of 2). In (b), the sampled data are shown after applying a one-dimensional unwrapping operator as described in Algorithm 9.1. The data series with the higher sampling density, denoted by squares, is reconstructed correctly, since all jumps between adjacent data points are less than  $\pi$ . For the series with the lower sampling rate, there are jumps larger than  $\pi$  (indicated by the arrow in (a)), and the unwrapping hence fails.

The simplest approach to unwrapping a wrapped discrete function  $\phi_w(n)$ ,  $n = 1, \dots, N$  is to take the first value  $\phi_w(1)$  as the reference, and assume that it was not wrapped.<sup>1</sup> Hence, the first point of the unwrapped function  $\phi_u(n)$  becomes  $\phi_u(1) = \phi_w(1)$ . The next step is to iterate through the function values, comparing the last unwrapped point ( $i - 1$ ) to its right-hand-side neighbor ( $i$ ) (the first wrapped point). If the difference between them exceeds  $\pm\pi$ , an integer multiple of  $2\pi$  can be added to the second point to make the difference smaller than  $\pi$ . This yields the unwrapped value for  $\phi_u(i)$ . This procedure is referred to as Itoh's method [205]. More formally, the algorithm can be formulated as shown in Algorithm 9.1 in pseudocode. It is important to emphasize

---

**Algorithm 9.1** A simple one-dimensional unwrapping algorithm

---

```

 $\phi_u(1) \leftarrow \phi_w(1)$ 
for  $i = 2$  to  $N$  do
  if  $|\phi_w(i) - \phi_u(i - 1)| > \pi$  then
     $\phi_u(i) \leftarrow \phi_w(i) + k \cdot 2\pi$ , where  $k$  is chosen such that  $|\phi_u(i) - \phi_u(i - 1)| < \pi$ .
  else
     $\phi_u(i) \leftarrow \phi_w(i)$ 
  end if
end for

```

---

the assumption underlying this algorithm: the phase difference between two adjacent points is *always* assumed to be  $\pi$  or less. If this is not the case, unwrapping will introduce artifacts, as illustrated in Figure 9.1. For a physical system, this means that  $\phi$  has to be a reasonably slowly varying function. However, if  $\phi$  is representative of viscoelastic behavior in an elastography experiment, there is no guarantee that the

---

<sup>1</sup> This assumption determines the global phase offset for the reconstructed function. Since there is no way to recover the true phase of the first point from the wrapped data, this assumption is as good as any other.



underlying parameter varies smoothly across organ boundaries or organ/air interfaces. Denser sampling of  $\phi(i)$ , corresponding to a higher image resolution, ameliorates this issue. However, as long as sampling remains discrete, there is always the probability of phase jumps exceeding  $\pi$  and thus giving rise to unwrapping artifacts.

From a mathematical point of view, phase unwrapping is an ill-posed problem, and there is no unique solution but an infinite number of solutions. In fact, if the unwrapping problem is stated as

$$\phi_u(i) = \phi_w(i) + 2\pi \cdot c(i), \quad (9.2)$$

where  $c$  is a list of integers representing additive phase offsets for each sampling point, then any choice for  $c$  yields a mathematically sound solution. The physically correct solution is just one of the infinitely many solutions, and, in the general case, there is nothing that distinguishes it from all the “false” solutions. Therefore, unwrapping is always dependent on an assumption about the nature of the function to be reconstructed. Smoothness, as assumed above, is one of the commonly used criteria. Other models might use different assumptions and hence require other mechanisms to perform successful unwrapping.

MRE typically yields three-dimensional (2D + time) or four-dimensional (3D + time) data sets. Coherence of the phase data is required along all dimensions, which renders any one-dimensional unwrapping approach unsuitable.<sup>2</sup> Two-dimensional phase unwrapping algorithms have been developed for various image-processing applications [206], and discussing them all is far beyond the scope of this book. Therefore, we will only introduce a small selection of unwrapping methods that are of particular relevance for MRE. Some of the algorithms can be scaled to three or more dimensions in a straightforward manner, whereas others are inherently limited to the two-dimensional case. However, computational complexity increases dramatically with the dimensionality of the problem, so that some algorithms are not feasible for higher-dimensional unwrapping due to computational costs.

Unwrapping can be performed by taking only the phase image into account, or by incorporating further information to improve the results. One common approach is to provide a quality map, which gives an estimate of the reliability for each voxel. Usually, these maps are generated from magnitude images, which map the relative signal strength in each voxel. Voxels with a stronger signal are considered less noisy than low-signal voxels, and their phase values are assumed to be less corrupted. Quality-guided algorithms usually process the voxels from high quality to low quality to prevent noise-induced artifacts from propagating excessively into the unwrapped phase image. Many available algorithms can work with and without a quality map.

## 9.1 Flynn's Minimum Discontinuity Algorithm

The minimum discontinuity approach was suggested by Flynn in 1997 as a two-dimensional phase unwrapping method [207]. This discussion follows the presentation in [206]. The method is based on the observation that a wrapped two-dimensional function, when plotted as a gray-scale image, has closed lines along which the color abruptly changes from black to white. These lines, henceforth referred

<sup>2</sup> Successive application of a one-dimensional unwrapper along all dimensions is not feasible, since every unwrapping step can destroy the effect of a previous unwrapping step along another dimension.

to as “fringe lines,” represent phase wraps, and they are easily spotted by the fact that the phase difference between adjacent pixels on both sides exceeds  $\pi$  (“phase jump”). If such a closed fringe line can be identified in the image, unwrapping can be performed by adding an integer multiple of  $2\pi$  as an offset to every pixel in the region encircled by the line. However, the presence of noise might corrupt the fringe lines, rendering them more difficult to identify (phase differences between adjacent pixels slightly larger than  $\pi$  are either indicators of phase wraps, or they have been induced by noise if the actual phase difference is less than  $\pi$ ). Alternatively, noise can cause fringe lines to be open-ended, so that there is no well-defined enclosed region.

Flynn’s approach is based on minimizing *jump counts*. The jump count between two horizontally adjacent voxels is defined in the wrapped phase image as

$$h(i, j) = \text{round} \left( \frac{\phi_w(i, j) - \phi_w(i + 1, j)}{2\pi} \right), \quad (9.3)$$

and the vertical jump count is

$$v(i, j) = \text{round} \left( \frac{\phi_w(i, j) - \phi_w(i, j + 1)}{2\pi} \right), \quad (9.4)$$

where  $\text{round}(x)$  rounds its argument to the nearest integer. A nonzero jump count between two adjacent voxels simply indicates that the phase difference between the voxels exceeds  $\pi$ .

Flynn introduced a grid in the image plane that has nodes wherever four voxels touch, that is, it is shifted with respect to the voxel raster by  $\Delta/2$  in both directions, where  $\Delta$  is the edge length of the square voxels. Adjacent nodes of the grid can be connected by horizontally or vertically directed *edges*. Edges exist wherever the jump count between adjacent voxels is nonzero. Every edge has one of four possible directions (up, down, left, and right). The edges have the following meaning:

- A horizontal edge indicates that a nonzero vertical jump count exists between the two voxels separated by the edge. If the jump count is positive ( $\text{round} \left( \frac{\phi_w(i, j) - \phi_w(i, j + 1)}{2\pi} \right) > 0$ ), the edge points to the left, whereas a right-pointing edge represents a negative jump count.
- Similarly, a vertical edge reveals a nonzero horizontal jump count. By convention, an edge points downward if it represents a positive jump count, and upward for a negative jump count.

The edges can therefore be interpreted as tangents to phase jumps. Hence, if one can find a closed path by following edges, this means that there is an area that is separated from its surroundings through a phase jump. Such a closed path is the equivalent of a closed fringe line. The objective of the algorithm is to add an appropriate offset (multiples of  $2\pi$ ) to all voxels within that region, which removes all phase jumps between the interior and exterior. Flynn’s unwrapping algorithm solves this task by calculating all phase jumps in a given image, translating them into the node-edge picture, and then continuously searching for closed paths in the edge space. The voxels enclosed by such a path are then unwrapped by adding an appropriate offset, the node-edge representation is updated and the process continues until no further closed paths exist. The edges are organized in a tree structure, which allows for an efficient implementation of the search and update procedures. The algorithm can also be extended to incorporate voxel-wise quality information. Further implementation details and source code can be found in [206].

## 9.2 Gradient Unwrapping

If the quantity of interest is not the phase itself but its first- or higher-order derivative (with respect to time or space), the chain rule of calculus provides a useful shortcut:

$$\frac{\partial}{\partial x} f(g(x)) = \frac{\partial f}{\partial g} \cdot \frac{\partial g}{\partial x}. \quad (9.5)$$

Instead of calculating derivatives of the (unknown) physical phase directly as  $\frac{\partial \phi}{\partial x}$ , we can instead look at the expression

$$\frac{\partial}{\partial x} e^{i\phi_w(x)}. \quad (9.6)$$

First, it is important to note that  $e^{ix}$  is  $2\pi$ -periodic, and since the values of  $\phi_w$  are restricted to a contiguous interval of length  $2\pi$ , the exponential function  $e^{i\phi_w(x)}$  is continuous in the complex plane, even in the vicinity of phase wraps. Furthermore,

$$e^{i\phi_w(x)} = e^{i\phi_u(x)} = e^{i\phi(x)} \quad (9.7)$$

for the same reason.<sup>3</sup> Applying the chain rule to Eq. (9.6) and dropping the argument  $x$  yields

$$\frac{\partial}{\partial x} e^{i\phi} = i \frac{\partial \phi}{\partial x} \cdot e^{i\phi} \quad (9.8)$$

$$\Rightarrow \frac{\partial \phi}{\partial x} = -i \cdot e^{-i\phi} \cdot \frac{\partial}{\partial x} e^{i\phi}. \quad (9.9)$$

On the right-hand side, we can now substitute  $e^{i\phi}$  with  $e^{i\phi_w}$  because of the identity Eq. (9.7) and obtain

$$\frac{\partial \phi}{\partial x} = -i \cdot e^{-i\phi_w} \cdot \frac{\partial}{\partial x} e^{i\phi_w}. \quad (9.10)$$

This means that we have found a way to calculate the derivative of the *physical* phase from the *wrapped* phase, with no explicit unwrapping step. In theory, one could also integrate the derivative to return to  $\phi(x)$ . However, there is a drawback. The chain rule, as formulated in Eq. (9.5), is only valid for continuous functions. In the case of discrete functions, where differentiation has to be approximated by finite differences between adjacent data points, the chain rule becomes an approximation itself. The quality of the approximation depends on the sampling density (i.e., on the distance  $\Delta x$  between adjacent points) and the rate of change of the function. The previously mentioned constraint that unwrapping will fail if the phase between neighboring points differs by more than  $\pi$  also holds true for derivative-based unwrapping. For a continuous function, if  $\phi_w$  is a real-valued function, the complex value on the right-hand side of Eq. (9.10) will also yield only real values. For a discrete function, due to discretization artifacts, the same expression will yield complex numbers with a small imaginary part. For practical purposes, it is advisable to discard the imaginary part and only use the real part of Eq. (9.10). This discrepancy is also the reason why integrating  $\frac{\partial \phi}{\partial x}$  is not

<sup>3</sup> Also, the wrapped phase is calculated by the scanner through the inverse process as  $\phi_w = \arctan \frac{\text{Im}(S)}{\text{Re}(S)}$ , where  $S = S_0 \cdot \exp(i\phi)$  is the complex MR signal.

a viable way to obtain unwrapped phase images, since integration will accumulate those discretization artifacts, which can corrupt the integrated image. However, if one wants to separate the field into longitudinal and transverse waves by applying the curl or divergence operator, as discussed in Section 4.9.2 (see Eqs. (4.141) and (4.143)), gradient unwrapping can directly provide first derivatives.

The name “gradient unwrapping” became established because derivatives can be calculated along all three spatial dimensions by means of the `gradient` function in Matlab. The method was first used in the context of MRE for taking temporal rather than spatial derivatives in cardiac MRE [208].

### 9.3 Laplacian Unwrapping

Similar to gradient unwrapping, Laplacian unwrapping [209] exploits the fact that  $e^{i\phi} = e^{i\phi_w}$ . However, instead of taking the first derivative, the Laplacian of the complex phase is calculated:

$$\Delta e^{i\phi_w} = \Delta e^{i\phi} = e^{i\phi} \left( i \Delta \phi - \left( \frac{\partial \phi}{\partial x} \right)^2 \right). \quad (9.11)$$

Hence, by dividing by  $e^{i\phi_w}$  and taking the imaginary part afterward, we obtain

$$\text{Im}(e^{-i\phi_w} \cdot \Delta e^{i\phi_w}) = \Delta \phi. \quad (9.12)$$

As a last step, we can calculate the unwrapped phase,  $\phi_u$ , by applying the inverse Laplacian:

$$\phi_u = \Delta^{-1} (\text{Im}(e^{-i\phi_w} \cdot \Delta e^{i\phi_w})). \quad (9.13)$$

By substituting  $e^{i\phi_w} = \cos(\phi_w) + i \cdot \sin(\phi_w)$  and  $e^{-i\phi_w} = \cos(\phi_w) - i \cdot \sin(\phi_w)$ , we can write this equivalently as

$$\phi_u = \Delta^{-1} (\text{Im}((\cos(\phi_w) - i \cdot \sin(\phi_w)) \cdot (\Delta \cos(\phi_w) + i \cdot \Delta \sin(\phi_w)))) \quad (9.14)$$

$$= \Delta^{-1} (\cos(\phi_w) \cdot \Delta \sin(\phi_w) - \sin(\phi_w) \cdot \Delta \cos(\phi_w)). \quad (9.15)$$

Matlab code illustrating the application of Eqs. (9.12) and (9.13) on multidimensional data is shown in Algorithm 9.2.

This last equation enables us to calculate the unwrapped phase by applying the discrete forward and inverse Laplacians. Different techniques exist to achieve these calculations. One is to utilize the matrix representation of the discrete Laplacian, which is introduced in Eq. (8.32). Alternatively, the discrete fast Fourier transform can be deployed [209]:

$$\Delta f(x, y) = -\frac{4\pi^2}{N^2} \text{FFT}^{-1}[(k_x^2 + k_y^2) \text{FFT}[f(x, y)]] \quad (9.16)$$

$$\Delta^{-1} f(x, y) = -\frac{N^2}{4\pi^2} \text{FFT}^{-1} \left[ \frac{1}{k_x^2 + k_y^2} \text{FFT}[f(x, y)] \right]. \quad (9.17)$$

In most cases, the Fourier-based method is faster and requires less memory than the matrix operator approach. The discrete cosine transform (DCT) has also been used instead of the fast Fourier transform to better accommodate boundary conditions [210, 211]. In either case, the implementation of the Laplacian and its inverse should be complementary (e.g., based on the same kernel), so that no numerical bias is introduced. As a second-order differential operator, the Laplacian removes the zeroth and first order (i.e., constant and linear terms) from the data. Applying the inverse Laplacian cannot recover these terms, so that two unknown constants of integration remain. This means that a constant offset and linear trends (as caused by global  $\mathbf{B}_0$  inhomogeneities) are suppressed, which can be a desirable effect.

---

**Algorithm 9.2** Matlab code for slice-based Laplacian unwrapping of a 4D (3D + time) or higher dimensional (including, e.g., displacement field components and different vibration frequencies) data set, as published in [69]. This approach is based on Eqs. (9.12) and (9.13) and the inversion of a finite-difference Laplacian operator. Temporal Fourier transform is used to extract only the vibration frequency.

---

```

% wWrapped is at least a 4D array (x,y,z,time) containing wrapped
% data scaled to [-pi, pi].
si = [size(wWrapped) 1 1 1 1];

% Finite difference Laplacian with Dirichlet boundary conditions
E = ones(si(1)*si(2),1);
L = spdiags([E E -4*E E E], [-si(1) -1:1 si(1)], si(1)*si(2), ...
            si(1)*si(2));

% Convert the real-valued phase into a phasor exp(1i*pi), and
% convert each 2D image into a row vector containing all voxels.
% Concatenate all row vectors into a big matrix that contains the
% full 4D dataset.
PHI = reshape(exp(1i*wWrapped), [si(1)*si(2) prod(si(3:end))]);

% Apply forward Laplacian to complex phase, then remove complex
% phase. laplacianPHI is equivalent to the Laplacian of the real-
% valued phase.
laplacianPHI = imag((L*PHI).*conj(PHI));

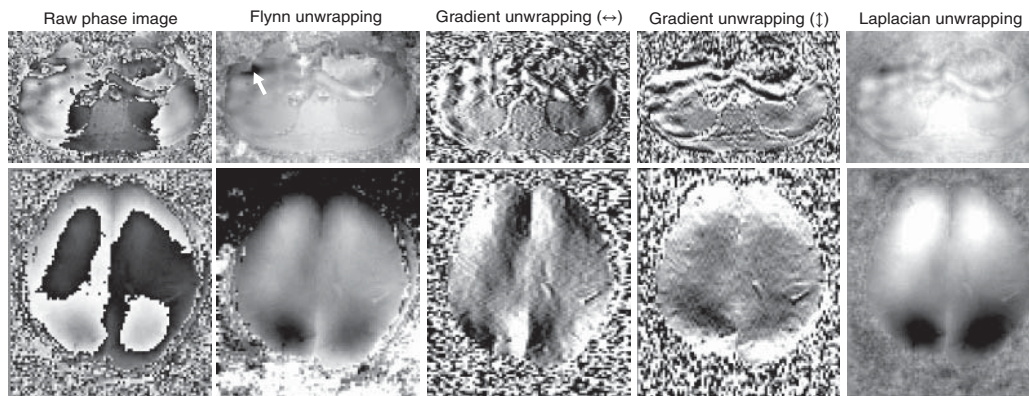
% perform temporal Fourier transform and extract the vibration
% frequency (which is stored at index 2 after FFT).
ft = fft(reshape(laplacianPHI, [prod(si(1:3)), si(4), ...
                               prod(si(5:end))]), [], 2);
wx = reshape(ft(:,2,:), [si(1)*si(2) prod([si(3) si(5:end)])]);

% numerical integration through inversion of the Laplacian
wUnwrapped = L\wx;

% convert the matrix representation of the data back to a
% multidimensional array
wUnwrapped = reshape(wUnwrapped, [si(1:3) si(5:end)]);

```

---



**Figure 9.2** Comparison of different 2D phase unwrapping methods in the liver (upper row) and brain (bottom row). While Flynn’s method performs well in the brain, it is disturbed in regions of multiple wraps in the liver (arrow). Furthermore, Flynn’s algorithm adds an arbitrary global phase offset  $n \cdot \pi$ ,  $n \in \mathbb{Z}$ . Gradient unwrapping, which is stable but direction-dependent and noisy, can be used as a high-pass filter or for subsequent curl calculations. Laplacian-based unwrapping is stable, noise-robust, and suppresses zeroth- and first-order components of the field, which are often undesirable. However, the Laplacian averages information from adjacent pixels, and unwrapping based on the Laplacian does not reconstruct the real wave field.

In Figure 9.2 we demonstrate the performance of the different unwrapping methods in the liver and the brain.

## 10

## Viscoelastic Parameter Reconstruction Methods

Data processing and parameter recovery in elastography always face an *inverse problem*. Specifically, the aim is to derive information about the spatial distribution of elastic parameters (shear modulus, Young's modulus, bulk modulus, etc.) from measured dynamic quantities, typically the displacement field  $\mathbf{u}(\mathbf{r}, t)$  or  $\tilde{\mathbf{u}}(\mathbf{r}, \omega)$ . In this chapter, we will discuss various methods to achieve this goal.

Constant or not constant?
---------------------------

<p>In the derivation of the general form of the elastic wave equation, Eq. (4.117), we neglected the spatial variation of the elastic parameters by discarding the spatial derivatives of the elasticity tensor <math>\mathbf{C}</math>. Mathematically, this is only admissible if the neglected terms are exactly zero, which would imply that the elastic properties are constant throughout the object. On the other hand, when we talk about wave inversion, we intend to calculate spatial maps of the distribution of the viscoelastic parameters, which only makes sense if there is some spatial variation. This is obviously a contradiction. The solution is that we assume the parameter variation to be small enough to yield no significant contribution to the wave equation. In this sense, every wave equation presented in this book is only an approximation. The treatment of the exact equations is more complicated, and solving for the elastic parameters and their spatial derivatives at the same time is not feasible by direct inversion (DI). Alternative approaches rely on finite elements approaches and can be applied to spatially varying parameters, as outlined later in this section.</p>
---

A wave equation – such as Eq. (4.129) – predicts the propagation of waves through a medium, if the parameter fields  $\mu(\mathbf{r})$  and  $\lambda(\mathbf{r})$  as well as the boundary conditions on the surface of the object (see Section 4.9.6) are known. The calculation of a wave field from these parameters is a typical *forward problem*, whereas the associated inverse problem constitutes the estimation of the mechanical parameters from the measured wave field. More generally, forward problems relate to predicting the behavior of a system if all of its defining parameters are known. Conversely, inverse problems revolve around calculating model parameters from measurements of the behavior of the model.

The inversion methods that have been established in the context of MRE can be broadly subdivided into two categories: iterative reconstruction and direct inversion (DI).

*Magnetic Resonance Elastography: Physical Background and Medical Applications*, First Edition.  
Sebastian Hirsch, Jürgen Braun, and Ingolf Sack.

© 2017 Wiley-VCH Verlag GmbH & Co. KGaA. Published 2017 by Wiley-VCH Verlag GmbH & Co. KGaA.

Iterative reconstruction transforms the solution of the inverse problem to repeated calculation of the related forward problem. An initial guess  $\zeta_0$  is used together with information about boundary conditions and the mechanical excitation pattern as the input to a finite-elements model (FEM), which is then used to calculate the resultant displacement field  $\mathbf{u}_{\text{calc}}$ . The deviation between  $\mathbf{u}_{\text{calc}}$  and the measured field  $\mathbf{u}_{\text{meas}}$  is then used to derive an update for the parameter estimate,  $\zeta_1$ , and  $\mathbf{u}_{\text{calc}}$  is calculated again. This process continues until the difference between  $\mathbf{u}_{\text{calc}}$  and  $\mathbf{u}_{\text{meas}}$  becomes lower (in a suitable metric) than a predefined threshold, and the parameters  $\zeta$  used in the last calculation step constitute the final result. Additional constraints can be integrated into the model, such as a compartmentalization derived from a priori anatomical information [212]. Furthermore, the resolution of the resultant parameter maps is determined by the density of the mesh used for the finite element model, which does not have to be identical to the image resolution. It has also been demonstrated that individual parameters can be reconstructed on meshes of different coarseness. On the other hand, the computational complexity of this method can be very high, demanding several hours of reconstruction time for a single data set on standard hardware. Furthermore, the model depends critically on the boundary conditions, and these cannot be measured reliably through an experiment. Hence, the assumptions made about boundary conditions can have a significant influence on the resultant parameter estimates [213].

For the DI strategy, it is necessary to formulate the wave equation as a general linear equation:

$$\rho \ddot{\mathbf{u}} = (\mathbf{D}\mathbf{u})\mathbf{M}(\zeta), \quad (10.1)$$

where  $\mathbf{D}\mathbf{u}$  is a matrix containing second-order spatial derivatives of the displacement field and  $\mathbf{M}$  is a vector whose entries depend only on the unknown parameters  $\zeta$ . If we use the Fourier domain representation for  $\mathbf{u}$  instead of the time domain representation, we can substitute  $\ddot{\mathbf{u}}$  with  $(-\omega^2 \ddot{\mathbf{u}})$ . Ideally, such an equation could be solved simply as

$$\mathbf{M}(\zeta) = -\rho\omega^2(\mathbf{D}\mathbf{u})^{-1} \cdot \mathbf{u}. \quad (10.2)$$

However, in most cases,  $\mathbf{D}\mathbf{u}$  is not a square matrix, so that its inverse does not exist. Instead, numerical optimization procedures can be deployed that yield parameter estimates  $\zeta$  which minimize the residual

$$N(|\rho\omega^2 \mathbf{u} + (\mathbf{D}\mathbf{u}) \cdot \mathbf{M}(\zeta)|), \quad (10.3)$$

where  $N$  is a suitable metric. The  $L^2$ -norm  $N(\mathbf{x}) = \sqrt{\sum_i x_i^2}$  is a common choice for  $N$ , thus minimizing the sum of squares of the data mismatch. One possibility to implement this strategy is to multiply Eq. (10.1) with the left Moore–Penrose pseudo-inverse of  $(\mathbf{D}\mathbf{u})$ :

$$\mathbf{M}(\zeta) = -\rho\omega^2(\mathbf{D}\mathbf{u})^+ \cdot \mathbf{u}. \quad (10.4)$$

Alternatively, other optimization or fitting techniques can be deployed to minimize the mismatch between the parameter estimate and the measured data. One example for DI will be presented in Section 10.3.

A second type of DI strategies is not based on the wave equation, but rather on one convenient property of harmonic waves: If we represent a wave by a complex-valued plane wave

$$\mathbf{u}(\mathbf{r}, t) = \mathbf{u}_0 \cdot e^{i(\mathbf{k} \cdot \mathbf{r} - \omega t)} = \mathbf{u}_0 \cdot e^{i\phi(\mathbf{r}, t)}, \quad (10.5)$$



we can simply extract the wave vector  $\mathbf{k}$  by applying the gradient operator to the phase of the wave:

$$\mathbf{k} = \nabla\phi = \nabla(\mathbf{k} \cdot \mathbf{r} - \omega t). \quad (10.6)$$

Since  $\phi$  is the phase of the motion-encoded complex MR signal, the above equation represents a straightforward way to calculate the wave vector from the acquired data. This method is known as *phase gradient* (PG), and will be discussed in Section 10.2.

## 10.1 Discretization and Noise

Two important sources of error have to be considered when dealing with measured data: discretization and noise. Both introduce a bias into the reconstruction of viscoelastic parameters, and it is essential to understand the effects of these factors when interpreting and comparing results.

We model noise as an independent additive contribution to a complex quantity  $Q$ . The measured value,  $Q_m$ , can thus be represented as

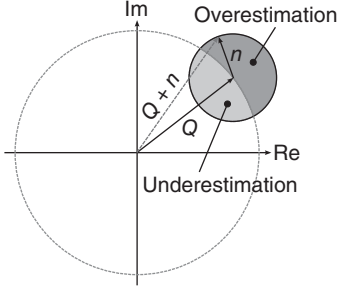
$$Q_m = Q + n \quad \text{with} \quad n = |n| \cdot e^{i\zeta}. \quad (10.7)$$

We assume that  $|n|$  is distributed over  $[0, \infty)$  according to some probability distribution function  $P(|n|) : \mathbb{R}_0^+ \rightarrow [0, 1]$ , and that the phase  $\zeta$  is uniformly distributed over the full circle  $[0, 2\pi)$ . The magnitude of the measured quantity is  $|Q_m| = |Q + n|$ , and it obeys the triangle inequality

$$\left| |Q| - |n| \right| \leq |Q + n| \leq |Q| + |n|. \quad (10.8)$$

Even though  $|Q_m|$  can be either smaller or larger than  $|Q|$ , noise generally leads to an overestimation of the magnitude of a complex quantity. A graphical explanation is given in Figure 10.1. The effect can also be explained by the fact that if  $n$  is Gaussian complex noise, the measured quantity  $|Q + n|$  will be distributed according to a Rician distribution, which is asymmetric and skewed toward larger values. The effect becomes stronger as  $|n|$  increases and  $|Q|$  decreases.

We can now use these findings to analyze the effect of noise during the reconstruction of viscoelastic parameters. The noise in the acquired displacement field  $u$  is determined by a number of measurement parameters, such as the vibration frequency, vibration amplitude, and motion sensitivity of the MR sequence and various MR sequence parameters. However, certain postprocessing steps, such as the calculation of derivatives, can further affect the noise level. For example, we will show in Section 10.3 that the magnitude of the complex modulus,  $|G^*|$ , can be calculated as  $|G^*| = \rho\omega^2|u|/|\Delta u|$ . Taking derivatives tends to amplify noise, since they act as high-pass filters, which can be easily seen from the  $k$ -space representation of the ideal derivative operator:  $\mathcal{F}[f'(x)] = k \cdot \mathcal{F}[f(x)]$ , applying a weight identical to the  $k$ -value. The term  $\Delta u$  is thus noisier than  $u$ . Therefore, when taking the absolute value of each, the denominator  $|\Delta u|$  receives a stronger bias toward larger values than the nominator  $|u|$ , which subsequently leads to an underestimation of  $|G^*|$ . The effect is more pronounced if  $u$  has a low signal-to-noise ratio (SNR). Multifrequency inversion methods based on the magnitude of  $\Delta u$  therefore tend to weight each frequency by the induced vibration amplitude to reduced artifacts from frequencies with low amplitudes, which we will discuss in Section 10.5.



**Figure 10.1** Illustration of the effect of noise on the magnitude of a measured signal in the complex plane. The true quantity  $Q$  is an arbitrary vector in the complex plane. We simulate the effect of noise by attaching a vector  $n$ , representing the noise contribution of the measurement, to the tip of  $Q$ , yielding the measured magnitude  $|Q_m| = |Q + n|$ . The dashed circle around the origin indicates all possible signals with a magnitude equal to  $|Q|$ . The solid circle around the tip of  $Q$  represents all possible values  $Q_m$  if  $|Q|$  and  $|n|$  are fixed and only the noise phase  $\zeta$  is variable. Since we assumed  $\zeta$  to be uniformly distributed over  $[0, 2\pi)$ , the measured signal is uniformly distributed over the black solid circle; and the probability of finding  $Q_m$  in a given segment of that circle is proportional to the arc length of the segment. The dashed circle divides the solid circle into two segments, the “inside” (light gray) and “outside” (dark gray). The arc length of the outside segment (where  $|Q_m| > |Q|$ ) is larger than the arc length of the inside segment, where  $|Q_m| < |Q|$ . Hence, the probability for  $|Q_m| > |Q|$  is larger than that for  $|Q_m| < |Q|$ . This means that, on average, noise tends to increase the magnitude of a complex quantity. The effect becomes more significant as the magnitude of the noise increases. This argument holds true if we consider the fact that usually the noise amplitude is not fixed, but distributed according to some probability density function.

Discretization artifacts arise when derivatives of the discrete displacement field have to be calculated. Since analytical derivatives are formulated as infinitesimal differences, a finite voxel spacing  $\delta x$  introduces deviations that can affect subsequent processing steps.

Assume that we calculate the Laplacian of the displacement field according to Eq. (8.28). In a one-dimensional scenario, we have

$$\Delta u = \frac{1}{\delta x^2} (u(x_{i-1}) - 2u_i + u(x_{i+1})). \quad (10.9)$$

We insert a plane wave with unit amplitude,  $u = \exp(ik \cdot x)$  (we neglect the time-dependent part  $e^{-i\omega t}$ , since it is irrelevant for spatial derivatives):

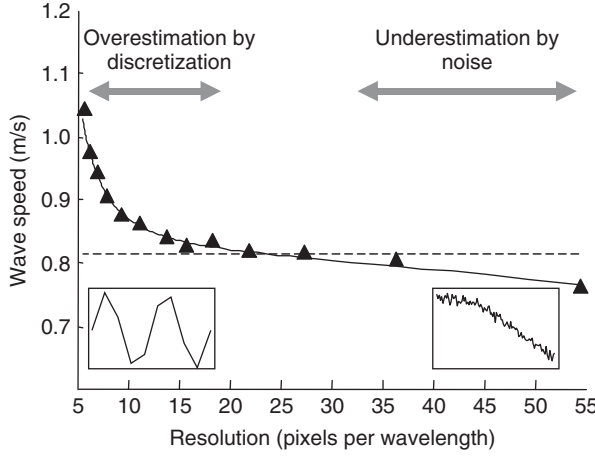
$$\Delta u = \frac{1}{\delta x^2} (e^{ik \cdot (x-\delta x)} - 2e^{ik \cdot x} + e^{ik \cdot (x+\delta x)}) = \frac{e^{ikr}}{\delta x^2} (e^{-ik \cdot \delta x} - 2 + e^{ik \cdot \delta x}) \quad (10.10)$$

$$= 2 \frac{e^{ikr}}{\delta x^2} (\cos(k \cdot \delta x) - 1). \quad (10.11)$$

In the limit of infinitesimal  $\delta x$ , using L'Hospital's rule twice, the result of the continuous case is reproduced:

$$\Delta u|_{\delta x=0} = 2 \frac{e^{ikr}}{\delta x^2} (\cos(k \cdot \delta x) - 1) \Big|_{\delta x=0} = 2e^{ikr} \cdot \frac{-k \sin(k \cdot \delta x)}{2\delta x} \Big|_{\delta x=0} \quad (10.12)$$

$$= 2e^{ikr} \cdot \frac{-k^2 \cdot \cos(k \cdot \delta x)}{2} \Big|_{\delta x=0} = -k^2 e^{ikr}. \quad (10.13)$$



**Figure 10.2** Illustration of the effect of discretization and noise on the reconstructed shear wave velocity. Displacement fields acquired at drive frequencies (and hence different wavelengths) from 10 to 100 Hz were subjected to algebraic Helmholtz inversion (AHI, Section 10.3) and the shear wave speed at each frequency was retrieved. It is obvious that for low resolution, discretization artifacts dominate and the wave speed (and hence the elastic modulus) is overestimated. For higher resolutions, discretization effects are suppressed and noise-induced underestimation of the wave speed and elastic modulus occurs. (Papazoglou 2008 [214]. Reproduced with permission of Institute of Physics Publishing.)

We substitute Eq. (10.11) into the Helmholtz equation to calculate the elastic modulus:

$$G^* = -\rho\omega^2 \frac{u}{\Delta u} = -\rho\omega^2 \frac{\delta x^2}{2(1 - \cos(k \cdot \delta x))}. \quad (10.14)$$

If  $\delta x$  is smaller than the wavelength  $\lambda = \frac{2\pi}{k}$ , so that  $k \cdot \delta x \ll 1$ , we can approximate the denominator by the Taylor series

$$1 - \cos(k \cdot \delta x) \approx 1 - (1 - k^2\delta x^2 + k^4\delta x^4) = k^2\delta x^2(1 - k^2\delta x^2) < k^2\delta x^2. \quad (10.15)$$

We can thus see that discretization leads to an underestimation of the denominator (the correct value would be  $k^2$ ), and hence to an overestimation of the modulus (see Figure 10.2):

$$G^* = -\rho\omega^2 \frac{1}{k^2(1 - k^2\delta x^2)} = \frac{(G^*)^{\text{true}}}{1 - k^2\delta x^2}. \quad (10.16)$$

We can also see that a singularity occurs in Eq. (10.14) if  $k \cdot \delta x = \frac{\pi}{2}$ . Therefore, inversion is only feasible if

$$\frac{\pi}{2} > k \cdot \delta x = \frac{2\pi}{\lambda} \cdot \delta x \implies \delta x < \frac{\lambda}{4}. \quad (10.17)$$

Hence, we need an absolute minimum resolution of more than four pixels per wavelength in order to perform inversion. However, discretization artifacts begin to manifest themselves much earlier, so that a much better resolution should be chosen to obtain reliable estimates for the elastic modulus. An approximation for the reconstructed shear wave speed in the presence of both noise and discretization is presented in [214] as

$$c \approx \frac{\omega}{k_0} \left( 1 - \frac{\sigma^2}{2} \left( \frac{1}{k_0^2 \delta x^2} - 1 \right) \right), \quad (10.18)$$

where  $k_0$  is the physically correct wave number and  $\sigma$  is the noise-to-signal ratio (reciprocal of SNR).

## 10.2 Phase Gradient

The *phase gradient* (PG) method is arguably the simplest way of deriving elastic information from a propagating wave. A single one-dimensional propagating wave with a potentially complex wave number  $k = k_r + ik_i$  can be represented as

$$u(x, t) = u_0 \cdot e^{i(k_r x - \omega t)} \cdot e^{-k_i x} = \underbrace{u_0 \cdot e^{i\phi}}_{\text{phasor}} \cdot \underbrace{e^{-k_i x}}_{\text{damping}}. \quad (10.19)$$

The phasor<sup>1</sup> determines the phase of the wave, whereas the damping part describes exponential attenuation along the propagation path in a dispersive medium. We can see that for a fixed time point, the phase of the wave is a linear function of the spatial coordinate:

$$\phi = k_r x - \omega t. \quad (10.20)$$

Applying a spatial derivative (which we will denote by  $\nabla$ , since it easily generalizes to three dimensions when applied to each vector component separately) to the phase will therefore yield the wave number:

$$\nabla \phi = k_r. \quad (10.21)$$

Since  $\phi$  is the motion-encoded phase directly obtained from an MRE measurement,<sup>2</sup> this is the most basic way of recovering elastic information from a wave image. The PG method only requires first-order spatial derivatives, in contrast to the wave equation-based methods discussed in Section 10.3, and is therefore more resilient toward noise. However, the PG method depends critically on spatial unwrapping, since every remaining phase wrap produces a spike in the derivative, which in turn taints the calculation of the wave number.

An alternative method of calculating the PG of a 1D discrete displacement field with voxel spacing  $\delta x$ , which is inspired by the gradient unwrapping method (cf. Section 9.2), is

$$k = \frac{1}{2\delta x} (\arg(u_{i-1}^* \cdot u_i) + \arg(u_i^* \cdot u_{i+1})) \quad (10.22)$$

$$= \frac{1}{2\delta x} (-\phi_{i-1} + \phi_i - \phi_i + \phi_{i+1}) \quad (10.23)$$

$$= \frac{1}{2\delta x} (\phi_{i+1} - \phi_{i-1}), \quad (10.24)$$

which is exactly the symmetric derivative scheme (Eq. (8.23c)) and thus yields an approximation to  $\nabla \phi$ . The method translates to multidimensional displacement field

<sup>1</sup> Some authors define the phasor such that it only contains the time-independent contribution, thus excluding the term  $\omega t$ .

<sup>2</sup> To suppress artifacts from an inhomogeneous susceptibility background, the temporally Fourier-transformed MRE signal, evaluated at the vibration frequency, should be used here instead of the raw phase.

in a straightforward manner by using the corresponding multidimensional central difference schemes.

Since only the real part of the wave vector contributes to the phase, the PG method is completely insensitive to damping, which is quantified by  $k_i$  instead. Furthermore, the PG cannot cope with a superposition of waves propagating along different directions, and it will yield incorrect results when applied to such a scenario. In Section 10.6, we will present a method which overcomes these two limitations by applying directional filters and normalizing the displacement field gradient.

### 10.3 Algebraic Helmholtz Inversion

The *Helmholtz equation* is the solution to the general wave equation for a monofrequency wave field. Formally, it can be derived from the wave equation by applying a temporal Fourier transform and exploiting its property (Eq. (8.30)):

$$\Delta u(x, t) = \frac{1}{c^2} \ddot{u}(x, t) \xrightarrow{\text{FFT}} \Delta \tilde{u}(x, \omega) = -\frac{\omega^2}{c^2} \tilde{u}(x, \omega). \quad (10.25)$$

As an added benefit, the Fourier transform suppresses nonmotion-related contributions to the MR signal phase, such as the static susceptibility background, and oscillations at frequencies other than the drive frequency, thus improving the quality of the inversion. The elastic properties of the tissue enter Eq. (10.25) via (see Eqs. (4.145) and (4.146))

$$c = \sqrt{\frac{\Gamma}{\rho}} \Rightarrow k^2 = \frac{\rho\omega^2}{\Gamma}, \quad (10.26)$$

where  $\Gamma$  is the elastic modulus that governs wave propagation.<sup>3</sup> In the case of a scalar wave field, Eq. (10.25) can be solved algebraically for  $k$ , such that the elastic properties can be assessed directly from the acquired wave field. However, the wave phenomena typically studied in elastography are two- or three-dimensional, and the displacement is therefore represented by a vector  $\tilde{\mathbf{u}}$ . In that case, Eq. (10.25) holds true for each vector component separately:

$$\Gamma_i = -\rho\omega^2 \frac{\tilde{u}_i}{\Delta \tilde{u}_i}. \quad (10.27)$$

If the medium is isotropic, every component should yield the same value for the modulus. In anisotropic media, however, the elastic properties depend on the direction of the displacement, and the moduli retrieved for the three vector components can differ.<sup>4</sup> This method of calculating elastic moduli from displacement fields is termed *Algebraic Helmholtz Inversion* (AHI) or *Direct Inversion* (DI).

If isotropy is assumed, the simplest type of inversion is to perform the Helmholtz inversion separately for the two or three components of the displacement field, and then to average the resultant moduli. One of the major issues with this approach is the second derivative in the denominator of Eq. (10.27). Derivatives exhibit noise-enhancing characteristics (which can be seen from the  $k$ -space representation of

<sup>3</sup> The shear modulus  $\mu$  or  $G^*$  for shear waves, the P-wave modulus  $M$  for pressure waves.

<sup>4</sup> In Section 10.8, we present a DI method for transverse isotropic media.

discrete derivative operators in Figures 8.12 and 8.13, where higher spatial frequencies are weighted more strongly than lower frequencies). Therefore, even relative small fluctuations in the wave field can be amplified by the double application of the derivative operator, with severe impact on the calculated modulus.

In multifrequency MRE, Helmholtz inversion is valid for each frequency component separately, so that the resulting modulus is also a function of frequency,  $\Gamma = \Gamma(\omega)$ . If  $\Gamma$  varies with frequency, this phenomenon is called *dispersion* and it occurs in all scenarios involving viscosity. The dispersion curve  $\Gamma(\omega)$  is equivalent to the frequency dependence of the viscoelastic models summarized in Figure 4.7 (with  $s = i\omega$ ) and can potentially yield valuable information about the viscoelastic properties of the tissue. In another approach, viscosity is neglected, and the values of  $\Gamma(\omega)$  obtained from single-frequency AHI are averaged over all acquired frequencies. However, a better approach for multifrequency MRE is discussed in Section 10.5.

Helmholtz inversion does not consider boundary effects. Therefore, standing waves caused by reflections at organ boundaries can cause nodes of the wave field, where no deflection occurs. In these regions, the modulus cannot be reliably reconstructed by Eq. (10.27). Instead, multifrequency inversion methods, which will be discussed in the following sections, can help to ameliorate these issues at the cost of losing information about the frequency dependence of the modulus.

In contrast to the PG discussed in Section 10.2, the Helmholtz equation can deal with superpositions of waves propagating along different directions, as long as their wave numbers  $k = |\mathbf{k}|$  are the same. We can easily verify this by substituting a superposition of two waves into the vector equivalent of Eq. (10.25):

$$\Delta(\mathbf{u}_1 \cdot e^{i(\mathbf{k}_1 \cdot \mathbf{r} - \omega_1 t)} + \mathbf{u}_2 \cdot e^{i(\mathbf{k}_2 \cdot \mathbf{r} - \omega_2 t)}) = -\mathbf{k}_1^2 \cdot \mathbf{u}_1 \cdot e^{i(\mathbf{k}_1 \cdot \mathbf{r} - \omega_1 t)} - \mathbf{k}_2^2 \cdot \mathbf{u}_2 \cdot e^{i(\mathbf{k}_2 \cdot \mathbf{r} - \omega_2 t)} \quad (10.28)$$

$$\ddot{\mathbf{u}} = -\omega_1^2 \cdot \mathbf{u}_1 \cdot e^{i(\mathbf{k}_1 \cdot \mathbf{r} - \omega_1 t)} - \omega_2^2 \cdot \mathbf{u}_2 \cdot e^{i(\mathbf{k}_2 \cdot \mathbf{r} - \omega_2 t)}. \quad (10.29)$$

If we now assume that the waves have equal wave number and frequency,  $\mathbf{k}_1^2 = \mathbf{k}_2^2 \equiv k^2$  and  $\omega_1 = \omega_2 \equiv \omega$ , we can combine these two equations:

$$-k^2(\mathbf{u}_1 \cdot e^{i\mathbf{k}_1 \cdot \mathbf{r}} + \mathbf{u}_2 \cdot e^{i\mathbf{k}_2 \cdot \mathbf{r}}) \cdot e^{-i\omega t} = -\frac{\omega^2}{c^2}(\mathbf{u}_1 \cdot e^{i\mathbf{k}_1 \cdot \mathbf{r}} + \mathbf{u}_2 \cdot e^{i\mathbf{k}_2 \cdot \mathbf{r}}) \cdot e^{-i\omega t} \quad (10.30)$$

$$\implies k^2 = \frac{\omega^2}{c^2}, \quad (10.31)$$

which is the same result as for a single wave. Therefore, inversion methods based on the wave equation are intrinsically capable of dealing with monofrequent waves traveling along different directions, and no directional filtering is necessary.

Real-world wave fields are typically a superposition of shear (transversal) and pressure (longitudinal) waves, which are governed by different elastic moduli. Applying AHI to such a wave field will result in erroneous results, since Eq. (10.27) is formulated with respect to only a single elastic modulus. There are two possibilities to resolve this issue: Multiparameter inversion, or separation of the two wave fields by means of Helmholtz decomposition. We will discuss both methods in the following two sections.

### 10.3.1 Multiparameter Inversion

AHI is only feasible for very simple material models that are characterized by a single elastic constant. However, more realistic models depend on two (in the isotropic case) or more parameters, and solving the equations of motion for these parameters simultaneously is nontrivial. Oliphant et al. published the first inversion method, termed *AIDE* (algebraic inversion of the differential equation), capable of retrieving multiple model parameters from an MRE scan with a sufficient number of independent measurements [215]. In this section, we will present a different formulation of a multiparameter inversion algorithm based on the two-parameter Navier equation.

We repeat the Navier equation (Eq. (4.132)) with elastic parameters  $\mu$  and  $\lambda$ :

$$\rho \ddot{\mathbf{u}} = (\lambda + \mu) \nabla(\nabla \bullet \mathbf{u}) + \mu \Delta \mathbf{u}. \quad (10.32)$$

The first term on the right-hand side relates exclusively to pressure waves ( $\nabla \bullet \mathbf{u} = 0$  for shear fields), whereas the second term contains both shear and volumetric deformation. In the case of a monofrequency oscillation, we can express the Navier equation in the Fourier domain, with  $\tilde{\mathbf{u}}$  being the temporally Fourier-transformed displacement field at the vibration frequency. Using the derivative property of the Fourier transform (see (8.30)) and reordering the right-hand side by elastic parameters, we obtain

$$-\rho \omega^2 \cdot \tilde{\mathbf{u}} = \lambda \cdot \nabla(\nabla \bullet \tilde{\mathbf{u}}) + \mu \cdot (\nabla(\nabla \bullet \tilde{\mathbf{u}}) + \Delta \tilde{\mathbf{u}}). \quad (10.33)$$

This allows us to express the right-hand side in vector notation:

$$-\rho \omega^2 \tilde{\mathbf{u}} = \underbrace{[\nabla(\nabla \bullet \tilde{\mathbf{u}}), \nabla(\nabla \bullet \tilde{\mathbf{u}}) + \Delta \tilde{\mathbf{u}}]}_{\equiv \mathbf{A}} \cdot \begin{pmatrix} \lambda \\ \mu \end{pmatrix}, \quad (10.34)$$

where the  $3 \times 2$  matrix  $\mathbf{A}$  is composed of second-order derivatives of the displacement field:

$$\mathbf{A} = \begin{pmatrix} \frac{\partial}{\partial x} \nabla \bullet \tilde{\mathbf{u}}, & \frac{\partial}{\partial x} \nabla \bullet \tilde{\mathbf{u}} + \Delta \tilde{u}_1 \\ \frac{\partial}{\partial y} \nabla \bullet \tilde{\mathbf{u}}, & \frac{\partial}{\partial y} \nabla \bullet \tilde{\mathbf{u}} + \Delta \tilde{u}_2 \\ \frac{\partial}{\partial z} \nabla \bullet \tilde{\mathbf{u}}, & \frac{\partial}{\partial z} \nabla \bullet \tilde{\mathbf{u}} + \Delta \tilde{u}_3 \end{pmatrix}. \quad (10.35)$$

We can now solve Eq. (10.34) for the elastic moduli:

$$\begin{pmatrix} \lambda \\ \mu \end{pmatrix} = -\rho \omega^2 \cdot (\mathbf{A}^T \mathbf{A})^{-1} \mathbf{A}^T \cdot \mathbf{u}. \quad (10.36)$$

The same procedure can be performed for other pairs of elastic parameters. For example, see [176] for the choice  $(\mu, K)$ .

### 10.3.2 Helmholtz Decomposition

We also discussed in Section 4.9.2 that the divergence and curl operators can be used to separate an arbitrary wave field into longitudinal and transversal displacement fields. We refer to that chapter for the mathematical background. As a result, we can separate

the Navier equation into two decoupled equations:

$$-\rho\omega^2 \mathbf{c} = \mu \cdot \Delta \mathbf{c} \quad (10.37)$$

$$-\rho\omega^2 d = \left(K + \frac{4}{3}\mu\right) \cdot \Delta d \quad (10.38)$$

with

$$\mathbf{c} \equiv \nabla \times \mathbf{u} \quad \text{and} \quad d \equiv \nabla \bullet \mathbf{u}. \quad (10.39)$$

These two equations are again of the Helmholtz type and can be solved for  $\mu$  and  $K$  by substituting  $\mathbf{c}$  and  $d$  for  $\mathbf{u}$  in Eq. (10.27). Two factors have to be considered when choosing Helmholtz decomposition for recovering elastic moduli: First, since  $\mathbf{c}$  and  $d$  are already first-order derivatives of the measured displacement field  $\mathbf{u}$ , the solution of Eqs. (10.37) and (10.38) requires third-order derivatives of the field, rendering the method even more noise-sensitive than regular AHI with its second-order derivatives. Second, Helmholtz decomposition is only exact for continuous functions. In the case of discrete displacement fields with numerically approximated derivatives, there can be a small amount of cross talk between the calculated longitudinal and transversal displacement fields. This latter effect becomes stronger as the spatial resolution decreases.

## 10.4 Local Frequency Estimation

*Local frequency estimation* (LFE) [216, 217] is a method to estimate the wave number<sup>5</sup>  $k$  from a wave image. It was first introduced into MRE by Manduca et al. [218]. LFE does not directly calculate spatial derivatives, as all previously discussed inversion methods. Instead, it is based on applying pairs of band-pass filters to the wave images and extracting the wave number from the ratio of the filtered images. The effect of the filters is similar to applying the gradient operator in  $k$ -space. A very thorough discussion of the method can be found in [219]; we will only present a general overview without going into implementational or mathematical details.

We recall the Fourier convolution theorem, which states that the convolution of two image space functions  $f(\mathbf{r})$  and  $g(\mathbf{r})$  can be equally expressed as the point-wise product of their Fourier transforms,  $\tilde{f}(\mathbf{k})$  and  $\tilde{g}(\mathbf{k})$ :

$$f(\mathbf{r}) \star g(\mathbf{r}) = \mathcal{F}^{-1}[\tilde{f}(\mathbf{k}) \cdot \tilde{g}(\mathbf{k})]. \quad (10.40)$$

We now look at a pair of filters  $H_1$  and  $H_2$  with the property that their  $k$ -space representations behave like

$$\frac{\tilde{H}_2(k, \vartheta)}{\tilde{H}_1(k, \vartheta)} = k^p, \quad (10.41)$$

where  $(k, \vartheta)$  represent polar coordinates of a two-dimensional  $k$ -space, and  $p \in \mathbb{R}$ . For a monofrequency plane wave  $\tilde{u}(k_0, \vartheta)$  with wave number  $k_0$  and arbitrary propagation

<sup>5</sup> The “frequency” in LFE relates to spatial frequencies, as quantified by the wave number, rather than oscillation frequencies.



direction, the filters  $H_1$  and  $H_2$  can extract the wave vector from the wave:

$$\frac{u \star H_2}{u \star H_1} = \frac{\mathcal{F}^{-1}[\tilde{u} \cdot \tilde{H}_2]}{\mathcal{F}^{-1}[\tilde{u} \cdot \tilde{H}_1]} = k_0^p. \quad (10.42)$$

If the wave is not truly monochromatic, but its spectrum is concentrated around some value  $k_0$ , Eq. (10.42) will instead yield an average wave number instead.

The filter functions used for LFE are drawn from a class known as *log-normal quadrature filters* [216, 217]. Their  $k$ -space representation is given by

$$\tilde{H}_1(k, \vartheta, k_c) = \exp\left(-\frac{1}{2 \ln 2} \ln^2\left(\frac{k}{k_c}\right)\right) \cdot \sum_{m=1}^{N_d} D_m(\vartheta), \quad (10.43)$$

where  $k_c$  is the characteristic frequency of the filter,  $N_d$  is the number of spatial dimensions, and

$$D_m(\vartheta) = \begin{cases} (\hat{\mathbf{k}} \cdot \hat{\mathbf{n}}_m)^2 & \text{if } \hat{\mathbf{k}} \cdot \hat{\mathbf{n}}_m > 0 \\ 0 & \text{else} \end{cases}, \quad (10.44)$$

where  $\hat{\mathbf{n}}_m$  is the unit vector along the  $m$ th dimension of  $k$ -space and  $\hat{\mathbf{k}} = \mathbf{k}/|\mathbf{k}|$ . Each  $D_m$  defines a directional filter that is aligned with one of the coordinate axes and only lets wave vectors with a component parallel (as opposed to antiparallel) to the coordinate axis pass.

A second filter can be defined as

$$\tilde{H}_2(k, \vartheta, k_c) = k \cdot \tilde{H}_1(k, \vartheta, k_c) = k_c \sqrt{2} \tilde{H}_1(k, \vartheta, 2 \cdot k_c). \quad (10.45)$$

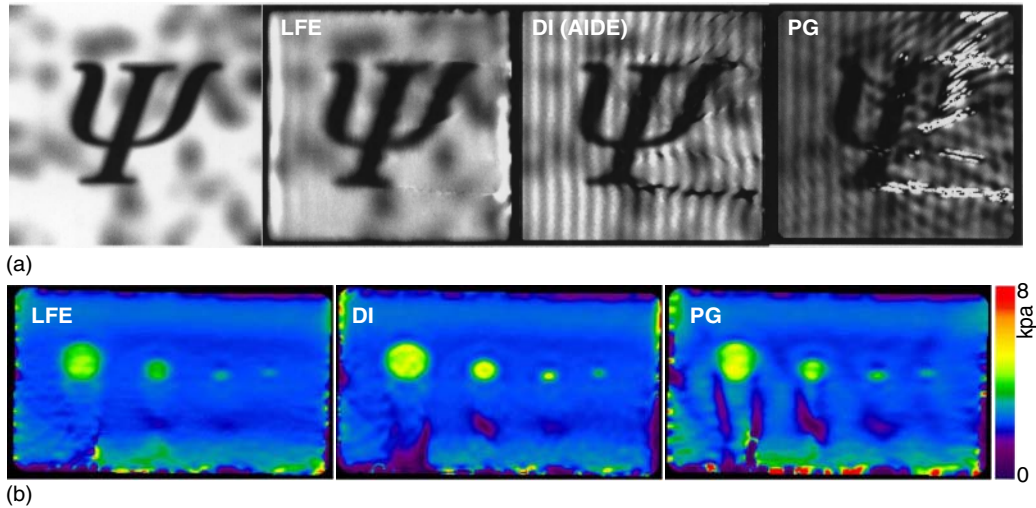
The filter pair  $(\tilde{H}_1, \tilde{H}_2)$  hence satisfies the relation (10.41) for  $p = 1$ , and one can therefore obtain an estimate of the local wave number (known as the “local frequency” in signal processing, hence the name of the method) by filtering the displacement field  $\mathbf{u}$  with both filters and taking the quotient of the results, as prescribed by Eq. (10.42). The wave number can then be converted into a wave velocity via  $k = \frac{\omega}{c}$ , and further into a shear modulus via  $\mu = \rho c^2$ .

Usually, the local wave number is not precisely known a priori, and it can also vary significantly over inhomogeneous tissue regions or in the vicinity of tissue boundaries. The two filters  $\tilde{H}_1$  and  $\tilde{H}_2$  vary by a factor 2 (one octave) in their characteristic frequency, according to Eq. (10.45). If the true local frequency does not fall into that interval, the estimate of  $k$  will be incorrect. Therefore, it is common practice to use a bank of filters with different center frequencies, and to inspect the output of pairs of filters whose characteristic frequencies differ by one octave.

Because of the relation

$$\mathcal{F}[f'(x)] = k \cdot \mathcal{F}[f(x)], \quad (10.46)$$

we can see from Eq. (10.45) that applying the filter  $\tilde{H}_2$  is similar to applying a spatial derivative to the output of the filter  $\tilde{H}_1$ . Solving for  $k$  by LFE is therefore comparable to the PG method discussed in Section 10.2, which is also based on a first spatial derivative of the displacement field and contrasts the (AHI) methods based on the inversion of the wave equation, which require second-order derivatives. Hence, LFE can be considered more resilient to noise than AHI because of the noise-amplifying characteristics of derivatives. On the downside, the application of filters with an extended spatial support



**Figure 10.3** Comparison of different inversion methods in the literature. (a) Simulated data and the LFE, direct inversion (DI, here: AIDE), and phase gradient (PG) reconstructions for the noiseless data (from left to right). LFE is smoother than DI and PG. Since no directional filters were used, PG is badly disturbed by phase discontinuities. (b) Phantom data reconstructed by LFE, DI, and PG, here including directional filters prior to the inversions. With directional filters, PG performs better; however, artifacts below the inclusions presumably due to diffraction are still more apparent than in other methods. Of note, phantom data comprise only a single wave field component at a single frequency. Multicomponent, multifrequency data can further reduce those artifacts toward the method described as  $k$ -MDEV inversion (see Section 10.6). (Manduca 2001 [194]. Reproduced with permission of Elsevier (a) and Manduca 2003 [220]. Reproduced with permission of Elsevier (b).)

means that in inhomogeneous tissue the reconstructed elasticities converge rather slowly toward their true value. This means that near a boundary between two different media, the boundary region becomes fuzzy, and the true elastic properties can only be reconstructed at a certain distance from the boundary. Similarly, the elastic estimates of small inclusions will be biased toward the elastic properties of the surrounding medium. The spatial resolution LFE is therefore determined by the width of the filters, and it can be dramatically lower than the actual image resolution.

In Figure 10.3, we present a comparison of different single-frequency inversion methods in numerically simulated data.

## 10.5 Multifrequency Inversion

The previously discussed inversion methods can be performed on data that were acquired using a single vibration frequency. However, single-frequency schemes suffer from a number of problems, including inhomogeneous illumination of the organ of interest due to standing wave nodes and attenuation especially in the higher frequency ( $\geq 60$ Hz) range. Standing waves are characterized by nodes with zero displacement amplitude. While under ideal, noise-free conditions, it is possible to recover correct moduli even for these nodes; in the presence of noise, the process is highly unstable and the results become random. Regions with low wave intensity tend to have lower

SNR and consequently yield lower elasticity estimates because of the noise-enhancing Laplacian in Eq. (10.27), for example. These issues can be ameliorated by performing averaging over several distinct vibration frequencies. This approach is implicitly based on the assumption the elastic moduli are independent of the vibration frequency, that is,  $G^* = G^*(\mathbf{r})$  rather than  $G^*(\mathbf{r}, \omega)$ . The absence of dispersion is strictly only true for purely elastic media, whereas viscous effects inevitably introduce dispersion (see Section 4.8.2 and Figure 4.7). However, for the sake of simplicity, we demonstrate the principle of frequency averaging for resolution improvement without relying on any particular viscoelastic model.

In Section 10.3, we mentioned that independently calculated  $G^*$  maps obtained at different vibration frequencies can be combined by averaging over frequencies. A better way than averaging over elastic moduli is to combine the raw wave fields acquired at these frequencies into a single composite wave field, which is then subjected to an inversion algorithm. The first version of this approach was published in [221] and termed *MDEV (multifrequency dual elasto-visco inversion)*.<sup>6</sup> In the following section, we will present an improved version of this method published in [69].

We begin the discussion by formulating the Helmholtz equation in terms of the complex shear modulus

$$G^* = |G^*| \cdot e^{i\varphi}. \quad (10.47)$$

The phase angle  $\varphi$  quantifies the ratio of elastic to viscous properties of the tissue.  $\varphi = 0$  corresponds to purely elastic characteristics, whereas  $\varphi = \frac{\pi}{2}$  designates pure viscosity. Values outside of this range are unphysical. The phase angle is also related to the interpolation parameter  $\alpha$  in the springpot model (see Eq. (4.106)) via  $\alpha = \frac{2}{\pi} \varphi$ . Thus, for a medium characterized by a springpot model,  $\varphi$  provides an intrinsic, frequency-independent property. The goal of multifrequency inversion is to reconstruct both parameters on the right-hand side of Eq. (10.47) independently.

### 10.5.1 Reconstruction of $\varphi$

Let  $\tilde{v}$  be an arbitrary component of the displacement field  $\tilde{\mathbf{u}}(\mathbf{r}, \omega)$ , then

$$G^*(\mathbf{r}) \cdot \Delta \tilde{v}(\mathbf{r}, \omega) = -\rho \omega^2 \tilde{v}(\mathbf{r}, \omega) \quad (10.48)$$

$$\implies \Delta \tilde{v} = -\frac{\rho \omega^2}{|G^*|} \cdot e^{-i\varphi} \tilde{v}, \quad (10.49)$$

which tells us that  $\Delta \tilde{v}$  is just a scaled (with factor  $-\frac{\rho \omega^2}{|G^*|}$ ) and rotated (with angle  $-\varphi$ ) copy of  $\tilde{v}$ . In order to retrieve the rotation angle  $\varphi$ , we can multiply both sides with  $(-\tilde{v}^\dagger)$ , where the dagger indicates complex conjugation:

$$-\tilde{v}^\dagger \cdot \Delta \tilde{v} = \frac{\rho \omega^2}{|G^*|} \cdot |\tilde{v}|^2 \cdot e^{-i\varphi}. \quad (10.50)$$

<sup>6</sup> The term “dual” alludes to the fact that elasticity and viscosity are retrieved from two mutually independent calculation steps.

The exponential function is the only complex quantity on the right-hand side. Therefore, we can retrieve  $\varphi$  by extracting the complex phase on both sides and exploiting the fact that  $\arg(a^\dagger \cdot b) = -\arg(a \cdot b^\dagger)$ :

$$\arg(-\tilde{v} \cdot \Delta\tilde{v}^\dagger) = \varphi. \quad (10.51)$$

Equation (10.51) yields the phase angle of the complex modulus for a measurement with a single vibration frequency  $\omega$  and one Cartesian component of the displacement field. If measurements at  $N$  different frequencies  $\omega_i$  and assessing all three components  $\tilde{u}_j$  of the field are performed, there are two options to combine these data into one value of  $\varphi$ . First, Eq. (10.51) could be evaluated for all frequencies and components separately, with  $v = \tilde{u}_j(\omega_i)$ , and then an average value of  $\varphi$  could be calculated. However, this would again be a single-frequency inversion with subsequent averaging, with all disadvantages discussed above. Second, assuming that there was no dissipation, all components should yield the same value inside the parentheses of the  $\arg$  function. Therefore, averaging can also be performed before the  $\arg$  is applied. The equation then reads<sup>7</sup>

$$\varphi = \arg\left(-\sum_{i=1}^N \sum_{j=1}^3 \tilde{u}_j(\omega_i) \cdot \Delta\tilde{u}_j^\dagger(\omega_i)\right). \quad (10.52)$$

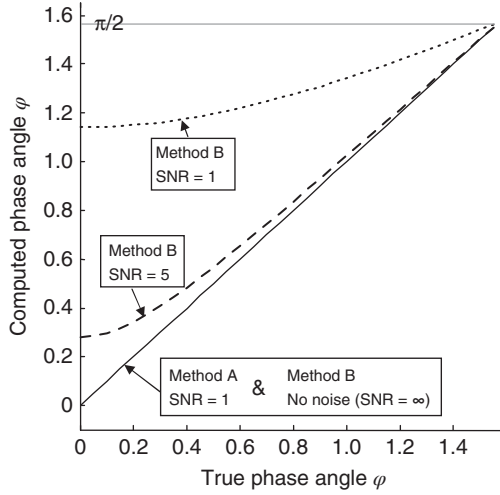
Each term in the sum is intrinsically weighted by the product  $|\tilde{u}_j(\omega_i)| \cdot |\Delta\tilde{u}_j(\omega_i)|$ . Weighting by  $|\tilde{u}_j|$  ensures that frequencies with higher vibration amplitude, and hence higher SNR, contribute more to the result than frequencies with lower amplitudes and lower signal quality. This prioritizes lower frequencies, which tend to have larger amplitudes than higher ones. Weighting by  $|\Delta\tilde{u}_j|$ , on the other hand, emphasizes waves with greater curvature, which corresponds to better SNR in the Laplacian of the wave field. Since curvature is inversely related to the wavelength, the curvature is larger for higher frequencies than for lower ones at the same vibration amplitude.

An alternative way of calculating the phase angle is to utilize the scalar product relation  $\mathbf{a} \bullet \mathbf{b} = |\mathbf{a}| \cdot |\mathbf{b}| \cdot \cos(\angle(\mathbf{a}, \mathbf{b}))$ . We can hence recover the phase angle as

$$\varphi = \arccos\left(-\frac{\tilde{v} \bullet \Delta\tilde{v}}{|\tilde{v}| \cdot |\Delta\tilde{v}|}\right), \quad (10.53)$$

if we treat  $\tilde{v}$  and  $\Delta\tilde{v}$  as two-dimensional vectors in the complex plane. For noiseless data, this is identical to Eq. (10.51). However, in the presence of noise, the two methods differ (see Figure 10.4). Imagine a purely elastic medium, with a phase angle  $\varphi = 0$  (i.e.,  $\tilde{v}$  and  $\Delta\tilde{v}$  are colinear). Measurement noise causes the actual value of  $\varphi$  to fluctuate around zero. If  $\varphi$  is calculated for each voxel separately and then averaged over the region of interest, these fluctuations cancel out and the resulting value of  $\varphi$  should be very close to zero. This is the result obtained when Eq. (10.51) is used. However, due to the definition of the arccosine function with image domain  $0 \leq \arccos(x) \leq \pi$ , small negative values of  $\varphi$  are actually mapped to small positive values. This means that the fluctuations over a region of interest cannot cancel, since each contribution is  $\geq 0$ . Therefore, the averaged value of  $\varphi$  obtained by the latter method is biased toward higher values of  $\varphi$ , thus overemphasizing the imaginary part. The effect becomes

<sup>7</sup> Since dividing by the number of components and frequencies inside the  $\arg$  function would have no effect on the phase, this factor is left out of the equation.



**Figure 10.4** Comparison of the two formulas for the reconstruction of  $\varphi$ , Eq. (10.52) (“method A”) and Eq. (10.53) (“method B”). Noisy one-dimensional waves were subjected to inversion at different SNR levels. Ideally, the true phase angle (which was used as the simulation parameter, plotted on the horizontal axis) should equal the calculated phase angle (obtained from the inversion, shown on the vertical axis). For method A, the agreement between the two values is indistinguishable from the ideal line  $\varphi_{\text{computed}} = \varphi_{\text{true}}$  even at a very low SNR = 1. For method B, we see a systematic overestimation of the calculated  $\varphi$ -value due to the bias of the arccos function toward positive values, especially when  $\varphi$  is close to zero. Method B only yields accurate results in the noise-free case. Every inversion step was repeated  $10^5$  times, and the averaged results are shown to minimize stochastic fluctuation. (Dittmann 2015 [69]. Reproduced with permission of Wiley.)

smaller as the viscosity of the medium increases, since in that case the true value of  $\varphi$  becomes larger, and noise is less likely to shift  $\varphi$  to negative values.

### 10.5.2 Reconstruction of $|G^*|$

For reconstructing the magnitude of  $G^*$ , we can take the absolute value of Eq. (10.49). Again, assuming that  $G^*$  is the same for all frequencies and field components, we can sum both sides of the equation over  $i$  and  $j$ :

$$\sum_{i=1}^N \sum_{j=1}^3 |G^*| \cdot |\Delta \tilde{u}_j(\omega_i)| = \sum_{i=1}^N \sum_{j=1}^3 \rho \omega_i^2 |\tilde{u}_j(\omega_i)| \quad (10.54)$$

$$\Rightarrow |G^*| = \rho \cdot \frac{\sum_{i=1}^N \sum_{j=1}^3 \omega_i^2 |\tilde{u}_j(\omega_i)|}{\sum_{i=1}^N \sum_{j=1}^3 |\Delta \tilde{u}_j(\omega_i)|} \quad (10.55)$$

Again, this is a true multifrequency inversion, since the wave fields are first averaged over all components and frequencies before the division is performed, as opposed to solving Eq. (10.49) for each  $(i, j)$  separately and averaging over the results.

The complex modulus can then be calculated using Eq. (10.47), with the values for  $|G^*|$  and  $\varphi$  obtained from Eq. (10.55) and Eq. (10.52) (or Eq. (10.53)), respectively.

It should be noted that parameters reconstructed by multifrequency inversion are influenced by tissue-specific wave attenuation properties. Those parameters represent a frequency-weighted average, and the relative weighting is likely to change as the wave moves deeper into the tissue, where higher frequencies experience stronger attenuation. Indeed, frequency-dependent attenuation is a challenge for all types of multifrequency elastography methods, especially for those relying on transient mechanical stimulations, such as many ultrasound-based methods. Viscosity of the tissue acts as a low-pass filter, hence lower frequencies dominate at longer sampling times in ultrasound-based elastography. Compared to transient impulses as, for example, used by acoustic radiation force impulse (ARFI) techniques (see Section 12.3), the frequency band exploited by MRE is relatively narrow. Nevertheless, frequency averaging by MDEV inversion ignores the fact that soft biological tissue displays frequency dispersion of  $|G^*|$  and thus depends on the used frequency range, similar to all other MRE methods not based on viscoelastic modeling. Comparisons of values between different types of tissue and cross-validation of parameters should be based on single-harmonic MRE even though the encountered inverse problem is often more affected by noise and amplitude nulls.

## 10.6 $k$ -MDEV

In Section 10.2, we introduced the PG method for estimating the wave number  $k$  based on first-order derivatives. We also mentioned the shortcomings of the methods, particularly its inability to cope with superposition of waves traveling in different directions. In this section, we demonstrate how these issues can be overcome through improved postprocessing and spatial filtering.

A novel inversion method has been devised recently and termed  $k$ -MDEV ( $k$ -based MDEV inversion) [222]. In contrast to the other inversion routines mentioned thus far (except LFE), it does not require second-order derivatives. It is built upon the principle that the real and imaginary parts of the complex wave vector,  $\mathbf{k}'$  and  $\mathbf{k}''$ , respectively, can be calculated from first-order spatial derivatives of the temporally Fourier-transformed displacement field. A full  $\mathbf{k}$  vector can be calculated for every component  $\tilde{u}_j$  of the displacement field. While it is in principle possible to obtain three-dimensional wave vectors, technical limitations have thus far restricted the method to in-plane applications, yielding two-dimensional  $\mathbf{k}$  vectors. We introduce the notation

$$\mathbf{k}_{(j)} = \mathbf{k}'_{(j)} + i\mathbf{k}''_{(j)} \quad \text{in-plane (2D) wave vector obtained from } \tilde{u}_j \quad (10.56)$$

$$k'_{(j)} = \|\mathbf{k}'_{(j)}\| \quad \text{Real part of the complex wave vector} \quad (10.57)$$

$$k''_{(j)} = \|\mathbf{k}''_{(j)}\| \quad \text{Imaginary part of the complex wave vector} \quad (10.58)$$

with the Euclidean in-plane norm

$$\|\chi\| = \sqrt{\chi_1^2 + \chi_2^2}. \quad (10.59)$$

For each of the three displacement field components, we calculate the magnitude of the real and imaginary parts of the wave vector as

$$k'_{(j)} = \left\| \nabla^{(2D)} \left( \frac{\tilde{u}_j}{|\tilde{u}_j|} \right) \right\| \quad (10.60)$$

$$k''_{(j)} = \frac{\left\| \nabla^{(2D)} |\tilde{u}_j| \right\|}{|\tilde{u}_j|} \quad (10.61)$$

with the in-plane gradient operator  $\nabla^{(2D)}$ . Normalization of  $\tilde{u}_j$  by  $|\tilde{u}_j|$  renders the reconstructed real part of the wave vector immune to bias from geometric attenuation (see Section 4.11.1), which would otherwise be mistaken for dissipative damping. However, for the imaginary part  $k''_{(j)}$ , geometric attenuation cannot be separated from dissipative damping, since the normalization is performed after calculating the gradient. Therefore,  $k''_{(j)}$  does not represent purely viscous properties, but it is tainted by geometrical factors. We will thus restrict the further discussion to  $k'_{(j)}$ .

Remember that  $k'_{(j)}$  refers to the magnitude of the wave vector,  $\|\mathbf{k}'_{(j)}\|$ , which is the *in-plane* wave vector derived from the  $j$ th Cartesian component of the displacement field, it is *not* the  $j$ th component of  $\mathbf{k}'$ . Ideally, in an isotropic medium, the relation  $\|\mathbf{k}'\| = k'_{(1)} = k'_{(2)} = k'_{(3)}$  should hold.

Equations (10.60) and (10.61) can be easily verified if a plane wave  $\tilde{u}_j = u_{0j} \cdot e^{i\mathbf{k}'_{(j)} \cdot \mathbf{x} - \mathbf{k}''_{(j)} \cdot \mathbf{x}}$  is inserted:

$$|\tilde{u}_j| = u_{0j} \cdot e^{-\mathbf{k}''_{(j)} \cdot \mathbf{x}} \quad (10.62)$$

$$\nabla^{(2D)} \left( \frac{\tilde{u}_j}{|\tilde{u}_j|} \right) = \nabla^{(2D)} e^{i\mathbf{k}'_{(j)} \cdot \mathbf{x}} = i\mathbf{k}'_{(j)} \cdot e^{i\mathbf{k}'_{(j)} \cdot \mathbf{x}} \quad (10.63)$$

$$\Rightarrow \left\| \nabla^{(2D)} \left( \frac{\tilde{u}_j}{|\tilde{u}_j|} \right) \right\| = \|\mathbf{k}'_{(j)}\| \quad (10.64)$$

$$\nabla^{(2D)} |\tilde{u}_j| = u_{0j} \nabla^{(2D)} e^{-\mathbf{k}''_{(j)} \cdot \mathbf{x}} = -\mathbf{k}''_{(j)} \cdot e^{-\mathbf{k}''_{(j)} \cdot \mathbf{x}} \quad (10.65)$$

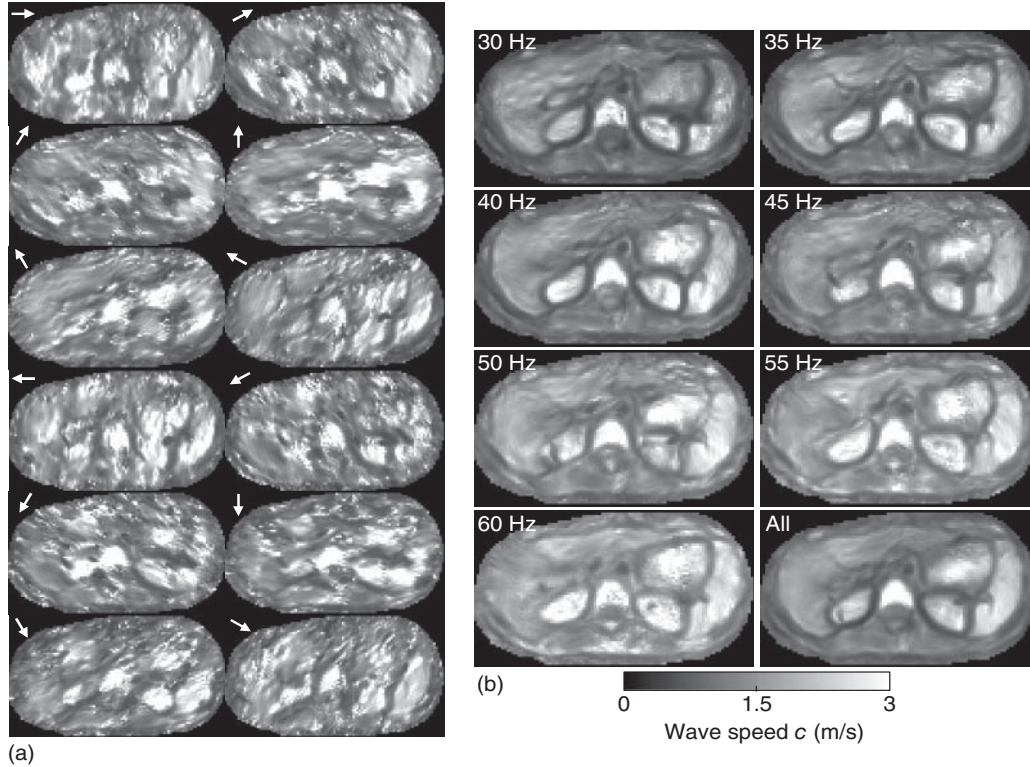
$$\Rightarrow \frac{\left\| \nabla^{(2D)} |\tilde{u}_j| \right\|}{|\tilde{u}_j|} = \frac{\|\mathbf{k}''_{(j)}\| \cdot u_{0j} \cdot e^{-\mathbf{k}''_{(j)} \cdot \mathbf{x}}}{u_{0j} \cdot e^{-\mathbf{k}''_{(j)} \cdot \mathbf{x}}} = \|\mathbf{k}''_{(j)}\|. \quad (10.66)$$

Using Eqs. (10.60) and (10.61) for the determination of the wave vector is heavily biased if the wave field is a superposition of several waves propagating in different directions.

Directional filters (Section 8.2) can be utilized to decompose the full wave field into waves propagating in different directions  $\vartheta_n$  prior to reconstruction of  $\mathbf{k}'_{(j)}$ . Finally, all wave field components (index  $j$ ), vibration frequencies (index  $i$ ), and propagation directions (index  $n$ ) can be combined into one inversion that yields the wave speed  $c(\mathbf{r})$ :

$$\frac{1}{c(\mathbf{r})} = \frac{\sum_{i,j,n} \frac{k'_{(j)}(\mathbf{r}, \omega_i, \vartheta_n)}{\omega_i} w_{i,j,n}}{\sum_{i,j,n} w_{i,j,n}} \quad (10.67)$$

with an empirical weight factor  $w_{i,j,n} = |u_j(\mathbf{r}, \omega_i, \vartheta_n)|^4$ . Equation (10.67) is similar to the MDEV principle for the solution of the Helmholtz equation for multiple frequencies and polarization components (Section 10.5), which inspired the name *k*-MDEV



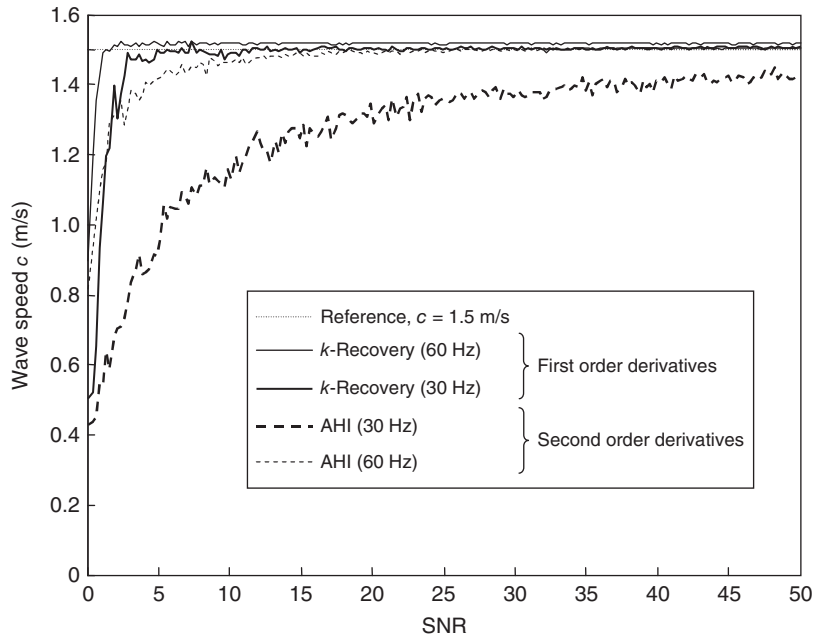
**Figure 10.5** Illustration of the principle behind  $k$ -MDEV in the abdomen. (a) 12 direction-filtered images at 45 Hz vibration. Each image is the superposition of the three displacement components, and the white arrows indicate the direction of the directional filter. (b) Wave speed images for individual frequencies, and the final imaging combining all frequencies (bottom right). Each single-frequency image is the superposition of 12 direction-filtered images, as shown in (a). The compound image thus incorporates all three Cartesian components of the displacement field, captured at seven vibration frequencies. (Tzschätzsch 2016 [222]. Reproduced with permission of Elsevier.)

for this method. The weighting factor emphasizes frequencies with high vibration amplitude and good SNR over those with lower amplitudes and poorer signal quality.

The wave velocity  $c$  can be converted into a shear modulus via  $c = \sqrt{\frac{|G'|}{\rho}}$ . An example of abdominal MRE using  $k$ -MDEV inversion is shown in Figure 10.5.

Figure 10.6 illustrates the noise robustness of  $k$ -MDEV as compared to DI by AHI. The graphs represent spatially averaged inversion results of simulated 1D complex-valued waves of 30 and 60 Hz vibration frequencies at different noise levels. AHI is demonstrated to result in severe underestimation of mean wave speed values, especially at low frequencies and high noise level (low SNR), even though the noise-suppressing filters were identical to those used in  $k$ -MDEV. As explained in Section 10.1, the effect of noise is predominant at low frequencies, whereas at high frequencies we note a slight overestimation due to discretization (as in  $k$ -MDEV at 60 Hz).





**Figure 10.6** Simulated sensitivity of  $k$ -MDEV and direct inversion to noise. Simulations were based on one-dimensional waves with  $c = 1.5$  m/s and two frequencies (30 and 60 Hz). Gaussian noise was added to a complex harmonic function  $u = e^{ik \cdot x}$  with 2 mm pixel spacing. The resulting noisy waves were subsequently analyzed by  $k$ -MDEV ( $k = \nabla \frac{u}{|u|}$ ) and direct inversion based on AHI ( $|G^*| = \rho \omega^2 \frac{|u|}{|\Delta u|}$ ).  $k$ -MDEV performs well even at low SNR whereas AHI severely underestimates values due to second-order derivatives in the Laplacian. (Tzschätzsch 2016 [222]. Reproduced with permission of Elsevier.)

## 10.7 Finite Element Method

*This chapter was coauthored by Abbas Samani from the Department of Electrical and Computer Engineering and the Department of Medical Biophysics, University of Western Ontario, Canada.*

The term “finite element method” (FEM) relates to a class of procedures that can be used to solve partial differential equations (PDEs). Different implementations of FEM vary significantly; however, all of them are founded on a weak form derived from the original PDE before their approximate solutions are obtained in a discretized form of the problem’s spatial domain. FEM is a very sophisticated and well-developed technique, with applications in almost all engineering fields. This chapter can barely scratch the surface of this topic and it is intended to provide a relevant introduction. Here, we will describe underlying principles of the method. For implementation pertaining to complex real-world applications, we refer the reader to specialized literature, for example, [223].

A typical FEM algorithm can be subdivided into a number of steps, which will be discussed below. The most fundamental part of FEM formulation is PDE conversion into one or more algebraic equations. There are a number of mathematical frameworks that

can be used for this conversion such as the *variational method* and *Galerkin method*. The main steps involved in a typical FEM algorithm are:

- 1) The problem domain is discretized into appropriate geometric primitives called finite elements. Typical choices are intervals of constant or variable length for 1D problems, triangles in 2D, and tetrahedra in 3D problems. Unknown problem parameters (e.g., displacements) are assigned at nodes of these finite elements.
- 2) A set of basis functions (*shape functions*) are introduced to interpolate the problem parameter inside the finite element in terms of the nodal parameters. In order to decrease computational complexity, each shape function has a small support limited to the domain of its associated finite element.
- 3) The governing PDE is converted into algebraic equations valid for the domain of each finite element using a suitable mathematical framework such as the variational method. This method involves the so-called weak formulation as it approximates the PDE such that the solution and boundary conditions do not match the PDE solution and the domain boundary conditions exactly, but approach them as the element size gets smaller. This framework involves the shape function of the elements, leading to algebraic equations in terms of these shape functions. The resulting algebraic equations are referred to as *element stiffness equations*.
- 4) The element stiffness equations are assembled in a systematic way to satisfy fundamental equations governing the problem (e.g., force equilibrium equations) at each node in the discretized domain. This leads to a system of algebraic equations governing the entire domain, called the global stiffness equations.
- 5) The problems boundary conditions are applied before the global stiffness equations are solved to calculate the unknown nodal parameters (e.g., displacements).

It is noteworthy that FEM is used for forward modeling where the object geometry, distribution of its viscoelastic properties, and loading are given to calculate displacement, stresses, and other parameters. In contrast, elastography is an inverse problem where the displacement field is given along loading to determine the viscoelastic parameter distribution inside the material. Inverse FEM is one of the several methods used to calculate an approximation of the viscoelastic parameter distribution. This can be done either directly using the measured displacements in conjunction with the global stiffness matrix arranged in terms of the unknown viscoelastic parameters. Another alternative for viscoelastic parameter reconstruction is using an iterative scheme, which uses the forward FEM equations iteratively to refine the parameters estimated by minimizing the mismatch between the FEM-simulated displacement field and its measured counterpart.

The following example will demonstrate how to formulate an FEM solution for the one-dimensional wave equation using the variational method as described in [204].

### 10.7.1 Weak Formulation of the One-Dimensional Wave Equation

In an incompressible medium, the single-component Navier equation (4.129) can be written in compact form as

$$\rho \ddot{u}(\mathbf{x}, t) - \mu(\mathbf{x}) \Delta u(\mathbf{x}, t) = f(\mathbf{x}, t), \quad (10.68)$$

where  $\rho$  is the mass density,  $\mu$  represents the elastic modulus of the medium, and  $f(\mathbf{x}, t)$  is the force applied to the medium. In this context, it is assumed that  $\mu$  is

position-dependent but slightly varying. Hence, all of its spatial derivatives in the equation can be neglected. By dropping the time and space annotation in the equation and moving all terms to one side, the following equation can be obtained:

$$\rho \ddot{u} - \mu \Delta u - f = 0. \quad (10.69)$$

In order to solve the wave equation in its spatial domain  $\Omega$ , which can be one-, two-, or three-dimensional, we define a vector space of *test functions*  $V = \{v | v : \Omega \rightarrow \mathbb{C}\}$  that map the problem domain into complex numbers space. Next, we multiply both sides of Eq. (10.68) with the arbitrary test function  $v(\mathbf{x}) \in V$  and integrate over  $\Omega$ . This is a mathematical trick, borrowed from the calculus of variations, that allows us to rewrite Eq. (10.68) into a more suitable form. We will see later that the obtained solution is independent of the choice of  $v$ . Therefore, we do not need to specify  $v$  explicitly:

$$\int_{\Omega} (\rho \ddot{u} - \mu \Delta u - f) \cdot v \, d\mathbf{x} = \int_{\Omega} 0 \cdot v \, d\mathbf{x} = 0. \quad (10.70)$$

We can rewrite the middle term of the integral on the left-hand side by exploiting the Gaussian divergence theorem

$$\int_{\Omega} \nabla \cdot \mathbf{F} \, d\mathbf{x} = \int_{\partial\Omega} \mathbf{F} \cdot \hat{\mathbf{n}} \, d\sigma \quad (10.71)$$

for an arbitrary vector field  $\mathbf{F}$ , where  $\hat{\mathbf{n}}$  is the outer normal unit vector to the surface element  $\sigma$  and  $\partial\Omega$  is the boundary of  $\Omega$ . Choosing  $\mathbf{F} = v \nabla u$  allows us to write

$$\int_{\Omega} \nabla \cdot (v \nabla u) \, d\mathbf{x} = \int_{\partial\Omega} (v \nabla u) \cdot \hat{\mathbf{n}} \, d\sigma \quad (10.72)$$

$$\Leftrightarrow \int_{\Omega} \nabla v \cdot \nabla u \, d\mathbf{x} + \int_{\Omega} v \Delta u \, d\mathbf{x} = \int_{\partial\Omega} (v \nabla u) \cdot \hat{\mathbf{n}} \, d\sigma \quad (10.73)$$

$$\Leftrightarrow \int_{\Omega} v \Delta u \, d\mathbf{x} = \int_{\partial\Omega} (v \nabla u) \cdot \hat{\mathbf{n}} \, d\sigma - \int_{\Omega} \nabla v \cdot \nabla u \, d\mathbf{x}. \quad (10.74)$$

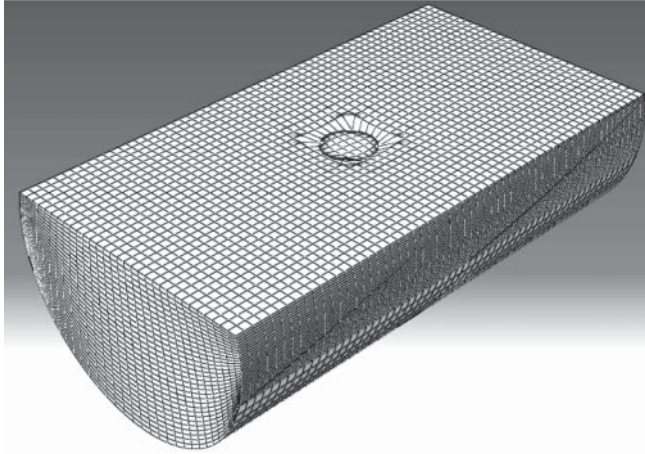
In the second line, we used the product rule of differentiation. This intermediate result allows us to rewrite Eq. (10.70) as

$$\int_{\Omega} (\rho \ddot{u} \cdot v + \mu \nabla v \cdot \nabla u - f \cdot v) \, d\mathbf{x} - \mu \int_{\partial\Omega} (v \nabla u) \cdot \hat{\mathbf{n}} \, d\sigma = 0. \quad (10.75)$$

The fundamental theorem of the calculus of variations states that a function  $u(\mathbf{x}, t)$  is a solution to Eq. (10.68) only if it satisfies Eq. (10.75) for any  $v \in V$ . The problem was hence reformulated from solving the PDE directly to finding a suitable solution  $u(\mathbf{x}, t)$  for Eq. (10.75). This in itself does not simplify the problem yet, as the solution space for  $u(\mathbf{x}, t)$  has infinite dimension. However, in a later step, we will substitute the general functions  $u$  and  $v$  with linear combinations of shape functions with small support, which will significantly reduce the size of the solution space.

### 10.7.2 Discretization of the Problem Domain

The concept underlying FEM is to substitute the continuous problem domain  $\Omega$  with a discretized domain. As a consequence, the solution is obtained at a certain set of points (called *nodes*) that sample the domain, whereas values for other points in the domain

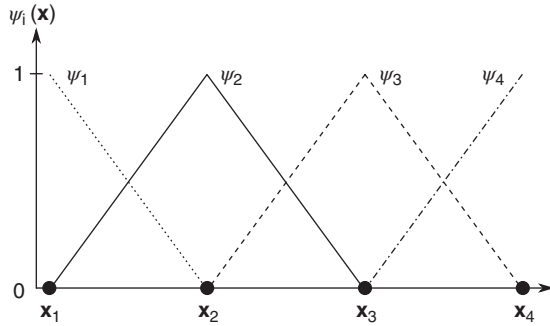


**Figure 10.7** Discretization of the problem domain in 3D. A block of material is indented locally, and the resulting deformation is reflected in the deformation of the mesh. (Reiter 2014 [224]. Reproduced with permission of Elsevier.)

have to be obtained by interpolation. For a one-dimensional problem, discretization means dividing the line domain into several small segments, where nodes are located at the two ends of each segment. In 2D and 3D, the domain is subdivided into geometric primitives, typically triangles and tetrahedra, but other primitives such as quadrilaterals and hexahedrons are also viable (Figure 10.7). The nodes coincide with the vertices of the primitives. High node density increases the accuracy of the solution at the cost of higher computational complexity. Variable node density can be prescribed in cases where the solution is expected to have local high gradients. In such cases, high node density is used in anticipated solutions including high gradient regions. In order to form a consistent FE mesh, element nodes can only intersect with other element nodes, that is, nodes cannot intersect with another element's edge. Nodes are denoted using a single index ( $\mathbf{x}_i, i = 1, \dots, N$ ). Together with the edges of the geometric primitives, the nodes form a mesh, called FE mesh, which defines the space on which calculations are performed. FEM provides the sought solution of unknown parameters (e.g., displacements) at the mesh nodes directly, while the parameters at other points within an element can be calculated using the element shape function. The notation  $\mathbf{x}$  will henceforth denote a node belonging to the FE mesh.

### 10.7.3 Basis Function in the Discretized Domain

Here, we introduce a set of simple shape functions that are involved in FEM formulation. We mentioned earlier that in order to facilitate computations, the shape functions should have local support and minimal overlap. This can be guaranteed if the shape functions are chosen such that their support is limited to exactly one node and one finite element containing that node (excluding the other nodes defining that element). In the 1D case, this simply means that the support of a shape function is limited to the one node and the space between that node and its nearest left- and right-hand-side neighbors where the function's value is 1 and 0 at the node and its neighboring nodes,



**Figure 10.8** Illustration of the shape functions  $\psi_i(\mathbf{x})$  on a one-dimensional mesh with  $N = 4$  equidistantly spaced nodes.

respectively. For a triangulation of a 2D surface, the support of a shape function corresponds to one node and one triangle adjacent to that node where the function's value is 1 and 0 at the node and its neighboring nodes, respectively.

For our 1D example, we define shape functions as *hat functions*, as illustrated in Figure 10.8. Each shape function  $\psi_i$  is equal to unity at the node  $\mathbf{x}_i$ , and scales linearly to zero toward its two neighbors. In this case, each node is associated with exactly one shape function. As a consequence, the shape functions are orthonormal with respect to the scalar product

$$\langle \psi_m, \psi_n \rangle \equiv \sum_{i=1}^N \psi_m(\mathbf{x}_i) \cdot \psi_n(\mathbf{x}_i) = \delta_{mn}. \quad (10.76)$$

Note that this scalar product only takes into account the nodes, and not points between nodes.

The scalar product (Eq. (10.76)) allows us to expand arbitrary functions  $g(\mathbf{x})$  in terms of the shape function  $\{\psi_i\}$ :

$$\check{g}(\mathbf{x}) = \sum_{i=1}^N a_i \cdot \psi_i(\mathbf{x}) \quad (10.77)$$

$$\text{with } a_i = \langle \psi_i, g \rangle. \quad (10.78)$$

The expansion  $\check{g}$  is exact only at the nodes, whereas along the edges,  $\check{g}$  and  $g$  can differ. The amount of deviation depends on the smoothness of  $g$  and how coarse the mesh is.

#### 10.7.4 FE Formulation of the Wave Equation

We now aim to express the weak formulation of the wave equation (10.75) in terms of the shape functions  $\{\psi_i\}$ . However, the solution  $u(\mathbf{x}, t)$  has an explicit time dependence. We can account for this by introducing time-dependent expansion coefficients  $\gamma_i(t)$ :

$$\check{u}(\mathbf{x}, t) = \sum_{i=1}^N \gamma_i(t) \cdot \psi_i(\mathbf{x}). \quad (10.79)$$

FEM provides a way to calculate the coefficients  $\gamma_i(t)$  so that the approximate solution  $\check{u}$  becomes a time-dependent linear combination of the spatial shape functions.

We also expand the arbitrary test function  $v(\mathbf{x})$  in terms of  $\{\psi_i\}$ :

$$\check{v}(\mathbf{x}) = \sum_{i=1}^N \beta_i \cdot \psi_i(\mathbf{x}) \quad (10.80)$$

$$\text{with } \beta_i = \langle \psi_i, v \rangle. \quad (10.81)$$

Since  $v$  is time-independent, the coefficients  $\beta_i$  are constant. Inserting the expansions (Eqs. (10.79) and (10.80)) into Eq. (10.75) yields

$$\begin{aligned} \sum_{i,j=1}^N \left( \int_{\Omega} (\rho \ddot{\gamma}_i \psi_i \cdot \beta_j \psi_j + \mu \gamma_i \beta_j \nabla \psi_i \bullet \nabla \psi_j - f \cdot \beta_j \psi_j) \, d\mathbf{x} \right. \\ \left. - \mu \int_{\partial\Omega} (\gamma_i \beta_j \psi_j \cdot \nabla \psi_i) \bullet \hat{\mathbf{n}} \, d\sigma \right) = 0. \end{aligned} \quad (10.82)$$

The coefficient  $\beta_j$  is contained in every term of the equation and can therefore be factored out:

$$\begin{aligned} \sum_{i,j=1}^N \beta_j \cdot \left( \int_{\Omega} (\rho \ddot{\gamma}_i \psi_i \cdot \psi_j + \mu \gamma_i \nabla \psi_i \bullet \nabla \psi_j - f \cdot \psi_j) \, d\mathbf{x} \right. \\ \left. - \mu \int_{\partial\Omega} (\gamma_i \psi_j \cdot \nabla \psi_i) \bullet \hat{\mathbf{n}} \, d\sigma \right) = 0. \end{aligned} \quad (10.83)$$

Equation (10.83) can be satisfied if the term in the parentheses vanishes for each value of  $j$  independently, leading to:

$$\begin{aligned} \rho \cdot \sum_{i=1}^N \ddot{\gamma}_i \underbrace{\int_{\Omega} \psi_i \cdot \psi_j \, d\mathbf{x}}_{=A_{ij}} + \mu \cdot \sum_{i=1}^N \gamma_i \underbrace{\int_{\Omega} \nabla \psi_i \bullet \nabla \psi_j \, d\mathbf{x}}_{=B_{ij}} - \mu \cdot \sum_{i=1}^N \gamma_i \underbrace{\int_{\partial\Omega} (\psi_j \cdot \nabla \psi_i) \bullet \hat{\mathbf{n}} \, d\sigma}_{=C_{ij}} \\ = \underbrace{\int_{\Omega} f \cdot \psi_j \, d\mathbf{x}}_{=f_j}. \end{aligned} \quad (10.84)$$

In vector notation, the equation can be expressed as follows:

$$\rho \cdot \ddot{\boldsymbol{\gamma}} \cdot \mathbf{A} + \mu(\mathbf{x}) \cdot \boldsymbol{\gamma} \cdot \mathbf{B} - \mu(\mathbf{x}) \cdot \boldsymbol{\gamma} \cdot \mathbf{C} = \mathbf{f}, \quad (10.85)$$

where  $\boldsymbol{\gamma}$  and  $\mathbf{f}$  are vectors composed of the entries  $\gamma_i$  and  $f_i$ , respectively. Equation (10.85) is a system of second-order ordinary differential equations, for which a number of solution algorithms exist [225]. The matrices  $\mathbf{A}$ ,  $\mathbf{B}$ , and  $\mathbf{C}$  are sparse, since the integrals in Eq. (10.84) vanish if  $i$  and  $j$  do not refer to the same or adjacent nodes because of the local support of  $\psi_i$ . It can be further seen that the solution  $\boldsymbol{\gamma}$  is independent of the choice of the test function  $v(\mathbf{x})$  as long as it is a linear combination of the shape functions. We can use Eq. (10.85) to calculate the resultant wave field for given force  $\mathbf{f}$  and elasticity distribution  $\mu(\mathbf{x})$ . As such, this equation can be used in an algorithm to solve the elastography inverse problem iteratively. In the first step of such algorithm, an initial guess for  $\mu(\mathbf{x})$  is used to calculate the field  $\check{u}$ . This field is compared to the measured displacement field. The estimate of  $\mu(\mathbf{x})$  can be refined using a mathematical framework (e.g., optimization) based on the difference between the calculated and

measured displacement fields. This procedure is repeated iteratively, until the mismatch is lower than a predefined threshold in a suitable metric. In order to enforce certain properties of the solution, such as smoothness of the field, additional constraints can be incorporated into the mismatch metric.

Another alternative to solve the elastography inverse problem is to solve Eq. (10.85) directly for  $\mu(\mathbf{x})$ :

$$\mu(\mathbf{x}) \cdot \boldsymbol{\gamma} \cdot (\mathbf{B} - \mathbf{C}) = \mathbf{f} - \rho \ddot{\boldsymbol{\gamma}} \cdot \mathbf{A}. \quad (10.86)$$

The measured displacement field  $u^{\text{meas}}(\mathbf{x})$  can be expanded in the discretized basis functions according to Eq. (10.79) by using the scalar product:

$$\gamma_i(t) = \langle \psi_i(\mathbf{x}), u^{\text{meas}}(\mathbf{x}, t) \rangle. \quad (10.87)$$

Equation (10.86) can then be solved by appropriate iterative or direct matrix inversion schemes.

It is noteworthy that the description provided here is only a rough overview of the FEM. As such, applying the above equations to actual displacement data may yield poor results. The method contains several parameters that could be tuned for optimal results. These include the shape functions, FE mesh composition, design of the cost function, and the numerical algorithms for matrix inversion. More detailed treatments of FEM in the context of MRE or ultrasound elastography can be found in [213].

The iterative finite element inversion and DI are two fundamentally different approaches to the same problem of deriving viscoelastic moduli from displacement fields. Both methods have their advantages and disadvantages, and neither is generally superior to the other. To conclude this section, we list the main differences between these methods.

- In contrast to DI methods, which make implicit assumptions about boundary conditions, iterative FEM inversion requires force or displacement boundary conditions to be explicitly specified. This can be an advantage if these boundary conditions are known. However, in medical applications, the geometry of organs and boundaries between them make it difficult to correctly model boundary conditions.
- Some formulations of FEM allow for numerical derivatives of the displacement field to be substituted with analytical derivatives of the shape functions, thus circumventing the noise amplification pertaining to the derivatives that DI algorithms have to cope with.
- Equation (10.68) is based on the assumption that the induced displacement field is purely transverse without any compressional waves. This is not always the case, and the full Navier equation (4.129) has to be used instead to account for a finite (though possibly very large) bulk modulus  $K$ , thus increasing the complexity of the model and hence computation time. In DI, the field can be separated into compressional and shear components by applying the divergence and curl operators, respectively (see Eqs. (4.141) and (4.143)). A similar concept for iterative FEM inversion was suggested in [226].
- Reconstruction time for iterative FEM inversion is often a matter of hours compared to seconds to minutes for DI methods.

## 10.8 Direct Inversion for a Transverse Isotropic Medium

In Section 4.10, we discussed the physical concept used to describe wave propagation in anisotropic media. For the special case of a transverse isotropic medium, the equations of motion were presented in Eq. (4.186). However, since the differential operator  $\hat{L}$ , defined in that equation, does not commute with the curl operator,

$$\nabla \times (\hat{L}\mathbf{u}) \neq \hat{L}(\nabla \times \mathbf{u}) = \hat{L}\mathbf{c}, \quad (10.88)$$

we cannot achieve a separation of the shear field by simply substituting  $\mathbf{u}$  with  $\mathbf{q} = \nabla \times \mathbf{u}$ , as we did in the isotropic case (Eqs. (4.141) and (4.143)). We will therefore present an alternative inversion strategy to determine the three complex viscoelastic constants  $\mu_{12}$  (shear modulus in the plane of isotropy),  $\mu_{13}$  (shear modulus along the fibers), and  $E_3$  (Young's modulus along the fibers) of an incompressible transverse isotropic medium.

Even though the operators do not commute, we can still apply the curl operator to both sides of Eq. (4.186). As a result, the equation of motion for shear waves in an incompressible transverse isotropic medium reads

$$\rho \cdot \ddot{\mathbf{q}} = \mu_{12} \cdot \Delta \mathbf{q} + \tau_1 \cdot \underbrace{\left[ \frac{\partial^2 \mathbf{q}}{\partial z^2} + \begin{pmatrix} \frac{\partial^3 u_3}{\partial y \partial x^2} + \frac{\partial^3 u_3}{\partial y^3} \\ -\frac{\partial^3 u_3}{\partial x^3} - \frac{\partial^3 u_3}{\partial x \partial y^2} \\ 0 \end{pmatrix} \right]}_{\mathbf{A}} + \tau_2 \cdot \underbrace{\begin{pmatrix} \frac{\partial^3 u_3}{\partial y \partial z^2} \\ -\frac{\partial^3 u_3}{\partial x \partial z^2} \\ 0 \end{pmatrix}}_{\mathbf{B}} \quad (10.89)$$

with

$$\tau_1 = \mu_{13} - \mu_{12} \quad (10.90)$$

$$\text{and } \tau_2 = E_3 - 3\mu_{13}. \quad (10.91)$$

The solution of this three-parameter model for complex-valued moduli  $\mu_{12}^*$ ,  $\mu_{13}^*$ , and  $E_3^*$  is given by

$$\mu_{12}^* = -\frac{\rho\omega^2}{\Gamma} \begin{pmatrix} B_2 A_3 \\ -B_1 A_3 \\ B_1 A_2 - B_2 A_1 \end{pmatrix} \cdot \mathbf{q} \quad (10.92)$$

$$\mu_{13}^* = -\frac{\rho\omega^2}{\Gamma} \begin{pmatrix} B_2(A_3 - \Delta q_3) \\ -B_1(A_3 - \Delta q_3) \\ B_1(A_2 - \Delta q_2) - B_2(A_1 - \Delta q_1) \end{pmatrix} \cdot \mathbf{q} \quad (10.93)$$

$$E_3^* = -\frac{\rho\omega^2}{\Gamma} \begin{pmatrix} 3B_2(A_3 - \Delta q_3) + A_2 \Delta q_3 - A_3 \Delta q_2 \\ -3B_1(A_3 - \Delta q_3) + A_3 \Delta q_1 - A_1 \Delta q_3 \\ 3B_1(A_2 - \Delta q_2) - 3B_2(A_1 - \Delta q_1) + A_1 \Delta q_2 - A_2 \Delta q_1 \end{pmatrix} \cdot \mathbf{q} \quad (10.94)$$

$$\text{with } \Gamma = (A_2 \Delta q_3 - A_3 \Delta q_2) B_1 + (A_3 \Delta q_1 - A_1 \Delta q_3) B_2.$$

Equations (10.92)–(10.94) therefore constitute a recipe for the calculation of the viscoelastic parameters from the curl of the measured displacement field  $\mathbf{u}$ .

It is important to keep in mind that the above equations are valid only in the special case that the fibers are aligned with the  $z$ -axis of the coordinate system. In muscles, where the fibers are fairly straight and their direction is known a priori, the image slices can be aligned with the fiber direction during the MRE scan, so that postprocessing is



straightforward. In other organs, such as the brain, where nerve fibers follow curved paths, additional information about fiber directions is necessary in order to apply the method to the displacement field. As an example, *diffusion tensor imaging* (DTI) is capable of providing maps indicating the principal direction of fiber tracts in each voxel. By using these data, it is possible to calculate a local coordinate system, in which the  $z$ -axis is aligned with the principal fiber direction in that respective voxel. Hence, a local rotation of the coordinate system has to be performed for each voxel individually prior to calculation of displacement field derivatives parallel and perpendicular to the local fiber direction. However, DTI itself is often compromised by noise, which affects the reliability of this approach. As an alternative, waveguide elastography based on directional Fourier decomposition is recommendable (see Section 10.9), since it obtains its directional information from reconstructed fiber tracts rather than from raw DTI data, the former being a smooth vector field.

## 10.9 Waveguide Elastography

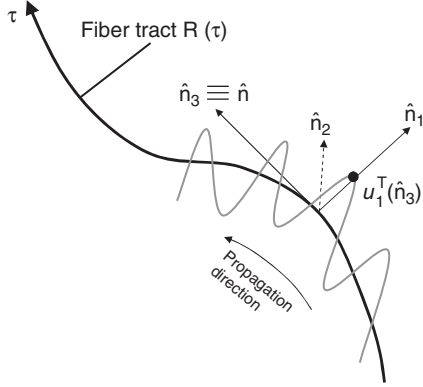
MR tractography, based on DTI, is capable of reconstructing fiber tracts as three-dimensional curves [227]. These data can be used for an alternative approach to wave analysis in fibrous media, termed *waveguide elastography* [72]. The underlying assumption is that fibrous structures, particularly nerve bundles in the brain, guide waves because of their highly anisotropic properties. Waveguide elastography is based on an orthotropic material model (see Eq. (4.34)) with nine independent elastic constants. We introduce a local coordinate system  $\{\hat{\mathbf{n}}_1, \hat{\mathbf{n}}_2, \hat{\mathbf{n}}_3\}$ , in which the  $\hat{\mathbf{n}}_3$ -direction is the local tangent to the fiber bundle, and  $\hat{\mathbf{n}}_1$  and  $\hat{\mathbf{n}}_2$  span a plane perpendicular to the fibers. With knowledge of the fiber directions in each voxel, we can use spatial–spectral filtering to separate the different wave modes propagating along and perpendicular to a fiber tract, which ultimately allows us to determine all nine constants of the orthotropic elasticity tensor. In the following discussion, we assume that the wave field,  $\mathbf{u}$ , and the position,  $\mathbf{r}$ , are already expressed in the local coordinate system, so that the components  $u_1, u_2, u_3$  correspond to the projections onto the local basis  $\{\hat{\mathbf{n}}_1, \hat{\mathbf{n}}_2, \hat{\mathbf{n}}_3\}$  and *not* onto the image coordinate system.<sup>8</sup>

In essence, the spatial–spectral filtering approach performs a one-dimensional Fourier transform along a local tangent or normal vector  $\hat{\mathbf{n}}$  to the fiber tract and picks all wave vectors from the wave field that are aligned with that vector (spatial filter), and which have a wave number within an interval  $I_k = [k_{\min}, k_{\max}]$  (spectral filtering). A fiber tract can be represented as a curve through three-dimensional space,  $\mathbf{R}(\tau)$ , where  $\tau$  can be understood as the position along the tract. For the derivation of the spatial–spectral filtering formula, we will use the tangent vector  $\hat{\mathbf{n}} \equiv \hat{\mathbf{n}}_3$ , but the result will also be valid if the normal vectors  $\hat{\mathbf{n}}_1$  and  $\hat{\mathbf{n}}_2$  are substituted for  $\hat{\mathbf{n}}$ .

The local tangent vector is then the normalized tangent to the tract at every point:

$$\hat{\mathbf{n}}(\mathbf{R}(\tau)) = \frac{d\mathbf{R}}{d\tau} \bigg/ \left| \frac{d\mathbf{R}}{d\tau} \right|. \text{ This is illustrated in Figure 10.9. Spatial–spectral filtering is then}$$

<sup>8</sup> The two coordinate systems are related by a rotation about two angles, which can be obtained from DTI. However, since fiber bundles are usually curved rather than straight, every voxel can have its own rotation matrix.



**Figure 10.9** Illustration of the local coordinate system used in waveguide elastography.

performed for each voxel along the curve separately and yields for each point only those waves that propagate locally parallel to the fiber with wavelengths that fall into a given window  $I_k$  (thus allowing one to separate pressure waves from shear waves based on their differences in wavelength).

The starting point for the mathematical treatment of the spatial–spectral filter is the Fourier transform in three dimensions:

$$\mathbf{U}(\mathbf{k}) = \int \mathbf{u}(\mathbf{r}) \cdot e^{-i\mathbf{k} \cdot \mathbf{r}} d\mathbf{r} \quad (10.95)$$

$$\mathbf{u}(\mathbf{r}) = \frac{1}{(2\pi)^3} \int \mathbf{U}(\mathbf{k}) \cdot e^{i\mathbf{k} \cdot \mathbf{r}} d\mathbf{k}. \quad (10.96)$$

Instead of performing the full three-dimensional Fourier transform, we calculate a local one-dimensional transform that follows the tangent vector along the curve  $\mathbf{R}(\tau)$ . We can then formulate a one-dimensional Fourier transform that only takes into account wave vectors  $\mathbf{k} = k\hat{\mathbf{n}}(\mathbf{R}(\tau))$  parallel to the local tangent vector:

$$\mathbf{U}(k\hat{\mathbf{n}}(\mathbf{R}(\tau))) = \int_{\mathbb{R}^3} \mathbf{u}(\mathbf{r}) \cdot e^{-ik\hat{\mathbf{n}}(\mathbf{R}(\tau)) \cdot \mathbf{r}} d\mathbf{r}. \quad (10.97)$$

Now,  $\mathbf{U}$  has been filtered with respect to the wave vector direction, but it contains all wave numbers  $0 \leq k < \infty$ . To constrain the analysis to only those wave components that have wave numbers in an interval  $I_k$ , the inverse transform can be restricted to integration over  $I_k$  instead of the full real axis:

$$\mathbf{u}_{\text{SF}}(\mathbf{R}(\tau)) = \frac{1}{2\pi} \int_{I_k} \mathbf{U}(k\hat{\mathbf{n}}(\mathbf{R}(\tau))) \cdot e^{ik\hat{\mathbf{n}}(\mathbf{R}(\tau)) \cdot \mathbf{R}(\tau)} dk. \quad (10.98)$$

For example, consider a plane wave component

$$\mathbf{u}(\mathbf{r}) = \mathbf{u}_0 \cdot e^{i\mathbf{q} \cdot \mathbf{r}}. \quad (10.99)$$

Insertion into Eq. (10.97) yields

$$\begin{aligned} \mathbf{U}(k\hat{\mathbf{n}}(\mathbf{R}(\tau))) &= \mathbf{u}_0 \int_{\mathbb{R}^3} e^{i\mathbf{q} \cdot \mathbf{r}} \cdot e^{-ik\hat{\mathbf{n}}(\mathbf{R}(\tau)) \cdot \mathbf{r}} d\mathbf{r} \\ &= \mathbf{u}_0 \int_{\mathbb{R}^3} e^{-i\mathbf{r} \cdot (k\hat{\mathbf{n}}(\mathbf{R}(\tau)) - \mathbf{q})} d\mathbf{r} \\ &= 2\pi \mathbf{u}_0 \cdot \delta(k\hat{\mathbf{n}}(\mathbf{R}(\tau)) - \mathbf{q}), \end{aligned} \quad (10.100)$$

that is, only plane wave components in the image with  $\mathbf{q} \parallel \hat{\mathbf{n}}$  show up as a peak in the  $k$ -space image. Insertion into Eq. (10.98) yields

$$\begin{aligned} \mathbf{u}_{\text{SF}}(\mathbf{R}(\tau)) &= \mathbf{u}_0 \int_{I_k} \delta(k\hat{\mathbf{n}}(\mathbf{R}(\tau)) - \mathbf{q}) \cdot e^{ik\hat{\mathbf{n}}(\mathbf{R}(\tau)) \cdot \mathbf{R}(\tau)} d\mathbf{k} \\ &= \begin{cases} \mathbf{u}_0 \cdot e^{i\mathbf{q} \cdot \mathbf{R}(\tau)} & \text{if } \mathbf{q} \parallel \hat{\mathbf{n}}(\mathbf{R}(\tau)) \text{ and } |\mathbf{q}| \in I_k. \\ \mathbf{0} & \text{else.} \end{cases} \end{aligned} \quad (10.101)$$

This technique allows one to reduce complex three-dimensional wave fields to one-dimensional waves that propagate along fibrous structures, which greatly simplifies wave inversion. By selecting suitable windows  $I_k$ , one can separate different wave modes based on their wavelengths. The same procedure can be performed for the two transverse directions  $\hat{\mathbf{n}}_1$  and  $\hat{\mathbf{n}}_2$ . The nine elements of the orthotropic elasticity tensor can then be reconstructed by solving the Helmholtz equation for different combinations of propagation direction and polarization. We use the notation  $u_i(\hat{\mathbf{n}}_j)$ , indicating the polarization component  $i$  that was extracted by a spatial-spectral filter in the direction  $\hat{\mathbf{n}}_j$ , as illustrated in Figure 10.9. In this notation,  $i = j$  represents a longitudinal (compression) wave, and  $i \neq j$  a transverse (shear) wave. We denote these two modes with L and T, respectively.

$$C_{11} \cdot \frac{\partial^2 u_1^L(\hat{\mathbf{n}}_1)}{\partial r_1^2} = -\rho\omega^2 u_1^L(\hat{\mathbf{n}}_1) \quad (10.102)$$

$$C_{22} \cdot \frac{\partial^2 u_2^L(\hat{\mathbf{n}}_2)}{\partial r_2^2} = -\rho\omega^2 u_2^L(\hat{\mathbf{n}}_2) \quad (10.103)$$

$$C_{33} \cdot \frac{\partial^2 u_3^L(\hat{\mathbf{n}}_3)}{\partial r_3^2} = -\rho\omega^2 u_3^L(\hat{\mathbf{n}}_3) \quad (10.104)$$

$$C_{44} \cdot \frac{\partial^2 u_3^T(\hat{\mathbf{n}}_2)}{\partial r_2^2} = -\rho\omega^2 u_3^T(\hat{\mathbf{n}}_2) \quad (10.105)$$

$$\text{and } C_{44} \cdot \frac{\partial^2 u_2^T(\hat{\mathbf{n}}_3)}{\partial r_3^2} = -\rho\omega^2 u_2^T(\hat{\mathbf{n}}_3) \quad (10.106)$$

$$C_{55} \cdot \frac{\partial^2 u_3^T(\hat{\mathbf{n}}_1)}{\partial r_1^2} = -\rho\omega^2 u_3^T(\hat{\mathbf{n}}_1) \quad (10.107)$$

$$\text{and } C_{55} \cdot \frac{\partial^2 u_1^T(\hat{\mathbf{n}}_3)}{\partial r_3^2} = -\rho\omega^2 u_1^T(\hat{\mathbf{n}}_3) \quad (10.108)$$

$$C_{66} \cdot \frac{\partial^2 u_2^T(\hat{\mathbf{n}}_1)}{\partial r_1^2} = -\rho\omega^2 u_2^T(\hat{\mathbf{n}}_1) \quad (10.109)$$

$$\text{and } C_{66} \cdot \frac{\partial^2 u_1^T(\hat{\mathbf{n}}_2)}{\partial r_2^2} = -\rho\omega^2 u_1^T(\hat{\mathbf{n}}_2). \quad (10.110)$$

For the three missing tensor elements  $C_{12}$ ,  $C_{13}$ , and  $C_{23}$ , we have to analyze longitudinal waves propagating in oblique directions. We define propagation unit vectors  $\hat{\mathbf{n}}_{12}$

(in the  $\hat{\mathbf{n}}_1-\hat{\mathbf{n}}_2$  plane),  $\hat{\mathbf{n}}_{13}$  (in the  $\hat{\mathbf{n}}_1-\hat{\mathbf{n}}_3$  plane), and  $\hat{\mathbf{n}}_{23}$  (in the  $\hat{\mathbf{n}}_2-\hat{\mathbf{n}}_3$  plane):

$$(C_{12} + C_{66}) \cdot \frac{\partial^2 u_2^L(\hat{\mathbf{n}}_{12})}{\partial r_1 \partial r_2} + C_{11} \cdot \frac{\partial^2 u_1^L(\hat{\mathbf{n}}_{12})}{\partial r_1^2} + C_{66} \cdot \frac{\partial^2 u_1^L(\hat{\mathbf{n}}_{12})}{\partial r_2^2} = -\rho\omega^2 u_1^L(\hat{\mathbf{n}}_{12}) \quad (10.111)$$

$$(C_{12} + C_{66}) \cdot \frac{\partial^2 u_1^L(\hat{\mathbf{n}}_{12})}{\partial r_1 \partial r_2} + C_{66} \cdot \frac{\partial^2 u_2^L(\hat{\mathbf{n}}_{12})}{\partial r_1^2} + C_{22} \cdot \frac{\partial^2 u_2^L(\hat{\mathbf{n}}_{12})}{\partial r_2^2} = -\rho\omega^2 u_2^L(\hat{\mathbf{n}}_{12}) \quad (10.112)$$

$$(C_{23} + C_{44}) \cdot \frac{\partial^2 u_3^L(\hat{\mathbf{n}}_{23})}{\partial r_2 \partial r_3} + C_{22} \cdot \frac{\partial^2 u_2^L(\hat{\mathbf{n}}_{23})}{\partial r_2^2} + C_{44} \cdot \frac{\partial^2 u_2^L(\hat{\mathbf{n}}_{23})}{\partial r_3^2} = -\rho\omega^2 u_2^L(\hat{\mathbf{n}}_{23}) \quad (10.113)$$

$$(C_{23} + C_{44}) \cdot \frac{\partial^2 u_2^L(\hat{\mathbf{n}}_{23})}{\partial r_2 \partial r_3} + C_{44} \cdot \frac{\partial^2 u_3^L(\hat{\mathbf{n}}_{23})}{\partial r_2^2} + C_{33} \cdot \frac{\partial^2 u_3^L(\hat{\mathbf{n}}_{23})}{\partial r_3^2} = -\rho\omega^2 u_3^L(\hat{\mathbf{n}}_{23}) \quad (10.114)$$

$$(C_{13} + C_{55}) \cdot \frac{\partial^2 u_3^L(\hat{\mathbf{n}}_{13})}{\partial r_1 \partial r_3} + C_{11} \cdot \frac{\partial^2 u_1^L(\hat{\mathbf{n}}_{13})}{\partial r_1^2} + C_{55} \cdot \frac{\partial^2 u_1^L(\hat{\mathbf{n}}_{13})}{\partial r_3^2} = -\rho\omega^2 u_1^L(\hat{\mathbf{n}}_{13}) \quad (10.115)$$

$$(C_{13} + C_{55}) \cdot \frac{\partial^2 u_1^L(\hat{\mathbf{n}}_{13})}{\partial r_1 \partial r_3} + C_{55} \cdot \frac{\partial^2 u_3^L(\hat{\mathbf{n}}_{13})}{\partial r_1^2} + C_{33} \cdot \frac{\partial^2 u_3^L(\hat{\mathbf{n}}_{13})}{\partial r_3^2} = -\rho\omega^2 u_3^L(\hat{\mathbf{n}}_{13}). \quad (10.116)$$

This is an overdetermined system of six equations that have to be solved for all three unknown quantities ( $C_{12}$ ,  $C_{13}$ , and  $C_{23}$ ) simultaneously (i.e., with the same basis vectors  $\hat{\mathbf{n}}_{12}$ ,  $\hat{\mathbf{n}}_{13}$ ,  $\hat{\mathbf{n}}_{23}$  for all equations). The angles of the basis vectors relative to the local coordinate system are chosen such that the geometric distance between the two solutions for each complex parameter is minimized. The separation of the wave field into transverse and longitudinal waves can be performed in  $k$ -space as follows:

$$\mathbf{U}^T(\mathbf{k}) = -\frac{\mathbf{k}}{|\mathbf{k}|^2} \cdot (\mathbf{k} \bullet \tilde{\mathbf{u}}(\mathbf{k})) \quad (10.117)$$

$$\mathbf{U}^L(\mathbf{k}) = -\frac{\mathbf{k}}{|\mathbf{k}|^2} \times (\mathbf{k} \times \tilde{\mathbf{u}}(\mathbf{k})). \quad (10.118)$$

A derivation of these relationships is provided in [72].

## 11

## Multicomponent Acquisition

The standard way of acquiring data in MRE is to sample one frequency and one Cartesian component of the displacement field in one scan. The measurement is repeated for different directions of the MEG to assess all three Cartesian components. In addition to that, the multifrequency inversion techniques presented in Sections 10.5 and 10.6, or single-frequency inversions aimed at sampling the dispersion of the viscoelastic moduli, require the acquisition of displacement fields at multiple vibration frequencies. Several strategies have been devised to achieve such a data acquisition scheme and will be presented in this chapter.

The most straightforward approach is to apply the individual vibration frequencies separately in subsequent scans. This strategy is the most commonly used method. Its major drawback is that the total scan time is proportional to the number of frequencies. The benefit of additional frequency information therefore has to be balanced against reduced patient comfort due to prolonged examination time. On the positive side, single-frequency measurements ensure that the entire vibration power is concentrated in a small interval around the vibration frequency, leading to optimal signal-to-noise ratio (SNR) in the resulting phase images. Furthermore, the parameters of the motion-encoding gradient (MEG) can be tuned to each vibration frequency independently, guaranteeing good motion sensitivity.

Another approach, first published in [33], exploits the high bandwidth of MEGs to gather information from several vibration frequencies in the same scan. The motion sensitivity curves shown in Figure 3.6b,c illustrate that oscillatory motion is still encoded when the MEG frequency and the oscillation frequency are unmatched (*fractional encoding*, [18]). The idea behind simultaneous acquisition of multiple vibration frequencies is to deploy a vibration waveform that is composed of several vibration frequencies, which are integer multiples of a common base frequency, and to use a wide-band MEG to detect all vibrations at the same time. Temporal Fourier transform then allows for a separation of the frequencies during postprocessing. In the original publication, the waveform was a superposition of four frequencies: 25, 37.5, 50, and 62.5 Hz. The corresponding base frequency is 12.5 Hz (note that the base frequency itself does not have to be contained in the waveform). The MEG comprised four cycles at a frequency of 50 or 60 Hz (depending on the organ). In total, 40 wave propagation phases were scanned with a temporal resolution of 2 ms, thus spanning an interval of  $40 \cdot 2 \text{ ms} = 80 \text{ ms}$ , one period of the base frequency. The frequency resolution after Fourier transform was therefore 12.5 Hz, so that the four vibration frequencies

were separated into adjacent bins in frequency space. Wave images at each vibration frequency could thus be generated separately.

The major advantage of this technique is that all frequencies are applied at the same time, and switching frequencies between measurements, as in the serial approach, is not necessary, thus avoiding user errors. However, this benefit comes at the cost of decreased image quality. First, the vibration energy is not concentrated around one frequency, but spread across all frequencies contained in the vibration waveform. The maximum achievable vibration amplitude is usually limited by either the maximum output level of the vibration generator or the strongest vibration tolerated by the patient. Therefore, in a simultaneous multifrequency measurement, the vibration amplitude per frequency is lower than in a single-frequency experiment. Second, since all vibration frequencies are encoded by the same MEG, the motion sensitivity cannot be tuned to the optimum for each frequency separately, but only a global maximum across all frequencies can be achieved. Both effects combined lead to a significantly lower SNR in the wave images than in the case of serial arrangement of single-frequency scans.

Rather than acquiring several frequencies simultaneously, a novel approach, termed *SLIM-MRE (Sample Interval Modulation)* [228, 229], aims to acquire all three Cartesian field components at the same time. The basic idea is somewhat similar to simultaneous multifrequency acquisition in that several data are stored in the MR signal phase and later separated through a temporal Fourier transform. In Section 3.1, we discussed the fundamental mechanism behind motion encoding, which can be summarized in a single equation

$$\phi(\psi) \propto \int_0^T G(t) \cdot \sin(\Omega t + \psi) dt, \quad (11.1)$$

where  $T$  is the duration of the MEG,  $\Omega$  is the vibration frequency, and  $\psi$  the initial vibration phase. For the following discussion, it will be advantageous to perform a temporal translation of the equation, so that the MEG starts at  $t = t_0$  and  $\psi = \Omega t_0$ :

$$\phi(\Omega t_0) \propto \int_{t_0}^{t_0+T} G(t) \cdot \sin(\Omega t + \Omega t_0) dt. \quad (11.2)$$

In Appendix B, we prove that  $\phi$  is  $2\pi$ -periodic with respect to its argument. Therefore, we can interfere the motion parameters from  $\phi$  if we sample Eq. (11.2) with different values of  $t_0$  and perform a temporal Fourier transform, as explained in Section 3.1.

The discrete Fourier transform has the property that the sampling time is equal to the period of the fundamental frequency. In other words, if we sample a signal with  $N$  points (assume that  $N$  is even for the sake of simplicity) and a temporal spacing  $\delta t$ , then the frequency spectrum after the Fourier transform is composed of data points at the frequencies

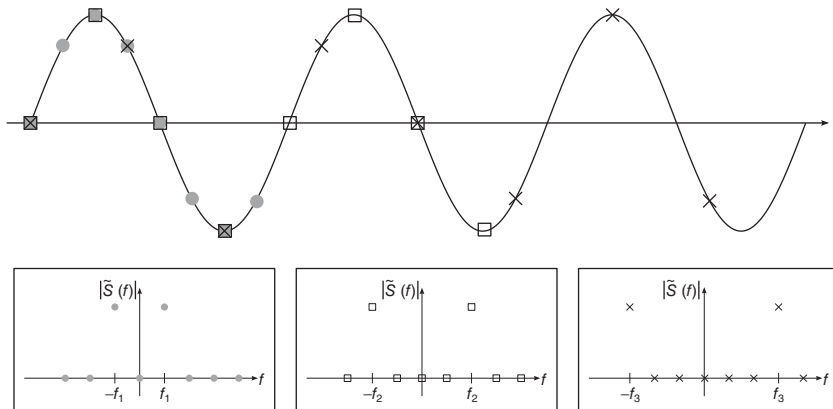
$$f_n = n \cdot \frac{1}{N \cdot \delta t}, \quad n = 0, \dots, \frac{N}{2}. \quad (11.3)$$

We will now look at a sinusoidal signal with period  $2\pi$  and three different sampling strategies. As visual representation of the process is shown in Figure 11.1. For the first sampling strategy, we choose a sampling interval  $\delta t_1$  such that  $N \cdot \delta t_1 \cdot f = 1$ . In other words, we distribute  $N$  sampling points equidistantly over one period of the signal. The signal hence corresponds to the fundamental frequency  $f_1$  after Fourier transform. For

the second strategy, we double the sampling interval, such that  $N \cdot \delta t_2 \cdot f = 2$ . In this case, we distribute  $N$  sample points over two cycles of the signal. As a consequence, the Fourier-transformed signal will have a peak at the second frequency  $f_2 = 2 \cdot f_1$  rather than at the fundamental frequency. For the third strategy, we triple the original sampling interval,  $N \cdot \delta t_3 \cdot f = 3$ , and hence sample  $N$  points across three signal cycles. Therefore, we will see the signal in the third frequency bin  $f_3 = 3 \cdot f_1$  after Fourier transform. This allows us to encode the information about the sampled signal in either of the three frequency bins:  $f_1$ ,  $f_2$ , or  $f_3$ , depending on how we choose the sampling interval  $\delta t$ . SLIM-MRE exploits this mechanism by encoding the three displacement field components into three different frequencies bin, which can then be separated by a Fourier transform over the sampled points.

In contrast to usual MRE sequences, which employ only one MEG at a time, SLIM-MRE uses three MEGs simultaneously. However, the timing of the gradients is not fixed, but it changes in every repetition. Assume that the vibration frequency is  $\Omega$ , and the vibration period is hence  $T_{\text{vib}} = \frac{2\pi}{\Omega}$ . In order to acquire  $N = 8$  sampling points, the conventional sampling interval would be  $\delta t = \frac{T_{\text{vib}}}{8}$ . In SLIM, three different intervals are used for the three MEGs:  $\delta t$ ,  $2\delta t$ , and  $3\delta t$ . This cannot be achieved by shifting the trigger pulse relative to the start of the MEG, as in normal MRE. Instead, the start times of the three MEGs are delayed in increments of  $\delta t$ ,  $2\delta t$ , and  $3\delta t$ . The motion-encoded phase is then a superposition of the contributions from the three MEG directions. However, due to the different sampling intervals, each direction is placed in a different frequency bin after Fourier transform (the Fourier-transformed signal would be the sum of the three spectra in Figure 11.1).

Since the start times of the MEGs are not fixed relative to the other parts of the sequence, additional delays have to be introduced into the sequence to allow for time-shifting the MEGs. This causes a significant increase of the echo time and thus a dramatic SNR reduction in the acquired image. For application in humans, where typically only one MEG cycle is utilized, the technique is therefore unfeasible. However, in animal experiments, vibration frequencies are much higher (up to  $\approx 1$  kHz), and



**Figure 11.1** Illustration of the encoding principle behind SLIM-MRE. A sinusoidal signal is sampled with eight points across one (●), two (□), and three (×) periods. The spectra resulting from these sampling strategies are shown in the three boxes. The original information is encoded in three different frequency bins of the frequency spectrum.

several MEG cycles are deployed to warrant sufficient motion sensitivity. In that case, the number of MEG cycles can be slightly reduced, and the resulting void intervals in the sequence can be used to shift the start times of the three MEGs, with only a small decrease in motion sensitivity and no adverse effect on the echo time and signal quality.

A second implementation of SLIM-MRE modulates the shape of the MEGs instead of shifting their start times [230]. This is easiest to understand in the case of sinusoidal MEGs. Instead of using an MEG waveform  $G(t)$ , a variable form  $G(t + \frac{q \cdot m}{N} T)$  is used for each of the  $N$  repetitions, and  $G(t)$  is treated as  $T$ -periodic. The index  $m$  iterates over the  $N$  sampling points, and  $q$  is set to 1, 2, or 3 for the three MEG directions. This modification of the gradient shape has the same effect as shifting the MEGs, but it does not require any additional delays within the echo time, thus allowing for better image quality than the previous approach. However, modulating the MEG shapes introduces different amounts of flow sensitivity in each single acquisition,<sup>1</sup> so that especially in organs with significant blood flow, such as the brain or liver, flow will be encoded as oscillatory motion and cannot be removed during postprocessing. For less flow-affected organs, or in scenarios where flow effects are negligible compared to the induced vibration, SLIM-MRE has a huge potential to accelerate MRE exams without any major drawback.

---

<sup>1</sup> A sinusoidal gradient has maximum sensitivity toward constant flow, whereas a cosinusoidal gradient is flow-compensated. Intermediate gradient possess varying levels of flow sensitivity.



## 12

## Ultrasound Elastography

*This chapter was coauthored by Heiko Tzschätzsch, Department of Radiology, Charité – Universitätsmedizin Berlin, Berlin, Germany.*

Medical elastography was developed in the ultrasound (US) imaging community in the 1980s, whereas the first application of MRE was not reported until 1995. Since then, a plethora of US-based elastography techniques have emerged, which differ both in the method of wave excitation and the data acquisition and processing technique. In this chapter, we will present an overview of the most common techniques of ultrasound elastography (USE).

An in-depth discussion of the principles underlying medical US is beyond the scope of this book. In general, US imaging involves the use of a transducer to send ultrasonic pulses (typically in the megahertz range) into the tissue, which are reflected by tissue boundaries or inhomogeneities and detected by a dedicated receiver, or, more commonly, the transducer operating in receive mode. The depth of the reflecting particle can be calculated from the time of flight of the echo (assuming a constant pressure wave speed of  $c = 1540$  m/s) via  $d = \frac{c \cdot t}{2}$  (the factor of 2 arises from the fact that the signal has to travel from the transducer to the location of reflection and back to the transducer in the given time). Being a sound wave, an ultrasonic pulse propagates as a compression wave and its velocity is determined by the P-wave modulus (see Eq. (4.145)). To guarantee that an echo is assigned the correct depth within the object, all echoes from a pulse must have returned before the next pulse is emitted. The *pulse repetition frequency* (PRF) is thus limited by the maximum depth. Three different acquisition modes are most commonly used in USE:

- *A-mode* (amplitude mode): The amplitude envelope of the reflected signal from a single straight line emanating from the transducer is recorded as a function of time. Time is then converted to a distance between the transducer and the reflecting particle, so that a depth profile is obtained. Since only a single line is scanned, the frame rate in this mode is very high.
- *B-mode* (brightness mode): Multiple A-mode scans are performed successively, and the line of sight is moved slightly in the lateral direction for each acquisition, so that a two-dimensional sector is sampled. The resulting data can be converted into a two-dimensional image. In comparison to A-mode scanning, the frame rate is reduced by a factor equivalent to the number of lines of sight.
- *M-mode* (motion mode): This is a hybrid between A- and B-mode. An image is sampled using B-mode. The central line of sight is sampled with much higher frequency

*Magnetic Resonance Elastography: Physical Background and Medical Applications*, First Edition.

Sebastian Hirsch, Jürgen Braun, and Ingolf Sack.

© 2017 Wiley-VCH Verlag GmbH & Co. KGaA. Published 2017 by Wiley-VCH Verlag GmbH & Co. KGaA.

than all other lines by interleaving it into acquisitions of other lines. As a result, a B-mode image and an A-mode scan are acquired, with the latter having a much higher frame rate than the former.

To focus, direct, and shape the ultrasonic beam, the transducer consists of a one-dimensional array of piezoelectric elements, which can be controlled independently. The resulting beam form can then be predicted by treating each element as a point source and applying Huygens' principle.

Whereas in magnetic resonance imaging (MRI) the image coordinates are referred to as slice-selection, phase-encode, and readout, US imaging distinguishes between axial (away from the transducer) and lateral (parallel to the transducer) directions.

A special US technique, termed *Doppler imaging*, can determine the axial velocity of the reflecting particle relative to the transmitter/receiver by detecting the frequency shift of the returned signal caused by the Doppler effect. Since this technique is capable of imaging functional physiological aspects, such as cardiac motion, it is also referred to as *functional ultrasound*.

US imaging is affected by speckles, which are caused by interference of echoes from adjacent scatterers (see Section 4.12). While this is considered an artifact that degrades image quality in conventional US imaging, tracking speckle patterns can yield valuable information on tissue deformation in USE.

One of the first USE methods used an external driver for shear wave generation and the Doppler technique for detecting induced tissue motion, thus requiring additional hardware for excitation. In 1990, Sugimoto presented a technique called *acoustic radiation force impulse* (ARFI), in which a focused US beam is used to generate a mechanical force in the tissue [231]. ARFI allows the excitation of shear waves directly in the region of interest. These shear waves can be detected with the same transducer and without the need for additional hardware.

Common US frame rates are on the order of tens of Hertz, which limits the observation of rapid events such as fast pulse waves or cardiac motion. A major development to increase the frame rate is *plane wave imaging*, which sends an unfocused wave using all piezo elements and focuses only during signal detection [232]. With plane wave imaging, the frame rate is equal to the PRF, which is on the order of several kilohertz; however, image quality is deteriorated. The decrease in image quality can be overcome by a method known as *coherent plane wave compounding* [233–235]. This method generates several plane wave images with different tilting angles of the plane wave. The quality of the compound image is comparable to conventional B-mode images, but the frame rate is on the order of a few hundred Hertz. This technique imposes very high demands on the acquisition speed of the scanner.

Unlike MRE, which typically aims to reconstruct (visco)elastic moduli, USE typically quantifies shear wave velocity (and sometimes its dispersion) instead. It is important to note that the excited shear waves propagate at much lower velocity than the compression waves that are used for US imaging. Furthermore, changes in shear wave velocity do not necessarily translate into changes in US velocity, which is assumed to be constant for image reconstruction.

Due to the wide variety of USE techniques available, many authors have published review articles over the last two decades [236–243]. We will briefly revise the most common techniques. Since many of these methods have been applied with numerous

variations, we will also reference review articles for each technique. A graphical overview is presented in Figure 12.1.

## 12.1 Strain Imaging (SI)

*Strain imaging* (SI) was developed in 1991 by Ophir et al. [244], and an overview is given in [245].

SI is based on imaging quasi-static (<10 Hz) tissue deformation. This can be accomplished by external and continuous or low-frequency manual deformation or internal excitation via respiration, cardiac muscle deformation, or cardiovascular sources. This deformation can be detected using Doppler imaging, which is only sensitive to the axial component, or speckle-tracking techniques, which are sensitive to both the axial and lateral deformation. Integration of displacement during deformation over time yields images of tissue strain in real time. When no information on the applied forces is available, SI is a qualitative rather than a quantitative technique, and only relative shear moduli can be reconstructed [246]. Due to its simplicity, SI requires no additional hardware, but should be performed by a well-trained investigator.

SI has been used for examinations of the breast, prostate, thyroid, muscle, and lymph nodes. In principle, all organs accessible to manual palpation can be examined.

## 12.2 Strain Rate Imaging (SRI)

*Strain rate imaging* (SRI) has its origin in the field of cardiac Doppler velocity measurement [247]. It is based on the fact that the gradient of the (normalized) displacement speed is equivalent to the strain rate, as we can easily see for the uniaxial deformation of a medium of original length  $L = L_0$  with displacement speed  $v = \frac{\partial L}{\partial t}$  [248]:

$$\dot{\epsilon} = \frac{\partial}{\partial t} \left( \frac{1}{L_0} \cdot \frac{\partial L}{\partial x} \right) = \frac{1}{L_0} \frac{\partial}{\partial x} \frac{\partial L}{\partial t} = \frac{1}{L_0} \frac{\partial v}{\partial x}. \quad (12.1)$$

The tissue deformation velocity resulting from cardiac motion is detected by Doppler (1D) or speckle tracking (2D). Calculating the spatial gradient of the velocity field enables real-time tracking of the strain rate, including information on tissue dilatation ( $\dot{\epsilon} > 0$ ) and contraction ( $\dot{\epsilon} < 0$ ).

SRI is only suitable for investigating tissue with an intrinsic motion source, such as the heart, muscles, and the gastrointestinal wall.

## 12.3 Acoustic Radiation Force Impulse (ARFI) Imaging

*Acoustic radiation force impulse imaging* (ARFI) was published in 2002 by Nightingale et al. [249] and 1998 by Sarvazyan et al. [250]. An overview is given in [251].

Instead of relying on an external driver or physiological motion as the strain source, ARFI uses focused US pulses, which induce rapid expansion of the heated tissue, thus generating shear deformations on the order of tens of micrometers. Repeatedly scanning the area surrounding the focus point allows sampling the propagating strain. ARFI

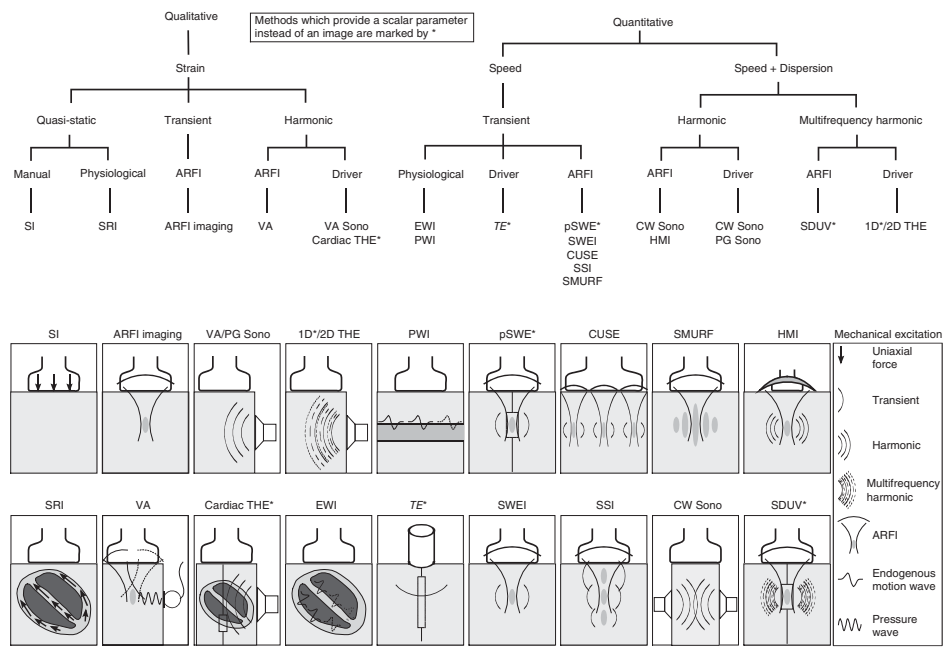


Figure 12.1 Categorization of the most common USE methods in terms of tissue excitation method and measurement quantity.

imaging has been applied to abdominal organs, the heart, vessels, breast, nerve, and prostate, and for monitoring of thermal ablation procedures. Since the depth of the focus point is limited to approximately 8 cm, deep organs or abdominal organs in obese patients can be inaccessible.

## 12.4 Vibro-Acoustography (VA)

*Vibro-acoustography* (VA) was developed by Fatemi and Greenleaf [252, 253] in 1998 and later reviewed by Urban et al. [254].

For tissue excitation, two ARFI beams of slightly different ultrasonic frequencies are focused at the same point within the tissue. Their superposition acts as a point source that pulsates at the difference frequency, which is typically in the range of 10–70 kHz. The sound waves emanating from this source are detected by a hydrophone. For image acquisition, the focus point is swept across the imaging region, and the region of interest is hence rasterized. VA images are speckle-free and highly sensitive to calcifications. The acquisition of a  $5 \times 5 \text{ cm}^2$  image using standard hardware takes several minutes; however, utilizing a linear transducer can reduce scan time to approximately 1 min.

VA has been applied to the breast, liver, thyroid, *ex vivo* prostate, and porcine arteries.

## 12.5 Vibration-Amplitude Sonoelastography (VA Sono)

*Vibration-amplitude sonoelastography* (VA Sono) was the first USE method based on harmonic shear waves and an external driver. It was developed by Lerner et al. [255] in 1988 and later reviewed by Parker [256]. The external driver generates one or multiple frequencies in the audible range of 20–1000 Hz. The resulting tissue motion is detected by Doppler imaging, and the vibration envelope is extracted in postprocessing. Tissue stiffness is then reconstructed qualitatively from the detected VA in a given voxel. Quantitative reconstruction is not possible, since this would require knowledge of the applied stresses.

VA Sono has been used to examine the liver, kidney, prostate, breast, eye, and to characterize lesions.

## 12.6 Cardiac Time-Harmonic Elastography (Cardiac THE)

*Cardiac time-harmonic elastography* (THE) was published in 2012 by Tzschätzsch et al. [257] based on results obtained with cardiac MRE [177, 208] and is similar to VA Sono.

An external driver is used to generate a harmonic 30 Hz vibration, and the resulting myocardial wall vibration is captured by A-mode scans acquired over several cardiac cycles. The time-resolved amplitude reflecting myocardial tension is displayed in real time. Wave amplitudes are thus low during contraction (systole) and higher during relaxation (diastole).

Cardiac THE has a potential application for diagnosing cardiac diastolic dysfunction, which is currently the domain of cardiac MRE.

## 12.7 Vibration Phase Gradient (PG) Sonoelastography

*Vibration phase gradient (PG) sonoelastography* is based on VA Sono, and was developed in 1990 by Yamakoshi et al. [258] and reviewed by Parker [256].

While setup and acquisition are similar to VA Sono, the PG technique captures the vibration phase in addition to the signal magnitude. A phase gradient method (see Section 10.2) is used to reconstruct shear wave speed in the image. When multifrequency excitation is used, the frequency dispersion of the shear wave speed can be calculated as well.

Vibration PG sonoelastography has been applied to skeletal muscle.

## 12.8 Time-Harmonic Elastography (1D/2D THE)

*Time-harmonic elastography (THE)* is related to vibration PG sonoelastography. The 1D version developed in 2014 by Tzschätzsch utilizes multifrequency excitation and A-mode acquisition of the waves along multiple profiles in the liver to provide a single shear wave speed value [259]. Zhao et al. extended this technique into a 2D quasi-harmonic method: *external vibration multidirectional ultrasound shear wave elastography (EVMUSE)* [260], which uses bursts of 50-Hz vibrations and captures tissue displacement during the relaxation phase a few milliseconds after stopping the vibration. In 2015, Tzschätzsch et al. presented 2D THE with multifrequency excitation [261].

For 2D THE, the tissue is excited by an external driver with a multifrequency wave form in a range of 30–60 Hz. Motion is captured by conventional B-mode scanning with a frame rate of 80 Hz. The shear waves corresponding to the different excitation frequencies can be reconstructed separately by using controlled aliasing in the frequency domain. After directional filtering (see Section 8.2) and wave normalization, the shear wave phase gradient is calculated (see Section 10.2). The shear wave speed is imaged over the entire B-mode size.

THE is currently used for imaging of the liver, spleen, and prostate.

## 12.9 Crawling Waves (CW) Sonoelastography

*Crawling waves (CW) sonoelastography* was developed in 2004 by Wu et al. [262] and later reviewed by Parker [256].

VA Sono only detects the envelope of the vibration; it is not fast enough to capture the entire wave. CW sonoelastography aims to overcome this limitation by generating slow waves. Two vibration sources,  $\omega - \frac{\Delta\omega}{2}$  and  $\omega + \frac{\Delta\omega}{2}$  in the range of 25–300 Hz, with a small frequency difference,  $\Delta\omega \ll \omega$ , are placed on opposite sides of the tissue sample. The envelope of the resulting interference pattern has a wavelength corresponding to the mean frequency  $\omega$  of the two sources, but the velocity of the envelope corresponds to  $v \approx \frac{\Delta\omega}{2\omega} \cdot v_{\text{shear}}$ , which is much slower than the proper shear wave velocity. Therefore, CW can be captured even with common frame rates. The observed wavelength can be converted to shear wave speed. In addition, dispersion can be detected. In order to overcome the requirement of two separate drivers, CW sonoelastography was implemented by using ARFI to generate wave sources [263, 264].

CW sonoelastography with external drivers has been demonstrated in *ex vivo* prostate and liver; and CW based on ARFI has been tested in skeletal muscle.

## 12.10 Electromechanical Wave Imaging (EWI)

*Electromechanical wave imaging* (EWI) was developed in 2005 by Pernot and Konofagou [265] and later reviewed by Konofagou et al. [266].

The periodic intrinsic electrical activation of the heart that triggers the heart beat causes electromechanical stimulation patterns that propagate across the myocardium. The resulting myocardial displacement can be captured by acquiring B-mode images with a very high frame rate on the order of 500 images per second. This is achieved by dividing the full B-mode image into sectors, which are acquired during successive heart beats. A speckle-tracking algorithm is used to calculate a strain image, and after segmentation, the isochrones<sup>1</sup> of tissue deflection due to electromechanical waves are reconstructed in 3D. Several studies have shown a linear correlation between electrical activation times and EWI isochrones. EWI can be used to visualize the spreading of electromechanical activation across the myocardium.

EWI has been demonstrated in mice and humans.

An alternative approach was developed in 2001 by Kanai and Koiwa to capture acoustic waves caused by the heart sounds [267]. By reducing the lines of sight to 16, a frame rate of 450 Hz can be achieved. Cross-correlation can be used to calculate and image the phase of shear waves. In addition, the phase along the septum is imaged in a time–distance image and the shear wave velocity can be estimated [268].

## 12.11 Pulse Wave Imaging (PWI)

*Pulse wave imaging* (PWI) was developed in 2007 by Pernot et al. [269] and reviewed by Konofagou et al. [266].

PWI aims at retrieving the Young's modulus of the aorta from the measurement of displacement of the aortic wall induced by the passing cardiac pulse wave. The pulse wave causes “bulging” of the aortic wall, which travels at the same velocity as the pulse wave inside the vessel. The pulse wave velocity,  $c$ , and the Young's modulus of the wall,  $E$ , are related via the Moens–Korteweg equation [266]:

$$E = \frac{2\rho Rc^2}{b}, \quad (12.2)$$

where  $R$  is the inner radius of the aorta and  $b$  and  $\rho$  are the thickness and density of the aortic wall, respectively.

An early method, devised by Kanai et al. [270] in 1994 identifies the arrival time of the pulse wave at two points on the aortic wall using Doppler ultrasound. The pulse wave velocity can then be calculated from the time delay between the two points and their distance. However, since measurements are only performed at two points, this is not an

<sup>1</sup> Isochrones are hypothetical lines connecting the points that receive the activation signal at the same time. They can also be interpreted as wave fronts of the electromechanical wave.

imaging method. PWI, on the other hand, uses high frame rates (plane wave imaging with up to 8000 frames per second) to capture the pulse wave displacement at multiple time points. From the time-resolved images, the progression of the pulse wave can be tracked and the velocity can be measured.

PWI has been used to investigate the aorta in mice and humans.

## 12.12 Transient Elastography (TE)

*Transient elastography (TE)* was developed in 2002 by Sandrin et al. to characterize stages of liver fibrosis [271].

An external piston driver generates shear waves by applying a transient burst of a single 50 Hz cycle. As a consequence, waves propagate from the body surface into the tissue; the tissue displacement is then recorded continuously by A-mode US along a single line. The shear wave modulates the signal reflected by moving scatterers toward and away from the transducer; and the shear wave velocity can be extracted algorithmically from the time-resolved data. *TE* only provides a single value for wave speed, and is hence not an imaging technique. *TE* is the most extensively studied USE method. It has also been tested in skeletal muscles, breast, skin, and blood clots. However, the technique is limited by a relatively low penetration depth of approximately 8 cm. Furthermore, due to the absence of a B-mode image, positioning the A-mode beam can be challenging.

## 12.13 Point Shear Wave Elastography (pSWE)

*Point shear wave elastography (pSWE)*, sometimes also referred to as *ARFI quantification*, was published in 2008 by Palmeri et al. [272] and reviewed by Nightingale [251].

Tissue is excited by transient ARFI, but in contrast to ARFI imaging, the resulting displacement is acquired outside the excitation region. A time-of-flight algorithm is used to estimate the averaged speed of the spherically propagating shear wave, from which the mean wave velocity inside the region is obtained. The method has been applied to prostate, liver, breast, kidney, spleen, and cardiac tissue.

## 12.14 Shear Wave Elasticity Imaging (SWEI)

*Shear wave elasticity imaging (SWEI)* was developed in 2003 by Nightingale et al. [273] based on previous work by Sarvazyan et al. [250]. An overview can be found in [251].

SWEI is based on the same principle as pSWE. However, instead of using a single point source, SWEI places the focus of the ARFI beam in different lateral positions within the region of interest in successive measurements. The group velocity of the spherically propagating wave is reconstructed by wave-peak detection and time-of-flight calculation at lateral ranges. As a result, the wave velocity is mapped in a small ( $3 \times 4 \text{ cm}^2$ ) region, unlike pSWE, which only yields one spatially averaged value. SWEI is applied to prostate, liver, and cardiac tissue.



### 12.15 Comb-Push Ultrasound Shear Elastography (CUSE)

*Comb-push ultrasound shear elastography* (CUSE) was developed in 2012 by Song et al. [274].

CUSE works similar to SWEI; however, multiple ARFI beams are applied simultaneously rather than successively. Plane wave imaging is used to acquire displacement maps with a frame rate in the kilohertz range, thus sampling the full image within a few milliseconds. Displacement is calculated using 2D autocorrelation; and, after directional filtering, the shear wave speed can be reconstructed using a time-of-flight algorithm. The shear wave speed is thus imaged in a small region ( $4 \times 4 \text{ cm}^2$ ).

CUSE was demonstrated in phantoms, breast, and thyroid.

### 12.16 Supersonic Shear Imaging (SSI)

*Supersonic shear imaging* (SSI) was developed in 2004 by Bercoff et al. [275].

Most ARFI-based shear wave methods create a single or multiple laterally distributed point sources with spherically propagating shear waves, yet invoke a plane wave model for wave speed reconstruction. SSI generates multiple point sources in quick succession along an axial line. This procedure is equivalent to moving a point source at supersonic speed (hence the name of the method) through the tissue. This excitation pattern results in a shear wave Mach cone with nearly cylindrical geometry. Displacement is captured laterally with a frame rate in the kilohertz range by plane wave imaging. A time-of-flight algorithm reconstructs shear wave speed, and an elastogram with a size of a few square centimeters is created at a frame rate of 3–4 Hz.

SSI has been applied to breast, thyroid, liver, spleen, prostate, skeletal muscle, and transplanted kidneys.

### 12.17 Spatially Modulated Ultrasound Radiation Force (SMURF)

*Spatially modulated ultrasound radiation force* (SMURF) was developed by McAleavey et al. [276] in 2007.

In contrast to most other methods, which prescribe the temporal characteristics of the deformation, for example, by utilizing time-harmonic excitation, SMURF dictates the wavelength of the excited wave by applying a laterally modulated ARFI pattern. The temporal characteristic, that is, the frequency of the oscillation, is then observed by repeatedly acquiring each image line with a high PRF. The shear wave speed can then be calculated according to  $c = \lambda \cdot f$ .

SMURF was demonstrated in a phantom and an *ex vivo* sample of porcine liver.

### 12.18 Shear Wave Dispersion Ultrasound Vibrometry (SDUV)

*Shear wave dispersion ultrasound vibrometry* (SDUV) was developed in 2004 by Chen et al. [277] and reviewed by Urban et al. [278].

For quantifying dispersion, elasticity has to be probed at different frequencies. SDUV achieves this by applying ARFI pulses at a base frequency and its first few harmonics, typically in the range of 200–800 Hz. The detected tissue displacement is then separated into the excited frequency components by Kalman filtering. For each frequency, the shear wave velocity is calculated by analyzing the oscillation phase shift at two points along a lateral propagation path. The Kelvin–Voigt model (see Section 4.8.3 and Figure 4.7) is then utilized to analyze the dispersion of elasticity and viscosity.

SDUV was demonstrated in *ex vivo* skeletal muscle, cardiac muscle, liver, in vitro kidney, prostate, and excised arterial vessels.

A variant of SDUV, termed *Lambwave dispersion ultrasound vibrometry* (LDUV), was used to analyze the variation of shear wave speed in the myocardium over the cardiac cycle [279]. However, the only application of the method thus far was in porcine myocardium during open-chest surgery.

## 12.19 Harmonic Motion Imaging (HMI)

The *harmonic motion imaging* (HMI) was developed by Konofagou and Hynynen in 2003 with the motivation to monitor viscoelastic behavior during thermal ablation with *high-intensity focused ultrasound* (HIFU) [280]. A short review is given in [281].

Harmonic vibration on the order of 50 Hz is accomplished by amplitude-modulated HIFU. A second imaging transducer is embedded in the HIFU transducer. Due to a limited number of lines of sight, the imaging transducer reaches a frame rate of a few hundred hertz and can hence capture vibration with sufficient temporal resolution. After temporal Fourier transform, the shear wave speed near the focus is calculated using a phase gradient method (see Section 10.2). The HMI setup is unique in that it permits to observe vibration during HIFU ablation in real time, which helps to control ablation duration. In addition, the phase shift between the excitation force and the tissue vibration can be measured. This phase is identical to the phase of the complex shear modulus.

**Part IV**

**Clinical Applications**

## 13

### MRE of the Heart

*This chapter was coauthored by Thomas Elgeti from the Department of Radiology, Charité – Universitätsmedizin Berlin, Berlin, Germany.*

The heart is the motor of blood circulation. It propels blood through the systemic and pulmonary circulatory systems by periodic contraction and dilatation of the four cardiac chambers. This mechanical action can be described in terms of a number of time-dependent physical parameters such as volume, strain, shear modulus, and pressure. Noninvasive quantification of these parameters is desirable for the assessment of vital aspects of cardiac function such as the generation of mechanical forces and pressure. However, so far only sparse and preliminary *in vivo* data on the myocardial shear modulus in volunteers have been reported in the literature – most of them obtained by MRE. A major reason for the lack of data is the requirement of synchronization of heart beat, breathing, image acquisition, and external harmonic stimulation. Ultrasound elastography (USE) studies based on acoustic radiation force impulse (ARFI) or external vibration (see Chapter 12) were invasive when applied to the heart and have thus focused on animal models or *ex vivo* hearts. Notwithstanding its current limitations, cardiac elastography using MRI and ultrasound has been shown to allow measurements of basic mechanofunctional properties of the living heart, and is thus of considerable clinical interest. Hence, the studies published on cardiac elastography can pave the way for further technical developments toward quantitative mechanical biomarkers of cardiac function. Before we continue with reviewing seminal studies in the field, we will briefly address a few fundamentals of normal heart physiology, which are necessary to understand the clinical motivation for the development of cardiac MRE.

#### 13.1 Normal Heart Physiology

The cardiac cycle can be divided into a relaxation phase, termed diastole, and a contraction phase, termed systole. From the state of relaxed myocardium at end-diastole to the contraction state at end-systole, pressure can increase as high as 20 kPa at a rate of change of 300 kPa/s. Such high left ventricular (LV) pressure alteration is necessary to propel blood through all tissues of the body supplied by the systemic circulation. The right heart pumps deoxygenated blood into the pulmonary circulation for reoxygenation. Blood transport and gas exchange in the lungs occur at a low systolic pressure on the order of 4 kPa. Oxygen-saturated blood in the lungs is directed through the pulmonary veins into the left atrium; it then passes into the left ventricle through the mitral

*Magnetic Resonance Elastography: Physical Background and Medical Applications*, First Edition.  
Sebastian Hirsch, Jürgen Braun, and Ingolf Sack.

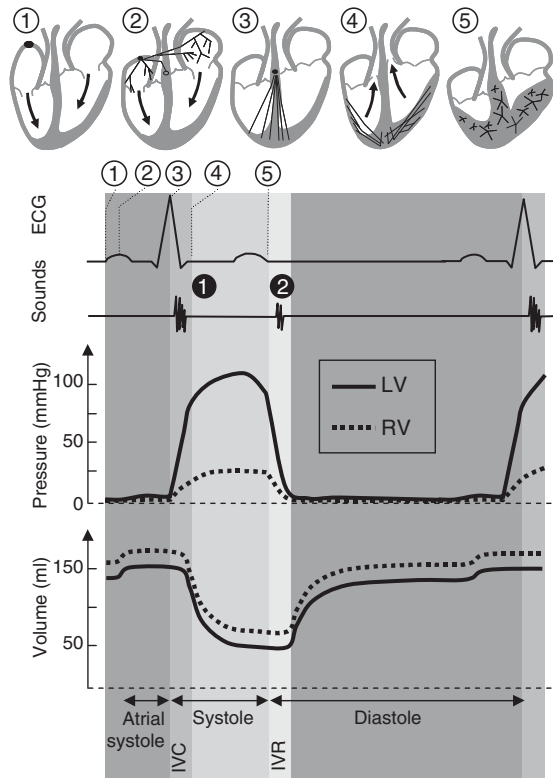
© 2017 Wiley-VCH Verlag GmbH & Co. KGaA. Published 2017 by Wiley-VCH Verlag GmbH & Co. KGaA.

valve. During the systolic ejection phase, the blood leaves the LV lumen through the aortic valve and the aorta to enter the systemic circulation for supplying the body with oxygen and nutrients and removing carbon dioxide and metabolic waste products. After delivery of oxygen through the highly branched vasculature of arterioles, capillaries, and venules, the oxygen-depleted blood returns to the heart through the superior and inferior vena cava, entering the right atrium and passing through the tricuspid valve into the right ventricle (RV). RV contraction propels the blood back into the pulmonary circuit for reoxygenation. The normal adult heart pumps between 5 and 25 l of blood per minute, depending on demand. Each contraction cycle of the heart is initiated by a synchronized depolarization of cardiac muscle cells. This electromechanical activation originates at the sinus node in the roof of the right atrium. In normal hearts, the sinus node generates 60–100 electrical impulses per minute, which propagate to the atrioventricular (AV) node located in the interatrial septum near the tricuspid valve. There, fibrous tissue acts as an insulator that prevents uncontrolled spread of electrical activation across the ventricular myocardium. The *bundle of His*, or AV bundle, is a collection of muscle cells specialized for electrical conduction that transmits the electrical activation further downstream from the AV node to the left and right bundle branch, Purkinje fibers, and cardiac myocytes.

In clinical routine, the propagation of the electrical impulse is measured by electrocardiography (ECG). There are five prominent signals in the ECG, identified as P, Q, R, S, and T waves, corresponding to major events of the electromechanical stimulation of the heart. While the P-wave reflects the depolarization of the atria toward the AV node, the QRS complex represents the rapid depolarization of the right and left ventricles. Since the ventricles have a larger muscle mass than the atria, the QRS complex has a much larger amplitude than the P-wave.<sup>1</sup> The T-wave indicates ventricular repolarization. Although several cellular mechanisms contribute to myocardial stiffness, the formation of actin–myosin cross-bridges is the major mechanism underlying the increase in myocardial stiffness during contraction. Therefore, as the electrical action potential stimulates cross-bridge formation, myocardial stiffness follows the electrical propagation paths [282, 283]. The increase in myocardial stiffness results in a significantly higher pressure inside the ventricle than that of the atrium. This pressure difference causes abrupt closure of the AV valves (mitral valve and tricuspid valve), thereby inducing acoustic vibration of myocardium and enclosed blood, which is the first heart sound. The second heart sound arises from closure of the semilunar valves (aortic valve and pulmonary valve) at the beginning of diastole. At early systole and early diastole, all heart valves are closed for short time periods, giving rise to an isovolumetric change in ventricular pressure. These periods are referred to as isovolumetric contraction time (IVC) and isovolumetric relaxation time (IVR), respectively. Figure 13.1 presents a diagram illustrating important features of normal heart physiology. Typical parameters used to assess cardiac function and values indicating normal cardiac function are summarized in the box on page 252.

---

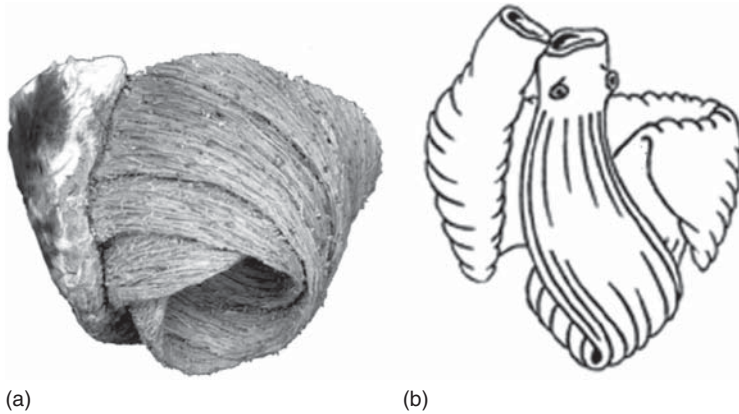
<sup>1</sup> The cardiac P-wave is unrelated to mechanical compression waves, which are also referred to as P-waves, particularly in the context of seismography.



**Figure 13.1** Normal heart physiology. The upper row schematically depicts electrical stimulation phases of the heart beginning with depolarization of the sinus in the right atrium ①, disseminated depolarization of right and left atria, which triggers atrial systole ②, depolarization of the right and left ventricles at early systole ③, ④ and the repolarization phase at the beginning of diastole ⑤. ① and ② demarcate the heart sounds produced by closure of the AV and semilunar valves, respectively. Note that stroke volumes are identical for LV and RV. Abbreviations: IVC – isovolumetric contraction time, IVR – isovolumetric relaxation time, LV – left ventricle, RV – right ventricle.

### 13.1.1 Cardiac Fiber Anatomy

Similar to skeletal muscle, the heart muscle, or myocardium, is composed of bundles of myocytes, which are oriented along a principal axis and hence induce transversely isotropic mechanical properties. However, cardiac myocytes are branched and their higher-order, macroscopic architecture is more complex than that of skeletal muscle. In fact, the heart demonstrates par excellence how mechanical requirements lead to the development of anatomical features. On a microscopic scale, the heart muscle is composed of linearly arranged myocytes, which develop uniaxial forces by sarcomere shortening. On a macroscopic level, the heart muscle is arranged in three-dimensional intertwined bands of counterdirectionally crossing fibers, which effectively translate forces that are aligned along the fibers within the walls into lateral forces, which produce volumetric ventricular strain. Figure 13.2 demonstrates a way to dissect the heart's macroscopic anatomy by unfolding a band of intertwined fiber bundles [284]. In this model, the myocardium is composed of a bilayer of endocardium and epicardium, which represent the ascending and descending branches of fibers with nearly orthogonally crossing directions in the left ventricle. A more detailed view reveals that fibers gradually change their directions from endocardium to epicardium. During systole and diastole, this helical loop architecture results in a spiral wall motion, imposing rotational flow. Streamlines of intraventricular flow can be measured by ultrasound Doppler techniques



**Figure 13.2** Myocardial fibers of the left ventricle around the apex of the heart. (a) Tissue specimen. (b) Simplified model of the helical ventricular myocardial band illustrating the crossing of fibers due to descendant and ascendant segments. (Kocica 2006 [284]. Reproduced with permission of Oxford Journals.)

or flow-sensitive MRI. From those techniques, it is known that normal flow inside the chambers, which results from in- and out-streaming blood, forms vortex rings due to rotational patterns imposed by the walls [285]. Vortex ring formation has wide implications for cardiac health, since vortices are thought to ameliorate convective pressure losses and facilitate fluid transport [286]. A further example of how tissue architecture is designed to address rheological needs can be seen in arterial walls, where spiral folds on the endoluminal surface impose spiral flow patterns [287]. Similar to the increased stability gained by precession of a bullet, which is imposed by spiral patterns inside a gun barrel, spiral flow is more stable, requires less energy to drive blood through the arterial system, and protects the vessel walls from laterally directed forces [287]. Analogously, the intricately intertwined helical structure of myocardial tissue appears to be optimized for the rheological needs of pulsatile chamber flow by enhancing turbulences, which better protect walls and propel blood more efficiently though the chamber than it is predicted for laminar flow [285]. Elastography has to account for those anatomical features when performed for parameter quantification in the heart. Alternatively, effective or apparent stiffness measures have been proposed, which, while oversimplifying myocardial structures, nevertheless provide mechanics-based imaging markers for clinical applications of cardiac elastography.

MRE of the biceps has shown that two different types of muscle contraction have to be distinguished (see Chapter 16). First, a muscle can contract without generating much force, for example, when the unloaded arm is flexed at the elbow. This state is distinguishable from the elongated state by an increase in  $T_2$ , whereas the MRE-derived shear modulus does not differ significantly [288]. Second, the contracting or contracted muscle can generate a force, for example, when lifting a weight or acting against a pulling force. This state is associated with an increase in shear modulus, which can be detected by MRE. In the myocardium, contraction of muscle fibers and the increase in shear modulus occur simultaneously. The contraction is necessary for decreasing the ventricular volume, which in turn is the prerequisite for pumping blood into the aorta. The force required to overcome the luminal pressure and to accelerate blood into the aorta

is effected by stiffening of the muscle in conjunction with the specific geometry of the myocardium, as we will explain in the next section.

The 3D volumetric strain of the heart chambers is directly translated into intraventricular pressure. As a result, the heart performs pressure–volume ( $p$ – $V$ ) work which – similar to adiabatic thermodynamic processes – can be described by the area enclosed in  $p$ – $V$  diagrams. This  $p$ – $V$  work represents the primary heart function. Hence, assessment of cardiac function requires *in vivo* imaging modalities sensitive to cardiac geometry and pressure. The cyclic alteration of the cardiac shear modulus  $\mu$  over the heart beat causes a cyclic alteration of ventricular pressure, as will be theoretically derived in the next section. Since elastography is sensitive to  $\mu$ , the  $\mu$ – $p$  relationship offers a way to noninvasively measure cardiac pressure by elastography, which can be combined with 3D ventricular imaging for a full assessment of cardiac function.

### 13.1.2 Wall Shear Modulus versus Cavity Pressure

We will now present a model that illustrates how the myocardial shear modulus is related to ventricular pressure. We therefore use Hooke’s law in spherical coordinates to find a relationship between shear modulus and pressure. Hence, we assume linear elastic, isotropic conditions, which clearly is an oversimplification of cardiac mechanics, but allows us to approximate the ventricle by a fluid-filled spherical shell in the regime of small displacements. In this model, fluid pressure inside the LV lumen is produced by the radial component of the stress field acting on the encased fluid:

$$\sigma_{rr} = -p_{\text{lumen}} \quad (13.1)$$

We note that large strains occur mainly during the ejection phase and the ventricular distension phase, that is, when the valves are open and blood streams into or out of the ventricles. By contrast, during isovolumetric phases IVC and IVR, the volumetric strain of the cardiac walls can be considered negligible while  $p_{\text{lumen}}$  rapidly rises or drops, respectively. How is a pressure change produced by a change in myocardial shear modulus? A straightforward answer is provided by Eq. (4.122) (in spherical coordinates), which, for the radial stress component, yields:

$$-p_{\text{lumen}} = \left(K + \frac{4}{3}\mu\right)\epsilon_{rr} + \left(K - \frac{2}{3}\mu\right) \cdot (\epsilon_{\theta\theta} + \epsilon_{\phi\phi}), \quad (13.2)$$

where  $K$  and  $\mu$  denote compression and shear modulus of the myocardium, respectively. Collecting volumetric strain  $\epsilon_{rr} + \epsilon_{\theta\theta} + \epsilon_{\phi\phi} = \text{tr}(\epsilon)$ , which denotes the volumetric strain inside the wall, we arrive at

$$-p_{\text{lumen}} = 2\mu\epsilon_{rr} - \frac{2}{3}\mu \cdot \text{tr}(\epsilon) + K \cdot \text{tr}(\epsilon). \quad (13.3)$$

For incompressible tissue, volumetric strains are very small, that is,  $\text{tr}(\epsilon) \ll \epsilon_{rr}$ , canceling out the second term in Eq. (13.3). In the third term, however,  $\text{tr}(\epsilon)$  is balanced by the very high compression modulus, giving rise to a finite value of  $K \cdot \text{tr}(\epsilon)$ , which we identify as intramural tissue pressure  $-p_{\text{wall}}$ . Equation (13.3) thus becomes

$$\mu\epsilon_{rr} = -\frac{1}{2}p_{\text{lumen}} + p_{\text{wall}}. \quad (13.4)$$



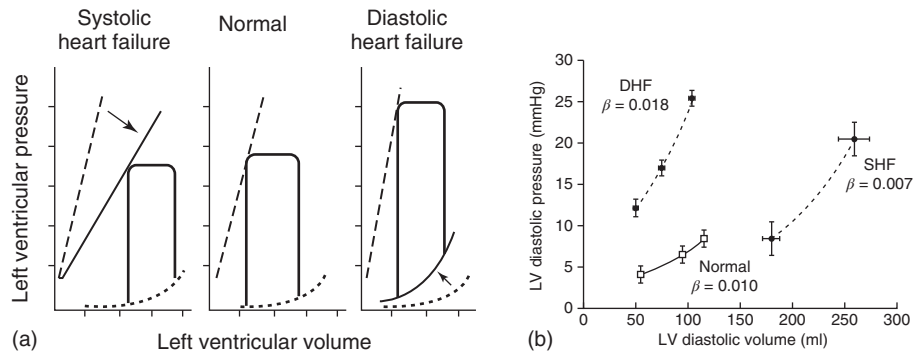
The right-hand side of Eq. (13.4) represents the ventricular pressure combining blood and myocardial tissue, which is proportional to the MRE-measured shear modulus  $\mu$ . An alternative derivation of the  $\mu$ - $p$  relationship is presented in [308], demonstrating that a spherical shear strain field of  $\text{tr}(\epsilon) = 0$  comprises a radial component if integrated over a sphere with an aperture. Such net radial strain gives rise to a radial stress, which, according to Eq. (13.4), relates to intraventricular pressure.

## 13.2 Clinical Motivation for Cardiac MRE

Heart failure is a major cause of death in Western societies and will become even more prevalent with increasing life expectancy. Early detection of cardiac abnormalities is key for the timely initiation of treatment of cardiovascular disease and reduction of the enormous death toll. As outlined above, the complete description of heart function including  $p$ - $V$  work by imaging markers is highly desirable for diagnosis and therapy monitoring in cardiology [290]. Today, one of the most important imaging markers for cardiac failure is the LV ejection fraction (EF). EF represents the total volumetric strain of the entire ventricle from diastole to systole (i.e., the stroke volume divided by end-diastolic volume). It is well known that EF is influenced by multiple parameters of heart physiology including preload, afterload, and myocardial contractility. Preload is the pressure that stretches the myocardial fibers prior to contraction, while afterload is the blood pressure against which the heart contracts to eject blood. Afterload arises from the downstream vascular system, comprising the aorta and its periphery for the left ventricle, whereas for the RV afterload originates from the pulmonary circulatory system [291]. Myocardial contractility refers to the ability of the heart muscle to contract. This parameter is normally quantified by the velocity of pressure generation ( $\dot{p}_{\text{lumen}}$ ) at a given ventricular volume. Cardiac preload, afterload, and contractility are intrinsic mechanical properties, whose quantification in humans *in vivo* presents a continuing challenge. By contrast, EF can be assessed by standard imaging methods and has therefore become established as a routine marker for heart failure associated with a reduced ejection capacity of the left ventricle. EF of the LV is also an important marker to discriminate systolic from diastolic heart failure. Both types of heart failure fundamentally differ in their  $p$ - $V$  performance and pose different challenges to diagnostic imaging, as will be explained in the next section.

### 13.2.1 Systolic Dysfunction versus Diastolic Dysfunction

Systolic function is characterized by blood ejection due to ventricular contraction and ventricular pressure generation against afterload. Different myocardial injuries or stresses lead to reduced myocardial contractility and increased volume – the dominant abnormalities in systolic dysfunction (SD). End-systolic pressure remains unchanged in SD since low contractility is compensated by increased muscle mass and volume. In general, an altered contractile behavior of the ventricle reflects widespread micromechanical changes and myocardial remodeling at the level of cardiomyocytes and the extracellular matrix. In most cases, SD arises from degradation and disruption of the collagen matrix. By contrast, accumulation of collagen causes increased passive



**Figure 13.3** LV pressure–volume relationship in normal hearts and hearts with abnormal systolic and diastolic function. (a) Schematic  $p$ - $V$  cycles, normal and altered by systolic dysfunction (SD) and diastolic dysfunction (DD). While left ventricular (LV) pressure is normal in SD, DD is characterized by a significantly elevated LV pressure. Conversely, as LV volumes are increased in SD (with reduced EF), DD does not change LV volumes, rendering an image-based diagnosis more challenging than the diagnosis of SD. (b) LV diastolic pressure–volume data from normal controls (solid line), patients with diastolic heart failure (DHF) (dotted line), and patients with systolic heart failure (SHF) (dashed line). In DHF, the  $p$ - $V$  cycle displays normal volumes but elevated pressure, indicating increased passive stiffness of myocardium. (Aurigemma 2006 [294]. Reproduced with permission of Wolters Kluwer.)

muscle stiffness, which often manifests in reduced distensibility or relaxivity of the ventricle. Such abnormal mechanical relaxation of the myocardium combined with normal EF and LV volume is the hallmark of diastolic dysfunction (DD). DD is highly prevalent in patients with cardiac failure – nearly half of the patients suffer from DD and face reduced survival [292]. Unlike SD, contractility and LV volume in DD remain widely unchanged, whereas increased passive myocardial stiffness gives rise to an elevated filling pressure. As seen in Figure 13.3, SD is revealed by a shift of the  $p$ - $V$  cycle along the  $V$ -axis, whereas DD is associated with an elevation of pressure and normal volume changes. For this reason, detection of DD remains challenging for morphometry-based imaging techniques. In the past, measurement of  $p$ - $V$  curves was considered the standard of reference for evaluation of DD. However, the high risks of catheterization such as hazardous aortic valve passage have limited the use of this procedure as a diagnostic tool for DD. Today, echocardiography with tissue Doppler techniques combined with serological parameters serves as the standard of reference for the diagnosis of DD in clinical routine. However, the exact parameters and threshold for the diagnosis of DD are still under debate. Recent reports suggest that LV hypertrophy, elevated LV filling pressure and high pulmonary artery pressure predict an increased cardiovascular death and hospitalization rate, which cannot be predicted by LV volumes and LV-EF alone [293]. Therefore, imaging techniques sensitive to myocardial relaxation during diastole are urgently required to assess LV dysfunction in heart failure with preserved EF and to detect preclinical stages of heart failure [290]. Detecting the altered myocardial shear modulus by MRE was demonstrated to be sensitive to myocardial relaxation abnormalities [79]. The quantification of myocardial stiffness in a time-resolved fashion is the major aim of cardiac MRE in the future.

Typical parameter values characterizing normal cardiac function	
Values from [56]:	
Isovolumetric contraction time (IVC):	40 ms
Isovolumetric relaxation time (IVR):	70 ms
Duration of systole:	280 ms @ 70 bpm, 250 ms @ 150 bpm
Duration of diastole:	580 ms @ 70 bpm, 150 ms @ 150 bpm
Values from [295]:	
LV end-diastolic volume:	86–178 ml (women), 106–214 ml (men)
LV end-systolic volume:	22–66 ml (women), 26–82 ml (men)
LV stroke volume:	57–117 ml (women), 72–144 ml (men)
LV ejection fraction:	57–77% (women), 57–77% (men)
LV mass:	56–140 g (women), 92–176 g (men)
RV end-diastolic volume:	77–201 ml (women), 118–250 ml (men)
RV end-systolic volume:	24–84 ml (women), 41–117 ml (men)
RV stroke volume:	48–120 ml (women), 68–144 ml (men)
RV ejection fraction:	51–71% (women), 52–72% (men)
RV mass:	21–49 g (women), 25–57 g (men)
Values from [296]:	
LV end-systolic pressure:	138 ± 15 mmHg
LV end-diastolic pressure:	10 ± 11 mmHg
LV $p$ - $V$ (stroke) work:	0.62 ± 0.14 J
RV end-systolic pressure:	26 ± 4 mmHg [297]
RV end-diastolic pressure:	6 ± 4 mmHg [297]
RV $p$ - $V$ (stroke) work:	≈ 0.1 J [56]

### 13.3 Cardiac Elastography

Despite the clear motivation and high relevance of cardiac MRE, a relatively low number of studies have been reported in the literature. The lack of data may be attributable to a number of technical challenges, including the highly complex geometry of the heart with multiple boundaries, its intricate microstructure, and the high temporal dynamics of parameter changes. Moreover, the position of the heart inside the thoracic cavity, protected by the lungs, diaphragm, fat, and bones effectively shields the heart from most types of exogenous mechanical stimuli. Therefore, cardiac elastography methods used in humans are based on time-harmonic waves in the low-frequency regime, which can penetrate the thorax better than transient stimuli. Time-harmonic cardiac elastography has been demonstrated to be feasible using MRI [289, 298] and ultrasound [257]. Transient ultrasonic methods such as acoustic radiation force impulse (ARFI) imaging and shear wave imaging (SWI) (see Chapter 12) have been studied in *ex vivo* hearts [299] or invasively [300, 301]. Table 13.1 summarizes principal approaches of cardiac elastography reported in the literature. Note that the term “cardiac elastography” is ambiguous, since it sometimes denotes measurement of intrinsically induced cardiac strain and

**Table 13.1** Overview of the currently available methods of cardiac elastography.

Mechanical stimulus, modality	Imaging modality	Reconstruction approach/ sought quantity	Application, reference
Time-harmonic 80 Hz, MRE	MRI	Inversion by LFE/shear modulus	<i>In vivo</i> , healthy volunteers [161]
Time-harmonic 25 Hz, MRE	MRI	Wave amplitude variation/relative shear modulus alteration	<i>In vivo</i> , patients with diastolic dysfunction [79]
Time-harmonic 30 Hz, THE	A-mode US	Wave amplitude variation/relative shear modulus variation	<i>In vivo</i> , healthy volunteers [302]
Time-harmonic 100–350 Hz, SDUV <sup>a)</sup>	B-mode US	Anti-symmetric Lamb waves/elasticity, viscosity	Pigs, invasive [303]
Transient, SWI <sup>b)</sup>	B-mode US	Time-of-flight/group velocity	Pigs, invasive [301]
Transient, ARFI <sup>c)</sup>	B-mode US	Strain/relative deflection	Dogs, invasive [282]
Endogeneous, intraventricular septum vibration	B-mode US	Anti-symmetric Lamb waves/elasticity, viscosity	<i>In vivo</i> , healthy volunteers [304]

a) SDUV = shear wave dispersion ultrasound vibrometry (see Section 12.18).

b) SWI = shear wave imaging (see Section 12.14).

c) ARFI = acoustic radiation force impulse (see Section 12.3).

Only methods assessing shear stiffness, shear viscosity, or other parameters related to external stimulations are considered here. Further details on ultrasound elastography are given in Chapter 12.

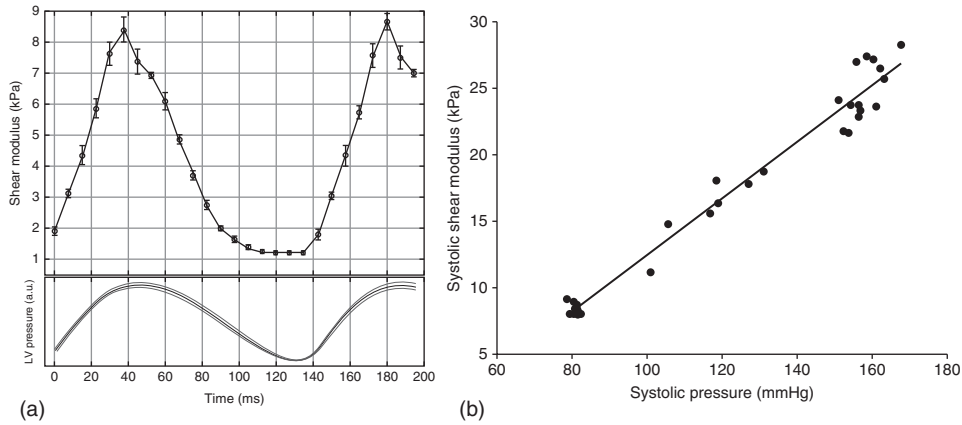
strain rate [305]. Albeit related to myocardial mechanics, these parameters alone cannot reveal intrinsic elastic properties, since the stress term in the balance of motion equation remains unknown. We will therefore disregard strain- and flow-sensitive methods in the further discussion. In the following sections, selected studies of cardiac elastography using ultrasound and MRI are presented to provide reference values and to demonstrate the sensitivity of cardiac MRE for future studies.

### 13.3.1 *Ex vivo* SWI

Shear wave imaging (SWI) was investigated in Langendorff perfused isolated adult rat hearts to measure the variation in shear modulus over the cardiac cycle [299]. The study was designed to simulate various physiological conditions and to measure the effect on elastography-derived stiffness values. Myocardial contractility was modified by infusion of isoproterenol, which resulted in a clear increase in systolic stiffness. Systolic stiffness was correlated with an increase in  $\dot{p}_{\text{lumen}}$ , as a direct measure of contractility, whereas diastolic stiffness remained unchanged. The major findings are summarized in Figure 13.4.

### 13.3.2 *In vivo* SDUV

Shear wave dispersion ultrasound vibrometry (SDUV) is based on the measurement of Lamb waves in the myocardial wall [303] (see Section 12.18). Lamb waves are two modes

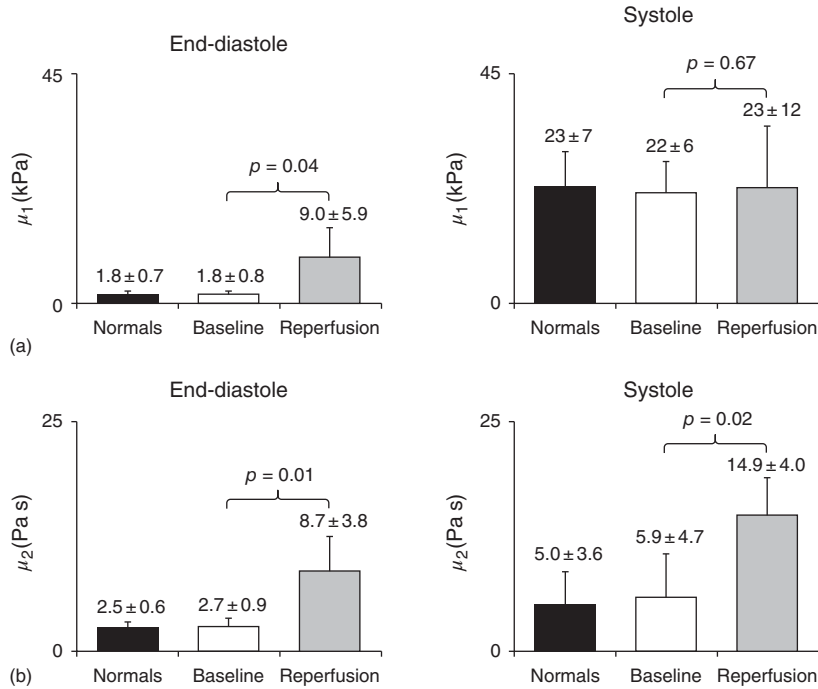


**Figure 13.4** Myocardial stiffness measured by SWI in a perfused Langendorff rat heart, and LV pressure evolution on the same time axis (a). (b) Linear relationship between systolic shear modulus of the LV wall and LV pressure. LV pressure was modified by isoproterenol infusion. (Pernot 2011 [299]. Reproduced with permission of Elsevier.)

of plate waves (parallel and antiparallel), whose velocities depend on the ratio between wavelength and plate thickness. Antisymmetric Lamb waves represent bending vibrations, which arise in the heart wall upon external stimulation by harmonic waves. SDUV measures the dispersion of Lamb wave speed over the excitation frequency, which can be fitted by a viscoelastic model such as the Voigt model (see Section 4.8). The Lamb wave model explicitly depends on the plate thickness; therefore, SDUV requires information on the finite plate thickness prior to inversion. Figure 13.5 shows normal values of myocardial elasticity and viscosity measured in porcine hearts exposed by sternotomy for measurement. In addition, myocardial infarction was induced by ligation of the anterior descending coronary artery, followed by reperfusion for 1–2 h. Similar to results obtained by SWI in *ex vivo* rat hearts (see Figure 13.4), the SDUV-measured shear modulus was higher in systole than in diastole ( $\approx 12$ -fold). Shear viscosity varied less over the cardiac cycle ( $\approx$  twofold). Infarction caused myocardial stiffening mainly in the relaxed heart phase, whereas no change was observed during systole. Myocardial viscosity after infarction was increased in both diastole and systole.

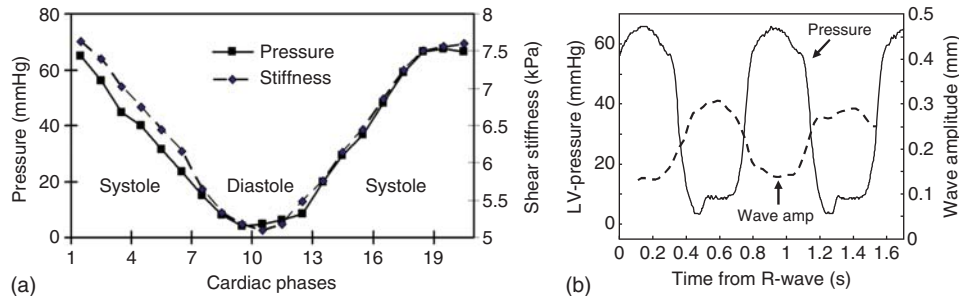
### 13.3.3 *In vivo* Cardiac MRE in Pigs

*In vivo* cardiac MRE in pigs was performed to measure shear modulus values across the cardiac cycle using 80-Hz harmonic vibration [298]. Reconstruction of effective myocardial stiffness was accomplished based on the flexural plate speed in a 2D spherical shell. By using this model, wave speed can be converted to a shear modulus as long as wall thickness is known. As a result of its 2D nature, this model shows in-plane singularities at the poles. Moreover, an unknown load term causes the stiffness measurements to be relative rather than reflecting intrinsic properties [306]. Shear moduli obtained in this study were  $\approx 9.3$  and  $\approx 6.0$  kPa for systole and diastole, respectively. This corresponds to a relatively small change ( $\approx 1.5$ -fold) compared to *ex vivo* SWI ( $\approx 7.3$ -fold) and *in vivo* SVDU ( $\approx 12.8$ -fold). Nevertheless, good correlation



**Figure 13.5** Shear wave dispersion ultrasound vibrometry (SDUV) of exposed pig hearts *in vivo*. Shear modulus  $\mu_1$  (a) and viscosity  $\mu_2$  (b) (corresponding to  $E$  and  $\eta$  of the Voigt model in Section 4.8) were measured in normal LV wall and after reperfused acute myocardial infarction. Notably, the highest increase in stiffness following infarction and reperfusion was observed in diastole. (Pislaru 2014 [303]. Reproduced with permission of Elsevier.)

between pressure and stiffness was observed in some animals, further corroborating the use of shear wave-based elastography for cardiac pressure measurement. This major finding was confirmed by a further cardiac MRE study in pigs following intravenous injection of dextran-40 to alter the end-diastolic cardiac load [306]. In this study, MRE confirmed the correlation between increased end-diastolic LV pressure and myocardial stiffening at different time intervals following dextran administration. In view of limitations of wave inversion in highly bounded media such as the heart, an alternative “inversion-free” approach was developed based on the simple relationship between wave amplitudes and shear modulus,  $|\mathbf{u}| \propto \sqrt{\mu}$  (see Eq. (4.213)) [208]. This approach is appealing since the change in  $\mu$  is directly reflected in the magnitude of shear wave amplitudes  $|\mathbf{u}|$  at the image resolution of the underlying imaging sequence. This method, often denoted wave amplitude variation (WAV) approach, does not rely on wave inversion and thus does not require high wave numbers. Instead, steady-state flux of shear wave energy is required to fulfill Eq. (4.213), which is better obtained by low vibration frequencies in the range of 20–30 Hz than at higher frequencies, where attenuation and reflections are more pronounced. More details on WAV-MRE sequences and postprocessing are given in the next section. To highlight the potential of WAV-MRE in measuring the cyclic variation of cardiac pressure, Figure 13.6 shows the reciprocal correlation between pressure and MRE-derived wave amplitudes in pigs.



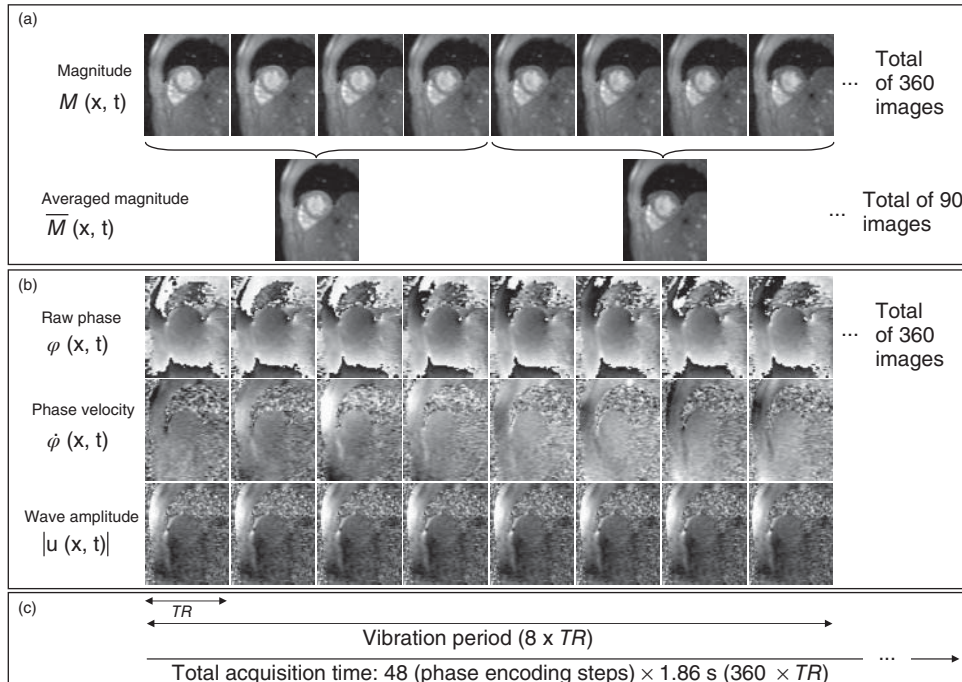
**Figure 13.6** Cardiac MRE in pigs to test the correlation between MRE and invasively measured LV pressure. ((a) Kolipaka 2010 [298]. Reproduced with permission of Wiley and (b) [308] used under CC BY 2.0 licence.)

### 13.3.4 *In vivo* Cardiac MRE in Humans

#### 13.3.4.1 Steady-State MRE (WAV-MRE)

The first cardiac MRE experiments in humans were conducted similar to measurement of wave amplitudes as shown in Figure 13.6 for pigs. Initially, a balanced steady-state free precession (bSSFP) MRE sequence was used, which is superior to other MRE methods in terms of signal-to-noise ratio (SNR) and image quality. However, as discussed in Section 3.4.2, bSSFP suffers from a nonlinear phase response to motion. This results in spatial modulation of the encoded motion phase, which does not reflect true displacement. Such displacement may result in apparently propagating waves when the offset phase changes during the heart beat. These propagating sensitivity patterns affect elasticity estimates by MRE. Therefore, [19] introduced the so-called phase preparation gradients for use with bSSFP-MRE, which produce parallel banding perpendicular to the gradient direction with regions of high signal magnitude in between. With increasing gradient amplitude, these stripes become narrower and increase in number. In the limit of fully dephased magnetization, the lines of high and low signals collapse into a single voxel, producing homogeneous image contrast, which basically resembles that of steady-state fast low-angle shot (FLASH). In contrast to bSSFP, FLASH ensures a linear relation between displacement amplitude and accumulated spin phase, as presented in Table 3.1. Therefore, steady-state FLASH was used for cardiac MRE [208]. A sequence scheme is displayed in Figure 7.1. This protocol creates a steady state of magnetization, during which time-harmonic waves are continuously excited. The patient is asked to hold his/her breath for approximately 1.8 s, during which one  $k$ -space line is acquired 360 times in quick succession. By repeating the same process for every  $k$ -space line, a time series of 360 images covering 1.8 s can be reconstructed. After each single line acquisition, a 2- to 3-s delay is inserted for breathing. This acquisition scheme provides high reproducibility for *in vivo* cardiac MRE. Figure 13.7 demonstrates the timing of steady-state FLASH MRE of the heart.

The relatively high temporal resolution of approximately 5 ms makes steady-state FLASH-MRE well suited for analysis of WAV during the heart beat. The change in shear wave energy or altered wave flux due to a change in the myocardial shear modulus gives rise to the WAV effect, which constitutes a relative measure of myocardial elasticity. Two experimental observations led to the development of WAV-MRE: (i) wave amplitudes

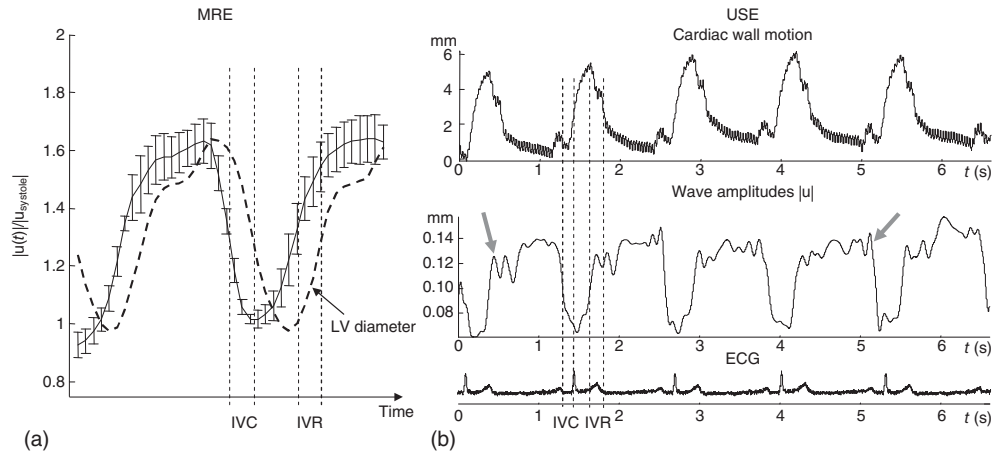


**Figure 13.7** Illustration of cardiac steady-state FLASH MRE (Elgeti 2010 [177]). (a) Collecting morphological information such as LV diameter from magnitude MRE images. (b) Analysis of phase MRE images comprising (i) unwrapping using gradient unwrapping corresponding to Eq. (9.10) but along the time axis, yielding phase velocity  $\dot{\varphi}$  and (ii) calculation of the wave deflection amplitude from  $\dot{\varphi}$  by accounting for all three vector field components of the displacement. Figure (c) illustrates the relative timing of the sequence.

change ahead of geometry (wall motion or LV volume) and (ii) wave amplitudes are not limited to myocardial tissue but can also be measured in the blood-filled LV lumen. The first observation is demonstrated in Figure 13.8 using both MRE and ultrasound-based cardiac elastography. The fact that geometry lags behind MRE-derived alterations in the shear modulus provides evidence for the aforementioned correlation between MRE and cardiac pressure. The time delay between MRE and geometry was exploited for the detection of isovolumetric times [177, 302].

Cardiac USE – in contrast to ultrasound-based cardiac strain measurement methods – was developed after the feasibility of WAV-MRE had been demonstrated in healthy volunteers [257]. As mentioned above, WAV-MRE requires a relatively high sampling rate to ensure that the continuous flux of shear wave energy through the heart is monitored with a sufficient time resolution. As a compromise, the WAV effect is analyzed inside the full ventricle and spatial resolution is sacrificed. Such a setup can be realized with even higher temporal resolution by using USE. Cardiac USE was introduced in the literature under the name “time-harmonic elastography” (THE, see Section 12.8) since it utilizes a time-harmonic monofrequency stimulus similar to that applied in cardiac MRE [257]. The THE–USE method measures a single wave field component, and the high sampling rate ( $\approx 1$  kHz) renders the method sensitive





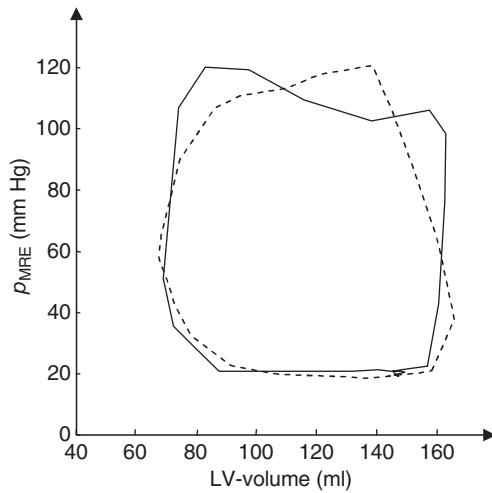
**Figure 13.8** *In vivo* WAV-based MRE and ultrasound-based cardiac elastography (USE) in healthy volunteers. The principal finding is that cardiac wall motion (geometry) lags behind wave amplitudes  $|u(t)|$  (elastography). The delay between the curves of geometry and elastography represents the isovolumetric contraction and relaxation times, IVC and IVR, respectively. Gray arrows in the USE plot point to modulations that are related to temporal scattering as explained in Section 4.12.2. ((a) Sack 2009 [208]. Reproduced with permission of Wiley. (b) Tzschätzsch 2012 [257]. Reproduced with permission of Elsevier.)

to the elasticity variation of the heart wall. This high temporal resolution sheds light on the interaction between shear waves and cardiac elasticity. Figure 13.8 illustrates modulations of shear wave amplitudes within elasticity transition times (IVC and IVR) measured by THE–USE. This frequently observed phenomenon is related to the mechanism explained in Figure 4.15, in which backward-running waves caused by a “temporal interface” (sudden changes in elasticity) interfere with forward-running waves. In other words, allowing the shear modulus to vary in the energy flux density Eq. (4.212) violates the underlying equality of potential and kinetic energy: elasticity changes influence the potential energy of a body, which must also affect the kinetic term in Eq. (4.212). Although WAV–MRE has a lower time resolution than THE–USE, this observation can help correctly determine cardiac time intervals in the future, as it was proposed in the studies reviewed below.

WAV–MRE was shown to allow noninvasive measurement of pressure–volume cycles in the human heart [289]. However, the relative change in wave amplitudes  $|u(t)|$  according to Eq. (4.213) had to be scaled by the peripherally measured systolic pressure,  $p_{systole}$ , in order to obtain an intracardiac pressure value  $p_{MRE}$ :

$$p_{MRE} = \frac{|u_{systole}|}{|u(t)|} \cdot p_{systole}. \quad (13.5)$$

Although  $p_{systole}$  provides only a rough approximation of systolic LV pressure, it enabled the quantification of the mechanical work performed during one  $p$ – $V$ , as  $0.84 \pm 0.19$  J which is on the order of invasively derived values for the normal heart (see the box on page 252). Figure 13.9 illustrates two  $p$ – $V$  cycles from a normal and a dysfunctional volunteer (mild mitral valve insufficiency). The latter volunteer had markedly lower



**Figure 13.9** *In vivo*  $p$ - $V$  cycles determined in two volunteers. The dashed line indicates mild mitral valve insufficiency, which results in a lower pressure increase than seen during normal IVC.  $p_{MRE}$  relates to Eq. (13.5). (Based on data published in [309].)

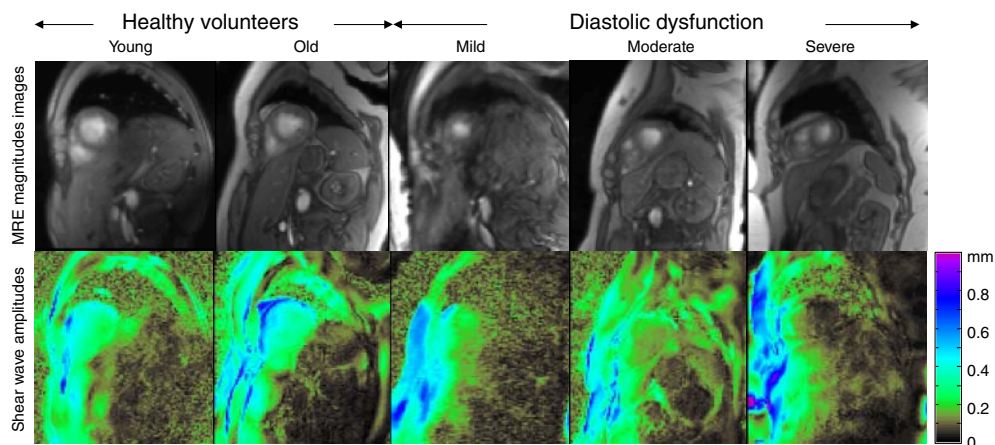
IVC pressure increase rate, indicating a symptomatically elevated volume change during pressure increase.

**Diastolic Dysfunction and Isovolumetric Cardiac Times** Elasticity-based IVC and IVR times were measured by WAV-MRE in 27 patients with relaxation abnormalities and 20 healthy controls [80]. The magnitude of the complex signal was used to deduce morphological information, and magnitude combined with the phase of the complex signal was used to derive tension relaxation information during systole and diastole. Wave amplitudes decreased during systolic contraction and increased during diastolic relaxation of the left ventricle. In healthy volunteers, mean IVC and IVR times were  $136 \pm 36$  and  $75 \pm 31$  ms, respectively. In patients with DD, IVC was only weakly altered ( $161 \pm 45$  ms), while IVR was significantly prolonged ( $133 \pm 57$  ms).

**Diastolic Dysfunction and Wave Amplitude Maps** As it is known that myocardial stiffness increases not only with myocardial disease but also with age, a young (18–39 years,  $N = 10$ ) and an old healthy group (40–68 years,  $N = 10$ ) were compared to patients with DD ( $N = 29$ ) [79]. LV wave amplitudes were normalized by wave amplitudes measured in a reference region anterior to the heart and adjacent to the RV. Normalized wave amplitudes decreased with age and DD severity, indicating progressive stiffening of myocardial tissue caused by aging or dysfunctional diastolic relaxation. A cutoff value of 0.43 for normalized wave amplitudes was found to be optimal for identifying patients with DD with an overall diagnostic performance of 0.92 as quantified by AUROC (area under the receiving operating characteristic curve) analysis and with 90% sensitivity and 89.7% specificity when compared with echocardiography as the reference standard. Figure 13.10 illustrates the DD-related decrease of LV wave amplitudes.

#### 13.3.4.2 Wave Inversion Cardiac MRE

The wave inversion (WI)-MRE approach uses excitation frequencies of 60–80 Hz, resulting in a temporal resolution of 50–100 ms in the heart. A standard gradient-echo MRE sequence with 160-Hz motion-encoding gradient (MEG) (thus using fractional encoding, see Section 3.1.3) allowed the acquisition of wave images in eight phases of the



**Figure 13.10** Shear wave amplitude maps generated using WAV-MRE (steady-state cardiac FLASH-MRE). Short-axis views of the heart and corresponding amplitude maps of a normal volunteer (young), a normal volunteer (old), and patients with mild, moderate, and severe diastolic dysfunction. The white solid line outlines the outer contour of the left ventricle during systole. The region of interest for normalizing the induced shear waves anterior to the heart is outlined by a white dashed line. (Elgeti 2014 [79]. Reproduced with permission of Radiological Society of North America.)

cardiac cycle at four samples over one vibration cycle [161]. Unlike data processing in swine, conventional local frequency estimation (LFE, see Section 10.4) was used to analyze these data, providing shear stiffness values similar to other MRE studies in larger organs such as the liver (discussed in Chapter 15). Using this approach, Wassenaar et al. [161] observed a weak linear correlation between stiffness and age. Interestingly, the deviation between end-systolic and end-diastolic stiffness was observed to increase with age, which was interpreted as an effect of higher afterload during systole attributable to changes in aortic compliance that occur with age.

### 13.3.5 MRE of the Aorta

In addition to the heart itself, the aorta is a major determinant of cardiovascular health and has recently gained attention as a potential clinical target of MRE. Large arteries such as the aorta deliver blood to peripheral tissues and serve as blood buffer according to the Windkessel principle: the walls of large arterial vessels distend when the blood pressure rises and recoil when the blood pressure falls. The distensibility of large elastic arteries is therefore analogous to a capacitor, which stores blood during systole and discharges blood during diastole. An estimated 50% of stroke volume is accumulated by the central large vessels during systole and delivered into the periphery during diastole. This effect enhances coronary blood flow, reduces afterload of the left ventricle, and improves ventricular relaxation [310]. With aging, the aorta stiffens, thus reducing the capacity to store blood during systole. This mechanical impairment of the aorta is accelerated by arterial hypertension [311]. A reduced mechanical compliance of the aorta also promotes vascular stenosis, formation of atherosclerotic plaques, and the risk of vascular rupture [312, 313], motivating the application of MRE to the central great arteries for assessing cardiovascular risk factors and monitoring antihypertensive therapy.

Current arterial MRE methods image and analyze harmonic shear wave propagation through the wall and lumen, considering arteries as fluid-filled tubes. Although shear waves do not propagate in fluids, vibration of the aortic wall causes the blood to vibrate with the same oscillatory pattern, thus enabling stiffness measurement in regions that incorporate both the wall and the lumen of the aorta [143]. Friction between blood and the oscillating vessel wall transfers kinetic energy to the blood and causes it to oscillate. Similar to WAV-MRE, which also relies on endoluminal vibrations, MRE of the aorta exploits the larger volume and high MRI signal of blood to indirectly capture the vibration properties of the adjacent vessel wall. Several studies investigated this approach adjusting the standard MRE setup used in liver examinations for the abdominal aorta [314–316]. Wave images in sagittal views of the abdominal aorta were acquired by gradient-echo MRE sequences [315]. Parameter reconstruction was either based on LFE assuming a boundary-free isotropic medium [316], by measuring wavelength along the principal axis of the aorta [315] or by a phase gradient method [314]. The MRE-derived stiffness values increased with age and were higher in systole than diastole [162, 315, 316]. Arterial stiffness can also be recovered from pulse wave velocity (PWV), that is, the speed at which the arterial pulse wave propagates through the vessel. PWV can accurately be determined by phase-contrast MRI and Doppler ultrasound methods [317, 318]. Recovery of arterial stiffness is usually based on the Moens–Korteweg equation (12.2), which is applicable in the linear elastic regime of elastic wall deformation for incompressible fluids and wall tissue [143]. In this simple model, PWV depends on either hydrostatic input pressure or the rate of deformation, which contradicts the observation reported by Xu et al., who found a strong correlation between pressure and PWV in porcine aorta [315]. Furthermore, it is known that PWV increases during systole and is influenced by variation in the heart rate [319]. It has to be noted that PWV and MRE provide different mechanical measures, which is confirmed by only moderate correlation between stiffness parameters retrieved with the two methods [162]. Future improvements of the method need to include faster acquisition (single-shot MRE), 3D data acquisition, and a more refined inversion algorithm. A preliminary application of aortic MRE in patients demonstrated high sensitivity of the method to hypertension [314], raising the prospect of future clinical applications of MRE for arterial wall stiffness measurement.

## 14

**MRE of the Brain**

MRE is unique among all testing methods that have been used to assess mechanical properties of brain tissue in that it is not restricted to the surface and that it can quantify viscoelastic parameters without opening the skull. Therefore, cerebral MRE can serve as the reference method for the measurement of *in vivo* shear modulus data of brain tissue [320]. Beyond the objective of providing a gold standard for numerical simulations or *ex vivo* methods, cerebral MRE has been developed to serve as a diagnostic imaging modality [321]. The use of MRE for neuroradiological examinations depends on a number of assumptions about the sensitivity of brain mechanical properties to disease, most of them still awaiting scientific confirmation. This illustrates the twofold challenges of brain MRE today: on the one hand, MRE has to evolve into a method which provides consistent and quantitative measures of cerebral shear moduli *in vivo* by accounting for individual and physiological variations. On the other hand, the clinical potential of measuring mechanical constants in the brain has to be investigated in a wide range of potential applications. Mechanical properties of the brain have never been used for diagnostic purposes, despite a few encouraging reports from clinical pilot studies in patients with tumors, hydrocephalus, multiple sclerosis (MS), or neurodegenerative diseases [3, 75, 110, 322]. Albeit promising, the reported diagnostic value of cerebral MRE has not yet reached its full potential and remains to be improved by further technical development of mechanical drivers, MRI sequences, and post-processing. Furthermore, basic studies are needed to elucidate the mechanical structures of brain tissue at multiple length scales and to understand the mechano-biological function of the living brain. Yet, cerebral MRE in the mouse has already revealed important insight into the mechanical response of the brain to a variety of physiological and pathological effects, including aging, inflammation, neuronal degeneration, and tumors [126, 128, 323, 324]. After more than a decade of development and research, MRE has opened a new window into the networks and interactions of brain tissue on a mechanical basis. This chapter is intended as an introduction to the basic concepts of cerebral MRE from a technical perspective as well as a summary of the current state of knowledge of brain MRE in humans and mice. Specific applications of cerebral MRE related to brain tumors are discussed in Chapter 17. Before reviewing selected experiments and findings, we will discuss some fundamental aspects and considerations of cerebral MRE.

## 14.1 General Aspects of Brain MRE

### 14.1.1 Objectives

The development of MRE of the human or murine brain is motivated by three aspects. First, any quantitative and reproducible imaging marker is highly valuable in clinical routine. MRE provides such parameters, which can be acquired in a fast and noninvasive way without administration of contrast agents. The mechanical characterization of brain tissue may contribute to the diagnosis of neuronal disorders related to changes in the mechanical support of neurons, altered vascularization, extracellular matrix (ECM) structures, or blood and cerebrospinal fluid (CSF) flow.

Second, cranial pressure is a highly relevant parameter for diseases associated with cerebral blood pressure and CSF flow obstruction. Neurosurgeons would benefit from an imaging technique capable of measuring cranial pressure noninvasively.

Third, the academic interest in structure-functional mechanisms of the brain including biophysical interactions at multiple scales is closely related to mechanical parameters. Scientists studying the brain want to understand the mechanisms of brain function and disease development in cerebral tissue. MRE adds new and unique information to this puzzle.

### 14.1.2 Determinants of Brain Stiffness

The contributors to brain stiffness remain to be identified and the search for them is still an active field of research. At any rate, multiple structures simultaneously contribute to the gross mechanical properties of the brain. Therefore, different dynamic regimes in MRE possess different sensitivities to different structures and processes. On the basis of the publications discussed later in more detail, there is growing evidence that the following effects are relevant for brain mechanical parameters:

- cell density and neuronal network density
- myelination of neurons
- inflammatory processes
- ECM structures
- vascular density
- blood and arterial pulse wave pressure
- functional activation.

### 14.1.3 Challenges for Cerebral MRE

Many challenges in brain MRE also apply to other organs; however, the combination of the following points makes cerebral MRE particularly demanding:

- high degree of mechanical shielding of the tissue
- high tissue heterogeneity/prevalent fluid–solid interfaces
- anisotropy of elastic parameters
- pulsation
- reflecting boundaries with subject dependent geometry

- high vascular density/fluid fraction
- high mechanical attenuation/shear modulus dispersion.

However, despite these challenges, some issues that are encountered in MRE of other organs do not apply to the brain, thus rendering cerebral MRE simpler than, for example, cardiac MRE (see Chapter 13). Three properties facilitate application of MRE to the brain:

- The brain is a volume organ in which normally more than one shear wavelength can be captured, permitting quantitative measurements of viscoelastic parameters.
- The brain does not move to the same extent as the heart, and breathing has so far not yet been reported as a confounding variable in brain MRE.
- Anisotropy and time variation of brain mechanical constants is not as pronounced as in the heart.

As a result of these challenges and advantages, most current methods are built on the following compromises:

- Property estimates based on viscoelastic models normally require spatial averaging over larger tissue volumes, thus diminishing spatial resolution.
- Higher spatial resolution based on multifrequency wave data is currently obtained only by ignoring or oversimplifying the dispersion relation of the shear modulus.
- Poroelastic effects are very subtle compared to shear waves and easily biased by physiological effects such as cardiac pulsation. Proper validation of poroelastic property estimates would require acquisition of the full 3D wave field using cardiac triggering or gating; however, the acquisition time for that would become prohibitively long.
- Reconstruction of anisotropic elastic parameters requires long scan times, including time-consuming techniques such as diffusion tensor imaging (DTI).

Brain MRE therefore ideally includes acquisition of the full 3D vector displacement field and multiple vibration frequencies to account for viscosity or to enable high-resolution MRE based on multifrequency inversion (see Section 10.5). In addition, complementary information, such as fiber tract directions derived from DTI, can be utilized for specialized inversion strategies including anisotropic inversion (Section 10.8) or waveguide elastography (Section 10.9).

## 14.2 Technical Aspects of Brain MRE

### 14.2.1 Clinical Setup for Cerebral MRE

Common MRE systems are detailed in Section 6.1; most of the systems discussed in that chapter have also been used for brain MRE. Because the ovoid geometry of human heads, geometry-induced field distortions are less prevalent in cerebral MRI than in other organs, making single-shot EPI-MRE favorable because of its acquisition speed. EPI-based MRE of the brain was the imaging method of choice in recent clinical studies [75, 108, 111]. Newer sequences include single-shot spin-echo EPI with retrospective slice reordering for a minimized acquisition time [69], spiral readout-based multislabs, multishot acquisition for whole-brain MRE [22, 325], and SLIM-MRE for optimized

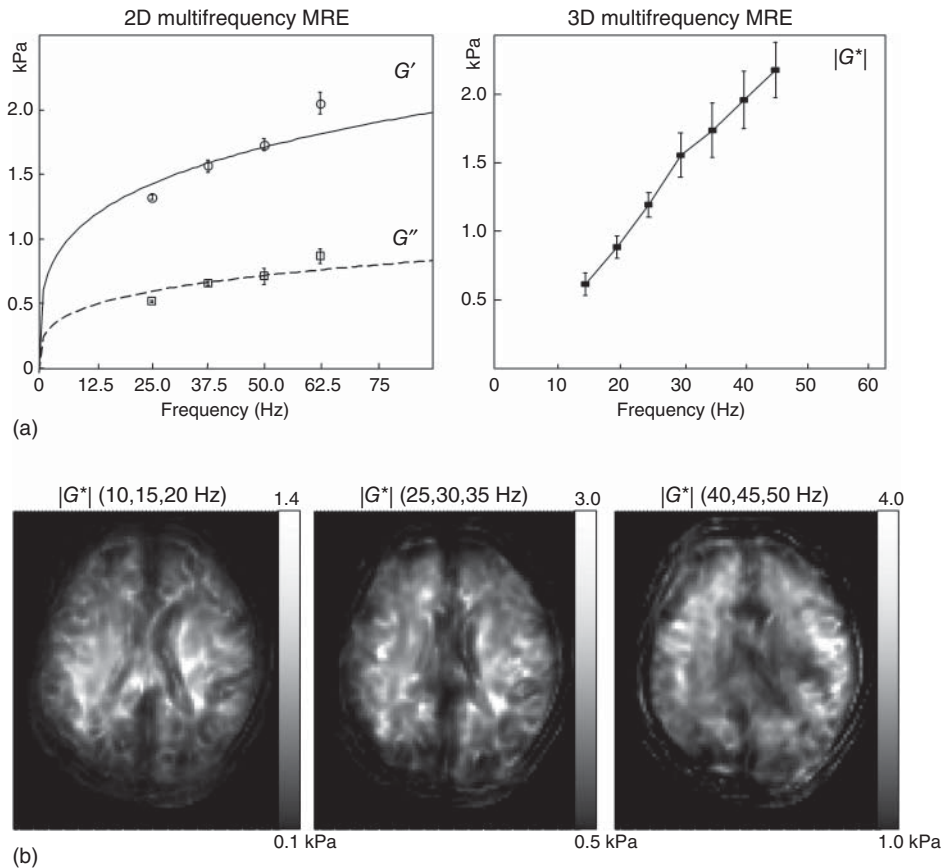
3D wave field acquisition in the brain [229]. These methods allow acquisition of multislice and multicomponent and multifrequency data in a short time (Chapter 11). For example, the method of Dittmann et al. [69] acquires a full 3D set of wave field data at three frequencies, 15 slices of  $2 \times 2 \times 4 \text{ mm}^3$  isotropic voxel size and eight time steps in approximately 3 min. Such short protocols can easily be integrated into clinical neuroradiological MRI examinations. Remaining challenges relate to motion artifacts and field distortions (“warping”). Fluctuations of motion phases across slices in 2D image acquisition are particularly relevant for all postprocessing methods involving derivative operators in the through-plane direction [176]. Such fluctuations arise from stochastic motion or pulsation, which are encoded in the motion phase of the wave signal. Furthermore, head motion including pulsation blurs spatial resolution in elastograms, which has to be accounted for in order for brain MRE to become a high-resolution modality. Field distortions at tissue-air interfaces cause geometric distortions of the object and impair estimates of wavelengths and elastic properties. However, such deteriorations mainly appear in images acquired by single-shot EPI sequences; and correction methods exist [326]. Finally, cardiac-gated multifrequency MRE acquisition using external wave stimulation relevant for poroelastic inversion has not yet been achieved in 3D.

In order to generate shear waves in the brain, MRE technology offers many solutions including bite bars, pneumatic pillows, head cradles, remote drivers based on a thorax mat, and compressed-air drivers. As a consequence of the high viscosity of brain tissue, shear wave amplitudes are more strongly attenuated at higher frequencies, motivating the use of low drive frequencies of  $< 60 \text{ Hz}$ . Figure 14.1a demonstrates two dispersion functions of the complex shear modulus,  $G^*$ , of *in vivo* brain tissue. Inducing frequencies in the 50–60 Hz range requires wave sources near the field of view, whereas lower frequencies of  $< 40 \text{ Hz}$  can also be produced farther away from the head, which greatly improves the clinical applicability of cerebral MRE [327]. Another aspect is hardware flexibility. A rigid head cradle, as proposed in [328, 329], requires adaptation of the setup to specific scanner hardware including RF coils and patient table for mounting the actuator on the table. This can be cumbersome when MRE hardware needs to be used on different scanner types. On the positive side, the head cradle does not require adaptation to body shape and surface and induces waves in a direct way without significant attenuation from the wave source to the actuator. Therefore, most studies in brain MRE were conducted using this type of actuator. By contrast, bite bar actuators need an individually molded polymer mouthguard, which is difficult to implement clinically [330], thus limiting this approach to fundamental studies with few subjects. Ideally, drivers for cerebral MRE should produce high amplitude shear waves inside the cranial cavity using a remote source and be adaptable to the individual’s physique and the MRI hardware used.

#### 14.2.2 Choice of Vibration Frequency

The requirement to induce intracranial shear waves in a gentle way seems to be fulfilled best by remote wave stimulation at low frequencies [327]. A recent analysis of viscoelasticity estimates by brain MRE obtained in a wide range of frequencies demonstrated that low-frequency elastograms can have the same resolution of anatomical detail as high-frequency elastograms [69]. Figure 14.1b shows elastograms from the literature





**Figure 14.1** Multifrequency MRE of the brain for recovery of shear modulus dispersion. (a) 2D MRE from 25 to 62.5 Hz vibration frequency and 3D MRE from 10 to 50 Hz vibration frequency reconstructed for magnitude shear modulus  $|G^*|$  by sliding window three-frequency MDEV inversion (Left-hand side: Sack 2009 [331]. Reproduced with permission of Wiley. Right-hand side: Based on data published in [69]. Reproduced with permission of Wiley.) Fit lines of storage and loss modulus data,  $G'$  and  $G''$ , represent springpot model dispersion. (b) Elastograms of  $|G^*|$  obtained by three-frequency MDEV inversion in three different frequency ranges. (Dittmann 2015 [69]. Reproduced with permission of Wiley.)

obtained with the use of different vibration frequencies, illustrating that brain MRE is feasible in a wide range of vibration frequencies from 10 to 60 Hz. However, patient comfort and detail resolution are not the only parameters that determine the best choice of frequencies in cerebral MRE. The sensitivity of mechanical constants to disease can vary with drive frequency. In view of the hierarchy and complexity of brain tissue networks, an optimal range of frequencies may exist for specific diseases. Würfel et al. [73] reported 2D multifrequency MRE in patients with MS to be more sensitive at 25 Hz compared to 37.5, 50, and 60 Hz. More data are needed here, especially in the range below 20 Hz, which is entirely unexplored in patients. Solid–fluid interactions are expected to be relevant in the lower frequency range, making low-frequency

**Table 14.1** Shear modulus values of brain tissue from the literature.

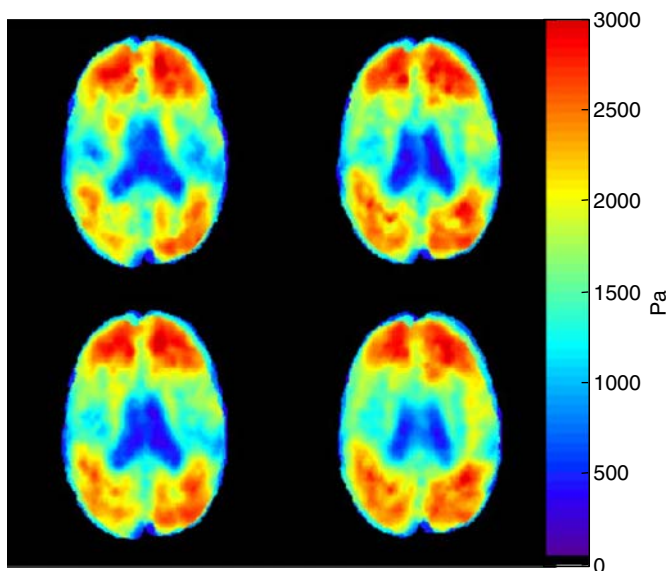
Frequency range (Hz)	Study	$G'$ (kPa)	$G''$ (kPa)	$G^*$ (kPa)	$\varphi$ (rad)	References
Static (micro indentation)	<i>Ex vivo</i> murine spinal cord (GM/WM)	0.13/0.07				[332]
Static (macro indentation)	<i>Ex vivo</i> porcine Bovine (GM/WM)	0.40/0.60 0.46/0.68				[333] [334]
20–30 Hz (shear test)	<i>Ex vivo</i> lamb (GM/WM)	0.29/0.4–0.62				[335]
1 Hz (arterial pulsation)	<i>In vivo</i> human	2.3				[336]
0.1	<i>Ex vivo</i> porcine	0.39	0.08	0.4	0.19	[131]
1.0		0.47	0.09	0.47	0.20	
10.0		0.65	0.19	0.68	0.28	
10–20	<i>In vivo</i> human	0.57	0.24	0.62	0.39	[69]
25–35		1.53	0.31	1.56	0.20	
40–50		2.12	0.52	2.18	0.24	
30	<i>In vivo</i> human	0.69	0.59	0.90	0.71	[337]
25	<i>In vivo</i> human	1.50	0.70	1.66	0.44	[78]
37.5		1.82	0.84	2.00	0.43	
50		1.94	0.98	2.17	0.47	
62.5		2.38	1.20	2.67	0.47	
50	<i>In vivo</i> human (GM/WM)	1.8/2.4	0.7/1.2	1.9/2.7	0.37/0.46	[325]
45	<i>In vivo</i> human (GM/WM)	2.8/3.7	0.8/1.3	2.9/3.9	0.28/0.34	[338]
60		3.1/3.3	1.7/2.0	3.5/3.9	0.50/0.54	
80		4.4/4.7	2.3/2.4	5.0/5.3	0.48/0.47	
90	<i>In vivo</i> human (GM/WM)	3.1/2.7	2.5/2.5	4.0/3.7	0.68/0.75	[339]

Only reports of complex shear modulus (either given as  $G'$  and  $G''$  or  $|G^*|$  and  $\varphi$ ) are listed, while wave speed values or reports on “shear stiffness” were not considered in this table. Static tests measuring Young’s modulus (scaled to  $G'$  by the factor 1/3) are presented for comparison purposes. Two values separated by a slash refer to gray matter (GM)/white matter (WM).

MRE potentially more sensitive to fluid-related diseases such as hydrocephalus than high-frequency MRE [78]. As seen in Figure 14.1, the pronounced shear modulus dispersion of *in vivo* brain tissue yields low values at frequencies between 10 and 20 Hz. In this frequency range,  $|G^*|$  values on the order of 0.6 kPa are measured. Table 14.1 lists published shear modulus values obtained at different vibration frequencies. Despite some variation, there seems to be agreement that brain matter is soft (between 1 and 3 kPa) at 50 Hz and very soft ( $\approx 0.5$  kPa) toward low frequency or quasi-static stimulation.

### 14.2.3 Driver-Free Cerebral MRE

Head stimulation and setup of driver hardware can be avoided by exploitation of endogenous brain motion. The brain is a pulsating organ with deflection amplitudes on the order of millimeters. The arterial pulse wave passes through the branched arterial system from the circle of Willis to parenchymal arteries. Arterial pulsation produces a propagating shear deformation of the vessel walls in the vascular tree. The speed of this effective-medium shear wave is determined by a number of parameters including the compression modulus of the fluid, the shear modulus of the vessel walls and the compliance of the embedding matrix. Elastographic parameter reconstruction based on the 1 Hz component of this pulse wave-driven shear wave was demonstrated by Weaver and colleagues [336]. Intriguingly, pulse wave-based shear modulus maps have similar detail resolution as the maps generated with most current inversion methods based on exogenous stimulation (see Figure 14.2). The mean shear modulus obtained by intrinsic MRE is in the order of 2.3 kPa and thus higher than the values obtained by external stimulation at low frequencies (see Table 14.1). However, the mechanism of shear wave generation differs considerably between both methods, and overlapping results are not expected. It would be interesting to see if this promising technique is sensitive to physiological conditions such as blood pressure, CO<sub>2</sub> saturation, and functional activation or diseases such as atherosclerosis or vascular dementia. A drawback of intrinsic methods is their higher susceptibility to physiological variations such as irregular heart rate and the need for cardiac gating. Retrospective gating discards and re-acquires nonmatching data, which results in longer acquisition times (on the order of 30 min [336] instead of 3 min as mentioned above). An alternative method of driver-free cerebral MRE exploits

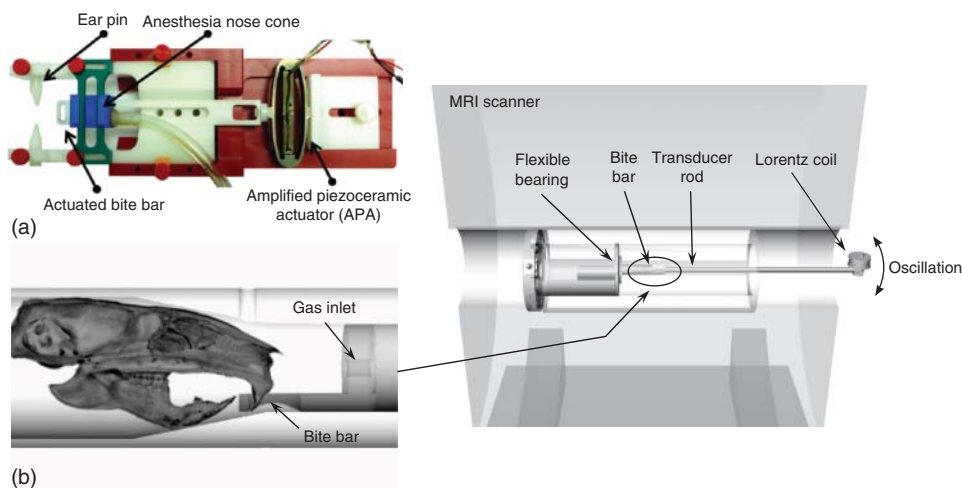


**Figure 14.2** Elastograms obtained by intrinsically activated MRE displaying the shear modulus corresponding to 1 Hz harmonic motion [336]. (Reproduced with kind permission of John Weaver and Keith Paulsen from Dartmouth College, USA.)

vibrations produced in the scanner by strong gradients. This approach demonstrates the sensitivity of MRE to low-frequency vibrations. Indeed, vibrations produced by an external driver at low frequencies, such as 25 Hz, are often reported by patients as less noticeable than the vibrations induced by the gradient system. For this reason, applying strong gradients with some time delay before motion encoding for stimulating waves is a feasible technique of cerebral MRE [340]. The main limitation here is the actual effort of vendors to avoid these vibrations. Patient tables decoupled from the scanner preclude those experiments. Furthermore, this approach is limited to a single frequency – the resonance frequency of the table – and transient effects have to be considered.

#### 14.2.4 MRE in the Mouse Brain

Investigation of the viscoelastic response of the mouse brain in disease models is a viable way to infer the relationship between mechanical constants and pathological processes. A number of technical solutions exist for performing MRE on the mouse brain. Figure 14.3 shows two examples based on a Lorentz coil in the fringe field of the MRI scanner and a piezo element vibrating inside the magnet. Images are normally acquired by spin-echo sequences with motion-encoding gradients (MEGs) symmetrically placed around the spin echo pulse (see Figure 3.10) or gradient recalled echo (GRE) pulse sequences with a single train of MEG's (see Figure 3.11). High excitation frequencies (in the range of 1 kHz) are required to capture shear waves with sufficiently short wavelengths inside the small mouse brain. Motion encoding synchronized to high-excitation frequencies, as often used at high field strengths, allows the application of multiple MEG cycles, constituting an ideal scenario for SLIM-MRE (see Chapter 11) [228]. SLIM-MRE is capable of acquiring the same amount of data as sequentially scanning the three wave field components in one-third of the time, which is important in view of the fact that mouse MRE is slower than MRE of the human brain. Susceptibility artifacts are more



**Figure 14.3** Two types of actuators for mouse brain MRE based on a piezo driver ((a), Clayton 2011 [341]. Reproduced with permission of Institute of Physics.) and a Lorentz coil in the fringe field of the MRI scanner (b) as it was used in multiple studies [121–124].

**Table 14.2** Overview of mouse brain MRE and ultrasound elastography (USE) studies published in the literature.

Frequency (Hz)	Mouse strain	$G'$ (kPa)	$G''$ (kPa)	Region	References
Transient, SSWI <sup>a</sup>	Sprague Dawley rats	11.6–12.3 <sup>b</sup>		Central brain	[342]
		8.6–10.0 <sup>b</sup>		Hippocampus	
		7.8–21.4 <sup>b</sup>		Corpus callosum	
1200	C57/BL6	13.8		Central cortical gray matter	[117]
600–1800	BALB/cAnNHsd	1.8–7.9	1.5–2.5	Central brain	[341]
900	SJL	6.1	2.0	Central brain	[124]
1500	WT	25.0		Central brain	[128]
180	Sprague Dawley rats	8.4	7.1	Central brain	[130]
1000	C57BL/6	7.8 <sup>c</sup>	5.5 <sup>c</sup>	Corpus callosum	[324]
900	C57BL/6	4.6	1.4	Hippocampus	[122]
900	C57BL/6	6.9	1.8	Central brain	[123]
900	C57BL/6	4.8	1.4	Cerebrum	[121]
		3.9	1.2	Cerebellum	

<sup>a</sup>Ultrasound-based elastography by supersonic shear wave imaging.

<sup>b</sup>Values dependent on the position of the of ultrasound probe (a large difference as in the corpus callosum indicates high anisotropy).

<sup>c</sup>Estimated from the relation  $G^* = |G^*| \cdot \exp(i\alpha\pi/2)$ .

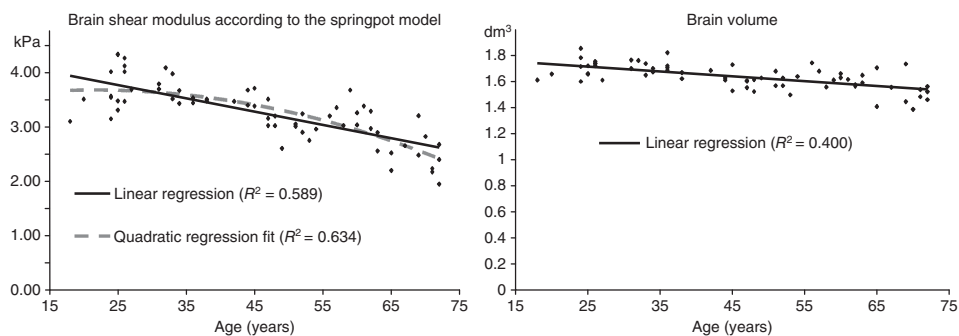
of a problem in the mouse brain than in cerebral MRE in humans due to the prevalence of tissue-air interfaces in the mouse head. Therefore, single-shot EPI-MRE has not yet been applied in the mouse, which considerably limits the amount of wave information accessible to preclinical MRE as compared to MRE in humans. The potential of MRE in the mouse is far from having been fully exploited with respect to detail resolution and consistency. Table 14.2 lists *in vivo* storage modulus values measured in the mouse brain.

### 14.3 Findings

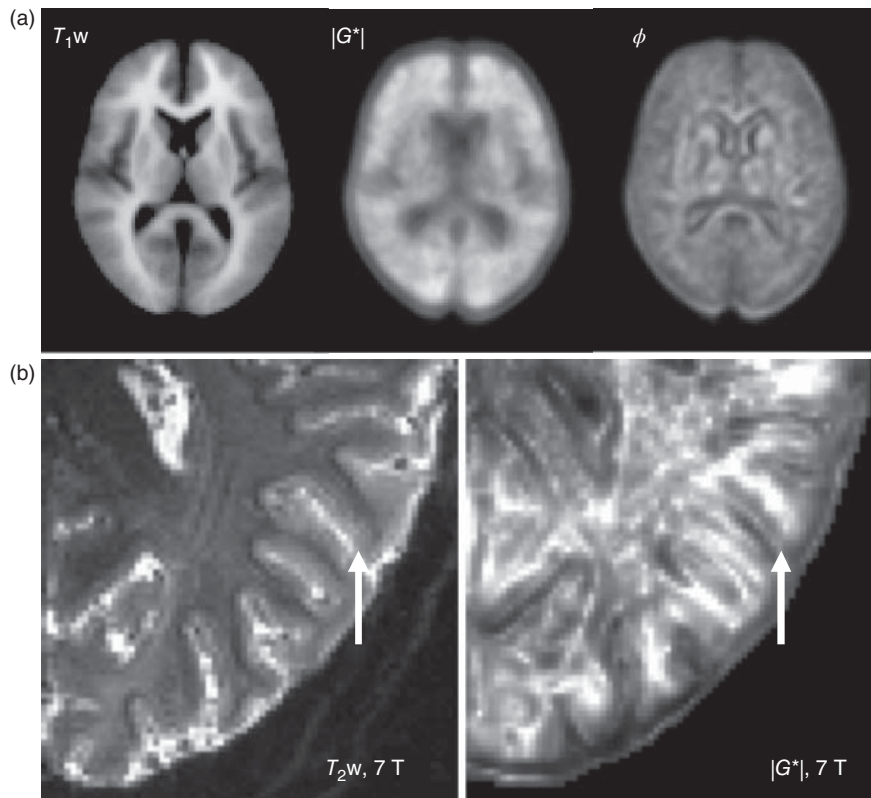
The results reviewed in Tables 14.1 and 14.2 illustrate the range of cerebral shear modulus values in healthy subjects and rodents. Note that there is a significant variation of values due to different excitation frequencies, imaging methods, and reconstruction approaches used. Nevertheless, similar to other more established mechanical testing methods, cerebral MRE is self-consistent (with less than 2% variation) within the same experimental protocol and postprocessing pipeline [343]. Significant variation in brain stiffness was observed among healthy subjects, which raises the question as to what degree the cerebral shear modulus is affected by physiological factors including age, sex, blood pressure, and hydration compared to the effect of diseases. In the following discussion, this question is addressed in the light of published evidence.

### 14.3.1 Brain Stiffness Changes with Age

A decrease in viscoelasticity of the adult brain over the lifespan was first reported in 2009 [331]. It was demonstrated by multifrequency MRE that the normal adult brain becomes considerably softer during aging at an annual rate of 0.7% at lower frequencies (25 Hz) and 0.4% at higher frequencies (50 Hz), which suggests that fluid compartments contribute to the age-related softening of brain tissue. Multifrequency data were combined into frequency-independent parameters  $\mu$  and  $\alpha$  using the springpot model (see Section 4.8 and the box on 82), which allowed separation of elastic effects from viscosity-related modulus dispersion. By this, an annual decay of shear elasticity ( $\mu$ ) of  $-15$  Pa was measured, while the slope of modulus dispersion as given by  $\alpha$  remained unchanged. The relative stability of  $\alpha$  was interpreted as an unchanged viscoelastic network topology – in contrast to the inherent network rigidity as quantified by  $\mu$ , which decreases with age. These initial findings were reproduced by 3D single-frequency MRE [70] and by the same 2D multifrequency MRE method correlated to volumetry [71]. Compared to MRE, brain volume was less affected by age with rates of change (full brain matter atrophy) of approximately 0.23% per year (see Figure 14.4). The highest rate of softening was observed in the frontal lobes [71] and in the temporal lobes [70]. Notably, these studies were performed in the adult brain (18–72 years [71], 56–89 years [70]), while children and adolescents are still unexplored. The linear regression model used in adults presumably requires extension toward a level of maximum elasticity in the juvenile age range. Such a maximum shear modulus during adolescence is suggested by the quadratic regression analysis in Figure 14.5, which suggests a plateau-like behavior in younger brains. In the mouse, only limited data exist on the influence of age on the viscoelasticity of neuronal tissue. All studies summarized in Table 14.2 reported age-pooled data and could not reveal significant softening of murine brain tissue as seen in humans. It has to be noted that most MRE experiments in small animals are conducted in a much higher frequency range than human studies. Static indenter tests in the rat brain (postmortem) showed an inverse age effect, meaning that stiffness increased from juvenile to adult rats [344]. In essence, brain MRE is sensitive to age effects in the human brain. This sensitivity needs to be accounted for in clinical studies by considering age as a confounding variable of brain stiffness.



**Figure 14.4** Brain shear modulus and brain volume in adults versus age. (Modified from [71] with permission.)



**Figure 14.5** High-resolution MRE based on multifrequency MRE from 30 to 60 Hz and MDEV inversion. (a) Group-averaged maps of magnitude shear modulus ( $|G^*|$ ) and shear modulus phase angle ( $\phi$ ) Guo [329]. (b) An MDEV-based elastogram ( $|G^*|$ ) together with a standard  $T_2$ -weighted image acquired at 7 T magnetic field strength. High signal intensities in  $|G^*|$  correspond to high stiffness. Scaling from 0 to 2 kPa. Image voxel size was  $1 \text{ mm}^3$ , allowing distinction of cortical gray matter from white matter based on their mechanical properties. (Braun 2014 [38]. Reproduced with permission of Elsevier.)

### 14.3.2 Male Brains Are Softer than Female Brains

Sexual dimorphism of brain architecture is known from MRI volumetry [345] and histological studies, which suggests differences in the number of neurons and glial cells [346, 347]. It is therefore not surprising that MRE revealed statistically significant differences in brain elasticity between men and women. Both 2D multifrequency MRE and 3D MRE were sensitive to gender differences, measuring lower stiffness in male brains compared to female brains [70, 331]. Arani et al. [70] reported female occipital and temporal lobes to be 230 and 90 Pa, respectively, stiffer than male ones of the same age, consistent with reports on springpot- $\mu$  of the central brain, which was about 180 Pa lower in men than in women [331]. The positive correlation between brain stiffness and volume does not imply a causal relationship. Instead, the observed gender-based disparity suggests that MRE measures intrinsic properties rather than geometry: since female brains are statistically smaller than male brains, their higher stiffness may relate to the higher neuronal

density found in many regions of the female brain [346, 347]. Yet, the effects of age or gender are weak relative to the variation in brain stiffness between individuals [328, 343]. It therefore remains an open question which contributors ultimately influence stiffness of *in vivo* brain tissue in healthy subjects. Gender and age appear to have a statistically significant but relatively weak effect compared to the variability between individuals.

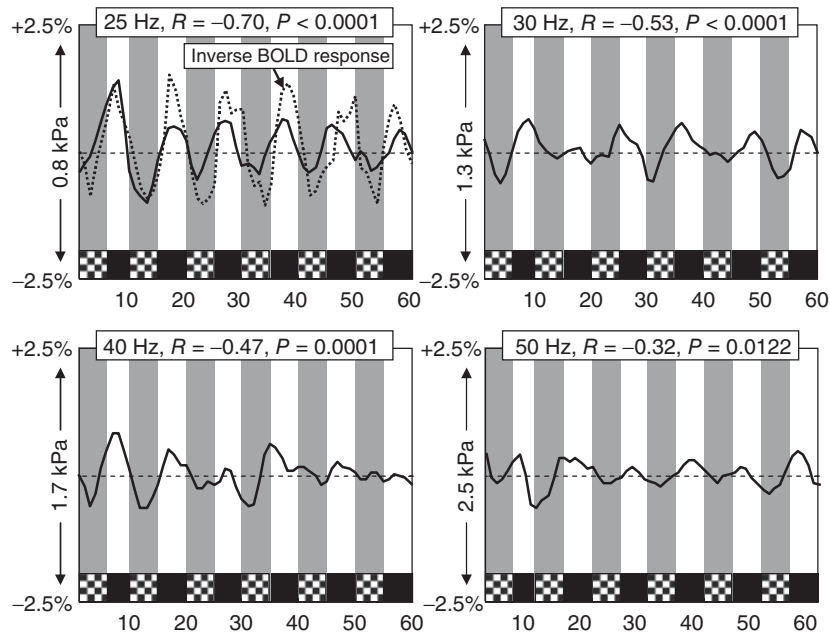
### 14.3.3 Regional Variation in Brain Stiffness

Much effort has been put into creating an atlas of brain mechanics, which, however, still has to be improved with respect to detail resolution and by cross-validation with different techniques of neuronal MRE. The most consistent mapping of  $|G^*|$  and  $\varphi$  derived from MDEV inversion (see Eqs. (10.52) and (10.55)) has been achieved by calculation of group averages after registering brain volumes. Exemplary maps are shown for illustration in Figure 14.5. In these maps, finer structures such as thalamus (TH), head of caudate nucleus (HCN), and genu of the corpus callosum (GCC) are delineable in order to tabulate group-averaged values for healthy adults. Corpus callosum (CC) and corona radiata (CR) were resolved by Johnson et al. [348], while [327] analyzed structures along the corticospinal tract (CST), namely capsula interna, crus cerebri, and pons. The reported values suggest a correlation of stiffness with the packing density of fibers, with both quantities exhibiting the highest values in corpus callosum and crus cerebri and lower values in regions, where fibers fan out (corona radiata) or cross (pons). Compared to the central cerebrum, the cerebellum appears to be softer [343, 349]. Using high-resolution MRI at 7 T with  $1 \times 1 \times 1 \text{ mm}^3$  resolution allowed delineation of cortical gray matter with a thickness of 3–6 pixels instead of 1–2 pixels as common in “normal” cerebral MRE of  $\approx 8 \text{ mm}^3$  voxel volume. Such high-resolution 7T MRE maps show cortical gray matter to be softer than white matter (Figure 14.6), consistent with [129, 160, 338, 348] (*in vivo* MRE) and [333–335] (*ex vivo* tests) but in conflict to [339] (*in vivo* MRE) and [332] (microindentation of the murine spinal cord).

### 14.3.4 Anisotropic Properties of Brain Tissue

To date, regional variations in viscoelastic constants in the brain were analyzed without consideration of anisotropic properties. The aforementioned correlation of stiffness with fiber density [327, 348] may point to direction-dependent (anisotropic) properties. Static tests on *ex vivo* white matter tissue samples measured anisotropic properties with a higher shear modulus when the shear was applied parallel to the direction of fibers, whereas no orientation dependence was detected for the shear moduli of gray matter samples [335]. Few data exist on *in vivo* anisotropic elastic constants in the human brain, and they have all been obtained using waveguide elastography (see Section 10.9) [72]. This method is capable of measuring the full orthotropic elastic tensor according to Eq. (4.34) with nine independent elastic constants, three of which representing shear moduli while the others are related to compression. In a waveguide, wave speeds (including the compression, i.e., longitudinal, wave speed) are related to the geometrical thickness of the vibrating rod, and thus represent effective properties of the material, which combine intrinsic properties and boundary conditions. Waveguide elastography presupposes that waves propagate along the nerve fibers, whose directions are deduced





**Figure 14.6** Preliminary functional MRE at four mechanical excitation frequencies. The global response of  $|G^*|$  to visual stimulation (averaged over five transverse slices) is shown for 60 experiments in which a checkerboard pattern was repeatedly (six times) shown during five consecutive MRE scans followed by five baseline scans without visual stimulation. In the 25 Hz response, the inverse BOLD effect (quantifying neuronal activity based on the oxygen level of the blood) is also included which was derived from the 3D fMRI data in the same subjects ( $N = 10$ ). In all cases, a decrease in  $|G^*|$  due to visual stimulation was observed. (Fehlner 2014 [358]. Reproduced with permission of ISMRM.)

by DTI-based tractography. Intriguingly, it was shown in five healthy volunteers that the full orthotropic elasticity tensor in the CST is redundant in seven elements (two in each of the diagonal, off-diagonal, and shear coefficients are equal plus the relationship  $C_{66} = \frac{1}{2}(C_{11} - C_{22})$  from transversely isotropic (TI) materials, see Eq. (4.37)), leaving five independent coefficients. As outlined in Section 4.6, such a material is characterized by a principal direction of the elasticity tensor along the fibers and a plane of isotropy perpendicular to them, hence the material is called TI. TI material models have been proposed for many fibrous soft tissue structures in the body. For example, skeletal muscles exhibit TI properties as validated *in vivo* by MRE, with a higher shear modulus parallel to the fibers than perpendicular to them [47, 48, 350, 351]. However, the ratio of shear stiffness in white matter seems to be the inverse of that found in muscle tissue: the CST displayed lower shear moduli parallel to the fibers ( $\mu_{13} = C_{44} = C_{55}$ ) than within the plane of isotropy ( $\mu_{12} = C_{66}$ ). While in lower leg muscles, the ratio  $\mu_{13}/\mu_{12}$  is on the order of 1.3 [47, 81], a ratio of 0.88 was measured in CST [72]. The same ratio in the corpus callosum and external capsula of the mouse brain measured by ultrasound-based elastography (SSWI) was even lower, on the order of 0.4–0.6 [342]. These results suggest that there is a principal difference between white matter tissue and “normal” TI materials (soft elastic matrix materials reinforced by stiffer fibers), which may relate to the fundamental structural differences between muscle fibers and nerve fibers. While

muscle architecture is essentially characterized by continuous parallel fibers, the myelin sheath of axons is highly organized in lipid bilayers oriented transversely to the main fiber direction, which – in addition to the presence of periodic discontinuities named *nodes of Ranvier* – could present a transverse rather than longitudinal mechanical element. Albeit not validated, this interpretation highlights the sensitivity of MRE to microstructures as a result of the scaling properties of the shear modulus (see the box on 124). Without further elucidation of the cause of this neuron-specific mechanical behavior, waveguide elastography was already performed in patients with amyotrophic lateral sclerosis (ALS) – a progressive neurodegenerative disease affecting the upper and lower motor neurons. Like other neurodegenerative diseases, ALS is difficult to detect based on imaging markers alone. ALS-related degradation of the cerebrospinal tract appears in DTI data as increased mean diffusivity and radial diffusivity. This suggests increased diffusion perpendicular to white matter fibers, which is indicative of disruption of myelin sheaths and modulation of extracellular spaces between myelin membranes [352]. Reduced shear moduli  $\mu_{13}$  and  $\mu_{12}$  were measured in patients with waveguide elastography, demonstrating that these pathoanatomical hallmarks of ALS can also affect the mechanical vibration characteristics of neuronal fiber bundles in the CST [353].

#### 14.3.5 The *in vivo* Brain Is Compressible

The basic concepts of compressibility of soft biological tissue are illustrated in Figure 5.1. For the sake of simplicity, we presume brain tissue to be a biphasic effective material consisting of a solid phase including interconnected cells and interstitial fluid and a liquid phase of blood and CSF, which can move independently of the solid phase. The unjacked scenario allows the fluid fraction to change volume, resulting in expansion and contraction of the entire brain. By contrast, the jacked scenario for incompressible constituents allows only a relative shift of particles with preservation of volume. This scenario results in slow and fast compression waves stimulated by external vibration according to Eq. (5.28). While the first scenario occurs in each physiological event that modulates the flow of fluids into or out of the brain (e.g., by arterial pulsation or the Valsalva maneuver), the second scenario applies to MRE, in which the fluid content is not affected by the waves. Both scenarios are characterized by their own specific effective-medium compression moduli, which – hypothetically – converge in the quasi-static limit. Unfortunately, very sparse data exist on the effective compression modulus of the brain. The lack of data can be explained by the challenge of applying *ex vivo* testing methods to perfused tissue. Moreover, compressibility as an intrinsic mechanical tissue property has not been in the workscope of scientists working on flow and perfusion quantification, leaving this field to the elastography community, which initially addressed compressibility using Poisson's ratio [354]. A very simple experiment to estimate the static (unjacked) compression modulus of the brain is the Valsalva maneuver combined with 3D MRI and image registration for calculation of volumetric strain:  $(V_{\text{Valsalva}} - V_{\text{normal}})/V_{\text{normal}}$ . Mousavi et al. measured this strain to be 3.1% in healthy volunteers [355]. Estimating the increase in intracranial pressure to be 775 Pa based on measurement of outblow pressure translates the measured volumetric strain into a compression modulus on the order of 26 kPa [355]. This very low value is not surprising in view of the fact that arterial pulsation causes an

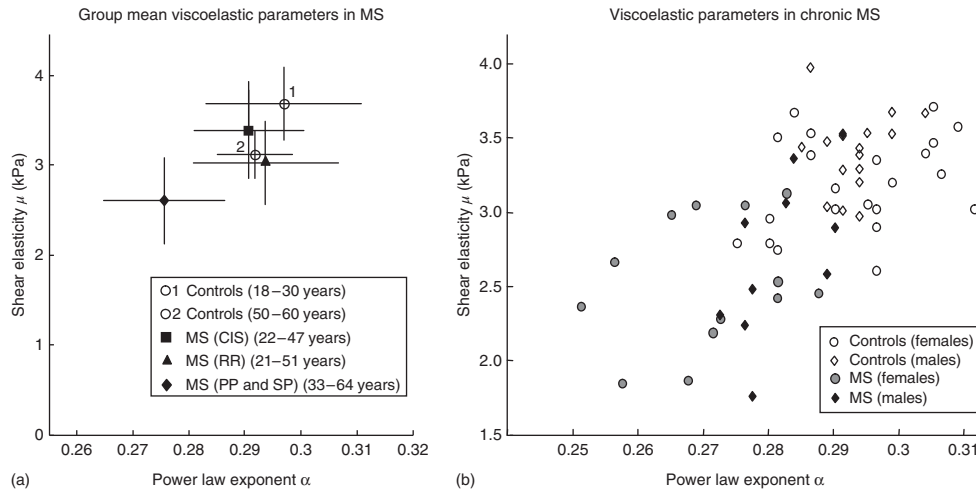
expansion of the brain on the order of a few millimeters. It seems as if our brains can be described by material properties of fluid-saturated sponges subjected to static or quasi-static compression. The situation changes when vibration stimuli are applied in MRE. Harmonic vibration in the acoustic frequency range of MRE is expected to induce motion in both fluid and solid phases, which, in a certain limit, can oscillate antiparallel to each other. The latter scenario gives rise to an effective compression modulus lower than that of the same material without independent motion but monophasic behavior. Using cardiac-triggered flow-encoding MRI, cerebral volumetric strain due to arterial pulsation was quantified with  $(2.8 \pm 1.9) \cdot 10^{-4}$ , which translates into an effective compression modulus on the order of several hundreds of kPa [176]. The large disparity of strain data between static and dynamic measurements illustrates the relevance of the considered frequency range in compression-sensitive MRE: while ultrasound in the regime of MHz barely encounters any biphasic properties of biological soft tissue, *in vivo* MRE with stimuli on the order of up to 50 Hz was demonstrated to be sensitive to volumetric strain in the brain [176], liver [356], and lung [85].

#### 14.3.6 Preliminary Findings of MRE with Functional Activation

The neuronal network transmits electrical signals within the brain and is central to brain function. However, its contribution to brain stiffness as a mechanical scaffold is still unknown. The mobility of fluids enables blood flow and ionic gradients, which are required to trigger neuronal activity, but it also attenuates tissue motion and influences the arterial, venous, and interstitial pressures within the cranium. It has been hypothesized that cerebrovascular flow and related mechanical tissue properties contribute to normal brain function and/or vice versa – brain function modulates cerebral hemodynamics, and concomitantly, brain tissue mechanics as measured by MRE [357]. A feasibility study of functional MRE (fMRE) is shown in Figure 14.6 [358]. During multifrequency MRE acquisition, a flickering (at 8 Hz) black–white checkerboard pattern was presented to healthy volunteers. Figure 14.6 presents an fMRE experiment in 2D for examining the time-resolved response of the cerebral shear modulus to visual stimulation. In a second experiment, using 3D fMRE, the spatial distribution of the effect was visualized and showed disseminated mechanical activation patterns. On the basis of the fast 2D fMRE experiments, Figure 14.6 demonstrates a negative correlation between shear modulus and stimulus (i.e., decrease in shear stiffness due to activation). Furthermore, frequency-resolved analysis revealed a decrease in the magnitude of the correlation coefficient ( $R$ ) with increasing drive frequency, suggesting the involvement of poroelastic effects since the fluid and vascular contributions to soft tissue viscoelastic properties are expected to be higher at lower vibration frequencies. While these first results indicate that a robust fMRE signal exists, more research is required on image-resolved mapping of mechanofunctional parameters including shear modulus and pressure-related parameters.

#### 14.3.7 Demyelination and Inflammation Reduce Brain Stiffness

MRI has improved early MS diagnosis by demonstrating spatiotemporal lesion dissemination. Notwithstanding this success, conventional MR parameters only moderately correlate with clinical disability – a phenomenon termed “clinico-radiological paradox”



**Figure 14.7** MRE in multiple sclerosis (MS). (a) The plot summarizes the MS-induced decrease in shear modulus,  $\mu$ , and power law exponent,  $\alpha$ , according to the springpot model. Three stages of MS are compared: the *clinically isolated syndrome* (CIS) is considered one of the earliest manifestations of MS, although the disease may remain silent in some cases; *remitting-relapsing* (RR) is a solid manifestation of MS, but still considered an early phase; *primary and secondary chronic progressive* disease (PP and SP) represent chronic phases of MS. Notably, reduction in  $\mu$  occurs at a very early time point of disease progression. (Fehlner 2015 [68]. Reproduced with permission of Wiley.) (b) Springpot constants  $\mu$  and  $\alpha$  for the detection of MS (PP&SP). The area under the receiver operator characteristics curve (AUROC) values for separating healthy volunteers from MS patients was 0.896 and 0.936 for  $\mu$  and  $\alpha$ , respectively. (Streitberger 2012 [74] used under CC BY 2.0 license.)

[359]. Therefore, the first clinical pilot study of cerebral MRE aimed at identifying new imaging markers for MS. Motivated by the scaling properties of the shear modulus, MRE was chosen to test the integrity of the multiscale neuronal network under the influence of demyelination and inflammation. Figure 14.7 summarizes MRE experiments in MS published in the literature [68]. Data of shear modulus  $\mu$  and power law exponent  $\alpha$  are based on the springpot model fitted to storage and loss moduli at several frequencies. The plot suggests that MS-related tissue degradation in the brain is associated with a decrease in both  $\mu$  and  $\alpha$ , indicating widespread degradation of tissue integrity beyond the few  $T_2$  lesions visible in conventional MR images [73]. In early MS, no alteration of  $\alpha$  was ascertainable in comparison to healthy volunteers, while there was a decrease<sup>1</sup> in  $\mu$  ( $\Delta\mu = -14.68\%$ ,  $\Delta\alpha = 0.29\%$  [74]). Conversely, chronic MS also had a significant effect on  $\alpha$  ( $\Delta\mu = -20.46\%$ ,  $\Delta\alpha = -6.07\%$  [74]). The areas under the receiver operator characteristics curve (AUROC) for separating healthy volunteers from patients with chronic MS were 0.896 and 0.936 for  $\mu$  and  $\alpha$ , respectively. Schregel et al. [324] demonstrated in a cuprizone mouse model of MS that the magnitude of the complex shear modulus decreases with both progressive demyelination and alterations in the structural integrity of the ECM. This work was confirmed by an MRE study in a model of experimental autoimmune encephalomyelitis (EAE), demonstrating a clear correlation between viscoelastic tissue alteration and the magnitude of perivascular T-cell infiltration [124].

<sup>1</sup> All values denoted by  $\Delta\mu$  and  $\Delta\alpha$  in this paragraph refer to the difference between normal and diseased, expressed in percent of the normal value.

A recent study in the mouse quantified macrophages and microglia in inflamed central nervous system tissue. This marker was linearly correlated with the magnitude of reduction in the storage modulus in the cerebellum ( $R = 0.9191$ ,  $P = 0.0096$ ) [121]. Of note, the EAE-related decrease in brain stiffness was not correlated with demyelination, but sensitive to early inflammatory processes in the brain.

#### 14.3.8 Neurodegeneration Reduces Brain Stiffness

Neurodegenerative disorders are characterized by a progressive loss of neurons and oligodendrocytes, which results in gross atrophy of affected brain regions. Atrophy can be quantified by volumetric MRI. However, in preclinical and early stages of neurodegenerative disorders, patterns of brain atrophy are subtle and difficult to detect by conventional MRI. It was hypothesized that the intrinsic mechanical properties of the brain are highly responsive to atrophy since reduced neuronal connectivity and lost neurons dilute the viscoelastic matrix of the brain, causing an overall reduction in brain stiffness. A mouse study in a model of Alzheimer's disease (AD) reported a disease-related decrease in brain stiffness [128]. This finding was reproduced by preliminary studies in seven patients with AD [76] and five patients with frontotemporal dementia [360]. Patients with idiopathic Parkinson's disease (PD) and progressive supranuclear palsy (PSP) were examined by MRE for differential diagnosis and assessment of the potential to rule out symptomatic Parkinsonism based on MRE [75]. Both neurodegenerative disorders have overlapping clinical symptoms but different neuropathology: PD is a rather slowly progressive neurodegenerative disease that affects focal regions including substantia nigra, locus coeruleus, and raphe nuclei. PSP, on the other hand, progresses rapidly by causing marked atrophy of the midbrain, superior cerebellar peduncle, and cerebellar dentate nucleus. The results show that cerebral viscoelasticity in PSP and PD is affected by the underlying neurodegeneration in different ways; whereas in PSP, a disseminated reduction of elasticity and viscosity was detected, a similar effect in PD attained significance only within the lentiform nucleus. In these groups, the impact of neurodegeneration on cerebral viscoelastic properties was also revealed by a significant negative correlation between clinical markers (disease severity in PD quantified by motor part of the UPDRS<sup>2</sup> during ON<sup>3</sup>; disease stage in PSP, staging system according to Golbe scale) and viscoelasticity parameters ( $|G^*|$  of the lentiform nucleus in PD, full brain  $|G^*|$  in PSP). Altogether, MRE in neurodegenerative diseases consistently revealed softening of brain matter, which confirms the initial hypothesis of reduced neuronal connectivity and loss of structural elements within the neuronal network. Since this viscoelastic network degradation was detected in different neurodegenerative and neuroinflammatory diseases, this mechanical signature appears to be a general response of affected brain tissue also in disorders that are not considered neurodegenerative diseases, such as normal pressure hydrocephalus (NPH). NPH is associated with CSF flow obstruction causing ventricular enlargement and severe clinical symptoms including gait disorder, dementia, and urinary incontinence, while CSF pressure measurements remain in the normal range. The occurrence of transient intracranial pressure peaks is discussed as a possible cause of symptoms. Consistent with previous studies in

<sup>2</sup> Unified Parkinson's disease rating scale.

<sup>3</sup> ON = phase with good response to medication.

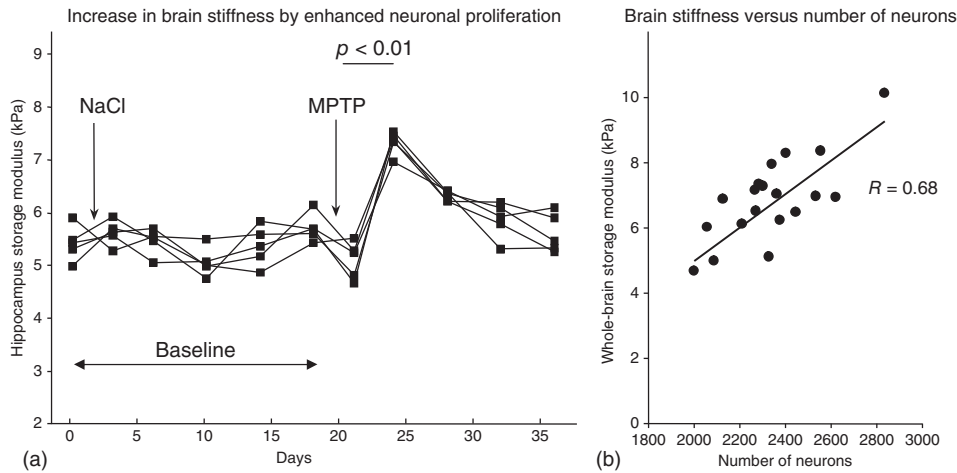
patients, MRE in NPH also demonstrated marked softening of brain tissue (decrease in springpot-related shear modulus  $\mu$ ) particularly within the periventricular regions [78]. In contrast to other diseases discussed above, NPH can be treated effectively by surgical implantation of a shunt to relieve obstructed CSF flow. Freimann et al. performed two MRE scans in the same group of patients, one pre-shunt and a second scan 3 months after the treatment [77]. The measured  $\mu$  parameter remained symptomatically low, while the power law exponent  $\alpha$  re-increased after shunting, suggesting reordering of viscoelastic structures without changes in inherent rigidity of structural elements [3, 77].

#### 14.3.9 The Number of Neurons Correlates with Brain Stiffness

After having reviewed these encouraging pilot studies of cerebral MRE in patients, it remains open whether the neuronal network itself is a mechanical supporter of brain matter. Lu et al. investigated the mechanical properties of single cells and measured a higher stiffness in neurons than in glial cells, which further supports the hypothesis that neurons establish the mechanical scaffold of the brain [361]. Evidence for this hypothesis was provided by two complementary MRE studies in mouse models. In one experiment, the number of neurons was reduced within one hemisphere of the mouse brain by middle cerebral arterial occlusion (MCAO) [123]. Neurons were counted histologically in both affected and contralateral hemispheres. The second experiment employed a mouse model of Parkinsonism based on the administration of 1-methyl-4-phenyl-1,2,3,6-tetrahydropyridine hydrochloride (MPTP), which induces dopaminergic neurodegeneration and enhances adult neurogenesis in the hippocampus [122]. Figure 14.8 presents results of both studies, demonstrating that elasticity increases in brain regions following enhanced proliferation of neurons. The plot on the right-hand side of Figure 14.8 complements this finding by demonstrating the correlation between number of neurons and whole-brain elasticity.

#### 14.3.10 Preliminary Conclusions on MRE of the Brain

The studies discussed here support the hypothesis of the neuronal network being a major contributor to the gross mechanical properties of the whole brain. We have seen that physiological aging or male gender as well as pathological processes such as neurodegeneration, inflammation, demyelination, and neuronal loss by ischemic infarction can cause reduction in brain stiffness. Conversely, one study, MRE in the MPTP mouse model, demonstrates the “positive” effect of enhanced neuronal proliferation on brain stiffness, suggesting a correlation between brain stiffness and neuronal network integrity and/or density. However, such a correlation does not imply a causal relationship. The simplified model of the neuronal network as the major viscoelastic lattice in the brain becomes more complicated when accounting for vascular contributions, pressure, and anisotropy. For example, an increased blood pressure as occurring with aging may lead to a higher proportion of fluid compartments in brain tissue, which in turn could reduce stiffness as, for example, observed with aging. An increase in brain perfusion may also explain the decrease in brain stiffness upon functional activation, as demonstrated in Figure 14.6. The influence of CSF, interstitial fluids, and blood perfusion may increase toward lower excitation frequencies. It is therefore important to account for the range of vibration frequencies used for MRE when analyzing brain mechanical properties. In



**Figure 14.8** Correlation between storage modulus  $\mu$  and number of neurons in the murine brain. (a) Time courses of the storage modulus in the hippocampus region in a Parkinson mouse model. MPTP (1-methyl-4-phenyl-1,2,3,6-tetrahydropyridine) was administered on day 20, causing a transient increase in neuronal proliferation. The significant increase in storage modulus on day 6 after injection followed by a decay to baseline values is correlated with the number of new neurons. (Based on data published in [122].) (b) Inversely to (a), a decrease in the number of neurons by middle cerebral artery occlusion (MCAO) correlates with a decline of the storage modulus in the mouse brain. (Based on data published in [123].)

tumors, the mechanical signatures of cell accumulation, ECM modulation, angiogenesis, necrosis, and tissue pressure overlap. This prevents a straightforward interpretation of viscoelastic constants in terms of tissue structure. We therefore discuss MRE in brain tumors to an extra chapter, which is dedicated to the viscoelastic properties of tumors in general (see Chapter 17). Altogether, MRE has the potential to become a new imaging biomarker for many neurological diseases as well as for fundamental research on the biophysical interactions in living brain tissue. In view of the latest developments in high-resolution mapping of viscoelastic and poroelastic properties, cerebral MRE can be expected to significantly contribute to both basic research and diagnostic neuroimaging in the future.

## 15

### MRE of Abdomen, Pelvis, and Intervertebral Disc

The abdominal cavity contains the digestive organs, including the stomach, small and large intestines, liver, gallbladder, spleen, and pancreas (Figure 15.1). The neighboring pelvic region hosts constituent parts of the female and male reproductive organs such as uterus and prostate. Many of these organs are prone to diseases, which are often associated with structural changes of the affected tissues. The lack of noninvasive biomarkers for the detection and staging of structural tissue changes motivates the ongoing search for a quantitative, biophysics-based imaging method such as MRE. In this chapter, current applications of MRE in abdominal and pelvic organs will be presented. We will start with the liver, since this organ covers major applications of MRE today, and then review MRE of the spleen, pancreas, kidneys, uterus, prostate, and intervertebral disc (IVD). Since the number of studies in the area of abdominal MRE is too large for a compact review within the scope of this textbook, we will present a selection of fundamental work. For further reading, we refer the reader to review articles on MRE of the abdomen [362] and the liver [363–367].

#### 15.1 Liver

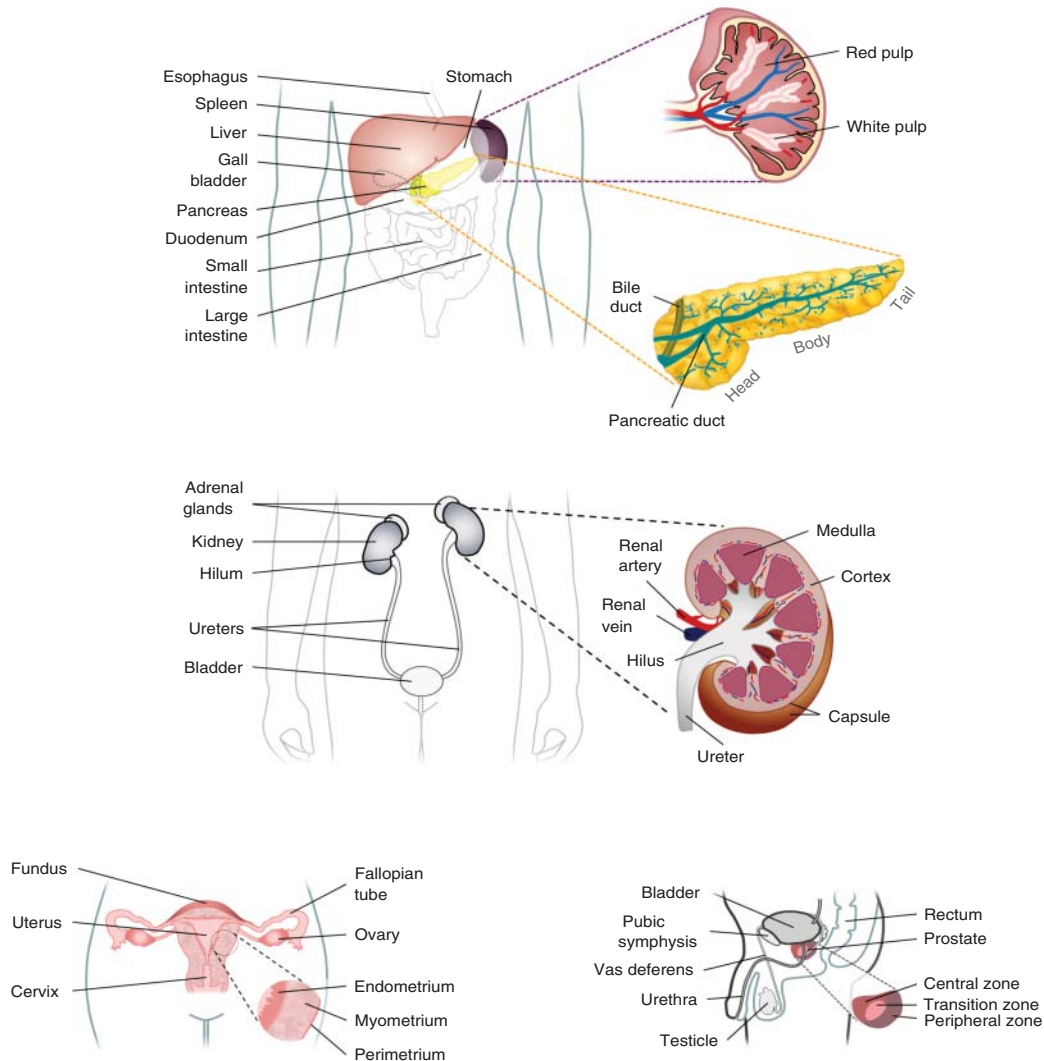
*This chapter was coauthored by Christian Hudert from the Clinic for Pediatric Endocrinology and Diabetology, Charité – Universitätsmedizin Berlin, Germany*

The liver is the largest parenchymatous organ in the body and part of the digestive system, accounting for roughly 3% of total body weight in adults. It consists of two main lobes, the larger right lobe and the smaller left lobe, both of which are further subdivided into segments. The two main lobes are separated by a band of tissue (falciform ligament or broad ligament), and a layer of connective tissue (Glisson's capsule) covers the entire liver. The liver is unique in that its blood supply is provided by two large vessels. One is the hepatic artery supplying oxygen-rich blood from the heart ( $\approx 25\%$  of the liver's total blood supply). The second is the portal vein carrying nutrient-rich blood from the digestive system to the liver ( $\approx 75\%$  of its total supply). These vessels branch into smaller vessels and finally into capillaries that end in thousands of lobules (see Figure 15.2). Liver lobules are the basic anatomical units of the liver and are mainly composed of hepatocytes. Hepatocytes monitor, add, and remove substances from blood and produce bile (see Figure 15.3). Sinusoids (see also Section 15.1.2.1) then drain into the central vein, and blood is removed from the liver through three main hepatic veins (right, middle,

*Magnetic Resonance Elastography: Physical Background and Medical Applications*, First Edition.  
Sebastian Hirsch, Jürgen Braun, and Ingolf Sack.

© 2017 Wiley-VCH Verlag GmbH & Co. KGaA. Published 2017 by Wiley-VCH Verlag GmbH & Co. KGaA.



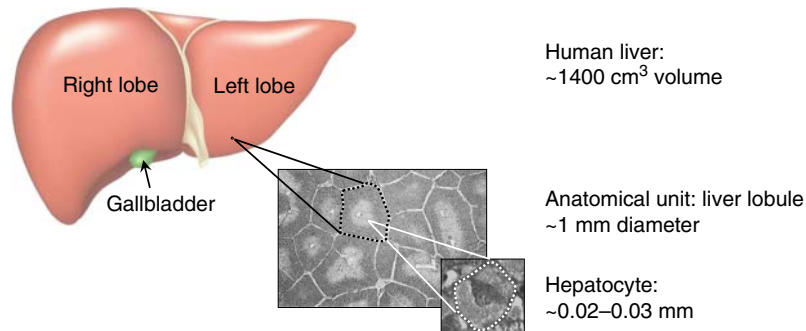


**Figure 15.1** Overview of abdominal organs, most of which have been studied using MRE. Organ-specific discussion will be presented in the following sections.

and left hepatic veins). Bile is gathered in bile ducts merging into common hepatic ducts before storage in the gallbladder or further transport to the small intestine.

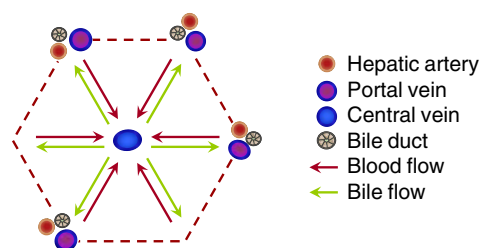
The liver performs a wide range of functions in human physiology comprising:

- Filtration and detoxification of blood to prevent accumulation of harmful substances coming from within (e.g., hormones) or outside (e.g., alcohol or other drugs) the body.
- Metabolism of proteins and carbohydrates, which are stored in the form of glycogen in the liver and released into the blood to maintain a normal blood sugar level.
- Production and secretion of bile in the small intestine, essential for absorbing lipids, cholesterol, and fat-soluble vitamins.



**Figure 15.2** Morphology of the liver and architecture of liver tissue with liver lobules as basic anatomical units and hepatocytes as the main constituents of liver parenchyma.

**Figure 15.3** Schematic cross-sectional view of a liver lobule illustrating blood and bile flow. The hepatic artery, portal vein, and bile duct are arranged in a distinctive pattern known as the portal triad or portal field at the center of liver lobules.



- Absorption and enzymatic processing of indirect bilirubin, which is formed from hemoglobin during red blood cell depletion, and is converted into water-soluble direct bilirubin by the liver.
- Production of plasma proteins, for example, albumin and nearly all blood-clotting factors.
- Storage of vitamins (A, D, E, K, and B12), minerals, and iron for the synthesis of new red blood cells.

In the industrialized world, chronic liver diseases (CLD) are a major cause of morbidity and mortality, and their prevalence is still increasing. The main contributors to the pathogenesis of CLD are nutritive-toxic conditions (alcohol abuse, obesity, and metabolic syndrome) and viral hepatitis. Pathophysiologically, CLD is heralded by progressive fibrosis, ultimately leading to cirrhotic transformation of the liver. A peculiarity of CLD is their often silent progression without serious, specific clinical symptoms until they reach a threshold stage characterized by the sudden and eventually often life-threatening onset of severe liver failure. The main reason why the diagnosis of liver disease is often delayed is the liver's unique capability to partially counterbalance functional deficits in localized steatotic, fibrotic, or cirrhotic regions by elevating the functional performance of still intact regions of the liver parenchyma. Against this background, better diagnostic tools for early diagnosis of ongoing liver disease are urgently needed in order to initiate treatment before the disease has reached an irreversible stage.

At present, monitoring of the disease course in patients with CLD is hampered by the unavailability of screening methods that can reliably quantify silent structural changes of liver tissue before morphological changes start to become apparent. Elastography – intrinsically sensitive to tissue structures across many length

scales – has become an important clinical marker of advanced hepatic fibrosis. Current technological improvements in the area of liver elastography aim at the detection of early fibrosis. This endeavor is challenged by the intrinsic variability of histology-based staging of hepatic fibrosis – the current gold standard for elastography. In fact, hepatic fibrosis is a heterogeneous and highly dynamic process, which is still incompletely understood. The next section will briefly review the epidemiology and basic physiological aspects of CLD.

### 15.1.1 Epidemiology of Chronic Liver Diseases

CLD usually have an insidious course and rarely cause any obvious signs or symptoms until they are fairly advanced and the liver is considerably damaged. Irrespective of etiology, chronic liver disease leads to liver fibrosis. Long-term consequences of progressive hepatic fibrosis are cirrhosis and increased risk for primary liver cancer, estimated to be responsible for around 170 000 and 47 000 deaths per year in the EU [368], respectively. Liver cirrhosis and primary liver cancer are the fifth most common cause of mortality in Europe. Furthermore, liver diseases are one of the major causes of death still increasing every year. Prevalence rates of CLD in the Western world are around 15% and have been stable over the last 15 years [368, 369]. Prevalence rates of hepatitis B and hepatitis C infections are slightly decreasing, while alcohol-induced liver disease has remained fairly stable over the last two decades. Of note is the prevalence of nonalcoholic fatty liver disease (NAFLD), which doubled in the last two decades. Today, NAFLD accounts for roughly 75% of CDL, a rate that is expected to grow even further given the increasing rate of obesity.

#### Major causes of CLD

- **Alcohol-related liver disease (ALD):** The liver is damaged after perennial misuse of alcohol.
- **Nonalcoholic fatty liver disease (NAFLD):** Storage of fat within liver cells (hepatic steatosis), usually seen in overweight or obese people without the necessity of other causes for secondary hepatic fat accumulation (e.g., heavy alcohol consumption) being present. NAFLD can be subdivided into fairly benign nonalcoholic fatty liver (NAFL) and nonalcoholic steatohepatitis (NASH). In NAFL, hepatic steatosis is present without evidence of significant inflammation, whereas in NASH, hepatic steatosis is associated with lobular inflammation (steatohepatitis) and progressive fibrosis.
- **Chronic viral hepatitis:** Chronic viral infection of the liver, for example, hepatitis B, C, D, E.
- **Hemochromatosis:** An inherited disorder characterized by gradual build up of iron in the body, usually around the liver.
- **Causes with lower prevalence:**
  - Autoimmune hepatitis
  - Primary biliary cirrhosis
  - Wilson's disease
  - Drug-induced liver injury

It is important to note that all types of liver disease can cause cirrhosis (scarring of the liver) and may lead to liver failure with the need for liver transplantation.

### 15.1.2 Liver Fibrosis

Liver fibrosis, or scarring of the liver, is a wound-healing response to injury resulting in the accumulation of excess extracellular matrix (ECM) material including fibrillar collagens, fibronectin, and proteoglycans. Sustained signals such as virus infection, drug exposure, or metabolic disorders are required to develop fibrosis. In advanced fibrosis, the liver contains approximately three to six times more ECM than normal<sup>1</sup> including fibril-forming collagens (types I and III) and matrix glycoconjugates such as proteoglycans, fibronectin, and hyaluronic acid.

#### ECM (Extracellular matrix):

The ECM can be defined as the collection of all secreted molecules that are immobilized outside a cell. Originally considered a mere support system for cells, ECM is now recognized as a central regulator with tissue-specific roles including structural support, transmission of forces, signaling, and macromolecular filtration. Under normal conditions, ECM continuously regenerates itself by remodeling while the original composition and structure is maintained. Once established, the ECM provides the cells with important biomechanical and biochemical cues that guide their morphology and function. ECM can be subdivided into the interstitial matrix and the basement membrane, which separates connective tissue from epithelia, endothelia, muscle fibers, and the nervous system. Major components of ECM are:

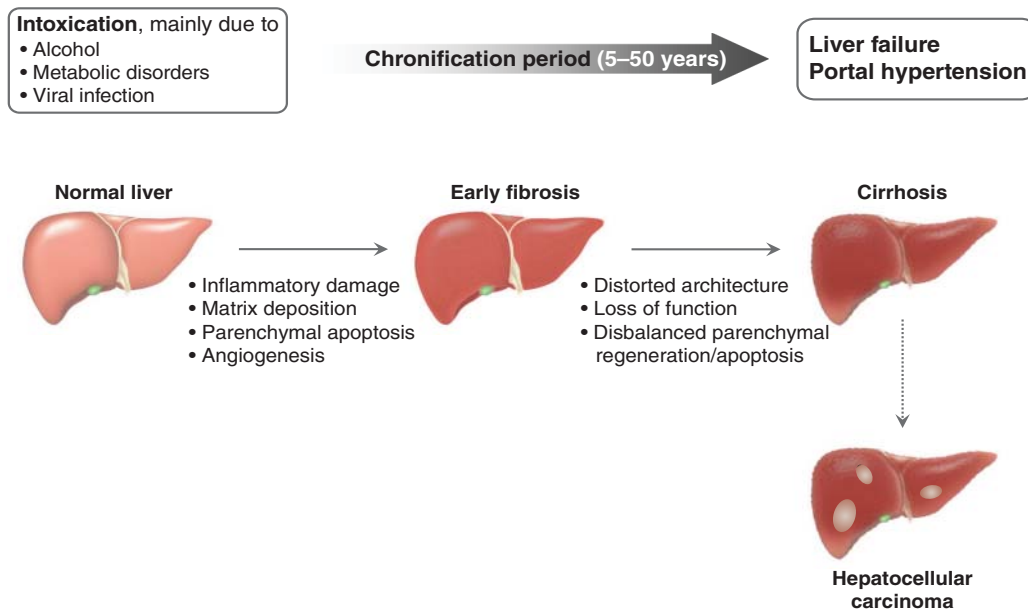
- **Fibrillar collagens:** collagen is a main structural protein in mammals, making up approximately 30% of the body's protein content. It has the capacity to bind to cell surface receptors, proteins, glycosaminoglycans, and nucleic acids. The most abundant types of collagens are type I (component of, e.g., organs, bone, and skin) and type III (component of reticular fibers). The fibrillar collagen types I and III self-assemble into a hierarchical collagen structure capable of withstanding tensile forces and thus providing mechanical integrity to the interstitial matrix.
- **Proteoglycans and glycosaminoglycans (GAGs):** proteoglycans form the basis of higher-order ECM structures. Proteoglycans consist of core proteins covalently linked to GAGs. GAGs are long, negatively charged, linear chains of disaccharide repeats. Major GAGs include heparan sulfate (component of the basement membrane), chondroitin sulfate (cartilage and neural ECM), dermatan sulfate (skin, blood vessels, tendons, lungs), hyaluronan, and keratan sulfate (cornea, cartilage, bone). Proteoglycans provide hydration and compressive resistance to ECM and hold numerous other biological functions including support of cell signaling, proliferation, and migration, as well as wound repair, binding of growth factors, cytokines,<sup>a</sup> and ECM proteins.
- **Fibronectin:** high-molecular-weight multidomain glycoprotein with binding capacities to cell surfaces through integrins and other biologically important molecules such as collagen and heparan sulfate proteoglycans. Fibronectin plays a major role in cell adhesion, growth, migration, and differentiation, and is involved in wound healing.

<sup>1</sup> ECM volume in healthy liver is approximately 3%.

- Nonfibrillar collagen type IV and the laminin family of glycoproteins: components of the basement membrane that form loose, sheet-like structures and influence cell differentiation, migration, adhesion, and angiogenesis.

<sup>a</sup>Cytokines are small proteins that are important in cell signaling and are involved, for example, in defense of infection, immune response, inflammation, and cancer.

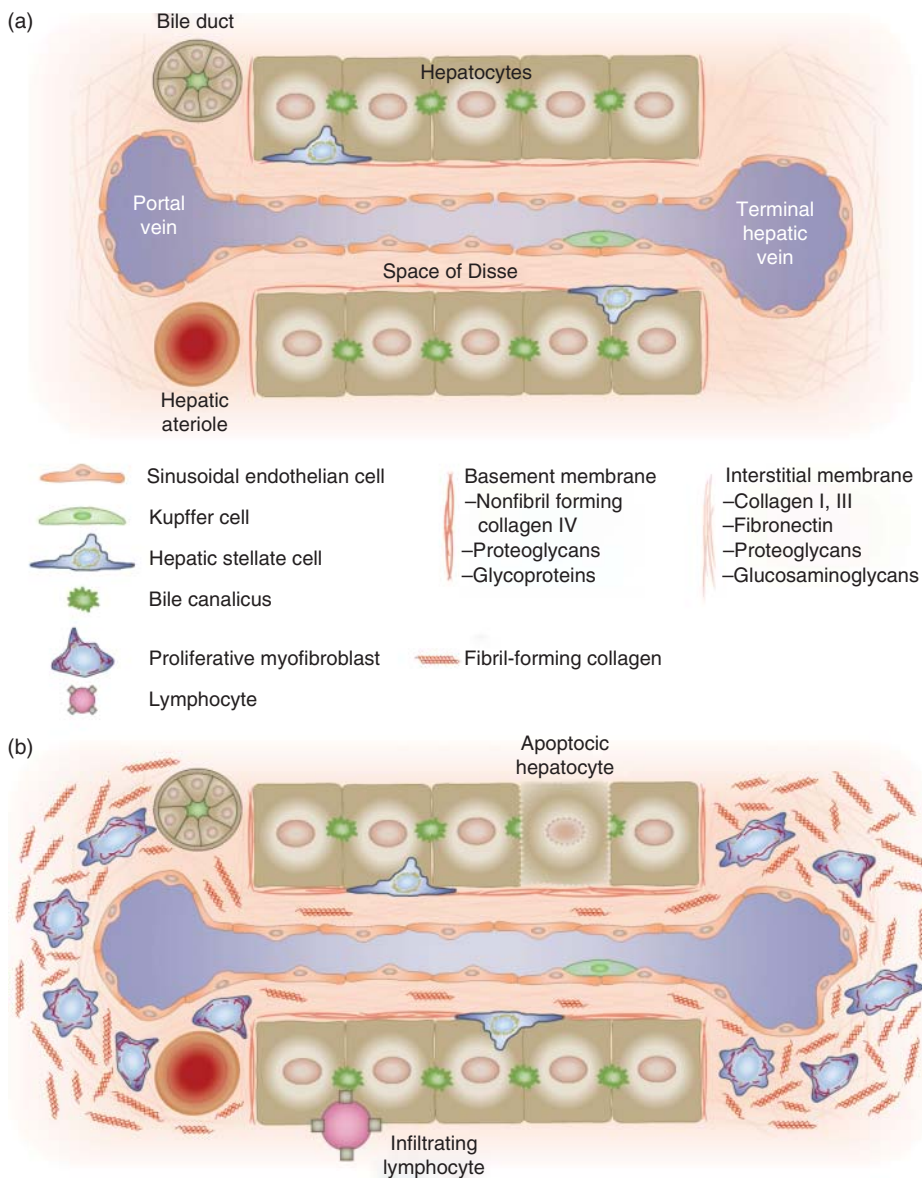
In case of time-limited injuries, changes in composition of ECM are reversible and both liver architecture and function are successfully restored. If injuries become chronic (see Figure 15.4), the structure of the liver parenchyma is progressively changed by the formation of fibrous scar tissue. During this period of ongoing reorganization processes (which can exceed some decades), most affected patients typically show only marginal and diffuse symptoms of disease. Progressive fibrosis ultimately leads to cirrhosis, which is characterized by the development of nodules of regenerating hepatocytes surrounded by fibrotic septa. Cirrhosis represents the end stage of liver pathology with hepatocellular dysfunction and increased intrahepatic resistance to blood flow, which further leads to portal hypertension and functional hepatic insufficiency. Patients with cirrhosis can remain free of major complications for several years (compensated cirrhosis) or develop various sequelae of hepatic decompensation, including variceal hemorrhage, ascites, hepatic encephalopathy, hepatic and renal failure, as well as hepatocellular carcinoma (HCC).



**Figure 15.4** Progression of liver fibrosis with characteristic changes in structure and function. Starting from initial insults and progression over many years, liver cirrhosis marks the end stage of liver diseases with an increased risk of hepatocellular carcinoma.

### 15.1.2.1 Pathogenesis of Liver Fibrosis

The organization and structure of healthy liver parenchyma is depicted in Figure 15.5a. The main constituents of healthy liver tissue are hepatocytes and endothelial cells. Hepatic stellate cells (HSCs) and Kupffer cells (KCs) are nonparenchymal cells residing in the subendothelial space of Disse and inside the sinusoids, respectively. The sinusoids



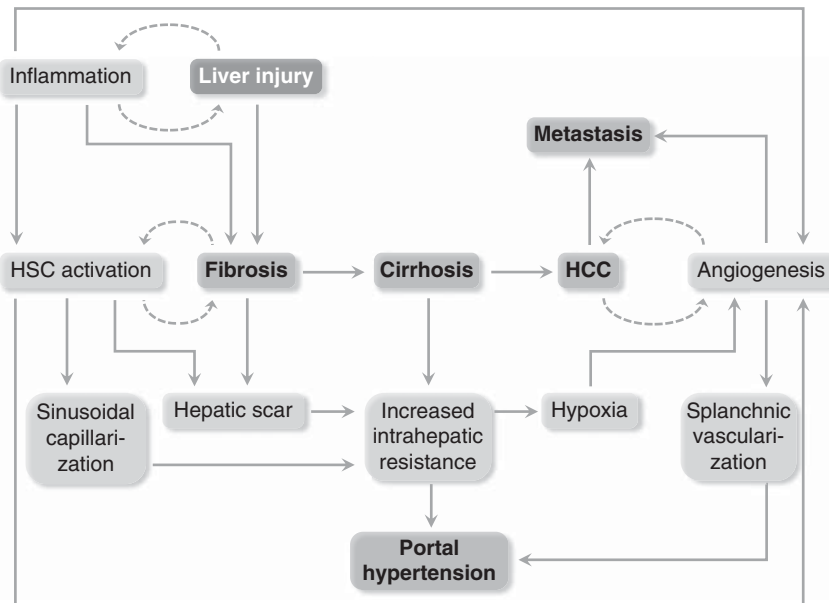
**Figure 15.5** (a) Schematic view of healthy liver parenchyma. (b) Schematic view of fibrotic liver parenchyma showing characteristic alterations such as an increase in activated myofibroblasts and fibril-forming collagens, enlarged portal fields, loss of endothelial fenestration, distortion of veins, as well as changes in the basal membrane.

are the smallest microvascular units of liver parenchyma, transferring inflowing blood from the portal vein and hepatic artery to the draining hepatic vein. Metabolic exchange between the bloodstream and hepatocytes occurs through two porous membrane-based structures in the space of Disse or perisinusoidal space. On the one hand, this is a fenestration of pores built by the endothelial lining of the sinusoids; on the other hand, this is the low-density basal membrane enclosing hepatocytes. Figure 15.5b illustrates the major structural changes in fibrotic liver. In the presence of injury, HSCs become activated mainly by paracrine stimulation (e.g., endothelial cell damage, hepatocyte apoptosis) and undergo transition from a quiescent vitamin A-rich cell to a proliferative, contractile, and highly fibrogenic myofibroblast (MF). Furthermore, HSCs communicate with inflammatory cells mediated by cytokines. Although HSCs are the main source of MFs in the liver, other cells such as portal fibroblasts, bone marrow-derived cells, and epithelial cells can undergo MF transition. The result is a loss of the carefully regulated balance of ECM synthesis and loss of degradation of excess collagen. This leads to an increase in fibril-forming collagens, enlarged portal fields, loss of endothelial fenestration, changes in the basement membrane (from the physiologic low-density type to an interstitial high-density matrix), loss of hepatocyte surface (loss of microvilli, not shown in Figure 15.5), and distortion of veins. Consequences are impairments of the bidirectional metabolic exchange between blood flow and hepatocytes and increased intrahepatic resistance to blood flow.

The distribution of this fibrotic material depends on the origin of the injury, the type of involved fibrogenic cells, and fibrogenic mechanisms. In alcohol-induced liver disease, fibrosis is observed in pericentral and perisinusoidal areas, whereas in chronic viral hepatitis and chronic cholestatic disorders (impairment of bile drainage from the liver) it is initially located around portal tracts. With the progression of liver fibrosis, initially isolated collagen bands become cross-linked. Figure 15.6 presents a simplified chart of the development of liver disease. As an initial insult, hepatotoxic agents progressively damage hepatocytes, Kupffer cells, and biliary cells, inducing the recruitment of inflammatory cells such as lymphocytes. Release of inflammatory cytokines mediates the activation of several intracellular signaling pathways including suppression of ECM degradation and activation of resident HSCs to highly proliferative MFs (see Table 15.2). HSC activation can further be perpetuated by hepatocytic apoptosis, HSC self-expressed cytokines, and mutual stimulation of inflammatory cells and HSCs. Furthermore, HSCs can also act as vasoactive mediators that can alter intrahepatic blood flow by influencing sinusoidal capillarization.

If the liver injury persists, the MFs synthesize large amounts of ECM structural proteins, and hepatic scarring increases. Progression of liver fibrosis with ongoing structural changes of liver parenchyma and an increasing loss of function ultimately lead to cirrhosis. The associated increase in intrahepatic resistance to blood flow causes portal hypertension as well as oxidative stress due to the decreased effective hepatocyte perfusion. Together with inflammation and HSC activation, the decrease in hepatocyte perfusion by itself is an elicitor of angiogenesis. In many ways, the liver's response to injury is angiogenic, including new blood vessel formation and sinusoidal remodeling. The development of new blood vessels plays a major role in the formation of primary cancer and metastases and affects portal systemic blood flow, resulting in many life-threatening complications of cirrhosis such as gastroesophageal varices, massive upper gastrointestinal bleeding, or ascites.





**Figure 15.6** Simplified process chart of the pathogenesis of liver diseases with liver injury caused by hepatotoxic agents. Bold font indicates liver diseases and dashed arrows indicate potential self-perpetuating processes. For further details, see text.

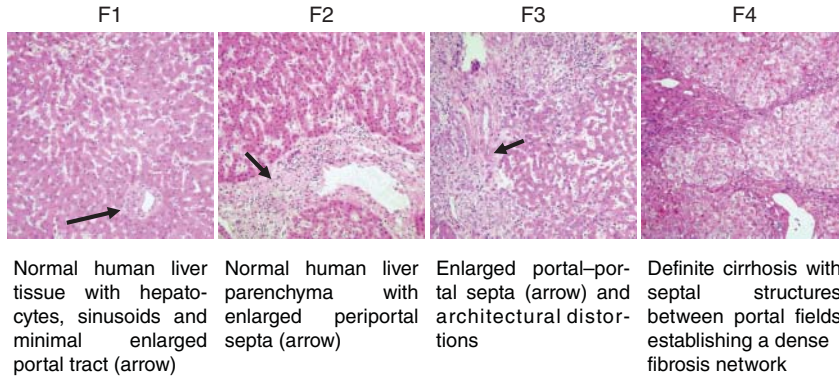
### 15.1.2.2 Staging of Liver Fibrosis

In many liver diseases, the determination of the degree of liver fibrosis is essential for diagnosis and treatment planning. Liver biopsy with successive histological analysis is still the gold standard for staging liver fibrosis (see Figure 15.7). It primarily provides information on the extent of established fibrosis (stage) and the degree of necroinflammatory activity (grade). While no generally accepted scoring system is available, most of the classification schemes in clinical use today are based on five to seven distinct categories ranging from healthy liver to cirrhosis. Common systems are METAVIR (Meta-analysis of Histological Data in Viral Hepatitis), the classification of the International Association for the Study of the Liver (IASL) and the more complex Ishak score (which distinguishes seven categories). For comparison, see Table 15.1 for histologic staging of liver fibrosis.

Although liver biopsy is still the gold standard for staging hepatic fibrosis, it has some generally acknowledged drawbacks:

- Significant complications with prolonged hospital stay occur in 2–6% of patients due to significant complications with a mortality rate of about 1:10 000 [374–376].
- Needle biopsy removes only about 1/50 000 of the liver volume and thus inherently carries substantial sampling error.
- Accuracy is limited, and cirrhosis may be missed in 25% of cases [377].
- Evaluation of liver pathology is subjective and prone to inter- and intraobserver error.
- Patients' refusal to undergo repeated biopsy limits its use for monitoring disease course and treatment response.





**Figure 15.7** Histological micrographs of human fibrotic liver showing fibrosis stages F1–F4 according to the METAVIR classification system. (Sack 2013 [3]. Reproduced with permission of Royal Society of Chemistry.)

**Table 15.1** Scoring systems for histologic staging of liver fibrosis.

Stage	METAVIR [371]	IASL [372]	Ishak [373]
0	No fibrosis	No fibrosis	No fibrosis
1	Periportal fibrotic expansion	Mild fibrosis	Fibrous expansion of some portal areas with or without short fibrous septa
2	Periportal septae	Moderate fibrosis	Fibrous expansion of most portal areas with or without short fibrous septa
3	Portocentral septae	Severe fibrosis	Fibrous expansion of most portal areas with occasional portal-to-portal bridging
4	Cirrhosis	Cirrhosis	Fibrous expansion of most portal areas with marked bridging (portal-to-portal and portal-to-central)
5			Marked bridging (portal-to-portal and portal-to-central) with occasional nodules (incomplete cirrhosis)
6			Cirrhosis

Source: Modified from [370].

### 15.1.2.3 Noninvasive Screening Methods for Liver Fibrosis

Liver fibrosis can be assessed noninvasively by determination of biomarkers and use of radiological modalities such as contrast-enhanced (CE) imaging or elastography. Serum biomarkers are categorized into two groups: (i) direct biomarkers, which reflect ECM turnover (fibrogenesis and fibrolysis) and/or fibrogenic cell changes mainly affecting HSC; (ii) indirect markers sensitive to molecules originating from hepatic inflammation or altered liver function. Table 15.2 lists some serum biomarkers and corresponding variables. For further information, refer to publications such as [378–380].

Advanced imaging modalities based on sonography and MRI for staging liver fibrosis include elastography, perfusion measurement, and diffusion-weighted and dynamic

**Table 15.2** Biomarkers of fibrosis.

Type	Category	Biomarkers
Direct	Collagen/ECM molecules and enzymes	Collagen type IV, fibronectin, hyaluronate, N-terminal pro-collagen peptide, MMP-2/-9
	Cytokines	TGF $\beta$ , TNF $\alpha$ , TIMP-1/-2
Indirect	Liver function tests	Aminotransaminases (ALT, AST), bilirubin, albumin gamma-glutamyl transpeptidase (GGT)
	Hematological parameters	Platelet count, prothrombin time
	Other	Globulins, insulin, apolipoprotein, cholesterol, haptoglobin

Abbreviations: MMP: matrix metalloproteinase (enzymatic degradation of collagenous and noncollagenous ECM substrates); TIMP: tissue inhibitor of metalloproteinase (cytokine responsible for inhibiting ECM degradation); TGF $\beta$ : transforming growth factor- $\beta$  (HSC-activating cytokine); TNF $\alpha$ : tumor necrosis factor- $\alpha$  (apoptosis-inducing cytokine).

imaging with extracellular or hepatobiliary contrast agents. At present, noninvasive biomarkers show high accuracy for determining advanced fibrosis and cirrhosis (METAVIR stage 4), while accuracy is only modest for mid-level stages (METAVIR stages 1–3). A comprehensive overview of the accuracy of noninvasive biomarkers for the diagnosis of diffuse liver diseases including elastography is given in Table 15.5.

#### 15.1.2.4 Reversibility of Liver Fibrosis

Against the longstanding paradigm of irreversibility of fibrotic changes, a reduction in ECM content has been observed in animal models and patients with alcoholic, viral, and metabolic fibrosis, and even cirrhosis. However, fibrosis regression may take years and does not necessarily restore normal ECM architecture. Mechanisms of fibrosis regression include enzymatic degradation of collagenous and noncollagenous ECM substrates by matrix metalloproteinase (MMP), upregulation of myofibroblast apoptosis,<sup>2</sup> and senescence<sup>3</sup> of activated HSCs to reduce the fibrogenic response to tissue damage. Liver transplantation is currently the only therapeutic option for liver failure due to cirrhosis. However, an increasing number of effective pharmaceuticals for treatment of liver fibrosis are becoming available.<sup>4</sup> With the advent of antifibrotic therapies, long-term monitoring of fibrosis regression by reliable noninvasive biomarkers such as elastography becomes increasingly important.

#### 15.1.2.5 Biophysical Signs of Liver Fibrosis

So far, we have focused on the biochemical description of the pathogenesis of liver fibrosis. However, cells also respond to mechanical forces such as shear or tensile stress [381–383]. Mechanical forces acting on cells can arise either from internal mechanochemical signals or from outside through the mechanical milieu, which is established by ECM, cellular adhesion, and interstitial fluids. Hence, mechanical

<sup>2</sup> Apoptosis is a highly regulated and controlled process of programmed cell death.

<sup>3</sup> Cellular senescence refers to the essentially irreversible arrest of cell proliferation that occurs when cells experience potentially oncogenic stress.

<sup>4</sup> For example, treatment of hepatitis C with agents acting against viral replication.

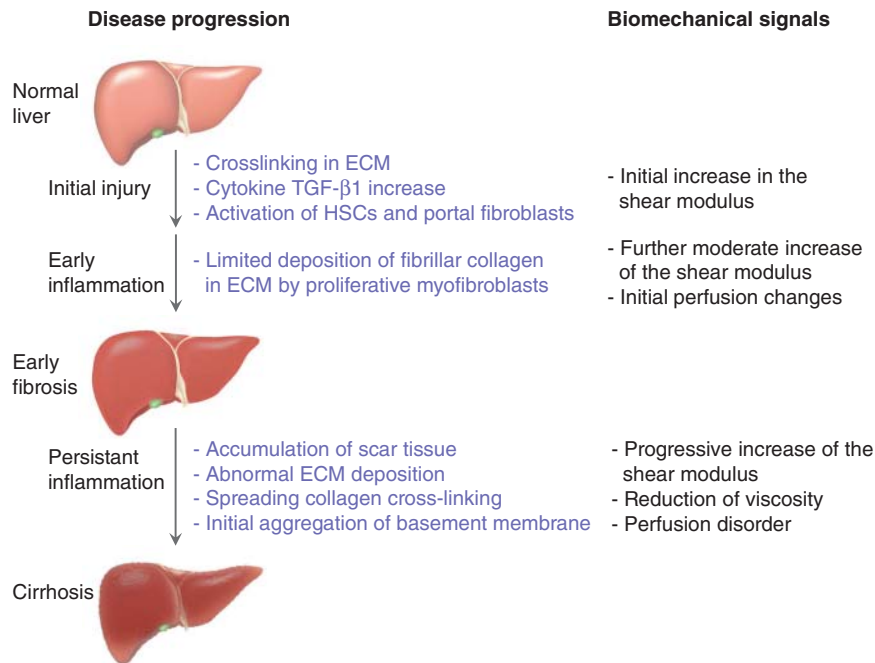
properties of both the cells and ECM environment are critical determinants of vital processes such as cell differentiation, oncogenic transformation, or hepatic fibrosis. Several experiments in animal models point to an intimate link between fibrogenesis and tissue stiffness by demonstrating that ECM cross-linking occurs before MF activation [383, 384]. Complementary experiments with primary cells from healthy liver corroborated that HSCs and portal fibroblasts produce both collagen and cross-linking enzymes [385]. Moreover, the expression of collagen and cross-linkers by HSCs is enhanced in the presence of TGF- $\beta$ 1, a cytokine of central importance in liver fibrosis (see Table 15.2) [386]. Interestingly, prestrained ECM releases higher rates of active TGF- $\beta$ 1 than unorganized or relaxed ECM [387]. This observation sheds light on the relevance of mechanical stress exerted on liver tissues as a possible precondition for the activation of HSCs and transformation to MF [388]. Taken together, these studies provide evidence that liver fibrosis is caused by changed biophysical properties of the ECM resulting from deposition and cross-linking of collagen fibers. In this process, HSCs and portal fibroblasts play a key role due to their ability of early expression of cross-linking enzymes and collagen. Of note, this function is distinct from their classic role as precursors of MFs, which are highly proliferative matrix-producing cells. Early ECM stiffening may further enhance the allocation of TGF- $\beta$ 1 and thus activation and transformation of HSCs and portal myofibroblasts into major collagen-secreting MF cells. Liver fibrosis would then result from the ongoing activation of mesenchymal cells to fibrogenic myofibroblasts, leading to a vicious circle of self-perpetuating effects. In this scenario, ECM stiffening occurs first and initiates the vicious circle leading to fibrosis rather than being a sequela of fibrosis (see also Figure 2 in Introduction). Figure 15.8 summarizes basic biomechanical signs associated with the progression of liver fibrosis.

### 15.1.3 MRE of the Liver

At present, quantification of viscoelastic parameters of the liver for staging hepatic fibrosis is one of the major applications of MRE. This is reflected by a large number of publications covering a wide range of methodological and application-related aspects including possible influencing factors such as etiology [389–394], ethnicity [395, 396], and age [397, 398]. For ease of reading, the following overview of major studies of MRE of the liver is organized into six broad topics: (i) studies of animals and tissue samples, (ii) early clinical studies and further developments, (iii) MRE in NAFLD, (iv) MRE in comparison to other noninvasive biomarkers, (v) further applications of liver MRE including assessment of portal hypertension and transplanted livers, and (vi) confounders.

#### 15.1.3.1 MRE in Animal Models of Hepatic Fibrosis and Liver Tissue Samples

The fundamental agreement between MRE and mechanical testing has been demonstrated in a cross-validation study using bovine liver samples [399]. The results show that mechanical tissue characterization by multifrequency MRE (MMRE) agrees well with oscillatory rheometry. Initial results of animal studies addressing hepatic fibrosis were published simultaneously with first studies in humans. In a knockout mouse model, a linear correlation between liver elasticity and degree of histologically proven fibrosis was found [134]. In this study, fatty infiltration – which is common in hepatic fibrosis – did not interfere with MRE-based fibrosis grading (see Section 15.1.3.3 below). The correlation of viscoelasticity parameters with toxin-induced hepatic



**Figure 15.8** Summary of microstructural changes associated with the pathogenesis of liver fibrosis as revealed by basic experiments in animal models and cell cultures. In the pre-inflammation stage of early liver injury, HSCs can express both collagen and collagen cross-linking enzymes, leading to ECM stiffening already at an initial stage of disease.

fibrosis was demonstrated in a rat model [400]. In this study, significant correlations were found between viscoelastic parameters and the extent of liver fibrosis. Liver slices from a similar rat model were analyzed by 3D MMRE [132]. When the frequency dispersion of viscoelastic parameters was fitted with a power law model, elasticity correlated significantly better with severity of liver fibrosis than viscosity.

Overall, these preclinical studies demonstrate that viscoelastic parameters quantified by MRE correlate well with established methods of mechanical materials testing. Furthermore, these studies indicate that liver elasticity increases with progression of fibrosis with only little influence of the amount of fat present in the liver. However, it should be noted that the influence of fat on the assessment of hepatic fibrosis by elastography is still under investigation. We further discuss this in light of more recent findings in the section dedicated to confounders.

### 15.1.3.2 Early Clinical Studies and Further Developments

First feasibility studies of liver MRE in healthy volunteers and patients with different stages of liver fibrosis were published in 2006. This preliminary work addressed basic methodological aspects such as the calculation of viscoelastic parameters [157, 185], driver positioning, directionality of motion encoding [182], and fractional encoding [185]. Technical parameters and results of the studies presented in this section are summarized in Table 15.3. These early studies already demonstrated that liver elasticity [157, 182, 185, 408] and viscosity [157, 408] are higher in patients with liver fibrosis

**Table 15.3** Fundamental *in vivo* studies of MRE of the liver.

Subjects [reference]	Stage of fibrosis	Sequence type	Encoding method	Vibration freq. (Hz)	Recon- struction	Stiffness (kPa)	Viscosity (Pa s)
5 volunteers [157] 25 patients		SE	3D	65	DI	2.1 ± 0.3	1.7 ± 0.2
11	0–1					2.2 ± 0.2	2.4 ± 0.9
4	2–3					2.6 ± 0.2	2.3 ± 0.4
10	4					4.7 ± 1.6	5.2 ± 1.9
12 volunteers [185] 2 patients		SSEFP <sup>a</sup> )	1D	150 <sup>a</sup> )	DI	2.6 ± 0.3	4.4 ± 2.0
	3						
12 volunteers [182] 11 patients		GRE	1D	80	DI	2.1 ± 0.3	5.6 ± 5.0
	1–4						
35 volunteers [88] 48 patients		GRE	1D	60	LFE	2.2 ± 0.3	5.8 ± 2.6
		0–4					
96 patients [402]		SE	3D	65	DI		
22	0					2.2 ± 0.2	
22	1					2.4 ± 0.1	
19	2					2.9 ± 0.2	
15	3					3.5 ± 0.5	
18	4					5.3 ± 0.7	
85 patients [90]		EPI	3D	50	DI		
56	0–1					1.6	
29	2–4					2.9	
21 patients [403]		GRE	1D	60	LFE		
1	0					2.1	
3	1					2.2	
4	2					3.1	
3	3					4.4	
10	4					5.7	
94 patients [404]		GRE	1D	65	LFE		
47	1–4					3.5 ± 0.3	
47	1–4					3.4 ± 0.2	
20 volunteers [405]		GRE	1D	60	LFE	2.1 ± 0.4	
49 volunteers [87]		GRE	1D	60	LFE	2.1	
20 volunteers [406] 10 patients		GRE	1D	60	LFE	2.4 ± 0.1	4.0 ± 0.5

*(continued overleaf)*

Table 15.3 (Continued)

Subjects [reference]	Stage of fibrosis	Sequence type	Encoding method	Vibration freq. (Hz)	Recon-struction	Stiffness (kPa)	Viscosity (Pa s)
10 volunteers [407]		EPI <sup>a)</sup>	3D	30–60	MDEV	1.3 ± 0.2	
10 volunteers [98]		EPI <sup>a)</sup>	3D	30–60	MDEV	1.4 ± 0.2	
4 patients						2.0 ± 1.0	

**Abbreviations:** SE – spin echo, GRE – gradient echo, SSFP – steady-state free precession GRE, 1D – single-displacement field component, 3D – full-displacement field, LFE – local frequency estimation, DI – direct inversion, MDEV – multifrequency dual elasto-visco inversion.

a) Fractional motion encoding.

“Stiffness” refers to  $\rho \cdot c^2$  (for LFE),  $|G^*|$  or  $G'$  (for DI, not specified), and  $|G^*|$  for MDEV inversion, “viscosity” refers to the shear viscosity as defined in [401]. All values are given as group mean ± standard deviation (if available).

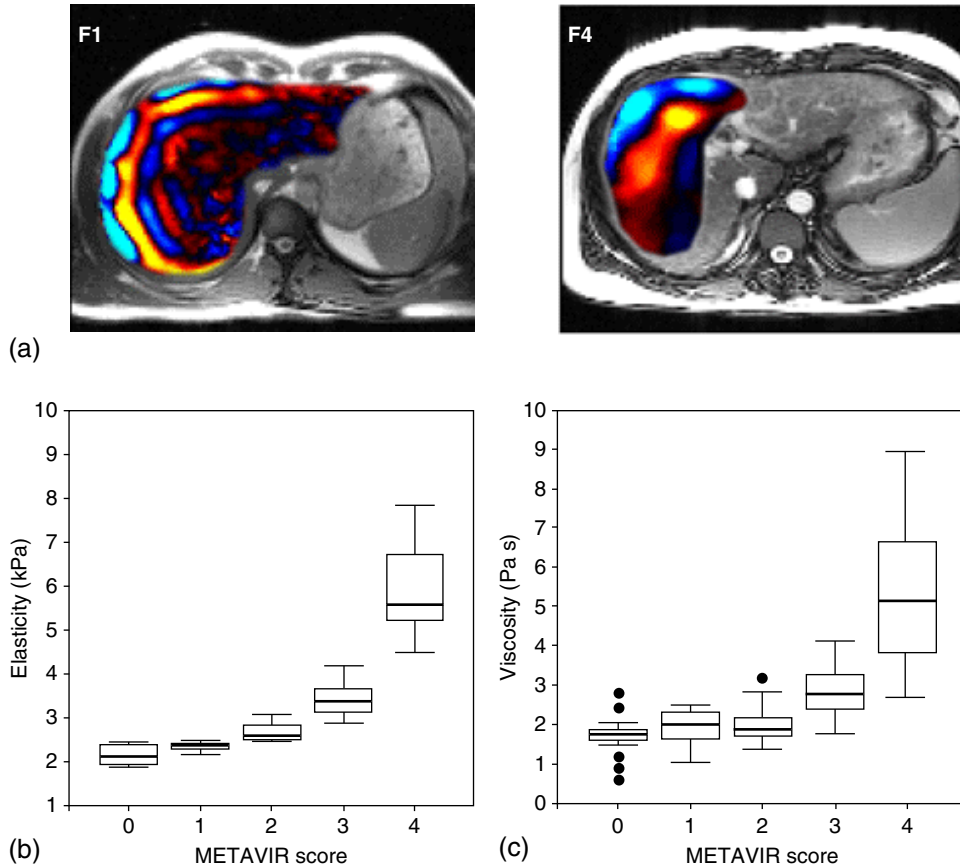
than healthy volunteers. Furthermore, it was shown that the measured viscoelasticity correlated well with the degree of liver fibrosis [157, 408], raising the prospect of MRE as a clinical tool for staging liver fibrosis. Figure 15.9 depicts some results of this early work.

Further important early work focused on the diagnostic accuracy of MRE in liver fibrosis and comparison with other noninvasive biomarkers. Yin et al. [88] compared MRE with MRI for fat quantification and estimated the influence of fatty infiltration on sensitivity and specificity of MRE for staging fibrosis. This study confirmed the previously observed increase in liver elasticity with fibrosis and, for the first time, demonstrated a high sensitivity and specificity of MRE for detecting all stages of fibrosis. Area under receiver operating characteristic (AUROC<sup>5</sup>) analysis provided evidence that MRE can discriminate between patients with any fibrosis ( $\geq$ stage 1), significant fibrosis ( $\geq$ stage 2), advanced fibrosis ( $\geq$ stage 3), and cirrhosis (stage 4) with AUROC values of 1.00, 0.92, 0.92, and 0.92, respectively (see Figure 15.10). The high sensitivity and specificity for the detection of all grades of liver fibrosis encouraged the further development and application of MRE as a noninvasive biomarker of liver fibrosis.

The comparison of success rate and diagnostic accuracy of MRE with other promising noninvasive biomarkers such as transient ultrasound elastography (*TE*, Section 12.12) and aspartate aminotransferase-to-platelets ratio index (APRI<sup>6</sup>) was studied in patients with chronic liver disease [402]. MRE was successfully completed in 94% and *TE* in 84% of all subjects. For diagnosis, MRE performed better than *TE* and APRI (see Figure 15.11). MRE discriminated patients with any fibrosis ( $\geq$ stage F1) from significant fibrosis ( $\geq$ stage F2), advanced fibrosis ( $\geq$ stage F3), and cirrhosis (stage F4)

<sup>5</sup> The AUROC measures discrimination. In the medical context, it is the ability of a test to correctly classify individuals with and without a disease. The accuracy depends on how well the test separates the group being tested into those with and without the disease in question. Accuracy is measured by the area under the ROC curve: an area of 1.0 represents a perfect test, whereas an area of 0.5 indicates random results. If not otherwise stated, AUROC values are normally given for a 95% confidence interval.

<sup>6</sup> APRI is a combination of serum markers calculated from the ratio of aspartate aminotransferase to platelet count.

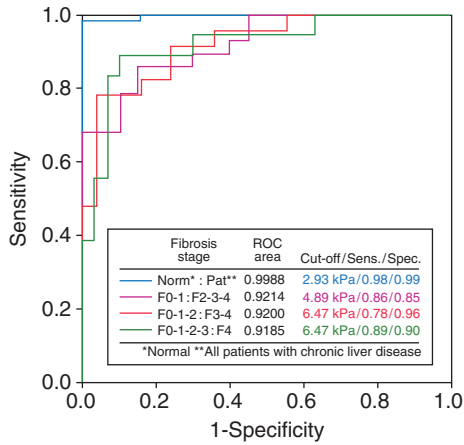


**Figure 15.9** Principle and early results of MRE of the liver. (a) Wave images of two patients with mild (F1) and severe (F4) fibrosis. The apparent increase in shear wavelength reflects stiffening of liver tissue with progressing fibrosis. (b,c) Box plots showing elasticity in kPa based on the Voigt model (b) and viscosity in Pa s (c) in patients with hepatic fibrosis. Both, elasticity and viscosity increase with the stage of fibrosis. (Huwart 2007 [408]. Reproduced with permission of Radiological Society of North America.)

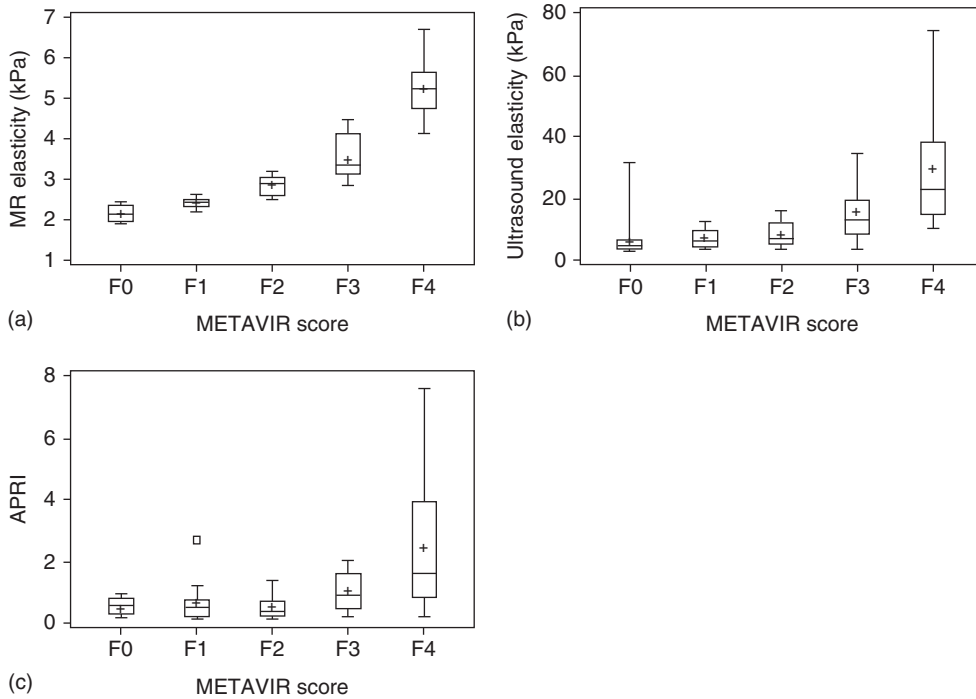
with AUROC values of 0.96, 0.99, 0.99, and 1.00, respectively, significantly better than *TE* (0.80, 0.84, 0.91, and 0.93) and APRI (0.68, 0.71, 0.82, and 0.82).

Numerous studies followed to further evaluate the diagnostic potential of MRE in the liver. The variability of liver biopsy was addressed in a study comparing the interobserver agreement of MRE with histopathological staging of liver fibrosis in a cohort of hepatitis patients [90]. Interestingly, interobserver agreement for the staging of liver fibrosis expressed by the intraclass correlation coefficient (ICC<sup>7</sup>) was significantly higher for MRE (ICC = 0.99) compared to histopathology (ICC = 0.91), corroborating

<sup>7</sup> ICC is a general measure of agreement or consensus between two or more raters or evaluation methods on the same set of subjects. ICC assesses the reliability of ratings by comparing the variability of different ratings of the same subject with the total variation across all ratings and all subjects. ICC has advantages over the calculation of correlation coefficients in that it is adjusted for the effects of the scale of measurements. A prominent application is the assessment of reproducibility of quantitative measurements made by different observers measuring the same quantity. If not otherwise stated, ICCs are given for a 95% confidence interval.



**Figure 15.10** AUROC analysis of the diagnostic accuracy of MRE for liver fibrosis staging. The inserted table shows the values for AUROC, cutoff values for liver elasticity, and the corresponding sensitivity and specificity for each test. (Yin 2007 [88]. Reproduced with permission of Elsevier.)



**Figure 15.11** Staging of hepatic fibrosis with different biomarkers. (a) MRE; (b) transient ultrasound elastography (*TE*, Section 12.12); and (c) APRI. (Huwart 2008 [402]. Reproduced with permission of Elsevier.)

the generally accepted fact that interobserver variability of liver biopsy is high. In this context, MRE was also compared with a morphology-based quantification algorithm (Fibro-C-Index<sup>8</sup>) of liver biopsy samples [409]. The study reported similar accuracies

<sup>8</sup> The Fibro-C-Index was developed to reduce high inter- and intraobserver discrepancies in the scoring of liver biopsies.



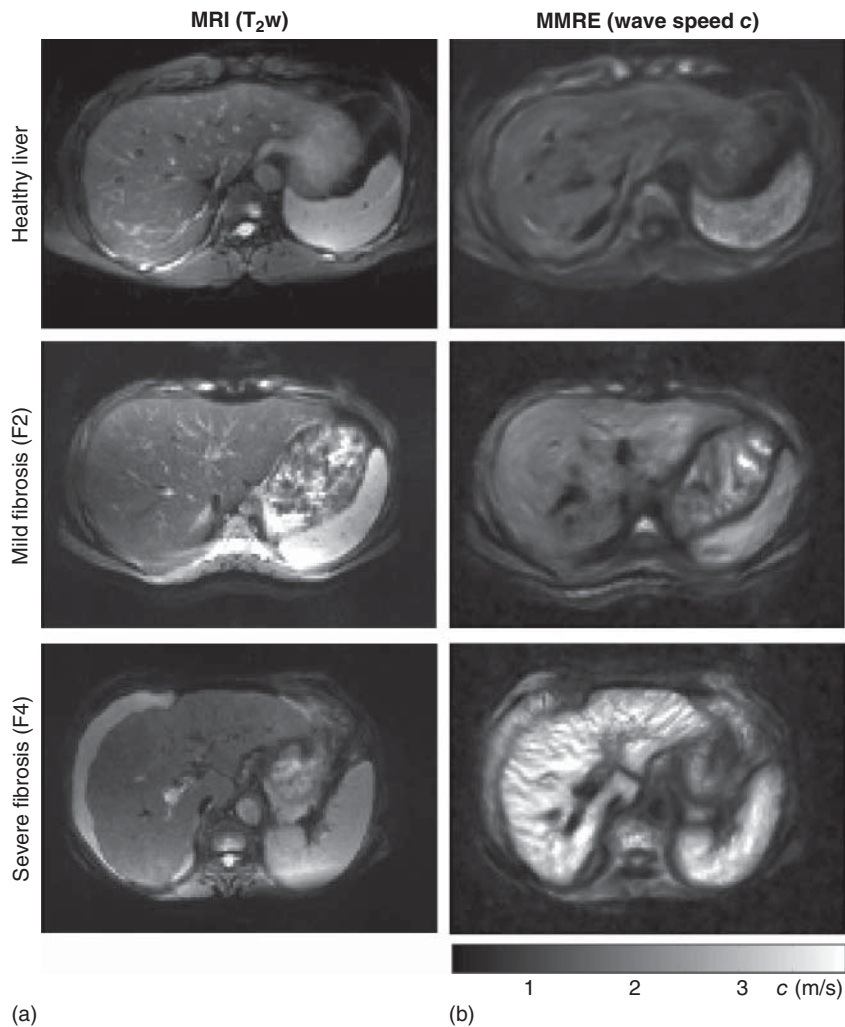
for MRE and Fibro-C-Index (AUROC MRE vs Fibro-C: 0.87 vs 0.81 for  $\geq F1$ , 0.95 vs 0.94 for  $\geq F2$ , 0.98 vs 0.96 for  $\geq F3$ , and 1.00 vs 0.92 for F4). The high interobserver reliability of MRE was confirmed in a further study on 110 patients (ICC = 0.91) [403]. Another study correlated MRE with liver biopsy addressed the reproducibility and repeatability of MRE [404]. In this study, ICC for intraobserver reliability was 0.96, repeat analysis of mean liver elasticity by one observer yielded an ICC of 0.83, and repeat measurements in patients gave an ICC of 0.95. Overall, similar experimental conditions with respect to driver location and patient positioning must be retained to ensure high reproducibility of MRE [410].

All studies presented so far determined liver viscoelasticity by averaging values over predefined regions of interest (ROIs) within the liver parenchyma. The influence of the choice of ROI was addressed by several studies showing that MRE values vary with placement [405] and size of ROIs [87, 405] in healthy volunteers but do not vary with age and gender [87]. The highest reproducibility was achieved by averaging over cross sections of the whole liver (ICC = 0.84) [405] or by averaging over a single-slice cross-sectional area of the liver (ICC = 0.85) [87].

Two meta-studies analyzing the diagnostic accuracy of MRE in liver fibrosis based on 989 patients [411] and 697 patients [412]. Su et al. [411] reported AUROC values of 0.95, 0.97, 0.96, and 0.99 for detection of fibrosis  $\geq F1$ ,  $\geq F2$ ,  $\geq F3$ , and F4, respectively. In a more recent analysis, MRE achieved lower precision with AUROC values of 0.84, 0.88, 0.93, and 0.92 for the diagnosis of the pooled five stages of liver fibrosis [412]. However, these meta-studies are limited by marked technical variations of the MRE methods used for acquisition of the included data. Therefore, thresholds calculated to separate distinct fibrosis stages showed different ranges and overlaps [411]. The trend toward fast acquisition techniques and MMRE might improve comparability of values in the future.

Excellent reproducibility of liver MRE parameters was demonstrated by a cross-platform study performed in two scanner systems on the same day and including the same groups of healthy volunteers and patients [98]. Since pulse sequences, drivers, and postprocessing methods were the same for both systems, almost identical results were reported. Further improvements in consistency of liver MRE can be expected from MMRE and noise-robust recovery such as  $k$ -MDEV (see Figure 15.12). The gradual increase of intensity in the liver elastograms with the degree of fibrosis is well perceptible – particularly in comparison with the spleen, which does not change to the same extent. As a drawback, MMRE is more time-consuming than the classic approach of MRE using a single excitation frequency. For this reason, the images shown in Figure 15.12 are based on fast single-shot echo-planar imaging (EPI) MRE, which is detailed in Section 3.4. Notably, the signal-to-noise-ratio (SNR) of EPI-based MRE of the liver has been found to be similar to that of standard spin – echo MRE [406].

Most work published on liver MRE is related to stiffness measures. Viscosity is another important source of diagnostic information in MRE. Roughly speaking, elasticity is related to the rigidity of a mechanical network as well as to the number of internal cross-links. By contrast, viscosity relates to the attenuation of mechanical energy, which is dramatically increased in polymer networks by the prevalence of free chains [413]. In general, the dispersion function of the global viscoelastic modulus of complex hierarchically ordered systems reveals information on the topology and geometry of the underlying mechanical network [414]. This phenomenological approach to viscoelastic



**Figure 15.12** Multifrequency MRE of the liver and spleen based on  $k$ -MDEV inversion (see Section 10.6). (a)  $T_2$ -weighted images of a healthy volunteer and patients with hepatic fibrosis of grades F2 and F4. (b) Stiffness maps, represented by shear wave speed. An increase in elasticity can be observed for both organs with fibrosis progression; however, this increase is clearly more pronounced in the liver than in the spleen. (Tzschätzsch 2016 [222]. Reproduced with permission of Elsevier.)

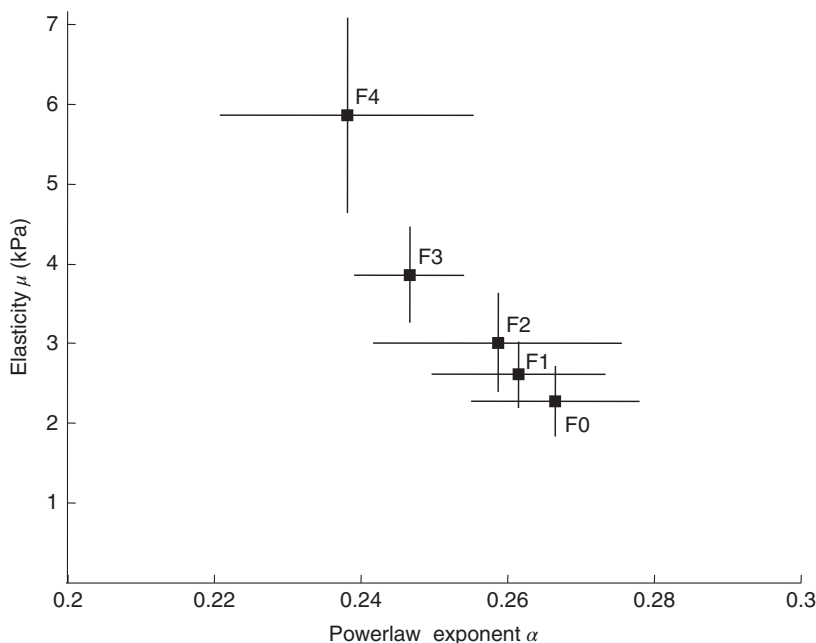
networks was established by methods from polymer physics and has been adopted for the interpretation of MRE data of biological tissues [3].

Measuring the dispersion of the complex shear modulus requires MMRE. An early technique of *in vivo* liver MMRE used a superposition of four harmonic drive frequencies and model fits based on rheological models frequently used in the literature including springpot, Voigt, Maxwell, and Zener models [33, 415, 416]. In these early studies, significant differences between healthy and fibrotic livers were detected based on the Zener and springpot model. The two-parameter springpot model (see Figure 4.7) is numerically more stable than the three-parameter Zener model (see Figure 4.7)

[33]. This observation motivated the further use of the springpot model for analysis of clinical MRE data. The validity of the springpot-inherent power law relationship of shear modulus in liver tissue was demonstrated in bovine liver specimens investigated by MMRE over a wide range of vibration frequencies from 25 to 800 Hz [125].

On a microscopic level, the viscoelasticity of healthy liver parenchyma is determined by the organization of sinusoids consisting of hepatocytes, endothelial cells, the space of Disse, blood, and bile vessels, which all integrate into very soft and highly viscous effective-medium properties. Fibrosis results in a dominating mechanical network characterized by extended, mechanically strong elements made up of fibrillary collagen. The replacement of soft hepatocytes by thick and extended connective tissue fibers translates into increased stiffness and decreased viscosity on the macroscopic scale. This was observed by springpot-based MMRE in 16 healthy volunteers and 74 patients with histologically proven fibrosis [89]. The springpot-related shear modulus  $\mu$  was found to accurately detect fibrosis  $\geq F1$ ,  $\geq F2$ ,  $\geq F3$ , and  $\geq F4$  with AUROC values of 0.91, 0.92, 0.97, and 0.99, respectively. Lower sensitivity was observed for the springpot parameter  $\alpha$ . A presentation of data of this study in the  $\mu - \alpha$  viscoelasticity space is shown in Figure 15.13.

The principal finding of increased stiffness and reduced viscosity due to liver fibrosis was reproduced by wideband MRE from 200 to 1200 Hz performed in a preclinical MRI scanner [224]. This study of human liver specimens combined preoperative *in vivo* functional tests with wideband MRE, static indentation experiments, histology, and biochemical quantification of connective tissue. Interestingly, MRE-based viscoelasticity parameters were more sensitive to the degree of fibrosis than other



**Figure 15.13** Changes in elasticity and the springpot parameter  $\alpha$  for progressing liver fibrosis (F0–F4). (Sack 2013 [3]. Reproduced with permission of Royal Society of Chemistry.)

measures. Quantification of collagen based on hydroxyproline was less correlated with fibrosis than MRE-measured elasticity. This result suggests that fibrogenesis causes cross-linking of collagen chains, resulting in increased stiffness and reduced viscosity of liver tissue. Since tissue structure is not directly linked to liver function, neither histology nor MRE correlated with the *in vivo* functional state of the liver.

### 15.1.3.3 MRE of Nonalcoholic Fatty Liver Disease

As introduced in Section 15.1.1, NAFLD has become one of the most common causes of chronic liver disease with increasing prevalence [417]. NAFLD describes the accumulation of fat in the liver not associated with alcohol abuse. NAFLD is becoming more common in children and is strongly associated with physical inactivity, obesity, and metabolic syndrome. NAFLD is characterized by four pathological features: (i) lipid storage; (ii) fibrosis; (iii) inflammation; and (iv) hepatocyte injury (ballooning). NAFLD covers a variety of diseases from simple isolated NAFL (also called steatosis) to NASH and advanced fibrosis and cirrhosis. NAFLD can be classified into four types [418]:

- type 1: fatty liver alone
- type 2: fat accumulation and lobular inflammation
- type 3: fat accumulation and ballooning degeneration
- type 4: fat accumulation, ballooning degeneration, and fibrosis.

In this classification scheme, types 1 and 2 correspond to NAFL. The sole presence of hepatic steatosis is considered as a benign condition. Types 3 and 4 are considered as NASH. Within the NAFLD spectrum, only NASH progresses to fibrosis and to end-stage liver disease. Detection of fibrosis, inflammation or liver injury is required to discriminate NASH from NAFL. Diagnostic tests can predict the degree of liver injury without the need for liver biopsy. For example, FibroMeter<sup>9</sup> has been shown to provide good predictive value and reliable diagnosis (AUROC = 0.94) for the detection of fibrosis in patients with NAFLD [419]. Medical imaging by sonography, CT and MRI can assess hepatic fat and liver size and can help to rule out other diseases. However, standard imaging techniques do not allow accurate determination of the severity of fibrosis in NAFLD.

MRE in NAFLD has to account for the complex interaction of confounders such as steatosis and inflammation. A fundamental study in NAFLD patients shows that liver elasticity is significantly higher in case of coexisting steatosis and lobular inflammation as compared to liver elasticity in the presence of steatosis alone [93]. Otherwise, liver elasticity is highest in patients with concurrent steatosis and fibrosis [93]. MRE was found to have high accuracy (AUROC = 0.93) for discriminating patients with NASH from those with simple steatosis [93], suggesting that benign steatosis affects neither hepatic elasticity nor the assessment of liver fibrosis.

These findings are in general agreement with results obtained in animals [133]. NASH was investigated by MRE in rat models of steatosis, steatohepatitis, and acute liver injury. It was observed that viscosity increased in rats with steatosis alone, while elasticity

<sup>9</sup> FibroMeters are blood tests for liver fibrosis comprising six different tests: one for staging and one for quantitation of liver fibrosis in each of the three main causes of chronic liver disease: chronic viral hepatitis, alcoholic liver disease, and NAFLD.

remained unchanged. By contrast, rats with steatohepatitis displayed an increased elasticity and viscosity of the liver due to the simultaneous presence of steatosis, inflammation, and myofibroblast activation. The highest increase in elasticity was observed in rats with acute liver injury, while fibrogenesis and inflammation were observed without substantial fibrosis or steatosis. The results of both studies indicate that the interaction of several symptoms inherent to the spectrum of NAFLD can be resolved by MRE, providing strong evidence for the potential of MRE in NAFLD. Furthermore, elasticity and viscosity were found to increase before the onset of fibrosis, which is presumably linked to changes of the ECM structure. This finding agrees with reports on early hepatic fibrosis in a rat model mentioned in Section 15.1.2.5.

Clinical MRE studies in NAFLD proposed optimal cutoff values for the detection of mild (F1–F2) and advanced fibrosis (F3–F4) in adults and children. The best discrimination between mild and advanced fibrosis was found for an elasticity threshold of 3.63 kPa (AUROC = 0.92) in adult patients [420] and 2.71 kPa (AUROC = 0.92) in children [421].

To date, only few medications for the treatment of NAFLD [422] exist; however, a growing need for large clinical trials of new medications monitored by quantitative imaging methods can be expected. MRE and MR-derived proton density fat fraction measurements were used in one study to examine the efficacy of an intestinal cholesterol absorption inhibiting drug in reducing liver fat [423]. Although this longitudinal study did not reveal a reduction of liver fat by the drug, it showed MRE to be a reliable imaging marker for monitoring the response to drug treatment in NASH. Several studies investigated the diagnostic accuracy of MRE in NAFLD based on pooled data from different centers. Singh et al. [424] analyzed MRE data from 232 NAFLD patients with liver biopsy, demonstrating good diagnostic accuracy with AUROC values of 0.86, 0.87, 0.90, and 0.91 for detecting fibrosis of  $\geq$ F1,  $\geq$ F2,  $\geq$ F3, and F4, respectively. Diagnostic accuracy was found to be independent of the degree of inflammation present. In a study of 102 patients with biopsy-proven NAFLD, the diagnostic accuracy of MRE was compared against that of eight noninvasive clinical lab tests. A major result of this study was that MRE had a significantly higher accuracy (AUROC = 0.96) than all clinical blood markers included (AUROC = 0.80–0.86) [425]. MRE also outperformed transient ultrasound elastography (*TE*) in 142 patients with liver fibrosis ( $F > 2$ ) and steatosis [426]. Similar mean AUROC values were found for MRE- and MRI-based proton density fat fraction (0.91 and 0.9), whereas *TE* yielded lower values for both elasticity and viscosity (0.82 and 0.73). A study comparing MRE with ARFI-based ultrasound elastography in 125 patients reported a lower difference between ultrasound elastography and MRE [94]: maximum AUROC values of 0.9 and 0.93 were found for ARFI and MRE, respectively. Interestingly, no significant difference between both methods was found in nonobese patients. This suggests that due to the limited penetration depth of ARFI-based elastography, obese patients seem to be more reliably investigated by MRE. Results and technical parameters of clinical MRE studies in NAFLD are summarized in Table 15.4.

#### 15.1.3.4 Comparison with other Noninvasive Imaging and Serum Biomarkers

The diagnostic accuracy of MRE for staging liver fibrosis was tested against a variety of noninvasive biomarkers. The studies presented here compared MRE with other MR-based imaging techniques, ultrasound elastography methods, and serum biomarkers. With the advent of MRI and sonography, a number of morphologic features

**Table 15.4** Data of published MRE studies on NAFLD patients.

NAFLD patients [reference]	Stage of fibrosis	Sequence type	Encoding method	Vibration freq. (Hz)	Reconstruction	Stiffness (kPa)
58 [93]		GRE	1D	60	DI	
22 simple steatosis						2.5
7 inflammation						3.2
29 fibrosis	1–4					4.2
117 [420]	0–4	GRE	1D	60	DI	$3.2 \pm 1.2^a$
142 [92]		GRE	1D	60		
50	0					$2.8 \pm 0.6$
34	1					$3.1 \pm 0.8$
12	2					$3.6 \pm 0.9$
10	3					$5.3 \pm 2.2$
36	4					$6.4 \pm 2.0$
50 [423]	0–4	GRE	ID	60	DI	$3.3 \pm 1.1/3.2 \pm 1.1^b$
		EPI	3D	40	DI	$2.1 \pm 0.9/2.2 \pm 1.0^b$
				60		$2.7 \pm 1.3/2.8 \pm 1.2^b$
232 [424]	0–4			60–62.5		$3.6 \pm 1.4^a$
102 [425]	0–4	GRE	1D	60	DI	$3.2 \pm 1.2^a$
142 [426]		GRE	1D	60	DI	
14	0					2.2
51	1					2.6
32	2					4.3
34	3					5.2
24	4					7.9
125 [94]	0–4	GRE	1D	60	DI	$3.1 \pm 1.27^a$

**Abbreviations:** GRE – gradient echo, EPI – echo planar imaging, 1D – single displacement field component, 3D – full displacement field, DI – direct inversion.

a) Average over all patients.

b) Baseline values of longitudinal study averaged over drug and placebo group, respectively.

“Stiffness” relates to  $|G^*|$  or  $G'$ , depending on the study. All values are given as group mean  $\pm$  standard deviation (if available).

were identified and have since been extensively used for the diagnosis of hepatic fibrosis. Different sets of features have been proposed for the best possible staging of liver fibrosis. One set of features includes (i) the texture of liver parenchyma, (ii) surface nodularity, (iii) signs of volumetric changes, and (iv) portal hypertension [409]. Another study [427] used a combination (i) the ratio of caudate to right lobe volume, (ii) nodularity, (iii) indirect assessment of portal venous hypertension, for example, due

to esophageal varices, (iv) posterior hepatic notch, (v) expanded gallbladder fossa, and (vi) right hepatic vein caliber. The use of both sets of morphology-based parameters showed a significantly lower diagnostic accuracy for the staging of fibrosis than MRE. AUROC values reported in [409] ranged between 0.71–0.81 and 0.61–0.80, which is significantly lower than the values reported for MRE (0.99 and 0.94, respectively).

Similar to MRE, diffusion-weighted imaging (DWI) is sensitive to tissue structures and promises sensitivity to liver fibrosis. However, a number of studies [428–431] showed that MRE outperforms DWI in discriminating different fibrosis stages (AUROC values 0.98 for MRE and 0.86 for DWI). An interesting option is the combination of DTI and MRE in the same examination, which is accomplished by deriving diffusion information from MRE motion-encoding gradients (see Section 3.3) [35]. It remains to be validated whether such a multiparametric approach can further improve staging of liver fibrosis.

Transient ultrasound elastography (*TE*) is a simple and cost-effective noninvasive method for the staging of liver fibrosis. Although confounding factors such as ascites and obesity exist, the method has been used more widely than other elastography methods for liver imaging. Due to methodological differences, absolute numbers of viscoelastic parameters measured by *TE* and MRE are not necessarily comparable. In a cross-validation study in cohorts with low and high grades of fibrosis, elasticities measured by *TE* were significantly different from those obtained with [432] for low and high fibrosis stages. By contrast, a phantom study covering the elasticity range typical for fibrosis patients (1–8 kPa) [433] showed no evidence of a systematic difference between MRE and *TE*. Published reports on the diagnostic accuracy of MRE compared to *TE* are somewhat inconsistent. A 3D EPI-based MRE study reported similar accuracy for *TE* [434] (AUROC MRE vs *TE*: 0.91 vs 0.91 for  $\geq F2$ , 0.93 vs 0.90 for  $\geq F3$ ). By contrast, a more recent study [91] based on analysis of 2D wave images found significantly higher diagnostic accuracy for MRE than for *TE* (AUROC MRE vs *TE*: 0.97 vs 0.87 for  $\geq F1$ , 0.98 vs 0.87 for  $\geq F2$ , and 0.97 vs 0.93 for  $F4$ ).

A comprehensive study [435] comparing MRE and ARFI-based elastography found MRE to be more accurate than ARFI, particularly in diagnosing early stages of hepatic fibrosis (AUROC MRE vs ARFI: 0.94 vs 0.82 for  $\geq F1$ , 0.97 vs 0.85 for  $\geq F2$ , 0.96 vs 0.94 for  $\geq F3$ , and 0.97 vs 0.94 for  $F4$ ).

Studies comparing ultrasound-based shearwave elastography (SWE) with MRE [436] showed similar diagnostic accuracy for both methods (AUROC: 0.99 for  $F4$  [436] and 0.85 for  $\geq F2$  [437]). Moreover, the number of patients who were successfully examined with both methods was comparable ( $\sim 96\%$ ) [437]. However, the sensitivity for the diagnosis of fibrosis  $\geq F2$  was significantly higher for MRE than SWE [437]. An earlier systematic review addressing the diagnostic accuracy and technical performance of several imaging modalities including DWI, ultrasonography (US), Doppler US, contrast-enhanced US, *TE*, ARFI, SWE, and MRE [438] found that most of these modalities allowed differentiation of normal and cirrhotic livers but failed in detecting mild fibrosis. DWI, MR elastography, and US elastography seemed to be the best candidates for accurate staging of hepatic fibrosis. At this time, only MRE was able to stage fibrosis or to diagnose mild degrees of fibrosis. Comparison of MRE with the serum-based aspartate aminotransferase-to-platelet ratio index (APRI) test found MRE to be superior [408] (AUROC MRE elasticity vs MRE viscosity: 1.00 and 0.86 for  $\geq F2$ , 1.00 and 0.96 for  $\geq F3$ , and 1.00 and 0.99 for  $F4$  compared to AUROC APRI: 0.85 for  $\geq F2$ , 0.89 for  $\geq F3$ , and 0.85 for  $F4$ ).

**Table 15.5** Noninvasive biomarkers of liver fibrosis.

Method	Parameter	AUROC <sup>a)</sup>			
		ALD	NAFLD	HCV	HBV
Fibrotest	Age, sex, bilirubin, GGT, $\alpha$ 2-M, haptoglobin, Apo-A1	0.83 [439]	0.85 [440]	0.85 [441]	0.78 [442]
Hepascore	Age, sex, bilirubin, GGT, $\alpha$ 2-M, HA	0.83 [439]	0.75 [443]	0.83 [444]	0.76 [445]
Fibrometer	Age, AST, platelets, $\alpha$ 2-M, HA, prothrombin index, urea	0.79 [389]	0.94 [419]	0.86 [446]	0.78 [445]
APRI	AST, platelets	0.59 [439]	0.73 [447]	0.76 [448]	0.72 [445]
ELF panel	Age, HA, TIMP-1, PNPIII	n.a.	0.82 [449]	0.82 [450]	n.a.
<i>TE</i>	Shear modulus	0.83 [451]	0.94 [452]	0.91 [453]	0.90 [454]
ARFI	Shear modulus	0.87 [455]	0.90 [456]	0.81 [457]	0.80 [458]
SSI	Shear modulus	0.95 [459]	0.88 [460]	0.95 [461]	n.a.
MRE	Shear modulus	0.92 [389]	0.96 [425]	0.98 [394]	0.96 [390]

a) Mean AUROC over all fibrosis stages.

Numbers in brackets denote literature references.

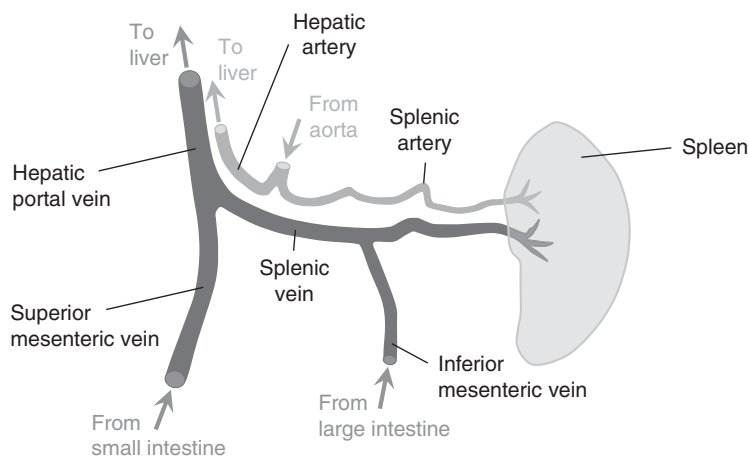
**Explanation:** ELF: European liver fibrosis panel, *TE*: transient elastography, ARFI: acoustic radiation force impulse ultrasound elastography, SSI: supersonic ultrasound elastography, Apo-A1: apolipoprotein-A1, AST: aspartate aminotransferase,  $\alpha$ 2-M:  $\alpha$ 2-macroglobulin, bilirubin: breakdown product of heme catabolism, GGT: Gamma-glutamyltransferase, HA: hyaluronic acid, haptoglobin: protein produced in the liver, platelets: correlate with thrombocyte concentration, PNPIII: procollagen N-terminal peptide III, prothrombin index: derived from measuring the clotting tendency of blood, TIMP-1: tissue inhibitor of metalloproteinases-1, n.a.: not available.

In essence, MRE is currently one of the most precise imaging modalities for the staging of liver fibrosis and outperforms most other noninvasive biomarkers. At present, only SWE shows a comparable high diagnostic performance. With improved elastography methods using both MRE and ultrasound, a further increase in diagnostic precision for early stages of hepatic fibrosis can be expected. An overview of the diagnostic accuracy of selected noninvasive serum and imaging biomarkers of liver fibrosis is given in Table 15.5 (see also Section 15.1.2.3 for the categorization of serum biomarkers).

#### 15.1.3.5 MRE of the Liver for Assessing Portal Hypertension

The liver is supplied with blood by two separate vascular circuits: the arterial system originating from the aorta for maintenance of vital liver functions and the hepatic portal venous system, which consists of numerous veins and tributaries, including the hepatic portal vein (see Figure 15.14). The portal venous system is responsible for directing blood from parts of the gastrointestinal tract into the liver. A proportion of 75% of the liver's blood supply depends on other organs including venous drainage from the gut, spleen, and pancreas. The multiscale hierarchic blood flow in the liver contributes to the

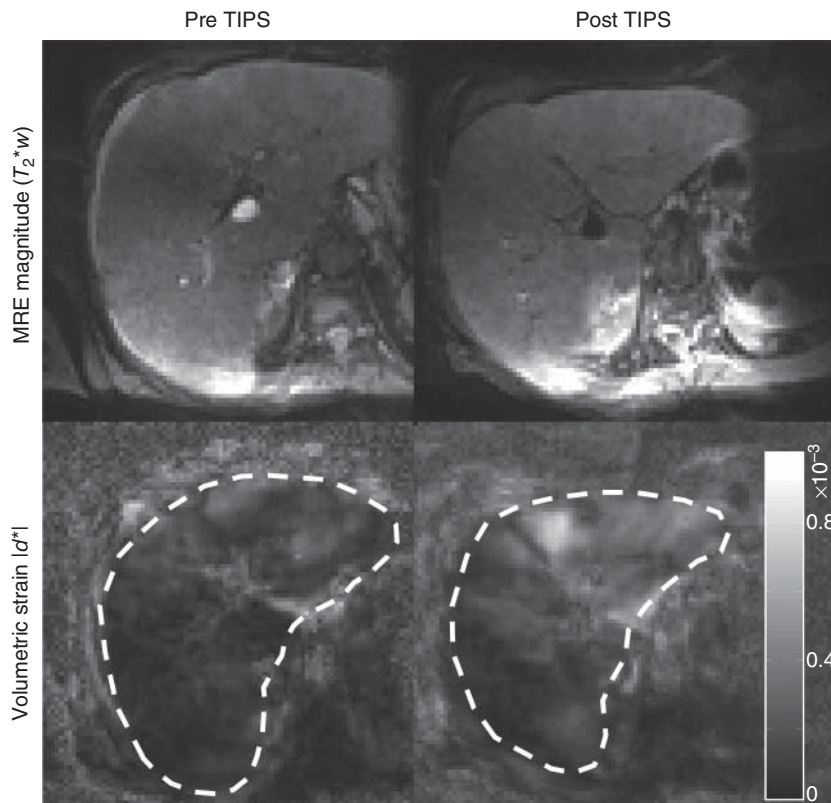




**Figure 15.14** Schematic representation of major vessels of the hepatic portal system. The hepatic portal vein is one of the largest veins in the abdomen, connecting the spleen and the gastrointestinal tract with the liver. The hepatic vein, which begins at the junction of the splenic vein and the superior mesenteric vein, drains the blood coming from the large and small intestine as well as from the spleen into the liver.

effective medium viscoelastic properties on the macroscopic scale [462]. The shear modulus measured by MRE in the liver reflects not only a solid tissue property but also fluid properties such as volume, viscosity and pressure of the blood phase and mechanical coupling between fluid phase and solid tissue. Conversely, the mechanical properties of the solid phase influence vascular flow in the liver. Increased flow resistance due to liver fibrosis results in portal hypertension, which contributes to the development of severe, frequently life-threatening complications such as ascites, esophageal varices and hepatic encephalopathy.

The gold standard for assessing portal hypertension is to measure the hepatic venous pressure gradient (HVPG) through invasive hepatic vein catheterization. MRE can be used to diagnose portal hypertension either based on the sensitivity of the effective medium shear modulus to liver perfusion or by directly assessing the compression properties of the liver through the measurement of volumetric strain. By nature of the intimately linked hepatic and splanchnic vasculature, MRE in portal hypertension has been concerned with both organs. We will therefore review more studies related to portal hypertension in the section dedicated to the spleen. Besides the shear modulus, volumetric strain measured by MRE can potentially serve as a biomarker for elevated HVPG values [356]. The idea and the basic concepts of compression-sensitive MRE are outlined in Chapter 5. A simple version of compression-sensitive MRE uses fast 3D vector field MRE followed by decomposing the wave field into its shear part (by the curl operator) and compression part (by the divergence operator). This approach was demonstrated in *ex vivo* sheep liver whose portal vein was connected to a water reservoir for adjusting portal inflow pressure [356]. While volumetric strain decreased with excess pressure in the portal vein, the shear field did not change. The same method was used in patients with pathologically increased HVPG (Figure 15.15), showing a significant increase in volumetric strain after reduction of HVPG as a result of decompression of the liver after a transjugular intrahepatic portosystemic shunt



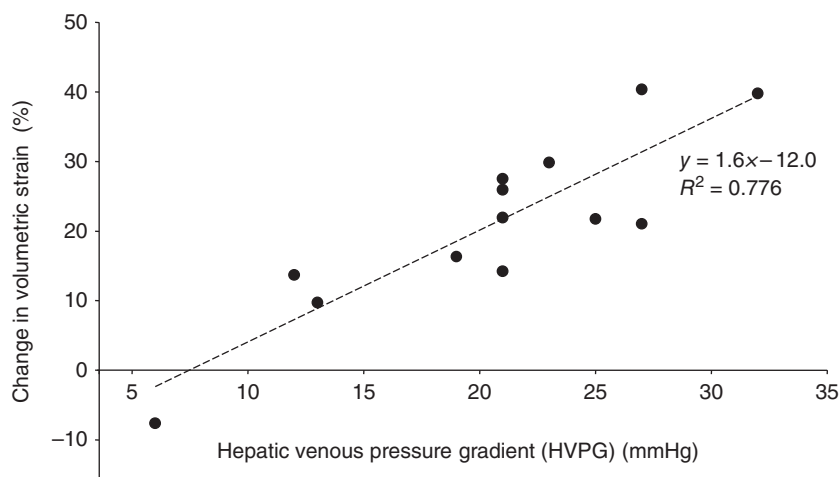
**Figure 15.15** Normal  $T_2$ -weighted MRI and maps of volumetric strain in a patient with hepatic hypertension before and after TIPS intervention demonstrating an increase in volumetric strain (reduced compression modulus) following TIPS. (Hirsch 2014 [356]. Reproduced with permission of Wiley.)

(TIPS<sup>10</sup>) procedure (Figure 15.16). Although this study did not reveal a significant effect of TIPS on the shear modulus of the liver, a more recent study based on MMRE and MDEV inversion showed exactly this [95]. However, it should be noted that decompression of the liver spleen vascular system by TIPS is more pronounced in the spleen. For this reason, other MRE studies and ultrasound-based elastography in portal hypertension focused on the spleen since the liver – due to abundant connective tissue in severe fibrosis stages – was reported to be less responsive to the relief of portal venous pressure by TIPS [95].

#### 15.1.3.6 MRE in Liver Grafts

Effective noninvasive methods for assessment of liver fibrosis are needed to guide transplant decisions, to monitor posttransplant structural changes, and to predict the risk of graft failure. In this context, MRE has successfully been used for the noninvasive

<sup>10</sup> TIPS is a procedure to create a direct connection between the portal vein and the hepatic vein. It is primarily used in patients with cirrhosis causing increased resistance to blood flow by architectural changes of the liver parenchyma.



**Figure 15.16** Linear regression analysis of the relative change in volumetric strain after TIPS versus HVPG. (Hirsch 2014 [356]. Reproduced with permission of Wiley.)

identification of appropriate donors and for identifying potential recurrence of liver fibrosis in transplanted organs and the heterogeneity of fibrosis progression based on MRE-guided biopsies.

Increased stiffness due to mild fibrosis and NASH, both contraindications to liver donation, was observed with MRE with AUROC values of 0.85 for  $F \geq 1$  [463]. For the stiffness-based detection of recurrent severe fibrosis ( $F \geq 3$ ) in liver transplant recipients, AUROC values of 0.92 [464] and 0.87 [465] were reported. Both studies reported lower AUROC values for staging lower grades of fibrosis (e.g., 0.65 for  $F \geq 2$  [465]) and no sensitivity was observed for the springpot parameter  $\alpha$  [465]. This finding suggests an influence of unknown confounding factors on the MRE-measured variables in liver grafts.

MRI-guided biopsy based on MRE data was proposed in a study which investigated the heterogeneity of fibrosis progression in transplant recipients [356]. This allowed a significant histology-based intraindividual discrimination of low- and high-grade fibrosis suggesting a nonuniform progression of liver fibrosis. Regional analysis by high-resolution MRE of the liver is becoming increasingly important to further improve the imaging-based characterization of liver fibrosis not only in transplant livers but also in all CLD independent of etiology.

#### 15.1.3.7 Confounders

Early studies showed that MRE in liver fibrosis is neither affected by the fat content of the liver [93, 399] nor by administration of contrast agents [466, 467]. However, ultrasound-based elastography studies in animal models and patients clearly demonstrated a decrease in elasticity due to the amount of fat in the liver [468, 469]. The influence of the postprandial state on MRE-measured liver elasticity was analyzed with partially controversial results. An MRE study of healthy volunteers showed no effect of food intake [470], whereas another study of volunteers and patients demonstrated liver stiffness to increase postprandially [471]. A postprandial increase was confirmed by time-harmonic elastography based on ultrasound, which was found to be sensitive

to pure water ingestion [472]. The guidelines for ultrasound elastography [473] include the postprandial status as confounder, and a defined fasting state is recommended for patients undergoing ultrasound elastography of the liver. Other studies demonstrated increased liver elasticity in an animal model of isolated portal hypertension [474] or, clinically more relevant, in the presence of active hepatitis [475] and necroinflammation in mild fibrosis [476]. Ultrasound elastography further demonstrated an overestimation of liver elasticity in patients with extrahepatic cholestasis [477] and congestive heart failure [478]. Although fewer confounders have been reported for MRE, similar sensitivities to liver perfusion, portal pressure, cholestasis, and fat accumulation as encountered in ultrasound elastography can be expected for MRE.

## 15.2 Spleen

The spleen is located in the left upper abdominal cavity (see Figure 15.1) and consists of a tree of branching arterial vessels, in which the smaller arterioles end in a venous sinusoidal system. The parenchyma of the spleen is divided into two types of tissue, red and white pulp. The red pulp constitutes the bulk of the splenic volume and is composed of a network of cell cords arranged in series with vascular sinuses. The splenic cords contain macrophages, plasma cells, lymphocytes, and other mature blood cells such as granulocytes and erythrocytes. White pulp is made up of lymphoid tissue that forms sheaths around the smaller branches of the arterial tree and contains T cells, B cells, and macrophages. Thus, the spleen is a major lymphoid and blood filtration organ responsible for antibacterial and antifungal immune reactivity as well as removal of older erythrocytes, blood-borne microorganisms, and cellular debris.

The spleen is also part of the hepatic portal system (see Figure 15.14). Due to the circulatory link between the liver and spleen, many diseases affect both organs. As mentioned earlier, portal hypertension alters blood flow throughout the hepatosplanchnic venous system and affects perfusion in the connected organs. Splenic syndromes such as splenomegaly are associated with severe complications of portal hypertension including ascites, esophageal varices, and hepatic encephalopathy. Being less prone to fibrosis than the liver, the spleen is more compliant to changes in vascular perfusion pressure as caused by portal hypertension. The resulting increase in effective stiffness of the spleen may render elastography sensitive to the noninvasive detection of portal hypertension. While invasive hepatic vein catheterization continues to be the gold standard for quantification of portal hypertension, it cannot routinely be used for diagnostic purposes only. Other possible noninvasive markers of portal hypertension such as spleen size or serum markers have limited diagnostic accuracy.

### 15.2.1 MRE of the Spleen

In healthy subjects, the spleen is stiffer than the liver as demonstrated by the elastograms shown in Figure 15.12. This figure presents a standard transverse MRE view through the liver, which also covers the spleen, thus underlining that both organs should be examined at the same time. Normal values of splenic stiffness measured by MRE were established in [479] with consideration of a number of physiologic parameters such as body mass index, arterial mean blood pressure, age, spleen volume, and liver stiffness. The results

**Table 15.6** MRE-measured stiffness of the spleen from the literature.

Study [reference]	Sequence type	Encoding method	Vibration freq. (Hz)	Reconstruction method	Stiffness spleen (kPa)	Stiffness liver (kPa)
16 volunteers [479]	GRE	1D	60	LFE	4.3 ± 0.6	
12 volunteers [97]	GRE	1D	60	LFE	3.6 ± 0.3	
38 patients					5.6 ± 5.0	
10 patients [95]	EPI <sup>a)</sup>	3D	25–60	MDEV		
Pre-TIPS					8.4 ± 1.4	8.3 ± 2.2
Post-TIPS					7.1 ± 1.3	7.0 ± 1.5
93 patients [480]	GRE	1D	60	DI		
49 no GEV					6.5 ± 2.1	4.0 ± 1.4
30 mild GEV					8.5 ± 2.9	5.6 ± 2.3
14 severe GEV					9.8 ± 1.7	6.1 ± 1.6
139 patients [481]	EPI <sup>a)</sup>	3D	60	LFE		
94 mild GEV					7.1	5.1
45 severe GEV					9.1	7.1
126 patients [482]	GRE	1D	60	LFE		
102 mild GEV						5.8 ± 2.3
24 severe GEV						8.5 ± 2.2
49 patients [483]	GRE	3D	60	DI		
40 noncirrhotic					5.2 ± 1.3	2.6 ± 1.2
9 cirrhotic					8.2 ± 2.0	4.6 ± 1.1
36 cirrhosis patients [96]	GRE <sup>a)</sup>	3D	28	DI	0.8	0.6
			56		4.4	3.1
			84		8.3	6.1

**Abbreviations:** 1D: single displacement field component, 3D: full displacement field, GRE: gradient echo, EPI: echo planar imaging, LFE: local frequency estimation, DI: direct inversion, MDEV: multifrequency dual elasto-visco inversion, TIPS: transjugular intrahepatic portosystemic shunt, GEV: gastro esophageal varices.

a) Fractional motion encoding.

“Stiffness” refers to  $\rho \cdot c^2$  (for LFE),  $|G^*|$  or  $G'$  (for DI, not specified), and  $|G^*|$  for MDEV inversion. Stiffness values are given as group mean value ± standard deviation (if available).

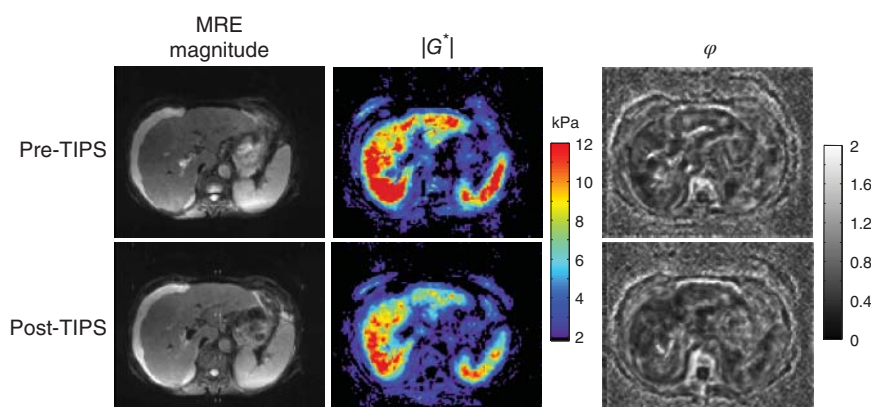
suggest that spleen stiffness is not significantly influenced by any of the physiologic criteria taken into consideration by the investigators. However, the investigators also used different actuator positions and found an effect on the results. Talwalkar et al. [97] shows that splenic elasticity is higher in patients with liver fibrosis than in healthy volunteers and that the stiffness values of the liver and spleen are correlated. Table 15.6 summarizes technical parameters and basic results from the literature on *in vivo* MRE of the human spleen compared to liver values.

The effect of portal hypertension on splenic stiffness was studied in a canine model of cholestatic chronic liver disease [164]. In this study, splenic and hepatic stiffness measured by MRE correlated well with the invasively measured HVPG. The results were confirmed by MRE in a porcine model of intra-arterial dextran infusion, which allowed the authors to adjust the level of portal hypertension [474]. Again, the stiffness values of both the liver and spleen were highly correlated with portal pressure.

Portal hypertension can be treated by the implantation of a TIPS, which diverts blood flow from passing through the liver by establishing a direct connection between portal and hepatic veins. HVPG is reduced after successful TIPS placement, making the intervention an appropriate model for testing the sensitivity of clinical MRE to portal hypertension. In [95], MMRE of the liver and spleen was performed in patients with portal hypertension before and after TIPS placement. This study reported a reduction of HVPG by TIPS based on the MRE-measured viscoelasticity ( $|G^*|$ ) in both the liver and spleen (see Figure 15.17). Notably,  $|G^*|$  was more sensitive to HVPG in the spleen as compared to liver values, giving rise to the correlation between relative changes in HVPG and relative changes in splenic viscoelasticity (see Figure 15.18).

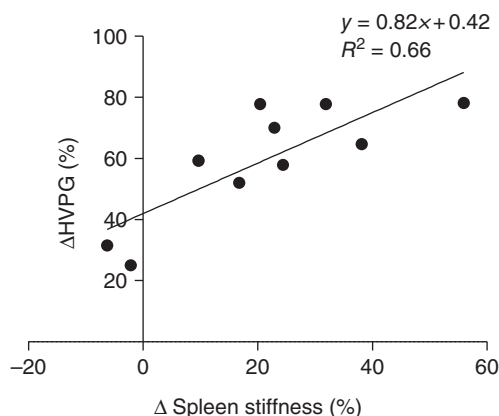
The diagnostic accuracy of spleen and liver elasticity for the prediction of esophageal varices was investigated in [95]. Liver elasticity, spleen elasticity, and spleen volume identified gastroesophageal varices in patients with chronic liver disease with AUROC values of 0.75, 0.76, and 0.73, respectively [95]. The high diagnostic value of splenic elasticity for detection of esophageal varices was confirmed by Shin et al. [481], reporting an AUROC value of 0.83. Additionally, the authors compared the diagnostic value of splenic elasticity with that of dynamic contrast-enhanced MRI, geometry (spleen length) and liver elasticity, which gave similar or lower results (AUROC = 0.84, 0.70, and 0.82, respectively). The highest diagnostic accuracy in the prediction of esophageal varices was reported by Sun et al. [482] for liver elasticity (AUROC = 0.86).

Viscosity-related parameters in the spleen are still subject of research. Encouraging findings were obtained in an MRE study of cirrhotic patients which included an analysis of splenic viscoelasticity, HVPG, and endoscopy to assess esophageal varices [96]. It was shown that splenic viscosity based on the loss modulus  $G''$  best enabled detection of



**Figure 15.17** MRE magnitude images and corresponding elastograms of a patient before and after TIPS demonstrating lower  $|G^*|$  values in liver and spleen in the post-TIPS experiment. (Guo 2015 [95]. Reproduced with permission of Wolters Kluwer.)

**Figure 15.18** Linear correlation between relative changes in spleen stiffness and relative changes in the HVPG ( $P = 0.013$ ). No such correlation was found for the liver. The relative changes are shown as percentages calculated by dividing the difference of pre-TIPS and post-TIPS values by the pre-TIPS values. (Guo 2015 [95]. Reproduced with permission of Wolters Kluwer.)



severe portal hypertension and high-risk esophageal varices (AUROC = 0.81 and 0.93, respectively), while liver and spleen elasticity were not correlated with HVPG.

The potential value of splenic viscosity for detection of an altered tissue perfusion is also indicated by  $\varphi$ , the phase angle of  $G^*$  retrieved by MDEV inversion [95, 98]. These studies reported higher  $\varphi$  values in the spleen in patients with hepatic fibrosis than in healthy volunteers ( $0.85 \pm 0.19$  (pre-TIPS) vs  $0.64 \pm 0.15$  [95]). However, the cause of higher  $\varphi$  values in patients is still unclear since, unlike  $|G^*|$ ,  $\varphi$  was not correlated with HVPG, suggesting an effect of an altered tissue structure such as vascular tree geometry or fibrosis rather than perfusion pressure.

### 15.3 Pancreas

The pancreas is part of the portal hepatic system and is important for proper digestion. It is supplied with blood by branches of the splenic, hepatic, and superior mesenteric arteries and is drained by veins that open into the portal vein. The pancreas is composed of exocrine and endocrine tissues. The exocrine pancreas is the larger part and secretes enzymes (pancreatic juice) for carbohydrate, protein, and fat digestion. The pancreatic juice is drained through the pancreatic duct, which merges with the common bile duct originating from the gallbladder and liver. The combined pancreatic juice and bile finally drain into the duodenum (see Figure 15.1). The duodenum is the first part of the small intestine that receives partially digested food from the stomach, absorbs nutrients, and passes digested food to the jejunum. A small number of the cells in the pancreas are endocrine cells secreting hormones for the regulation of blood glucose concentration, such as insulin and glucagon, into the blood. Insulin lowers the amount of sugar in the blood by stimulating the liver, muscles, and fatty tissues to absorb and store glucose. The antagonist of insulin is glucagon, which increases the amount of sugar in the blood by stimulating the liver and other tissues to release stored sugar.

The detection of pancreatic diseases is limited by the relative inaccessibility of the pancreas, being located behind the stomach and surrounded by other organs, such as the spleen, liver, and small intestine. Despite progress in blood testing and imaging-based detection and characterization, there are instances in which surgical

exploration is the only way to confirm the diagnosis of pancreatic disease. Pancreatic cancer is the fourth most common cause of cancer death in men and the fifth in women, growing insidiously over years with inconspicuous symptoms. It is resistant to many standard treatments including chemotherapy and radiation therapy. If detected early, pancreatic cancer can be cured by surgical resection. However, differentiation of pancreatic cancer from other diseases such as chronic pancreatitis can be difficult. Chronic pancreatitis is a progressive disorder associated with the destruction of the pancreas. Patients with advanced chronic pancreatitis may develop diabetes mellitus.

### 15.3.1 MRE of the Pancreas

The number of reports on elastography, including ultrasound methods, for assessment of the pancreas is still small. It still remains to be determined to which extent mechanical properties of the pancreas vary with disease. Therefore, current ultrasound elastography practice guidelines do not recommend elastography-based imaging and analysis for diagnostic evaluation of the pancreas [241]. However, tissue stimulation by time-harmonic waves as used in MRE is potentially better suited to efficiently excite the very soft and viscous pancreatic tissue, which is surrounded by mechanically absorbing tissues and organs, than transient ultrasound elastography methods. For this reason, efforts have been undertaken to utilize MRE for examinations of the pancreas. Shi et al. proposed a pancreatic MRE setup using the Resoundant system for inducing 40 and 60 Hz vibrations, EPI-MRE with fractional encoding and 3D direct inversion [100]. Mean stiffness values (based on  $\rho \cdot c^2$  according to Eq. (4.154)) in a group of 20 healthy volunteers were  $1.2 \pm 0.2$  kPa for 40 Hz, and  $2.1 \pm 0.3$  kPa for 60 Hz, suggesting very soft tissue properties. Similar values were measured in the liver at 60 Hz ( $2.1 \pm 0.2$  kPa), whereas stiffness of the liver was higher at 40 Hz ( $1.6 \pm 0.2$  kPa), indicating stronger viscoelastic dispersion of pancreatic tissue compared to liver tissue. Furthermore, the results suggest that the use of lower vibration frequencies is preferable since the intrasubject variation coefficient was lower at 40 Hz than 60 Hz. Although this sole study of pancreatic MRE needs to be reproduced and extended in a clinical pilot study, these very encouraging results suggest that MRE is a promising candidate for staging chronic pancreatitis and for early detection, differential diagnosis and treatment monitoring in patients with pancreatic cancer.

## 15.4 Kidneys

The kidneys are composed of highly complex tissues such as the outer renal cortex and the inner renal medulla. Each kidney hosts 8–18 cone-shaped renal lobes known as the renal pyramids. Each pyramid comprises a segment of the outer renal cortex and the inner renal medulla (see Figure 15.1). The smallest functional units of the kidney are the nephrons, which extend from the cortex via medulla into collecting ducts and hilus for drainage of urine. The main task of the kidneys is related to blood filtration. From a total of 900 l of blood passing both kidneys per day, 160 l of water are washed out, from which 158 l become reabsorbed, while 2 l of urine remain as waste [484]. This intricate filter function is accomplished in millions of nephrons and is important for maintaining extracellular homeostasis of pH and blood components such as glucoses



and electrolytes. Kidney failure causes a number of syndromes that affect other organs or the entire cardiovascular system. For this reason, early detection of renal dysfunction is of great importance for initiating or adapting treatment to improve long-term outcome and preserve native kidney function or to ensure renal graft survival in kidney transplant recipients. Current clinical practice relies on a multimodal approach including blood tests (serum creatinine level) and urinalysis for evaluating kidney function, and routine biopsy for histology. However, there are no specific biochemical markers for chronic renal injury in general. MRE might be a suitable biomarker of renal function for two reasons: (i) its sensitivity to the effective perfusion pressure in highly perfused organs such as the spleen and (ii) its sensitivity to fibrosis and excessive ECM accumulation. Renal fibrosis – a severe condition which develops in virtually every type of chronic kidney disease – is associated with increased tissue stiffness [485]. On the other hand, the kidneys are shielded by the vertebra and spinal muscles, which has so far limited *in vivo* studies of MRE and ultrasound elastography in the native kidneys. Furthermore, renal tissue is – on the macroscopic scale – more complex than liver tissue, featuring a high degree of heterogeneity and anisotropy, which poses a great challenge for measurement of meaningful *in vivo* viscoelasticity constants [486].

#### 15.4.1 MRE of the Kidneys

Preclinical renal MRE has been performed to assess renal fibrosis in the cortex [138], deposition of calcium salts in the renal medulla (nephrocalcinosis) [139], and the influence of blood circulation on renal stiffness [487]. In [138], renal fibrosis secondary to renal artery stenosis was studied in a pig model. Despite histological evidence of renal fibrosis, MRE detected increased stiffness only in the medulla while cortical stiffness was not significantly different from normal. In [139], a decrease in renal blood flow led to a gradual decrease of cortical stiffness while medullary stiffness decreased only when there was total interruption of blood flow. Both results suggest that hemodynamic variables may modulate kidney stiffness measured by MRE and may mask the presence of fibrosis. By contrast, deposition of calcium salts in the medulla led to an increase in stiffness persisting even beyond calcium exposure. This might also be attributed to altered fluid dynamics. Altogether, these preclinical experiments suggest that renal stiffness measured by MRE is highly influenced by hemodynamic factors.

So far, most human MRE studies addressed the feasibility and reproducibility of MRE or optimization of imaging protocols. To maximize the pixel count of kidney parenchyma, a coronal slice orientation has been proposed [488]. Gradient-echo MRE was optimized to achieve high accuracy of 6% test–retest variability [103] despite the long scan times of 56–105 min. More recent publications proposed fast single-shot spin-echo EPI-MRE [489] and demonstrated high repeatability and interrater agreement. MMRE based on single-shot EPI and MDEV inversion has been proposed recently by Streitberger et al. [102]. The total acquisition time of less than 10 min achieved in this study [102] may allow incorporation of this examination into clinical MRI protocols. Renal cortex, medulla, and hilus showed significant differences in elasticity (see Table 15.7 and Figure 15.19a).

Renal MRE in patients is preferably performed in transplant kidneys due to the better accessibility compared with native kidneys. Lee et al. [104] investigated kidney recipients in whom fibrosis was determined by needle biopsy according to the Banff score.

The authors discussed the small sample size, missing baselines studies of renal stiffness immediately after transplantation, and technical limitations as possible reasons for a nonsignificant correlation between renal stiffness and fibrosis. The feasibility of MRE for detection of decreased renal function in patients with hepatorenal syndrome was demonstrated in [168]. Renal elasticity was significantly lower in patients with impaired kidney function compared to patients with normal kidney function. The reported AUROC values increased with increasing vibration frequencies (AUROC=0.89 at 60 Hz vs 0.94 at 90 Hz), indicating the need for a large enough number of shear waves in smaller organs for direct inversion at a single frequency. In a recent study [222],  $k$ -MDEV inversion (see Section 10.6) was used to address this issue by reevaluating data from [102]. Figure 15.19 demonstrates the superior wavespeed contrast in the kidney as compared to noise-sensitive MDEV inversion.

A compilation of published viscoelastic parameters measured by renal MRE is presented in Table 15.7.

**Table 15.7** Results of renal MRE studies in healthy volunteers and kidney transplant recipients

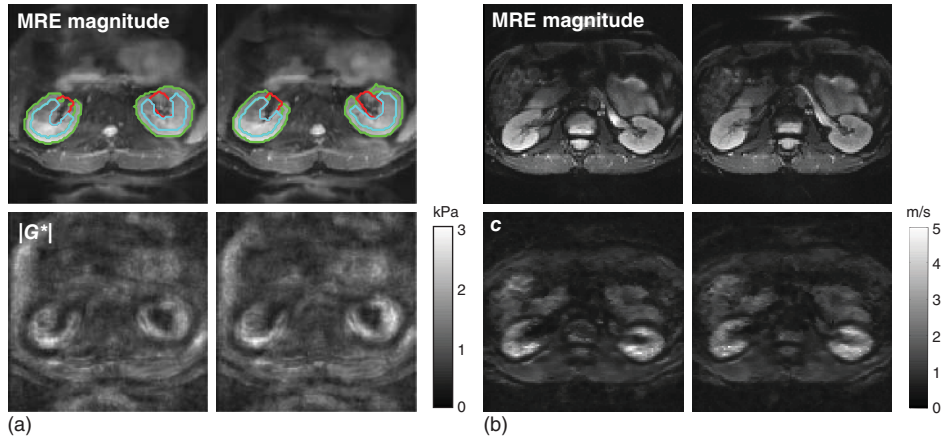
Study [reference]	Actuator position	Encoding method	Vibration freq. (Hz)	Recon-struction	Stiffness renal hilus (kPa)	Stiffness medulla (kPa)	Stiffness cortex (kPa)
11 volunteers [488]	Below ribcage	1D	60	LFE	6.8 ± 0.1	5.5 ± 0.5	4.4 ± 0.3
10 volunteers [103]	Back/under kidneys	3D	45	LFE		5.4 ± 0.7	4.8 ± 0.6
			76			9.6 ± 1.4	9.4 ± 1.0
16 volunteers [489]	Back/under kidneys	3D	60	LFE		− 3.5 ± 0.5 <sup>R</sup> , 3.5 ± 0.5 <sup>L</sup>	–
			90			− 6.0 ± 3.4 <sup>R</sup> , 5.4 ± 1.9 <sup>L</sup>	–
9 volunteers [102]	Kidney belt	3D	30–60	MDEV	1.2 ± 0.2	2.7 ± 0.5	1.6 ± 0.2
Ktx patients [104]	Over allograft	3D	90	DI			
1 ns							− 6.9 <sup>a)</sup> –
6 mild							− 6.0 <sup>a)</sup> –
2 mod							− 7.2 <sup>a)</sup> –
HRS patients [168]	Back/under kidneys	3D	60/90	LFE			
6 normal function							− 3.4 <sup>a)</sup> /5.1 <sup>a)</sup> –
14 reduced function							− 2.6 <sup>a)</sup> /3.3 <sup>a)</sup> –

**Abbreviations:** 1D: single displacement field component, 3D: full displacement field, LFE: local frequency estimation, MDEV: multifrequency dual elasto reconstruction, DI: direct inversion, R,L: group mean value of stiffness for entire right/left kidneys ± standard deviation values given in brackets represent group mean values of stiffness for whole kidneys.

a) Group mean value of stiffness of kidneys without hilus ± standard deviation (if available).

Ktx: kidney transplant recipients, ns: no significant fibrosis, mild: mild fibrosis, mod: moderate fibrosis (fibrosis staging according to Banff score), HRS: hepatorenal syndrome.

Stiffness corresponds to  $\rho \cdot c^2$  according to Eq. (4.154) for LFE and DI whereas for MDEV inversion,  $|G^*|$  is reported. Stiffness values are given as group mean value ± standard deviation (if available).



**Figure 15.19** Renal MRE. (a) MMRE and MDEV inversion of central slices in a healthy volunteer. The anatomical regions for spatial averaging of  $|G^*|$  are encircled by green (cortex), cyan (medulla), and red (hilus) lines. (Streitberger 2014 [102]. Reproduced with permission of Elsevier.) (b) MMRE and  $k$ -MDEV inversion showing superior detail resolution in the wavespeed maps.

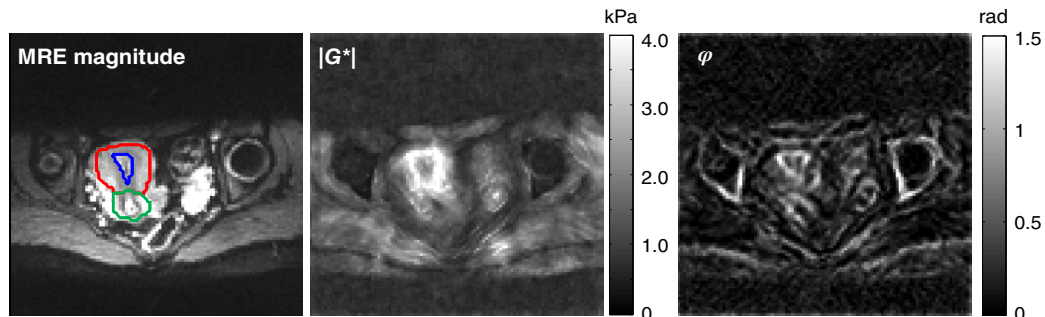
## 15.5 Uterus

The uterus is a major female reproductive organ and mostly consists of a smooth muscle layer known as myometrium, which surrounds the uterine cavity. The endometrium is the inner layer of the myometrium adjacent to the uterine cavity. The functional layer of the endometrium is built up periodically during the menstrual cycle under the influence of ovarian hormones and are shed or reabsorbed if no pregnancy occurs. The perimetrium is the outer layer enveloping the uterus. The cervix connects the body of the uterus with the vagina (see Figure 15.1).

MRE may contribute to the differentiation of benign uterine fibroids or leiomyomas from cervical cancer. Both conditions present with the same clinical symptoms of pain and bleeding. Uterine fibroids are estrogen-dependent benign tumors that originate in the smooth muscle layer of the uterus. They are one of the most common health problems in women during the third and fourth decades of life. As fibroids are muscular in origin and have a solid consistency, they are stiffer than the uterine fundus. Cervical cancer is the most common malignancy of the genital tract in women. Malignant lesions are significantly stiffer than healthy tissue [490].

### 15.5.1 MRE of the Uterus

So far, only two MRE studies of the uterus have been published [105, 166]. Challenges of uterine MRE are related to the irregular shape and high heterogeneity of the uterus, periodically varying baseline values and high wave attenuation for mechanical stimulation. In published work, piezoelectric [105] and pneumatic [166] actuators were employed, both positioned on the anterior surface directly above the uterine cervix. Baseline values for healthy volunteers taking different phases of the menstrual cycle and regional variations into account were reported in [105]. The study combined multifrequency EPI-MRE in the frequency range from 30 to 60 Hz with MDEV inversion. An intriguing finding



**Figure 15.20** MMRE of the uterus from [105]. Shown are standard  $T_2$ -weighted MRI (MRE magnitude),  $|G^*|$ , and  $\varphi$  in a representative image slice of the uterus of a healthy volunteer. The uterine corpus, endometrium, and cervix are demarcated by red, blue, and green lines, respectively. (Jiang 2014 [105]. Reproduced with permission of Springer.)

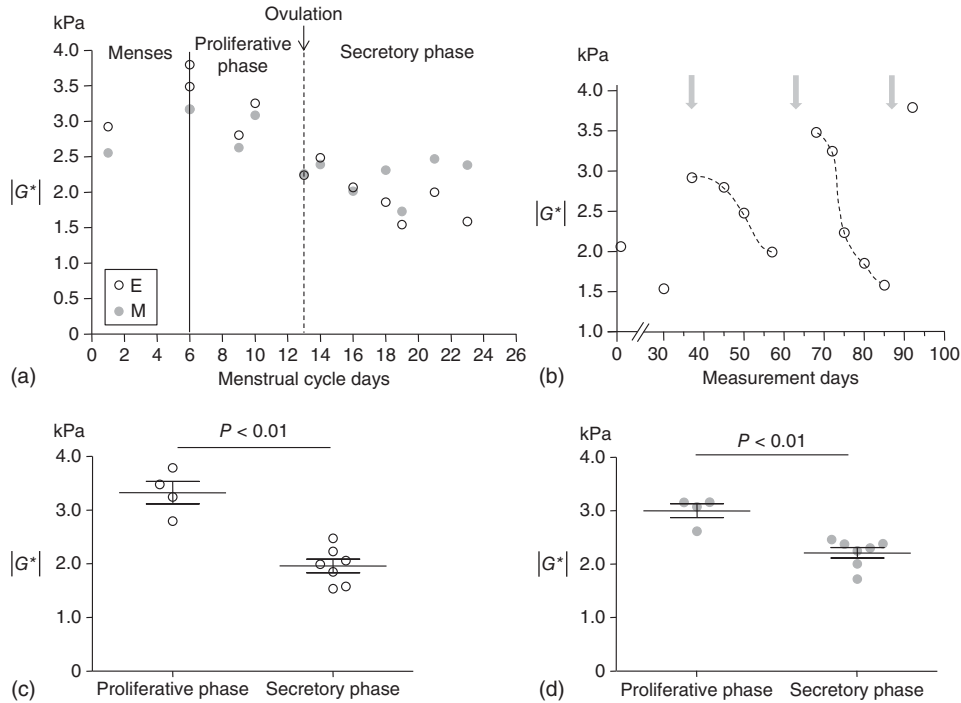
of this study is the higher stiffness of the uterine body as compared to the cervix ( $|G^*| = 2.6 \pm 0.5$  vs  $2.0 \pm 0.3$  kPa) (see Figure 15.20). Viscosity-related  $\varphi$  was similar in both regions (uterine corpus:  $\varphi = 0.5 \pm 0.1$  rad; cervix:  $0.6 \pm 0.1$  rad). High reproducibility was demonstrated by repeat measurements over 2 months in one volunteer (uterine corpus:  $|G^*| = 3.5 \pm 0.1$  kPa,  $\varphi = 0.60 \pm 0.05$  rad; cervix:  $|G^*| = 1.9 \pm 0.1$  kPa,  $\varphi = 0.53 \pm 0.10$  rad). Significant variation of  $|G^*|$  was observed with the menstruation cycle (see Figure 15.21). Myometrial stiffness was lower in the secretory phase than in the proliferative phase ( $2.2 \pm 0.3$  kPa vs  $3.0 \pm 0.3$  kPa), similar to the stiffness of the endometrium ( $2.0 \pm 0.3$  kPa vs  $3.3 \pm 0.4$  kPa). These results were reproduced by  $k$ -MDEV-based data evaluation [222]. Taken together, these experiments provide the baseline for future clinical studies of MRE of the uterus.

A preliminary study tested the feasibility of MRE for the detection of uterine fibroids in subjects with body mass indices ranging from 23 to 38 [166]. On the basis of GE-MRE and LFE reconstruction, fibroid stiffness values ranging from 4.0 to 6.7 kPa were found. Further studies of uterine MRE in patients are necessary for a definitive assessment of its diagnostic potential.

## 15.6 Prostate

The prostate is an exocrine gland and is part of the male reproductive and urinary systems. The size of the prostate varies individually from the size of a walnut to a small apple. The prostate is covered by a layer of connective tissue called the prostatic capsule. The gland itself consists of different cell types including fibrous cells providing the supportive structure, cells producing the fluid portion of semen, and smooth muscle cells controlling urine flow and ejaculation. As shown in the magnification of Figure 15.1, the gland can be subdivided into three zones:

- **Peripheral zone:** The largest zone of the prostate and closest to the rectum. Thus, it can be palpated by physicians in a digital rectal examination. Approximately 75% of all prostate tumors arise in the peripheral zone.



**Figure 15.21** Variation of  $|G^*|$  over the menstruation cycle in a healthy volunteer: (a)  $|G^*|$  of myometrium (filled circles) and endometrium (open circles) plotted separately over the normalized menstrual cycle days. (b)  $|G^*|$  of endometrium covering two complete menstrual cycles, the beginning of menstruation is indicated by arrows. Mean values and standard deviations of  $|G^*|$  in the endometrium (c) and the myometrium (d) in the proliferative (PP) and the secretory phase (SP). (Jiang 2014 [105]. Reproduced with permission of Springer.)

- **Transition zone:** The part between the peripheral and central zones surrounding the urethra and comprising approximately 20% of the volume of the prostate gland until the age of 40. After that age, the transition zone starts to enlarge (benign prostatic hyperplasia) and ultimately becomes the largest region of the prostate.
- **Central zone:** The part of the prostate that is farthest away from the rectum. Therefore, prostate tumors in this zone are difficult to assess by digital rectal examination.

The main function of the prostate is to secrete the fluid portion of semen. The prostate also plays a role in controlling the flow of urine.

### 15.6.1 MRE of the Prostate

The use of elastography for examining the prostate is motivated by the clinically established practice of digital rectal examination, in which the mechanical rigidity of the gland is manually assessed. This palpation is performed to identify prostatic disorders, notably inflammation, tumors, and benign prostatic hyperplasia. So far, MRE of the prostate has focused on the characterization of tumors and is therefore described in Section 17.3.3. In Table 15.8, we tabulate *in vivo* MRE values for normal and diseased prostate tissue published in the literature.

**Table 15.8** *In vivo* data of MRE studies of the prostate in healthy volunteers and patients with prostate tumors.

Study [reference]	Gleason score	Actuator position	Encoding method	Vibration freq. (Hz)	Recon-struction	Stiffness CZ (kPa)	Stiffness PZ (kPa)	Stiffness TZ (kPa)
12 volunteers [107]		Endorectal	1D	100	LFE	2.5 ± 0.7	2.7 ± 0.6	
				200		9.0 ± 2.0	9.0 ± 2.0	
				300		19.0 ± 5.0	17.0 ± 3.0	
6 volunteers [153]	7	Transperineal	3D	70	FEM	3.3 ± 0.5	2.6 ± 0.3	
1 patient						2.7 ± 1.1	3.1 ± 4.1	
6 volunteers [116]	6–8	Transperineal	3D	70	FEM	4.6 ± 1.5	3.8 ± 1.0	4.4 ± 1.7
11 patients						3.2 ± 1.0	2.5 ± 0.6	3.0 ± 1.1
7 volunteers [493]		Pubic bone	3D	65	DI	2.2 ± 0.3	3.3 ± 0.5	
10 volunteers [494]		Pubic bone	3D	100	n.s.		2.3 ± 0.5	
2 patients	5					–	5.8 <sup>a)</sup>	–
3 patients	6					–	6.0 <sup>a)</sup>	–
2 patients	7					–	7.5 <sup>a)</sup>	–
1 patient	8					–	8.0 <sup>a)</sup>	–

**Abbreviations:** 1D: single-displacement field component, 3D: full-displacement field, LFE: local frequency estimation, FEM: finite element method based on the wave equation (see text), DI: direct inversion, n.s.: not specified, CZ: central zone, PZ: peripheral zone, TZ: transition zone, the data given are averaged over the respective zone.

a) Group mean stiffness for the entire gland.

Stiffness refers to  $\rho \cdot c^2$  for LFE and DI (according to Eq. (4.154)) and  $\frac{1}{3} E$  (shear modulus calculated from the Young's modulus assuming incompressibility). Stiffness values are given as group mean value for respective zones ± standard deviation (if available).

## 15.7 Intervertebral Disc

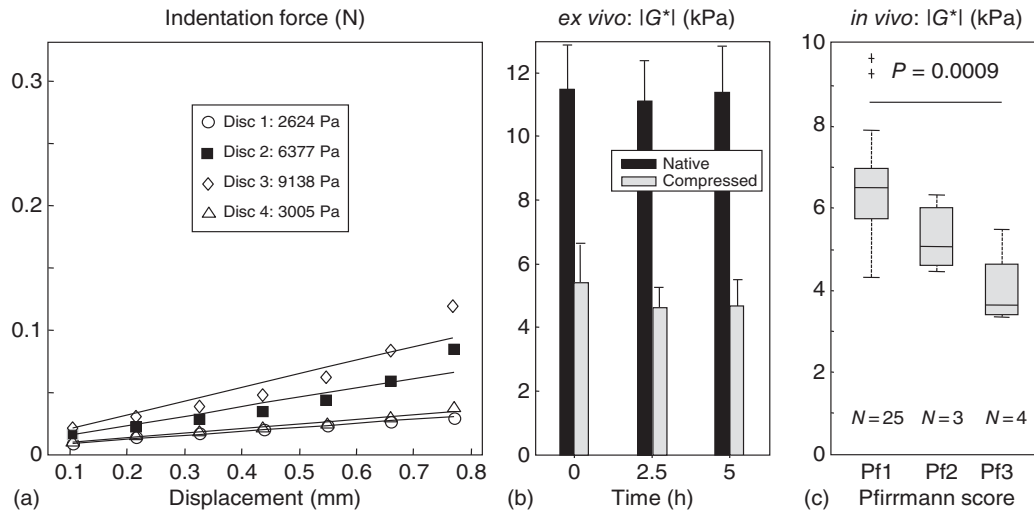
The IVD is a fibrocartilaginous joint that acts as a shock absorber in the vertebral column while at the same time facilitating complex spinal movement. Structurally, the IVD can be subdivided into the gelatinous nucleus pulposus (NP), the annulus fibrosus (AF) made up of fibrocartilage tissue, a transition zone between NP and AF, and the cartilaginous endplates [491]. Being predominantly composed of type I collagen fibers organized in concentric lamellae, the AF is a stiff solid material with cartilage-like properties characterized by high shear modulus on the order of MPa. By contrast, the NP is soft and viscous due to high water content and a disordered ECM, which is composed of type II collagen fibers and proteoglycans, leading to a high water storage capacity. At low dynamics (on the order of minutes), the NP cannot bear static shear stress, suggesting fluid-like rather than solid material properties, while at higher dynamics (on the order of less than a second), the NP shows distinct solid behavior and transmits

shear forces [492]. This duality of fluid–solid properties may reflect an important functional property of NP in the adsorption of shock and sudden transient load.

Since the dual function of the disc is to provide mechanical support and ensure mobility of the spine, MRE has high potential to directly assess the IVD functional state by medical imaging. Accurate staging of IVD degeneration is of high socioeconomic relevance since degenerative disc disease is a common cause of chronic back pain – a costly and widely prevalent health disorder in Western countries. IVD degeneration is characterized by progressive cell death, tissue dehydration, and aging of the endplates. As a result, blood vessels and nerves can invade the disc, causing pain and inflammation. In addition, the IVD becomes vulnerable to shear stress-related microtrauma, making degenerative disc disease a possible precursor of IVD herniation [495]. Various classification systems exist for assessing the grade of disc degeneration. The grading system proposed by Pfirrmann et al. is the most accepted tool due to its high feasibility using  $T_2$ -weighted MRI and accurate reliability [496]. Although the Pfirrmann score is widely used in radiological routine, the morphological MRI appearance of the IVD is not significantly correlated with the severity of symptoms or the risk of future herniation events. Other less validated MRI-based biomarkers for IVD degeneration include changes in water diffusivity, sodium content, and ECM macromolecule contents [497].

### 15.7.1 MRE of the Intervertebral Disc

In terms of MRI signal intensities and shear elasticity, NP is well accessible by *in vivo* MRE. By contrast, AF has not yet been analyzed by MRE due to short signal relaxation times and very high stiffness, which is on the order of MPa. Mechanical tests of *ex vivo* NP specimens, *ex situ* and *in situ*, were performed to investigate compression, poroelastic, hyperelastic, and shear elastic properties over a wide dynamic range from static to a few hundred hertz [498–502]. The reported NP shear modulus values vary between 10.5 and 17.4 kPa [492] and nearly 1000 kPa [500]. This variability indicates that the results are strongly influenced by mechanical testing conditions, osmotic swelling pressure, and whether the tissue was examined *in vivo* or *ex vivo*. MRE of human motion segments (vertebra–disc–vertebra) yielded shear modulus values of 661 kPa (normal IVD), 135 kPa (mild degeneration), and 71 kPa (severe degeneration) using a mechanical frequency of 1250 Hz and a finite element-based inversion method (see Section 10.7). A preliminary study using MRE at 1000 Hz in two baboon lumbar spine motion segments (L3/L4) reproduced these findings, yielding an averaged LFE-based shear stiffness of 79 kPa [503]. However, lower values were measured at lower frequencies. Streitberger et al. analyzed NP properties of *ex vivo* bovine discs by mechanical indentation and by MMRE at different precompression states in the frequency range between 50 and 70 Hz and reported values of  $G' = 5.3$  kPa (indentation),  $|G^*| = 11.3$  kPa (uncompressed state, MRE), and  $|G^*| = 4.9$  kPa (compressed state, MRE) [101]. The marked reduction of  $|G^*|$  after compression suggests that degeneration leads to softening of NP tissue. This was validated in the same study in the lumbar spine (IVD L3/4 and L4/5) of healthy volunteers covering a range of Pfirrmann scores. Averaged  $|G^*|$  values decreased with increasing Pfirrmann scores of 1, 2, and 3 by 6.51, 5.29, and 4.03 kPa, respectively (see Figure 15.22). This encouraging study is the reference for further *in vivo* MRE studies of the IVD based on noise-robust  $k$ -MDEV inversion. Tzschätzsch et al. [222] used the same data as reported by Streitberger et al. [101] and obtained similar stiffness values



**Figure 15.22** Results of MRE of the IVD obtained in *ex vivo* bovine samples by static indentation (a) or by MRE at two different states of the disc, once in its native state and a second time in a compressed state to simulate tissue degeneration (b). (c) Results from *in vivo* experiments in healthy volunteers of two IVD (L3/4, L4/5) with varying degrees of degeneration according to the Pfirmann score. (Streitberger 2015 [101]. Reproduced with permission of Wiley.)

based on wave speed ( $3.22 \pm 0.71$  m/s). An ultrasound-based SWE study found a similar range of wave speed values in the NP ( $3.0 \pm 0.4$  m/s) with softening over age [504]. Notably, the NP of IVD is visible in many *k*-MDEV-based elastograms acquired in an axial abdominal plane (cf. Figures 10.5 and 15.12), where it normally appears to be much stiffer than other tissues. The clinical use of this new information still awaits validation.



## 16

**MRE of Skeletal Muscle**

*This chapter was coauthored by Jing Guo from the Department of Radiology, Charité – Universitätsmedizin Berlin, Germany*

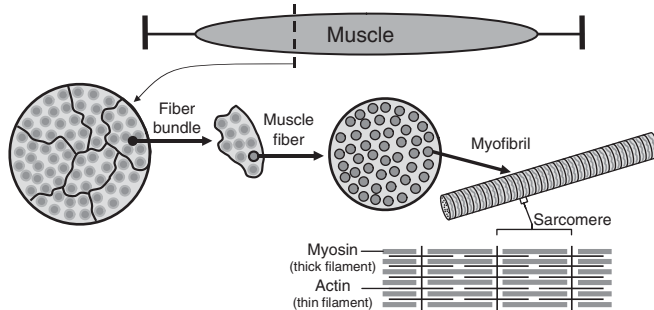
Skeletal muscle tissue is composed of macromolecular functional units, the actin–myosin filaments, which are organized into a hierarchy of sarcomeres, myofibrils, myocytes, and bundles of fibers (see Figure 16.1). The actin–myosin filaments of synchronized myofibrils generate the macroscopic contraction force, which acts via tendons on the bones. The directionality of forces generated in muscle implies a principal direction of the effective mechanical network of muscle tissue. As such, muscle tissue is anisotropic, which is visible to the naked eye by the alignment of the fascicles surrounding the fiber bundles. In longitudinally arranged fusiform muscles (e.g., the biceps brachii), fibers run parallel to the axis of force generation. In unipennate muscles (e.g., vastus lateralis), the fibers are all oriented at the same angle relative to the axis of force generation. Bipennate muscles (e.g., rectus femoris) are made of fibers arranged in V-shaped patterns. Multipennate muscle fibers are arranged at multiple angles relative to the axis of force generation, and are the most general and most common architecture of skeletal muscle.

The fibrous structure of muscle tissue implies – at least locally – rotational symmetry of the mechanical network. Applying rotational symmetry to the full orthotropic elasticity tensor results in the transversely isotropic (TI) elasticity tensor (Eq. (4.38)). The full TI elasticity tensor has five independent elements, which reduce to three free constants in case of incompressibility (Eq. (4.190)). Green's function of the solution of the wave equation accounts for both wave polarization and wave propagation direction (see Section 4.9.5). Therefore, the full solution of the elastodynamic wave equation including anisotropy needs to account for the directionalities of motion encoding and wave propagation in MRE wave data. Possible waveform scenarios in TI materials considering MRE imaging plane, wave field polarization, and wave propagation direction are schematically drawn in Figure 4.10. Early work in ultrasound elastography of skeletal muscles used transient elastography with shear waves of a preferred propagation direction [505]. The axis of the exciter rod was rotated so that the shear waves are propagated at controlled angles relative to the muscle fibers. The measured wave speed values reflected the shear modulus properties  $\mu_{12}$  and  $\mu_{13}$  (see Eq. (4.64)). Unlike MRE, ultrasound elastography is limited in acquiring the full wave field and cannot resolve the full anisotropic elasticity tensor [506]. Two more requirements are needed to retrieve all elements of the orthotropic elasticity tensor as achieved by waveguide elastography: (i) knowledge of the local coordinate system of elasticity and (ii) wave propagation

*Magnetic Resonance Elastography: Physical Background and Medical Applications*, First Edition.

Sebastian Hirsch, Jürgen Braun, and Ingolf Sack.

© 2017 Wiley-VCH Verlag GmbH & Co. KGaA. Published 2017 by Wiley-VCH Verlag GmbH & Co. KGaA.



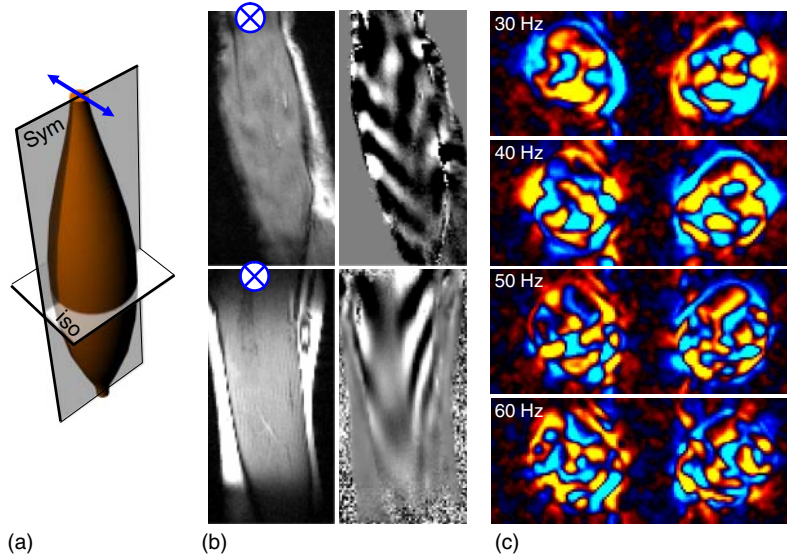
**Figure 16.1** Sketch of the hierarchy of tissue architecture in skeletal muscle.

parallel and perpendicular to the local fiber direction. The first point can be addressed by diffusion tensor imaging (DTI), which retrieves the local fiber direction and thus the local principal axis in TI materials. The second requirement ensures that directional filtering as applied in waveguide elastography results in sufficient wave amplitude in each field component and that all elasticity components  $C_{11}$  to  $C_{66}$  (Eqs. (10.102)–(10.110)) can be determined. A simplified version of waveguide elastography is the curl-based direct inversion as outlined in Section 10.8, which yields the three independent constants of an incompressible TI material:  $\mu_{12}$ ,  $\mu_{13}$ , and  $E_3$  (Eq. (4.190)) [47]. However, this approach also requires knowledge of the local fiber direction, from either a priori assumptions (see Figure 16.2) or additional experimental information from DTI. So far, neither waveguide elastography nor DTI-based three-parameter direct inversion have been applied to skeletal muscle tissue. All published studies of MRE of anisotropic media, specifically of skeletal muscle, made several assumptions to reduce the complexity of the five-parameter problem in TI materials or the three-parameter problem in incompressible TI materials. Group velocity inversion was proposed to determine the wave propagation speed of the slow transverse (ST) wave along different directions relative to the muscle fibers, which basically yields  $\mu_{12}$  and  $\mu_{13}$  similar to the aforementioned *TE* approach [48]. Simplification was achieved here by adapting the experiment, so that only ST-waves were induced, similar to studies in thigh muscles [82, 507] or by employing profile-based determination of wavelengths of unidirectional filtered waves [508, 509].

## 16.1 *In vivo* MRE of Healthy Muscles

The variation of approaches in MRE of skeletal muscle with respect to anisotropy, reconstruction, mechanical excitation frequency, and studied muscle groups hampers a direct comparison of values. For example, *in vivo* MRE of the lower extremity measured elastic modulus values between 1 and 2 kPa in thigh muscle at 50 Hz vibration frequency [82], but higher values of 3.7–7.5 kPa were obtained in the frequency range of 90–120 Hz [508]. Soleus elasticity was measured by MRE to be 12.5 kPa at 100 Hz [170].

Anisotropic shear moduli of lower leg extremity muscles obtained using *in vivo* MRE at 60 Hz were reported to be  $\mu_{13} = 0.8 \pm 0.22$  kPa and  $\mu_{12} = 0.65 \pm 0.13$  kPa



**Figure 16.2** Appearance of shear waves in MRE of skeletal muscle. (a): Imaging planes relative to the muscle. Two typical scenarios are shown for measuring the ST wave mode (polarization/propagation directions are perpendicular/parallel to the principal axis of the muscle, respectively) in a plane of symmetry (sym) or the plane of isotropy (iso). Therefore, vibration is induced at the distal or proximal end of the muscle (blue arrow) and free wave propagation is captured within the imaging planes aligned with the coordinate axes of the elasticity system (sym and iso). (b): Example MRE magnitude images (left) and wave images (right) showing the preferred direction of wave propagation along the muscle fibers within the plane of symmetry. Both motion encoding and vibration direction are through-plane (blue cross). This scenario corresponds to the lower left panel in Figure 4.10. (c): Appearance of shear waves (in-plane curl component,  $\frac{\partial u_2}{\partial r_1} - \frac{\partial u_1}{\partial r_2}$ ) in the lower extremity muscles (right leg and left leg) at different frequencies. In contrast to (b) and as prescribed by the plane of isotropy in TI media, no preferred directionality of the shear wave patterns is apparent.

in the soleus;  $\mu_{13} = 0.86 \pm 0.15$  kPa and  $\mu_{12} = 0.66 \pm 0.19$  kPa in the gastrocnemius; and  $\mu_{13} = 0.78 \pm 0.24$  kPa and  $\mu_{12} = 0.66 \pm 0.16$  kPa in the tibialis [81]. The modulus ratios ( $\mu_{13}/\mu_{12}$ ) obtained in these three muscles were 1.3, 1.3, and 1.2, respectively, which are lower than the same shear modulus ratio observed in the biceps brachii using supersonic shear wave imaging ( $3.7$ ,  $\mu_{13} = 5.86 \pm 0.20$  kPa,  $\mu_{12} = 1.58 \pm 0.15$  kPa) [510]. *TE*-based ultrasound elastography of the biceps reported a much higher modulus ratio of 16 [505]. The same ratio was derived by waveform analysis of MRE data acquired in the biceps muscle at 200 Hz ( $\mu_{13} = 54 \pm 3$  kPa,  $\mu_{12} = 3.4 \pm 1.1$  kPa) [511]. In this study,  $E_3$  was preliminarily derived from a plane stress model with  $185 \pm 60$  kPa, which is  $\sim 3.5 \cdot \mu_{13}$ , lower than the ratio  $E_3/\mu_{13}$  of five as measured in the soleus based on three-parameter inversion [47]. Group velocity inversion of biceps MRE data acquired at approximately 100 Hz yielded a shear modulus ratio of 5.7 with  $\mu_{13} = 29.3 \pm 6.3$  kPa and  $\mu_{12} = 5.5 \pm 0.29$  kPa [48]. It has to be noted that  $\mu_{12}$  values of the biceps vary to a large extent throughout the literature. Gennisson et al. [512] measured very low values of  $0.927 \pm 0.55$  kPa by transient elastography at 150 Hz, indicating the influence of prestretching and positioning on the elasticity of relaxed muscle.

Table 16.1 *In vivo* MRE of skeletal muscle of healthy volunteers in the literature.

Muscle group [reference]	Subgroup	Vibration freq. (Hz)	Muscle state	Inversion	Stiffness in (kPa)
Upper extremities [181]	Biceps	150	Load range 0–10 kPa	$\lambda$	$14.5 \pm 1.8$ per kg load
Thigh [508]	Vastus medialis	90 120	Resting	$\lambda$	3.73
			10% MVC		6.11
			20% MVC		8.49
	Vastus lateralis		Resting		3.91
			10% MVC		4.83
Sartorius	20% MVC	6.40			
		Resting		7.53	
Thigh [509]	Rectus femoris	90	Resting	$\lambda$	$3.9 \pm 10.16$
	Vastus medialis				$3.95 \pm 0.32$
	Vastus intermedius				$4.23 \pm 0.25$
	Vastus lateralis				$3.74 \pm 0.23$
	Sartorius				$5.15 \pm 0.18$
	Gracilis				$6.15 \pm 0.45$
	Semimembranosus				$4.22 \pm 0.14$
	Semitendinosus				$5.32 \pm 0.10$
	Biceps				$4.07 \pm 0.19$
Thigh [507]	Quadriceps femoris	25 37.5 50 62.7 25 37.5 50 62.7	Resting	iso-DI $\mu_{13}$	$0.77 \pm 0.14$
			Resting		$1.18 \pm 0.15$
			Resting		$1.52 \pm 0.10$
			Resting		$2.02 \pm 0.14$
			Contracted		$0.67 \pm 0.07$
			Contracted		$1.41 \pm 0.16$
			Contracted		$2.05 \pm 0.19$
			Contracted		$2.67 \pm 0.27$

(continued overleaf)

Table 16.1 (Continued)

Muscle group [reference]	Subgroup	Vibration freq. (Hz)	Muscle state	Inversion	Stiffness in (kPa)	
Thigh [82]		50		iso-DI		
	Rectus femoris		Resting lift	$\mu_{13}$	$0.98 \pm 0.23$ $1.46 \pm 0.98$	
	Vastus medialis		Resting lift		$1.93 \pm 0.38$ $2.44 \pm 0.76$	
	Vastus intermedius		Resting lift		$1.47 \pm 0.23$ $1.59 \pm 0.53$	
	Vastus lateralis		Resting lift		$1.73 \pm 0.54$ $2.10 \pm .57$	
	Extremities [170]	Biceps brachii	142	Resting	n.a.	$17.9 \pm 5.5$
		Flexor digitorum profundus	142			$8.7 \pm 2.8$
Soleus		100			$12.5 \pm 7.3$	
Gastrocnemius		100			$9.9 \pm 6.8$	
Shoulder [518]	Trapezius	90	Resting	n.a.	$2.72 \pm 0.60$	
		120			$4.66 \pm 1.20$	
	Infra-spinatus	90			$3.20 \pm 0.52$	
		120			$4.38 \pm 0.92$	
Upper extremities [48]	Biceps brachii	99	Resting	GVI		
				$\mu_{12}$	$5.5 \pm 0.9$	
				$\mu_{13}$	$29.3 \pm 6.2$	
Lower extremities [81]	Soleus	60	Resting	2para-DI		
				$\mu_{12}$	$0.65 \pm 0.13$	
	$\mu_{13}$			$0.83 \pm 0.22$		
	Gastrocnemius			$\mu_{12}$	$0.66 \pm 0.19$	
				$\mu_{13}$	$0.86 \pm 0.15$	
	Tibialis			$\mu_{12}$	$0.66 \pm 0.16$	
$\mu_{13}$		$0.78 \pm 0.24$				
Lower extremities [47]	Soleus	30–60	Resting	3para-MDEV		
				$\mu_{12}$	$1.06 \pm 0.12$	
				$\mu_{13}$	$1.33 \pm 0.10$	
				$E_3$	$6.92 \pm 0.95$	

(continued overleaf)

Table 16.1 (Continued)

Muscle group [reference]	Subgroup	Vibration freq. (Hz)	Muscle state	Inversion	Stiffness in (kPa)
	Gastrocnemius			$\mu_{12}$	$0.90 \pm 0.11$
				$\mu_{13}$	$1.30 \pm 0.15$
				$E_3$	$8.22 \pm 1.37$
	Tibialis			$\mu_{12}$	$1.26 \pm 0.15$
				$\mu_{13}$	$1.27 \pm 0.10$
				$E_3$	$9.26 \pm 1.65$

**Abbreviations:**  $\lambda$ : wavelength estimation by profiles (in most cases, profiles were placed along the principal fiber direction, thus reported values reflect  $\mu_{13}$  rather than  $\mu_{12}$ , but deviations are likely). iso-DI: isotropic direct inversion applied within the plane of isotropy to waves polarized along the fiber direction, thus analyzing the FT-wave mode, which yields  $\mu_{13}$ . GVI: group velocity inversion yielding  $\mu_{13}$  and  $\mu_{12}$ . 2para-DI: two-parameter anisotropic direct inversion yielding  $\mu_{13}$  and  $\mu_{12}$ . 3para-MDEV: three-parameter anisotropic MDEV inversion yielding  $\mu_{12}$ ,  $\mu_{13}$ , and  $E_3$  (Young's modulus along the muscle fibers). MVC: maximum voluntary contraction.

Not only elasticity, but also viscosity of skeletal muscle is anisotropic [510]. Only a few studies have investigated the *in vivo* viscous properties of skeletal muscle so far. In the gastrocnemius, Hoyt et al. [513] measured a shear modulus of approximately 5 kPa and shear viscosity of 9.3 Pa s using sonoelastography and Voigt model fitting in a frequency range between 80 and 200 Hz. Klatt et al. used a specialized MRE setup to quantify the springpot-model based parameter  $\mu_{13}$  in the femoral muscle between 25 and 62.5 Hz [507].

So far, we have not considered muscle contraction. Since muscle function is based on contraction and relaxation, MRE-measured parameters in different states of contraction are intrinsically sensitive to muscle function. One of the first *in vivo* studies of MRE addressed the relationship between muscle stiffness and load [181]. In this study, the authors demonstrated that MRE is capable of assessing muscle function *in vivo* and reported a positive linear relationship between shear stiffness and muscle load. Many other studies in the field used different loading paradigms and proposed nonmagnetic load apparatuses for applying muscle load in different regions in a reproducible manner. Table 16.1 provides a summary of major studies in the field including the used definition of muscle activity.

## 16.2 MRE in Muscle Diseases

Table 16.2 summarizes clinical MRE studies of skeletal muscle. Since muscular dysfunction is the impairment of the muscle's capability to perform mechanical work, the MRE-measured shear modulus is a direct image-based biomarker for muscle disease.

The first *in vivo* application of MRE to diseased muscles was reported in [155], where lower extremity muscle stiffness was significantly higher in patients with neurologic

**Table 16.2** *In vivo* MRE of skeletal muscle in patients.

Muscle type [reference]	Subgroup	Vibration freq. (Hz)	Muscle state	Inversion	Shear stiffness (kPa)
Patients with lower extremity neuromuscular dysfunction					
Lower extremity	Tibialis anterior	150	Resting	$\lambda$	Pat: $38.2 \pm 81.89$ Con: $12.03 \pm 0.39$
Muscles [155]	Medial gastrocnemius				Pat: $47.48 \pm 1.23$ Con: $24.86 \pm 0.71$
	Lateral gastrocnemius				Pat: $38.40 \pm 0.77$ Con: $16.16 \pm 0.19$
	Soleus				Pat: $51.79 \pm 1.82$ Con: $16.77 \pm 0.24$
Patients with Duchenne muscular dystrophy					
Thigh muscle [514]	Vastus medialis	90	Resting	$\lambda$	Pat: $4.75 \pm 0.50$ Con: $3.06 \pm 0.21$
			10% MVC		Pat: $7.50 \pm 0.62$ Con: $15.89 \pm 2.38$
			20% MVC		Pat: $10.96 \pm 0.60$ Con: $15.13 \pm 2.96$
Hypogonadal patients before and after testosterone substitution therapy					
Lower extremity muscles [515]	Soleus	100	Resting with ankle $\sim 90^\circ$	LFE	Pat(pre): $13.42 \pm 0.92$ Pat(post): $19.54 \pm 2.19$ Con: $15.96 \pm 1.00$
			5% MVC		Pat(pre): $14.02 \pm 1.05$ Pat(post): $18.93 \pm 1.85$ Con: $18.52 \pm 1.26$
			10% MVC		Pat(pre): $15.96 \pm 1.03$ Pat(post): $20.49 \pm 2.09$ Con: $19.18 \pm 1.21$
			15% MVC		Pat(pre): $17.11 \pm 1.13$ Pat(post): $21.00 \pm 2.28$ Con: $19.13 \pm 1.11$
			20% MVC		Pat(pre): $16.44 \pm 0.99$ Pat(post): $22.63 \pm 3.01$ Con: $19.75 \pm 0.99$

*(continued overleaf)*

Table 16.2 (Continued)

Muscle type [reference]	Subgroup	Vibration freq. (Hz)	Muscle state	Inversion	Shear stiffness (kPa)
Hyperthyroid patients before and after medical treatment					
Thigh muscle [84]	Vastus medialis	90	Resting	$\lambda$	Pat(pre): $2.11 \pm 0.61$ Pat(post): $4.56 \pm 0.40$ Con: $5.52 \pm 1.52$

**Abbreviations:**  $\lambda$ : wavelength estimation by profiles (in most cases profiles were placed along the principal fiber direction, thus reported values reflect  $\mu_{13}$  rather than  $\mu_{12}$ , but deviations are likely). LFE: isotropic inversion based on local frequency estimation, Pat: patients, Con: controls, pre: MRE prior to therapy, post: MRE after therapy, MVC: maximum voluntary contraction.

disease than that in the control subjects under resting state. In addition, the muscles stiffened with increased load in both controls and patients. Quite recently, MRE was employed to investigate elastic properties of the vastus medialis (VM) in children with Duchenne muscular dystrophy (DMD) in both relaxed and contracted states [514]. It was observed that due to muscle fibrosis and lack of muscle contractile properties, VM stiffness in DMD was higher in the resting state and lower in the contracted state than the healthy control muscle. MRE was also used to evaluate therapeutic effects in patients with hypogonadism [515] and hyperthyroidism [84] with muscular effects. In hypogonadal patients, a significant increase of the VM shear modulus of was observed after 6 months of testosterone therapy, which was comparable to the healthy age-related control group. In patients with hypogonadism, VM stiffness was lower than in healthy controls. An increase in stiffness after treatment was observed in hyperthyroid patients in the resting state. The only *in vivo* MRE study on animal skeletal muscles was performed on mdx mice, a model of muscular dystrophy [127]. In this study, the mechanical anisotropic ratio ( $\mu_{13}/\mu_{12}$ ) was calculated for the lateral gastrocnemius and plantaris muscles. This mechanical anisotropic ratio was found to be sensitive for distinguishing the muscles of mdx and wild-type mice and correlate with the percentage of necrotic muscle area.

In essence, MRE of skeletal muscle is an active area of research including both principal studies on anisotropic elastic constants of soft tissues and clinical applications toward better characterization of muscular dysfunction. Using advanced driver technologies, 3D wave field acquisition, and sophisticated anisotropic inversion strategies, MRE is capable of recovering all elements of the unknown TI elasticity tensor. These experiments have been complimented by numerical simulations [516] and studies using anisotropic phantom materials [517]. However, these methods still need validation in clinical applications by accounting for complex muscle geometries, locally changing fiber directions and different loading states of the muscle.



## 17

## Elastography of Tumors

Tumor growth is associated with extensive alterations of tissue structures resulting from a number of processes such as neovascularization, accumulation of cells, and remodeling of the extracellular matrix (ECM). Furthermore, leaky tumor blood vessels and impaired lymphatic drainage lead to interstitial fluid accumulation and elevated hydrostatic pressure. The altered structure and fluid turnover are mirrored by significant changes in the effective shear modulus of the tumor. Therefore, tumors frequently present as rigid masses, which are well detectable by manual palpation. In fact, the high sensitivity of palpation for the detection of stiff tumors was one of the initial motivations for the development of elastography. Today, ultrasound elastography is a routine clinical method for tumor diagnosis and treatment monitoring. Clinical trials have demonstrated that the macroscopic mechanical properties of tumors provide a rich source of diagnostic information. The success of *in vivo* tumor elastography has been paralleled by intriguing discoveries of mechanosensitivity, mechanosignaling, and mechanical interactions in cancer cells and their ECM. Over the last decade, biophysical methods have uncovered the significance of mechanical tissue properties for the progression and malignant transformation of tumors.

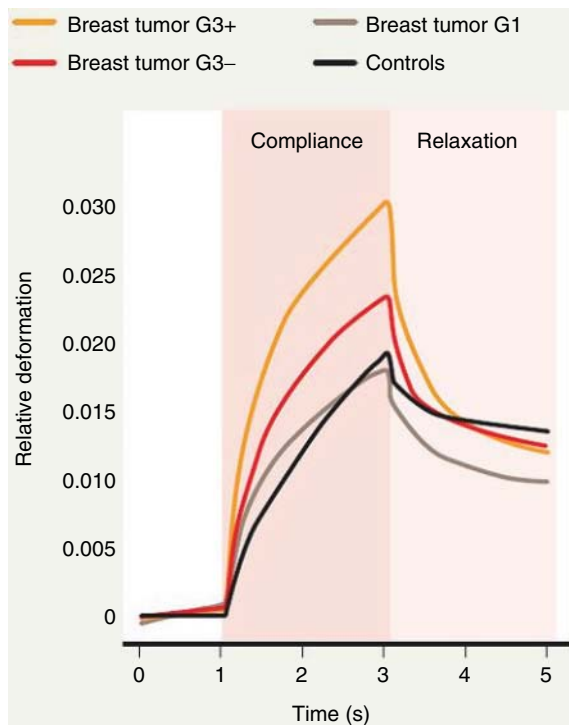
### 17.1 Micromechanical Properties of Tumors

From a clinical perspective, malignant transformation is the most dramatic process in tumorigenesis. Malignant tumors can invade other organs, spread to distant locations by metastases, and become life-threatening. Cancer metastases are still largely incurable and are closely related to patient death [519]. Formation of metastases involves escape of cancerous cells from the primary tumor, migration through ECM, and spread to distant organs. Thus, the metastatic potential of a tumor increases with the number of cells that are able to leave the solid tumor [520]. Invasive cells have often undergone significant changes in cell–cell adhesion and cytoskeletal composition, suggesting that escape from the tumor mass is also controlled by specific changes in mechanical properties of both individual cells and the surrounding tissue [521]. From a physics perspective, cells must overcome energy barriers [522] caused by various biological, chemical, and physical mechanisms, such as adhesion-induced tissue cohesion or jamming effects [523], to escape from the primary tumor and to migrate through the surrounding ECM.

*Magnetic Resonance Elastography: Physical Background and Medical Applications*, First Edition.  
Sebastian Hirsch, Jürgen Braun, and Ingolf Sack.

© 2017 Wiley-VCH Verlag GmbH & Co. KGaA. Published 2017 by Wiley-VCH Verlag GmbH & Co. KGaA.

Cancer cell invasion falls predominantly into two categories: mesenchymal invasion (“path generating”) and amoeboid invasion (“path finding”) [524]. Mesenchymal invasion requires proteolytic activity to digest the surrounding ECM and to open a path for invading cancer cells. Amoeboid invasion involves dynamic cell shape changes, allowing cells to squeeze into small gaps when finding their way through ECM pores. Amoeboid motility is improved by soft and contractile cell properties, making it easier for cells to migrate through the ECM. Cellular stiffness and contractility is regulated by the cytoskeleton, which consists of intermediate filament bundles. During mitosis, thick filament fibers are degraded and replaced by diffusely distributed smaller elements, giving rise to greater mechanical compliance of dividing cells [525]. It is therefore not surprising that the high proliferation rate of tumor cells is often associated with cell softening. In fact, results obtained by micromechanical test methods such as the optical cell stretcher<sup>1</sup> suggest that, with tumor progression, cancer cells become softer against small deformations [527]. Moreover, high-grade cancer cells show faster relaxation, which is related to reduced viscosity and increased contractility (see Figure 17.1). Fast mechanical relaxation after mechanical stimulation of the cells correlates, to some extent, with the invasiveness of cancer cells [528]. In general, the biophysical signature of softening combined with reduced viscosity (increased contractility) seems to endow cancer cells with the flexibility required for their migration through ECM and tissue boundaries.



**Figure 17.1** Creep experiments with the optical cell stretcher (each curve is the average of more than 500 cells, G3- and G3+ denote stage 3 cancer without and with nodal metastasis, respectively). Cancer cell compliance increases with the tumor stage. Cancer cells become softer, but show faster relaxation due to increased contractility. This tendency is more pronounced for breast cancer and is in agreement with observations that breast cancer is more invasive than cervical cancer. (Jonietz 2012 [527]. Reproduced with permission of Nature publishing group.)

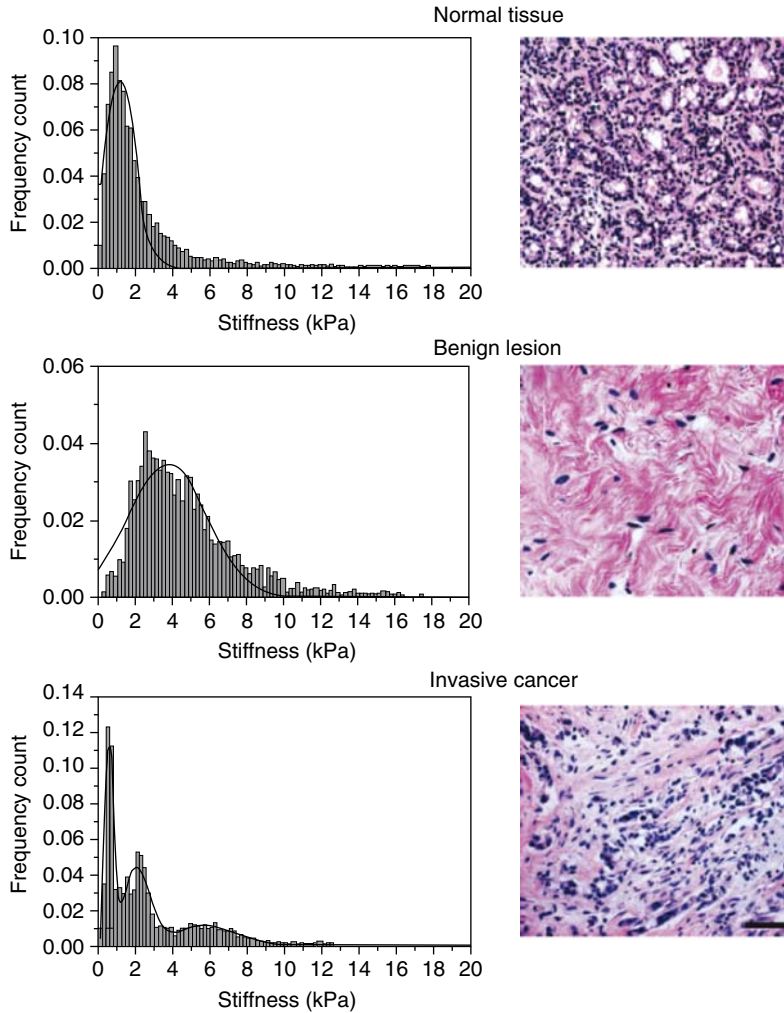
<sup>1</sup> The optical stretcher is a device that measures elasticity of single cells by deforming them with focused laser beams [526].

Cell proliferation is always associated with displacement of masses. Therefore, a growing tumor expanding against surrounding tissue produces mechanical pressure acting on the tumor boundaries. Beyond a threshold, this “homeostatic pressure” impedes further tumor progression and invasiveness [529, 530]. Plants prevent cancer cell migration by rigid cell membranes and stiff ECM structures [531]. In animal and human tissue, tumors favorably grow at membranes, folds, or boundaries between tissues, where solid stress is lower than that in regions with homogeneous dense tissue [529]. The mechanical environment influences tumor growth and metastatic dissemination and – vice versa – tumor cells can gain control of their microenvironment by ECM degradation and remodeling to make it permissive for invasion [532, 533]. For example, malignancies frequently deposit collagen in their ECM to prepare “invasion highways” for accelerated migration of metastatic cells [534]. Pathologists use excessive ECM deposition as a marker of poor prognosis [535]. However, in areas where fibrillary proteins are absent, such as the brain, the tumor’s ability to produce its own stiff ECM is limited and alternative ways of invasion are exploited.<sup>2</sup> This may explain why high-grade neuronal tumors, unlike malignant breast tumors, are softer than the surrounding parenchyma [108, 126, 322]. Breast tumors – similar to other malignancies which have access to connective tissues – appear stiffer due to abundant cross-linked collagen fibers in their ECM [537]. The fibrillar proteins expressed in the ECM of such tumors may conceal to large-scale test methods that embedded tumor cells have undergone malignant transition. Conversely, micromechanical methods such as atomic force microscopy (AFM) can elicit this clinically important mechanical footprint. Using AFM of breast tumor samples, Plodinec et al. demonstrated stiffness to be heterogeneous in cancerous lesions, whereas premalignant lesions displayed more homogeneous stiffness patterns [538]. Results of this study are presented in Figure 17.2 and show that – in agreement with palpation – healthy glandular tissue is softer than tissue from a benign breast lesion. However, a prominent peak arises in the histogram at low elasticity values, which indicate patches of infiltrating and aggressive cells. This “soft cancer” peak is contrasted by a distinct portion of stiff tissue consistent with the overall fibrotic structure of the tumor. The integrated stiffness response of the tumor as it presents to the fingers would be that of a solid mass. *In vivo* MRE might be sensitive to the presence of soft spots in solid tumor tissue and identify malignant cancer cells provided that sufficient detail resolution and precise measurement of elasticity and viscosity can be achieved.

In essence, mechanical forces acting on cancer cells determine growth, malignant state, and aggressiveness of tumors, and should therefore be measured by *in vivo* elastography to aid cancer diagnosis. Given the unique scaling properties of the shear modulus, ultrasound elastography and MRE are potentially sensitive to the highly specific micromechanical properties of tumors. It remains an eminent goal of elastography for the future to translate the mechanical predictions from biophysical models into predictive diagnostic markers of tumor progression and tumor boundary identification.

---

<sup>2</sup> For example, it was observed that glioma cells can directly exploit existing stiff myelin sheath bundles as migration routes [536].



**Figure 17.2** Stiffness response of breast tumor samples to microindentation. Left-hand side: Biopsy-wide histograms showing stiffness distribution for normal glandular breast tissue, benign lesion, and invasive cancer. Normal tissue appears to be homogeneously soft. The benign lesion exhibits a similar unimodal stiffness distribution, however, with a higher stiffness than healthy breast tissue. By contrast, invasive cancer is identified by heterogeneous stiffness distribution with a characteristic soft peak for malignant tumor tissue. Corresponding micrographs of H&E-stained histological sections are shown on the right-hand side (scale bar applies to all images, 50  $\mu\text{m}$ ). (Plodinec 2012 [538]. Reproduced with permission of Nature publishing group.)

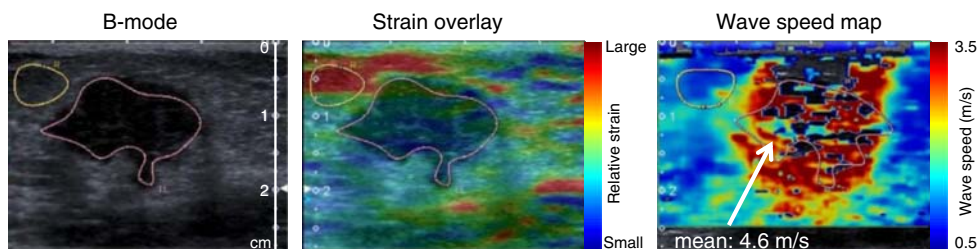
## 17.2 Ultrasound Elastography of Tumors

*This chapter was coauthored by Thomas Fischer from the Department of Radiology and Ultrasound Research Laboratory, and Anke Thomas from the Departments of Gynecology and Obstetrics, and Ultrasound Research Laboratory, both at Charité – Universitätsmedizin Berlin, Berlin, Germany.*

Since the early 1990s, the term sonoelastography has been used as a cover term for a variety of ultrasound (US) techniques that were developed to assess the elasticity of biological tissues [244, 258, 539]. Some of these techniques are discussed in Chapter 12. An important clinical advantage of sonoelastography is that it is generally available and quick to perform at little extra cost. The high spatial resolution of US allows determination of the elastic properties of small structures (less than 5 mm). Real-time strain imaging is widely used in clinical examinations today, but becomes increasingly substituted by quantitative methods based on shear wave speed measurements. As compared to MRE, sonoelastography has some technical disadvantages including the limited penetration depth of only 5–6 cm, the susceptibility to artifacts related to acoustic shading, and examiner dependence. Examples of the diagnostic value of sonoelastography are applications to tumorous lesions in the breast and prostate.

### 17.2.1 Ultrasound Elastography in Breast Tumors

Inclusion of tissue elasticity as an additional diagnostic parameter for breast lesions has been shown to increase specificity and to improve the separation of benign and malignant tumors classified as BIRADS (Breast Imaging Reporting and Data System [540]) category 3 or 4. This improvement reduces the number of false-positive findings and could thus spare many women unnecessary breast biopsies in the future. In women with involuted glandular tissue, qualitative strain-based real-time elastography has been shown to increase specificity from 69% to 80% [541]. By contrast, the diagnostic accuracy of B-mode US decreases with involution of breast parenchyma. A multicenter study of 779 women has confirmed these results [542]. For further standardization of strain-based elastography, the fat-to-lesion strain ratio (FLR) has been developed [543]. FLR estimates the degree of strain in a lesion in relation to that in fat [544, 545] by assuming individual differences being less pronounced in fat than normal mammary gland. In a European patient population, an FLR cutoff value for discrimination of benign and malignant lesions ranging between 2.3 and 2.5 has been identified using different US systems [544, 546]. This range of values was lower than that reported for a Chinese population [547], possibly due to ethnic variations in normal glandular breast density [546], precluding the definition of a single standardized FLR. Nevertheless, FLR is a simple accessible and reproducible parameter for the characterization of known breast lesions and a first large meta-analysis of RTE was conducted in 2012, including 5511 breast lesions [548]. This study reported some interesting results: (i) in agreement with previous studies [541, 542], inclusion of mechanical strain as a diagnostic parameter increases the specificity of US imaging in breast tumors from 70% to 88% and thus reduces the need for breast biopsy in screening populations with low risk of breast cancer; (ii) in low-risk populations, strain measurements should be applied after B-mode US indicated breast lesions; (iii) in high-risk populations, strain measurements should be used in combination with FLR to ensure the highest possible correct classification rate. Limitations of FLR exist for the differentiation of recurrent breast cancer from scar tissue, the latter developing after surgery and radiotherapy. Both tissue types exhibit comparable stiffness and can thus not be distinguished with FLR alone. Therefore, MRI or biopsy with US guidance [544] are still indispensable for ruling out cancer recurrence. Because of general limitations of strain measurements, such as interexaminer variability, limited reproducibility, and qualitative values [549, 550], quantitative US shear wave



**Figure 17.3** Strain-based elastography and quantitative shear wave elastography for characterization of invasive ductal mammary carcinoma. The tumor presents with irregularly shaped boundaries and perifocal edema in B-mode US. Both strain and shear wave speed maps indicate high tumor stiffness (corresponding to low strain amplitudes), which is typical for invasive ductal carcinoma. The shear wave speed map is confused by artifacts related to the near field of the US probe.

imaging methods promise further improvements in the specificity of breast US imaging (Figure 17.3). Supersonic shear wave imaging (SSI, see Section 12.16) was applied in a multinational study to 939 BIRADS-classified breast masses [551]. It was shown that inclusion of quantitative stiffness information to BIRADS-feature analysis improved specificity of breast US mass assessment without loss of sensitivity (AUROC = 0.96).

An almost identical AUROC value was found for the differentiation of malignant and benign breast lesions in a meta-analysis [552], which aimed to assess the diagnostic performance of quantitative ARFI elastography (see Section 12.3) based on 1408 breast lesions from 1245 women. It was also observed that the identification of breast mucinous carcinoma and breast carcinoma *in situ* was limited. A recent comprehensive meta study on 5838 lesions from 5397 patients analyzed the pooled diagnostic performance of SSI and ARFI [456]. AUROC values of 0.94, 0.92, and 0.94 were found by pooling data of both methods, and for the ARFI and SSI subgroups, respectively.

In practice, ultrasound elastography of the breast fits seamlessly to standard examination protocols. Today, ultrasound elastography is an adjunct to conventional sonography to (i) improve the differentiation between benign and malignant lesions and (ii) refine the BIRADS score. With the increasing standardization of quantitative methods such as ARFI or SSI, objective measures for differentiating malignant from benign breast lesions might find a broad application in the diagnosis of breast masses.

### 17.2.2 Ultrasound Elastography in Prostate Cancer

Men with an elevated prostate-specific antigen (PSA) level or abnormal prostate findings in digital rectal examination undergo workup by transrectal ultrasound (TRUS) in combination with systematic biopsy for histologic confirmation [553]. In a subgroup of these patients, TRUS-guided biopsy fails to detect cancer despite increasing PSA levels, and multiple biopsies may be necessary before a diagnosis can be made [554–557]. Many suggestions have been made to improve the cancer detection rate of TRUS. Since it is known that prostate cancer is associated with changes in metabolism, perfusion, and stiffness [558], techniques such as color Doppler US and contrast-enhanced ultrasound (CEUS) as well as elastography have been proposed for prostate cancer detection, however, without achieving decisive progress [559–563]. Data on TRUS elastography,

for example, are highly variable with reported sensitivities for prostate cancer detection ranging from 25% to 92% [564, 565].

A breakthrough was finally achieved by combining multiparametric 3T-MRI for localizing suspicious lesions with subsequent use of these data for real-time MRI/US fusion biopsy [566]. Initial results with MRI/US fusion biopsy in subgroups of patients showed detection rates that were comparable to those of the more time-consuming and expensive method of MRI-guided biopsy [567]. Fusion biopsy can also be performed using a multiparametric approach combining color Doppler, CEUS and elastography (see Figure 17.4). The advantage of this technique is in the assessment of focal lesions in a given plane, which takes the high detection rate of prostate cancer by MRI into account. Both CEUS and strain elastography have shown high specificity in multiparametric US imaging [568].

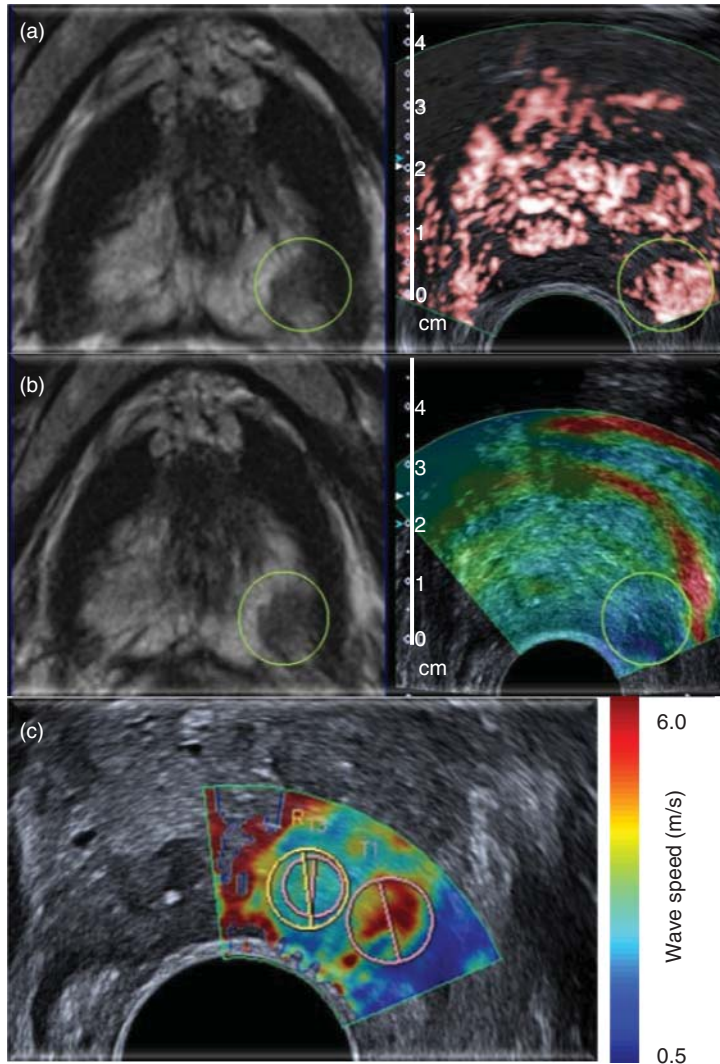
Quantitative ultrasound elastography methods yielding absolute values for focal lesions are of particular interest for the identification of suspicious lesions and subsequent targeted biopsy with routine TRUS-based techniques. Recently, the combination of B-mode and acoustic radiation force impulse (ARFI, see Section 12.3) imaging has been proposed to complement multiparametric MRI for diagnosis and treatment planning of prostate cancer [569]. This feasibility study showed the possible demarcation of different prostatic zones on ARFI images as well as good geometrical agreement of B-mode and  $T_2$ -weighted MRI. Initial publications based on shear wave elastography (SWEI, see Section 12.14) have proposed cutoff values on the order of 35 kPa for discriminating benign from malignant lesions [570].

It remains to be determined whether the limited penetration depth of ARFI and SWEI can be improved further and whether these initial results can be confirmed by multi-center trials. US elastography has the potential to provide supplementary information that could be used for routine TRUS-guided biopsy in patients with abnormal B-mode findings [570].

### 17.3 MRE of Tumors

Notwithstanding the initial motivation for exploring the potential of MRE in the detection and characterization of neoplasms, a relatively low number of studies investigating tumor diagnosis by MRE have been published. A major limitation of tumor MRE in the past was its low detail resolution and, as a result, low consistency. More studies are being published now as MRE methods have improved, making it easier to generate elastograms with higher resolution. This development contributes to a growing overall awareness of the relevance of biophysical properties of cancer and *in vivo* mechanical imaging markers. Many cancer research groups have started to show an interest in bridging micromechanical test methods with *in vivo* MRE. Mouse tumor models represent a viable way of testing the viscoelastic parameters of tumors under *in vivo* conditions and investigate the changes in tissue structures by histology. This effort is paralleled by clinical MRE studies addressing the diagnostic potential of mechanical parameters for tumor detection and differentiation of benign and malignant tumors. Until now, MRE has been investigated for tumor imaging in the breast, liver, prostate, and brain. Mouse tumor models of lymphoma, colon cancer, and intracranial tumors were studied by MRE. A brief overview of these studies is given in the following sections.





**Figure 17.4** Multiparametric image fusion in prostate cancer. (a) hypointense tumor in  $T_2$ -weighted MRI (left) and contrast-enhanced ultrasound (CEUS) showing increased perfusion related to high aggressiveness of the tumor (Gleason-score 4+4, right). (b)  $T_2$ -weighted MRI (left) with strain image showing the tumor as a solid-encapsulated mass. (c) Shear wave elastography revealing high stiffness within the tumor boundaries. This elasticity-based contrast could be used for guidance of the biopsy. Notably, this patient received previously two biopsies without result. SWE could increase the detection rate of prostate tumors.

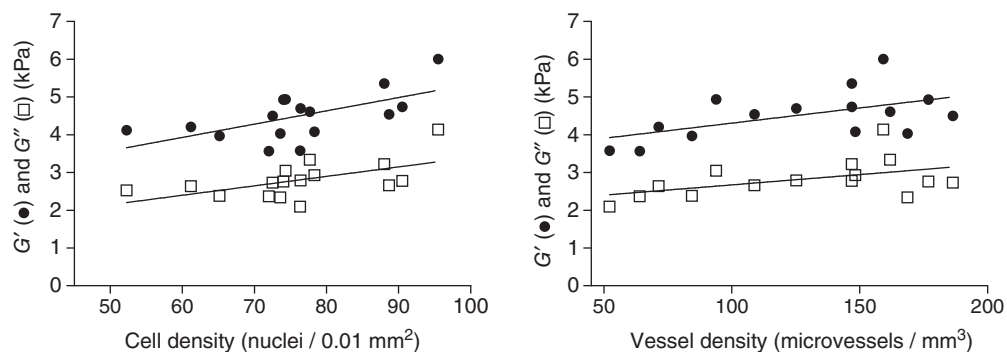
### 17.3.1 MRE of Tumors in the Mouse

Intracranial tumors implanted in the mouse were investigated by MRE in [126] and [571]. Specifically, Jamin et al. used human glioblastoma cells, rat glioma cells, and human breast carcinoma cells to induce tumors in the mouse brain for studying the



viscoelastic properties of intracranial tumors in relation to their invasiveness [126]. Guo et al. studied tumor properties relative to surrounding brain tissue in a mouse glioblastoma model [571]. Consistent with cues from biophysics, all studied tumors were softer than surrounding brain parenchyma. Furthermore, Jamin et al. [126] observed reduced tumor viscosity, corroborating the predicted correlation between contractility and invasiveness of cancer cells (cf. Figure 17.1). Beyond this “reductionist view” on single cells [527], larger-scale structures such as vessels, ECM, or cell clotting need to be accounted for the interpretation of global values. Figure 17.5 presents results from [126], which correlated MRE-derived storage modulus and loss modulus with the tumor’s cell density and microvessel density. Good correlation was observed between MRE and cell density, while correlation with microvessel density was only moderate. The correlation between MRE and cell density suggests that either the cohesiveness of intracranial tumors increases with increasing cell adhesion at higher cell numbers or that cellular viscoelasticity is higher than that of the ECM, resulting in an overall increase in MRE parameters with an increasing number of cells. In the latter case, cellular properties would dominate the gross mechanical response of neuronal tumors and allow MRE to be directly correlated with mechanical cell tests such as the optical stretcher. A preliminary study of human neuronal tumors, reviewed below, reported exactly this correlation [572] (see Figure 17.6).

However, as indicated by Figure 17.5, other structure elements such as microvessels significantly contribute to an overall increase in MRE parameters. MRE in colon tumors implanted in mice reproduced this principal finding [141]. Furthermore, the effect of antivasular treatment was demonstrated by showing a significant decrease in complex shear modulus  $|G^*|$  with reduction of vascularity after treatment. The observed effect on  $|G^*|$  was even higher than that of water diffusion measured by the apparent diffusion coefficient (ADC), which also increased after treatment [141]. In general, tumor treatment by cytotoxic and antivasular agents reduces tissue integrity, degrades membranes and vascular architecture, and decreases cell–cell contact. The induced necrosis ultimately leads to tissue liquefaction. Intuitively, these processes are associated with a reduction in MRE-derived stiffness parameters and an increase in free water diffusion. Comparing the sensitivity of MRE and ADC in monitoring tumor response to treatment



**Figure 17.5** MRE-derived viscoelasticity (storage modulus  $G'$ , loss modulus  $G''$ ) versus cell density and microvessel density obtained in mouse models of intracranial tumors. (Data courtesy of Yann Jamin and Simon Robinson (The Institute of Cancer Research, London) [126].)

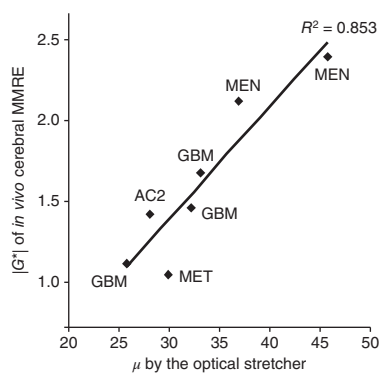
reveals that MRE detects vascular disruption earlier than water diffusion [573]. A possible explanation is the scaling property of the shear modulus, as outlined on page 124, which provides sensitivity across multiple scales of a vascular tree with fractal geometry. The decrease in tumor stiffness in response to treatment was also detected by MRE in a lymphoma mouse model [574]. The authors discussed their results in view of micromechanical methods, which predict that cells exposed to chemotherapy become stiffer due to their reduced metastatic potential [575, 576]. However, it should be noted that chemotherapeutic agents massively affect the integrity of the entire tumor including ECM and vascular tree, which ultimately causes a reduction of viscoelasticity parameters due to the decomposition of tumorous tissue by treatment.

### 17.3.2 MRE in Liver Tumors

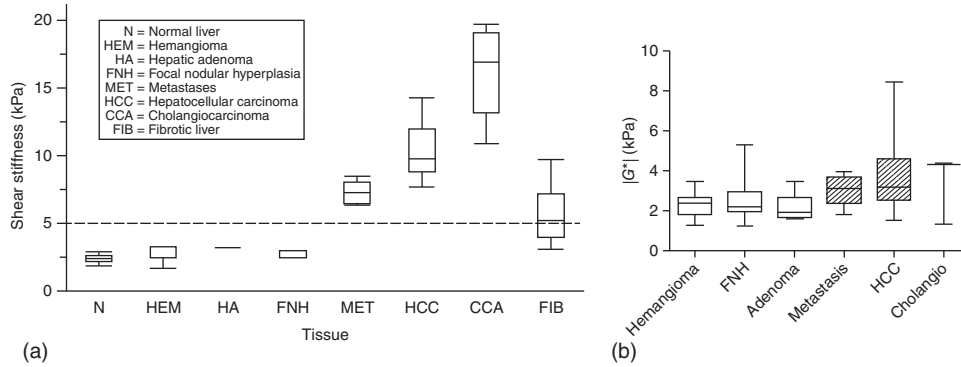
Higher liver stiffness increases the risk of hepatocellular carcinoma [577]. Thus, the progression and metastatic potential of liver tumors is intimately linked to the mechanical properties of the liver [530]. As reviewed in Section 15.1, liver viscoelasticity is altered by a number of processes, among which fibrosis is one of the most relevant ones. Measuring liver viscoelastic constants by MRE may provide a unique biomarker for assessing whether or not the mechanical milieu in which a tumor grows is favorable for the tumor's further progression and invasiveness. Moreover, the viscoelastic properties of a lesion itself may contribute to multiparametric MRI, which is superior to radiological reading based on single-parameter maps alone for characterizing liver tumors [578].

So far, two studies using single-frequency MRE analyzed the averaged viscoelastic properties of liver tumors [114, 115]. On the basis on the mean shear stiffness of the entire tumor, Venkatesh et al. concluded that malignant liver tumors are stiffer than benign tumors [114]. By contrast, Garteiser et al. found a significant increase in malignant versus benign tumors only for their loss properties [115]. Venkatesh et al. [114] reported that cholangiocarcinoma had the highest stiffness among all tumors, followed by hepatocellular carcinomas. Similar results were reported based on  $|G^*|$  [115] (see Figure 17.7).

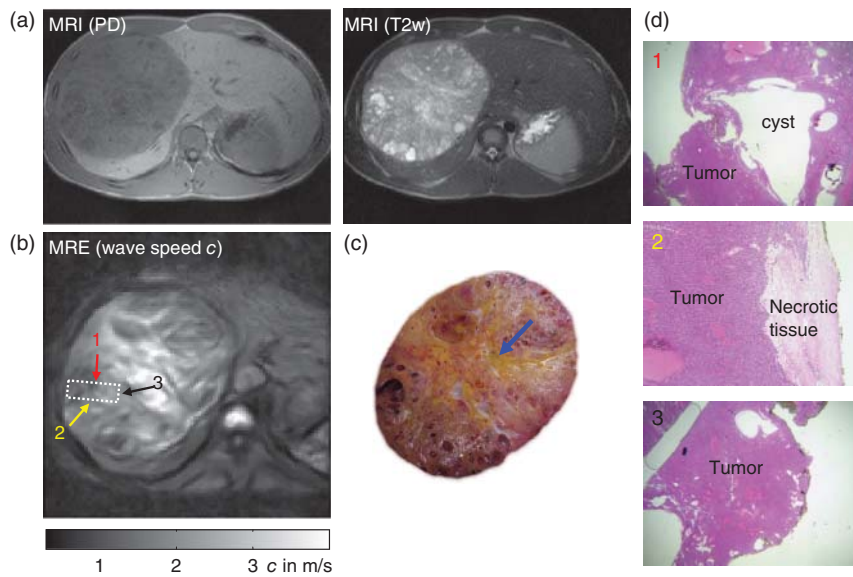
Measurement of intratumor heterogeneity of viscoelastic constants may improve the sensitivity and specificity of MRE. Multifrequency MRE combined with multifrequency parameter recovery based on MDEV or  $k$ -MDEV inversion (see Sections 10.5 and 10.6, respectively) showed promising preliminary results. Figure 17.8 illustrates a case



**Figure 17.6** Mechanical properties of seven *in vivo* tumors (three glioblastoma multiforme (GBM), one metastasis (MET), one astrocytoma WHO II (AC2), two meningioma (MEN)) measured by multifrequency MRE (MMRE) and the optical stretcher. (Sack 2015 [572]. Reproduced with permission of ISMRM.)



**Figure 17.7** *In vivo* MRE of liver tumors. (a) A stiffness threshold of 5 kPa separates malignant liver tumors from benign tumors (Venkatesh 2008 [114]. Reproduced with permission of American Journal of Roentgenology.) (b) Separation of benign from malignant tumors based on  $|G^*|$  was less pronounced according to Garteiser et al. [115]. This study found a significant separation based on the loss modulus  $G''$  of the tumors. (Garteiser 2012 [115]. Reproduced with permission of Springer.)



**Figure 17.8**  $k$ -MDEV-based multifrequency MRE in a patient with hepatocellular carcinoma. (a) Standard proton-density (PD) and  $T_2$ -weighted ( $T_2w$ ) MRI. (b) Wave speed map. (c) Cross-sectional view through the excised tumor. (d) Micrographs of histological analysis (H&E stain) corresponding to regions identified by arrows 1–3 in the  $c$  map shown in (b). Specimens were taken from the edges of a rectangular tissue sample demarcated by the dashed line in (b). (Tzschätzsch 2016 [222]. Reproduced with permission of Elsevier.)

analyzed by  $k$ -MDEV inversion of seven frequencies acquired by full-field, single-shot spin-echo EPI MRE [222]. The figure shows standard MRI (proton-density and  $T_2$ -weighted sequences), a wave speed map, and a cross-sectional view of the excised tumor, which corresponds to the other images. The blue arrow indicates regions of excessive cholestasis with obstructed bile flow – often the result of mechanical

obstruction by a tumor. These regions are characterized by high wave speed values. On average, the tumor is stiffer than the surrounding, unaffected tissue, which is consistent with reports of [114, 115] summarized in Figure 17.7. The high detail resolution in the wave speed map in Figure 17.8 allows pixel-wise correlation of MRE and histopathology. The micrographs show three tissue portions whose locations have been identified inside the elastogram. Tissue 1 (red arrow) indicates a region that consists mainly of tumor and cysts with wave speeds (soft,  $\approx 1.2$  m/s). Areas characterized by a mixture of tumorous and necrotic tissue (yellow arrow) show intermediate wave speed values ( $\approx 1.9$  m/s), while  $c$  is higher in regions consisting mainly of tumor (black arrow,  $\approx 2.3$  m/s).

### 17.3.3 MRE of Prostate Cancer

Prostate cancer is the most prevalent type of cancer in men. Currently, prostate cancer is commonly detected by PSA levels, digital rectal examination, US imaging, and MRI. However, histological confirmation remains indispensable for diagnosis and therapeutic decision making despite the limitations of biopsy in screening and follow-up examinations. Hence, research is being conducted to improve the diagnostic power of medical imaging in prostate cancer screening. Currently, multiparametric MRI based on  $T_2$ -weighted, diffusion-weighted, and dynamic contrast-enhanced imaging provides the best anatomic and functional imaging of the prostate [579]. MRI-derived parameters are combined in the PI-RADS (Prostate Imaging Reporting and Data System) scale for assessing the likelihood of prostate malignancy by assigning a score of 1–5 [580]. Reported by trained radiologists, PI-RADS provides an excellent negative predictive power, whereas the positive predictive value of the method is only moderate [579]. This means that current multiparametric MRI will typically not miss out significant prostate cancer lesions while resulting in a substantial number of unnecessary biopsies. Therefore, adding viscoelasticity to multiparametric MRI could help to increase specificity of imaging-based detection of prostate cancer. This motivation is supported by current reports on ADC-based diffusion measurement and MRE in prostate cancer, showing that MRE performs better than ADC in distinguishing normal from cancerous tissue [140].

#### 17.3.3.1 *Ex Vivo* Studies

Many studies investigating *ex vivo* tissue samples suggest that prostate cancer lesions are stiffer than healthy glandular tissue. Using a mechanical indenter device in 113 specimens, Krouskop et al. reported shear modulus values for 2% precompressed healthy prostate tissue, benign prostatic hyperplasia (BPH), and cancerous prostate tissue on the order of 20, 12, and 33 kPa, respectively (calculated from Young's moduli by assuming incompressibility) [581]. The observation that prostate cancer is stiffer than healthy glandular tissue was confirmed by Zhang et al. based on stress relaxation tests combined with Kelvin–Voigt fractional derivative model fitting (see Figure 4.7) [582]. Hoyt et al. investigated prostate samples in the relevant dynamic range of *in vivo* elastography (0.1–150 Hz) and measured shear modulus values of 1.3–5.3 kPa for healthy prostate tissue and of 2.6–13.5 kPa for cancerous tissue [583]. The first prostate specimen MRE was presented by Dresner et al. [584] in 1999. The so far most comprehensive study of MRE in human prostate specimens with correlation to histopathology was published by Sahebjavaheer et al. [140]. In this study, 112 tumors were analyzed, revealing storage

moduli in the peripheral zone of 65 kPa (normal tissue) versus 69 kPa (cancer) and in the central zone of 55 kPa (normal tissue) versus 63 kPa (cancer). However, effects of fixation of the specimens were observed, which reduced the discriminative power of the method.

### 17.3.3.2 *In Vivo* Studies

First *in vivo* MRE of the prostate was published by Kemper et al. using an external actuator attached to the pubic bone [493]. The shear modulus measured in healthy prostate correlated with the zonal anatomy of the gland with values of 2.2 kPa for the central gland and 3.3 kPa for the peripheral zone. A similar setup was used by Li et al. in a clinical pilot study of 10 patients with prostatitis and cancer lesions [494]. At 100 Hz vibration frequency, shear stiffness of the healthy peripheral zone was 2.3 kPa, while prostatitis and cancer were associated with 2.0 and 6.5 kPa, respectively [494]. An alternative strategy of mechanical excitation was proposed by Sahebjavaher et al., who used a transperineal driver setup, once based on hydraulic force transmission [585] and, more recently, by vibrating Lorentz coils [116]. The latter setup was used in a pilot study of 11 patients with prostate cancer. At 70 Hz single-frequency excitation, elasticity was measured to be 8.2, 7.5, 9.7, and 9.0 kPa in the prostate capsule, peripheral zone, central gland, and transition zone, respectively. The authors found cancerous tissue to be not always stiffer than normal tissue, resulting in only moderate diagnostic performance [116]. Further studies of *in vivo* MRE of the prostate used endorectal and transurethral drivers [107, 158, 586], which allowed application of higher vibration frequencies (100–300 Hz) and enabled higher detail resolution than surface-based prostate MRE. Values obtained by endorectal MRE in 12 volunteers fall into the range obtained by other methods (2.5–19 kPa for the central gland and 2.7–17 kPa for the peripheral zone) [107]. When using MRE as a screening method, endorectal actuators appear less suited than surface-based drivers. In the future, surface-based drivers combined with multifrequency MRE might add information on microstructural changes to multiparametric MRI of the prostate, which cannot be measured by other techniques.

### 17.3.4 MRE of Breast Tumors

Breast cancer is the most common type of cancer in Western women. Most women who die of breast cancer are not killed by the primary tumor but by its metastases at distant sites. Current biomarkers only poorly reflect the risk for metastasis in an individual patient, which leads to many unnecessary treatments by chemotherapy or mastectomy. MRE may improve the specificity of MRI breast screening, once the biophysical signatures of malignant transformation as shown in Figures 17.1 and 17.2 can be reproduced *in vivo*. Furthermore, the mechanical forces measured by MRE acting on tumor boundaries or being exerted by the tumor on the surrounding tissue may contribute to the differential diagnosis and staging of breast tumors.

Early work on the viscoelastic properties of breast tissue was performed using *ex vivo* tissue samples. Krouskop et al., using the same indenter-based test method as in prostate specimens, investigated 142 samples of breast tissue [581]. The shear modulus at 5% pre-compression and 4 Hz frequency (computed from Young's modulus via  $\mu = \frac{1}{3} E$ ) was 7.3, 11.7, 38.7, 8.7, and 37.3 kPa for fat, glandular tissue, fibrous tissues, intraductal

**Table 17.1** Young's modulus values for different breast lesions measured by inversion-based indentation.

Breast tissue type	Number of samples	Young's modulus (kPa) mean $\pm$ std
Normal fat	71	3.25 $\pm$ 0.91
Normal fibroglandular tissue	26	3.24 $\pm$ 0.61
Fibroadenoma	16	6.41 $\pm$ 2.86
Low-grade infiltrating ductal carcinoma (IDC)	12	10.40 $\pm$ 2.60
Infiltrating lobular carcinoma (ILC)	4	15.62 $\pm$ 2.64
Ductal carcinoma <i>in situ</i> (DCIS)	4	16.38 $\pm$ 1.55
Fibrocystic disease	4	17.11 $\pm$ 7.35
Intermediate-grade IDC	21	19.99 $\pm$ 4.20
High-grade IDC	9	42.52 $\pm$ 12.47
Invasive mucinous carcinoma (IMC)	1	20.21
Fat necrosis	1	4.45

Values should be divided by 3 for comparison with MRE shear modulus values.

Source: From [587] with permission.

carcinoma, and infiltrating ductal carcinoma, respectively [581]. Samani and coworkers investigated 169 breast tissue samples by an inversion-based indentation technique [587]. Results are listed in Table 17.1. The data show that fibroadenomas are softer than most breast pathologies but stiffer than fat and fibroglandular tissue. This is particularly relevant for MRE as a means to improve the specificity of dynamic contrast-enhanced MRI of the breast, in which fibroadenomas can frequently enhance in a manner similar to many breast cancers, leading to a high number of unnecessary biopsies. By contrast, differentiation of other tissues such as malignant lesions solely based on their macroscopic elastic properties may not be possible.

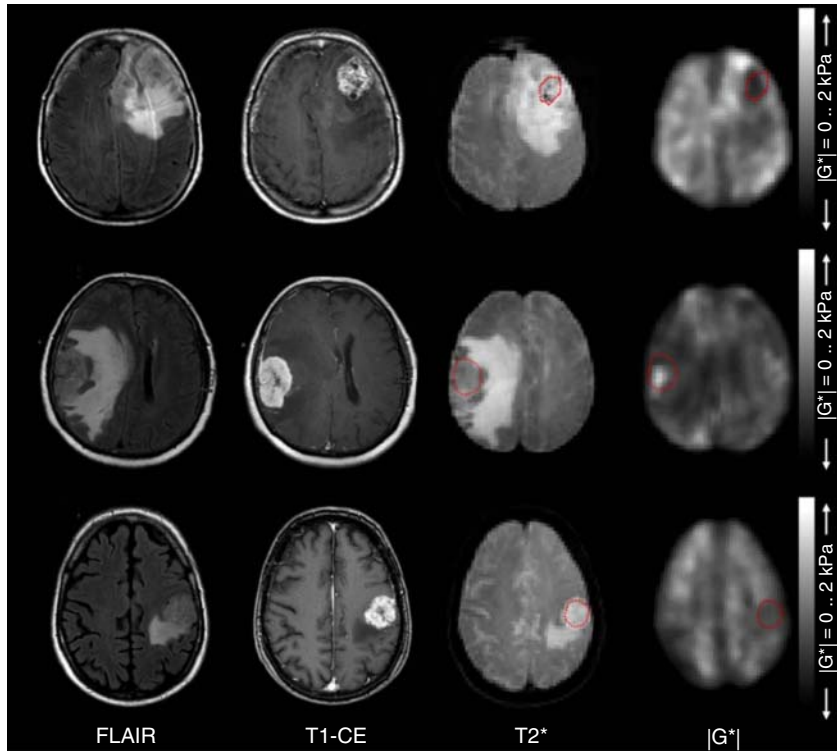
#### 17.3.4.1 *In Vivo* MRE of Breast Tumors

The technical feasibility of MRE for the mechanical characterization of breast tumors was demonstrated by Sinkus et al. [401, 588], Plewes et al. [589], and van Houten et al. [590]. Although aimed at breast tumors, these studies introduced general approaches to imaging, mechanical excitation, and postprocessing in MRE, which stimulated further developments in the field. A preliminary clinical test in six healthy women and six patients with known breast cancer was published by McKnight et al. [112]. The elastograms of patients with breast cancer showed focal areas of high shear stiffness, corresponding to the sites of known cancer within the breast. A total of 39 malignant and 29 benign lesions were investigated by *in vivo* 3D MRE and 3D reconstruction in a study by Sinkus et al. [156]. Storage and loss modulus as well as the springpot power law exponent were analyzed for their sensitivities to the degree of malignancy predefined by the BI-RADS score [156]. The authors observed a significantly increased storage and loss modulus of the tumors. In addition, the springpot power law exponent was found to be higher in tumors, which the authors suggested might be related to more liquid-like tissue properties. Altogether, the specificity of breast cancer diagnosis could be increased by approximately 20%. A second pilot study from the same group investigated 57 patients

and reproduced prior findings of increased specificity (from 75% to 90% at 90% sensitivity) by combined analysis of MRE with contrast-enhanced MRI [113]. Again, a higher discriminative power of benign versus malignant lesions was obtained by accounting for viscosity rather than elasticity, which explains the high diagnostic value of the power law exponent. The authors concluded that malignant lesions are significantly more liquid than benign lesions despite higher elasticity values [113].

### 17.3.5 MRE of Intracranial Tumors

Neuroradiological assessment of brain tumors and image-based differential diagnosis of intracranial masses is challenging [591, 592]. As a consequence, diagnostic biopsy remains inevitable for a definitive diagnosis despite possible complications [593]. MRE may add important information to established neuroradiological tumor markers and hence increase the diagnostic precision of imaging of intracranial tumors. Specifically, quantification of the tumor's intrinsic cohesiveness, heterogeneity, or infiltration into surrounding tissue could benefit from MRE. Furthermore, preoperative information on the mechanical consistency of a tumor as well as adhesion of a tumor to surrounding tissue is of high clinical relevance for treatment planning. For example, resection of harder tumors is often more challenging than treatment of softer tumors. The latter types of tumors can sometimes be treated by minimally invasive approaches such as suction, which minimizes the risk of damage to healthy tissue. Meanwhile, both motivations for MRE assessment of intracranial tumors – tissue mechanical characterization and treatment planning – have been supported by reports in the literature. The diagnostic capability of MRE is highlighted by Figure 17.9, in which three cases are shown: anaplastic oligoastrocytoma (WHO III), benign meningioma (WHO I), and high-grade glioblastoma (WHO IV). These cases presented with high similarity on conventional MRI, whereas the MRE property maps clearly differentiated the tumor entities as already visible to the naked eye [322]. This preliminary study relied on MRE with mechanical single-frequency vibration of 45 Hz and was thus limited by providing only coarse detail resolution. Therefore, a revised setup of multifrequency MRE (30–60 Hz) was used in two subsequent studies addressing the *in vivo* mechanical characterization of altogether 49 tumors [108, 109]. Figure 17.10 presents the averaged intratumor MDEV inversion parameters  $|G^*|$  and  $\varphi$  from both studies. Both parameters are plotted as ratios between tumor tissue and normal-appearing white matter. On average, normalized  $|G^*|$  was lower in high-grade glioblastoma (GB) than in meningioma despite significant overlap of values.  $\varphi$  fully separates both types of tumors, suggesting lower attenuation properties or more elastic behavior of GB than meningioma. It remains to be determined if this large difference in  $\varphi$  is related to the increased contractility (reduced viscosity) of malignant cells as observed by the optical stretcher (see Figure 17.1). The heterogeneity of values as seen on the  $|G^*|$  axis did not correlate with tumor size but reflected minor influences of geometry and tumor morphology [108]. Morphology-based tumor scores vary largely due to the presence of heterogeneous tissue fractions such as solid, cystic, and necrotic portions inside a single lesion. This heterogeneity is more markedly reflected in  $|G^*|$  than in  $\varphi$ .  $\varphi$  represents an attenuation-related measure, which appears to be more markedly influenced by how efficiently waves are introduced into the tumor, which in turn reflects the tumor's invasiveness into surrounding tissue. To account for the heterogeneity of  $|G^*|$  values, Streitberger et al. further assessed GBs by measuring

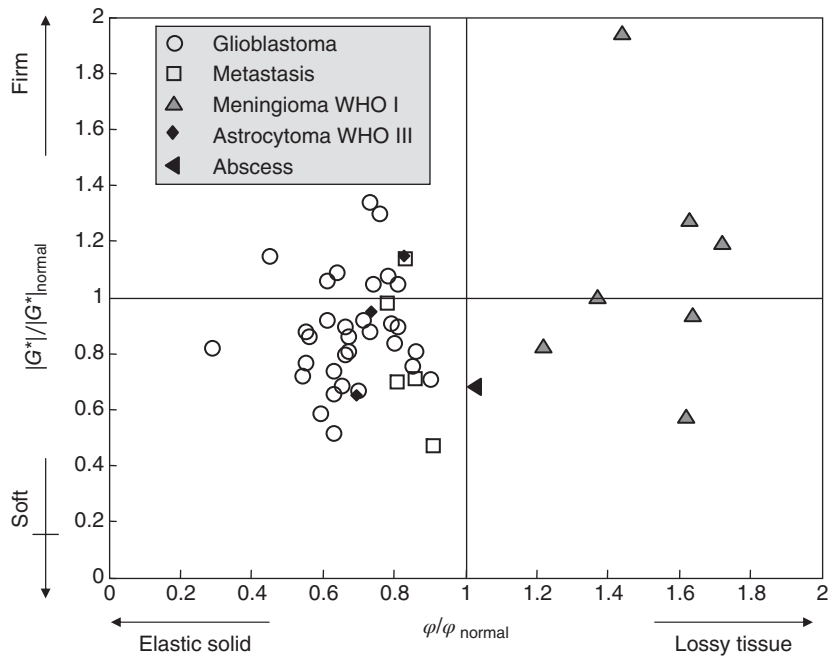


**Figure 17.9** Anatomical scans and parameter maps of three cases with high similarity on conventional MRI (FLAIR and  $T_1$ -weighted MRI). By contrast, the parameter maps derived from  $|G^*|$  measured by MRE clearly differentiate these three tumor entities. (From [322]. Reproduced with permission from Institute of Physics.)

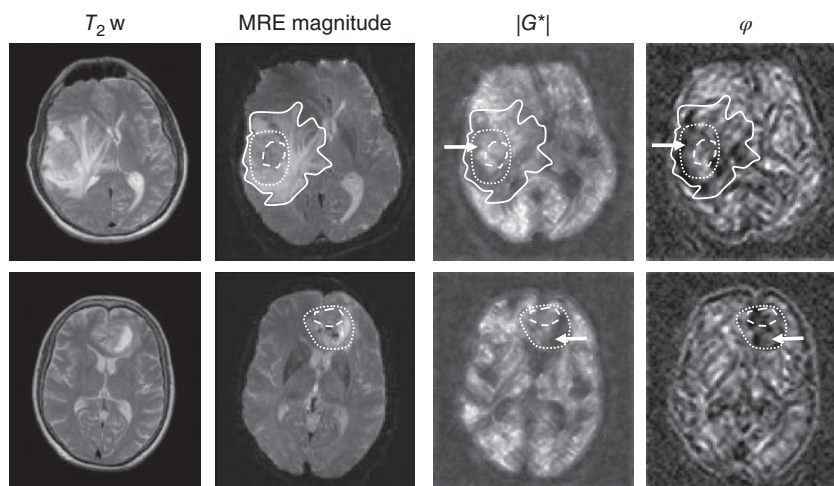
$|G^*|$  values in three regions: tumor, edema, and intratumor homogeneous-appearing matter [108]. An outline of these regions is presented in Figure 17.11 for two cases. Interestingly, tissue in homogeneous regions within the tumor displayed higher  $|G^*|$  values than full tumor regions without significant differences to healthy tissue, suggesting that homogenous tissue in GB is less affected than the remaining tumor. Some of the lesions investigated in [109] were further studied by the optical stretcher [572]. In this preliminary study, tissue samples were obtained in seven patients who underwent surgery after MRE (see Figure 17.6). On the basis of MRI, the surgeon defined the regions in which the tissue was obtained for cell dissociation and further analysis by the optical stretcher. Within these regions, MRE-measured  $|G^*|$  values were averaged and correlated with the shear modulus of cells of the same tissue obtained with the optical stretcher. Despite the preliminary nature of this study, the excellent correlation between *in vivo* MRE and optical stretcher shown in Figure 17.6 is encouraging in that it raises the prospect for the translation of the high sensitivity and specificity obtained by micromechanical methods into a quantitative imaging marker for staging tumors.

Two studies of brain MRE addressed the preoperative assessment of meningioma stiffness for treatment planning [110, 111]. Both studies showed an excellent agreement between meningioma stiffness measured *in vivo* and haptic assessment by the surgeon,

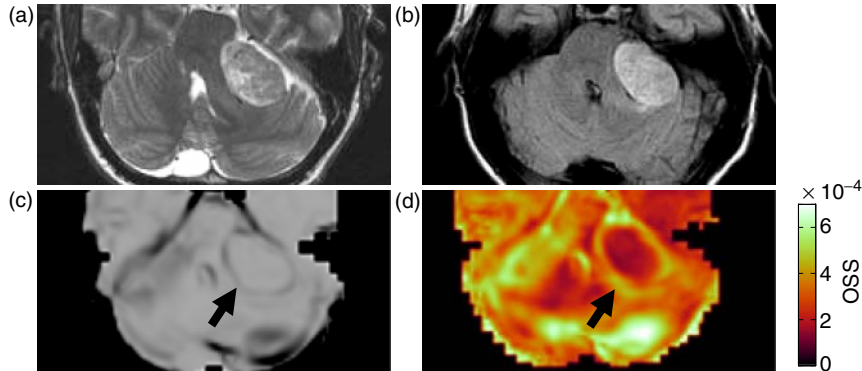




**Figure 17.10** Viscoelastic properties of intracranial tumors based on the parameter ratios of  $|G^*|$  and  $\varphi$  between tumor and healthy reference tissue (normal) as published in [109] and [108].



**Figure 17.11** Anatomical  $T_2$ -weighted images ( $T_2w$ ), MRE magnitude images, and MDEV inversion-based parameter maps ( $|G^*|$  and  $\varphi$ ) of two glioblastoma patients (upper row: 61-year-old man with a tumor with central necrosis and hemorrhage; bottom row: 72-year-old woman with a cystic tumor without hemorrhage). The selected regions demarcate the tumor (dotted lines), edema (solid line), and the region of homogeneous-appearing matter (dashed line). The arrows indicate compartments of soft tissue properties (low  $|G^*|$ ) but different dissipative behavior ( $\varphi$ ) in both tumors.  $|G^*|$  was scaled from 0 to 3 kPa;  $\varphi$  was scaled from 0 to 2.5 rad. (From [108]. Reproduced with permission of PLoS.)



**Figure 17.12** Images of a 32-year-old man with a left vestibular schwannoma. (a)  $T_2$ -weighted fast spin echo (FSE) and (b)  $T_2$ -weighted FLAIR images. The CSF cleft is classified as a partial cleft. The slip interface can be observed as a (c) low-signal shear line with (d) large OSS values around the whole surface of the tumor, indicating independent motion between the tumor and the adjacent tissues, classified as a complete slip interface. Surgical findings demonstrated no adhesion between the tumor–brainstem interfaces, in agreement with the slip interface imaging [595] predictions. (Reproduced with kind permission of Dr Ziyang Yin, Mayo Clinic College of Medicine, USA.)

in particular for lesions smaller than 3.5 cm. However, tumors below this threshold or vascular tumors were found to be softer than scored by the surgeon. Higher detail resolution achieved by multifrequency acquisition could potentially increase the accuracy of the method for measuring the consistency of intracranial tumors in the routine clinical setting.

A further interesting prospect for MRE in brain tumors is the evaluation of shear forces around lesions for quantification of tumor adhesion to surrounding brain parenchyma. Well-encapsulated tumors with slip boundaries to surrounding healthy tissue have a better prognosis and are easier to remove by the surgeon than invasively growing tumors with poorly defined boundaries. Low-frequency shear waves propagating through the brain become scattered at interfaces between compartments with relatively large differences in impedance [594]. Scattering also occurs at slip boundaries, which can be regarded as an intermediate layer of very soft tissue [51]. Scattering changes the amplitudes of shear waves. If this occurs at the edge of a tumor, the steep change in wave amplitude gives rise to a high shear strain, as demonstrated in Figure 17.12 in a case of a vestibular schwannoma [595]. Quantification of octahedral shear strain (see Section 4.3) in nine patients with vestibular schwannomas excellently matched the intraoperative assessment of tumor adhesion to brain parenchyma [595].

## References

- 1 Bar-Yosef, O. (2002) The upper paleolithic revolution. *Annual Review of Anthropology*, **31** (1), 363–393.
- 2 Georges, P.C., Hui, J.J., Gombos, Z., McCormick, M.E., Wang, A.Y., Uemura, M., Mick, R., Janmey, P.A., Furth, E.E., and Wells, R.G. (2007) Increased stiffness of the rat liver precedes matrix deposition: implications for fibrosis. *American Journal of Physiology. Gastrointestinal and Liver Physiology*, **293** (6), G1147–G1154, doi: 10.1152/ajpgi.00032.2007.
- 3 Sack, I., Jöhrens, K., Würfel, J., and Braun, J. (2013) Structure-sensitive elastography: on the viscoelastic powerlaw behavior of in vivo human tissue in health and disease. *Soft Matter*, doi: 10.1039/c3sm50552a.
- 4 Posnansky, O., Guo, J., Hirsch, S., Papazoglou, S., Braun, J., and Sack, I. (2012) Fractal network dimension and viscoelastic powerlaw behavior: I. A modeling approach based on a coarse-graining procedure combined with shear oscillatory rheometry. *Physics in Medicine and Biology*, **57** (12), 4023–4040, doi: 10.1088/0031-9155/57/12/4023.
- 5 Guo, J., Posnansky, O., Hirsch, S., Scheel, M., Taupitz, M., Braun, J.J., and Sack, I. (2012) Fractal network dimension and viscoelastic powerlaw behavior: II. An experimental study of structure-mimicking phantoms by magnetic resonance elastography. *Physics in Medicine and Biology*, **57** (12), 4041–4053, doi: 10.1088/0031-9155/57/12/4041.
- 6 Lambert, S.A., Näsholm, S.P., Nordsletten, D., Michler, C., Juge, L., Serfaty, J.M., Bilston, L., Guzina, B., Holm, S., and Sinkus, R. (2015) Bridging three orders of magnitude: multiple scattered waves sense fractal microscopic structures via dispersion. *Physical Review Letters*, **115** (9), 094301, doi: 10.1103/PhysRevLett.115.094301.
- 7 Haken, H. and Wolf, H.C. (2004) *Atom- und Quantenphysik*, 8th edn, Springer-Verlag.
- 8 Liang, Z.P. and Lauterbur, P.C. (2000) *Principles of Magnetic Resonance Imaging*, IEEE Press, Piscataway, NJ.
- 9 Hanson, L.G. (2008) Is quantum mechanics necessary for understanding magnetic resonance? *Concepts in Magnetic Resonance*, **32A** (5), 329–340, doi: 10.1002/cmra.

*Magnetic Resonance Elastography: Physical Background and Medical Applications*, First Edition.  
Sebastian Hirsch, Jürgen Braun, and Ingolf Sack.

© 2017 Wiley-VCH Verlag GmbH & Co. KGaA. Published 2017 by Wiley-VCH Verlag GmbH & Co. KGaA.

- 10 Haacke, E.M., Brown, R.W., Thompson, M.R., and Venkatesan, R. (1999) *Magnetic Resonance Imaging: Physical Principles and Sequence Design*, John Wiley & Sons, Inc., New York.
- 11 Bernstein, M.A., King, K.F., and Zhou, X.J. (2004) *Handbook of MRI Pulse Sequences*, Elsevier Academic Press.
- 12 Stanisz, G., Odrobina, E.E., Pun, J., Escaravage, M., Graham, S.J., Bronskill, M.J., and Henkelman, R.M. (2005) T1 , T2 relaxation and magnetization transfer in tissue at 3T. *Magnetic Resonance in Medicine*, **54**, 507–512, doi: 10.1002/mrm.20605.
- 13 Haase, A., Frahm, J., Matthaei, D., Hänicke, W., and Merboldt, K.D. (1986) FLASH imaging. Rapid NMR imaging using low flip-angle pulses. *Journal of Magnetic Resonance*, **67** (2), 258–266, doi: 10.1016/j.jmr.2011.09.021.
- 14 McRobbie, D.W., Moore, E.A., Graves, M.J., and Prince, M.R. (2003) *MRI from Picture to Proton*, Cambridge University Press, Cambridge.
- 15 Oppelt, A., Graumann, R., Barfuss, H., Fischer, H., Hartl, W., and Schajor, W. (1986) FISP - a new fast MRI sequence. *Electromedica*, **54**, 15–18.
- 16 Patz, S. (1988) Some factors that influence the steady state in steady-state free precession. *Magnetic Resonance Imaging*, **6** (4), 405–413.
- 17 Bieri, O., Maderwald, S., Ladd, M.E., and Scheffler, K. (2006) Balanced alternating steady-state elastography. *Magnetic Resonance in Medicine*, **55** (2), 233–241.
- 18 Rump, J., Klatt, D., Braun, J., Warmuth, C., and Sack, I. (2007) Fractional encoding of harmonic motions in MR elastography. *Magnetic Resonance in Medicine*, **57** (2), 388–395, doi: 10.1002/mrm.21152.
- 19 Rump, J., Warmuth, C., Braun, J., and Sack, I. (2008) Phase preparation in steady-state free precession MR elastography. *Magnetic Resonance Imaging*, **26** (2), 228–235.
- 20 Mansfield, P. (1977) Multi-planar image formation using NMR spin echoes. *Journal of Physics C: Solid State Physics*, **10** (3), L55–L58, doi: 10.1088/0022-3719/10/3/004.
- 21 Schmitt, F., Stehling, M.K., and Turner, R. (1998) *Echo-Planar Imaging*, Springer-Verlag, Berlin Heidelberg.
- 22 Johnson, C.L., McGarry, M.D.J., Van Houten, E.E.W., Weaver, J.B., Paulsen, K.D., Sutton, B.P., and Georgiadis, J.G. (2013) Magnetic resonance elastography of the brain using multishot spiral readouts with self-navigated motion correction. *Magnetic Resonance in Medicine*, **70** (2), 404–412, doi: 10.1002/mrm.24473.
- 23 Kim, D.H., Adalsteinsson, E., and Spielman, D.M. (2003) Simple analytic variable density spiral design. *Magnetic Resonance in Medicine*, **50** (1), 214–219, doi: 10.1002/mrm.10493.
- 24 Pruessmann, K.P., Weiger, M., Scheidegger, M.B., and Boesiger, P. (1999) SENSE: sensitivity encoding for fast MRI. *Magnetic Resonance in Medicine*, **42** (5), 952–962.
- 25 Griswold, M.A., Jakob, P.M., Heidemann, R.M., Nittka, M., Jellus, V., Wang, J., Kiefer, B., and Haase, A. (2002) Generalized autocalibrating partially parallel acquisitions (GRAPPA). *Magnetic Resonance in Medicine*, **47** (6), 1202–1210, doi: 10.1002/mrm.10171.

- 26 Uecker, M., Zhang, S., Voit, D., Karaus, A., Merboldt, K.D., and Frahm, J. (2010) Real-time MRI at a resolution of 20 ms. *NMR in Biomedicine*, **23** (8), 986–994, doi: 10.1002/nbm.1585.
- 27 Hennig, J., Welz, A.M., Schultz, G., Korvink, J., Liu, Z., Speck, O., and Zaitsev, M. (2008) Parallel imaging in non-bijective, curvilinear magnetic field gradients: a concept study. *Magnetic Resonance Materials in Physics, Biology and Medicine*, **21** (1-2), 5–14, doi: 10.1007/s10334-008-0105-7.
- 28 Blaimer, M., Breuer, F., Mueller, M., Heidemann, R.M., Griswold, M.A., and Jakob, P.M. (2004) SMASH, SENSE, PILS, GRAPPA: how to choose the optimal method. *Topics in Magnetic Resonance Imaging*, **15** (4), 223–236.
- 29 Deshmane, A., Gulani, V., Griswold, M.A., and Seiberlich, N. (2012) Parallel MR imaging. *Journal of Magnetic Resonance Imaging*, **36** (1), 55–72, doi: 10.1002/jmri.23639.
- 30 Chenevert, T.L., Skovoroda, A.R., O'Donnell, M., and Emelianov, S.Y. (1998) Elasticity reconstructive imaging by means of stimulated echo MRI. *Magnetic Resonance in Medicine*, **39** (3), 482–490, doi: 10.1002/mrm.1910390319.
- 31 Steele, D.D., Chenevert, T.L., Skovoroda, A.R., and Emelianov, S.Y. (2000) Three-dimensional static displacement, stimulated echo NMR elasticity imaging. *Physics in Medicine and Biology*, **45** (6), 1633–1648, doi: 10.1088/0031-9155/45/6/316.
- 32 Axel, L. and Dougherty, L. (1989) MR imaging of motion with spatial modulation of magnetization. *Radiology*, **171** (3), 841–845.
- 33 Klatt, D., Hamhaber, U., Asbach, P., Braun, J., and Sack, I. (2007) Noninvasive assessment of the rheological behavior of human organs using multifrequency MR elastography: a study of brain and liver viscoelasticity. *Physics in Medicine and Biology*, **52** (24), 7281–7294, doi: 10.1088/0031-9155/52/24/006.
- 34 Glaser, K.J., Felmlee, J.P., Manduca, A., and Ehman, R.L. (2003) Shear stiffness estimation using intravoxel phase dispersion in magnetic resonance elastography. *Magnetic Resonance in Medicine*, **50** (6), 1256–1265.
- 35 Yin, Z., Magin, R.L., and Klatt, D. (2014) Simultaneous MR elastography and diffusion acquisitions: diffusion-MRE (dMRE). *Magnetic Resonance in Medicine*, **71** (5), 1682–1688, doi: 10.1002/mrm.25180.
- 36 Braun, J., Buntkowsky, G., Bernarding, J., Tolxdorff, T., and Sack, I. (2001) Simulation and analysis of magnetic resonance elastography wave images using coupled harmonic oscillators and Gaussian local frequency estimation. *Magnetic Resonance Imaging*, **19**, 703–713.
- 37 Baron, C.A., Lebel, R.M., Wilman, A.H., and Beaulieu, C. (2012) The effect of concomitant gradient fields on diffusion tensor imaging. *Magnetic Resonance in Medicine*, **68** (4), 1190–1201, doi: 10.1002/mrm.24120.
- 38 Braun, J., Guo, J., Lützkendorf, R., Stadler, J., Papazoglou, S., Hirsch, S., Sack, I., and Bernarding, J. (2014) High-resolution mechanical imaging of the human brain by three-dimensional multifrequency magnetic resonance elastography at 7T. *Neuroimage*, **90**, 308–314.
- 39 Maderwald, S., Uffmann, K., Galbán, C.J., de Greiff, A., Ladd, M.E., and Galban, C.J. (2006) Accelerating MR elastography: a multiecho phase-contrast

- gradient-echo sequence. *Journal of Magnetic Resonance Imaging*, **23** (5), 774–780, doi: 10.1002/jmri.20570.
- 40 Landau, L.D. and Lifschitz, E.M. (1986) *Theory of Elasticity*, 3rd edn, Pergamon Press, Oxford.
- 41 Aki, K. and Richards, P.G. (2002) *Quantitative Seismology*, 2nd edn, University Science Books, Sausalito, CA.
- 42 Lai, W.M., Rubin, D., and Krempf, E. (1993) *Introduction to Continuum Mechanics*, 3rd edn, Butterworth Heinemann Ltd.
- 43 McGarry, M.D., Van Houten, E.E.W., Perriñez, P.R., Pattison, A.J., Weaver, J.B., and Paulsen, K.D. (2011) An octahedral shear strain-based measure of SNR for 3D MR elastography. *Physics in Medicine and Biology*, **56** (13), N153–N164, doi: 10.1088/0031-9155/56/13/n02.
- 44 Mainardi, F. (2010) *Fractional Calculus and Waves in Linear Viscoelasticity: An Introduction to Mathematical Models*, 1st edn, Imperial College Press, London.
- 45 Scott Blair, G.W. (1947) The role of psychophysics in rheology. *Journal of Colloid Science*, **2** (1), 21–32.
- 46 Graff, K.F. (1991) *Wave Motion in Elastic Solids*, 1st edn, Dover Publications, New York.
- 47 Guo, J., Hirsch, S., Scheel, M., Braun, J., and Sack, I. (2015) Three-parameter shear wave inversion in MR elastography of incompressible transverse isotropic media: application to in vivo lower leg muscles. *Magnetic Resonance in Medicine*, doi: 10.1002/mrm.25740.
- 48 Papazoglou, S., Rump, J., Braun, J., and Sack, I. (2006) Shear-wave group-velocity inversion in MR elastography of human skeletal muscle. *Magnetic Resonance in Medicine*, **56** (3), 489–497.
- 49 Klatt, D., Papazoglou, S., Braun, J., and Sack, I. (2010) Viscoelasticity-based MR elastography of skeletal muscle. *Physics in Medicine and Biology*, **55** (21), 6445–6459, doi: 10.1088/0031-9155/55/21/007.
- 50 Fedorov, F.I. (1968) *Theory of Elastic Waves in Crystals*, Plenum Press.
- 51 Papazoglou, S., Hamhaber, U., Braun, J., and Sack, I. (2007) Horizontal shear wave scattering from a nonwelded interface observed by magnetic resonance elastography. *Physics in Medicine and Biology*, **52** (3), 675–684, doi: 10.1088/0031-9155/52/3/010.
- 52 Ben-Avraham, D. and Havlin, S. (2000) *Diffusion and Reactions and Disordered Systems*, Cambridge University Press, Cambridge.
- 53 Fink, M. (1992) Time reversal of ultrasonic fields. I. Basic principles. *IEEE Transactions on Ultrasonics, Ferroelectrics, and Frequency Control*, **39** (5), 555–566, doi: 10.1109/58.156174.
- 54 Sheng, P. (2006) *Introduction to Wave Scattering, Localization and Mesoscopic Phenomena*, Springer-Verlag, Berlin Heidelberg, New York.
- 55 Papazoglou, S., Braun, J., Klatt, D., and Sack, I. (2012) Shear wave diffusion observed by magnetic resonance elastography, in *New Developments in the Visualization and Processing of Tensor Fields* (eds D.H. Laidlaw and A. Vilanova), Springer-Verlag, Berlin Heidelberg, pp. 157–168.

- 56 Schmidt, R.F., Lang, F., and Heckmann, M. (2011) *Physiologie des Menschen*, 31st edn, Springer-Verlag, Berlin, Heidelberg.
- 57 Ernst, T., Kreis, R., and Ross, B.D. (1993) Absolute quantitation of water and metabolites in the human brain. 1. Compartments and water. *Journal of Magnetic Resonance Series B*, **102** (1), 1–8.
- 58 Biot, M.A. (1941) General theory of three-dimensional consolidation. *Journal of Applied Physics*, **12** (2), 155–164, doi: 10.1063/1.1712886.
- 59 Biot, M.A. (1955) Theory of elasticity and consolidation for a porous anisotropic solid. *Journal of Applied Physics*, **26** (2), 182–185, doi: 10.1063/1.1721956.
- 60 Biot, M.A. (1956) Theory of propagation of elastic waves in a fluid-saturated porous solid. I. Low-frequency range. *Journal of the Acoustical Society of America*, **28** (2), 168–178, doi: 10.1121/1.1908239.
- 61 Biot, M.A. (1956) Theory of propagation of elastic waves in a fluid-saturated porous solid. II. Higher frequency range. *Journal of the Acoustical Society of America*, **28** (2), 179–191, doi: 10.1121/1.1908241.
- 62 Leiderman, R., Barbone, P.E., Oberai, A.A., and Bamber, J.C. (2006) Coupling between elastic strain and interstitial fluid flow: ramifications for poroelastic imaging. *Physics in Medicine and Biology*, **51** (24), 6291–6313, doi: 10.1088/0031-9155/51/24/002.
- 63 Berry, G.P., Bamber, J.C., Miller, N.R., Barbone, P.E., Bush, N.L., and Armstrong, C.G. (2006) Towards an acoustic model-based poroelastic imaging method: II. Experimental investigation. *Ultrasound in Medicine & Biology*, **32** (12), 1869–1885, doi: 10.1016/j.ultrasmedbio.2006.07.013.
- 64 Perrañez, P.R., Kennedy, F.E., Van Houten, E.E.W., Weaver, J.B., and Paulsen, K.D. (2010) Magnetic resonance poroelastography: an algorithm for estimating the mechanical properties of fluid-saturated soft tissues. *IEEE Transactions on Medical Imaging*, **29** (3), 746–755.
- 65 Perrañez, P.R., Kennedy, F.E., Van Houten, E.E.W., Weaver, J.B., and Paulsen, K.D. (2009) Modeling of soft poroelastic tissue in time-harmonic MR elastography. *IEEE Transactions on Biomedical Engineering*, **56** (3), 598–608, doi: 10.1109/TBME.2008.2009928.
- 66 Norris, A.N. (1985) Radiation from a point source and scattering theory in a fluid-saturated porous solid. *Journal of the Acoustical Society of America*, **77** (6), 2012–, doi: 10.1121/1.391773.
- 67 Dai, Z., Peng, Y., Mansy, H.A., Sandler, R.H., and Royston, T.J. (2014) Comparison of poroviscoelastic models for sound and vibration in the lungs. *Journal of Vibration and Acoustics*, **136**, 051012–, doi: 10.1115/1.4026436.
- 68 Fehlner, A., Behrens, J.R., Streitberger, K.J., Papazoglou, S., Braun, J., Bellmann-Strobl, J., Ruprecht, K., Paul, F., Würfel, J., and Sack, I. (2015) Higher-resolution MR elastography reveals early mechanical signatures of neuroinflammation in patients with clinically isolated syndrome. *Journal of Magnetic Resonance Imaging*.
- 69 Dittmann, F., Hirsch, S., Tzschätzsch, H., Guo, J., Braun, J., and Sack, I. (2015) In vivo wideband multifrequency MR elastography of the human brain and liver. *Magnetic Resonance in Medicine*, doi: 10.1002/mrm.26006.

- 70 Arani, A., Murphy, M.C., Glaser, K.J., Manduca, A., Lake, D.S., Kruse, S.A., Jack, C.R. Jr., Ehman, R.L., and Huston, J. III (2015) Measuring the effects of aging and sex on regional brain stiffness with MR elastography in healthy older adults. *NeuroImage*, **111**, 59–64, doi: 10.1016/j.neuroimage.2015.02.016.
- 71 Sack, I., Streitberger, K.J., Krefting, D., Paul, F., and Braun, J. (2011) The influence of physiological aging and atrophy on brain viscoelastic properties in humans. *PLoS ONE*, **6** (9), e23451.
- 72 Romano, A.J., Scheel, M., Hirsch, S., Braun, J., and Sack, I. (2012) In vivo waveguide elastography of white matter tracts in the human brain. *Magnetic Resonance in Medicine*, **68** (5), 1410–1422, doi: 10.1002/mrm.24141.
- 73 Würfel, J., Paul, F., Beierbach, B., Hamhaber, U., Klatt, D., Papazoglou, S., Zipp, F., Martus, P., Braun, J., and Sack, I. (2010) MR-elastography reveals degradation of tissue integrity in multiple sclerosis. *NeuroImage*, **49** (3), 2520–2525.
- 74 Streitberger, K.J., Sack, I., Krefting, D., Pfuller, C., Braun, J., Paul, F., and Würfel, J. (2012) Brain viscoelasticity alteration in chronic-progressive multiple sclerosis. *PLoS ONE*, **7** (1), e29888.
- 75 Lipp, A., Trbojevic, R., Paul, F., Fehlner, A., Hirsch, S., Scheel, M., Noack, C., Braun, J., and Sack, I. (2013) Cerebral magnetic resonance elastography in supranuclear palsy and idiopathic Parkinson's disease. *NeuroImage: Clinical*, **3**, 381–387.
- 76 Murphy, M.C., Huston, J. III, Jack, C.R. Jr., Glaser, K.J., Manduca, A., Felmlee, J.P., and Ehman, R.L. (2011) Decreased brain stiffness in Alzheimer's disease determined by magnetic resonance elastography. *Journal of Magnetic Resonance Imaging*, **34** (3), 494–498, doi: 10.1002/jmri.22707.
- 77 Freimann, F.B., Streitberger, K.J., Klatt, D., Lin, K., McLaughlin, J.R., Braun, J., Sprung, C., and Sack, I. (2012) Alteration of brain viscoelasticity after shunt treatment in normal pressure hydrocephalus. *Neuroradiology*, **54** (3), 189–196, doi: 10.1007/s00234-011-0871-1.
- 78 Streitberger, K.J., Wiener, E., Hoffmann, J., Freimann, F.B., Klatt, D., Braun, J., Lin, K., McLaughlin, J.R., Sprung, C., Klingebiel, R., and Sack, I. (2011) In vivo viscoelastic properties of the brain in normal pressure hydrocephalus. *NMR in Biomedicine*, **24** (4), 385–392, doi: 10.1002/nbm.1602.
- 79 Elgeti, T., Knebel, F., Hättasch, R., Hamm, B., Braun, J., and Sack, I. (2014) Shear-wave amplitudes measured with cardiac MR elastography for diagnosis of diastolic dysfunction. *Radiology*, **271** (3), 681–687, doi: 10.1148/radiol.13131605.
- 80 Elgeti, T., Steffen, I.G., Knebel, F., Hättasch, R., Hamm, B., Braun, J., and Sack, I. (2016) Time-resolved analysis of left ventricular shear wave amplitudes in cardiac elastography for the diagnosis of diastolic dysfunction. *Investigative Radiology*, **51** (1), 1–6, doi: 10.1097/RLI.000000000000198.
- 81 Green, M.A., Geng, G., Qin, E., Sinkus, R., Gandevia, S.C., and Bilston, L.E. (2013) Measuring anisotropic muscle stiffness properties using elastography. *NMR in Biomedicine*, **26** (11), 1387–1394, doi: 10.1002/nbm.2964.
- 82 Barnhill, E., Kennedy, P., Hammer, S., van Beek, E.J.R., Brown, C., and Roberts, N. (2013) Statistical mapping of the effect of knee extension on thigh muscle



- viscoelastic properties using magnetic resonance elastography. *Physiological Measurement*, **34** (12), 1675–1698, doi: 10.1088/0967-3334/34/12/1675.
- 83 McCullough, M.B., Domire, Z.J., Reed, A.M., Amin, S., Ytterberg, S.R., Chen, Q., and An, K.N. (2011) Evaluation of muscles affected by myositis using magnetic resonance elastography. *Muscle & Nerve*, **43** (4), 585–590, doi: 10.1002/mus.21923.
- 84 Bensamoun, S.F., Ringleb, S.I., Chen, Q., Ehman, R.L., An, K.N.N., and Brennan, M. (2007) Thigh muscle stiffness assessed with magnetic resonance elastography in hyperthyroid patients before and after medical treatment. *Journal of Magnetic Resonance Imaging*, **26** (3), 708–713, doi: 10.1002/jmri.21073.
- 85 Hirsch, S., Posnansky, O., Papazoglou, S., Elgeti, T., Braun, J., and Sack, I. (2013) Measurement of vibration-induced volumetric strain in the human lung. *Magnetic Resonance in Medicine*, **69** (3), 667–674, doi: 10.1002/mrm.24294.
- 86 Mariappan, Y.K., Glaser, K.J., Levin, D.L., Vassallo, R., Hubmayr, R.D., Mottram, C., Ehman, R.L., and McGee, K.P. (2013) Estimation of the absolute shear stiffness of human lung parenchyma using 1 H spin echo, echo planar MR elastography. *Journal of Magnetic Resonance Imaging*, **40** (5), 1230–1237, doi: 10.1002/jmri.24479.
- 87 Lee, D.H., Lee, J.M., Han, J.K., and Choi, B.I. (2013) MR elastography of healthy liver parenchyma: normal value and reliability of the liver stiffness value measurement. *Journal of Magnetic Resonance Imaging*, **38** (5), 1215–1223, doi: 10.1002/jmri.23958.
- 88 Yin, M., Talwalkar, J.A., Glaser, K.J., Manduca, A., Grimm, R.C., Rossman, P.J., Fidler, J.L., and Ehman, R.L. (2007) Assessment of hepatic fibrosis with magnetic resonance elastography. *Clinical Gastroenterology and Hepatology*, **5** (10), 1207–1213.e2, doi: 10.1016/j.cgh.2007.06.012.
- 89 Asbach, P., Klatt, D., Schlosser, B., Biermer, M., Muche, M., Rieger, A., Loddenkemper, C., Somasundaram, R., Berg, T., Hamm, B., Braun, J.J., and Sack, I. (2010) Viscoelasticity-based staging of hepatic fibrosis with multifrequency MR elastography. *Radiology*, **257** (1), 80–86, doi: 10.1148/radiol.10092489.
- 90 Runge, J.H., Bohte, A.E., Verheij, J., Terpstra, V., Nederveen, A.J., van Nieuwkerk, K.M.J., de Kneegt, R.J., Baak, B.C., Jansen, P.L.M., Sinkus, R., and Stoker, J. (2014) Comparison of interobserver agreement of magnetic resonance elastography with histopathological staging of liver fibrosis. *Abdominal Imaging*, **39** (2), 283–290, doi: 10.1007/s00261-013-0063-z.
- 91 Ichikawa, S., Motosugi, U., Morisaka, H., Sano, K., Ichikawa, T., Tatsumi, A., Enomoto, N., Matsuda, M., Fujii, H., and Onishi, H. (2015) Comparison of the diagnostic accuracies of magnetic resonance elastography and transient elastography for hepatic fibrosis. *Magnetic Resonance Imaging*, **33** (1), 26–30, doi: 10.1016/j.mri.2014.10.003.
- 92 Kim, D., Kim, W.R., Talwalkar, J.A., Kim, H.J., and Ehman, R.L. (2013) Advanced fibrosis in nonalcoholic fatty liver disease: noninvasive assessment with MR elastography. *Radiology*, **268** (2), 411–419, doi: 10.1148/radiol.13121193.
- 93 Chen, J., Talwalkar, J.A., Yin, M., Glaser, K.J., Sanderson, S.O., and Ehman, R.L. (2011) Early detection of nonalcoholic steatohepatitis in patients with nonalcoholic fatty liver disease by using MR elastography. *Radiology*, **259** (3), 749–756, doi: 10.1148/radiol.11101942.

- 94 Cui, J., Heba, E., Hernandez, C., Haufe, W., Hooker, J., Andre, M.P., Valasek, M.A., Aryafar, H., Sirlin, C.B., and Loomba, R. (2015) MRE is superior to ARFI for the diagnosis of fibrosis in patients with biopsy-proven NAFLD: a prospective study. *Hepatology*, **63** (2), 453–461, doi: 10.1002/hep.28337.
- 95 Guo, J., Büning, C., Schott, E., Kröncke, T., Braun, J., Sack, I., and Althoff, C. (2015) In vivo abdominal magnetic resonance elastography for the assessment of portal hypertension before and after transjugular intrahepatic portosystemic shunt implantation. *Investigative Radiology*, **50** (5), 347–351, doi: 10.1097/RLI.000000000000136.
- 96 Ronot, M., Lambert, S., Elkrief, L., Doblaz, S., Rautou, P.E., Castera, L., Vilgrain, V., Sinkus, R., Van Beers, B.E., and Garteiser, P. (2014) Assessment of portal hypertension and high-risk oesophageal varices with liver and spleen three-dimensional multifrequency MR elastography in liver cirrhosis. *European Radiology*, **24** (6), 1394–1402, doi: 10.1007/s00330-014-3124-y.
- 97 Talwalkar, J.A., Yin, M., Venkatesh, S., Rossman, P.J., Grimm, R.C., Manduca, A., Romano, A.J., Kamath, P.S., and Ehman, R.L. (2009) Feasibility of in vivo MR elastographic splenic stiffness measurements in the assessment of portal hypertension. *American Journal of Roentgenology*, **193** (1), 122–127, doi: 10.2214/AJR.07.3504.
- 98 Hirsch, S., Guo, J., Reiter, R., Papazoglou, S., Kroencke, T.J., Braun, J.J., and Sack, I. (2014) MR elastography of the liver and the spleen using a piezoelectric driver, single-shot wave-field acquisition, and multifrequency dual parameter reconstruction. *Magnetic Resonance in Medicine*, **71** (1), 267–277, doi: 10.1002/mrm.24674.
- 99 Yasar, T.K., Wagner, M., Bane, O., Besa, C., Babb, J.S., Kannengiesser, S., Fung, M., Ehman, R.L., and Taouli, B. (2015) Interplatform reproducibility of liver and spleen stiffness measured with MR elastography. *Journal of Magnetic Resonance Imaging*, doi: 10.1002/jmri.25077.
- 100 Shi, Y., Glaser, K.J., Venkatesh, S.K., Ben-Abraham, E.I., and Ehman, R.L. (2015) Feasibility of using 3D MR elastography to determine pancreatic stiffness in healthy volunteers. *Journal of Magnetic Resonance Imaging*, **41** (2), 369–375, doi: 10.1002/jmri.24572.
- 101 Streitberger, K.J., Diederichs, G., Guo, J., Fehlner, A., Hamm, B., Braun, J., and Sack, I. (2015) In vivo multifrequency magnetic resonance elastography of the human intervertebral disk. *Magnetic Resonance in Medicine*, **74** (5), 1380–1387, doi: 10.1002/mrm.25505.
- 102 Streitberger, K.J., Guo, J., Tzschätzsch, H., Hirsch, S., Fischer, T., Braun, J., and Sack, I. (2014) High-resolution mechanical imaging of the kidney. *Journal of Biomechanics*, **47** (3), 639–644, doi: 10.1016/j.jbiomech.2013.11.051.
- 103 Rouvière, O., Souchon, R., Pagnoux, G., Ménager, J.M., and Chapelon, J.Y. (2011) Magnetic resonance elastography of the kidneys: feasibility and reproducibility in young healthy adults. *Journal of Magnetic Resonance Imaging*, **34** (4), 880–886, doi: 10.1002/jmri.22670.
- 104 Lee, C.U., Glockner, J.F., Glaser, K.J., Yin, M., Chen, J., Kawashima, A., Kim, B., Kremers, W.K., Ehman, R.L., and Gloor, J.M. (2012) MR elastography in renal

- transplant patients and correlation with renal allograft biopsy: a feasibility study. *Academic Radiology*, **19** (7), 834–841, doi: 10.1016/j.acra.2012.03.003.
- 105 Jiang, X., Asbach, P., Streitberger, K.J., Thomas, A., Hamm, B., Braun, J., Sack, I., and Guo, J. (2014) In vivo high-resolution magnetic resonance elastography of the uterine corpus and cervix. *European Radiology*, **24** (12), 3025–3033, doi: 10.1007/s00330-014-3305-8.
- 106 Sahebjavaher, R.S., Baghani, A., Honarvar, M., Sinkus, R., and Salcudean, S.E. (2013) Transperineal prostate MR elastography: initial in vivo results. *Magnetic Resonance in Medicine*, **69** (2), 411–420, doi: 10.1002/mrm.24268.
- 107 Arani, A., Da Rosa, M., Ramsay, E., Plewes, D.B., Haider, M.A., and Chopra, R. (2013) Incorporating endorectal MR elastography into multi-parametric MRI for prostate cancer imaging: initial feasibility in volunteers. *Journal of Magnetic Resonance Imaging*, **38** (5), 1251–1260, doi: 10.1002/jmri.24028.
- 108 Streitberger, K.J., Reiss-Zimmermann, M., Freimann, F.B., Bayerl, S., Guo, J., Arlt, F., Wuerfel, J., Braun, J., Hoffmann, K.T., and Sack, I. (2014) High-resolution mechanical imaging of glioblastoma by multifrequency magnetic resonance elastography. *PLoS ONE*, **9** (10), e110588, doi: 10.1371/journal.pone.0110588.
- 109 Reiss-Zimmermann, M., Streitberger, K.J., Sack, I., Braun, J., Arlt, F., Fritzsche, D., and Hoffmann, K.T. (2014) High resolution imaging of viscoelastic properties of intracranial tumours by multi-frequency magnetic resonance elastography. *Clinical Neuroradiology*, **25** (4), 371–378, doi: 10.1007/s00062-014-0311-9.
- 110 Murphy, M.C., Huston, J. III, Glaser, K.J., Manduca, A., Meyer, F.B., Lanzino, G., Morris, J.M., Felmlee, J.P., and Ehman, R.L. (2013) Preoperative assessment of meningioma stiffness using magnetic resonance elastography. *Journal of Neurosurgery*, **118** (3), 643–648, doi: 10.3171/2012.9.JNS12519.
- 111 Hughes, J.D., Fattahi, N., Van Gompel, J., Arani, A., Meyer, F., Lanzino, G., Link, M.J., Ehman, R., and Huston, J. (2015) Higher-resolution magnetic resonance elastography in meningiomas to determine intratumoral consistency. *Neurosurgery*, **77** (4), 653–659, doi: 10.1227/NEU.0000000000000892.
- 112 McKnight, A.L., Kugel, J.L., Rossman, P.J., Manduca, A., Hartmann, L.C., and Ehman, R.L. (2002) MR elastography of breast cancer: preliminary results. *American Journal of Roentgenology*, **178** (6), 1411–1417, doi: 10.2214/ajr.178.6.1781411.
- 113 Siegmann, K.C., Xydeas, T., Sinkus, R., Kraemer, B., Vogel, U., and Claussen, C.D. (2010) Diagnostic value of MR elastography in addition to contrast-enhanced MR imaging of the breast-initial clinical results. *European Radiology*, **20** (2), 318–325, doi: 10.1007/s00330-009-1566-4.
- 114 Venkatesh, S.K., Yin, M., Glockner, J.F., Takahashi, N., Araoz, P.A., Talwalkar, J.A., and Ehman, R.L. (2008) MR elastography of liver tumors: preliminary results. *American Journal of Roentgenology*, **190** (6), 1534–1540, doi: 10.2214/AJR.07.3123.
- 115 Garteiser, P., Doblbas, S., Daire, J.L.L., Wagner, M., Leitao, H., Vilgrain, V., Sinkus, R., and Van Beers, B.E. (2012) MR elastography of liver tumours: value of viscoelastic properties for tumour characterisation. *European Radiology*, **22** (10), 2169–2177, doi: 10.1007/s00330-012-2474-6.

- 116 Sahebjavaher, R.S., Nir, G., Honarvar, M., Gagnon, L.O., Ischia, J., Jones, E.C., Chang, S.D., Fazli, L., Goldenberg, S.L., Rohling, R., Kozlowski, P., Sinkus, R., and Salcudean, S.E. (2015) MR elastography of prostate cancer: quantitative comparison with histopathology and repeatability of methods. *NMR in Biomedicine*, **28** (1), 124–139, doi: 10.1002/nbm.3218.
- 117 Atay, S.M., Kroenke, C.D., Sabet, A., and Bayly, P.V. (2008) Measurement of the dynamic shear modulus of mouse brain tissue in vivo by magnetic resonance elastography. *Journal of Biomechanical Engineering*, **130** (2), 21 013, doi: 10.1115/1.2899575.
- 118 Boulet, T., Kelso, M.L., and Othman, S.F. (2013) Long-term in vivo imaging of viscoelastic properties of the mouse brain after controlled cortical impact. *Journal of Neurotrauma*, **30** (17), 1512–1520, doi: 10.1089/neu.2012.2788.
- 119 Boulet, T., Kelso, M.L., and Othman, S.F. (2011) Microscopic magnetic resonance elastography of traumatic brain injury model. *Journal of Neuroscience Methods*, **201** (2), 296–306, doi: 10.1016/j.jneumeth.2011.08.019.
- 120 Othman, S.F., Curtis, E.T., Plautz, S.A., Pannier, A.K., Butler, S.D., and Xu, H. (2012) MR elastography monitoring of tissue-engineered constructs. *NMR in Biomedicine*, **25** (3), 452–463, doi: 10.1002/nbm.1663.
- 121 Millward, J.M., Guo, J., Berndt, D., Braun, J., Sack, I., and Infante-Duarte, C. (2015) Tissue structure and inflammatory processes shape viscoelastic properties of the mouse brain. *NMR in Biomedicine*, **28** (7), 831–839, doi: 10.1002/nbm.3319.
- 122 Klein, C., Hain, E.G., Braun, J., Riek, K., Mueller, S., Steiner, B., and Sack, I. (2014) Enhanced adult neurogenesis increases brain stiffness: in vivo magnetic resonance elastography in a mouse model of dopamine depletion. *PLoS ONE*, **9** (3), e92 582, doi: 10.1371/journal.pone.0092582.
- 123 Freimann, F.B., Müller, S., Streitberger, K.J., Guo, J., Rot, S., Ghori, A., Vajkoczy, P., Reiter, R., Sack, I., and Braun, J. (2013) MR elastography in a murine stroke model reveals correlation of macroscopic viscoelastic properties of the brain with neuronal density. *NMR in Biomedicine*, **26** (11), 1534–1539, doi: 10.1002/nbm.2987.
- 124 Riek, K., Millward, J.M., Hamann, I., Mueller, S., Pfueller, C.F., Paul, F., Braun, J., Infante-Duarte, C., and Sack, I. (2012) Magnetic resonance elastography reveals altered brain viscoelasticity in experimental autoimmune encephalomyelitis. *NeuroImage: Clinical*, **1** (1), 81–90, doi: 10.1016/j.nicl.2012.09.003.
- 125 Riek, K., Klatt, D., Nuzha, H., Mueller, S., Neumann, U., Sack, I., and Braun, J. (2011) Wide-range dynamic magnetic resonance elastography. *Journal of Biomechanics*, **44** (7), 1380–1386, doi: 10.1016/j.jbiomech.2010.12.031.
- 126 Jamin, Y., Boulton, J.K.R., Li, J., Popov, S., Garteiser, P., Ulloa, J.L., Cummings, C., Box, G., Eccles, S.A., Jones, C., Waterton, J.C., Bamber, J.C., Sinkus, R., and Robinson, S.P. (2015) Exploring the biomechanical properties of brain malignancies and their pathologic determinants in vivo with magnetic resonance elastography. *Cancer Research*, **75** (7), 1216–1224, doi: 10.1158/0008-5472.CAN-14-1997.
- 127 Qin, E.C., Jugé, L., Lambert, S.A., Paradis, V., Sinkus, R., and Bilston, L.E. (2014) In vivo anisotropic mechanical properties of dystrophic skeletal muscles measured by anisotropic MR elastographic imaging: the mdx mouse model of muscular dystrophy. *Radiology*, **273** (3), 726–735, doi: 10.1148/radiol.14132661.

- 128 Murphy, M.C., Curran, G.L., Glaser, K.J., Rossman, P.J., Huston, J. III, Poduslo, J.F., Jack, C.R. Jr., Felmlee, J.P., and Ehman, R.L. (2012) Magnetic resonance elastography of the brain in a mouse model of Alzheimer's disease: initial results. *Magnetic Resonance Imaging*, **30** (4), 535–539, doi: 10.1016/j.mri.2011.12.019.
- 129 Pattison, A.J., Lollis, S.S., Perrañez, P.R., Perreard, I.M., McGarry, M.D.J., Weaver, J.B., and Paulsen, K.D. (2010) Time-harmonic magnetic resonance elastography of the normal feline brain. *Journal of Biomechanics*, **43** (14), 2747–2752, doi: 10.1016/j.jbiomech.2010.06.008.
- 130 Vappou, J., Breton, E., Choquet, P., Willinger, R., and Constantinesco, A. (2008) Assessment of in vivo and post-mortem mechanical behavior of brain tissue using magnetic resonance elastography. *Journal of Biomechanics*, **41** (14), 2954–2959, doi: 10.1016/j.jbiomech.2008.07.034.
- 131 Vappou, J., Breton, E., Choquet, P., Goetz, C., Willinger, R., and Constantinesco, A. (2007) Magnetic resonance elastography compared with rotational rheometry for in vitro brain tissue viscoelasticity measurement. *Magnetic Resonance Materials in Physics, Biology and Medicine*, **20** (5-6), 273–278, doi: 10.1007/s10334-007-0098-7.
- 132 Ronot, M., Lambert, S.A., Wagner, M., Garteiser, P., Doblus, S., Albuquerque, M., Paradis, V., Vilgrain, V., Sinkus, R., and Van Beers, B.E. (2014) Viscoelastic parameters for quantifying liver fibrosis: three-dimensional multifrequency MR elastography study on thin liver rat slices. *PLoS ONE*, **9** (4), e94679, doi: 10.1371/journal.pone.0094679.
- 133 Salameh, N., Larrat, B.B., Abarca-Quinones, J., Pallu, S., Dorvillius, M., Leclercq, I., Fink, M., Sinkus, R., and Van Beers, B.E. (2009) Early detection of steatohepatitis in fatty rat liver by using MR elastography. *Radiology*, **253** (1), 90–97, doi: 10.1148/radiol.2523081817.
- 134 Yin, M., Woollard, J., Wang, X., Torres, V.E., Harris, P.C., Ward, C.J., Glaser, K.J., Manduca, A., and Ehman, R.L. (2007) Quantitative assessment of hepatic fibrosis in an animal model with magnetic resonance elastography. *Magnetic Resonance in Medicine*, **58** (2), 346–353, doi: 10.1002/mrm.21286.
- 135 McGee, K.P., Lake, D., Mariappan, Y.K., Hubmayr, R.D., Manduca, A., Ansell, K., and Ehman, R.L. (2011) Calculation of shear stiffness in noise dominated magnetic resonance elastography data based on principal frequency estimation. *Physics in Medicine and Biology*, **56** (14), 4291–4309, doi: 10.1088/0031-9155/56/14/006.
- 136 McGee, K.P., Mariappan, Y.K., Hubmayr, R.D., Carter, R.E., Bao, Z., Levin, D.L., Manduca, A., and Ehman, R.L. (2012) Magnetic resonance assessment of parenchymal elasticity in normal and edematous, ventilator-injured lung. *Journal of Applied Physiology*, **113** (4), 666–676, doi: 10.1152/jappphysiol.01628.2011.
- 137 McGee, K.P., Hubmayr, R.D., and Ehman, R.L. (2008) MR elastography of the lung with hyperpolarized  $^3\text{He}$ . *Magnetic Resonance in Medicine*, **59** (1), 14–18, doi: 10.1002/mrm.21465.
- 138 Korsmo, M.J., Ebrahimi, B., Eirin, A., Woollard, J.R., Krier, J.D., Crane, J.A., Warner, L., Glaser, K., Grimm, R., Ehman, R.L., and Lerman, L.O. (2013) Magnetic resonance elastography noninvasively detects in vivo renal medullary fibrosis secondary to swine renal artery stenosis. *Investigative Radiology*, **48** (2), 61–68, doi: 10.1097/RLI.0b013e31827a4990.

- 139 Shah, N.S., Kruse, S.A., Lager, D.J., Farell-Baril, G., Lieske, J.C., King, B.F., and Ehman, R.L. (2004) Evaluation of renal parenchymal disease in a rat model with magnetic resonance elastography. *Magnetic Resonance in Medicine*, **52** (1), 56–64, doi: 10.1002/mrm.20101.
- 140 Sahebjavaher, R.S., Nir, G., Gagnon, L.O., Ischia, J., Jones, E.C., Chang, S.D., Yung, A., Honarvar, M., Fazli, L., Goldenberg, S.L., Rohling, R., Sinkus, R., Kozlowski, P., and Salcudean, S.E. (2015) MR elastography and diffusion-weighted imaging of ex vivo prostate cancer: quantitative comparison to histopathology. *NMR in Biomedicine*, **28** (1), 89–100, doi: 10.1002/nbm.3203.
- 141 Jugé, L., Doan, B.T.T., Seguin, J., Albuquerque, M., Larrat, B., Mignet, N., Chabot, G.G., Scherman, D., Paradis, V., Vilgrain, V., Van Beers, B.E., and Sinkus, R. (2012) Colon tumor growth and antivasular treatment in mice: complementary assessment with MR elastography and diffusion-weighted MR imaging. *Radiology*, **264** (2), 436–444, doi: 10.1148/radiol.12111548.
- 142 Xu, L., Chen, J., Yin, M., Glaser, K.J., Chen, Q., Woodrum, D.A., and Ehman, R.L. (2012) Assessment of stiffness changes in the ex vivo porcine aortic wall using magnetic resonance elastography. *Magnetic Resonance Imaging*, **30** (1), 122–127, doi: 10.1016/j.mri.2011.09.009.
- 143 Woodrum, D.A., Romano, A.J., Lerman, A., Pandya, U.H., Brosh, D., Rossman, P.J., Lerman, L.O., and Ehman, R.L. (2006) Vascular wall elasticity measurement by magnetic resonance imaging. *Magnetic Resonance in Medicine*, **56** (3), 593–600, doi: 10.1002/mrm.20991.
- 144 Litwiller, D.V., Lee, S.J., Kolipaka, A., Mariappan, Y.K., Glaser, K.J., Pulido, J.S., and Ehman, R.L. (2010) MR elastography of the ex vivo bovine globe. *Journal of Magnetic Resonance Imaging*, **32** (1), 44–51, doi: 10.1002/jmri.22217.
- 145 Ipek-Ugay, S., Drießle, T., Ledwig, M., Guo, J., Hirsch, S., Sack, I., and Braun, J. (2015) Tabletop magnetic resonance elastography for the measurement of viscoelastic parameters of small tissue samples. *Journal of Magnetic Resonance*, **251**, 13–18, doi: 10.1016/j.jmr.2014.11.009.
- 146 Doyley, M.M., Perreard, I., Pattison, A.J., Weaver, J.B., and Paulsen, K.M. (2010) The performance of steady-state harmonic magnetic resonance elastography when applied to viscoelastic materials. *Medical Physics*, **37** (8), 3970–3979.
- 147 Okamoto, R.J., Clayton, E.H., and Bayly, P.V. (2011) Viscoelastic properties of soft gels: comparison of magnetic resonance elastography and dynamic shear testing in the shear wave regime. *Physics in Medicine and Biology*, **56** (19), 6379–6400, doi: 10.1088/0031-9155/56/19/014.
- 148 Othman, S.F., Xu, H., Royston, T.J., and Magin, R.L. (2005) Microscopic magnetic resonance elastography (microMRE). *Magnetic Resonance in Medicine*, **54** (3), 605–615, doi: 10.1002/mrm.20584.
- 149 Yasar, T.K., Royston, T.J., and Magin, R.L. (2013) Wideband MR elastography for viscoelasticity model identification. *Magnetic Resonance in Medicine*, **70** (2), 479–489, doi: 10.1002/mrm.24495.
- 150 Liu, Y., Yasar, T.K., and Royston, T.J. (2014) Ultra wideband (0.5–16 kHz) MR elastography for robust shear viscoelasticity model identification. *Physics in Medicine and Biology*, **59** (24), 7717–7734, doi: 10.1088/0031-9155/59/24/7717.

- 151 Tse, Z.T.H., Janssen, H., Hamed, A., Ristic, M., Young, I., and Lamperth, M. (2009) Magnetic resonance elastography hardware design: a survey. *Proceedings of the Institution of Mechanical Engineers, Part H: Journal of Engineering in Medicine*, **223** (4), 497–514.
- 152 Ehman, E.C., Rossman, P.J., Kruse, S.A., Sahakian, A.V., and Glaser, K.J. (2008) Vibration safety limits for magnetic resonance elastography. *Physics in Medicine and Biology*, **53** (4), 925–935.
- 153 Sahebjavaher, R.S., Frew, S., Bylinskii, A., ter Beek, L., Garteiser, P., Honarvar, M., Sinkus, R., and Salcudean, S. (2014) Prostate MR elastography with transperineal electromagnetic actuation and a fast fractionally encoded steady-state gradient echo sequence. *NMR in Biomedicine*, **27** (7), 784–794, doi: 10.1002/nbm.3118.
- 154 Hamhaber, U., Klatt, D., Papazoglou, S., Hollmann, M., Stadler, J., Sack, I., Bernarding, J., and Braun, J. (2010) In vivo magnetic resonance elastography of human brain at 7 T and 1.5 T. *Journal of Magnetic Resonance Imaging*, **32** (3), 577–583.
- 155 Basford, J.R., Jenkyn, T.R., An, K.N., Ehman, R.L., Heers, G., and Kaufman, K.R. (2002) Evaluation of healthy and diseased muscle with magnetic resonance elastography. *Archives of Physical Medicine and Rehabilitation*, **83** (11), 1530–1536.
- 156 Sinkus, R., Siegmann, K., Xydeas, T., Tanter, M., Claussen, C., and Fink, M. (2007) MR elastography of breast lesions: understanding the solid/liquid duality can improve the specificity of contrast-enhanced MR mammography. *Magnetic Resonance in Medicine*, **58** (6), 1135–1144, doi: 10.1002/mrm.21404.
- 157 Huwart, L., Peeters, F., Sinkus, R., Annet, L., Salameh, N., ter Beek, L.C., Horsmans, Y., and Van Beers, B.E. (2006) Liver fibrosis: non-invasive assessment with MR elastography. *NMR in Biomedicine*, **19** (2), 173–179, doi: 10.1002/nbm.1030.
- 158 Thörmer, G., Reiss-Zimmermann, M., Otto, J., Hoffmann, K.T.T., Moche, M., Garnov, N., Kahn, T., and Busse, H. (2013) Novel technique for MR elastography of the prostate using a modified standard endorectal coil as actuator. *Journal of Magnetic Resonance Imaging*, **37** (6), 1480–1485, doi: 10.1002/jmri.23850.
- 159 Latta, P., Gruwel, M.L.H., Debergue, P., Matwiy, B., Sbotto-Frankensteen, U.N., and Tomanek, B. (2011) Convertible pneumatic actuator for magnetic resonance elastography of the brain. *Magnetic Resonance Imaging*, **29** (1), 147–152, doi: 10.1016/j.mri.2010.07.014.
- 160 Kruse, S.A., Rose, G.H., Glaser, K.J., Manduca, A., Felmlee, J.P., Jack, C.R. Jr., and Ehman, R.L. (2008) Magnetic resonance elastography of the brain. *NeuroImage*, **39** (1), 231–237.
- 161 Wassenaar, P.A., Eleswarpu, C.N., Schroeder, S.A., Mo, X., Raterman, B.D., White, R.D., and Kolipaka, A. (2015) Measuring age-dependent myocardial stiffness across the cardiac cycle using MR elastography: a reproducibility study. *Magnetic Resonance in Medicine*, **75** (4), 1586–1593.
- 162 Kenyhercz, W.E., Raterman, B., Illapani, V.S., Dowell, J., Mo, X., White, R.D., and Kolipaka, A. (2015) Quantification of aortic stiffness using magnetic resonance elastography: measurement reproducibility, pulse wave velocity comparison, changes over cardiac cycle, and relationship with age. *Magnetic Resonance in Medicine*, **75** (5), 1920–1926.

- 163 Yin, M., Glaser, K.J., Talwalkar, J.A., Chen, J., Manduca, A., and Ehman, R.L. (2016) Hepatic MR elastography: clinical performance in a series of 1377 consecutive examinations. *Radiology*, **278** (1), 114–124, doi: 10.1148/radiol.2015142141.
- 164 Nedredal, G.I., Yin, M., McKenzie, T., Lillegard, J., Luebke-Wheeler, J., Talwalkar, J., Ehman, R.L., and Nyberg, S.L. (2011) Portal hypertension correlates with splenic stiffness as measured with MR elastography. *Journal of Magnetic Resonance Imaging*, **34** (1), 79–87, doi: 10.1002/jmri.22610.
- 165 Itoh, Y., Takehara, Y., Kawase, T., Terashima, K., Ohkawa, Y., Hirose, Y., Koda, A., Hyodo, N., Ushio, T., Hirai, Y., Yoshizawa, N., Yamashita, S., Nasu, H., Ohishi, N., and Sakahara, H. (2016) Feasibility of magnetic resonance elastography for the pancreas at 3T. *Journal of Magnetic Resonance Imaging*, **43** (2), 384–390, doi: 10.1002/jmri.24995.
- 166 Stewart, E.A., Taran, F.A., Chen, J., Gostout, B.S., Woodrum, D.A., Felmlee, J.P., and Ehman, R.L. (2011) Magnetic resonance elastography of uterine leiomyomas: a feasibility study. *Fertility and Sterility*, **95** (1), 281–284, doi: 10.1016/j.fertnstert.2010.06.004.
- 167 Chakouch, M.K., Pouletaut, P., Charleux, F., and Bensamoun, S.F. (2015) Viscoelastic shear properties of in vivo thigh muscles measured by MR elastography. *Journal of Magnetic Resonance Imaging*, **43**(6), 1423–1433, doi: 10.1002/jmri.25105.
- 168 Low, G., Owen, N.E., Joubert, I., Patterson, A.J., Graves, M.J., Alexander, G.J.M., and Lomas, D.J. (2015) Magnetic resonance elastography in the detection of hepatorenal syndrome in patients with cirrhosis and ascites. *European Radiology*, **25** (10), 2851–2858, doi: 10.1007/s00330-015-3723-2.
- 169 Uffmann, K., Maderwald, S., de Greiff, A., and Ladd, M.E. (2004) Determination of gray and white matter elasticity with MR elastography. *Proceedings of the 11th Annual Meeting of ISMRM*, p. 1768.
- 170 Uffmann, K., Maderwald, S., Ajaj, W., Galban, C.G., Mateiescu, S., Quick, H.H., and Ladd, M.E. (2004) In vivo elasticity measurements of extremity skeletal muscle with MR elastography. *NMR in Biomedicine*, **17** (4), 181–190.
- 171 Arani, A., Plewes, D., Krieger, A., and Chopra, R. (2011) The feasibility of endorectal MR elastography for prostate cancer localization. *Magnetic Resonance in Medicine*, **66** (6), 1649–1657, doi: 10.1002/mrm.22967.
- 172 Braun, J., Hirsch, S., Heinze, T., and Sack, I. (2015) Feasibility of a new actuator type for magnetic resonance elastography based on transient air pressure impulses. *Proceedings of the 23rd Annual Meeting of ISMRM*, Toronto, p. 1826.
- 173 Dittmann, F., Tzschätzsch, H., Guo, J., Hirsch, S., Braun, J., and Sack, I. (2016) In vivo multifrequency MR elastography of the human prostate using a surface-based compressed air driver operated in the lower frequency regime. *Proceedings of the 24th Annual Meeting of ISMRM*, Singapore.
- 174 Corbin, N., Vappou, J., Breton, E., Boehler, Q., Barbé, L., Renaud, P., and de Mathelin, M. (2015) Interventional MR elastography for MRI-guided percutaneous procedures. *Magnetic Resonance in Medicine*, **75** (3), 1110–1118, doi: 10.1002/mrm.25694.



- 175 Mariappan, Y.K., Glaser, K.J., Hubmayr, R.D., Manduca, A., Ehman, R.L., and McGee, K.P. (2011) MR elastography of human lung parenchyma: technical development, theoretical modeling and in vivo validation. *Journal of Magnetic Resonance Imaging*, **33** (6), 1351–1361, doi: 10.1002/jmri.22550.
- 176 Hirsch, S., Klatt, D., Freimann, F.B., Scheel, M., Braun, J., and Sack, I. (2013) In vivo measurement of volumetric strain in the human brain induced by arterial pulsation and harmonic waves. *Magnetic Resonance in Medicine*, **70** (3), 671–683, doi: 10.1002/mrm.24499.
- 177 Elgeti, T., Beling, M., Hamm, B., Braun, J., and Sack, I. (2010) Elasticity-based determination of isovolumetric phases in the human heart. *Journal of Cardiovascular Magnetic Resonance*, **12** (60), 1–8, doi: 10.1186/1532-429X-12-60.
- 178 Muthupillai, R., Lomas, D.J., Rossman, P.J., Greenleaf, J.F., Manduca, A., and Ehman, R.L. (1995) Magnetic resonance elastography by direct visualization of propagating acoustic strain waves. *Science*, **269** (5232), 1854–1857.
- 179 Muthupillai, R., Rossman, P.J., Lomas, D.J., Greenleaf, J.F., Riederer, S.J., and Ehman, R.L. (1996) Magnetic resonance imaging of transverse acoustic strain waves. *Magnetic Resonance in Medicine*, **36** (2), 266–274, doi: 10.1002/mrm.1910360214.
- 180 Kruse, S.A., Dresner, M.A., Rossman, P.J., Felmlee, J.P., Jack, C.R., and Ehman, R.L. (1999) Palpation of the brain using magnetic resonance elastography. *Proceedings of the 7th Annual Meeting of ISMRM*, Philadelphia, PA, p. 258.
- 181 Dresner, M.A., Rose, G.H., Rossman, P.J., Muthupillai, R., Manduca, A., and Ehman, R.L. (2001) Magnetic resonance elastography of skeletal muscle. *Journal of Magnetic Resonance Imaging*, **13** (2), 269–276.
- 182 Rouvière, O., Yin, M., Dresner, M.A., Rossman, P.J., Burgart, L.J., Fidler, J.L., and Ehman, R.L. (2006) MR elastography of the liver: preliminary results. *Radiology*, **240** (2), 440–448, doi: 10.1148/radiol.2402050606.
- 183 Bieri, O., Maderwald, S., Ladd, M.E., and Scheffler, K. (2005) Balanced alternating steady-state elastography. *Proceedings of the 13th Annual Meeting of ISMRM*, Miami, FL, p. 97.
- 184 Rump, J., Klatt, D., Warmuth, C., Braun, J., Hamhaber, U., Papazoglou, S., and Sack, I. (2005) Synchronisation of shear vibrations and balanced steady state free precession in MR Elastography (SSFP-MRE). *Proceedings of the 13th Annual Meeting of ISMRM*, Miami, FL, p. 2384.
- 185 Klatt, D., Asbach, P., Rump, J., Papazoglou, S., Somasundaram, R., Modrow, J., Braun, J.J., and Sack, I. (2006) In vivo determination of hepatic stiffness using steady-state free precession magnetic resonance elastography. *Investigative Radiology*, **41** (12), 841–848, doi: 10.1097/01.rli.0000244341.16372.08.
- 186 Braun, J., Bernarding, J., Tolxdorff, T., and Sack, I. (2002) In vivo magnetic resonance elastography of the human brain using ultrafast acquisition techniques. *Proceedings of the 10th Annual Meeting of ISMRM*, Vol. 10, Honolulu, HI, p. 2597.
- 187 Yin, M., Grimm, R.C., Manduca, A., and Ehman, R.L. (2006) Rapid EPI-based MR elastography of the liver. *Proceedings of the 14th Annual Meeting of ISMRM*, Seattle, WA, p. 2268.

- 188 Aletras, A.H., Ding, S., Balaban, R.S., and Wen, H. (1999) DENSE: displacement encoding with stimulated echoes in cardiac functional MRI. *Journal of Magnetic Resonance*, **137** (1), 247–252, doi: 10.1006/jmre.1998.1676.
- 189 Robert, B., Sinkus, R., Gennisson, J.L., and Fink, M. (2009) Application of DENSE-MR-elastography to the human heart. *Magnetic Resonance in Medicine*, **62** (5), 1155–1163, doi: 10.1002/mrm.22124.
- 190 Vaseghi, S.V. (2008) *Advanced Digital Signal Processing and Noise Reduction*, John Wiley & Sons, Ltd.
- 191 Mallat, S. (2008) *A Wavelet Tour of Signal Processing: The Sparse Way*, Academic press.
- 192 Kolipaka, A., McGee, K.P., Manduca, A., Romano, A.J., Glaser, K.J., Araoz, P.A., and Ehman, R.L. (2009) Magnetic resonance elastography: inversions in bounded media. *Magnetic Resonance in Medicine*, **62** (6), 1533–1542, doi: 10.1002/mrm.22144.
- 193 Kruse, S.A., Kolipaka, A., Manduca, A., and Ehman, R.L. (2009) Feasibility of evaluating the spinal cord with MR elastography. *Proceedings of the 17th Annual Meeting of ISMRM*, p. 629.
- 194 Manduca, A., Oliphant, T.E., Dresner, M.A., Mahowald, J.L., Kruse, S.A., Amromin, E., Felmlee, J.P., Greenleaf, J.F., and Ehman, R.L. (2001) Magnetic resonance elastography: non-invasive mapping of tissue elasticity. *Medical Image Analysis*, **5** (4), 237–254.
- 195 Savitzky, A. and Golay, M.J.E. (1964) Smoothing and differentiation of data by simplified least squares procedures. *Analytical Chemistry*, **36** (8), 1627–1639.
- 196 Schafer, R.W. (2011) What is a Savitzky-Golay filter? [lecture notes]. *IEEE Signal Processing Magazine*, **28** (4), 111–117.
- 197 Prandoni, P. and Vetterli, M. (2008) *Signal Processing for Communications*, CRC Press.
- 198 Tramel, E.W., Kumar, S., Giurghi, A., and Montanari, A. (2014) Statistical Estimation: From Denoising to Sparse Regression and Hidden Cliques. *arXiv preprint arXiv:1409.5557*.
- 199 Vetterli, M., Kovačević, J., and Goyal, V.K. (2014) *Foundations of Signal Processing*, Cambridge University Press, Cambridge.
- 200 Selesnick, I.W., Baraniuk, R.G., and Kingsbury, N.C. (2005) The dual-tree complex wavelet transform. *IEEE Signal Processing Magazine*, **22** (6), 123–151.
- 201 Anderssen, R.S. and de Hoog, F.R. (1984) Finite difference methods for the numerical differentiation of non-exact data. *Computing*, **33** (3), 259–267.
- 202 Mclaughlin, J., Renzi, D., Yoon, J.R., Ehman, R.L., and Manduca, A. (2006) Variance controlled shear stiffness images for MRE data. *3rd IEEE International Symposium on Biomedical Imaging: Nano to Macro, 2006*, pp. 960–963, doi: 10.1109/ISBI.2006.1625079.
- 203 Anderssen, R.S. and Hegland, M. (1999) For numerical differentiation dimensionality can be a blessing. *Mathematics of Computation*, **68** (227), 1121–1141.
- 204 Lehtinen, J. (2003) Time-domain numerical solution of the wave equation, [http://www.cs.unm.edu/williams/cs530/wave\\_eqn.pdf](http://www.cs.unm.edu/williams/cs530/wave_eqn.pdf).
- 205 Itoh, K. (1982) Analysis of the phase unwrapping algorithm. *Applied Optics*, **21** (14), 2470.

- 206 Ghiglia, D.C. and Pritt, M.D. (1998) *Two-Dimensional Phase Unwrapping: Theory, Algorithms, and Software*, John Wiley & Sons, Inc., New York.
- 207 Flynn, T.J. (1997) Two-dimensional phase unwrapping with minimum weighted discontinuity. *Journal of the Optical Society of America A*, **14** (10), 2692–2701.
- 208 Sack, I., Rump, J., Elgeti, T., Samani, A., and Braun, J. (2009) MR elastography of the human heart: noninvasive assessment of myocardial elasticity changes by shear wave amplitude variations. *Magnetic Resonance in Medicine*, **61** (3), 668–677, doi: 10.1002/mrm.21878.
- 209 Schofield, M.A. and Zhu, Y. (2003) Fast phase unwrapping algorithm for interferometric applications. *Optics Letters*, **28** (14), 1194–1196, doi: 10.1364/OL.28.001194.
- 210 Barnhill, E., Kennedy, P., Johnson, C.L., Mada, M., and Roberts, N. (2014) Real-time 4D phase unwrapping applied to magnetic resonance elastography. *Magnetic Resonance in Medicine*, **00**, 1–11, doi: 10.1002/mrm.25332.
- 211 Jeught, S., Sijbers, J., and Dirckx, J. (2015) Fast fourier-based phase unwrapping on the graphics processing unit in real-time imaging applications. *Journal of Imaging*, **1** (1), 31–44, doi: 10.3390/jimaging1010031.
- 212 Pattison, A.J., McGarry, M.D., Weaver, J.B., and Paulsen, K.D. (2014) Spatially-resolved hydraulic conductivity estimation via poroelastic magnetic resonance elastography. *IEEE Transactions on Medical Imaging*, **33** (6), 1373–1380, doi: 10.1109/TMI.2014.2311456.Spatially-Resolved.
- 213 Park, E. and Maniatty, A.M. (2006) Shear modulus reconstruction in dynamic elastography: time harmonic case. *Physics in Medicine and Biology*, **51** (15), 3697–3721, doi: 10.1088/0031-9155/51/15/007.
- 214 Papazoglou, S., Hamhaber, U., Braun, J., and Sack, I. (2008) Algebraic Helmholtz inversion in planar magnetic resonance elastography. *Physics in Medicine and Biology*, **53** (12), 3147–3158, doi: 10.1088/0031-9155/53/12/005.
- 215 Oliphant, T.E., Manduca, A., Ehman, R.L., and Greenleaf, J.F. (2001) Complex-valued stiffness reconstruction for magnetic resonance elastography by algebraic inversion of the differential equation. *Magnetic Resonance in Medicine*, **45** (2), 299–310.
- 216 Westin, C.F. (1994) A tensor framework for multidimensional signal processing. PhD thesis. Linköping University, <http://www.diva-portal.org/smash/get/diva2:302457/FULLTEXT01.pdf> (accessed 21 June 2016).
- 217 Knutsson, H., Westin, C.F., and Granlund, G. (1994) Local multiscale frequency and bandwidth estimation. *Proceedings of the IEEE International Conference on Image Processing*, Vol. 1, pp. 36–40.
- 218 Manduca, A., Muthupillai, R., Rossman, P.J., Greenleaf, J.F., and Ehman, R.L. (1996) Image processing for magnetic resonance elastography, in *Proceedings of SPIE Medical Imaging*, Vol. **2710** (eds M.H. Loew and K.M. Hanson), pp. 616–623.
- 219 Oliphant, T.E. (2001) Direct methods for dynamic elastography reconstruction: optimal inversion of the interior helmholtz problem. PhD thesis. Mayo Graduate School, Rochester, MN, <http://www.mayo.edu/research/documents/oliphantpdf/DOC-10027444> (accessed 21 June 2016).

- 220 Manduca, A., Lake, D.S., Kruse, S.A., and Ehman, R.L. (2003) Spatio-temporal directional filtering for improved inversion of MR elastography images. *Medical Image Analysis*, **7** (4), 465–473.
- 221 Papazoglou, S., Hirsch, S., Braun, J., and Sack, I. (2012) Multifrequency inversion in magnetic resonance elastography. *Physics in Medicine and Biology*, **57** (8), 2329–2346, doi: 10.1088/0031-9155/57/8/2329.
- 222 Tzschätzsch, H., Guo, J., Dittmann, F., Hirsch, S., Barnhill, E., Jöhrens, K., Braun, J., and Sack, I. (2016) Tomoelastography by multifrequency wave number recovery from time-harmonic propagating shear waves. *Medical Image Analysis*, **30**, 1–10, doi: 10.1016/j.media.2016.01.001.
- 223 Reddy, J.N. (2005) *An Introduction to the Finite Element Method*, 3rd edn, McGraw-Hill.
- 224 Reiter, R., Freise, C., Jöhrens, K., Kamphues, C., Seehofer, D., Stockmann, M., Somasundaram, R., Asbach, P., Braun, J., Samani, A., and Sack, I. (2014) Wideband MRE and static mechanical indentation of human liver specimen: sensitivity of viscoelastic constants to the alteration of tissue structure in hepatic fibrosis. *Journal of Biomechanics*, **47** (7), 1665–1674, doi: 10.1016/j.jbiomech.2014.02.034.
- 225 Press, W.H., Teukolsky, S.A., Vetterling, W.T., and Flannery, B.P. (2007) *Numerical Recipes*, 3rd edn, Cambridge University Press, New York.
- 226 Honarvar, M., Sahebjavaher, R., Sinkus, R., Rohling, R., and Salcudean, S.E. (2013) Curl-based finite element reconstruction of the shear modulus without assuming local homogeneity: time harmonic case. *IEEE Transactions on Medical Imaging*, **32** (12), 2189–2199, doi: 10.1109/TMI.2013.2276060.
- 227 Basser, P.J., Pajevic, S., Pierpaoli, C., Duda, J., and Aldroubi, A. (2000) In vivo fiber tractography using DT-MRI data. *Magnetic Resonance in Medicine*, **44** (4), 625–632.
- 228 Klatt, D., Yasar, T.K., Royston, T.J., and Magin, R.L. (2013) Sample interval modulation for the simultaneous acquisition of displacement vector data in magnetic resonance elastography: theory and application. *Physics in Medicine and Biology*, **58** (24), 8663–8675, doi: 10.1088/0031-9155/58/24/8663.
- 229 Klatt, D., Johnson, C.L., and Magin, R.L. (2015) Simultaneous, multidirectional acquisition of displacement fields in magnetic resonance elastography of the in vivo human brain. *Journal of Magnetic Resonance Imaging*, **42** (2), 297–304, doi: 10.1002/jmri.24806.
- 230 Kearney, S.P., Brinker, S.T., Burns, D.A., Royston, T.A., and Klatt, D. (2015) SLIM-MRE without prolonged echo time for the simultaneous acquisition of the 3D displacement vector applied to in vivo mouse brain. In *Proceedings of the 23rd Annual Meeting of ISMRM*, Toronto, p. 1054.
- 231 Sugimoto, T., Ueha, S., and Itoh, K. (1990) Tissue hardness measurement using the radiation force of focused ultrasound. *Ultrasonics Symposium, 1990*, pp. 1377–1380, doi: 10.1109/ULTSYM.1990.171591.
- 232 Lu, J.Y. (1997) 2D and 3D high frame rate imaging with limited diffraction beams. *IEEE Transactions on Ultrasonics, Ferroelectrics, and Frequency Control*, **44** (4), 839–856, doi: 10.1109/58.655200.
- 233 Song, T.K. and Chang, J.H. (2004) Synthetic Aperture Focusing Method for Ultrasound Imaging Based on Planar Waves.

- 234 Cheng, J. and Lu, J.Y. (2006) Extended high-frame rate imaging method with limited-diffraction beams. *IEEE Transactions on Ultrasonics, Ferroelectrics, and Frequency Control*, **53** (5), 880–899, doi: 10.1109/TUFFC.2006.1632680.
- 235 Montaldo, G., Tanter, M., Bercoff, J., Benech, N., and Fink, M. (2009) Coherent plane-wave compounding for very high frame rate ultrasonography and transient elastography. *IEEE Transactions on Ultrasonics, Ferroelectrics, and Frequency Control*, **56** (3), 489–506, doi: 10.1109/TUFFC.2009.1067.
- 236 Greenleaf, J.F., Fatemi, M., and Insana, M. (2003) Selected methods for imaging elastic properties of biological tissues. *Annual Review of Biomedical Engineering*, **5** (1), 57–78, doi: 10.1146/annurev.bioeng.5.040202.121623.
- 237 Parker, K.J., Taylor, L.S., Gracewski, S., and Rubens, D.J. (2005) A unified view of imaging the elastic properties of tissue. *Journal of the Acoustical Society of America*, **117** (5), 2705, doi: 10.1121/1.1880772.
- 238 Sarvazyan, A., Hall, T.T.J., Urban, M.M.W., Fatemi, M., Aglyamov, S.R., and Garra, B.S. (2011) An overview of elastography - an emerging branch of medical imaging. *Current Medical Imaging Reviews*, **7** (4), 255–282, doi: 10.2174/157340511798038684.
- 239 Parker, K.J., Dooley, M.M., and Rubens, D.J. (2012) Corrigendum: imaging the elastic properties of tissue: the 20 year perspective. *Physics in Medicine and Biology*, **57** (16), 5359–5360, doi: 10.1088/0031-9155/57/16/5359.
- 240 Bamber, J., Cosgrove, D., Dietrich, C.F., Fromageau, J., Bojunga, J., Calliada, F., Cantisani, V., Correas, J.M., D’Onofrio, M., Drakonaki, E.E., Fink, M., Friedrich-Rust, M., Gilja, O.H., Havre, R.F., Jenssen, C., Klausner, A.S., Ohlinger, R., Saftoiu, A., Schaefer, F., Sporea, I., and Piscaglia, F. (2013) EFSUMB guidelines and recommendations on the clinical use of ultrasound elastography. Part 1: Basic principles and technology. *Ultraschall in der Medizin*, **34** (2), 169–184, doi: 10.1055/s-0033-1335205.
- 241 Cosgrove, D., Bamber, J., Piscaglia, F., Bojunga, J., Correas, J.M., Gilja, O.H., Klausner, a.S., Sporea, I., Calliada, F., Cantisani, V., D’Onofrio, M., Drakonaki, E.E., Fink, M., Friedrich-Rust, M., Fromageau, J., Havre, R.F., Jenssen, C., Ohlinger, R., S?ftoiu, A., Schaefer, F., and Dietrich, C.F. (2013) EFSUMB guidelines and recommendations on the clinical use of ultrasound elastography. Part 2: Clinical applications. *Ultraschall in der Medizin*, **34** (3), 238–253, doi: 10.1055/s-0033-1335375.
- 242 Sarvazyan, A.P., Urban, M.W., and Greenleaf, J.F. (2013) Acoustic waves in medical imaging and diagnostics. *Ultrasound in Medicine & Biology*, **39** (7), 1133–1146, doi: 10.1016/j.ultrasmedbio.2013.02.006.
- 243 Zaleska-Dorobisz, U., Kaczorowski, K., Pawluś, A., Puchalska, A., and Ingot, M. (2014) Ultrasound elastography - review of techniques and its clinical applications. *Advances in Clinical and Experimental Medicine*, **23** (4), 645–655.
- 244 Ophir, J., Céspedes, I., Ponnekanti, H., Yazdi, Y., and Li, X. (1991) Elastography: a quantitative method for imaging the elasticity of biological tissues. *Ultrasonic Imaging*, **13** (2), 111–134, doi: 10.1016/0161-7346(91)90079-W.
- 245 Varghese, T. (2009) Quasi-static ultrasound elastography. *Ultrasound Clinics*, **4** (3), 323–338, doi: 10.1016/j.cult.2009.10.009.

- 246 Oberai, A.A., Gokhale, N.H., Goenezen, S., Barbone, P.E., Hall, T.J., Sommer, A.M., and Jiang, J. (2009) Linear and nonlinear elasticity imaging of soft tissue in vivo: demonstration of feasibility. *Physics in Medicine and Biology*, **54** (5), 1191–1207, doi: 10.1088/0031-9155/54/5/006.
- 247 Fleming, A.D., Xia, X., McDicken, W.N., Sutherland, G.R., and Fenn, L. (1994) Myocardial velocity gradients detected by Doppler imaging. *British Journal of Radiology*, **67**, 679–688, doi: 10.1259/0007-1285-67-799-679.
- 248 Dandel, M., Lehmkuhl, H., Knosalla, C., Suramelashvili, N., and Hetzer, R. (2009) Strain and strain rate imaging by echocardiography - basic concepts and clinical applicability. *Current Cardiology Reviews*, **5** (2), 133–148, doi: 10.2174/157340309788166642.
- 249 Nightingale, K.R., Stutz, D., and Trahey, G. (2002) Acoustic radiation force impulse imaging of in vivo vastus medialis muscle under varying isometric load. *Ultrasonic Imaging*, **24** (2), 100–108.
- 250 Sarvazyan, A.P., Rudenko, O.V., Swanson, S.D., Fowlkes, J.B., and Emelianov, S.Y. (1998) Shear wave elasticity imaging: a new ultrasonic technology of medical diagnostics. *Ultrasound in Medicine & Biology*, **24** (9), 1419–1435, doi: [http://dx.doi.org/10.1016/S0301-5629\(98\)00110-0](http://dx.doi.org/10.1016/S0301-5629(98)00110-0).
- 251 Nightingale, K.R. (2011) Acoustic radiation force impulse (ARFI) imaging: a review. *Current Medical Imaging Reviews*, **7** (4), 328–339, doi: 10.2174/157340511798038657.Acoustic.
- 252 Fatemi, M. and Greenleaf, J.F. (1998) Ultrasound-stimulated vibro-acoustic spectrography. *Science*, **280** (5360), 82–85, doi: 10.1126/science.280.5360.82.
- 253 Fatemi, M. and Greenleaf, J.F. (1999) Vibro-acoustography: an imaging modality based on ultrasound-stimulated acoustic emission. *Proceedings of the National Academy of Sciences of the United States of America*, **96** (12), 6603–6608, doi: 10.1073/pnas.96.12.6603.
- 254 Urban, M.W., Alizad, A., Aquino, W., Greenleaf, J.F., and Fatemi, M. (2011) A review of vibro-acoustography and its applications in medicine. *Current Medical Imaging Reviews*, **7** (4), 350–359, doi: 10.2174/157340511798038648.
- 255 Lerner, R.M., Parker, K.J., Holen, J., Gramiak, R., and Waag, R.C. (1988) Sono-elasticity: medical elasticity images derived from ultrasound signals in mechanically vibrated targets, in *Acoustical Imaging*, Vol. **16** (eds L. Kessler), Springer US, pp. 317–327, doi: 10.1007/978-1-4613-0725-9\_31.
- 256 Parker, K.J. (2011) The evolution of vibration sonoelastography. *Current Medical Imaging Reviews*, **7** (4), 283–291, doi: 10.2174/157340511798038675.
- 257 Tzschätzsch, H., Elgeti, T., Rettig, K., Kargel, C., Klaua, R., Schultz, M., Braun, J., and Sack, I. (2012) In vivo time harmonic elastography of the human heart. *Ultrasound in Medicine & Biology*, **38** (2), 214–222, doi: 10.1016/j.ultrasmedbio.2011.11.002.
- 258 Yamakoshi, Y., Sato, J., and Sato, T. (1990) Ultrasonic imaging of internal vibration of soft tissue under forced vibration. *IEEE Transactions on Ultrasonics, Ferro-electrics, and Frequency Control*, **37** (2), 45–53, doi: 10.1109/58.46969.

- 259 Tzschätzsch, H., Ipek-Ugay, S., Guo, J., Streitberger, K.J., Gentz, E., Fischer, T., Klaua, R., Schultz, M., Braun, J., and Sack, I. (2014) In vivo time-harmonic multi-frequency elastography of the human liver. *Physics in Medicine and Biology*, **59** (7), 1641–1654, doi: 10.1088/0031-9155/59/7/1641.
- 260 Zhao, H., Song, P., Meixner, D., Kinnick, R., Callstrom, M., Sanchez, W., Urban, M., Manduca, A., Greenleaf, J., and Chen, S. (2014) External vibration multi-directional ultrasound shearwave elastography (EVMUSE): application in liver fibrosis staging. *IEEE Transactions on Medical Imaging*, **33** (11), 2140–2148, doi: 10.1109/TMI.2014.2332542.
- 261 Tzschätzsch, H., Braun, J., and Sack, I. (2015) 2D time harmonic ultrasound elastography at low frame rates. *International Tissue Elasticity Conference XIV*.
- 262 Wu, Z., Taylor, L.S., Rubens, D.J., and Parker, K.J. (2004) Sonoelastographic imaging of interference patterns for estimation of the shear velocity of homogeneous biomaterials. *Physics in Medicine and Biology*, **49** (6), 911–922, doi: 10.1088/0031-9155/49/6/003.
- 263 Hazard, C., Hah, Z., Rubens, D., and Parker, K. (2012) Integration of crawling waves in an ultrasound imaging system. Part 1: System and design considerations. *Ultrasound in Medicine & Biology*, **38** (2), 296–311, doi: 10.1016/j.ultrasmedbio.2011.10.026.
- 264 Hah, Z., Hazard, C., Mills, B., Barry, C., Rubens, D., and Parker, K. (2012) Integration of crawling waves in an ultrasound imaging system. Part 2: Signal processing and applications. *Ultrasound in Medicine & Biology*, **38** (2), 312–323, doi: 10.1016/j.ultrasmedbio.2011.10.014.
- 265 Pernot, M. and Konofagou, E.E. (2005) Electromechanical imaging of the myocardium at normal and pathological states. *Proceedings - IEEE Ultrasonics Symposium*, Vol. 2 (C), 1091–1094, doi: 10.1109/ULTSYM.2005.1603040.
- 266 Konofagou, E., Lee, W.N., Luo, J., Provost, J., and Vappou, J. (2011) Physiologic cardiovascular strain and intrinsic wave imaging. *Annual Review of Biomedical Engineering*, **13**, 477–505, doi: 10.1146/annurev-bioeng-071910-124721.
- 267 Kanai, H. and Koiwa, Y. (2001) Myocardial rapid velocity distribution. *Ultrasound in Medicine & Biology*, **27** (4), 481–498, doi: 10.1016/S0301-5629(01)00341-6.
- 268 Kanai, H. (2009) Propagation of vibration caused by electrical excitation in the normal human heart. *Ultrasound in Medicine & Biology*, **35** (6), 936–948.
- 269 Pernot, M., Fujikura, K., Fung-Kee-Fung, S.D., and Konofagou, E.E. (2007) ECG-gated, mechanical and electromechanical wave imaging of cardiovascular tissues in vivo. *Ultrasound in Medicine & Biology*, **33** (7), 1075–1085, doi: 10.1016/j.ultrasmedbio.2007.02.003.
- 270 Kanai, H., Kawabe, K., Takano, M., Murata, R., Chubachi, N., and Koiwa, Y. (1994) New method for evaluating local pulse wave velocity by measuring vibrations on arterial wall. *Electronics Letters*, **30** (7), 534–536.
- 271 Sandrin, L., Tanter, M., Gennisson, J.L., Catheline, S., and Fink, M. (2002) Shear elasticity probe for soft tissues with 1-D transient elastography. *IEEE Transactions on Ultrasonics, Ferroelectrics, and Frequency Control*, **49** (4), 436–446.

- 272 Palmeri, M.L., Wang, M.H., Dahl, J.J., Frinkley, K.D., and Nightingale, K.R. (2008) Quantifying hepatic shear modulus in vivo using acoustic radiation force. *Ultrasound in Medicine & Biology*, **34** (4), 546–558, doi: 10.1016/j.ultrasmedbio.2007.10.009.
- 273 Nightingale, K., McAleavey, S., and Trahey, G. (2003) Shear-wave generation using acoustic radiation force: in vivo and ex vivo results. *Ultrasound in Medicine & Biology*, **29** (12), 1715–1723, doi: 10.1016/j.ultrasmedbio.2003.08.008.
- 274 Song, P., Zhao, H., Manduca, A., Urban, M.W., Greenleaf, J.F., and Chen, S. (2012) Comb-push ultrasound shear elastography (CUSE): a novel method for two-dimensional shear elasticity imaging of soft tissues. *IEEE Transactions on Medical Imaging*, **31** (9), 1821–1832, doi: 10.1109/TMI.2012.2205586.
- 275 Bercoff, J., Tanter, M., and Fink, M. (2004) Supersonic shear imaging: a new technique. *IEEE Transactions on Ultrasonics, Ferroelectrics, and Frequency Control*, **51** (4), 396–409, doi: 10.1109/TUFFC.2004.1295425.
- 276 McAleavey, S.A., Menon, M., and Orszulak, J. (2007) Shear-modulus estimation by application of spatially- modulated impulsive acoustic radiation force. *Ultrasonic Imaging*, **104** (2007), 87–104.
- 277 Chen, S., Fatemi, M., and Greenleaf, J.F. (2004) Quantifying elasticity and viscosity from measurement of shear wave speed dispersion. *Journal of the Acoustical Society of America*, **115** (6), 2781–2785, doi: 10.1121/1.1739480.
- 278 Urban, M.W., Chen, S., and Fatemi, M. (2012) A review of shearwave dispersion ultrasound vibrometry (SDUV) and its applications. *Current Medical Imaging Reviews*, **8** (1), 27–36, doi: 10.2174/157340512799220625.
- 279 Nenadic, I.Z., Urban, M.W., Mitchell, S.A., and Greenleaf, J.F. (2011) Lamb wave dispersion ultrasound vibrometry (LDUV) method for quantifying mechanical properties of viscoelastic solids. *Physics in Medicine and Biology*, **56** (7), 2245–2264, doi: 10.1088/0031-9155/56/7/021.
- 280 Konofagou, E.E. and Hynynen, K. (2003) Localized harmonic motion imaging: theory, simulations and experiments. *Ultrasound in Medicine & Biology*, **29** (10), 1405–1413, doi: 10.1016/S0301-5629(03)00953-0.
- 281 Konofagou, E.E., Maleke, C., and Vappou, J. (2012) Harmonic motion imaging (HMI) for tumor imaging and treatment monitoring. *Current Medical Imaging Reviews*, **8** (1), 16–26, doi: 10.1016/j.micin.2011.07.011.Innate.
- 282 Hsu, S.J., Byram, B.C., Bouchard, R.R., Dumont, D.M., Wolf, P.D., and Trahey, G.E. (2012) Acoustic radiation force impulse imaging of mechanical stiffness propagation in myocardial tissue. *Ultrasonic Imaging*, **34** (3), 142–158.
- 283 Provost, J., Lee, W.N., Fujikura, K., and Konofagou, E.E. (2011) Imaging the electromechanical activity of the heart in vivo. *Proceedings of the National Academy of Sciences of the United States of America*, **108** (21), 8565–8570.
- 284 Kocica, M.J., Corno, A.F., Carreras-Costa, F., Ballester-Rodes, M., Moghbel, M.C., Cueva, C.N., Lackovic, V., Kanjuh, V.I., and Torrent-Guasp, F. (2006) The helical ventricular myocardial band: global, three-dimensional, functional architecture of the ventricular myocardium. *European Journal of Cardio-Thoracic Surgery*, **29** (Suppl. 1), S21–S40.



- 285 Gharib, M., Rambod, E., Kheradvar, A., Sahn, D.J., and Dabiri, J.O. (2006) Optimal vortex formation as an index of cardiac health. *Proceedings of the National Academy of Sciences of the United States of America*, **103** (16), 6305–6308.
- 286 Bermejo, J., Benito, Y., Alhama, M., Yotti, R., Martinez-Legazpi, P., Del Villar, C.P., Perez-David, E., Gonzalez-Mansilla, A., Santa-Marta, C., Barrio, A., Fernandez-Aviles, F., and Del Alamo, J.C. (2014) Intraventricular vortex properties in nonischemic dilated cardiomyopathy. *American Journal of Physiology*, **306** (5), H718–H729.
- 287 Stonebridge, P.A. and Brophy, C.M. (1991) Spiral laminar flow in arteries? *Lancet*, **338** (8779), 1360–1361.
- 288 Rump, J., Braun, J., Papazoglou, S., Taupitz, M., and Sack, I. (2006) Alterations of the proton-T2 time in relaxed skeletal muscle induced by passive extremity flexions. *Journal of Magnetic Resonance Imaging*, **23** (4), 541–546.
- 289 Elgeti, T., Rump, J., Klatt, D., Hamhaber, U., Papazoglou, S., Braun, J., Hamm, B., and Sack, I. (2008) Non invasive measurement of the volume-pressure work of the human heart by cardiac MR elastography. *Proceedings of the 16th Annual Meeting of ISMRM*, Toronto, p. 705.
- 290 Cikes, M. and Solomon, S.D. (2015) Beyond ejection fraction: an integrative approach for assessment of cardiac structure and function in heart failure. *Eur Heart J*. 2016 Jun 1; **37** (21), 1642–1650.
- 291 Haddad, F., Doyle, R., Murphy, D.J., and Hunt, S.A. (2008) Right ventricular function in cardiovascular disease, Part II: Pathophysiology, clinical importance, and management of right ventricular failure. *Circulation*, **117** (13), 1717–1731.
- 292 McMurray, J.J. and Pfeffer, M.A. (2005) Heart failure. *Lancet*, **365** (9474), 1877–1889.
- 293 Shah, A.M., Claggett, B., Sweitzer, N.K., Shah, S.J., Anand, I.S., O'Meara, E., Desai, A.S., Heitner, J.F., Li, G., Fang, J., Rouleau, J., Zile, M.R., Markov, V., Ryabov, V., Reis, G., Assmann, S.F., McKinlay, S.M., Pitt, B., Pfeffer, M.A., and Solomon, S.D. (2014) Cardiac structure and function and prognosis in heart failure with preserved ejection fraction: findings from the echocardiographic study of the Treatment of Preserved Cardiac Function Heart Failure with an Aldosterone Antagonist (TOP-CAT) Trial. *Circulation: Heart Failure*, **7** (5), 740–751.
- 294 Aurigemma, G.P., Zile, M.R., and Gaasch, W.H. (2006) Contractile behavior of the left ventricle in diastolic heart failure: with emphasis on regional systolic function. *Circulation*, **113** (2), 296–304.
- 295 Kawel-Boehm, N., Maceira, A., Valsangiacomo-Buechel, E.R., Vogel-Claussen, J., Turkbey, E.B., Williams, R., Plein, S., Tee, M., Eng, J., and Bluemke, D.A. (2015) Normal values for cardiovascular magnetic resonance in adults and children. *Journal of Cardiovascular Magnetic Resonance*, **17**, 29.
- 296 Alter, P., Rupp, H., Rominger, M.B., Klose, K.J., and Maisch, B. (2008) A new methodological approach to assess cardiac work by pressure-volume and stress-length relations in patients with aortic valve stenosis and dilated cardiomyopathy. *Pflügers Archiv - European Journal of Physiology*, **455** (4), 627–636.
- 297 Redington, A.N., Gray, H.H., Hodson, M.E., Rigby, M.L., and Oldershaw, P.J. (1988) Characterisation of the normal right ventricular pressure-volume relation

- by biplane angiography and simultaneous micromanometer pressure measurements. *British Heart Journal*, **59** (1), 23–30.
- 298 Kolipaka, A., Araoz, P.A., McGee, K.P., Manduca, A., and Ehman, R.L. (2010) Magnetic resonance elastography as a method for the assessment of effective myocardial stiffness throughout the cardiac cycle. *Magnetic Resonance in Medicine*, **64** (3), 862–870.
- 299 Pernot, M., Couade, M., Mateo, P., Crozatier, B., Fischmeister, R., and Tanter, M. (2011) Real-time assessment of myocardial contractility using shear wave imaging. *Journal of the American College of Cardiology*, **58** (1), 65–72.
- 300 Hsu, S.J., Bouchard, R.R., Dumont, D.M., Wolf, P.D., and Trahey, G.E. (2007) In vivo assessment of myocardial stiffness with acoustic radiation force impulse imaging. *Ultrasound in Medicine & Biology*, **33** (11), 1706–1719.
- 301 Lee, W.N., Pernot, M., Couade, M., Messas, E., Bruneval, P., Bel, A., Hagege, A.A., Fink, M., and Tanter, M. (2012) Mapping myocardial fiber orientation using echocardiography-based shear wave imaging. *IEEE Transactions on Medical Imaging*, **31** (3), 554–562.
- 302 Tzschätzsch, H., Hättasch, R., Knebel, F., Klaua, R., Schultz, M., Jenderka, K.V., Braun, J., and Sack, I. (2013) Isovolumetric elasticity alteration in the human heart detected by in vivo time-harmonic elastography. *Ultrasound in Medicine & Biology*, **39** (12), 2272–2278, doi: 10.1016/j.ultrasmedbio.2013.07.003.
- 303 Pislaru, C., Urban, M.W., Pislaru, S.V., Kinnick, R.R., and Greenleaf, J.F. (2014) Viscoelastic properties of normal and infarcted myocardium measured by a multifrequency shear wave method: comparison with pressure-segment length method. *Ultrasound in Medicine & Biology*, **40** (8), 1785–1795, doi: 10.1016/j.drugalcdep.2008.02.002.A.
- 304 Kanai, H. (2005) Propagation of spontaneously actuated pulsive vibration in human heart wall and in vivo viscoelasticity estimation. *IEEE Transactions on Ultrasonics, Ferroelectrics, and Frequency Control*, **52** (11), 1931–1942.
- 305 Konofagou, E.E., D’Hooge, J., and Ophir, J. (2002) Myocardial elastography—a feasibility study in vivo. *Ultrasound in Medicine & Biology*, **28** (4), 475–482.
- 306 Kolipaka, A., McGee, K.P., Manduca, A., Anavekar, N., Ehman, R.L., and Araoz, P.A. (2011) In vivo assessment of MR elastography-derived effective end-diastolic myocardial stiffness under different loading conditions. *Journal of Magnetic Resonance Imaging*, **33** (5), 1224–1228.
- 307 Sack, I., Beierbach, B., Würfel, J., Klatt, D., Papazoglou, S., Hamhaber, U., Martus, P., and Braun, J. (2009) The impact of aging and gender on cerebral viscoelasticity. *Proceedings of the 17th Annual Meeting of ISMRM*, Honolulu, HI.
- 308 Elgeti, T., Laule, M., Kaufels, N., Schnorr, J., Hamm, B., Samani, A., Braun, J., and Sack, I. (2009) Cardiac MR elastography: comparison with left ventricular pressure measurement. *Journal of Cardiovascular Magnetic Resonance*, **11** (1), 44, doi: 10.1186/1532-429X-11-44.
- 309 Elgeti, T., Rump, J., Hamhaber, U., Papazoglou, S., Hamm, B., Braun, J., and Sack, I. (2008) Cardiac magnetic resonance elastography: initial results. *Investigative Radiology*, **43** (11), 762–772.

- 310 Belz, G.G. (1995) Elastic properties and Windkessel function of the human aorta. *Cardiovascular Drugs and Therapy*, **9** (1), 73–83.
- 311 Cavalcante, J.L., Lima, J.A., Redheuil, A., and Al-Mallah, M.H. (2011) Aortic stiffness: current understanding and future directions. *Journal of the American College of Cardiology*, **57** (14), 1511–1522.
- 312 Dijk, J.M., van der Graaf, Y., Grobbee, D.E., Banga, J.D., and Bots, M.L. (2004) Increased arterial stiffness is independently related to cerebrovascular disease and aneurysms of the abdominal aorta: the Second Manifestations of Arterial Disease (SMART) Study. *Stroke*, **35** (7), 1642–1646.
- 313 Wilson, K.A., Lee, A.J., Lee, A.J., Hoskins, P.R., Fowkes, F.G., Ruckley, C.V., and Bradbury, A.W. (2003) The relationship between aortic wall distensibility and rupture of infrarenal abdominal aortic aneurysm. *Journal of Vascular Surgery*, **37** (1), 112–117.
- 314 Kolipaka, A., Aggarwal, S.R., McGee, K.P., Anavekar, N., Manduca, A., Ehman, R.L., and Araoz, P.A. (2012) Magnetic resonance elastography as a method to estimate myocardial contractility. *Journal of Magnetic Resonance Imaging*, **36** (1), 120–127, doi: 10.1002/jmri.23616.
- 315 Xu, L., Chen, J., Glaser, K.J., Yin, M., Rossman, P.J., and Ehman, R.L. (2013) MR elastography of the human abdominal aorta: a preliminary study. *Journal of Magnetic Resonance Imaging*, **38** (6), 1549–1553.
- 316 Damughatla, A.R., Raterman, B., Sharkey-Toppen, T., Jin, N., Simonetti, O.P., White, R.D., and Kolipaka, A. (2015) Quantification of aortic stiffness using MR elastography and its comparison to MRI-based pulse wave velocity. *Journal of Magnetic Resonance Imaging*, **41** (1), 44–51.
- 317 Li, R.X., Qaqish, W., and Konofagou, E.E. (2015) Performance assessment of Pulse Wave Imaging using conventional ultrasound in canine aortas and normal human arteries. *Artery Research*, **11**, 19–28.
- 318 Markl, M., Wallis, W., Strecker, C., Gladstone, B.P., Vach, W., and Harloff, A. (2012) Analysis of pulse wave velocity in the thoracic aorta by flow-sensitive four-dimensional MRI: reproducibility and correlation with characteristics in patients with aortic atherosclerosis. *Journal of Magnetic Resonance Imaging*, **35** (5), 1162–1168.
- 319 Lantelme, P., Mestre, C., Lievre, M., Gressard, A., and Milon, H. (2002) Heart rate: an important confounder of pulse wave velocity assessment. *Hypertension*, **39** (6), 1083–1087.
- 320 Chatelin, S., Constantinesco, A., and Willinger, R. (2010) Fifty years of brain tissue mechanical testing: from in vitro to in vivo investigations. *Biorheology*, **47** (5-6), 255–276.
- 321 Glaser, K.J., Manduca, A., and Ehman, R.L. (2012) Review of MR elastography applications and recent developments. *Journal of Magnetic Resonance Imaging*, **36** (4), 757–774.
- 322 Simon, M., Guo, J., Papazoglou, S., Scholand-Engler, H., Erdmann, C., Melchert, U., Bonsanto, M., Braun, J., Petersen, D., Sack, I., and Wuerfel, J. (2013) Non-invasive characterization of intracranial tumors by MR-Elastography. *New Journal of Physics*, **15**, 85 024.

- 323 Riek, K., Hamann, I., Millward, J.M., Pfueller, C., Hirsch, S., Klatt, D., Braun, J., Infante-Duarte, C., and Sack, I. (2011) MR elastography of mice in experimental autoimmune encephalitis. *Proceedings of the 19th Annual Meeting of ISMRM*, Montreal, p. 1476.
- 324 Schregel, K., Wuerfel, E., Garteiser, P., Gemeinhardt, I., Prozorovski, T., Aktas, O., Merz, H., Petersen, D., Wuerfel, J., and Sinkus, R. (2012) Demyelination reduces brain parenchymal stiffness quantified in vivo by magnetic resonance elastography. *Proceedings of the National Academy of Sciences of the United States of America*, **109** (17), 6650–6655.
- 325 Johnson, C.L., Holtrop, J.L., McGarry, M.D., Weaver, J.B., Paulsen, K.D., Georgiadis, J.G., and Sutton, B.P. (2014) 3D multislabs, multishot acquisition for fast, whole-brain MR elastography with high signal-to-noise efficiency. *Magnetic Resonance in Medicine*, **71** (2), 477–485.
- 326 Andersson, J.L.R., Skare, S., and Ashburner, J. (2003) How to correct susceptibility distortions in spin-echo echo-planar images: application to diffusion tensor imaging. *NeuroImage*, **20** (2), 870–888, doi: 10.1016/S1053-8119(03)00336-7.
- 327 Fehlner, A., Papazoglou, S., McGarry, M.D., Paulsen, K.D., Guo, J., Streitberger, K.J., Hirsch, S., Braun, J., and Sack, I. (2015) Cerebral multifrequency MR elastography by remote excitation of intracranial shear waves. *NMR in Biomedicine*, **28** (11), 1426–1432.
- 328 Sack, I., Beierbach, B., Hamhaber, U., Klatt, D., and Braun, J. (2008) Non-invasive measurement of brain viscoelasticity using magnetic resonance elastography. *NMR in Biomedicine*, **21** (3), 265–271.
- 329 Guo, J., Hirsch, S., Fehlner, A., Papazoglou, S., Scheel, M., Braun, J., and Sack, I. (2013) Towards an elastographic atlas of brain anatomy. *PLoS ONE*, **8** (8), e71807, doi: 10.1371/journal.pone.0071807.
- 330 Hamhaber, U., Beierbach, B., Klatt, D., Papazoglou, S., Sack, I., Braun, J., Hollmann, M., Bernarding, J., and Stadler, J. (2008) Comparison of dynamic MR elastography of living brain at 7 T and 1.5 T. In *Proceedings of the 16th Annual Meeting of ISMRM*, Toronto, p. 1546.
- 331 Sack, I., Beierbach, B., Würfel, J., Klatt, D., Hamhaber, U., Papazoglou, S., Martus, P., and Braun, J. (2009) The impact of aging and gender on brain viscoelasticity. *NeuroImage*, **46** (3), 652–657, doi: 10.1016/j.neuroimage.2009.02.040.
- 332 Koser, D.E., Moeendarbary, E., Hanne, J., Kuerten, S., and Franze, K. (2015) CNS cell distribution and axon orientation determine local spinal cord mechanical properties. *Biophysical Journal*, **108** (9), 2137–2147.
- 333 Kaster, T., Sack, I., and Samani, A. (2011) Measurement of the hyperelastic properties of ex vivo brain tissue slices. *Journal of Biomechanics*, **44** (6), 1158–1163.
- 334 Budday, S., Nay, R., de Rooij, R., Steinmann, P., Wyröbek, T., Ovaert, T.C., and Kuhl, E. (2015) Mechanical properties of gray and white matter brain tissue by indentation. *Journal of the Mechanical Behavior of Biomedical Materials*, **46**, 318–330.
- 335 Feng, Y., Okamoto, R.J., Namani, R., Genin, G.M., and Bayly, P.V. (2013) Measurements of mechanical anisotropy in brain tissue and implications for transversely

- isotropic material models of white matter. *Journal of the Mechanical Behavior of Biomedical Materials*, **23C**, 117–132.
- 336 Weaver, J.B., Pattison, A.J., McGarry, M.D., Perreard, I.M., Swienckowski, J.G., Eskey, C.J., Lollis, S.S., and Paulsen, K.D. (2012) Brain mechanical property measurement using MRE with intrinsic activation. *Physics in Medicine and Biology*, **57** (22), 7275–7287, doi: 10.1088/0031-9155/57/22/7275.
- 337 Hatt, A., Cheng, S., Tan, K., Sinkus, R., and Bilston, L.E. (2015) MR elastography can be used to measure brain stiffness changes as a result of altered cranial venous drainage during jugular compression. *American Journal of Neuroradiology*, **36** (10), 1971–1977.
- 338 Clayton, E.H., Genin, G.M., and Bayly, P.V. (2012) Transmission, attenuation and reflection of shear waves in the human brain. *Journal of The Royal Society Interface*, **9** (76), 2899–2910.
- 339 Green, M.A., Bilston, L.E., and Sinkus, R. (2008) In vivo brain viscoelastic properties measured by magnetic resonance elastography. *NMR in Biomedicine*, **21** (7), 755–764.
- 340 Gallichan, D., Robson, M.D., Bartsch, A., and Miller, K.L. (2009) TREMR: table-resonance elastography with MR. *Magnetic Resonance in Medicine*, **62** (3), 815–821.
- 341 Clayton, E.H., Garbow, J.R., and Bayly, P.V. (2011) Frequency-dependent viscoelastic parameters of mouse brain tissue estimated by MR elastography. *Physics in Medicine and Biology*, **56** (8), 2391–2406, doi: 10.1088/0031-9155/56/8/005.
- 342 Macé, E., Cohen, I., Montaldo, G., Miles, R., Fink, M., and Tanter, M. (2011) In vivo mapping of brain elasticity in small animals using shear wave imaging. *IEEE Transactions on Medical Imaging*, **30** (3), 550–558, doi: 10.1109/TMI.2010.2079940.
- 343 Murphy, M.C., Huston, J. III, Jack, C.R. Jr., Glaser, K., Senjem, M.L., Chen, J., Manduca, A., Felmlee, J., and Ehman, R.L. (2013) Measuring the characteristic topography of brain stiffness with magnetic resonance elastography. *PLoS ONE*, **8** (12), e81668, doi: 10.1371/journal.pone.0081668.
- 344 Finan, J.D., Elkin, B.S., Pearson, E.M., Kalbian, I.L., and Morrison, B. III, (2012) Viscoelastic properties of the rat brain in the sagittal plane: effects of anatomical structure and age. *Annals of Biomedical Engineering*, **40** (1), 70–78.
- 345 Giedd, J.N., Snell, J.W., Lange, N., Rajapakse, J.C., Casey, B.J., Kozuch, P.L., Vaituzis, A.C., Vauss, Y.C., Hamburger, S.D., Kaysen, D., and Rapoport, J.L. (1996) Quantitative magnetic resonance imaging of human brain development: ages 4–18. *Cerebral Cortex*, **6** (4), 551–560.
- 346 Witelson, S.F., Glezer, I.I., and Kigar, D.L. (1995) Women have greater density of neurons in posterior temporal cortex. *Journal of Neuroscience*, **15** (5 Pt 1), 3418–3428.
- 347 Pelvig, D.P., Pakkenberg, H., Stark, A.K., and Pakkenberg, B. (2008) Neocortical glial cell numbers in human brains. *Neurobiology of Aging*, **29** (11), 1754–1762.
- 348 Johnson, C.L., McGarry, M.D.J., Gharibans, A.A., Weaver, J.B., Paulsen, K.D., Wang, H., Olivero, W.C., Sutton, B.P., and Georgiadis, J.G. (2013) Local mechanical properties of white matter structures in the human brain. *NeuroImage*, **79**, 145–152, doi: 10.1016/j.neuroimage.2013.04.089.

- 349 Zhang, J., Green, M.A., Sinkus, R., and Bilston, L.E. (2011) Viscoelastic properties of human cerebellum using magnetic resonance elastography. *Journal of Biomechanics*, **44** (10), 1909–1913.
- 350 Kruse, S.A., Smith, J.A., Lawrence, A.J., Dresner, M.A., Manduca, A., Greenleaf, J.F., and Ehman, R.L. (2000) Tissue characterization using magnetic resonance elastography: preliminary results. *Physics in Medicine and Biology*, **45** (6), 1579–1590.
- 351 Sack, I., Bernarding, J., and Braun, J. (2002) Analysis of wave patterns in MR elastography of skeletal muscle using coupled harmonic oscillator simulations. *Magnetic Resonance Imaging*, **20** (1), 95–104.
- 352 Agosta, F., Pagani, E., Petrolini, M., Caputo, D., Perini, M., Prella, A., Salvi, F., and Filippi, M. (2010) Assessment of white matter tract damage in patients with amyotrophic lateral sclerosis: a diffusion tensor MR imaging tractography study. *American Journal of Neuroradiology*, **31** (8), 1457–1461.
- 353 Romano, A.J., Guo, J., Prokscha, T., Meyer, T., Hirsch, S., Braun, J., Sack, I., and Scheel, M. (2013) In vivo waveguide elastography: effects of neurodegeneration in patients with amyotrophic lateral sclerosis. *Magnetic Resonance in Medicine*, **00**, 1–7, doi: 10.1002/mrm.25067.
- 354 Konofagou, E.E., Harrigan, T.P., Ophir, J., and Krouskop, T.A. (2001) Poroelastography: imaging the Poroelastic Properties of Tissues. *Ultrasound in Medicine & Biology*, **27** (10), 1387–1397.
- 355 Mousavi, S.R., Fehlner, A., Streitberger, K.J., Braun, J., Samani, A., and Sack, I. (2014) Measurement of in vivo cerebral volumetric strain induced by the Valsalva maneuver. *Journal of Biomechanics*, **47** (7), 1652–1657, doi: 10.1016/j.jbiomech.2014.02.038.
- 356 Hirsch, S., Guo, J., Reiter, R., Schott, E., Somasundaram, R., Braun, J., Sack, I., Kroencke, T.J., and Büning, C. (2014) Towards compression-sensitive magnetic resonance elastography of the liver: sensitivity of harmonic volumetric strain to portal hypertension. *Journal of Magnetic Resonance Imaging*, **39** (2), 298–306, doi: 10.1002/jmri.24165.
- 357 Tyler, W.J. (2012) The mechanobiology of brain function. *Nature Reviews Neuroscience*, **13** (12), 867–878.
- 358 Fehlner, A., Guo, J., Streitberger, K., Hirsch, S., Braun, J., and Sack, I. (2014) The viscoelastic response of the human brain to functional activation detected by magnetic resonance elastography. *Proceedings of the 22nd Annual Meeting of ISMRM*, Milan.
- 359 Barkhof, F. (2002) The clinico-radiological paradox in multiple sclerosis revisited. *Current Opinion in Neurology*, **15** (3), 239–245.
- 360 Huston, J. III, Murphy, M.C., Boeve, B.F., Fattahi, N., Arani, A., Glaser, K.J., Manduca, A., Jones, D.T., and Ehman, R.L. (2015) Magnetic resonance elastography of frontotemporal dementia. *Journal of Magnetic Resonance Imaging*, **43** (2), 474–478.
- 361 Lu, Y.B., Franze, K., Seifert, G., Steinhäuser, C., Kirchhoff, F., Wolburg, H., Guck, J., Janmey, P., Wei, E.Q., Kas, J., and Reichenbach, A. (2006) Viscoelastic properties of individual glial cells and neurons in the CNS. *Proceedings of the National Academy of Sciences of the United States of America*, **103** (47), 17 759–17 764.

- 362 Venkatesh, S.K. and Ehman, R.L. (2015) Magnetic resonance elastography of abdomen. *Abdominal Imaging*, **40** (4), 745–759, doi: 10.1007/s00261-014-0315-6.
- 363 Venkatesh, S.K. and Ehman, R.L. (2014) Magnetic resonance elastography of liver. *Magnetic Resonance Imaging Clinics of North America*, **22** (3), 433–446, doi: 10.1016/j.mric.2014.05.001.
- 364 Venkatesh, S.K., Yin, M., and Ehman, R.L. (2013) Magnetic resonance elastography of liver: technique, analysis, and clinical applications. *Journal of Magnetic Resonance Imaging*, **37** (3), 544–555, doi: 10.1002/jmri.23731.
- 365 Tang, A., Cloutier, G., Szeverenyi, N.M., and Sirlin, C.B. (2015) Ultrasound elastography and MR elastography for assessing liver fibrosis: Part 1, Principles and techniques. *American Journal of Roentgenology*, **205** (1), 22–32, doi: 10.2214/AJR.15.14552.
- 366 Tang, A., Cloutier, G., Szeverenyi, N.M., and Sirlin, C.B. (2015) Ultrasound elastography and MR elastography for assessing liver fibrosis: Part 2, Diagnostic performance, confounders, and future directions. *American Journal of Roentgenology*, **205** (1), 33–40, doi: 10.2214/AJR.15.14553.
- 367 Venkatesh, S.K., Yin, M., and Ehman, R.L. (2013) Magnetic resonance elastography of liver: clinical applications. *Journal of Computer Assisted Tomography*, **37** (6), 887–896, doi: 10.1097/RCT.0000000000000032.
- 368 Blachier, M., Leleu, H., Peck-Radosavljevic, M., Valla, D.C., and Roudot-Thoraval, F. (2013) The burden of liver disease in Europe: a review of available epidemiological data. *Journal of Hepatology*, **58** (3), 593–608, doi: 10.1016/j.jhep.2012.12.005.
- 369 Younossi, Z.M., Stepanova, M., Afendy, M., Fang, Y., Younossi, Y., Mir, H., and Srishord, M. (2011) Changes in the prevalence of the most common causes of chronic liver diseases in the United States from 1988 to 2008. *Clinical Gastroenterology and Hepatology*, **9** (6), 524–530.e1; quiz e60, doi: 10.1016/j.cgh.2011.03.020.
- 370 Ghany, M.G., Strader, D.B., Thomas, D.L., and Seeff, L.B. (2009) Diagnosis, management, and treatment of hepatitis C: an update. *Hepatology (Baltimore, MD)*, **49** (4), 1335–1374, doi: 10.1002/hep.22759.
- 371 Bedossa, P. and Poinard, T. (1996) An algorithm for the grading of activity in chronic hepatitis C. The METAVIR Cooperative Study Group. *Hepatology*, **24** (2), 289–293, doi: 10.1002/hep.510240201.
- 372 Desmet, V.J., Gerber, M., Hoofnagle, J.H., Manns, M., and Scheuer, P.J. (1994) Classification of chronic hepatitis: diagnosis, grading and staging. *Hepatology*, **19** (6), 1513–1520.
- 373 Ishak, K., Baptista, A., Bianchi, L., Callea, F., De Groote, J., Gudat, F., Denk, H., Desmet, V., Korb, G., MacSween, R.N., Phillips, M.J., Portmann, B.G., Poulsen, H., Scheuer, P.J., Schmid, M., and Thaler, H. (1995) Histological grading and staging of chronic hepatitis. *Journal of Hepatology*, **22** (6), 696–699.
- 374 Thampanitchawong, P. and Piratvisuth, T. (1999) Liver biopsy: complications and risk factors. *World Journal of Gastroenterology*, **5** (4), 301–304.
- 375 Perrault, J., McGill, D.B., Ott, B.J., and Taylor, W.F. (1978) Liver biopsy: complications in 1000 inpatients and outpatients. *Gastroenterology*, **74** (1), 103–106.

- 376 Piccinino, F., Sagnelli, E., Pasquale, G., and Giusti, G. (1986) Complications following percutaneous liver biopsy. A multicentre retrospective study on 68,276 biopsies. *Journal of Hepatology*, **2** (2), 165–173.
- 377 Maharaj, B., Maharaj, R.J., Leary, W.P., Cooppan, R.M., Naran, A.D., Pirie, D., and Pudifin, D.J. (1986) Sampling variability and its influence on the diagnostic yield of percutaneous needle biopsy of the liver. *Lancet*, **1** (8480), 523–525.
- 378 Papastergiou, V., Tsochatzis, E., and Burroughs, A.K. (2012) Non-invasive assessment of liver fibrosis. *Annals of Gastroenterology*, **25** (3), 218–231.
- 379 Adams, L.A. (2011) Biomarkers of liver fibrosis. *Journal of Gastroenterology and Hepatology*, **26** (5), 802–809, doi: 10.1111/j.1440-1746.2010.06612.x.
- 380 Parkes, J., Guha, I.N., Roderick, P., and Rosenberg, W. (2006) Performance of serum marker panels for liver fibrosis in chronic hepatitis C. *Journal of Hepatology*, **44** (3), 462–474, doi: 10.1016/j.jhep.2005.10.019.
- 381 Chen, B., Ji, B., and Gao, H. (2015) Modeling active mechanosensing in cell-matrix interactions. *Annual Review of Biophysics*, **44**, 1–32, doi: 10.1146/annurev-biophys-051013-023102.
- 382 Ingber, D.E. (2006) Cellular mechanotransduction: putting all the pieces together again. *FASEB Journal*, **20** (7), 811–827, doi: 10.1096/fj.05-5424rev.
- 383 Karsdal, M.A., Nielsen, M.J., Sand, J.M., Henriksen, K., Genovese, F., Bay-Jensen, A.C., Smith, V., Adamkewicz, J.I., Christiansen, C., and Leeming, D.J. (2013) Extracellular matrix remodeling: the common denominator in connective tissue diseases. Possibilities for evaluation and current understanding of the matrix as more than a passive architecture, but a key player in tissue failure. *Assay and Drug Development Technologies*, **11** (2), 70–92, doi: 10.1089/adt.2012.474.
- 384 Desmoulière, A., Darby, I., Costa, A.M., Raccurt, M., Tuchweber, B., Sommer, P., and Gabbiani, G. (1997) Extracellular matrix deposition, lysyl oxidase expression, and myofibroblastic differentiation during the initial stages of cholestatic fibrosis in the rat. *Laboratory Investigation*, **76** (6), 765–778.
- 385 Perepelyuk, M., Terajima, M., Wang, A.Y., Georges, P.C., Janmey, P.A., Yamauchi, M., and Wells, R.G. (2013) Hepatic stellate cells and portal fibroblasts are the major cellular sources of collagens and lysyl oxidases in normal liver and early after injury. *American Journal of Physiology. Gastrointestinal and Liver Physiology*, **304** (6), G605–G614, doi: 10.1152/ajpgi.00222.2012.
- 386 Guvendiren, M., Perepelyuk, M., Wells, R.G., and Burdick, J.A. (2014) Hydrogels with differential and patterned mechanics to study stiffness-mediated myofibroblastic differentiation of hepatic stellate cells. *Journal of the Mechanical Behavior of Biomedical Materials*, **38**, 198–208, doi: 10.1016/j.jmbbm.2013.11.008.
- 387 Klingberg, F., Chow, M.L., Koehler, A., Boo, S., Buscemi, L., Quinn, T.M., Costell, M., Alman, B.A., Genot, E., and Hinz, B. (2014) Prestress in the extracellular matrix sensitizes latent TGF- $\beta$ 1 for activation. *Journal of Cell Biology*, **207** (2), 283–297, doi: 10.1083/jcb.201402006.
- 388 Olsen, A.L., Bloomer, S.A., Chan, E.P., Gaça, M.D.A., Georges, P.C., Sackey, B., Uemura, M., Janmey, P.A., and Wells, R.G. (2011) Hepatic stellate cells



- require a stiff environment for myofibroblastic differentiation. *American Journal of Physiology. Gastrointestinal and Liver Physiology*, **301** (1), G110–G118, doi: 10.1152/ajpgi.00412.2010.
- 389** Bensamoun, S.F., Leclerc, G.E., Debernard, L., Cheng, X., Robert, L., Charleux, F., Rhein, C., and Latrive, J.P. (2013) Cutoff values for alcoholic liver fibrosis using magnetic resonance elastography technique. *Alcoholism, Clinical and Experimental Research*, **37** (5), 811–817, doi: 10.1111/acer.12025.
- 390** Ichikawa, S., Motosugi, U., Morisaka, H., Sano, K., Ichikawa, T., Enomoto, N., Matsuda, M., Fujii, H., and Onishi, H. (2015) Validity and reliability of magnetic resonance elastography for staging hepatic fibrosis in patients with chronic hepatitis B. *Magnetic Resonance in Medical Sciences*, **14** (3), 211–221, doi: 10.2463/mrms.2014-0150.
- 391** Enomoto, M., Morikawa, H., Tamori, A., and Kawada, N. (2014) Noninvasive assessment of liver fibrosis in patients with chronic hepatitis B. *World Journal of Gastroenterology*, **20** (34), 12 031–12 038, doi: 10.3748/wjg.v20.i34.12031.
- 392** Venkatesh, S.K., Wang, G., Lim, S.G., and Wee, A. (2014) Magnetic resonance elastography for the detection and staging of liver fibrosis in chronic hepatitis B. *European Radiology*, **24** (1), 70–78, doi: 10.1007/s00330-013-2978-8.
- 393** Wu, W.P., Chou, C.T., Chen, R.C., Lee, C.W., Lee, K.W., and Wu, H.K. (2015) Non-invasive evaluation of hepatic fibrosis: the diagnostic performance of magnetic resonance elastography in patients with viral hepatitis B or C. *PLoS ONE*, **10** (10), e0140068, doi: 10.1371/journal.pone.0140068.
- 394** Ichikawa, S., Motosugi, U., Ichikawa, T., Sano, K., Morisaka, H., Enomoto, N., Matsuda, M., Fujii, H., and Araki, T. (2012) Magnetic resonance elastography for staging liver fibrosis in chronic hepatitis C. *Magnetic Resonance in Medical Sciences*, **11** (4), 291–297.
- 395** Venkatesh, S.K., Wang, G., Teo, L.L., and Ang, B.W. (2014) Magnetic resonance elastography of liver in healthy asians: normal liver stiffness quantification and reproducibility assessment. *Journal of Magnetic Resonance Imaging*, **39** (1), 1–8, doi: 10.1002/jmri.24084.
- 396** Kim, B.H., Lee, J.M., Lee, Y.J., Lee, K.B., Suh, K.S., Han, J.K., and Choi, B.I. (2011) MR elastography for noninvasive assessment of hepatic fibrosis: experience from a tertiary center in Asia. *Journal of Magnetic Resonance Imaging*, **34** (5), 1110–1116, doi: 10.1002/jmri.22723.
- 397** Serai, S.D., Towbin, A.J., and Podberesky, D.J. (2012) Pediatric liver MR elastography. *Digestive Diseases and Sciences*, **57** (10), 2713–2719, doi: 10.1007/s10620-012-2196-2.
- 398** Binkovitz, L.A., El-Youssef, M., Glaser, K.J., Yin, M., Binkovitz, A.K., and Ehman, R.L. (2011) Pediatric MR elastography of hepatic fibrosis: principles, technique and early clinical experience. *Pediatric Radiology*, **42** (4), 402–409, doi: 10.1007/s00247-011-2298-6.
- 399** Klatt, D., Friedrich, C., Korth, Y., Vogt, R., Braun, J., and Sack, I. (2010) Viscoelastic properties of liver measured by oscillatory rheometry and multifrequency magnetic resonance elastography. *Biorheology*, **47** (2), 133–141, doi: 10.3233/BIR-2010-0565.

- 400 Salameh, N., Peeters, F., Sinkus, R., Abarca-Quinones, J., Annet, L., Ter Beek, L.C., Leclercq, I., and Van Beers, B.E. (2007) Hepatic viscoelastic parameters measured with MR elastography: correlations with quantitative analysis of liver fibrosis in the rat. *Journal of Magnetic Resonance Imaging*, **26** (4), 956–962, doi: 10.1002/jmri.21099.
- 401 Sinkus, R., Tanter, M., Catheline, S., Lorenzen, J., Kuhl, C., Sondermann, E., and Fink, M. (2005) Imaging anisotropic and viscous properties of breast tissue by magnetic resonance-elastography. *Magnetic Resonance in Medicine*, **53** (2), 372–387, doi: 10.1002/mrm.20355.
- 402 Huwart, L., Sempoux, C., Vicaut, E., Salameh, N., Annet, L., Danse, E., Peeters, F., ter Beek, L.C., Rahier, J., Sinkus, R., Horsmans, Y., and Van Beers, B.E. (2008) Magnetic resonance elastography for the noninvasive staging of liver fibrosis. *Gastroenterology*, **135** (1), 32–40, doi: 10.1053/j.gastro.2008.03.076.
- 403 Motosugi, U., Ichikawa, T., Sano, K., Sou, H., Muhi, A., Koshiishi, T., Ehman, R.L., and Araki, T. (2010) Magnetic resonance elastography of the liver: preliminary results and estimation of inter-rater reliability. *Japanese Journal of Radiology*, **28** (8), 623–627, doi: 10.1007/s11604-010-0478-1.
- 404 Ji Lee, Y., Lee, J.M., Lee, J.E., Lee, K.B., Lee, E.S., Yoon, J.H., Yu, M.H., Baek, J.H., Shin, C.I., Han, J.K., and Choi, B.I. (2014) MR elastography for noninvasive assessment of hepatic fibrosis: reproducibility of the examination and reproducibility and repeatability of the liver stiffness value measurement. *Journal of Magnetic Resonance Imaging*, **39** (2), 326–331, doi: 10.1002/jmri.24147.
- 405 Rusak, G., Zawada, E., Lemanowicz, A., and Serafin, Z. (2015) Whole-organ and segmental stiffness measured with liver magnetic resonance elastography in healthy adults: significance of the region of interest. *Abdominal Imaging*, **40** (4), 776–782, doi: 10.1007/s00261-014-0278-7.
- 406 Hines, C.D.G., Bley, T.A., Lindstrom, M.J., and Reeder, S.B. (2010) Repeatability of magnetic resonance elastography for quantification of hepatic stiffness. *Journal of Magnetic Resonance Imaging*, **31** (3), 725–731, doi: 10.1002/jmri.22066.
- 407 Guo, J., Hirsch, S., Streitberger, K.J., Kamphues, C., Asbach, P., Braun, J., and Sack, I. (2014) Patient-activated three-dimensional multifrequency magnetic resonance elastography for high-resolution mechanical imaging of the liver and spleen. *RöFo: Fortschritte auf dem Gebiete der Röntgenstrahlen und der Nuklearmedizin*, **186** (3), 260–266, doi: 10.1055/s-0033-1350510.
- 408 Huwart, L., Sempoux, C., Salameh, N., Jamart, J., Annet, L., Sinkus, R., Peeters, F., ter Beek, L.C., Horsmans, Y., and Van Beers, B.E. (2007) Liver fibrosis: noninvasive assessment with MR elastography versus aspartate aminotransferase-to-platelet ratio index. *Radiology*, **245** (2), 458–466, doi: 10.1148/radiol.2452061673.
- 409 Venkatesh, S.K., Yin, M., Takahashi, N., Glockner, J.F., Talwalkar, J.A., and Ehman, R.L. (2015) Non-invasive detection of liver fibrosis: MR imaging features vs. MR elastography. *Abdominal Imaging*, **40** (4), 766–775, doi: 10.1007/s00261-015-0347-6.
- 410 Bohte, A.E., Garteiser, P., De Niet, A., Groot, P.F.C., Sinkus, R., Stoker, J., and Nederveen, A.J. (2013) MR elastography of the liver: defining thresholds for detecting viscoelastic changes. *Radiology*, **269** (3), 768–776, doi: 10.1148/radiol.13122669.

- 411 Su, L.N., Guo, S.L., Li, B.X., and Yang, P. (2014) Diagnostic value of magnetic resonance elastography for detecting and staging of hepatic fibrosis: a meta-analysis. *Clinical Radiology*, **69** (12), e545–e552, doi: 10.1016/j.crad.2014.09.001.
- 412 Singh, S., Venkatesh, S.K., Wang, Z., Miller, F.H., Motosugi, U., Low, R.N., Hassanein, T., Asbach, P., Godfrey, E.M., Yin, M., Chen, J., Keaveny, A.P., Bridges, M., Bohte, A., Murad, M.H., Lomas, D.J., Talwalkar, J.A., and Ehman, R.L. (2015) Diagnostic performance of magnetic resonance elastography in staging liver fibrosis: a systematic review and meta-analysis of individual participant data. *Clinical Gastroenterology and Hepatology*, **13** (3), 440–451.e6, doi: 10.1016/j.cgh.2014.09.046.
- 413 Urayama, K., Kawamura, T., and Kohjiya, S. (2009) Structure-mechanical property correlations of model siloxane elastomers with controlled network topology. *Polymer*, **50** (2), 347–356, doi: 10.1016/j.polymer.2008.10.027.
- 414 Gurtovenko, A.A. and Blumen, A. (2005) Generalized Gaussian structures: models for polymer systems with complex topologies, in *Polymer Analysis, Polymer Theory*, Vol. **182**, Springer-Verlag, Berlin, pp. 171–282, doi: 10.1007/b135561,<Go to ISI>://000234477500004.
- 415 Asbach, P., Klatt, D., Hamhaber, U., Braun, J., Somasundaram, R., Hamm, B., and Sack, I. (2008) Assessment of liver viscoelasticity using multifrequency MR elastography. *Magnetic Resonance in Medicine*, **60** (2), 373–379, doi: 10.1002/mrm.21636.
- 416 Klatt, D., Asbach, P., Somasundaram, R., Hamm, B., Braun, J., and Sack, I. (2008) Assessment of the solid-liquid behavior of the liver for the diagnosis of diffuse disease using magnetic resonance elastography. *RöFo: Fortschritte auf dem Gebiete der Röntgenstrahlen und der Nuklearmedizin*, **180** (12), 1104–1109, doi: 10.1055/s-2008-1027697.
- 417 Vernon, G., Baranova, A., and Younossi, Z.M. (2011) Systematic review: the epidemiology and natural history of non-alcoholic fatty liver disease and non-alcoholic steatohepatitis in adults. *Alimentary Pharmacology & Therapeutics*, **34** (3), 274–285, doi: 10.1111/j.1365-2036.2011.04724.x.
- 418 Matteoni, C.A., Younossi, Z.M., Gramlich, T., Boparai, N., Liu, Y.C., and McCullough, A.J. (1999) Nonalcoholic fatty liver disease: a spectrum of clinical and pathological severity. *Gastroenterology*, **116** (6), 1413–1419.
- 419 Castera, L., Vilgrain, V., and Angulo, P. (2013) Noninvasive evaluation of NAFLD. *Nature Reviews. Gastroenterology & Hepatology*, **10** (11), 666–675, doi: 10.1038/nrgastro.2013.175.
- 420 Loomba, R., Wolfson, T., Ang, B., Hooker, J., Behling, C., Peterson, M., Valasek, M., Lin, G., Brenner, D., Gamst, A., Ehman, R., and Sirlin, C. (2014) Magnetic resonance elastography predicts advanced fibrosis in patients with nonalcoholic fatty liver disease: a prospective study. *Hepatology (Baltimore, MD)*, **60** (6), 1920–1928, doi: 10.1002/hep.27362.
- 421 Xanthakos, S.A., Podberesky, D.J., Serai, S.D., Miles, L., King, E.C., Balistreri, W.F., and Kohli, R. (2014) Use of magnetic resonance elastography to assess hepatic fibrosis in children with chronic liver disease. *Journal of Pediatrics*, **164** (1), 186–188, doi: 10.1016/j.jpeds.2013.07.050.

- 422 Chalasani, N., Younossi, Z., Lavine, J.E., Diehl, A.M., Brunt, E.M., Cusi, K., Charlton, M., and Sanyal, A.J. (2012) The diagnosis and management of non-alcoholic fatty liver disease: practice guideline by the American Gastroenterological Association, American Association for the Study of Liver Diseases, and American College of Gastroenterology. *Gastroenterology*, **142** (7), 1592–1609, doi: 10.1053/j.gastro.2012.04.001.
- 423 Loomba, R., Sirlin, C.B., Ang, B., Bettencourt, R., Jain, R., Salotti, J., Soaft, L., Hooker, J., Kono, Y., Bhatt, A., Hernandez, L., Nguyen, P., Noureddin, M., Haufe, W., Hooker, C., Yin, M., Ehman, R., Lin, G.Y., Valasek, M.A., Brenner, D.A., and Richards, L. (2015) Ezetimibe for the treatment of nonalcoholic steatohepatitis: assessment by novel magnetic resonance imaging and magnetic resonance elastography in a randomized trial (MOZART trial). *Hepatology*, **61** (4), 1239–1250, doi: 10.1002/hep.27647.
- 424 Singh, S., Venkatesh, S.K., Loomba, R., Wang, Z., Sirlin, C., Chen, J., Yin, M., Miller, F.H., Low, R.N., Hassanein, T., Godfrey, E.M., Asbach, P., Murad, M.H., Lomas, D.J., Talwalkar, J.A., and Ehman, R.L. (2015) Magnetic resonance elastography for staging liver fibrosis in non-alcoholic fatty liver disease: a diagnostic accuracy systematic review and individual participant data pooled analysis. *European Radiology*, doi: 10.1007/s00330-015-3949-z.
- 425 Cui, J., Ang, B., Haufe, W., Hernandez, C., Verna, E.C., Sirlin, C.B., and Loomba, R. (2015) Comparative diagnostic accuracy of magnetic resonance elastography vs. eight clinical prediction rules for non-invasive diagnosis of advanced fibrosis in biopsy-proven non-alcoholic fatty liver disease: a prospective study. *Alimentary Pharmacology & Therapeutics*, **41** (12), 1271–1280, doi: 10.1111/apt.13196.
- 426 Imajo, K., Kessoku, T., Honda, Y., Tomeno, W., Ogawa, Y., Mawatari, H., Fujita, K., Yoneda, M., Taguri, M., Hyogo, H., Sumida, Y., Ono, M., Eguchi, Y., Inoue, T., Yamanaka, T., Wada, K., Saito, S., and Nakajima, A. (2015) Magnetic resonance imaging more accurately classifies steatosis and fibrosis in patients with nonalcoholic fatty liver disease than transient elastography. *Gastroenterology*, doi: 10.1053/j.gastro.2015.11.048.
- 427 Rustogi, R., Horowitz, J., Harmath, C., Wang, Y., Chalian, H., Ganger, D.R., Chen, Z.E., Bolster, B.D., Shah, S., Miller, F.H., Bolster, B.D. Jr., Shah, S., and Miller, F.H. (2012) Accuracy of MR elastography and anatomic MR imaging features in the diagnosis of severe hepatic fibrosis and cirrhosis. *Journal of Magnetic Resonance Imaging*, **35** (6), 1356–1364, doi: 10.1002/jmri.23585.
- 428 Ichikawa, S., Motosugi, U., Morisaka, H., Sano, K., Ichikawa, T., Enomoto, N., Matsuda, M., Fujii, H., and Onishi, H. (2015) MRI-based staging of hepatic fibrosis: Comparison of intravoxel incoherent motion diffusion-weighted imaging with magnetic resonance elastography. *Journal of Magnetic Resonance Imaging*, **42** (1), 204–210, doi: 10.1002/jmri.24760. Epub 2014 Sep 15.
- 429 Park, H.S., Kim, Y.J., Yu, M.H., Choe, W.H., Jung, S.I., and Jeon, H.J. (2014) Three-Tesla magnetic resonance elastography for hepatic fibrosis: comparison with diffusion-weighted imaging and gadoxetic acid-enhanced magnetic resonance imaging. *World Journal of Gastroenterology*, **20** (46), 17 558–17 567, doi: 10.3748/wjg.v20.i46.17558.

- 430 Wang, Q.B., Zhu, H., Liu, H.L., and Zhang, B. (2012) Performance of magnetic resonance elastography and diffusion-weighted imaging for the staging of hepatic fibrosis: a meta-analysis. *Hepatology (Baltimore, MD)*, **56** (1), 239–247, doi: 10.1002/hep.25610.
- 431 Wang, Y., Ganger, D.R., Levitsky, J., Sternick, L.A., McCarthy, R.J., Chen, Z.E., Fasanati, C.W., Bolster, B., Shah, S., Zuehlsdorff, S., Omary, R.A., Ehman, R.L., and Miller, F.H. (2011) Assessment of chronic hepatitis and fibrosis: comparison of MR elastography and diffusion-weighted imaging. *American Journal of Roentgenology*, **196** (3), 553–561, doi: 10.2214/AJR.10.4580.
- 432 Motosugi, U., Ichikawa, T., Amemiya, F., Sou, H., Sano, K., Muhi, A., Enomoto, N., and Araki, T. (2012) Cross-validation of MR elastography and ultrasound transient elastography in liver stiffness measurement: discrepancy in the results of cirrhotic liver. *Journal of Magnetic Resonance Imaging*, **35** (3), 607–610, doi: 10.1002/jmri.22845.
- 433 Oudry, J., Chen, J., Glaser, K.J., Miette, V., Sandrin, L., and Ehman, R.L. (2009) Cross-validation of magnetic resonance elastography and ultrasound-based transient elastography: a preliminary phantom study. *Journal of Magnetic Resonance Imaging*, **30** (5), 1145–1150, doi: 10.1002/jmri.21929.
- 434 Bohte, A.E., de Niet, A., Jansen, L., Bipat, S., Nederveen, A.J., Verheij, J., Terpstra, V., Sinkus, R., van Nieuwkerk, K.M.J., de Knegt, R.J., Baak, B.C., Jansen, P.L.M., Reesink, H.W., and Stoker, J. (2014) Non-invasive evaluation of liver fibrosis: a comparison of ultrasound-based transient elastography and MR elastography in patients with viral hepatitis B and C. *European Radiology*, **24** (3), 638–648, doi: 10.1007/s00330-013-3046-0.
- 435 Guo, Y., Parthasarathy, S., Goyal, P., McCarthy, R.J., Larson, A.C., and Miller, F.H. (2015) Magnetic resonance elastography and acoustic radiation force impulse for staging hepatic fibrosis: a meta-analysis. *Abdominal Imaging*, **40** (4), 818–834, doi: 10.1007/s00261-014-0137-6.
- 436 Yoon, J.H., Lee, J.M., Woo, H.S., Yu, M.H., Joo, I., Lee, E.S., Sohn, J.Y., Lee, K.B., Han, J.K., and Choi, B.I. (2013) Staging of hepatic fibrosis: comparison of magnetic resonance elastography and shear wave elastography in the same individuals. *Korean Journal of Radiology*, **14** (2), 202–212, doi: 10.3348/kjr.2013.14.2.202.
- 437 Yoon, J.H., Lee, J.M., Joo, I., Lee, E.S., Sohn, J.Y., Jang, S.K., Lee, K.B., Han, J.K., and Choi, B.I. (2014) Hepatic fibrosis: prospective comparison of MR elastography and US shear-wave elastography for evaluation. *Radiology*, **273** (3), 772–782, doi: 10.1148/radiol.14132000.
- 438 Bonekamp, S., Kamel, I., Solga, S., and Clark, J. (2009) Can imaging modalities diagnose and stage hepatic fibrosis and cirrhosis accurately? *Journal of Hepatology*, **50** (1), 17–35, doi: 10.1016/j.jhep.2008.10.016, <Go to ISI>://000261902900006.
- 439 Naveau, S., Gaudé, G., Asnacios, A., Agostini, H., Abella, A., Barri-Ova, N., Dauvois, B., Prévot, S., Ngo, Y., Munteanu, M., Balian, A., Njiké-Nakseu, M., Perlemuter, G., and Poynard, T. (2009) Diagnostic and prognostic values of non-invasive biomarkers of fibrosis in patients with alcoholic liver disease. *Hepatology (Baltimore, MD)*, **49** (1), 97–105, doi: 10.1002/hep.22576.

- 440 Poynard, T., Lassailly, G., Diaz, E., Clement, K., Caiazzo, R., Tordjman, J., Munteanu, M., Perazzo, H., Demol, B., Callafe, R., Pattou, F., Charlotte, F., Bedossa, P., Mathurin, P., and Ratziu, V. (2012) Performance of biomarkers FibroTest, ActiTest, SteatoTest, and NashTest in patients with severe obesity: meta analysis of individual patient data. *PLoS ONE*, **7** (3), e30325, doi: 10.1371/journal.pone.0030325.
- 441 Castéra, L., Vergniol, J., Foucher, J., Le Bail, B., Chanteloup, E., Haaser, M., Darriet, M., Couzigou, P., and De Lédinghen, V. (2005) Prospective comparison of transient elastography, Fibrotest, APRI, and liver biopsy for the assessment of fibrosis in chronic hepatitis C. *Gastroenterology*, **128** (2), 343–350.
- 442 Myers, R.P., Tainturier, M.H., Ratziu, V., Piton, A., Thibault, V., Imbert-Bismut, F., Messous, D., Charlotte, F., Di Martino, V., Benhamou, Y., and Poynard, T. (2003) Prediction of liver histological lesions with biochemical markers in patients with chronic hepatitis B. *Journal of Hepatology*, **39** (2), 222–230.
- 443 Adams, L.A., George, J., Rossi, E., Van der Poorten, D., Kench, J., and De Boer, W. (2008) AASLD abstracts 443-675. *Hepatology*, **48** (S1), 506A–608A, doi: 10.1002/hep.22642.
- 444 Becker, L., Salameh, W., Sferruzza, A., Zhang, K., Chen, R., Malik, R., Reitz, R., Nasser, I., and Afdhal, N.H. (2009) Validation of hepascore, compared with simple indices of fibrosis, in patients with chronic hepatitis C virus infection in United States. *Clinical Gastroenterology and Hepatology*, **7** (6), 696–701.
- 445 Zhou, K., Gao, C.F., Zhao, Y.P., Liu, H.L., Zheng, R.D., Xian, J.C., Xu, H.T., Mao, Y.M., Zeng, M.D., and Lu, L.G. (2010) Simpler score of routine laboratory tests predicts liver fibrosis in patients with chronic hepatitis B. *Journal of Gastroenterology and Hepatology*, **25** (9), 1569–1577, doi: 10.1111/j.1440-1746.2010.06383.x.
- 446 Leroy, V., Hilleret, M.N., Sturm, N., Trocme, C., Renversez, J.C., Faure, P., Morel, F., and Zarski, J.P. (2007) Prospective comparison of six non-invasive scores for the diagnosis of liver fibrosis in chronic hepatitis C. *Journal of Hepatology*, **46** (5), 775–782, doi: 10.1016/j.jhep.2006.12.013.
- 447 Shah, A.G., Lydecker, A., Murray, K., Tetri, B.N., Contos, M.J., and Sanyal, A.J. (2009) Comparison of noninvasive markers of fibrosis in patients with nonalcoholic fatty liver disease. *Clinical Gastroenterology and Hepatology*, **7** (10), 1104–1112, doi: 10.1016/j.cgh.2009.05.033.
- 448 Shaheen, A.A.M. and Myers, R.P. (2007) Diagnostic accuracy of the aspartate aminotransferase-to-platelet ratio index for the prediction of hepatitis C-related fibrosis: a systematic review. *Hepatology (Baltimore, MD)*, **46** (3), 912–921, doi: 10.1002/hep.21835.
- 449 Guha, I.N., Parkes, J., Roderick, P., Chattopadhyay, D., Cross, R., Harris, S., Kaye, P., Burt, A.D., Ryder, S.D., Aithal, G.P., Day, C.P., and Rosenberg, W.M. (2008) Noninvasive markers of fibrosis in nonalcoholic fatty liver disease: validating the European Liver Fibrosis Panel and exploring simple markers. *Hepatology (Baltimore, MD)*, **47** (2), 455–460, doi: 10.1002/hep.21984.
- 450 Cobbold, J.F.L., Crossey, M.M.E., Colman, P., Goldin, R.D., Murphy, P.S., Patel, N., Fitzpatrick, J., Vennart, W., Thomas, H.C., Cox, I.J., and Taylor-Robinson, S.D. (2010) Optimal combinations of ultrasound-based and serum markers of disease

- severity in patients with chronic hepatitis C. *Journal of Viral Hepatitis*, **17** (8), 537–545, doi: 10.1111/j.1365-2893.2009.01209.x.
- 451 Nguyen-Khac, E., Chatelain, D., Tramier, B., Decrombecque, C., Robert, B., Joly, J.P., Brevet, M., Grignon, P., Lion, S., Le Page, L., and Dupas, J.L. (2008) Assessment of asymptomatic liver fibrosis in alcoholic patients using fibroscan: prospective comparison with seven non-invasive laboratory tests. *Alimentary Pharmacology & Therapeutics*, **28** (10), 1188–1198, doi: 10.1111/j.1365-2036.2008.03831.x.
- 452 Wong, V.W.S., Vergniol, J., Wong, G.L.H., Foucher, J., Chan, H.L.Y., Le Bail, B., Choi, P.C.L., Kowo, M., Chan, A.W.H., Merrouche, W., Sung, J.J.Y., and de Lédinghen, V. (2010) Diagnosis of fibrosis and cirrhosis using liver stiffness measurement in nonalcoholic fatty liver disease. *Hepatology (Baltimore, MD)*, **51** (2), 454–462, doi: 10.1002/hep.23312.
- 453 Afdhal, N.H., Bacon, B.R., Patel, K., Lawitz, E.J., Gordon, S.C., Nelson, D.R., Challies, T.L., Nasser, I., Garg, J., Wei, L.J., and McHutchison, J.G. (2015) Accuracy of fibroscan, compared with histology, in analysis of liver fibrosis in patients with hepatitis B or C: a United States multicenter study. *Clinical Gastroenterology and Hepatology*, **13** (4), 772–779.e1–3, doi: 10.1016/j.cgh.2014.12.014.
- 454 Chon, Y.E., Choi, E.H., Song, K.J., Park, J.Y., Kim, D.Y., Han, K.H., Chon, C.Y., Ahn, S.H., and Kim, S.U. (2012) Performance of transient elastography for the staging of liver fibrosis in patients with chronic hepatitis B: a meta-analysis. *PLoS ONE*, **7** (9), e44930, doi: 10.1371/journal.pone.0044930.
- 455 Zhang, D., Li, P., Chen, M., Liu, L., Liu, Y., Zhao, Y., and Wang, R. (2015) Non-invasive assessment of liver fibrosis in patients with alcoholic liver disease using acoustic radiation force impulse elastography. *Abdominal Imaging*, **40** (4), 723–729, doi: 10.1007/s00261-014-0154-5.
- 456 Liu, H., Fu, J., Hong, R., Liu, L., and Li, F. (2015) Acoustic radiation force impulse elastography for the non-invasive evaluation of hepatic fibrosis in non-alcoholic fatty liver disease patients: a systematic review & meta-analysis. *PLoS ONE*, **10** (7), e0127782, doi: 10.1371/journal.pone.0127782.
- 457 Sporea, I., Bota, S., Peck-Radosavljevic, M., Sirli, R., Tanaka, H., Iijima, H., Badea, R., Lupsor, M., Fierbinteanu-Braticicevici, C., Petrisor, A., Saito, H., Ebinuma, H., Friedrich-Rust, M., Sarrazin, C., Takahashi, H., Ono, N., Piscaglia, F., Borghi, A., D'Onofrio, M., Gallotti, A., Ferlitsch, A., Popescu, A., and Danila, M. (2012) Acoustic Radiation Force Impulse elastography for fibrosis evaluation in patients with chronic hepatitis C: an international multicenter study. *European Journal of Radiology*, **81** (12), 4112–4118, doi: 10.1016/j.ejrad.2012.08.018.
- 458 Park, M.S., Kim, S.W., Yoon, K.T., Kim, S.U., Park, S.Y., Tak, W.Y., Kweon, Y.O., Cho, M., Kim, B.K., Park, J.Y., Kim, D.Y., Ahn, S.H., and Han, K.H. (2016) Factors influencing the diagnostic accuracy of acoustic radiation force impulse elastography in patients with chronic hepatitis B. *Gut and Liver*, **10** (2), 275, doi: 10.5009/gnl14391.
- 459 Thiele, M., Detlefsen, S., Sevelsted Møller, L., Madsen, B.S., Fuglsang Hansen, J., Fialla, A.D., Trebicka, J., and Krag, A. (2016) Transient and 2-dimensional shear-wave elastography provide comparable assessment of alcoholic liver fibrosis and cirrhosis. *Gastroenterology*, **150** (1), 123–133, doi: 10.1053/j.gastro.2015.09.040.

- 460 Cassinotto, C., Boursier, J., De Ledinghen, V., Lebigot, J., Lapuyade, B., Cales, P., Hiriart, J.B., Michalak, S., Le Bail, B., Cartier, V., Mouries, A., Oberti, F., Fouchard-Hubert, I., Vergniol, J., and Aube, C. (2016) Liver stiffness in nonalcoholic fatty liver disease: a comparison of supersonic shear imaging, FibroScan and ARFI with liver biopsy. *Hepatology*, **63** (6), 1817–1827, doi: 10.1002/hep.28394.
- 461 Bavu, E., Gennisson, J.L., Couade, M., Bercoff, J., Mallet, V., Fink, M., Badel, A., Vallet-Pichard, A., Nalpas, B., Tanter, M., and Pol, S. (2011) Noninvasive in vivo liver fibrosis evaluation using supersonic shear imaging: a clinical study on 113 hepatitis C virus patients. *Ultrasound in Medicine & Biology*, **37** (9), 1361–1373, doi: 10.1016/j.ultrasmedbio.2011.05.016.
- 462 Parker, K.J. (2015) Experimental evaluations of the microchannel flow model. *Physics in Medicine and Biology*, **60** (11), 4227–4242, doi: 10.1088/0031-9155/60/11/4227.
- 463 Yoon, J.H., Lee, J.M., Suh, K.S., Lee, K.W., Yi, N.J., Lee, K.B., Han, J.K., and Choi, B.I. (2015) Combined use of MR fat quantification and MR elastography in living liver donors: can it reduce the need for preoperative liver biopsy? *Radiology*, **276** (2), 453–464, doi: 10.1148/radiol.15140908.
- 464 Crespo, S., Bridges, M., Nakhleh, R., McPhail, A., Pungpapong, S., and Keaveny, A.P. (2013) Non-invasive assessment of liver fibrosis using magnetic resonance elastography in liver transplant recipients with hepatitis C. *Clinical Transplantation*, **27** (5), 652–658, doi: 10.1111/ctr.12180.
- 465 Kamphues, C., Klatt, D., Bova, R., Yahyazadeh, A., Bahra, M., Braun, J., Klauschen, F., Neuhaus, P., Sack, I., and Asbach, P. (2012) Viscoelasticity-based magnetic resonance elastography for the assessment of liver fibrosis in hepatitis C patients after liver transplantation. *RöFo: Fortschritte auf dem Gebiete der Röntgenstrahlen und der Nuklearmedizin*, **184** (11), 1013–1019, doi: 10.1055/s-0032-1313126.
- 466 Hallinan, J.T.P.D., Alsaiif, H.S., Wee, A., and Venkatesh, S.K. (2015) Magnetic resonance elastography of liver: influence of intravenous gadolinium administration on measured liver stiffness. *Abdominal Imaging*, **40** (4), 783–788, doi: 10.1007/s00261-014-0275-x.
- 467 Motosugi, U., Ichikawa, T., Sou, H., Sano, K., Muhi, A., Ehman, R.L., and Araki, T. (2012) Effects of gadoteric acid on liver elasticity measurement by using magnetic resonance elastography. *Magnetic Resonance Imaging*, **30** (1), 128–132, doi: 10.1016/j.mri.2011.08.005.
- 468 Kazemirad, S., Zhang, E., Chayer, B., Destrempes, F., Nguyen, B., Bilodeau, M., Bodson-Clermont, P., Cloutier, G., and Tang, A. (2015) Detection of steatohepatitis in a rat model: low versus high frequency ultrasound elastography for assessment of liver shear stiffness. *Proceedings of the 14th International Tissue Elasticity Conference*, Bardolino, p. 47.
- 469 Yoneda, M., Suzuki, K., Kato, S., Fujita, K., Nozaki, Y., Hosono, K., Saito, S., and Nakajima, A. (2010) Nonalcoholic fatty liver disease: US-based acoustic radiation force impulse elastography. *Radiology*, **256** (2), 640–647, doi: 10.1148/radiol.10091662.



- 470 Hines, C.D.G., Lindstrom, M.J., Varma, A.K., and Reeder, S.B. (2011) Effects of postprandial state and mesenteric blood flow on the repeatability of MR elastography in asymptomatic subjects. *Journal of Magnetic Resonance Imaging*, **33** (1), 239–244, doi: 10.1002/jmri.22354.
- 471 Yin, M., Talwalkar, J.A., Glaser, K.J., Venkatesh, S.K., Chen, J., Manduca, A., and Ehman, R.L. (2011) Dynamic postprandial hepatic stiffness augmentation assessed with MR elastography in patients with chronic liver disease. *American Journal of Roentgenology*, **197** (1), 64–70, doi: 10.2214/AJR.10.5989.
- 472 Ipek-Ugay, S., Tzschentsch, H., Hudert, C., Marticorena Garcia, S.R., Fischer, T., Braun, J., Althoff, C., and Sack, I. (2016) Time harmonic elastography reveals sensitivity of liver stiffness to water ingestion. *Ultrasound in Medicine & Biology*, **42** (6), 1289–1294, doi: 10.1016/j.ultrasmedbio.2015.12.026.
- 473 Ferraioli, G., Filice, C., Castera, L., Choi, B.I., Sporea, I., Wilson, S.R., Cosgrove, D., Dietrich, C.F., Amy, D., Bamber, J.C., Barr, R., Chou, Y.H., Ding, H., Farrokh, A., Friedrich-Rust, M., Hall, T.J., Nakashima, K., Nightingale, K.R., Palmeri, M.L., Schafer, F., Shiina, T., Suzuki, S., and Kudo, M. (2015) WFUMB guidelines and recommendations for clinical use of ultrasound elastography: Part 3: Liver. *Ultrasound in Medicine & Biology*, **41** (5), 1161–1179, doi: 10.1016/j.ultrasmedbio.2015.03.007.
- 474 Yin, M., Kolipaka, A., Woodrum, D.A., Glaser, K.J., Romano, A.J., Manduca, A., Talwalkar, J.A., Araoz, P.A., Mcgee, K.P., Anavekar, N.S., and Ehman, R.L. (2013) Hepatic and splenic stiffness augmentation assessed with MR elastography in an in vivo porcine portal hypertension model. *Journal of Magnetic Resonance Imaging*, **38** (4), 809–815, doi: 10.1002/jmri.24049.
- 475 Ichikawa, S., Motosugi, U., Nakazawa, T., Morisaka, H., Sano, K., Ichikawa, T., Enomoto, N., Matsuda, M., Fujii, H., and Onishi, H. (2015) Hepatitis activity should be considered a confounder of liver stiffness measured with MR elastography. *Journal of Magnetic Resonance Imaging*, **41** (5), 1203–1208, doi: 10.1002/jmri.24666.
- 476 Shi, Y., Guo, Q., Xia, F., Dzyubak, B., Glaser, K.J., Li, Q., Li, J., and Ehman, R.L. (2014) MR elastography for the assessment of hepatic fibrosis in patients with chronic hepatitis B infection: does histologic necroinflammation influence the measurement of hepatic stiffness? *Radiology*, **273** (1), 88–98, doi: 10.1148/radiol.14132592.
- 477 Millonig, G., Reimann, F.M., Friedrich, S., Fonouni, H., Mehrabi, A., Büchler, M.W., Seitz, H.K., and Mueller, S. (2008) Extrahepatic cholestasis increases liver stiffness (FibroScan) irrespective of fibrosis. *Hepatology*, **48** (5), 1718–1723, doi: 10.1002/hep.22577.
- 478 Millonig, G., Friedrich, S., Adolf, S., Fonouni, H., Golriz, M., Mehrabi, A., Stiefel, P., Pöschl, G., Büchler, M.W., Seitz, H.K., and Mueller, S. (2010) Liver stiffness is directly influenced by central venous pressure. *Journal of Hepatology*, **52** (2), 206–210, doi: 10.1016/j.jhep.2009.11.018.
- 479 Mannelli, L., Godfrey, E., Joubert, I., Patterson, A.J., Graves, M.J., Gallagher, F.A., and Lomas, D.J. (2010) MR elastography: spleen stiffness measurements in healthy volunteers—preliminary experience. *American Journal of Roentgenology*, **195** (2), 387–392, doi: 10.2214/AJR.09.3390.

- 480 Morisaka, H., Motosugi, U., Ichikawa, S., Sano, K., Ichikawa, T., and Enomoto, N. (2015) Association of splenic MR elastographic findings with gastroesophageal varices in patients with chronic liver disease. *Journal of Magnetic Resonance Imaging*, **41** (1), 117–124, doi: 10.1002/jmri.24505.
- 481 Shin, S.U., Lee, J.M., Yu, M.H., Yoon, J.H., Han, J.K., Choi, B.I., Glaser, K.J., and Ehman, R.L. (2014) Prediction of esophageal varices in patients with cirrhosis: usefulness of three-dimensional MR elastography with echo-planar imaging technique. *Radiology*, **272** (1), 143–153, doi: 10.1148/radiol.14130916.
- 482 Sun, H.Y., Lee, J.M., Han, J.K., and Choi, B.I. (2014) Usefulness of MR elastography for predicting esophageal varices in cirrhotic patients. *Journal of Magnetic Resonance Imaging*, **39** (3), 559–566, doi: 10.1002/jmri.24186.
- 483 Dyvorne, H.A., Jajamovich, G.H., Besa, C., Cooper, N., and Taouli, B. (2015) Simultaneous measurement of hepatic and splenic stiffness using MR elastography: preliminary experience. *Abdominal Imaging*, **40** (4), 803–809, doi: 10.1007/s00261-014-0255-1.
- 484 Fuhrhop, J.H. and Wang, T. (2008) *Sieben Moleküle: Die chemischen Elemente und das Leben*, Wiley-VCH Verlag GmbH.
- 485 Liu, Y. (2006) Renal fibrosis: new insights into the pathogenesis and therapeutics. *Kidney International*, **69** (2), 213–217, doi: 10.1038/sj.ki.5000054.
- 486 Gennisson, J.L., Grenier, N., Combe, C., and Tanter, M. (2012) Supersonic shear wave elastography of in vivo pig kidney: influence of blood pressure, urinary pressure and tissue anisotropy. *Ultrasound in Medicine & Biology*, **38** (9), 1559–1567, doi: 10.1016/j.ultrasmedbio.2012.04.013.
- 487 Warner, L., Yin, M., Glaser, K.J., Woollard, J.A., Carrascal, C.A., Korsmo, M.J., Crane, J.A., Ehman, R.L., and Lerman, L.O. (2011) Noninvasive In vivo assessment of renal tissue elasticity during graded renal ischemia using MR elastography. *Investigative Radiology*, **46** (8), 509–514, doi: 10.1097/RLI.0b013e3182183a95.
- 488 Bensamoun, S.F., Robert, L., Leclerc, G.E., Debernard, L., and Charleux, F. (2011) Stiffness imaging of the kidney and adjacent abdominal tissues measured simultaneously using magnetic resonance elastography. *Clinical Imaging*, **35** (4), 284–287, doi: 10.1016/j.clinimag.2010.07.009.
- 489 Low, G., Owen, N.E., Joubert, I., Patterson, A.J., Graves, M.J., Glaser, K.J., Alexander, G.J.M., and Lomas, D.J. (2015) Reliability of magnetic resonance elastography using multislice two-dimensional spin-echo echo-planar imaging (SE-EPI) and three-dimensional inversion reconstruction for assessing renal stiffness. *Journal of Magnetic Resonance Imaging*, **42** (3), 844–850, doi: 10.1002/jmri.24826.
- 490 Du, L. (2013) Evaluation of cervical cancer detection with acoustic radiation force impulse ultrasound imaging. *Experimental and Therapeutic Medicine*, **5** (6), 1715–1719, doi: 10.3892/etm.2013.1057.
- 491 Baer, A.E., Laursen, T.A., Guilak, F., and Setton, L.A. (2003) The micromechanical environment of intervertebral disc cells determined by a finite deformation, anisotropic, and biphasic finite element model. *Journal of Biomechanical Engineering*, **125** (1), 1–11.

- 492 Iatridis, J.C., Weidenbaum, M., Setton, L.A., and Mow, V.C. (1996) Is the nucleus pulposus a solid or a fluid? Mechanical behaviors of the nucleus pulposus of the human intervertebral disc. *Spine*, **21** (10), 1174–1184.
- 493 Kemper, J., Sinkus, R., Lorenzen, J., Nolte-Ernsting, C., Stork, A., and Adam, G. (2004) MR elastography of the prostate: initial in-vivo application. *RöFo: Fortschritte auf dem Gebiete der Röntgenstrahlen und der Nuklearmedizin*, **176** (8), 1094–1099, doi: 10.1055/s-2004-813279.
- 494 Li, S.Y., Chen, M., Wang, W.C., Zhao, W.F., Wang, J.Y., Zhao, X.N., and Zhou, C. (2011) A feasibility study of MR elastography in the diagnosis of prostate cancer at 3.0T. *Acta Radiologica*, **52** (3), 354–358, doi: 10.1258/ar.2010.100276.
- 495 Lama, P., Le Maitre, C.L., Dolan, P., Tarlton, J.F., Harding, I.J., and Adams, M.A. (2013) Do intervertebral discs degenerate before they herniate, or after? *The Bone & Joint Journal*, **95-B** (8), 1127–1133, doi: 10.1302/0301-620X.95B8.31660.
- 496 Pfirrmann, C.W., Metzendorf, A., Zanetti, M., Hodler, J., and Boos, N. (2001) Magnetic resonance classification of lumbar intervertebral disc degeneration. *Spine*, **26** (17), 1873–1878.
- 497 Majumdar, S. (2006) Magnetic resonance imaging and spectroscopy of the intervertebral disc. *NMR in biomedicine*, **19** (7), 894–903, doi: 10.1002/nbm.1106.
- 498 Panjabi, M.M., Oxland, T.R., Yamamoto, I., and Crisco, J.J. (1994) Mechanical behavior of the human lumbar and lumbosacral spine as shown by three-dimensional load-displacement curves. *Journal of Bone and Joint Surgery American*, **76** (3), 413–424.
- 499 Iatridis, J.C., Setton, L.A., Weidenbaum, M., and Mow, V.C. (1997) The viscoelastic behavior of the non-degenerate human lumbar nucleus pulposus in shear. *Journal of Biomechanics*, **30** (10), 1005–1013.
- 500 Cortes, D.H., Magland, J.F., Wright, A.C., and Elliott, D.M. (2014) The shear modulus of the nucleus pulposus measured using magnetic resonance elastography: a potential biomarker for intervertebral disc degeneration. *Magnetic Resonance in Medicine*, **72** (1), 211–219, doi: 10.1002/mrm.24895.
- 501 Antoniou, J., Epure, L.M., Michalek, A.J., Grant, M.P., Iatridis, J.C., and Mwale, F. (2013) Analysis of quantitative magnetic resonance imaging and biomechanical parameters on human discs with different grades of degeneration. *Journal of Magnetic Resonance Imaging*, **38** (6), 1402–1414, doi: 10.1002/jmri.24120.
- 502 Nerurkar, N.L., Elliott, D.M., and Mauck, R.L. (2010) Mechanical design criteria for intervertebral disc tissue engineering. *Journal of Biomechanics*, **43** (6), 1017–1030, doi: 10.1016/j.jbiomech.2009.12.001.
- 503 Ben-Abraham, E.I., Chen, J., Felmlee, J.P., Rossman, P., Manduca, A., An, K.N., and Ehman, R.L. (2015) Feasibility of MR elastography of the intervertebral disc. *Magnetic Resonance Imaging*, doi: 10.1016/j.mri.2015.12.037.
- 504 Vergari, C., Rouch, P., Dubois, G., Bonneau, D., Dubouset, J., Tanter, M., Gennisson, J.L., and Skalli, W. (2014) Non-invasive biomechanical characterization of intervertebral discs by shear wave ultrasound elastography: a feasibility study. *European Radiology*, **24** (12), 3210–3216, doi: 10.1007/s00330-014-3382-8.
- 505 Gennisson, J.L., Catheline, S., Chaffai, S., and Fink, M. (2003) Transient elastography in anisotropic medium: application to the measurement of slow and fast

- shear wave speeds in muscles. *Journal of the Acoustical Society of America*, **114** (1), 536–541.
- 506 Royer, D., Gennisson, J.L., Defieux, T., and Tanter, M. (2011) On the elasticity of transverse isotropic soft tissues. *The Journal of the Acoustical Society of America*, **129** (5), 2757–2760, doi: 10.1121/1.3559681.
- 507 Klatt, D., Papazoglou, S., Braun, J., and Sack, I. (2010) Viscoelasticity-based Magnetic resonance elastography of skeletal muscle. *Physics in Medicine and Biology*, **55**, 6445–6459.
- 508 Bensamoun, S.F., Ringleb, S.I., Littrell, L., Chen, Q., Brennan, M., Ehman, R.L., and An, K.N. (2006) Determination of thigh muscle stiffness using magnetic resonance elastography. *Journal of Magnetic Resonance Imaging*, **23** (2), 242–247.
- 509 Chakouch, M.K., Charleux, F., and Bensamoun, S.F. (2015) Quantifying the elastic property of nine thigh muscles using magnetic resonance elastography. *PLoS ONE*, **10** (9), e0138873, doi: 10.1371/journal.pone.0138873.
- 510 Gennisson, J.L., Defieux, T., Mace, E., Montaldo, G., Fink, M., and Tanter, M. (2010) Viscoelastic and anisotropic mechanical properties of in vivo muscle tissue assessed by supersonic shear imaging. *Ultrasound in Medicine & Biology*, **36** (5), 789–801, doi: 10.1016/j.ultrasmedbio.2010.02.013, <Go to ISI>://000278012600012.
- 511 Papazoglou, S., Braun, J., Hamhaber, U., and Sack, I. (2005) Two-dimensional waveform analysis in MR elastography of skeletal muscles. *Physics in Medicine and Biology*, **50** (6), 1313–1325.
- 512 Gennisson, J.L., Cornu, C., Catheline, S., Fink, M., and Portero, P. (2005) Human muscle hardness assessment during incremental isometric contraction using transient elastography. *Journal of Biomechanics*, **38** (7), 1543–1550.
- 513 Hoyt, K., Kneezel, T., Castaneda, B., and Parker, K.J. (2008) Quantitative sonoelastography for the in vivo assessment of skeletal muscle viscoelasticity. *Physics in Medicine and Biology*, **53** (15), 4063–4080.
- 514 Bensamoun, S., Charleux, F., Debernard, L., Themar-Noel, C., and Voit, T. (2015) Elastic properties of skeletal muscle and subcutaneous tissues in Duchenne muscular dystrophy by magnetic resonance elastography (MRE): a feasibility study. *IRBM*, **36** (1), 4–9, doi: 10.1016/j.irbm.2014.11.002.
- 515 Brauck, K., Galban, C.J., Maderwald, S., Herrmann, B.L., and Ladd, M.E. (2007) Changes in calf muscle elasticity in hypogonadal males before and after testosterone substitution as monitored by magnetic resonance elastography. *European Journal of Endocrinology*, **156** (6), 673–678.
- 516 Tweten, D.J., Okamoto, R.J., Schmidt, J.L., Garbow, J.R., and Bayly, P.V. (2015) Estimation of material parameters from slow and fast shear waves in an incompressible, transversely isotropic material. *Journal of Biomechanics*, **48** (15), 4002–4009, doi: 10.1016/j.jbiomech.2015.09.009.
- 517 Namani, R., Wood, M.D., Sakiyama-Elbert, S.E., and Bayly, P.V. (2009) Anisotropic mechanical properties of magnetically aligned fibrin gels measured by magnetic resonance elastography. *Journal of Biomechanics*, **42** (13), 2047–2053, doi: 10.1016/j.jbiomech.2009.06.007.
- 518 Hong, S.H., Hong, S.J., Yoon, J.S., Oh, C.H., Cha, J.G., Kim, H.K., and Bolster, B. (2015) Magnetic resonance elastography (MRE) for measurement of muscle

- stiffness of the shoulder: feasibility with a 3 T MRI system. *Acta Radiologica*, doi: 10.1177/0284185115571987.
- 519 Chaffer, C.L. and Weinberg, R.A. (2011) A perspective on cancer cell metastasis. *Science*, **331** (6024), 1559–1564.
- 520 Wirtz, D., Konstantopoulos, K., and Searson, P.C. (2011) The physics of cancer: the role of physical interactions and mechanical forces in metastasis. *Nature Reviews Cancer*, **11** (7), 512–522.
- 521 Seltmann, K., Fritsch, A.W., Kas, J.A., and Magin, T.M. (2013) Keratins significantly contribute to cell stiffness and impact invasive behavior. *Proceedings of the National Academy of Sciences of the United States of America*, **110** (46), 18 507–18 512.
- 522 Amack, J.D. and Manning, M.L. (2012) Knowing the boundaries: extending the differential adhesion hypothesis in embryonic cell sorting. *Science*, **338** (6104), 212–215.
- 523 Nnetu, K.D., Knorr, M., Käs, J., and Zink, M. (2012) The impact of jamming on boundaries of collectively moving weak-interacting cells. *New Journal of Physics*, **14**, 115 012.
- 524 Hecht, I., Bar-El, Y., Balmer, F., Natan, S., Tsarfaty, I., Schweitzer, F., and Ben-Jacob, E. (2015) Tumor invasion optimization by mesenchymal-amoeboid heterogeneity. *Scientific Reports*, **5**, 10 622.
- 525 Fritsch, A., Hockel, M., Kiessling, T., Nnetu, K.D., Wetzel, F., Zink, M., and Kas, J.A. (2010) Are biomechanical changes necessary for tumour progression? *Nature Physics*, **6** (10), 730–732, <Go to ISI>://WOS:000283570000011.
- 526 Guck, J., Ananthakrishnan, R., Mahmood, H., Moon, T.J., Cunningham, C.C., and Käs, J. (2001) The optical stretcher: a novel laser tool to micromanipulate cells. *Biophysical Journal*, **81** (2), 767–784, doi: 10.1016/S0006-3495(01)75740-2.
- 527 Jonietz, E. (2012) Mechanics: the forces of cancer. *Nature*, **491** (7425), S56–S57.
- 528 Koch, T.M., Munster, S., Bonakdar, N., Butler, J.P., and Fabry, B. (2012) 3D traction forces in cancer cell invasion. *PLoS ONE*, **7** (3), e33 476.
- 529 Basan, M., Risler, T., Joanny, J.F., Sastre-Garau, X., and Prost, J. (2009) Homeostatic competition drives tumor growth and metastasis nucleation. *HFSP Journal*, **3** (4), 265–272.
- 530 Leal-Egana, A., Fritsch, A., Heidebrecht, F., Diaz-Cuenca, A., Nowicki, M., Bader, A., and Kas, J. (2012) Tuning liver stiffness against tumours: an in vitro study using entrapped cells in tumour-like microcapsules. *Journal of the Mechanical Behavior of Biomedical Materials*, **9**, 113–121, doi: 10.1016/j.jmbbm.2012.01.013.
- 531 Greaves, M.F. (2002) *Cancer: The Evolutionary Legacy*, Oxford University Press, Oxford.
- 532 Paszek, M.J., Zahir, N., Johnson, K.R., Lakins, J.N., Rozenberg, G.I., Gefen, A., Reinhart-King, C.A., Margulies, S.S., Dembo, M., Boettiger, D., Hammer, D.A., and Weaver, V.M. (2005) Tensional homeostasis and the malignant phenotype. *Cancer Cell*, **8** (3), 241–254.
- 533 Butcher, D.T., Alliston, T., and Weaver, V.M. (2009) A tense situation: forcing tumour progression. *Nature Reviews Cancer*, **9** (2), 108–122, doi: 10.1038/nrc2544.

- 534 Egeblad, M., Rasch, M.G., and Weaver, V.M. (2010) Dynamic interplay between the collagen scaffold and tumor evolution. *Current Opinion in Cell Biology*, **22** (5), 697–706.
- 535 Anastassiades, O.T. and Pryce, D.M. (1974) Fibrosis as an indication of time in infiltrating breast cancer and its importance in prognosis. *British Journal of Cancer*, **29** (3), 232–239.
- 536 Novak, U. and Kaye, A.H. (2000) Extracellular matrix and the brain: components and function. *Journal of Clinical Neuroscience*, **7** (4), 280–290.
- 537 Levental, K.R., Yu, H., Kass, L., Lakins, J.N., Egeblad, M., Erler, J.T., Fong, S.F., Csiszar, K., Giaccia, A., Weninger, W., Yamauchi, M., Gasser, D.L., and Weaver, V.M. (2009) Matrix crosslinking forces tumor progression by enhancing integrin signaling. *Cell*, **139** (5), 891–906.
- 538 Plodinec, M., Loparic, M., Monnier, C.A., Obermann, E.C., Zanetti-Dallenbach, R., Oertle, P., Hyotyla, J.T., Aebi, U., Bentires-Alj, M., Lim, R.Y., and Schoenenberger, C.A. (2012) The nanomechanical signature of breast cancer. *Nature Nanotechnology*, **7** (11), 757–765.
- 539 Lerner, R.M., Huang, S.R., and Parker, K.J. (1990) “Sonoelasticity” images derived from ultrasound signals in mechanically vibrated tissues. *Ultrasound in Medicine & Biology*, **16** (3), 231–239, doi: 10.1016/0301-5629(90)90002-T.
- 540 Mendelson, E.B., Böhm-Vélez, M., and Berg, W.A. (2013) ACR BI-RADS ultrasound, in *ACR BI-RADS Atlas, Breast Imaging Reporting and Data System*, American College of Radiology, Reston, VA.
- 541 Thomas, A., Kümmel, S., Fritzsche, F., Warm, M., Ebert, B., Hamm, B., and Fischer, T. (2006) Real-time sonoelastography performed in addition to B-mode ultrasound and mammography: improved differentiation of breast lesions? *Academic Radiology*, **13** (12), 1496–1504, doi: 10.1016/j.acra.2006.08.012.
- 542 Wojcinski, S., Farrokh, A., Weber, S., Thomas, A., Fischer, T., Slowinski, T., Schmidt, W., and Degenhardt, F. (2010) Multicenter study of ultrasound real-time tissue elastography in 779 cases for the assessment of breast lesions: improved diagnostic performance by combining the BI-RADS<sup>®</sup>-US classification system with sonoelastography. *Ultraschall in der Medizin*, **31** (5), 484–491, doi: 10.1055/s-0029-1245282.
- 543 Zhi, H., Xiao, X.Y., Yang, H.Y., Wen, Y.L., Ou, B., Luo, B.M., and Liang, B.L. (2008) Semi-quantitating stiffness of breast solid lesions in ultrasonic elastography. *Academic Radiology*, **15** (11), 1347–1353, doi: 10.1016/j.acra.2008.08.003.
- 544 Thomas, A., Degenhardt, F., Farrokh, A., Wojcinski, S., Slowinski, T., and Fischer, T. (2010) Significant differentiation of focal breast lesions: calculation of strain ratio in breast sonoelastography. *Academic Radiology*, **17** (5), 558–563, doi: 10.1016/j.acra.2009.12.006.
- 545 Fischer, T., Peisker, U., Fiedor, S., Slowinski, T., Wedemeyer, P., Diekmann, F., Grigoryev, M., and Thomas, A. (2012) Significant differentiation of focal breast lesions: raw data-based calculation of strain ratio. *Ultraschall in der Medizin*, **33** (4), 372–379, doi: 10.1055/s-0031-1273222.
- 546 Sadigh, G., Carlos, R.C., Neal, C.H., and Dwamena, B.A. (2012) Accuracy of quantitative ultrasound elastography for differentiation of malignant and benign breast

- abnormalities: a meta-analysis. *Breast Cancer Research and Treatment*, **134** (3), 923–931, doi: 10.1007/s10549-012-2020-x.
- 547 Zhi, H., Xiao, X.Y., Yang, H.Y., Ou, B., Wen, Y.L., and Luo, B.M. (2010) Ultrasonic elastography in breast cancer diagnosis: strain ratio vs 5-point scale. *Academic Radiology*, **17** (10), 1227–1233, doi: 10.1016/j.acra.2010.05.004.
- 548 Sadigh, G., Carlos, R.C., Neal, C.H., and Dwamena, B.A. (2012) Ultrasonographic differentiation of malignant from benign breast lesions: a meta-analytic comparison of elasticity and BIRADS scoring. *Breast Cancer Research and Treatment*, **133** (1), 23–35, doi: 10.1007/s10549-011-1857-8.
- 549 Yoon, J.H., Kim, M.H., Kim, E.K., Moon, H.J., Kwak, J.Y., and Kim, M.J. (2011) Interobserver variability of ultrasound elastography: how it affects the diagnosis of breast lesions. *American Journal of Roentgenology*, **196** (3), 730–736, doi: 10.2214/AJR.10.4654.
- 550 Weismann, C., Mayr, C., Egger, H., and Auer, A. (2011) Breast sonography - 2D, 3D, 4D ultrasound or elastography? *Breast Care*, **6** (2), 98–103, doi: 10.1159/000327504.
- 551 Berg, W.A., Cosgrove, D.O., Doré, C.J., Schäfer, F.K.W., Svensson, W.E., Hooley, R.J., Ohlinger, R., Mendelson, E.B., Balu-Maestro, C., Locatelli, M., Tourasse, C., Cavanaugh, B.C., Juhan, V., Stavros, A.T., Tardivon, A., Gay, J., Henry, J.P., and Cohen-Bacrie, C. (2012) Shear-wave elastography improves the specificity of breast US: the BE1 multinational study of 939 masses. *Radiology*, **262** (2), 435–449, doi: 10.1148/radiol.11110640.
- 552 Li, D.D., Guo, L.H., Xu, H.X., Liu, C., Xu, J.M., Sun, L.P., Wu, J., Liu, B.J., Liu, L.N., and Xu, X.H. (2015) Acoustic radiation force impulse elastography for differentiation of malignant and benign breast lesions: a meta-analysis. *International Journal of Clinical and Experimental Medicine*, **8** (4), 4753–4761.
- 553 Colombo, T., Schips, L., Augustin, H., Gruber, H., Hebel, P., Petritsch, P.H., and Hubmer, G. (1999) Value of transrectal ultrasound in preoperative staging of prostate cancer. *Minerva Urologica e Nefrologica*, **51** (1), 1–4.
- 554 Greenlee, R.T., Hill-Harmon, M.B., Murray, T., and Thun, M. (2001) Cancer statistics, 2001. *CA: A Cancer Journal for Clinicians*, **51** (1), 15–36.
- 555 Keetch, D.W., Catalona, W.J., and Smith, D.S. (1994) Serial prostatic biopsies in men with persistently elevated serum prostate specific antigen values. *Journal of Urology*, **151** (6), 1571–1574.
- 556 Ellis, W.J. and Brawer, M.K. (1995) Repeat prostate needle biopsy: who needs it? *Journal of Urology*, **153** (5), 1496–1498.
- 557 Nagata, M., Sato, T., Un-no, T., Nagae, H., Mugiya, S., Takayama, T., Suzuki, K., and Fujita, K. (2002) Repeat prostate biopsy in patients with previous negative biopsies. *Hinyokika Kyo. Acta Urologica Japonica*, **48** (10), 589–592.
- 558 Dang, C.V. and Semenza, G.L. (1999) Oncogenic alterations of metabolism. *Trends in Biochemical Sciences*, **24** (2), 68–72.
- 559 Bartsch, G., Horninger, W., Klocker, H., Reissigl, A., Oberaigner, W., Schönitzer, D., Severi, G., Robertson, C., and Boyle, P. (2001) Prostate cancer mortality after introduction of prostate-specific antigen mass screening in the Federal State of Tyrol, Austria. *Urology*, **58** (3), 417–424.

- 560 Tanaka, N., Samma, S., Joko, M., Akiyama, T., Takewa, M., Kitano, S., and Okajima, E. (1999) Diagnostic usefulness of endorectal magnetic resonance imaging with dynamic contrast-enhancement in patients with localized prostate cancer: mapping studies with biopsy specimens. *International Journal of Urology*, **6** (12), 593–599.
- 561 Frauscher, F., Pallwein, L., Klauser, A., Berger, A.P., Koppelstaetter, F., Gradl, J., Schurich, M., Bektic, J., Pinggera, G.M., Halpern, E.J., Horninger, W., Bartsch, G., and zur Nedden, D. (2005) [Ultrasound contrast agents and prostate cancer]. *Der Radiologe*, **45** (6), 544–551, doi: 10.1007/s00117-005-1193-2.
- 562 Forsberg, F., Merton, D.A., Liu, J.B., Needleman, L., and Goldberg, B.B. (1998) Clinical applications of ultrasound contrast agents. *Ultrasonics*, **36** (1-5), 695–701.
- 563 Pallwein, L., Mitterberger, M., Gradl, J., Aigner, F., Horninger, W., Strasser, H., Bartsch, G., zur Nedden, D., and Frauscher, F. (2007) Value of contrast-enhanced ultrasound and elastography in imaging of prostate cancer. *Current Opinion in Urology*, **17** (1), 39–47, doi: 10.1097/MOU.0b013e328011b85c.
- 564 Yan, Z., Jie, T., Yan-Mi, L., Xiang, F., Liu-Quan, C., En-Hui, H., and Qiu-Yang, L. (2011) Role of transrectal real-time tissue elastography in the diagnosis of prostate cancer. *Acta Academiae Medicinae Sinicae*, **33** (2), 175–179, doi: 10.3881/j.issn.1000-503X.2011.02.015.
- 565 Nelson, E.D., Slotoroff, C.B., Gomella, L.G., and Halpern, E.J. (2007) Targeted biopsy of the prostate: the impact of color Doppler imaging and elastography on prostate cancer detection and Gleason score. *Urology*, **70** (6), 1136–1140, doi: 10.1016/j.urology.2007.07.067.
- 566 Durmus, T., Stephan, C., Grigoryev, M., Diederichs, G., Saleh, M., Slowinski, T., Maxeiner, A., Thomas, A., and Fischer, T. (2013) Detection of prostate cancer by real-time MR/ultrasound fusion-guided biopsy: 3T MRI and state of the art sonography. *RöFo: Fortschritte auf dem Gebiete der Röntgenstrahlen und der Nuklearmedizin*, **185** (5), 428–433, doi: 10.1055/s-0032-1330704.
- 567 Maxeiner, A., Fischer, T., Stephan, C., Cash, H., Slowinski, T., Kilic, E., and Durmus, T. (2014) Real-time MRI/US fusion-guided biopsy improves detection rates of prostate cancer in pre-biopsied patients. *Aktuelle Urologie*, **45** (3), 197–203, doi: 10.1055/s-0034-1375682.
- 568 Maxeiner, A., Stephan, C., Durmus, T., Slowinski, T., Cash, H., and Fischer, T. (2015) Added value of multiparametric ultrasonography in magnetic resonance imaging and ultrasonography fusion-guided biopsy of the prostate in patients with suspicion for prostate cancer. *Urology*, **86** (1), 108–114, doi: 10.1016/j.urology.2015.01.055.
- 569 Palmeri, M.L., Miller, Z.A., Glass, T.J., Garcia-Reyes, K., Gupta, R.T., Rosenzweig, S.J., Kauffman, C., Polascik, T.J., Buck, A., Kulbacki, E., Madden, J., Lipman, S.L., Rouze, N.C., and Nightingale, K.R. (2015) B-mode and acoustic radiation force impulse (ARFI) imaging of prostate zonal anatomy: comparison with 3T T2-weighted MR imaging. *Ultrasonic Imaging*, **37** (1), 22–41, doi: 10.1177/0161734614542177.
- 570 Correas, J.M., Tissier, A.M., Khairoune, A., Vassiliu, V., Méjean, A., Hélénon, O., Memo, R., and Barr, R.G. (2015) Prostate cancer: diagnostic performance of



- real-time shear-wave elastography. *Radiology*, **275** (1), 280–289, doi: 10.1148/radiol.14140567.
- 571 Guo, J., Bayerl, S., Braun, J., Vajkoczy, P., and Sack, I. (2015) Mechanical characterization of a mouse GL261 glioma model using MR elastography, in *Proceedings of the 23rd Annual Meeting of ISMRM* (ed. I.P.o.t.s.A.M. of ISMRM), Toronto, p. 1101.
- 572 Sack, I., Fritsch, A., Pawlizak, S., Reiss-Zimmermann, M., Hoffmann, K.T., Arlt, F., Mueller, W., Guo, J., Braun, J., and Kaes, J.A. (2015) In vivo high resolution multifrequency MR elastography of neuro tumors compared to single cell mechanical properties, in *Proceedings of the 23rd Annual Meeting of ISMRM* (ed. I.P.o.t.s.A.M. of ISMRM), Toronto, p. 1128.
- 573 Li, J., Jamin, Y., Boulton, J.K., Cummings, C., Waterton, J.C., Ulloa, J., Sinkus, R., Bamber, J.C., and Robinson, S.P. (2014) Tumour biomechanical response to the vascular disrupting agent ZD6126 in vivo assessed by magnetic resonance elastography. *British Journal of Cancer*, **110** (7), 1727–1732.
- 574 Pepin, K.M., Chen, J., Glaser, K.J., Mariappan, Y.K., Reuland, B., Ziesmer, S., Carter, R., Ansell, S.M., Ehman, R.L., and McGee, K.P. (2014) MR elastography derived shear stiffness—a new imaging biomarker for the assessment of early tumor response to chemotherapy. *Magnetic Resonance in Medicine*, **71** (5), 1834–1840.
- 575 Lam, W.A., Rosenbluth, M.J., and Fletcher, D.A. (2007) Chemotherapy exposure increases leukemia cell stiffness. *Blood*, **109** (8), 3505–3508.
- 576 Guck, J., Schinkinger, S., Lincoln, B., Wottawah, F., Ebert, S., Romeyke, M., Lenz, D., Erickson, H.M., Ananthakrishnan, R., Mitchell, D., Kas, J., Ulvick, S., and Bilby, C. (2005) Optical deformability as an inherent cell marker for testing malignant transformation and metastatic competence. *Biophysical Journal*, **88** (5), 3689–3698.
- 577 Singh, S., Fujii, L.L., Murad, M.H., Wang, Z., Asrani, S.K., Ehman, R.L., Kamath, P.S., and Talwalkar, J.A. (2013) Liver stiffness is associated with risk of decompensation, liver cancer, and death in patients with chronic liver diseases: a systematic review and meta-analysis. *Clinical Gastroenterology and Hepatology*, **11** (12), 1573–1579, doi: 10.1016/j.cgh.2013.07.034.
- 578 Van Beers, B.E., Daire, J.L., and Garteiser, P. (2015) New imaging techniques for liver diseases. *Journal of Hepatology*, **62** (3), 690–700.
- 579 Thompson, J.E., van Leeuwen, P.J., Moses, D., Shnier, R., Brenner, P., Delprado, W., Pulbrook, M., Bohm, M., Haynes, A.M., Hayen, A., and Stricker, P.D. (2015) The diagnostic performance of multiparametric magnetic resonance imaging to detect significant prostate cancer. *Journal of Urology*.
- 580 Barentsz, J.O., Richenberg, J., Clements, R., Choyke, P., Verma, S., Villeirs, G., Rouviere, O., Logager, V., and Futterer, J.J. (2012) ESUR prostate MR guidelines 2012. *European Radiology*, **22** (4), 746–757.
- 581 Krouskop, T.A., Wheeler, T.M., Kallel, F., Garra, B.S., and Hall, T. (1998) Elastic moduli of breast and prostate tissue under compression. *Ultrasonic Imaging*, **20** (4), 260–274, doi: 10.1177/016173469802000403.

- 582 Zhang, M., Nigwekar, P., Castaneda, B., Hoyt, K., Joseph, J.V., di Sant'Agnese, A., Messing, E.M., Strang, J.G., Rubens, D.J., and Parker, K.J. (2008) Quantitative characterization of viscoelastic properties of human prostate correlated with histology. *Ultrasound in Medicine & Biology*, **34** (7), 1033–1042.
- 583 Hoyt, K., Castaneda, B., Zhang, M., Nigwekar, P., di Sant'agnese, P.A., Joseph, J.V., Strang, J., Rubens, D.J., and Parker, K.J. (2008) Tissue elasticity properties as biomarkers for prostate cancer. *Cancer Biomark*, **4** (4-5), 213–225.
- 584 Dresner, M.A., Rossmann, P.J., Kruse, S.A., and Ehman, R.L. (1999) MR elastography of the prostate. *Proceedings of the 10th Annual Meeting of ISMRM*, Philadelphia, PA, p. 526.
- 585 Sahebjavaher, R.S., Baghani, A., Honarvar, M., Sinkus, R., and Salcudean, S.E. (2012) Transperineal prostate MR elastography: initial in vivo results. *Magnetic Resonance in Medicine*, **69** (2), 411–420, doi: 10.1002/mrm.24268.
- 586 Chopra, R., Arani, A., Huang, Y., Musquera, M., Wachsmuth, J., Bronskill, M., and Plewes, D.B. (2009) In vivo MR elastography of the prostate gland using a transurethral actuator. *Magnetic Resonance in Medicine*.
- 587 Samani, A., Zubovits, J., and Plewes, D.B. (2007) Elastic moduli of normal and pathological human breast tissues: an inversion-technique-based investigation of 169 samples. *Physics in Medicine and Biology*, **52** (6), 1565–1576.
- 588 Sinkus, R., Lorenzen, J., Schrader, D., Lorenzen, M., Dargatz, M., and Holz, D. (2000) High-resolution tensor MR elastography for breast tumour detection. *Physics in Medicine and Biology*, **45** (6), 1649–1664.
- 589 Plewes, D.B., Bishop, J., Samani, A., and Sciarretta, J. (2000) Visualization and quantification of breast cancer biomechanical properties with magnetic resonance elastography. *Physics in Medicine and Biology*, **45** (6), 1591–1610.
- 590 Van Houten, E.E.W., Doyley, M.M., Kennedy, F.E., Weaver, J.B., and Paulsen, K.D. (2003) Initial in vivo experience with steady-state subzone-based MR elastography of the human breast. *Journal of Magnetic Resonance Imaging*, **17** (1), 72–85.
- 591 Essig, M., Anzalone, N., Combs, S.E., Dorfner, A., Lee, S.K., Picozzi, P., Rovira, A., Weller, M., and Law, M. (2012) MR imaging of neoplastic central nervous system lesions: review and recommendations for current practice. *American Journal of Neuroradiology*, **33** (5), 803–817.
- 592 Faehndrich, J., Weidauer, S., Pilatus, U., Oszvald, A., Zanella, F.E., and Hattingen, E. (2011) Neuroradiological viewpoint on the diagnostics of space-occupying brain lesions. *Clinical Neuroradiology*, **21** (3), 123–139.
- 593 Bernstein, M. and Parrent, A.G. (1994) Complications of CT-guided stereotactic biopsy of intra-axial brain lesions. *Journal of Neurosurgery*, **81** (2), 165–168.
- 594 Papazoglou, S., Xu, C., Hamhaber, U., Siebert, E., Bohner, G., Klingebiel, R., Braun, J., and Sack, I. (2009) Scatter-based magnetic resonance elastography. *Physics in Medicine and Biology*, **54** (7), 2229–2241.
- 595 Yin, Z., Glaser, K.J., Manduca, A., Van Gompel, J.J., Link, M.J., Hughes, J.D., Romano, A., Ehman, R.L., and Huston, J. III, (2015) Slip interface imaging predicts tumor-brain adhesion in vestibular schwannomas. *Radiology*, **277** (2), 507–517.

- 596 Barnhill, E., Sack, I., Braun, J., Jens, W., Brown, C., van Beek, E., and Roberts, N. (2015) Stationary super-resolution multi-frequency magnetic resonance elastography (SSR-MMRE) of the human brain. *Proceedings of the 23rd Annual Meeting of ISMRM*, Toronto, p. 1057.
- 597 Serai, S.D., Yin, M., Wang, H., Ehman, R.L., and Podberesky, D.J. (2015) Cross-vendor validation of liver magnetic resonance elastography. *Abdominal Imaging*, **40** (4), 789–794, doi: 10.1007/s00261-014-0282-y.
- Color details: 1C Page 367First Page 367Last Page 415Page 416 will be a blank Page 416

## Part V

### Outlook

During the period of slightly more than 20 years between the advent and publication of this book, magnetic resonance elastography (MRE) has evolved into a mature imaging technique with applications in clinical routine as well as preclinical and clinical research. Over the years, MRE has seen many gradual improvements, adaptations, and extensions, and we have done our best to incorporate most of them into the contents of this book. However, the development of MRE is still far from being complete, and a number of challenges remain to be solved in the future to either improve existing techniques or open up new areas of application for MRE. The authors of this book subjectively identified four key issues to be addressed in future MRE research, which relate to the high dimensionality of MRE data, exploitation of sparsity, heterogeneity of mechanical tissue properties, and comparability and reproducibility of MRE parameters across platforms. These points will be briefly discussed in the final chapters of this book.

#### Dimensionality

Material waves are represented by vector fields in 3D space, resulting in four-dimensional data structures.<sup>1</sup> Adding time and vibration frequency readily extends the dimensionality of MRE data to six. By contrast, most MRE sequences are still slice-based, that is, a 3D volume is sampled slice by slice. Single-shot sequences, such as echo-planar imaging (EPI), acquire images of a single slice with just one radiofrequency (RF) excitation pulse, whereas segmented sequences require several excitations for the same purpose. In both cases, the acquired data set consists of a stack of independently scanned slices. For 3D inversion techniques, it is necessary to calculate derivatives of the displacement field not only within each slice but also across adjacent slices (“through-slice derivative”). While this is not an issue in theory, some practical issues remain to be solved. First, in pulsatile organs, such as the heart and brain, the recorded MR signal represents not only the induced oscillatory tissue motion but also contributions from pulsation and blood flow that are encoded by the imaging gradients and the motion-encoding gradients (MEGs). Temporal Fourier transform is not capable of fully separating these different components, so that a certain amount of motion will erroneously be classified as oscillation. This can become an issue when adjacent slices are acquired during different phases of the cardiac cycle. For example, in

---

<sup>1</sup> three spatial coordinates + polarization component.

the brain, the arrival of the cardiac pulse wave causes a strong expansive motion of the brain parenchyma [176], along with elevated flow velocities in the cerebral arteries and arterioles. This phase is shorter than the diastolic phase, during which the brain relaxes back to its equilibrium state. Images acquired during the two phases will differ significantly, even if they represent the same wave information, and calculating through-plane derivatives will therefore be tainted by these effects. Standard gating strategies such as retrospective electrocardiogram (ECG) triggering are not viable here, since MRE needs synchrony between image acquisition and externally induced vibrations. 3D  $k$ -space acquisition as proposed in [22] helps; however, appropriate  $k$ -space segmentation and gating to physiological motion should be maintained. More research in this direction would be desirable to better understand the effects of physiological processes, such as pulsation, on different data acquisition strategies, with the ultimate goal of finding optimal artifact suppression methods.

The high dimensionality of MRE data is associated with some common problems in postprocessing such as consistent denoising or phase unwrapping. Because of its relevance in numerous fields of signal processing, phase unwrapping is a topic of ongoing research. However, the majority of available algorithms are limited to 2D or 3D. For MRE, on the other hand, it would be desirable to have phase unwrapping algorithms that are not restricted to slices or volumes, but are capable of operating across the spatial, temporal, and field component dimensions simultaneously to achieve optimal data consistency prior to reconstruction of elastic moduli. Some existing algorithms are inherently limited to a certain dimension and cannot be generalized to a higher-dimensional space. Others can be formulated for an arbitrary number of dimensions, but computational complexity increases overwhelmingly with dimensionality, so that application to more than three dimensions is unfeasible. Ideally, an algorithm tailored for the specific needs of MRE would also account for the time-harmonic property of the signal to improve the conditioning of the problem at hand. While some of these aspects have been considered already, algorithms satisfying all of these requirements simultaneously are still lacking.

### Sparsity

The frequency domain representation of an MRE data set is highly sparse, and the spectrum should only contain the drive frequency (or frequencies) as notable peaks, since all other frequency components are caused by noise. Therefore, in principle, MRE is an ideal candidate for accelerated acquisition techniques, such as compressed sensing, which exploit sparsity to reduce the amount of data – and hence acquisition time – that is necessary to reconstruct the data set. However, only a few studies have investigated methods to accelerate MRE acquisition, among them SLIM [228] for the simultaneous acquisition of multiple displacement field components. Shorter acquisition would increase patient comfort or could allow radiologists to perform exams that would be too long for clinical application when unaccelerated acquisition techniques are used. As an example, because of the aforementioned pulsation-induced artifacts, it would be beneficial to perform MRE acquisitions in synchrony with the heart beat by using cardiac triggering. However, current data acquisition strategies are not fast enough to

accomplish this goal for 3D volumes within a reasonable time span. Therefore, acquisition schemes with fewer repetitions could open up new perspectives for more accurate and reproducible 3D MRE of pulsating organs.

### **Heterogeneity**

Most inversion techniques are implicitly based on the assumption of spatially constant moduli, and they neglect the spatial derivatives of the viscoelastic moduli to be reconstructed. Clearly, this assumption is violated in highly inhomogeneous tissues or close to boundaries, where mechanical properties are discontinuous. Strategies which do not assume local homogeneity can be found in the literature, mostly based on finite-element formulations of the inverse problem. Apart from high computational costs, some of these methods are limited by a high demand on data consistency with respect to field components, time behavior, and a priori knowledge of boundary conditions. Consequently, more elaborate inversion strategies accounting for heterogeneities often fail for *in vivo* MRE data affected by physiological motion, inconsistent boundary conditions or noise, and still need to be proven robust for clinical MRE. New strategies may include concepts such as super-resolution, which can reconstruct viscoelastic parameter maps at higher resolution than the underlying scans, thus reducing artifacts near boundaries and improving detection of small anatomical structures [596]. Irrespective of which inversion method is chosen, this rich field of research steadily enhances the amount of information that can be extracted from mechanical wave fields by MRE.

### **Reproducibility**

Various viscoelastic parameter reconstruction algorithms have been devised by a number of research groups worldwide, each with its specific strengths and weaknesses. As with any quantitative method, MRE values should be as close to ground truth as possible. Material properties are related to neither the imaging system or the dynamic range of the measurement nor the postprocessing method. In a clinical context, standardized, platform-independent values would greatly improve diagnosis, treatment planning, and longitudinal therapy monitoring. Notably, the search for quantitative, platform-independent imaging markers exceeds the field of MRE, and has been identified by the broader imaging community as an urgent research goal. On the one hand, MRE has been demonstrated to be highly reproducible across platforms [597]. On the other hand, every reconstruction algorithm has its own characteristics in terms of sensitivity to noise, boundary conditions, and other parameters that cannot be controlled in a clinical environment. Therefore, a certain degree of standardization of viscoelastic parameter reconstruction procedures would be desirable. As a first step in that direction, the International Society for Magnetic Resonance in Medicine (ISMRM) founded an MRE study group in 2015. The objectives of this group include manufacturing standardized phantoms and providing sample MRE data sets that can be used to compare different reconstruction algorithms.

In conclusion, MRE has already evolved into a mature and robust noninvasive imaging modality with applications in both clinical diagnostics and medical research. The use of externally stimulated waves as a “physical contrast agent” has the potential to replace magnetic resonance imaging (MRI) contrast agents and invasive procedures – such as

biopsies – in a number of diseases. With more ready-to-use MRE hardware and software packages becoming available from MRI scanner manufacturers and third-party vendors, MRE is expected to evolve into an affordable routine tool that improves diagnostic accuracy and patient comfort at the same time. Simultaneously, a growing number of scientific groups committed to research in this field worldwide address open issues and aim to further refine all aspects of MRE, thus advancing this exciting technology to its fullest potential.

## A

## Simulating the Bloch Equations

In a real MR experiment, there are many sources of magnetic fields in addition to  $\mathbf{B}_0$ . The *chemical shift* modulates the effective field strength that a nucleus experiences due to shielding effects of the electron shell. The strength of the effect depends on the bonding state of the hydrogen atom, and is therefore different for spins constituting free water and those that are part of lipids, giving rise to the *fat–water shift*. In addition to  $\mathbf{B}_1$ -fields used to flip the magnetization into the transverse plane, position-dependent magnetic field gradients along the  $z$ -axis (see Section 1.6.1) are used to manipulate the magnetization during the experiment. We can therefore express the effective magnetic field in the rotating frame as

$$\mathbf{B}' = \begin{pmatrix} B'_{1,x} \\ B'_{1,y} \\ B_0 + B_{\text{chem. shift}} + G_x + G_y + G_z \end{pmatrix}. \quad (\text{A1})$$

Of all these field components,  $B_0$  is the strongest with a typical magnitude of 1.5 or 3 T on clinical magnetic resonance imaging (MRI) scanners. The gradients typical induce field variations in the order of a few tens of millitesla.  $B_1$  usually has a magnitude in the range of tens of  $\mu\text{T}$ . The chemical shift is very weak, causing a field modulation of 1.3 ppm (parts per million) between water and fat. It is therefore only relevant for  $B_0$  and is negligible for all other field components.  $B_1$  fields are designed to rotate in the  $(x, y)$ -plane and therefore do not have a  $z$ -component. The precession in such a complex setting can be parameterized by a precession frequency vector

$$\boldsymbol{\omega}' = \begin{pmatrix} \omega'_1 \\ \omega'_2 \\ \omega'_3 \end{pmatrix} = \gamma \mathbf{B}', \quad (\text{A2})$$

and the angle between the magnetization and the magnetic field is given by

$$\alpha' = \boldsymbol{\omega}' t \quad (\text{A3})$$

if  $\mathbf{M}'$  was aligned with  $\mathbf{B}$  at  $t = 0$ .



With this vector notation, we can express the precession in the rotating frame<sup>1</sup> as

$$\frac{\partial \mathbf{M}'}{\partial t} = \mathbf{M}' \times \gamma \mathbf{B}' = \gamma \begin{pmatrix} M'_2 \cdot B'_3 - M'_3 \cdot B'_2 \\ M'_3 \cdot B'_1 - M'_1 \cdot B'_3 \\ M'_1 \cdot B'_2 - M'_2 \cdot B'_1 \end{pmatrix} = \begin{pmatrix} 0 & \omega'_3 & -\omega'_2 \\ -\omega'_3 & 0 & \omega'_1 \\ \omega'_2 & -\omega'_1 & 0 \end{pmatrix} \cdot \mathbf{M}'. \quad (\text{A4})$$

By adding  $T_1$  and  $T_2$  relaxation terms, we can express the Bloch equation (1.26) in the rotating frame as

$$\frac{\partial \mathbf{M}'}{\partial t} = \mathbf{W}' \cdot \mathbf{M}' + \frac{1}{T_1} \mathbf{M}_0 \quad (\text{A5})$$

with

$$\mathbf{W}' = \begin{pmatrix} -\frac{1}{T_2} & \omega'_3 & -\omega'_2 \\ -\omega'_3 & -\frac{1}{T_2} & \omega'_1 \\ \omega'_2 & -\omega'_1 & -\frac{1}{T_1} \end{pmatrix} \quad (\text{A6})$$

and the longitudinal equilibrium magnetization  $\mathbf{M}_0$  as defined in Eq. (1.7) (which is independent of the coordinate system and therefore not marked with a prime). In order to solve the differential equation (A5), we introduce the quantity  $\mathbf{h}'$ :

$$\mathbf{h}' = \mathbf{M}' + \frac{1}{T_1} (\mathbf{W}')^{-1} \mathbf{M}_0. \quad (\text{A7})$$

By taking the temporal derivative, we see that

$$\frac{\partial \mathbf{h}'}{\partial t} = \frac{\partial \mathbf{M}'}{\partial t} = \mathbf{W}' \cdot \mathbf{M}' + \frac{1}{T_1} \mathbf{M}_0 = \mathbf{W}' \cdot \mathbf{h}', \quad (\text{A8})$$

which can be solved by a matrix exponential function:

$$\mathbf{h}'(t) = \mathbf{h}_0 \cdot e^{\mathbf{W}' \cdot t}. \quad (\text{A9})$$

The initial value  $\mathbf{h}_0 = \mathbf{h}'(0)$  translates to

$$\mathbf{h}_0 = \mathbf{M}'(0) + \frac{1}{T_1} (\mathbf{W}')^{-1} \mathbf{M}_0, \quad (\text{A10})$$

and reversing the substitution Eq. (A7) yields

$$\mathbf{M}'(t) = e^{\mathbf{W}' \cdot t} \cdot \mathbf{M}'(0) + e^{\mathbf{W}' \cdot t} \cdot \frac{1}{T_1} (\mathbf{W}')^{-1} \cdot \mathbf{M}_0 - \frac{1}{T_1} (\mathbf{W}')^{-1} \mathbf{M}_0. \quad (\text{A11})$$

In order to simulate the time evolution of the magnetization, Eq. (A11) can be solved for a number of time steps  $t_k = k \cdot \delta t$ . It is important to note that Eq. (A11) was derived under the assumption of a constant matrix  $\mathbf{W}'$ , implying a constant  $\mathbf{B}'$ -vector in the rotating frame. This means that to simulate experiments with time-variable magnetic fields, Eq. (A11) has to be solved in small time steps, for which all magnetic fields can be assumed to be constant.

<sup>1</sup> For the following discussion, we chose the rotating frame since it will allow for a time-independent matrix representation of the time evolution operator. In the laboratory frame, the same description would be more complicated.

## B

### Proof that Eq. (3.8) Is Sinusoidal

Section 3.1 uses the fact that

$$\phi(\varphi) = \gamma \mathbf{u}_0 \cdot \mathbf{G}_0 \cdot \int_0^T \sin(\Omega t + \varphi) \cdot \sin(\omega_G t) dt$$

is a sinusoidal function with respect to  $\varphi$ . As a proof, it will be shown that

$$g(\varphi) = \int_{t_0}^{t_1} \sin(t + \varphi) \cdot f(t) dt$$

is sinusoidal for any real-valued integrable function  $f(t)$  and arbitrary limits  $t_0 \neq t_1$ .

*Proof:* Taking the second derivative of  $g$  with respect to  $\varphi$  yields

$$\begin{aligned} \frac{d^2 g}{d\varphi^2} &= \frac{\partial^2}{\partial \varphi^2} \int_{t_0}^{t_1} \sin(t + \varphi) \cdot f(t) dt \\ &= - \int_{t_0}^{t_1} \sin(t + \varphi) \cdot f(t) dt \\ &= -g(\varphi), \end{aligned} \tag{B1}$$

which is a second-order differential equation with two linearly independent real-valued solutions  $\sin(\varphi)$  and  $\cos(\varphi)$ , both of which are sinusoidal. They constitute a complete basis of the solution space, such that any solution to Eq. (B1) is a linear combination of these, and therefore is sinusoidal itself.

## C

## Proof for Eq. (4.1)

To be shown:

$$\sum_{j=1}^3 \frac{\partial u_i}{\partial r_j} \delta r_j = \frac{1}{2} \sum_{j=1}^3 \left( \frac{\partial u_i}{\partial r_j} + \frac{\partial u_j}{\partial r_i} \right) \delta r_j + \frac{1}{2} ((\nabla \times \mathbf{u}) \times \delta \mathbf{r})_i. \quad (\text{C1})$$

*Proof:* The cross product can be expressed in index notation as

$$(\mathbf{a} \times \mathbf{b})_i = \sum_{j,k=1}^3 \epsilon_{ijk} a_j b_k \quad (\text{C2})$$

with the totally antisymmetric *Levi-Civita tensor*  $\epsilon_{ijk}$ . Translating the last term in Eq. (C1) to this notation yields

$$\begin{aligned} \frac{1}{2} ((\nabla \times \mathbf{u}) \times \delta \mathbf{r})_n &= \frac{1}{2} \sum_{i,m=1}^3 \underbrace{\sum_{j,k=1}^3 \epsilon_{ijk} \frac{\partial u_k}{\partial r_j} \epsilon_{nim}}_{(\nabla \times \mathbf{u})_i} \delta r_m \\ &= \frac{1}{2} \sum_{i,j,k,m=1}^3 \epsilon_{ijk} \epsilon_{imn} \frac{\partial u_k}{\partial r_j} \delta r_m. \end{aligned} \quad (\text{C3})$$

In the second step, the fact that  $\epsilon_{abc}$  is invariant under cyclic permutations of the indices was used:  $\epsilon_{abc} = \epsilon_{bca} = \epsilon_{cab}$ . Equation (C3) can be further simplified by contracting the two  $\epsilon$  tensors over the common index  $i$ :

$$\sum_{i=1}^3 \epsilon_{ijk} \epsilon_{imn} = \delta_{jm} \delta_{kn} - \delta_{jn} \delta_{km}. \quad (\text{C4})$$

Substituting Eq. (C4) into Eq. (C3) yields

$$\begin{aligned} \frac{1}{2} ((\nabla \times \mathbf{u}) \times \delta \mathbf{r})_n &= \frac{1}{2} \sum_{j,k,m=1}^3 (\delta_{jm} \delta_{kn} - \delta_{jn} \delta_{km}) \frac{\partial u_k}{\partial r_j} \delta r_m \\ &= \frac{1}{2} \sum_{m=1}^3 \left( \frac{\partial u_n}{\partial r_m} \delta r_m - \frac{\partial u_m}{\partial r_n} \delta r_m \right). \end{aligned} \quad (\text{C5})$$

After performing the index substitution  $n \rightarrow i$  and  $m \rightarrow j$ , Eq. (C5) can be substituted into the right-hand side of Eq. (C1):

$$\begin{aligned} & \frac{1}{2} \sum_{j=1}^3 \left( \frac{\partial u_i}{\partial r_j} + \frac{\partial u_j}{\partial r_i} \right) \delta r_j + \frac{1}{2} ((\nabla \times \mathbf{u}) \times \delta \mathbf{r})_i \\ &= \frac{1}{2} \sum_{j=1}^3 \left( \frac{\partial u_i}{\partial r_j} + \frac{\partial u_j}{\partial r_i} + \frac{\partial u_i}{\partial r_j} - \frac{\partial u_j}{\partial r_i} \right) \delta r_j \\ &= \sum_{j=1}^3 \frac{\partial u_i}{\partial r_j} \delta r_j. \end{aligned}$$

## D

### Wave Intensity Distributions

#### D.1 Calculation of Intensity Probabilities

In this section, we will show how to calculate intensity probabilities for different types of waves. First, we will derive the general formula for intensity probabilities, and then apply them to several wave phenomena.

From the conservation of energy, we know that in an unattenuated medium, the energy that was emitted by an isotropic point source over the time interval  $t_0 \leq t \leq t_1$  is evenly distributed across a spherical shell with inner radius  $R = c(t - t_0)$  and thickness  $\Delta R = c(t_1 - t_0)$ . The radius is obviously a function of time; hence, as the wave propagates, the radius of the shell increases. The shell volume can be calculated as

$$V(t) = 4\pi R(t)^2 \cdot \Delta R. \quad (\text{D1})$$

The wave intensities at the inner and outer surfaces of the shell are  $I(R)$  and  $I(R) + \Delta I = I(R - \Delta R)$ , respectively. By using a minus sign in front of  $\Delta R$ , we account for the fact that the intensity decreases with increasing radius, so this trick allows us to have  $\Delta I$  and  $\Delta R$  both positive. For the following analysis, we need to find a way to convert  $\Delta I$  to  $\Delta R$ . We can achieve this by means of a Taylor expansion:

$$I(R) + \Delta I = I(R - \Delta R) = I(R) - \frac{dI}{dr}(r = R) \cdot \Delta R \quad (\text{D2})$$

$$\Rightarrow \Delta R = -\left(\frac{dI}{dr}(r = R)\right)^{-1} \Delta I. \quad (\text{D3})$$

Second, we also need to invert the relation  $I(r)$ , so that we can calculate the distance from the source at which we find the intensity  $I$ . This step of course depends on the actual form of  $I(r)$ , but in any case it will yield a function  $r(I)$ .

From these steps, we can assemble the sought intensity probability distribution. First, we calculate the volume  $V(I, \Delta I)$  of the shell, in which the intensities  $I_0 \leq I \leq I_0 + \Delta I$  are located. The probability of finding an intensity in that range is then

$$P(I) \Delta I = \frac{V(I, \Delta I)}{V}, \quad (\text{D4})$$

where  $V$  is the total volume illuminated by the source. We start by rewriting Eq. (D1) in terms of  $I$  instead of  $r$ :

$$V(I, \Delta I) = -4\pi r(I)^2 \cdot \left( \frac{dI}{dr}(r = r(I)) \right)^{-1} \Delta I. \quad (\text{D5})$$

The total volume  $V$ , on the other hand, can be calculated as the volume of a ball with radius  $R_{\max}$ , where  $R_{\max}$  is the distance of the first emitted wave front from the source. We thus have

$$V = \frac{4}{3}\pi R_{\max}^3. \quad (\text{D6})$$

We can see that this formula is divergent for  $R_{\max} \rightarrow \infty$ , so that  $P(I)$  is not properly defined in the long-term limit  $t \rightarrow \infty$ . We are now prepared to apply these formulas to different wave phenomena.

## D.2 Point Source in 3D

For a point source in three-dimensional space with an isotropic radiation characteristic and a nonabsorbing medium, conservation of energy dictates that the intensity behaves as

$$I(r) \propto \frac{1}{r^2}. \quad (\text{D7})$$

For the sake of simplicity, we will set all involved proportionality constants to one and ignore all arising inconsistencies regarding physical units; this allows us to write

$$I(r) = \frac{1}{r^2}. \quad (\text{D8})$$

Hence, we have

$$r(I) = \frac{1}{\sqrt{I}} \quad (\text{D9})$$

$$\text{and } \frac{dI}{dr} = -\frac{2}{r^3} = -2 I^{\frac{3}{2}}. \quad (\text{D10})$$

Substituting these findings into Eq. (D5) yields

$$V(I, \Delta I) = -4\pi \left( \frac{1}{\sqrt{I}} \right)^2 \cdot \left( -2 I^{\frac{3}{2}} \right)^{-1} \Delta I = \frac{2\pi}{I^{\frac{5}{2}}} \Delta I. \quad (\text{D11})$$

If the source has been turned on for a duration  $T$ , the first emitted wave front has propagated a distance  $R_{\max} = cT$ . We can therefore calculate the intensity probability from Eqs. (D4) and (D6):

$$P(I)\Delta I = \frac{3}{2} \frac{1}{I^{\frac{5}{2}} \cdot c^3 T^3} \Delta I. \quad (\text{D12})$$

Finally, we have to account for the fact that the smallest occurring intensity  $I_{\min} = I(R_{\max})$  is found at the first emitted wave front, further away all intensities are zero everywhere. Thus, we will not be able to find intensities in the interval

$0 < I < I_{\min}$ . We therefore have to correct Eq. (D12) manually by introducing a case distinction:

$$P(I)\Delta I = \begin{cases} \frac{3}{2} \frac{1}{I^{\frac{5}{2}} \cdot c^3 T^3} \Delta I & \text{if } I \geq I(cT) \\ 0 & \text{otherwise.} \end{cases} \quad (\text{D13})$$

However, we can also incorporate this constraint by using proper integration boundaries, such as  $R_{\max} = cT$  instead of  $\infty$ .

A plot of that function for a fixed time  $T$  is presented in Figure 4.18a. Note that for  $T \rightarrow \infty$  the intensity probability tends toward zero everywhere, but more slowly for small intensities than for larger ones, because large intensities can only be found in a relatively small region in the vicinity of the source, whereas the major part of the illuminated volume only receives comparatively small intensities.

In order to be consistent with the discussion of diffusive waves in Section 4.12.3, we would have to normalize the intensity to the average intensity over the entire illuminated volume. Calculating this spatial average is equivalent to calculating the average intensity from the probability function:

$$\langle I \rangle = \frac{3}{4\pi R_{\max}^3} \int_0^{R_{\max}} 4\pi r^2 I(r) dr = \int_{I(R_{\max})}^{\infty} I \cdot P(I) dI = \frac{3}{R_{\max}^2}. \quad (\text{D14})$$

Hence, in order to obtain normalized amplitudes, one would have to substitute

$$I \rightarrow \frac{R_{\max}^2}{3} I \quad (\text{D15})$$

$$\Delta I \rightarrow \frac{3}{R_{\max}^2} \Delta I \quad (\text{D16})$$

in Eq. (D12). However, this only rescales the function and does not affect its overall shape.

### D.3 Classical Diffusion

Note that this section treats actual diffusion, as in the case of mass concentrations, and not the diffusion of wave amplitudes discussed in Section 4.12.3. It serves only as a comparison to illustrate some fundamental differences between those two diffusive phenomena.

The solution to the three-dimensional diffusion equation is given by Green's function

$$G(\mathbf{r}, \mathbf{r}', t) = \frac{1}{(4\pi Dt)^{\frac{3}{2}}} \cdot \exp\left(-\frac{|\mathbf{r} - \mathbf{r}'|^2}{4Dt}\right). \quad (\text{D17})$$

This means that if we assume an infinitely short excitation at  $t = 0$ ,  $\mathbf{r}' = \mathbf{0}$ , the distribution of the diffusing quantity will be

$$A(\mathbf{r}, t) = \frac{1}{(4\pi Dt)^{\frac{3}{2}}} \cdot \exp\left(-\frac{|\mathbf{r}|^2}{4Dt}\right) \quad \text{for } t \geq 0. \quad (\text{D18})$$

If we associate  $A$  with a wave amplitude, the resulting intensity will be given by  $I = A^2$ :

$$I(\mathbf{r}, t) = \frac{1}{(4\pi Dt)^3} \cdot \exp\left(-\frac{|\mathbf{r}|^2}{2Dt}\right) \quad \text{for } t \geq 0. \quad (\text{D19})$$

Inverting this relation to obtain  $r(I)$  yields

$$r(I) = \sqrt{-2Dt \cdot \ln((4\pi Dt)^3 I)} \quad (\text{D20})$$

and the scaling factor between  $\Delta R$  and  $\Delta I$  is

$$\frac{dI}{dr} = -\frac{r}{64\pi^3 D^4 t^4} \cdot \exp\left(-\frac{r^2}{2Dt}\right) = -\frac{I \cdot \sqrt{-2Dt \cdot \ln((4\pi Dt)^3 \cdot I)}}{Dt}. \quad (\text{D21})$$

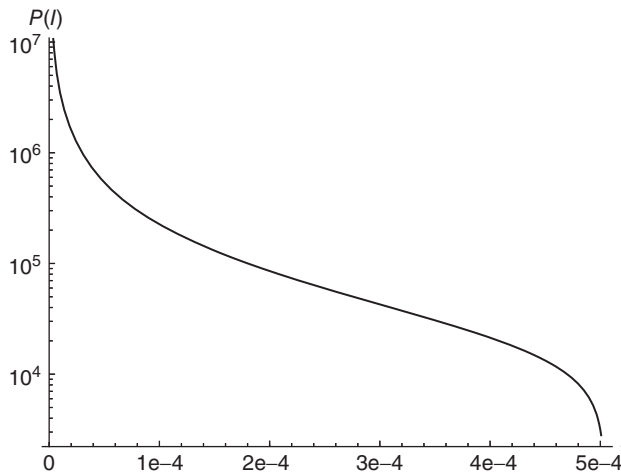
The square root is real-valued for  $0 \leq I \leq I_{\max}$  with

$$I_{\max} = \frac{1}{(4\pi Dt)^3}. \quad (\text{D22})$$

Combining these results according to Eq. (D5) results in

$$P(I)\Delta I = \begin{cases} \frac{4\sqrt{2\pi D^2 t^2 \cdot \sqrt{-\ln((4\pi Dt)^3 I)}}}{\sqrt{Dt \cdot I}} \Delta I & \text{if } 0 \leq I \leq I_{\max} \\ 0 & \text{otherwise} \end{cases} \quad (\text{D23})$$

which is shown in Figure D1. We can see that this is clearly different from the  $e^{-I}$  law presented in Section 4.12.3. The reason is that the diffusion model presented in this section is based on real-valued amplitudes, which were merely squared in order to obtain intensities. In a physically correct treatment, the relative phase between interfering waves at a given point would have to be considered, and doing so yields fundamentally different results. The derivation of the  $e^{-I}$  law is presented, for example, in [54].



**Figure D1** Intensity probability distribution for a hypothetical case of intensity diffusion.

1 Note that this is just a thought experiment and that such a wave would offend conservation of energy. Also, we are ignoring any proportionality constants between  $A$  and  $I$  by setting them to unity.



## D.4 Damped Plane Wave

In analogy to the previous section, we will now calculate the intensity distribution of a damped plane wave. In contrast to the previous examples, a plane wave does not have spherical symmetry, so that the above formulas have to be adapted for the one-dimensional case.

The intensity of the wave along the propagation direction is given by

$$I(x) = I_0 \cdot \exp\left(-2 \frac{x}{L}\right). \quad (\text{D24})$$

The damping length  $L$  is usually defined for the damping of the amplitude  $A$ , which explains the factor 2 in the exponential because of  $I \propto A^2$ . Inverting this relation yields

$$x(I) = -\frac{\lambda}{2} \ln\left(\frac{I}{I_0}\right). \quad (\text{D25})$$

The intensities between  $I$  and  $I + \Delta I$  are located in a strip between  $x(I + \Delta I)$  and  $x(I)$ , and its width  $\Delta x(I, \Delta I)$  is equal to the volume  $V(I, \Delta I)$ , which we need to calculate. Thus, we convert Eq. (D5) from the 3D spherical case to the 1D linear case and obtain

$$V(I, \Delta I) = \Delta x(I, \Delta I) = -\left(\frac{dI}{dx}\right)^{-1} \Delta I = \frac{L}{2I} \Delta I. \quad (\text{D26})$$

Again we assume that the wave source was switched on at  $t_0$ , so that the first wave front has traveled a distance  $X_{\max} = c(t - t_0)$ . This first wave front has experienced the most damping, and has hence the lowest intensity. The maximum intensity, on the other hand, can be found directly at the source. All other intensities must therefore lie between these extreme cases  $I_{\min} = I(X_{\max}) = I_0 \cdot \exp\left(-\frac{2X_{\max}}{L}\right)$  and  $I_{\max} = I(0) = I_0$ :

$$P(I)\Delta I = \begin{cases} \frac{L}{2X_{\max}I} \Delta I & \text{if } I_{\min} \leq I \leq I_{\max} \\ 0 & \text{otherwise.} \end{cases} \quad (\text{D27})$$

A plot of this function for a fixed propagation time is shown in Figure 4.18a.

As in the previous section, we will finish the discussion by transcribing the intensity probability to normalized intensities, as introduced in Section 4.12.3. First, we calculate the average intensity over the entire illuminated region:

$$\langle I \rangle = \frac{1}{X} \int_0^X I(x) dx = \int_{I_{\min}}^{I_{\max}} I \cdot P(I) dI = \frac{I_0 L}{2X} \left(1 - e^{-2\frac{X}{L}}\right). \quad (\text{D28})$$

We can therefore translate Eq. (D27) to normalized intensities by substituting

$$I \rightarrow \left(\frac{I_0 L}{2X} \left(1 - e^{-2\frac{X}{L}}\right)\right)^{-1} I \quad (\text{D29})$$

$$\Delta I \rightarrow \frac{I_0 L}{2X} \left(1 - e^{-2\frac{X}{L}}\right) \Delta I. \quad (\text{D30})$$

## Index

### a

Abbe limit 4  
 abdominal cavity 283  
 abdominal organs 284  
 acoustic radiation force impulse (ARFI)  
   imaging 214, 234–235, 237, 245  
 alcohol-related liver disease (AL) 286  
 algebraic Helmholtz inversion (AHI)  
   Helmholtz decomposition 207–208  
   isotropy 205  
   multifrequency MRE 206  
   multiparameter inversion 207  
 Algebraic inversion of the differential  
   equation (AIDE) 207  
 Alzheimer's disease (AD) 279  
 amoeboid invasion 334  
 aminotransferase-to-platelets ratio index  
   297, 306  
 amplitude mode 233  
 amyotrophic lateral sclerosis (ALS) 276  
 Anderssen gradients  
   discretization effects 186  
   frequency response plots 186–187  
   low noise levels 186  
   symmetric difference kernel 184  
 anti-symmetric gradients 46  
 anulus fibrosus (AF) 321  
 aorta, MRE of 260–261  
 apparent diffusion coefficient (ADC) 341  
 areas under receiver operator  
   characteristics (AUROC) 297  
 ARFI elastography 338  
 atrioventricular (AV) node 246  
 autocalibration scans (ACS) 36  
 auxetic materials 76

### b

balanced steady-state free precession  
   (bSSFP) 28–30, 55, 256  
   nonlinear phase response 56  
 balanced waveform 49  
 balance of momentum 92–95  
 band-pass filtering 172  
 bandwidth 27  
 benign prostatic hyperplasia (BPH) 344  
 biphasic material, composition of 133  
 biphasic poroelastic tissue model  
   continuity equation 142  
   hydrogen density 142  
 Bloch equations 14–15  
 boundary conditions 103–104  
 boxcar filters 170  
 brain MRE 263 *see also* Cerebral MRE  
   brain stiffness determinants 264  
   challenges, cerebral MRE 264  
   compressibility 276  
   mouse model 270  
   multifrequency 267  
   objectives 264  
   preliminary findings, functional  
     activation 277  
     technical aspects of 265–271  
 brain shear modulus 272  
 brain stiffness  
   changes with age 272  
   demyelination and inflammation  
     277–279  
   gender differences 273–274  
   neurodegeneration 279–280  
   regional variation in 274

- brain tissue, anisotropic properties 274–276
- brain volume 272
- Breast Imaging Reporting and Data System (BIRADS) 337
- breast lesions 337
- breast tumors 335
  - MRE of 345–347
  - stiffness response of 336
  - ultrasound elastography 337–338
- brightness mode 233
- bSSFP-MRE 55–57
- bulk modulus 77–79
- bundle of His/AV bundle 246
- C**
- Cardiac cycle 245
- cardiac elastography
  - ex vivo* shear wave imaging 253
  - in vivo* shear wave dispersion ultrasound vibrometry 253–254
  - in vivo* cardiac MRE in humans 256–260
- cardiac fiber anatomy 247–249
- cardiac FLASH sequence, diagram 161
- cardiac MRE
  - clinical motivation 250
  - in pigs 254–256
  - wave inversion 259–260
- cardiac steady-state FLASH MRE, timing 257
- Cartesian imaging techniques 23
- causal phenomena 125
- cell proliferation 335
- cerebral MRE 264 *see also* Brain MRE
  - clinical setup for 265
  - driver-free 269
- cerebrospinal fluid (CSF) flow 264
- cervical cancer 318
- Christoffel equation 105–106
- chronic liver diseases (CLD) 285
  - causes 286
  - epidemiology 286
- coherent plane wave compounding 234
- compliance tensor transverse isotropy 325
- compliance *vs.* elasticity 70
- compressibility 77–79
- compression modulus 100
- constant-coefficient difference equation (CCDE) 168
- corticospinal tract 274
- corona radiata 274
- corpus callosum 274
- cranial pressure 264
- crawling waves (CW) sonoelastography 238–239
- d**
- damped plane wave 365
- Darcy's law 131
- decay time constant 14
- deformation
  - gradient 66
  - magnitude 66
  - of three-dimensional object 64
- demyelination and inflammation, brain
  - stiffness 277–279
- denoising, in MRE
  - description 165
  - frequency domain filtering 168–172
  - ordinary least squares 167–168
  - polynomial fitting 167–168
  - process, schematic illustration 166
  - Savitsky–Golay filter 167
- dephaser–rephaser gradients 17
- diastolic dysfunction
  - and isovolumetric cardiac times 259
  - vs.* systolic dysfunction 250–251
  - and wave amplitude maps 259
- differential operator 179
- diffusion, classical 363
- diffusion-encoding process 52
- diffusion tensor imaging (DTI) 225, 265
- diffusion-weighted imaging (DWI) 52, 306
- diffusion-weighted MRE 52
- diffusive waves 126–129
- 3D inversion techniques 351
- direct inversion (DI) 199–201
  - for transverse isotropic medium 224–225
- directional filters
  - 2D directional filters 176, 179
- Dirichlet boundary condition 103
- discrete cosine transform (DCT) 197

- discrete Fourier transform (DFT) 23
- discrete time Fourier transform (DTFT) 170
- discretization artifacts 202–203
- dispersion 206
- 2D  $k$ -space, acquisition of 31
- Doppler imaging 234
- 2D phase unwrapping methods, in liver and brain 198
- Duchenne muscular dystrophy (DMD) 332
- dwelt time 27
- dynamic deformation
  - balance of momentum 92–95
  - boundary conditions 103–104
  - compression modulus and oscillating volumetric strain 100
  - elastodynamic Green's function 101–103
  - mechanical waves 96–98
  - Navier–Stokes equation 99–100
- e**
- echoes 21
  - gradient 17
  - spin 15–17
- echo-planar imaging (EPI) 30–32, 161, 300
- echo time 21
- ejection fraction (EF) 250
- elastic wave equation 199
- elastodynamic Green's function 101–103
- electrocardiography (ECG), signals in 246
- electromechanical wave imaging (EWI) 239
- encoding efficiency 46
  - of sinusoidal MEGs 48
  - of trapezoidal MEGs 48
- encoding sensitivity 50
- endocardium 247
- endometrium 318
- energy density and flux 110–114
  - geometric attenuation 113–114
- energy gap 9
- epicardium 247
- EPI-MRE 57–59
- Ernst angle 28
- Eulerian description 99
- experimental autoimmune
  - encephalomyelitis (EAE) 278
- external vibration multidirectional
  - ultrasound shear wave elastography (EVMUSE) 238
- extracellular matrix (ECM) 264, 287, 333
- f**
- fast Fourier transform (FFT) 23
- fast imaging
  - partial Fourier imaging 34–37
  - SNR and scan time impact 37–39
  - strategies 33
- fast low-angle shot (FLASH) 27, 37, 161, 256
- fast transverse (FT) 108
- fast wavelet transform (FWT) 176
- FE mesh 220
- fibrillar collagens 287
- fibronectin 287
- finite difference methods 187–190
- finite element method (FEM)
  - algorithm, steps involved in 217–218
  - description 217
  - vs. direct inversion 223
  - one-dimensional wave equation 218–219
  - wave equation, formulation of 221–223
  - discretization
    - node density 220
    - one-dimensional problem 220
    - in three dimension 220
  - discretized domain, basis function in 220–221
  - forward FEM equations 218
- finite impulse response (FIR) filter
  - averaging 168–170
  - characterization 168
  - convolution 168
  - kernel 168
- finite strain theory 65
- FLASH-MRE sequence 53–55
  - for cardiac MRE 161–162
- flip angle 11
- Flynn's minimum discontinuity algorithm 193–194

forces, in continuous media 92  
 forward FEM equations 218  
 Fourier domain gradient operator 186  
 fourth-order Butterworth low-pass filter 172  
 fractional calculus 124  
 fractional encoding 50–51, 229  
 free induction decay (FID) 15, 31  
 frequency domain ( $k$ -space) filtering 168  
   *see also* Finite impulse response (FIR) filter  
   band-pass filtering 172  
   LTI system (*see* Linear time-invariant (LTI) system)  
 frequency encoding, MRI 20–21  
 fringe lines 194  
 functional MRE (fMRE) 277  
 functional ultrasound 234

**g**

Galerkin method 218  
 Gaussian complex noise 201  
 Gaussian filter 172  
 Gaussian-type filter kernels 170  
 GE –EPI sequence  
   structure of 59  
   timing diagram of 59  
 geometric attenuation 113–114  
 Gibbs ringing 178, 182  
 glioblastoma 341  
 global stiffness equations 218  
 glycosaminoglycans (GAGs) 287  
 gradient echoes 17, 53  
 gradient moment nulling, orders of 50  
 gradient spoiling 28  
 gradient unwrapping 195–196, 204  
 gradient waveform 45, 49  
 GRAPPA 36–37  
 Green's function 125–126  
 group velocity 106

**h**

head of caudate nucleus (HCN) 274  
 heart physiology 247  
 Helmholtz decomposition 96, 207–208

Helmholtz equation 205  
 hemochromatosis 286  
 hepatic fibrosis staging 299  
 hepatic steatosis 286  
 hepatic stellate cell (HSC) 289  
 hepatic venous pressure gradient 308  
 hepatocellular carcinoma (HCC) 288  
 higher-order gradient moment nulling 45  
 high-intensity focused ultrasound (HIFU) 242  
 Hooke's law 69–70  
 Huygens' principle 102, 234

**i**

imaging concepts  
   fast imaging 33–39  
    $k$ -space 23–26  
    $k$ -space sampling strategies 26–33  
 impulse response 168  
 incident wave, reflection and transmission 115  
 infinite impulse response 168  
 infinitesimal strain tensor 64  
 in-plane magnetization 56  
   2D Fourier transform 20  
 intervertebral disc (IVD) 283, 321  
   annulus fibrosus 321  
   MRE 322–323  
   nucleus pulposus 321  
 intraclass correlation coefficient (ICC) 298  
 intracranial tumors, MRE of 347–350  
 intra-voxel phase dispersion 51–52  
 invariants 68–69  
 inversion methods  
   direct inversion 200–201  
   iterative reconstruction 200  
 isochromat, magnetization of 16  
 isovolumetric contraction time (IVC) 246  
 isovolumetric relaxation time (IVR) 246  
 iterative reconstruction 200  
 Itoh's method 192

**j**  
 jacketed scenario 132  
 jamming effects 333

**k**

Kelvin–Voigt model 83  
 kernel 168  
 kidney, MRE of 315–318  
   functional units 315  
   viscoelasticity 316  
 kMDEV  
   in abdomen 216  
   directional filters 215  
   geometric attenuation 215  
   noise robustness 216  
   principle 214  
   simulated sensitivity 217  
   wave vector 214–215  
*k*-space  
   artefacts 26  
   data points 23  
   description 23  
   DFT 23  
   echo-planar imaging 30–32  
   non-Cartesian imaging 32–33  
   Nyquist–Shannon sampling theorem 23–24  
   readout 26  
   readout and phase-encode directions 23  
   sampling strategies 26–33  
   segmented image acquisition 27–30  
*k*-space representation, of iso surfaces 109  
 Kupffer cell (KC) 289

**l**

Lagrangian description 99  
 Lamb wave dispersion ultrasound vibrometry (LDUV) 242  
 Lamé–Navier equation 95  
 Lamé’s first parameter 77  
 Laplace transforms, in viscoelastic models 84–85  
 Laplacian unwrapping 196–198  
 Larmor frequency 11, 12, 56  
 left ventricular (LV) pressure 245, 251  
 LFE *see* Local frequency estimation (LFE)  
 linear shift invariant 168  
 linear slip 115  
 linear strain theory 65  
 linear time-invariant (LTI) system

Fourier domain 170–172  
 frequency response plots 171  
   five-tap moving average filter 171  
   fourth-order Butterworth low-pass filter 172  
   Gaussian filter 172  
   in-spectrum loss/attenuation 171  
 mapping 168  
 liver  
   blood supply 283  
   chronic liver disease, epidemiology of 286  
   elasticity 313  
   functions 284  
   grafts, MRE in 309–310  
   injury 290–291  
   lobules 283  
   morphology 285  
   MRE 294–311  
   MRE portal hypertension 307–309  
   parenchyma 289  
   transplantation 293  
   tumors, MRE in 342–344  
 liver fibrosis 287  
   biomarkers of 293  
   biophysical signs of 293–294  
   microstructural changes 295  
   noninvasive screening methods 292–293  
   pathogenesis of 289–291  
   progression of 288  
   reversibility of 293  
   scoring systems 292  
   staging of 291–292  
 local frequency estimation (LFE) 208–210  
   description 208  
   direct inversion *vs.* phase gradient 210  
   filter effects 208  
   filter functions 209  
   Fourier convolution theorem 208  
   noise-amplifying characteristics 209  
   spatial resolution 210  
 log-normal quadrature filters 209  
 longer motion-encoding periods 50  
 longitudinal equilibrium magnetization 12

- loss tangent 90
- lung, poroelastic tissue in 131
- m**
- magnetic field
  - inhomogeneities and susceptibility effects 41
  - protons in 9–10
- magnetic resonance imaging (MRI) 17–21
  - frequency encoding 20–21
  - phase encoding 19–20
  - slice selection 19
  - spatial encoding 18–21
- magnetization
  - of isochromat 16
  - precession of 10–13
  - quadrature detection 11–13
  - thermal equilibrium state 13
  - time evolution of 12
- matrix metalloproteinase (MMP) 293
- matrix representation, of derivative operators 182–183
- Maxwell model 83, 89
- Maxwell's equations 15
- mechanical waves
  - complex moduli and wave speed 98–99
  - Navier equation 96
- mesenchymal invasion 334
- meta-analysis of histological data in viral hepatitis (METAVIR) 291
- midpoint rule 180
- mitral valve 246
- mixed boundary conditions 104
- motion encoding gradient (MEG) 28, 43
  - fractional encoding 50–51
  - gradient moment nulling 44–46
  - time-harmonic motion encoding 46–50
- motion-induced phase 47
- motion mode 233
- multifrequency dual elasto-visco inversion (MDEV) 211
- multifrequency inversion 210–214
- multifrequency MRE (MMRE) 210, 229
- multiparameter inversion 207
- multiple sclerosis (MS) 263, 278
- multi-resolution analysis (MRA)
  - vs. FFT 174–175
  - wavelets 172–174
- muscular dystrophy 332
- myocardial contractility 250
- myocardial fibers 248
- myocardial stiffness measurement 254
- myocardium 247
- myofibroblast (MF) 290
- myometrium 318
- n**
- Navier equation 95
- Navier–Cauchy equation 95
- Navier–Stokes equation 99–100
- Navier's equation, for biphasic medium
  - elasticity tensor 134
  - Helmholtz theorem 136
  - momentum equations 134
  - one-dimensional system 136
- neurodegeneration, brain stiffness 279–280
- neurodegenerative diseases 263
- noise 52
  - in acquired displacement field 201
  - numerical derivative schemes, sensitivity of 186
  - sensor noise 165
  - signal processing definition of 165
- nonalcoholic fatty liver disease (NAFLD) 286
- nonalcoholic steatohepatitis (NASH) 286
  - MRE 303–304
- non-Cartesian imaging 32–33
- noninvasive biomarkers, of liver fibrosis 307
- nonwelded interface 115
- normal pressure hydrocephalus (NPH) 279–280
- nuclear magnetic resonance (NMR)
  - Bloch equations 14–15
  - echoes 15–17
  - magnetic field, protons in 9–10
  - magnetic resonance imaging 17–21
  - magnetization precession 10–13
  - relaxation process 13–14

- nucleus pulposus 321–322
- numerical derivatives
  - Anderssen gradients 183–186
  - boundary conditions 180–181
  - differential operator 179
  - Fourier transform 181
  - frequency response, of derivative operators 186–187
  - matrix representation, of derivative operators 182–183
  - midpoint rule 180
  - Nyquist criterion 182
- Nyquist–Shannon sampling theorem 23–26, 170
  
- o**
- octahedral shear strain (OSS) 68, 69
- OLS *see* Ordinary least squares (OLS)
- one-dimensional unwrapping algorithm 192
- optimal motion sensitivity 57
- ordinary least squares (OLS) 167
- orthotropic elasticity tensor, elements of 227, 228
- oscillating volumetric strain 100
  
- p**
- pancreas
  - diseases of 314
  - MRE 315
- parallel imaging
  - description 35
  - GRAPPA 36–37
  - image space-based methods 36
  - k*-space-based methods 36
  - reconstruction 36
- Parkinson's disease (PD) 279
- partial Fourier imaging 34–35
- pelvic region 283
- Pfirrmann scores 322
- phase difference image 43
- phase encoding 19–20, 26–27
- phase gradient (PG) 204–205
  - spatial unwrapping 204
- phase unwrapping 41
  - algorithms 191
  - gradient unwrapping 195–196
  - Itoh's method 192
  - Laplacian unwrapping 196–198
  - one-dimensional function 191–192
  - quality map 193
  - smoothness 193
- phase wraps 191
- plane of isotropy 74
- plane wave imaging 234
- point source, in 3D 362–363
- Poisson's ratio 75–76
- poroelasticity theory 131
- poroelastic media
  - pressure waves in 136–140
  - shear waves in 140–141
- poroelastic MRE 133
- poroelastic signal equation 142–144
- porosity 133
- portal hypertension
  - assessment 307–309
  - splenic stiffness 313
- position-dependent precession frequencies 14
- precession frequency, spatial modulation of 17
- pressure waves, in poroelastic media 136–140
- principal strains 68
- progressive supranuclear palsy (PSP) 279
- prostate
  - MRE 320–321
  - zones of 319–320
- prostate cancer
  - MRE 344–345
  - ultrasound elastography 338–339
- prostate-specific antigen (PSA) 338
- prostate, zones of 319–320
- proteoglycans 287
- protons
  - in magnetic field 9–10
  - magnetic moments of 10
  - quantum-mechanical nature of 10
- pulse repetition frequency (PRF) 233
- pulse sequences 53
- pulse wave velocity (PWV) 261



**q**

quadrature detection 11–13  
 quality-guided algorithms 193  
 quality map 193

**r**

radiofrequency (RF) pulses 26  
 relaxation process 13–14  
 renal pyramids 315  
 repetition time 31  
 right ventricle (RV) contraction 246  
 RO gradient waveforms 32

**s**

sample interval modulation-MRE  
 (SLIM-MRE) 230  
 sampling time 38  
 Savitsky–Golay filter 167  
 scatterers 234  
 second-order gradient moment nulling 45  
 segmented image acquisition  
 balanced steady-state free precession  
 28–30  
 description 27  
 FLASH 27–28  
 sensor noise 165  
 serum biomarkers, liver 304–307  
 sexual dimorphism, brain architecture 273  
 shape function 218–221  
 shear horizontal (SH) wave 115  
 shear modulus  
 and Lamé’s first parameter 76–77  
 shear strain, octahedral 68–69  
 shear vertical (SV) wave 115  
 shear wave amplitude maps 260  
 shear wave dispersion ultrasound  
 vibrometry (SDUV) 241–242  
 shear wave elasticity imaging (SWEI) 240  
 shearwave elastography (SWE) 306  
 shear wave imaging (SWI) 252  
 shear wave scattering  
 description 114  
 interface 115  
 mean free path length 114  
 mode conversion 115  
 plane interfaces 115–118  
 shear horizontal and vertical wave 115

spatial and temporal interfaces 118–121  
 speckle patterns 114  
 three-layer model 117–118  
 wave diffusion 121  
 amplitudes and intensities 126–129  
 diffusion coefficient 123  
 discrete waves 121  
 Green’s function 125–126  
 grid spacing 124  
 propagation velocity 123  
 random walk 121–122  
 scaling property 124  
 stochastic nature 123  
 unattenuated plane wave 121  
 unattenuated propagating wave 121  
 welded and nonwelded interface 115  
 shear waves, in poroelastic media  
 140–141  
 shear waves, in transverse isotropic medium  
 nomenclature 108  
 wave modes 109  
 signal dephasing 14  
 signal sampling 31  
 signal-to-noise ratio (SNR) 25, 52  
 single-channel RF transmit system 29  
 skeletal muscle  
 composition 325  
 tissue architecture in 326  
 skeletal muscle MRE 326–330  
 slice-based Laplacian unwrapping, Matlab  
 code for 197  
 slice-select gradient 19, 30  
 slice selection, MRI 19  
 SLIM (Sample Interval Modulation) 230  
 slow transverse (ST) mode 108  
 Snell’s law 117  
 Sommerfeld (nonreflecting) boundary  
 condition 103  
 sonoelastography 337  
 spatial encoding, MRI 18–21  
 speckles 128  
 spin echo (SE) 14, 57, 59  
 EPI–MRE sequence 43  
 MRI 15–17  
 signal formation 30  
 spin–echo sequence, MEG placement 59  
 spin quantum number 9

- spleen
    - elasticity 313
    - location 311
    - splenic stiffness 311, 313
  - spoiler gradients 28
  - springpot and fractional viscoelasticity 89–90
  - square of viscoelasticity 2, 3
  - standard linear solid (SLS) model 89
  - standing waves 210
  - static magnetic field 9
  - steatohepatitis 286, 303
  - steatosis 286, 303
  - strain 63–66
    - finite strain theory 65
    - linear strain theory 65
    - principal strains 68
    - shear strain 65–66, 68
    - tensor 65
  - strain-based elastography 338
  - strain-energy function 70–71
  - supersonic shear imaging (SSI) 241
  - surface coils 35
  - symmetric difference 180
  - symmetries 71–75
  - systolic vs. diastolic dysfunction 250–252
- t**
- temporal resolution 163
  - thalamus 274
  - three-dimensional  $k$ -space 32
  - time-dependent magnetic fields 10
  - time-harmonic elastography (THE) 237–238, 257
  - time-harmonic motion encoding 46–50
  - time-translation invariance 45
  - time-varying magnetic fields 15
  - timing diagram, of FLASH pulse sequence 28
  - tortuosity 135, 136
  - transient ultrasound elastography (TE) 306
  - transjugular intrahepatic portosystemic shunt (TIPS) 308–309
  - transmission and reflection coefficients, for welded and slip interface 117–118
  - transverse isotropy 73
  - transversely isotropic elasticity tensor 325
  - transversely isotropic (TI) material
    - compliance and elasticity tensor 79–80
    - models 275
  - transverse magnetization 11, 13, 16, 19, 29, 55, 57
    - creation of 26
    - decay of 14
    - first-order differential equation 13
    - $k$ -space 23
    - magnitude of 17
    - RF pulses 28
  - tricuspid valve 246
  - trigger pulse 55, 147, 231
  - tumors
    - growth 333
    - micromechanical properties 333–336
    - MRE 339–350
    - ultrasound elastography 336–339
  - two-dimensional phase unwrapping
    - algorithms 193
- u**
- ultrasound-based cardiac strain
    - measurement methods 257
  - ultrasound elastography (USE) 233, 245, 271
    - breast tumors 337–338
    - prostate cancer 338–339
  - uniaxial loading 75
  - unjacketed condition 132
  - unwrapped phase 191
  - uterus, MRE of 318–319
- v**
- variational method 218
  - vertical edge 194
  - vibration energy 230
  - vibration frequency 231
    - choice of 266–268
  - vibration period 55
  - vibration phase gradient (PG)
    - sonoelastography 238
  - vibro-acoustography (VA) 237
  - viscoelasticity 80

- viscoelastic models
    - dashpot (viscous model) 82
    - description 80
    - Laplace transform 84–85
    - spring (elastic model) 81
    - springpot and fractional viscoelasticity 89–90
    - stress–strain relations 83–84, 86
  - viscoelastic parameter reconstruction
    - algebraic Helmholtz inversion 205–208
    - algorithms 353
    - discretization and noise 201–204
    - finite element method 217–223
    - inversion methods 199–200
    - $k$ -MDEV 214–217
    - local frequency estimation 208–210
    - multifrequency inversion 210–214
    - phase gradient 204–205
    - transverse isotropic medium, direct inversion for 224–225
    - waveguide elastography 225–228
  - viscoelastic theory
    - assumptions 63
    - engineering constants
      - compliance and elasticity tensor 79–80
      - compressibility and bulk modulus 77–79
      - Lamé’s first parameter 77
      - shear modulus 76–77
      - Young’s modulus and Poisson’s ratio 75–76
    - Hooke’s law 69–70
    - invariants 68–69
    - strain 63–66
    - strain-energy function 70–71
    - stress 67–68
    - symmetries 71–75
  - viscosity-related parameters, spleen 313
  - Voigt model 83, 89
  - volume resonator/body coil 35
  - volumetric deformation modes 132
  - von Neumann boundary condition 103
- W**
- wall shear modulus *versus* cavity pressure 249–250
  - WAV-based MRE 258
  - wave(s)
    - in anisotropic media
      - Christoffel equation 105–106
      - transversely isotropic medium 104–109
    - image 43
    - intensity 112
    - oscillation cycle, phases of 41
    - wave phenomena, intensity and radial profiles 128
  - wave amplitude variation (WAV) 255
  - waveguide elastography 228
    - local coordinate system 226
    - principle 225
    - spatial–spectral filtering
      - description 225
      - Fourier transform 226
    - plane wave component 226–227
    - tangent vector 225
  - wave inversion cardiac MRE 259–260
  - wavelets 173
  - welded interfaces 115
  - wrapped phase 191
- Y**
- Young’s modulus 75–76
- Z**
- Zener model 89